Author:
De Leeuw, Lawrence W

Title:
Interface shear response of polypropylene pipe coatings and influencing pipe buckling using enhanced textures

Interface shear response of polypropylene pipe coatings and influencing pipe buckling using enhanced textures

Lawrence Willem de Leeuw

A dissertation submitted to the University of Bristol in accordance with the requirements for award of the degree of Doctor of Philosophy in the Faculty of Civil, Aerospace, and Mechanical Engineering, Department of Civil Engineering, September 2020.

Abstract

Pipelines are an integral part of offshore infrastructure supporting the oil and gas industry and the consequences of their failure have severe economic and environmental ramifications. Changes in pipe internal pressures and temperatures from the as-laid condition to their operational state cause large thermal expansions. When axial strain from thermal expansion is resisted by the pipe-soil friction, the effective axial force in an unburied pipeline is relieved by lateral friction-sliding-buckling. The phenomenon of pipeline buckling is a significant challenge in managing the global stability of high pressure-high temperature offshore on-bottom pipelines. Pipelines are commonly given a protecting coating to aid in protection from damage and to provide thermal insulation. The use of polypropylene in this application is prevalent but relatively recent so correct quantification of the interface shear strength between marine sand soils and polypropylene is key to robust global stability design.

Herein, an extensive campaign of soil and interface shearbox testing has been undertaken to determine and evaluate the shear response of polypropylene surfaces. Parameters such as soil grading, density, surface texture, stress level, and cyclic behaviour have been investigated. The results show that the efficiency of the interface is strongly dependant on the soil grading and the surface texture at the interface. The shear response of soils at the interface with smooth surfaces is bilinear, characterised by an initially linearly elastic response at very small horizontal displacements, that transitions rapidly to a near constant shear stress plateau. Surfaces with greater roughness provoke a dilatant soil shear response more typical of a soil-only behaviour. Greater magnitude of surface texture engenders greater dilation leading to greater peak shear strengths. A relationship has been developed which can aid designers in predicting interface friction for polypropylene surfaces and sandy soils given surface texture, soil grain size, and stress level input parameters.

The application of the experimental results to real-world problems was investigated through numerical modelling in Abaqus of an approximately 5 km long pipe on a rigid seafloor using friction penalty and non-linear springs to model pipe-soil interaction and force-displacement response. The impact on global stability and buckling parameters of changes in pipe-soil friction and of applying a differential friction regime along the pipe was investigated. Numerical analysis results showed that such techniques are able to significantly change the distribution and magnitude of buckles.

Acknowledgements

This research was not funded by any research council grant or institution scholarship. However, I must acknowledge the funding and support from the European Union EXCHANGE-RISK project that enabled a six-month research secondment to University of Toronto, Canada, in 2019.

I express my sincere appreciation and thanks to my supervisor, Dr. Andrea Diambra, for his experience, guidance, and support throughout this work and in the preparation of this, and other, manuscripts. Further, I would like to thank Dr. Matt Dietz for his involvement and insight on a range of topics within this work, and Prof. George Mylonakis for his oversight and support.

Of particular importance to this work was the invaluable laboratory experience and good humour of Mr. Gary Martin who presided over the geomechanics laboratory and without whom much of the experimental work would have been challenging or impossible to accomplish.

Considerable experimental parts of this research were inspired and commissioned by an industrial partner, TechnipFMC, and I appreciate in particular the input of Mr. Henry Milewski.

I also thank Prof. Anastasios Sextos for giving me the opportunity to go to University of Toronto for six months on research secondment and to Prof. Oh-Sung Kwon for being my host there.

Numerous other technical, research, and administrative staff at University of Bristol are deserving of my thanks but they are too many to name here.

Outputs

The work detailed in this thesis has generated a number of research outputs. In addition to the publications detailed below, various parts of this work have been presented in talks at the *17th European Conference on Soil Mechanics and Geotechnical Engineering*, Reykjavik, and the *7th International Symposium on Deformation Characteristics of Geomaterials, Glasgow*, both in 2019. In 2021 the numerical modelling aspects are due to be presented at the *4th International Symposium on Frontiers in Offshore Geotechnics* in Austin, Texas.

De Leeuw, L.W., Dietz, M.S., Milewski, H., Mylonakis, G., Diambra, A. The relationship between polypropylene texture and interface friction for sand at low stress levels. *Canadian Geotechnical Journal*. Under review.

De Leeuw, L.W., Diambra, A., Dietz, M.S., Milewski, H., Mylonakis, G., Kwon, O-S., Sextos, A. 2020. Using coating roughness to control pipe-soil friction and influence pipeline global buckling behaviour. In: *Proceedings of the 4th International Symposium in Frontiers in Offshore Geotechnics*, Austin, Texas.

Milewski, H., Diambra, A., De Leeuw, L.W., Dietz, M.S. 2020. Axial resistance of rough polymer pipelines on sand. In: *Proceedings of the 4th International Symposium in Frontiers in Offshore Geotechnics*, Austin, Texas.

De Leeuw, L.W., Martin, G., Milewski, H., Dietz, M.S., Diambra, A. 2020. Polypropylene interface strength on marine sandy soils with varying coarse fraction. *Geotechnical Engineering*. DOI: 10.1680/jgeen.19.00137

De Leeuw, L.W., Diambra, A., Dietz, M.S., Mylonakis, G., Milewski, H. 2019. Cyclic polypropylene pipeline coating interface strength with granular materials at low stress. In: *Proceedings of the 17th European Conference on Soil Mechanics and Geotechnical Engineering*, Reykjavik, Iceland.

De Leeuw, L.W., Diambra, A., Dietz, M.S., Mylonakis, G., Milewski, H. 2019. Interface shear strength of polypropylene pipeline coatings and granular materials at low stress level. In: *E3S Web of Conference*, 92, pp.13010. EDP Sciences, 2019.

Milewski, H., Dietz, M., Diambra, A., De Leeuw, L.W. 2019. Axial resistance of smooth polymer pipelines on sand. In: *Proceedings of the 38th International Conference on Ocean, Offshore and Arctic Engineering*, Glasgow, UK.

Declaration

I declare that the work in this dissertation was carried out in accordance with the requirements of the University's Regulations and Code of Practice for Research Degree Programmes and that it has not been submitted for any other academic award. Except where indicated by specific reference in the text, the work is my own work. Work done in collaboration with, or with the assistance of, others, is indicated as such. Any views expressed in the dissertation are those of the author.

SIGNED: ……. DATE: ……

Contents

Notation

The notation used throughout this thesis are listed here for easy reference. Some descriptions are general in nature and specific technical definitions are included in the text when the term appears. The list is not exhaustive and additional notation is identified in the text where necessary. Unless otherwise stated, all units are in the SI system of measurement.

A_{buck}	amplitude of pipe buckle
A_e	pipe external cross-sectional area
A_i	pipe internal cross-sectional area
A_p	cross-sectional area of pipe wall
A_s	cross sectional area of shearbox
e	void ratio
c	soil cohesion
C_c	coefficient of curvature
C_u	coefficient of soil uniformity
e_{max}	maximum void ratio
e_{min}	minimum void ratio
d	horizontal shear displacement
D	pipe diameter
D_r	relative density (of soils)
D_{50}	grain size at which 50% of the soil by mass is finer
E	Young's modulus
f_y	yield stress
F_a	average surface form
F_A	drained axial resistance
F_C	Coulomb frictional resistance
F_h	total soil horizontal resistance force
F_r	passive resistance
G_s	specific gravity
H	residual stress (residual lay tension)
I	second moment of area
k_n	Hobbs (1984) buckle constant
l	Internal width of shearbox
L	profilometry profile measuring length
L_a	arc length in embedded soil
L_c	profilometry (high-pass) cut-off filter
L_T	pipeline total length
L_w	wavelength
L_z	length of buckle
M_{buck}	maximum moment induced in a buckle
M_i	mechanical indentability
M_s	mass of solids (in soil)
N	normally orientated load
N_c	bearing capacity factor

N_q	bearing capacity factor
N_γ	bearing capacity factor
OD	pipe outside diameter
P	normal stress
P_{buck}	residual force in a buckle
P_e	pipe external pressure
P_i	pipe internal pressure
P_{op}	maximum operating pressure
P_z	pipe critical buckling force
P_0	pipe steel wall force
Q	shear stress
Q_f	ultimate bearing capacity
R	pipe radius
R_a	average surface roughness
R_{max}	maximum surface roughness
R_n	normalised surface roughness
$R_{relative}$	relative surface roughness
S_{eff}	pipe effective axial stress
S_t	soil sensitivity
S_u	undrained shear strength of soil
S_y	yield force
T	force measured by load cell
T_a	average surface texture
T_{amb}	ambient temperature
T_{max}	maximum surface texture
T_{op}	maximum operating temperature
$T_{relative}$	relative surface texture
v	Poisson's ratio
V_s	volume of solids (in soil)
V_t	total volume of soil
V_v	volume of voids (in soil)
W_a	average surface waviness
W_s	pipe submerged weight
W_t	pipe wall thickness
y_z	buckle amplitude
z	pipe nominal embedment
z_i	pipe initial embedment

Greek letters

α	adhesion factor
α_t	coefficient of linear thermal expansion
γ_{max}	maximum soil density
γ_{min}	minimum soil density
γ_s	soil saturated unit weight
δ	angle of interface friction
δ_{peak}	peak angle of interface friction

δ_{ult}	ultimate angle of interface friction
δ_{res}	residual angle of interface friction
δ_{ss}	sand-steel interface angle of friction
ε_T	thermal strain
ζ_{peak}	peak angle of interface dilation
ϕ	angle of internal soil friction
ϕ_{cs}	critical state angle of soil friction
ϕ_{peak}	peak angle of soil friction
ϕ_{ult}	ultimate angle of soil friction
K	peak strength dilatancy coefficient
M	friction coefficient
μ_a	axial pipe-soil friction coefficient
μ_l	lateral pipe-soil friction coefficient
σ_n	average normal stress
P	density
ρ_{max}	maximum density
ρ_{min}	minimum density
T	horizontal shear stress
ψ	angle of soil dilation
ω	lateral position along pipe relative to straight
ω_0	maximum lateral amplitude along pipeline (at $L_w/2$)

Special characters

‘	effective stress signifier
∇	pipe embedment wedging factor
Δ	denotes “change in”
ϵ	work done (energy) during pipe displacement

List of Tables

List of Figures

1 Introduction

1.1 Overview

Past ages of human history are typically referred to by their technological or cultural paradigm, the Stone Age, Bronze Age, Iron Age, the Industrial Age even. It has been said that we currently are living in an information age of electronic technology and computers. However, it could perhaps more accurately be said that we live in an Oil Age (Maugeri, 2006) – much of our technology, lifestyle, and recent civilisation is wholly dependent on exploitation and refinement of petroleum products. Oil has advanced or shaped societal development throughout the 20th Century and looks set to continue to do so.

Hydrocarbon products such as tar and bitumen appear to have been in use for at least 70,000 years (Boëda *et al*., 2008) by *Homo Neanderthalensis* and by *Homo Sapiens;* bitumen products were used for waterproofing and as adhesives by the Indus Valley Civilisations at least 6000 years ago (McIntosh, 2008). Herodotus noted the use of bitumen and tar products in the construction of the walls of ancient Babylon 4000 years ago, and oil is known to have been used as a fuel as early as the fourth century BCE in ancient China. It was not until the invention of the internal combustion engine in the late 19th Century though, and the commercial production of internal combustion engine motor vehicles by Karl Benz in 1886, that oil and petroleum products started to become the major economic and political drivers that they are today. The genesis of recognisably modern onshore oil drilling is generally considered to be near Baku in modern-day Azerbaijan. The first modern offshore drilling also began in Azerbaijan in the mid-20th Century but the practise soon spread following oil discoveries around the world. In Europe, the biggest offshore reservoirs are under the North Sea and exploration in the UK-sector began in earnest in 1964 seeing a proliferation in oil and gas wells throughout the 1960s and 1970s.

Offshore engineering of structures and infrastructure related to hydrocarbons exploration raises a host of problems not normally considered onshore; very low effective stresses, the effect of buoyancy, more pronounced cyclic wind and tidal effects, height of structures above the foundation level, loose and weak surface soils, varying hydrodynamic and soil transport regimes, and more besides. In addition to the platforms, a network of flowlines and pipelines transport hydrocarbons and water from wellheads to platforms, and back to shore which presents additional design problems for stiff structures traversing long distances with variable substrate properties.

1.2 Pipelines

Pipelines (transporting hydrocarbon from the oil field back to shore) and flowlines (transporting hydrocarbons and water intrafield between wellheads and platforms) are at the same time both geotechnically resilient and delicate structures. Pipelines traverse large expanses of seafloor with varying soil properties and behaviours, and in the case of deep-water exploration traverse the continental slope which exposes them to submarine landslide hazards and potentially tectonism. Conversely, limit states on pipelines are governed mostly by the structural performance of the pipe and junctions with ancillary infrastructure. Large strains and displacements are not typically limit states for the pipeline itself which gives significant design flexibility. In recent decades exploration has moved into deeper waters to exploit geologically deeper oil reservoirs which have increasingly higher reservoir temperatures and pressures. So called High Pressure High Temperature (HPHT) reservoirs require pipelines which are assumed to accommodate similar conditions and operating loads. Pipelines are generally considered HPHT when internal pressures and temperatures exceed 68,500 kPa (10,000 psi) and 149°C (300°F) respectively (Shadravan and Amani, 2012). The large difference between the as-laid conditions at ambient seafloor temperatures and pressures, and the operational HPHT conditions causes expansion of the pipeline which is usually relieved by upheaval (vertical) or lateral buckling, depending on the pipe installation mode, and can cause global axial movement of the pipeline called pipeline walking.

An important component of pipeline construction is the application of a coating to the outside of the pipe. Coatings have numerous benefits including protection from corrosion, and from damage during installation or from anchor strikes and fishing gear. Coatings also provide thermal insulation to maintain the hydrocarbon viscosity and prevent phase separation inside the pipeline. In the case of concrete coatings, it can also provide a ballast function to weigh down otherwise buoyant pipes. A variety of coating technologies have been used; concrete, bitumen, FBE (fusion bonded epoxy), polyethylene, and polypropylene amongst the most prevalent. It is immediately obvious that concrete, bitumen, and polypropylene all have very different mechanical and surface properties and given that these materials form the outer surface of the pipeline, it is no surprise that they wield a significant influence on the nature of pipe-soil interaction.

1.3 Motivation

Considerable energy has been directed at the investigation of pipe-soil interaction on cohesive seafloors (e.g. White *et al.*, 2011; Randolph *et al*., 2012; Westgate *et al*., 2018), but there is a paucity of information relating to the interaction of sandy seafloors and polypropylene pipelines coatings despite its wide-spread and dominant use as a coating technology. Figure 1.1a

shows the distribution of sediments across the North Sea basin and Figure 1.1b is a map of oil and gas pipeline routes across the North Sea. It can be imagined that the nature of pipe-soil interaction may vary significantly across the length of a pipeline and that there may be advantage to developing additional tools to predict and control pipeline behaviour.

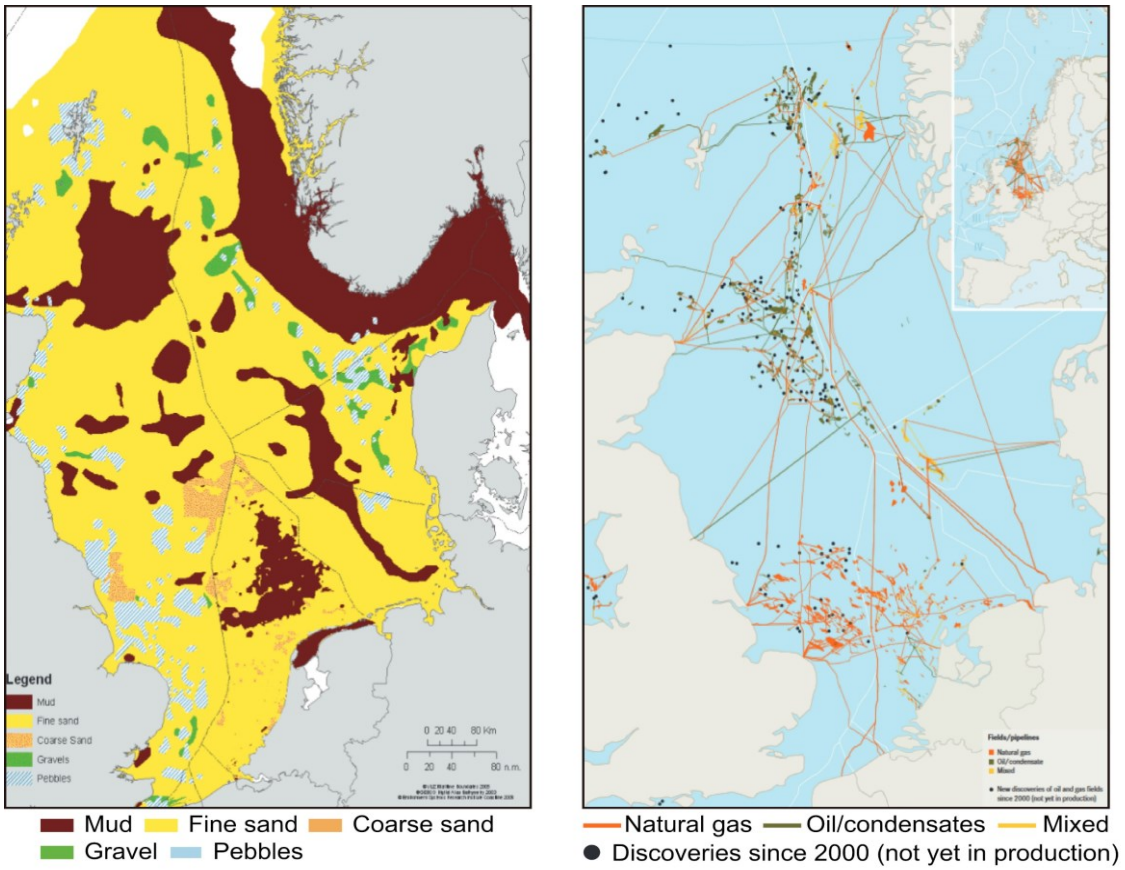

(a) Distribution of North Sea sediments **(b) Map of North Sea pipelines and fields**

Figure 1.1 (a) Distribution of seafloor sediments across the North Sea basin from MEFEPO (Paramor *et al.,* 2009) and (b) distribution of pipelines and oil and gas fields in the North Sea from OSPAR (2010).

Quantification of frictional behaviour and understanding its nature within the context of pipe-soil interaction and interface friction is a key component to predicting both global and local pipeline behaviour in response to axial loading from expansion effects. Numerous techniques are currently employed to improve pipeline stability which often require extra time ship time or voyages which are a significant financial burden on the installation cost of the project. The key motivations for this research project are to seek to address both these concerns with better quantification of polypropylene pipe-soil interaction on sandy seafloors and to explore the possibility of engineering surface textures to enhance performance.

It is necessary to note that the application to the hydrocarbon industry is obvious, but that the fundamental problem under investigation has uses in other circumstances as well. In

the offshore sector, the increasingly important renewables sector also has significant supporting infrastructure such as cables where appropriate soil-surface interface strength is a key parameter. Furthermore, in seismic settings where ground motions impose displacement and loads on a buried pipe, the interface friction determines the amount of force that is imposed on the pipe (Psyrras *et al.*, 2019; Psyrras *et al*., 2020).

1.4 Scope

The field of pipeline geotechnics and interfaces is broad with multiple avenues for investigation. A small number of aspects are explored in this thesis within the following scope:

- Evaluate the nature of interface shear response for polypropylene coating materials with variously smooth, rough, and intermediate surface textures.
- Investigate the effect on interface shear strength of test parameters such as soil density, grading, grain size, and confining stress level.
- Assess the most appropriate methodology for quantification of surface texture applicable to surfaces with random texture with reference to relevant industry standards and the literature.
- Identify any trends in the data across the parameters tested such that the interface friction coefficient of a given polypropylene pipeline coating and seafloor substrate might be predicted.
- Test the notion that manipulation of pipe-soil interface friction coefficient could be used as an alternative tool for influencing the formation and distribution of pipeline buckles.

1.5 Thesis structure

This thesis is divided into eight chapters including this introductory chapter. More detailed plots and results than space in the main body allows are included in appendices. Additionally, raw test data is contained on an attached SD card.

Chapter 2 – Literature Review

The literature review of this thesis is extensive as it needs to cover a range of interacting topics across pipeline geotechnics, soil mechanics and laboratory testing, some aspects of materials science and characterisation, and a summary of relevant existing works in the field. Each of these areas are addressed and gaps in the literature identified along with the basis for the work described in this thesis.

Chapter 3 – Materials and Methodology

Various materials are used in this research including a range of soils and polypropylene surfaces. Chapter 3 details the test materials, including their sourcing and preparation, and discusses the approach to testing, the apparatus used, and best available techniques.

Chapter 4 – Shear Response of Polypropylene Pipe Coatings

Chapter 4 deals with the laboratory investigation into the interface shear response of typical polypropylene pipe coating specimens with a range of test sands. Tests are summarised with shear response graphs and their results discussed and put into context. Trends are identified and compared with the literature including a discussion on surface texture evolution.

Chapter 5 – Enhanced Polypropylene Textures

Four additional surface specimen types were prepared to investigate the nature of the interface shear response with surfaces of enhanced texture. Their preparation is detailed along with summaries of tests and shear responses. The results are discussed with reference to results from Chapter 4 and also to established trends in the literature. A novel methodology for the assessment and quantification of high-bandwidth surface textures is developed. A unique relationship is identified to predict polypropylene interface friction from surface texture, soil mean grain size, and stress level.

Chapter 6 – Cyclic Interface Response

This chapter details a limited investigation into the nature of cyclic shear response. Pipe coating specimens were subject to cyclic shear to establish what, if any, effect this would have on cardinal test parameters and if there was any evolution in the surface texture.

Chapter 7 – Application to Pipeline Engineering

Chapter 7 details a numerical investigation into pipeline global stability drawing on the possibilities identified in this thesis for pipeline engineers to control the pipe-soil interaction friction coefficient. Abaqus finite element software is used to study lateral buckling phenomena in relation to variable interface friction input parameters and to show how their distribution can be influenced by a designer.

Chapter 8 – Conclusions

Chapter 8 brings together the conclusions of each chapter to provide a concise summary of the key conclusions and findings of this research with a short discussion on limitations and scope for future work.

2 Literature Review

The research presented in this thesis draws on various aspects of soil mechanics, offshore and pipeline geotechnics, laboratory testing, and properties of materials. The first section explores relevant aspects of pipeline geotechnics including an overview of drained and undrained conditions, various phenomena relating to pipe behaviour when they are laid and subjected to high internal pressures and temperatures, and a look at methods of modelling and controlling it. The second part looks at pertinent aspects of soil mechanics including peak and ultimate states, stress dilatancy and flow rules. This discussion is closely followed by a review of testing precedents and methods in the literature for determination of interface shear strengths including a discussion on interface shear mechanics. The final part of the literature review looks at existing work including already established relationships.

2.1 Geotechnics of offshore pipelines

Pipeline geotechnics is a relatively recent specialism within the field of pipeline and geotechnical engineering, having grown out of the need to comprehensively understand the complicated, multi-facetted, and often conflicting interactions between hot on-bottom pipelines in deep water and seafloor sediments. Pipelines may be either buried in shallow trenches, left unburied on the seafloor, or covered over with extra material post-laying, each of which scenarios brings unique combinations of geotechnical considerations. A critical important first step of pipeline geotechnics is to acquire an as comprehensive as possible characterisation of seafloor soils to avoid major, potentially unsafe or overly conservative, assumptions; geotechnical parameters of interest include soil classification (particle size distribution, index tests, shear resistance), in-situ density, and undrained shear strength in the case of cohesive soils (Cathie *et al*., 2005).

There are a number of specialist considerations and unique geotechnical challenges which apply to pipeline engineering compared to conventional foundation engineering, principally related to limit states, soil-structure interaction, and relationship to the environment in which they sit. A comparison is presented in Table 2.1 after White and Cathie (2011) and White and Gaudin (2008).

Table 2.1 Comparison of pipeline geotechnics and conventional foundation engineering from White and Cathie (2011) after White and Gaudin (2008).

	Foundation	On-bottom pipeline
Problem geometry	Known, controlled	Uncertain. Embedment affected by lay process and metocean conditions. Subsequent pipeline movements disturb seabed topography
Design criteria for in-service behaviour	To remain fixed, limited movement	May be required to displace significantly, through hundreds of cycles of operation or hydrodynamic loading
Surrounding soil conditions	Similar to in-situ state. Relatively unaffected by installation.	Soft soil is significantly affected by installation. Remoulding, heave and reconsolidation affect the local strength.
Soil-structure interaction	Usually minimal. Imposed loads are not strongly affected by foundation displacements.	Often significant. Local pipe-soil load displacement relationship affects overall pipeline response.
Soil-ocean interaction	Scour and wave-induced liquefaction may require mitigation.	Scour and wave-induced liquefaction can dominate behaviour.
Single conservative design approach	Usually available. Can assume lowest credible geotechnical capacity.	Often unavailable. Both upper and lower bound geotechnical capacity may adversely affect structural response.

2.2 Drainage considerations

As in all geotechnics there are important differences between drained and undrained conditions and the behaviour of cohesive and granular soils. Differences in pore water pressure generation and effective stress at the pipe-soil interface have an important impact on the nature of interface shear and embedment response. Drained or undrained soil behaviour depends on the rate of loading with respect to the soil permeability. Cohesive soil behaviour is generally considered to be undrained due to the very low permeability of clays, and granular soil behaviour is generally considered to be drained. Therefore, clays are typically considered in terms of an undrained shear strength, S_u, and granular soils are considered in terms of angle of internal friction which relates the shear resistance to the normal stress by a slope, ϕ. In both cases the controlling parameter (normal stress for drained, undrained shear strength for undrained) is modulated by a coefficient, μ for drained or α for undrained. Cathie *et al.* (2005) report that it is common practise to assume that operational

loads in pipelines develop sufficiently slowly that even clay soils can be considered as drained soils for axial loading (Finch *et al*. 2000).

A useful illustration of how drained and undrained conditions may vary is presented in Figure 2.1 from Hill *et al*. (2012) and White *et al*. (2012) which plots the schematic relationships between various mechanisms affecting axial pipe-soil friction. All vertical axes are friction coefficient (analogous to interface shear strength). The green section relates the roughness of the interface surface to friction coefficient with interface strength being equal to soil strength forming an upper bound. The red section deals with stress level and recognises that strength envelopes of geomaterials are generally non-linear. The blue section deals with pore water drainage; where drained conditions prevail, there is no further modification of the friction coefficient, but when conditions become undrained the strength evolves over time and through cycling in response to pore water pressure dissipation. Affecting each of these mechanisms is the wedging factor, the purple section, which is related to the degree of pipe embedment affecting the pipe-soil contact area.

The extremes of the blue section, representing full drained and full undrained conditions are clear-cut, but the transition zone is less straight-forward to assess for a given soil-surface system. The velocity of the shearing process, even in soils generally considered to be drained, may generate fully undrained conditions or localised areas of excess pore water pressure (Boukpeti and White, 2017). The coupled process of pore water generation and dissipation, the balance of which represents the partial-drainage state, was modelled in a simplified way as an infinite slab by Randolph *et al*. (2012). Boukpeti and White (2017) show the transition from undrained to drained resulting in a three-fold increase in interface friction.

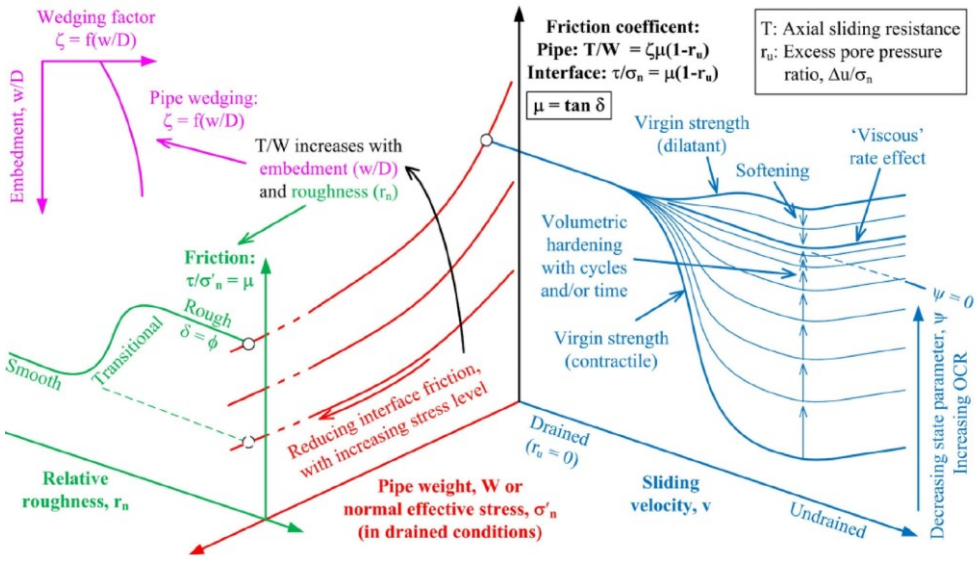

Figure 2.1 Mechanisms affecting axial pipe-soil interaction (from Hill *et al*., 2012 and White *et al*., 2012).

It is obvious from Figure 2.1 that the blue section which deals with drained and undrained behaviour, has the largest effect on the friction coefficient with a potential range in excess of other mechanisms. In the case of granular soils, which are considered to have fully drained behaviour, the blue section does not apply. Pipe-soil interaction friction is, therefore, a function of surface texture and stress level.

Clays make up a considerable portion of the seabed, with finer grained sediments becoming more prevalent with increasing water depth and distance from shore. In recent decades, the majority of new exploration is occurring in deeper waters where undrained conditions are likely to dominate. Considerable energy in the literature has been directed at the behaviour of pipelines on clay soils including laboratory (e.g. Boukpeti and White, 2017; Westgate *et al*., 2018), theoretical (e.g. Bruton *et al*., 2007; Cheuk *et al.,* 2008), numerical (e.g. Wang *et al.,* 2010; Ansari *et al*., 2014), scale model (e.g. Cheuk *et al.,* 2006; Dingle *et al.,* 2008), and full-scale or field survey (e.g. Schaminee *et al*., 1990; White and Cathie, 2010) investigations.

In spite of the prevalence of fine-grained soils on the seabed globally, granular soils still form large and important parts of the seabed with certain basins being dominated by sand. The map extract from Paramor *et al*. (2009) shown in Chapter 1 shows that as a conservative estimate, over 60% of the North Sea seabed substrate is fine sand or coarser. In the case of clay soils, pipes become embedded into the soil such that passive resistance from soil berms becomes more important in influencing pipe behaviour with interface friction of secondary importance (White and Dingle, 2011). However, in the case of granular soils there is limited embedment so the pipe-soil friction coefficient is the dominating parameter in influencing pipe stability. Numerous studies have looked at pipeline stability problems in sands (e.g. Schupp *et al*., 2006; Daiyan *et al*., 2011) including phenomena unique to sandy seabeds such as scour (Draper *et al*., 2018) and the mobile nature of sediments (Griffiths *et al*., 2018).

2.2.1 Pipe embedment

Pipe embedment is the depth to which a pipe penetrates the soil upon which it is laid with respect to the undisturbed seabed prior to laying, sometimes called the nominal or far-field embedment as it is unaffected by local soil upheaval caused by the embedment itself. The mechanism of embedment is largely a bearing capacity problem with the majority occurring immediately upon laying but some additional embedment may occur over time due to creep, additional loading when operational, or hydrodynamic loading from wave and current action. Lay effects dependent on the sea state can also cause increased embedment. Embedment relative to local soil upheaval may be called local embedment or near-field embedment.

Nominal and local embedment differences become important when considering thermal insulation effects, passive resistance to lateral sliding, and additional axial resistance offered by the larger contact area from an abutting soil berm. Local embedment may typically be ~50% greater than the nominal embedment in clays (Dingle *et al.,* 2008; Zhou *et al.,* 2008) though for non-cohesive soils embedment depths are generally much less overall owing to their greater stiffness (White and Randolph, 2007). A schematic from Bruton *et al.* (2008) is presented in Figure 2.2 depicting embedment and identifying notation pertinent to this phenomenon. In contrast to clay seabeds, granular soil seabeds (sometimes referred to as mobile seabeds) can change significantly over short periods of time depending on the local sediment transport regimes (Griffiths *et al*., 2010; Draper *et al.,* 2018). Scour (removal of material away from a structure) or build-up of berms can rapidly change the pipe-soil contact area or lead to further subsidence and needs consideration in any detailed stability analysis.

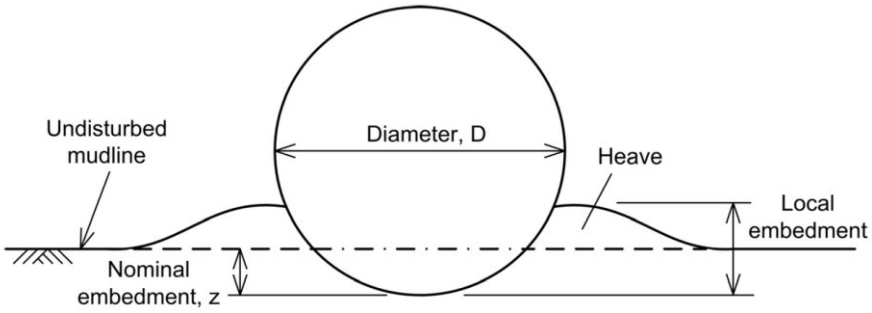

Figure 2.2 Schematic representation of pipe embedment and pertinent notation from Bruton *et al.* (2008).

As pipe embedment is effectively a bearing capacity problem, an estimation can be made by comparison of the soil ultimate bearing capacity and the load from the pipe by classical methods. Assuming the pipe resting on the seabed is analogous to a superficial strip footing:

$$Q_f = c \cdot N_c + \gamma_s \cdot z_i \cdot N_q + \frac{1}{2} \cdot \gamma_s \cdot B \cdot N_\gamma \qquad (Eq. 2.1)$$

$$z < \frac{D}{2} \ldots\ldots\ldots\ldots\ldots B = 2\sqrt{z \cdot (D - z)} \qquad (Eq. 2.2)$$

$$z > \frac{D}{2} \ldots\ldots\ldots\ldots\ldots B = D \qquad (Eq. 2.3)$$

where:

Q_f = ultimate bearing capacity (kPa)

c = cohesion (kPa)

γ_s = soil saturated unit weight (kN/m^3)

z_i = pipe initial embedment (m)

D = pipe outside diameter (m)

N_c, N_q, N_γ = bearing capacity factors (Hansen, 1970)

In the case of cohesive undrained soils, it is normal to assume $\phi = 0$ and that cohesion equals the undrained shear strength. In the case of granular soils cohesion is assumed to be zero so in both the case of drained and undrained soils Equation 2.1 can be simplified as some parameters become zero. Langford *et al*. (1989) discuss various expressions for relating bearing capacity to pipeline settlement in clays. A range of analytical solutions are also proposed by various authors based on industry studies and laboratory model testing which vary according to drained and undrained conditions.

Drained conditions

Verley and Sotberg (1994) derived an analytical solution for estimating pipe embedment on granular soils using a large body of empirical evidence from PIPESTAB (Brennodden *et al.,* 1986), DHI (Palmer *et al*., 1988), and AGA (Brennodden *et al*., 1989) to develop and calibrate their models. Initial pipe embedment may be calculated by their solution with the equation from Youssef and Cassidy (2014):

$$\left(\frac{z_i}{D}\right) = 0.037\left(\frac{\gamma_s \cdot D^2}{W_s}\right)^{-0.67} \qquad (Eq.2.4)$$

where:

W_s = pipe submerged weight (kN/m)

In practice, analytical methods for calculating pipe embedment on granular soil seabeds tend to underestimate pipe embedment giving typically only a few percent of the pipe diameter. In reality, lay effects, stress concentration at the touch-down point, and additional loading resulting from the sea state affecting the laying ship results in greater embedment. Lund (2000) compared the calculated penetration depth of a 1.2 m diameter pipe, laid mostly on sand, to the actual embedment. Actual embedment was found to be between 5 and 8 times greater than calculated and reached up to 30% in places.

Undrained conditions

Multiple models have been developed to predict pipe embedment on cohesive soils. The Murff *et al*. (1989) method uses the following expression:

$$\left(\frac{W_s}{R \cdot S_u}\right) = 4(1 + \Theta) \times cos(\Theta) + 4\left(\frac{z_i}{R}\right) \qquad (Eq. 2.5)$$

$$\Theta = sin^{-1}\left(1 - \frac{z_i}{R}\right) \qquad (Eq. 2.6)$$

where:

R = pipe radius (m)

S_u = soil undrained shear strength (kPa)

Verley and Lund (1995) used data from industry studies to derive an expression for pipe embedment due to self-weight in cohesive soils in terms of normalised pipe penetration:

$$\left(\frac{z_i}{D}\right) = 0.0071\left(\frac{W_s}{D \cdot S_u} \times \frac{S_u}{D \cdot \gamma_s}^{0.3}\right)^{3.2} + 0.062\left(\frac{W_s}{D \cdot S_u} \times \frac{S_u}{D \cdot \gamma_s}^{0.3}\right)^{0.7} \qquad (Eq. 2.7)$$

Bruton *et al*. (2006) developed a method from historical and model test data to determine the pipe penetration from a given load:

$$\left(\frac{z_i}{D}\right) = \frac{S_t}{45}\left(\frac{W_s}{D \cdot S_u}\right)^2 \qquad (Eq. 2.8)$$

where:

S_t = soil sensitivity

Figure 2.3 compares the Murff *et al.* (1989), Verley and Lund (1995), and Bruton *et al*. (2006) methods for determining pipe embedment. On the axis labels *F* is the vertical load per unit length of soil, S_u is the undrained shear strength, *D* is the pipeline diameter, *z* is the penetration, and *r* is the pipe radius.

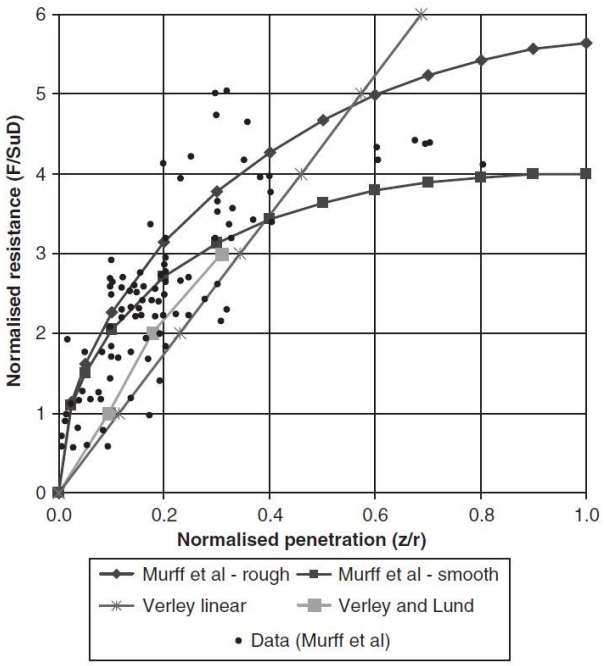

Figure 2.3 Comparison of undrained soil pipe penetration models from Cathie *et al.* (2005). Plotted data (Wagner *et al.,* 1987; Murff *et al.,* 1989; Verley and Lund, 1995; Bruton *et al*., 2006).

It can be seen that each curve lies within a similar range but that there is considerable scatter in the data so there is a potential for large errors between the fit and the data. No single curve can be said to satisfactorily fit the data, and up to z/r of 0.4 there is little to suggest a linear or nonlinear shape to the relationship. Many of the data are from Wagner *et al*., (1987) which applies to remoulded clay with undrained shear strengths of approximately 1 kPa. A potential source of such a scatter in the data is the very low stresses that prevail at the seafloor near-surface, which makes undisturbed in-situ testing and sample recovery difficult.

2.2.2 Axial force

The term effective axial force is used in contrast to “true” axial force to avoid problems of integrating pressure effects over double-curve surfaces in the event of pipe buckling (Fyrileiv and Collberg, 2005). It resolves conflicting internal and external pressures and the steel wall force driven by thermal expansion. It is the axial effective force which is recognised to be the driver of global buckling of pipelines (DNV, 2013). Before startup, a pipeline experiences only residual lay tension and an external pressure force; effects which act against pipe expansion. During operation thermal expansion, restrained by soil resistance, gives rise to the steel-wall force given by the expression (Hobbs, 1981), and which provides an upper bound estimate on the maximum force in the pipe:

$$P_0 = E \cdot A_e \cdot \alpha_t \cdot \Delta T \qquad (Eq. 2.9)$$

where:

P_0 = steel wall force (kN)

E = Young's Modulus (kN/m^2)

A_e = pipe external cross-sectional area (m^2)

α_t = coefficient of linear thermal expansion (1/°C)

T = temperature (°C)

Hoop stress and Poisson's effect also need to be considered and the external pipe pressure can be discounted as it remains unchanged between as-laid and operational states. Chee *et al.* (2018) distils these various components into one workable expression to calculate the effective axial force when the pipe is fully constrained and cannot expand:

$$S_{eff} = H - \Delta P_i \cdot A_i(1 - 2v) + E \cdot A_e \cdot \alpha_t \cdot \Delta T \qquad (Eq. 2.10)$$

where:

S_{eff} = effective axial force (kN)

H = residual lay tension (kN)

P_i = pipe internal pressure (kPa)

A_i = pipe internal cross-sectional area (m^2)

v = Poisson ratio

The opposing actions of thermal expansion and internal pressure is illustrating in a free body diagram presented in Figure 2.4.

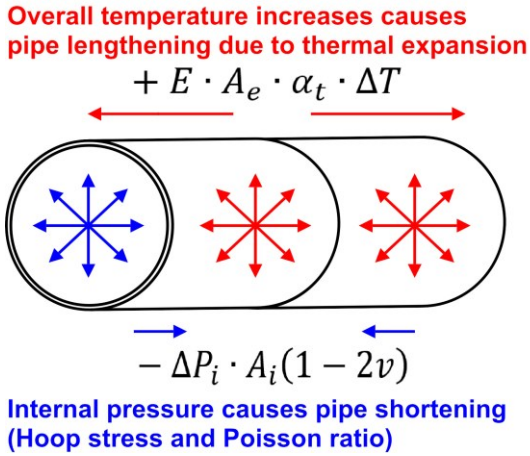

Figure 2.4 Free body diagram showing schematically the actions of Eq. 2.10 on a pipe section

2.2.3 Axial soil resistance

The mobilised soil resistance has principally two orientations, there is an axial resistance which acts longitudinally in the pipe's axial direction, and a lateral component which resists movement laterally away from the pipe axial plane. The axial resistance controls the degree to which axial strain from thermal expansion is constrained and therefore, directly and proportionally controls the build-up effective axial stress in the pipeline.

Drained conditions

Axial resistance in fully drained conditions can be modelled using a method analogous to the *beta* effective stress method for assessing axial shaft capacity for foundation piles (White and Cathie, 2010). Contact stresses between pipe and seabed are known as they are wholly due to the pipe self-weight and there is only a modest enhancement due to a wedging effect used to account for the horizontal component of contact between an embedded pipe and soil. The drained axial resistance is given from Bruton *et al.* (2008) by the expression:

$$F'_A = W_s \cdot \nabla \cdot \mu_a \qquad (Eq. 2.11)$$

where:

F'_A = drained axial resistance (kN/m)

∇ = wedging factor

μ_a = axial friction coefficient

The wedging factor, ∇, is given by the equation:

$$\nabla = \frac{2sin\theta}{\theta + sin\theta \cdot cos\theta} \qquad (Eq. 2.12)$$

$$\theta = cos^{-1}\left(1 - 2 \cdot \frac{z}{D}\right) \qquad (Eq. 2.13)$$

where:

z = pipe nominal embedment (m)

The dominating factor for drained axial resistance is the self-weight of the pipe and how much of that contact force is available for resisting shear which is modulated by the friction coefficient. The friction coefficient can be determined by a number of laboratory tests which are discussed later and is simply the ratio of the shear resistance to the normal force. It determines what proportion of the normal stress that a given interface or contact is

experiencing can be mobilised to resist a shear load. The greater the friction coefficient, the greater the shear load a given surface contact or soil-surface interface is able to resist before displacement occurs under a given normal stress.

Undrained conditions

Although loading is often slow enough that drained conditions can dominate, even with cohesive soils, loading maybe sometimes be rapid enough to elicit an undrained response. Axial resistance in undrained conditions can be calculated:

$$F_A = \alpha \cdot S_u \cdot L_a \qquad (Eq. 2.14)$$

where:

α = adhesion factor

L_a = arc length in embedded soil (m)

Cathie *et al*. (2005) report that in absence of any specific data an adhesion factor of 1 is appropriate for peak resistance and for residual strength may be related to the soil sensitivity by $\alpha = 1/S_t$. Soil sensitivity is the ratio of the peak to remoulded shear strength.

Effective axial stress

Axial resistance is a cumulative parameter and relates directly to the units of submerged pipe weight in the equation and the length along the pipe. Axial strain in the pipe is directly constrained by the axial resistance so the rate of build-up and magnitude of axial resistance is equal to the axial stress at any given point along the pipeline. Stress levels relevant to pipelines are very low, typically down to 1 kPa (White and Cathie, 2011) so the rate of build-up of axial soil resistance along the pipe length is slow. It may be many kilometres before there is sufficient axial soil resistance to fully constrain thermally-induced axial strain. The build-up of axial force as a straight pipe becomes cumulatively constrained along its length is illustrated in Figure 2.5 with a free body diagram showing the relevant actions in Figure 2.6. Higher axial friction (μ_a) results in a faster build-up until it becomes fully constrained. At lower axial friction, the pipe may never become fully constrained. The fully constrained force line in red gradually reduces along its length to reflect the thermal gradient between the hotter and colder end of the pipe.

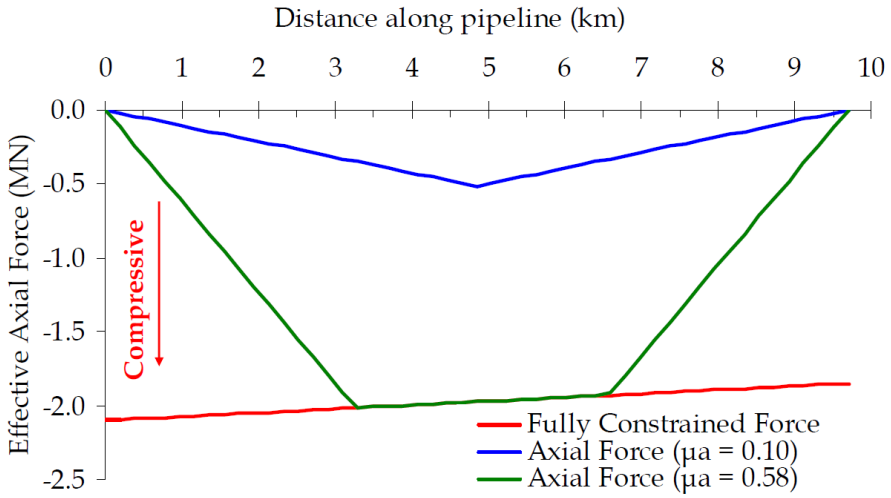

Figure 2.5 Effective axial force in a straight pipe from Bruton *et al*. (2008).

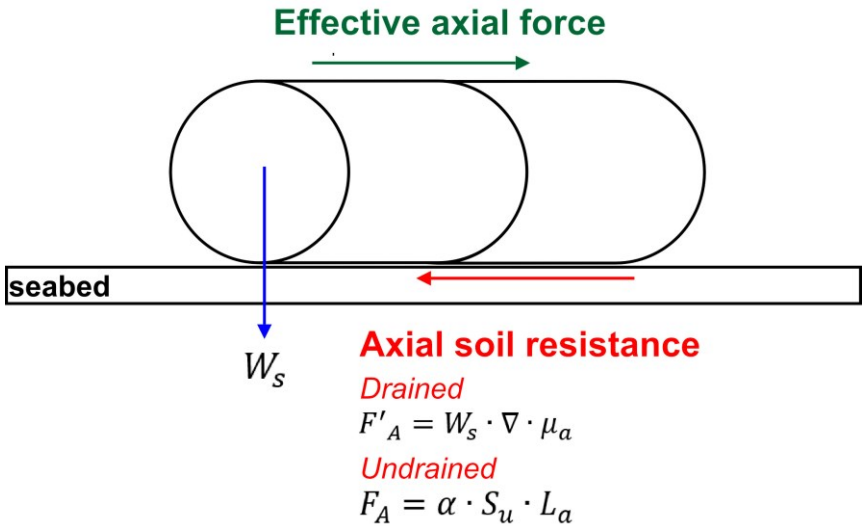

Figure 2.6 Free body diagram of a pipe laying on the seabed

2.2.4 Pipeline axial walking

As a pipeline heats up it expands and the expansion is opposed by axial resistance between pipe and soil. Conversely during shutdown, the pipe cools and contracts but is similarly opposed by the axial resistance. In theory the expansion and contraction between cycles is steady state in relation to the pipe ends but local variations in seafloor topography, temperature differentials along the pipe from cooling of the pipe contents, and end of pipeline tension, can lead to global axial movement of the pipe (Bruton *et al.,* 2003). Long-term axial movement of a pipeline is termed “pipeline walking” and is generally a feature of “short” pipelines (Tornes *et al*., 2000; Carr *et al*., 2003). “Short” pipelines are ones which do not become fully restrained over their length such that thermal strains manifest primarily as axial extension. When pipelines walk, they can put significant stress on risers or other connecting

infrastructure, so expansion spools (zigzag, or right-angled sections of pipe) are incorporated to accommodate these movements (Choi *et al.*, 2010). In contrast, if a pipeline is sufficiently long that enough pipe-soil resistance accumulates causing axial strain to be restrained, then the pipe is said to be "long" and is likely instead to be vulnerable to lateral buckling. Figure 2.7 (from Carr *et al.*, 2003) illustrates the phenomenon of asymmetric and progressive thermal gradients in a pipeline. Heat loss to the surrounding water slows the heat transfer along the pipe such that only after 15 cycles does the thermal gradient come close to zero.

Repeated cycling can accumulate axial movement through soil ratcheting and is termed pipeline walking (Tornes *et al.,* 2000; Carr *et al.,* 2003) which, although not usually considered a limit state, requires consideration to prevent damage at end connections to other infrastructure. If a pipeline does not become fully constrained over its length due to soil resistance then the pipeline may expand over its entire length.

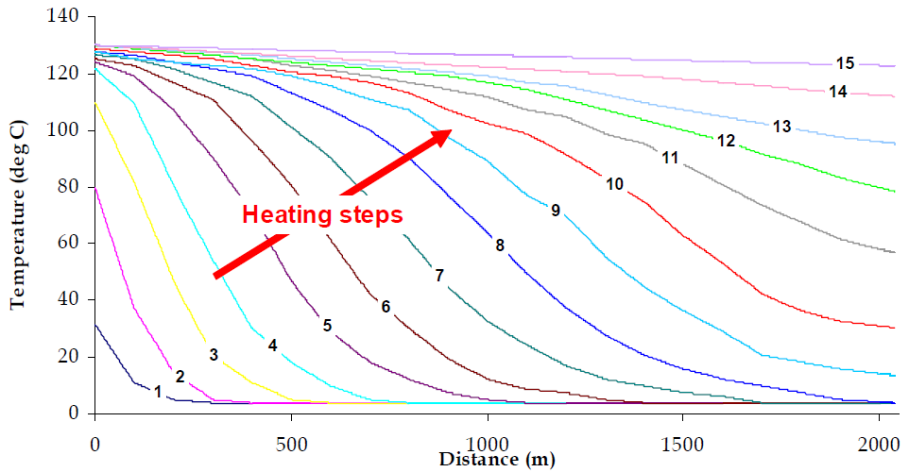

Figure 2.7 Effective axial force for a range of friction in a straight pipe from Bruton *et al*. (2008).

Pipe walking is highly sensitive to axial friction, with lower axial friction precipitating greater potential for pipeline walking. Carr *et al*. (2003) provides an example of how the axial friction coefficient can influence the cyclic walking displacement of a free-ended 4 km pipeline with a submerged weight of 1.224 kN/m. Their figures are presented in Table 2.2 and show that with a large thermal gradient greater axial friction leads to much larger displacement per cycle, whereas the reverse is true with a small thermal gradient although overall magnitudes are also lower.

Table 2.2 Cyclic walking displacement of a free-ended 4 km pipeline with submerged weight of 1.244 kN/m (mm/cycle)

Gradient of thermal transient (°C/km)	Axial friction coefficient		
	0.2	0.4	0.6
3.36	5.65	3.16	2.09
33.6	140.4	210.5	214.9

2.2.5 Lateral soil resistance

Cathie *et al*. (2005) drew attention to three general approaches for assessing lateral resistance; a Coulomb-type single friction coefficient approach to determine shear resistance as a proportion of the normal stress relating to submerged pipe weight, a two component model comprising shear resistance and an additional passive resistance offered by a wedge of soil, an example is shown in Figure 2.8, (Nyman, 1984; Wagner *et al*., 1987; Verley and Sotberg, 1994), or a plasticity model approach (Zhang *et al*., 1999; 2002; Hodder and Cassidy, 2010). In general, pipe embedment is greater for pipes laid on clays so passive resistance offered by soil berms is of greater consequence to lateral soil resistance (Merifield *et al*., 2008). Pipes laid on granular soils tend to embed less so the Coulomb friction interaction distilled to a friction coefficient between pipe and soil is the more important component (Brennodden *et al*., 1986). The total horizontal resistance to pipe movement is assumed to have two components; the Coulomb friction component and the passive resistance caused by a soil berm or due to pipe embedment:

$$F_h = F_C + F_r \qquad (Eq.2.15)$$

$$F_C = \mu \cdot W_s \qquad (Eq.2.16)$$

where:

F_h = total soil horizontal resistance force (kN/m)

F_C = Coulomb frictional resistance (kN/m)

F_r = passive resistance (kN/m)

μ = friction coefficient

The friction component is analogous to the axial resistance which is a function of the net pipe submerged weight and the interface friction coefficient. The energy-based passive soil resistance model developed by Verley and Sotberg (1994), alluded to previously for pipe embedment, is shown in Figure 2.8 from Youssef and Cassidy (2014).

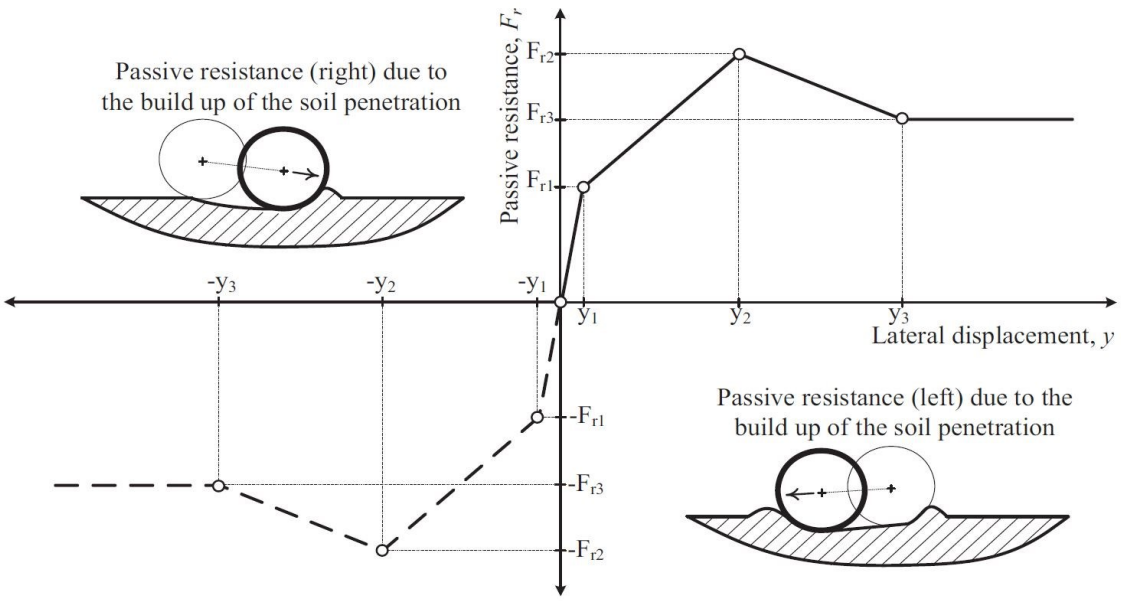

Figure 2.8 Schematic representation of Verley and Sotberg (1994) silica sand soil resistance model from Youssef and Cassidy (2014).

The Verley and Sotberg (1994) lateral passive resistance model for silica sand soils comprises four regions, clearly distinguishable in Figure 2.8:

- An elastic region where lateral displacement is less than 0.02 pipe diameters (*D*) where no work is done and pipe vertical penetration is equal to the initial penetration.
- A region up to 0.5*D* where lateral displacement is accompanied by additional vertical penetration.
- The breakout region, from 0.5*D* to 1.0*D* where peak breakout resistance is reached and passed and is accompanied by a reduction in pipe penetration.
- From lateral displacement of 1.0*D* penetration and passive resistance remains constant.

Analytical solutions for passive breakout resistance are given by Youssef and Cassidy (2014) arranged based on the work of Verley and Sotberg (1994). The three nodes of the force displacement model shown in Figure 2.8 are dependent on the lateral displacements and the force which is a function of pipe embedment at each lateral position. Pipe embedment at z_1 in the elastic zone is assumed to be the same as initial embedment with no work done. The initial pipe embedment was discussed previously but is reproduced for clarity, although it may be that instead of using this analytical solution it is more appropriate to assume embedment to be 5-20% to avoid underestimation.

$$\left(\frac{z_i}{D}\right) = 0.037\left(\frac{\gamma_s \cdot D^2}{W_s}\right)^{-0.67} \qquad (Eq.\,2.17)$$

Pipe penetration at breakout, z_2, which corresponds to lateral displacement y_2, is calculated:

$$\left(\frac{z_2 - z_i}{D}\right) = 0.23\left(\frac{\epsilon}{\gamma_s \cdot D^3}(K_s)^{-1}\left(\frac{y}{D}\right)^{-0.5}\right)^{0.31} \qquad (Eq.\,2.18)$$

$$K_S = \frac{\gamma_s \cdot D^2}{W_s} \qquad (Eq.\,2.19)$$

where:

y = pipe lateral displacement (m)

ϵ = energy (kN·m/m)

Residual pipe penetration, z_3, is calculate by the following equations:

$$\left(\frac{z_2}{D}\right) \leq 0.1 \ldots\ldots\ldots\ldots\ldots \left(\frac{z_3}{z_2}\right) = 0.82 - \left(\frac{z_2}{D}\right) \qquad (Eq.\,2.20)$$

$$\left(\frac{z_2}{D}\right) > 0.1 \ldots\ldots\ldots\ldots\ldots \left(\frac{z_3}{z_2}\right) = 0.5 \qquad (Eq.\,2.21)$$

Using pipe penetrations calculate as above, the peak passive resistance force, F_{r2}, is given:

$$K_S \leq 20 \ldots\ldots\ldots\ldots\ldots F_{r2} = \gamma_s \cdot D^2(5 - 0.15K_s)\left(\frac{z_2}{D}\right)^{1.25} \qquad (Eq.\,2.22)$$

$$K_S > 20 \ldots\ldots\ldots\ldots\ldots F_{r2} = 2\gamma_s \cdot D^2\left(\frac{z_2}{D}\right)^{1.25} \qquad (Eq.\,2.23)$$

The residual passive force, F_{r3}, can be calculated simply by substituting z_3 into *Eq. 2.22* or *Eq. 2.23* as appropriate. The passive resistance force in the elastic region, F_{r1} is assumed to be $0.3F_{r2}$.

Although passive resistance offered by soil wedging and pipe embedment are deserving of attention and consideration in pipeline stability design, low initial embedment on granular soil seafloors (White and Randolph, 2007) means it only makes a modest contribution to overall lateral soil resistance. The larger component of soil resistance is provided by the contact between pipe and soil so the interface contact friction coefficient remains the dominant factor (Brennodden *et al*., 1986), particularly beyond the initial breakout zone.

2.2.6 Pipeline buckling

Pipelines are inherently long and slender structures which, when subject high pressures and temperatures, makes them vulnerable to Euler-type column buckling. Pipelines buried in trenches are more prone to buckling vertically, called upheaval buckling, whilst those laid directly on the seafloor are more prone to lateral buckling. Global buckling (with respect to pipe geometry across the seafloor as opposed to structural buckling affecting the pipe section) is triggered when a critical buckling force is reached. Uncontrolled buckling can lead to large, localised plastic deformation potentially causing buckling collapse or fatigue during operation cycles (Perinet and Simon, 2011). Buckling collapse does not always lead to a loss of containment, but it is a significant risk, and did happen in Guanabara Bay, Brazil in 2000 where a 4 m lateral buckle snap-through led to pipe rupture and the loss of 7000 barrels (approximately 1.1 million litres) of oil. Buckles are typically initiated where localised pipe imperfections, out-of-straightness from the lay process, seafloor topography or substrate variations cause local reductions in the critical buckling force which promotes buckle initiation at those points. A side-scan sonar image of a laterally buckled pipeline section is shown in Figure 2.9 from Bruton *et al*. (2005).

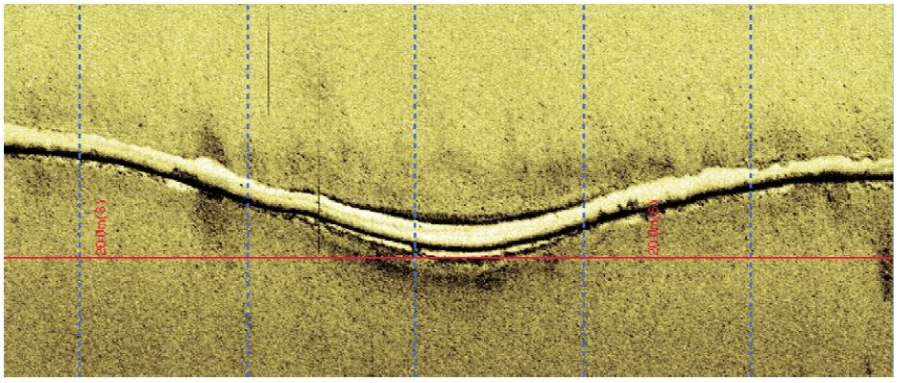

Figure 2.9 Side-scan sonar image of a lateral buckle from Bruton *et al.* (2005).

Euler-type column buckling adopts four deflection modes, schematically depicted in Figure 2.10 from Hobbs and Liang (1989). For buried or trenched pipes Mode 1 is most common but for unburied pipes Mode 3 becomes most prevalent due the lack of horizontal reaction force offered at the buckle shoulders when deforming laterally.

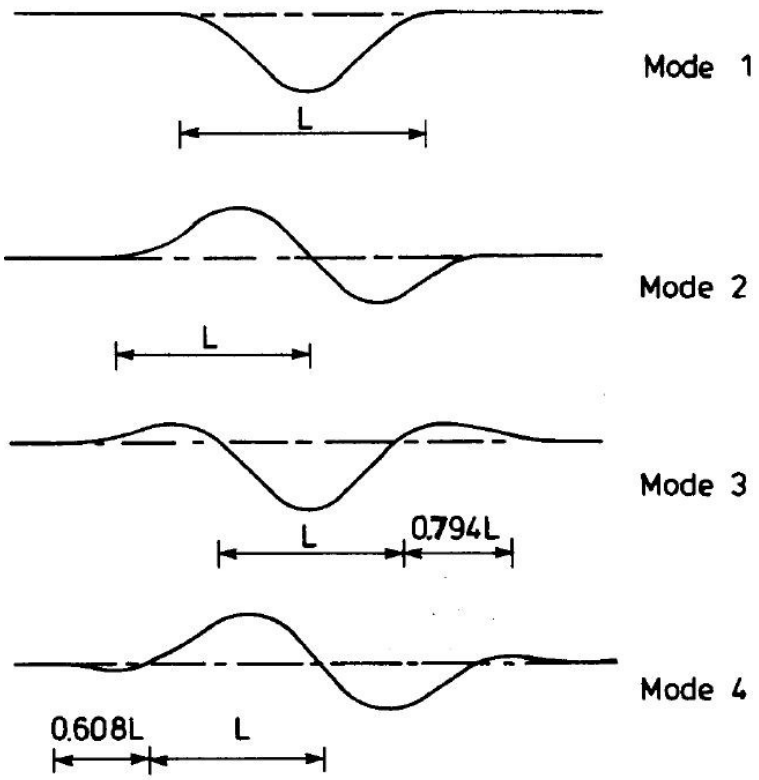

Figure 2.10 Lateral buckling modes from Hobbs and Liang (1989).

Determination of lateral buckling parameters can be achieved using the Hobbs (1984) method. The effective axial force required to initiate buckling, also termed the critical buckling force, is expressed as:

$$P_z = \frac{k_1 \cdot E \cdot I}{(L_z)^2} + k_3 \cdot \mu_a \cdot L_z \cdot W_s \left\{ \left[1 + \frac{k_2 \cdot E \cdot A_e \cdot {u_l}^2 W_s \cdot {L_z}^4}{\mu_a (E \cdot I)^2} \right]^{0.5} - 1 \right\} \qquad (Eq. 2.24)$$

Buckle amplitude is given by:

$$A_{buck} = \frac{k_4 \cdot \mu_l \cdot W_s \cdot {L_z}^4}{E \cdot I} \qquad (Eq. 2.25)$$

Leaving a residual force in the buckle given by:

$$P_{buck} = \frac{k_1 \cdot E \cdot I}{{L_z}^2} \qquad (Eq. 2.26)$$

And maximum moment induced in the buckle:

$$M_{buck} = k_5 \cdot \mu_l \cdot W_s \cdot {L_z}^2 \qquad (Eq. 2.27)$$

where:

P_z = critical buckling threshold (kN)

L_z = buckle length (m)

μ_a = axial pipe-soil friction coefficient

μ_l = lateral pipe-soil friction coefficient

I = second moment of area (m^4)

k_n = buckle constant

The buckle constant, k_n, varies according to the buckle mode (Figure 2.10), and they are summarised in Table 2.3.

Table 2.3 Buckling constants *k* for buckling modes

Buckle mode	k_1	k_2	k_3	K_4	k_5
1	80.76	6.391e-05	0.500	2.407e-03	0.0694
2	39.48	1.743e-04	1.000	5.532e-03	0.1088
3	34.06	1.668e-04	1.294	1.032e-02	0.1434
4	28.20	2.144e-04	1.608	1.047e-02	0.1483

In Figure 2.5 it was shown how a compressive force can build up in the pipeline until all axial strain is resisted by the interaction with the surrounding soil and the fully constrained force is reached. However, when the critical buckling force is reached and a buckle is triggered, the axial force in the pipe is relieved causing a local reduction in the effective axial stress. The midpoints between buckles are said to be virtually anchored as they become artificial nodes about which pipe expansions and strains reverse their direction. The phenomenon is schematically explained in Figure 2.11.

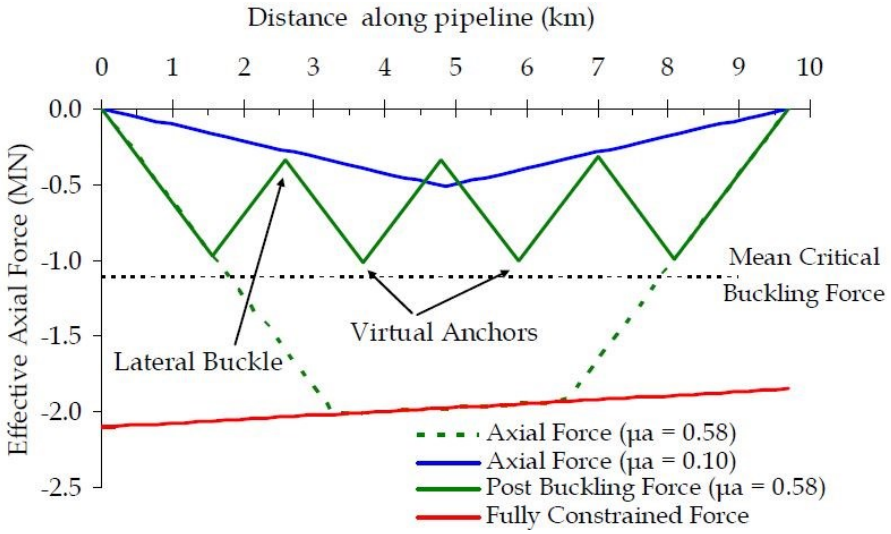

Figure 2.11 Effective axial force and virtual anchor points from Bruton et al. (2008).

The relationship between pipe-soil friction coefficient, pipe end expansion, and buckling is complex but is best illustrated by Figure 2.12 from Bruton *et al*. (2008).

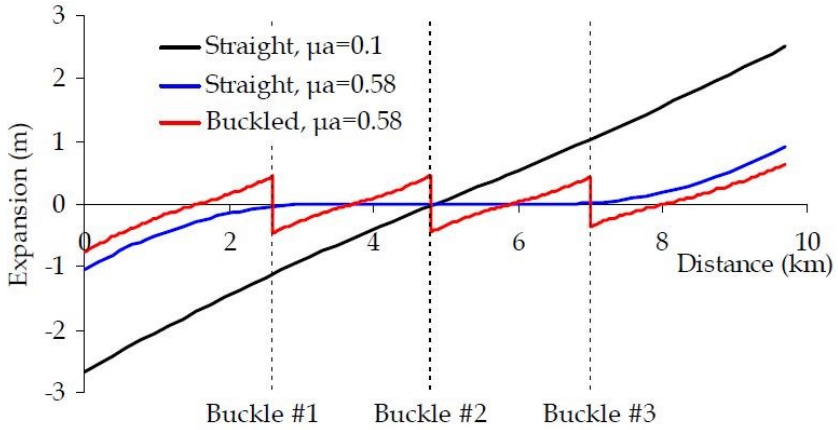

Figure 2.12 Pipeline buckling and end expansion relationship from Bruton *et al*. (2008).

What Figure 2.12 shows is that for a straight, unbuckled, pipe with a low pipe-soil friction coefficient (meaning the pipe does not become fully constrained), expansion can occur unimpeded resulting in net expansions of approximately 2.5 m at each end. In the case of a straight, unbuckled, pipe with a high pipe-soil friction coefficient (meaning the pipe becomes fully constrained across the central section) axial expansion can only occur in sections which are not fully constrained resulting in expansions of approximately 1 m at each end. If a high pipe-soil friction coefficient pipe buckles then the pipe does not become fully constrained at any point so axial expansion is free to occur at all points along the pipe. However, as the direction of expansion changes around the virtual anchor points shown in Figure 2.11, the overall net expansion at the pipe ends is only approximately 0.7 m in the example given.

The design challenges of these conflicting effects of low or high friction are unique. Low friction pipelines are much less susceptible to buckling but controlling the extreme end expansions and likelihood of pipeline walking then becomes problematic. Conversely, high friction pipelines are vulnerable to buckling over much of their length and the design challenge is to limit these events such that the severity of deformation does not compromise the integrity of the pipeline.

2.2.7 Control of walking and buckling

Bruton *et al*. (2005) discuss a wide range of methods that are in use to help influence the movement of pipelines subject to walking or buckling phenomena. Solutions involving the geometry of the as-laid pipe such as snake lay or pre-stressing the pipe as it is unspooled from the ship, promote the formation of buckles by exacerbating the geometry imparted during laying of the pipe. In this way the nature of pipe deformation becomes predictable. Snake-lay is schematically shown in Figure 2.13 from Bruton *et al*. (2005).

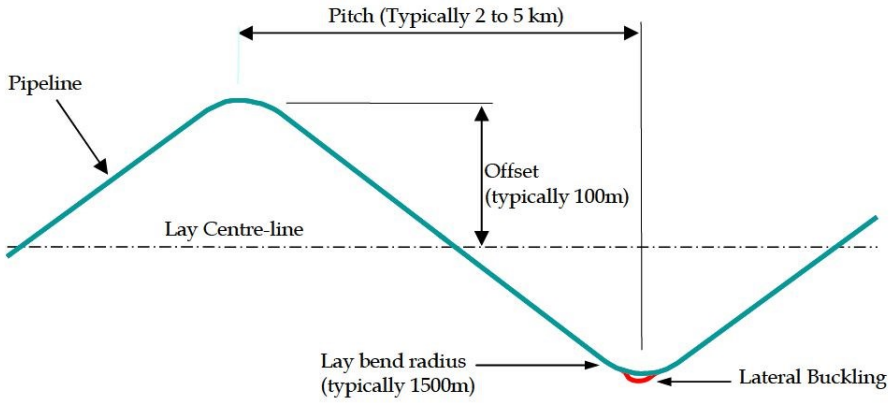

Figure 2.13 Typical Snake Lay configuration (with exaggerated vertical scale) from Bruton *et al*. (2005).

Other methods to provoke buckling include the placement of sleepers (Figure 2.14) or sliders on the seafloor, typically 25 to 50 m long spaced 2 to 3 km apart, over which the pipeline is laid. Such devices provide a vertical upset and cause a localised reduction in friction between pipe and slider which promotes the formation of a buckling in this area. A similar effect can be induced by attaching buoyancy modules to a typically 100 m long section of the pipe (Figure 2.15) to reduce the normal contact force between pipe and seafloor which also promotes pipe deflection in this area.

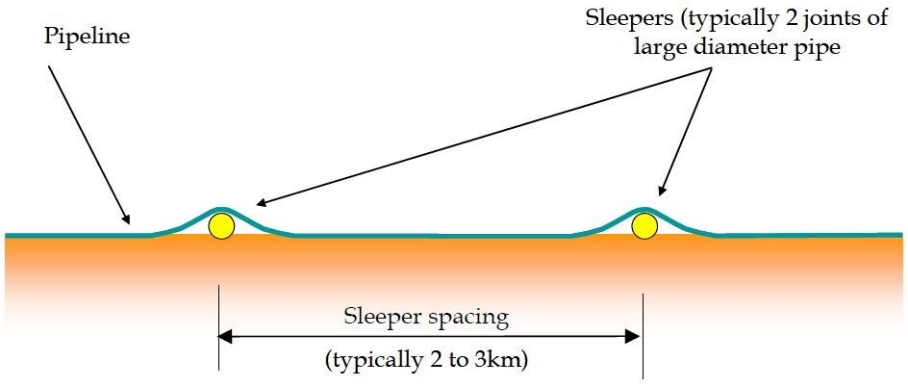

Figure 2.14 Buckle initiation using sleepers from Bruton *et al*. (2005).

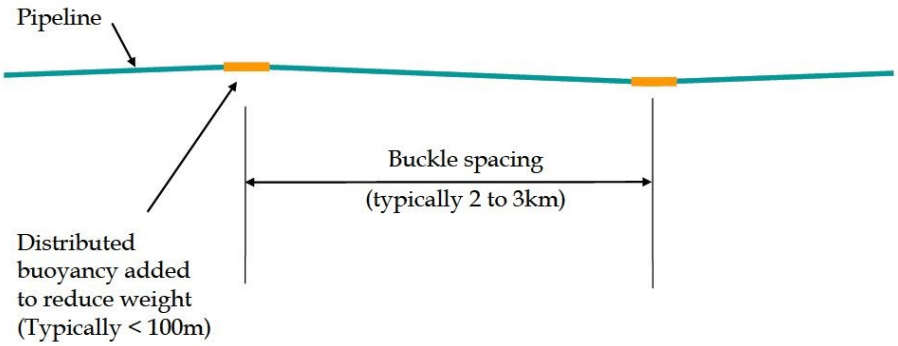

Figure 2.15 Buckle initiation using distributed buoyancy from Bruton *et al*. (2005).

Besides promoting buckling, methods such as rock dump (Figure 2.16) or the application of concrete mattresses (Figure 2.17) over the as-laid pipe increase the weight of the pipe and provide greater resistance to movement to restrict or eliminate any pipe deformation.

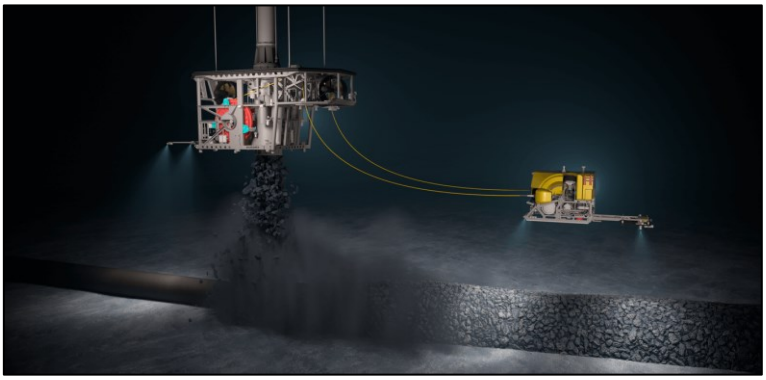

Figure 2.16 Depiction of rock dump over a pipeline (Seatools, 2020).

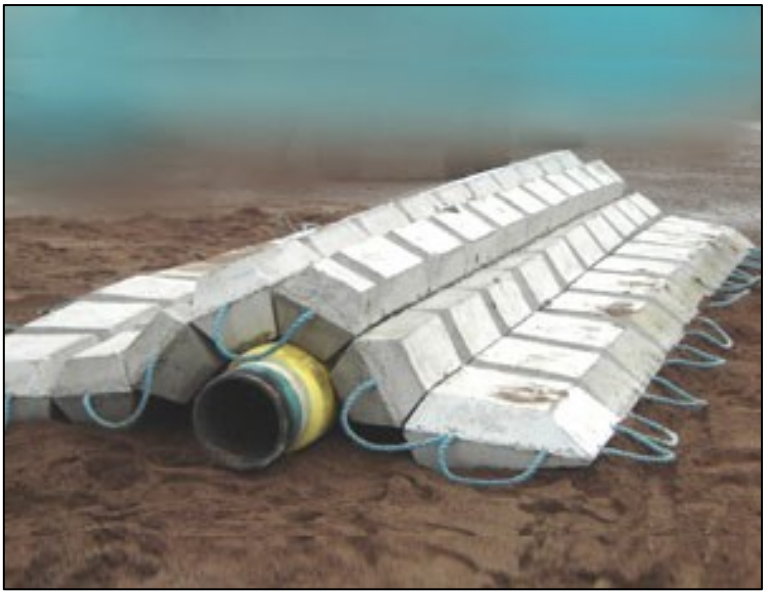

Figure 2.17 Concrete mattress applied to a pipeline (SPS, 2020)

2.2.8 Pipe coatings

Pipelines, as indeed are other types of seafloor infrastructure, are typically given an exterior coating which has a number of functions including corrosion prevention, protection from damage, and thermal insulation. A number of coating solutions have been in use historically including bitumen, fusion-bonded epoxy (FBE), polyethylene (PE), and polypropylene (PP). The relative benefits of each coating solution are scored in Table 2.4 after Guidetti *et al*. (1996) with a score of 5 being excellent and 1 being very poor.

The benefits of polypropylene coating solutions are clear from Table 2.4 where it equals or outperforms the other options hence its widespread use in modern offshore applications. Polypropylene solutions are usually applied to pipelines as a three-layer coating bonded skin (Connelly *et al*., 1989). The inside of the coating is a thin layer of epoxy resin to bond the coating to the pipe. The outer layer is polypropylene and sandwiched between is an intermediate layer of modified polypropylene co-polymer. The outer and intermediate layers are completely chemically compatible ensuring good adhesion. The inner surface of the epoxy primer bonds strongly with oxides of the metal and also the outer surface with polar groups grafted onto the intermediate layer polypropylene. Examples of polypropylene-coated pipe sections are shown in Figure 2.18 which shows the variable thickness of coatings as applied to pipes. Different thicknesses of coating reflect different requirements from the coating relating to the vulnerability of the pipe to damage, buoyancy and/or ballast considerations and how much thermal insulation is required to maintain the liquids inside in the appropriate phase and viscosity.

Table 2.4 Relative performance comparison of pipeline coating technologies adapted after (Guidetti *et al.*, 1996)

Property	PP	PE	FBE	Bitumen
Transport, handling, and laying				
Impact strength	5	4	3	2
Weathering resistance	4	4	4	3
Abrasion resistance	5	3	3	2
Damage resistance	5	3	3	2
Environmental impact	5	5	4	2
Corrosion protection				
Adhesion	5	4	5	2
Cathodic disbanding resistance	5	5	5	4
Water impermeability	5	5	2 - 4	2
Oxygen impermeability	4	4	5	2
Volume resistivity	5	5	4	1
Properties during operation				
Soil stress resistance	5	4	5	1
Fungi and bacteria resistance	5	5	3	1
Penetration resistance	5	4	5	1
Flexibility	5	5	3	1
Low temperature resistance	5	5	4	2
High temperature resistance	5	3	4	1

Figure 2.18 Polypropylene coated pipe samples at University of Bristol.

Given that interaction between soil and pipeline is via the coating-soil interface, correct quantification and understanding of the interface mechanics and shear strength of coatings is key to properly understanding the transmission of stress from pipe to soil and vice versa.

2.2.9 Relevant standards and industry projects

Due to the importance to global pipeline stability of properly understanding the pipe-soil interaction and the mechanisms involved contributing to buckling, a joint industry project (JIP), called SAFEBUCK, was launched in 2002. The SAFEBUCK JIP was led by Atkins and included multiple stakeholders including contractors, consultants, designers, operators, and academia. The project ran until 2015 with four phases and from a pipe-soil interaction point of view, was primarily concerned with the development of plasticity models to predict lateral force-displacement responses of pipes embedded in clay soils through operational cycles over the pipeline's life cycle. More recently, the STABLEpipe JIP sought to address analogous problems related to pipelines laid on mobile seabeds (seabeds comprising granular soils which are susceptible to liquefaction, scour, and fluidisation). Common to both these projects is the need to adequately determine appropriate pipe-soil friction coefficients, either by in-situ tests or by laboratory testing of comparable soil samples and surface specimens.

Numerous authors have determined equivalent friction coefficients for clay soils of between 0.3 and 0.8 depending on the strain rate and over consolidation ratio (e.g. Hill *et al.*, 2012; Boukpeti and White, 2017) or between 0.1 and 1.0 when considering the roughness of surfaces and depending on drainage state (e.g. Westgate *et al.*, 2018). It is more typical to treat clays according to their undrained shear strength. They are not considered true friction coefficients as, although they relate the available shear resistance to the normal stress, the response is governed much more by the clay soil properties and strain rate than by interaction with the surface. In the case of sand soils and pipelines, particularly polymer coatings, O'Rourke *et al*. (1990) is an authority and established that smooth polymers may have a wide range of interface efficiencies (the ratio of interface to soil-only shear strength) which depends largely on the hardness of the surface.

For drained soils, DNVGL Recommended Practice F114 (DVNGL, 2017b) suggests a residual interface friction coefficient of between 0.3 and 1.0 for non-carbonate sandy soils, or up to 1.4 for clay or silty soils but notes that suitable interface testing should be carried out to determine the appropriate value. To the author's knowledge there is no database of publicly available information that would allow pipeline designers to make an estimation of pipe-soil interface friction for polypropylene (or indeed other polymers) coated pipes and granular seabed substrates.

2.3 Soil and soil-interface mechanics

The nature of interface stress response depends largely on the soil response which varies between granular and cohesive soils just as if it were only the soil response being investigated. Cohesive soils are not part of this investigation so only the relevant aspects of granular soil mechanics are discussed.

2.3.1 Peak and ultimate states

When dense granular soils shear their stress displacement behaviour is characterised by an initial peak strength mobilised in the early stages of shearing followed by a reduction in shear strength which settles to a near constant value at large displacement. These states are often referred to as peak and ultimate, respectively. Ultimate is sometimes also referred to as postpeak or critical state though these are not always analogous terms. Loose soils do not exhibit peak behaviour but instead only mobilise a large displacement ultimate strength which is of the same magnitude as that reached by dense soils. Figure 2.19 from Wood (1990) after Taylor (1948) illustrates the concept showing strength (in terms of a ratio between shear stress, Q, and normal stress, P) with horizontal displacement.

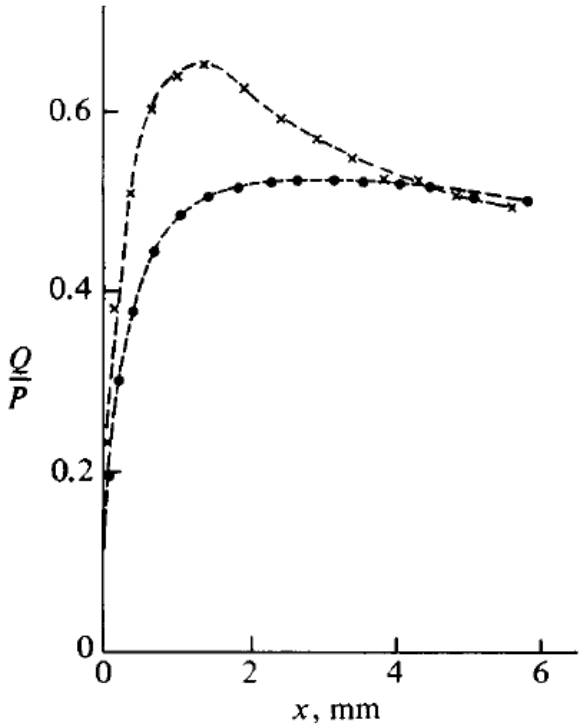

Figure 2.19 Shear stress behaviour of sand in a direct shear apparatus for loose (dots) and dense (crosses) samples from Wood (1990) after Taylor (1948).

The generation of peak strengths for denser soil samples is easily explained by considering grain packing. In addition to overcoming the inherent friction generated by the grain to grain contact (represented by the ultimate strength), grains which are tightly arranged need to override their neighbours to allow them to become “unlocked” and participate in shearing. The extra energy required to unpack interlocked soil grains manifests as the peak shear strength. This model of grain interaction is sometimes referred to as the saw-tooth model.

2.3.2 Stress dilatancy

Considering the “unlocking” of tightly arranged grains that is required to override their neighbours during shearing, the overall density along the shear band must reduce as the volume occupied increases. Similarly, it is easily imagined that loosely arranged soils will see grains adopt a more compact arrangement as grains are forced to rearrange and settle. It is therefore not surprising that a dense soil sample tested in the laboratory will tend to expand, or dilate, during shearing and a loose soil sample tends to settle, or contract. Figure 2.20 from Wood (1990) after Taylor (1948) illustrates this phenomenon and should be considered together with Figure 2.19 and the relationship between shear stress, horizontal, and vertical displacement appreciated.

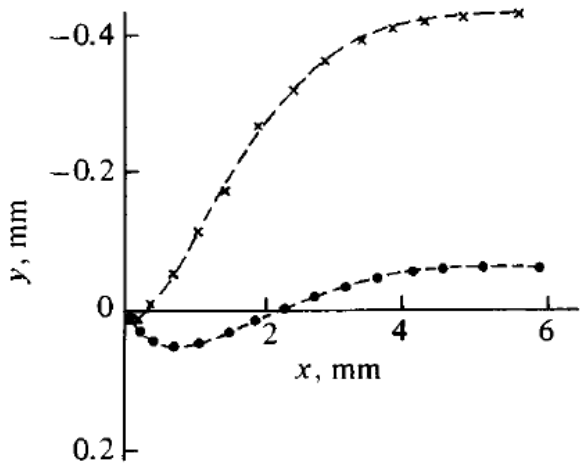

Figure 2.20 Vertical displacement in the DSA for loose (dots) and dense (crosses) samples from Wood (1990) after Taylor (1948).

It has been seen that the density of a soil sample influences the peak (if any) shear strength of the soils. It follows that as the ultimate strength of both initially loose and initially dense samples is the same that by the end of the test the density (at least, along the shear band) and sample volume, is the same regardless of initial sample density. Another term for describing ultimate strength is, therefore, constant volume shear strength.

2.3.3 Shear test cardinal parameters

The direct shear apparatus (DSA), discussed in more detail later, is one of the most commonly used laboratory apparatus for determination of shear strength of granular materials. Measurements taken during direct shear testing are limited to the force resisting shearing and displacement in horizontal or vertical orientations. From these measures the average vertical confining stress (or normal stress) and average horizontal shear stress can be calculated. It is not possible to derive strain (vertical, volumetric, or horizontal) because the thickness and orientation of shear bands within the shear zone are not known. Principle cardinal parameters generated by the DSA are shear stress, τ, normal stress, σ_n, and horizontal and vertical displacement, Δh and Δv respectively. From these can be derived the soil friction angle, ϕ, and angle of dilation, ψ, (assuming all dilation occurs within a simple shear zone) given by the following equations:

$$tan\phi = \frac{\tau}{\sigma_n} \qquad (Eq. 2.28)$$

where:
ϕ = soil friction angle
τ = average horizontal shear stress
σ_n = average normal stress

$$tan\psi = \frac{\Delta v}{\Delta h} \qquad (Eq. 2.29)$$

where:
ψ = angle of dilation
Δv = vertical displacement
Δh = horizontal displacement

Equations 2.28 and 2.29 describe the conventional interpretation of what occurs within the direct shear box and assumes a horizontal shear plane where principle strain and stress are coincident. The Mohr circle for this interpretation is presented in Figure 2.21. In this scenario the soil is assumed to be elastic until failure, whereas in reality soils can be argued to behave plastically before failure.

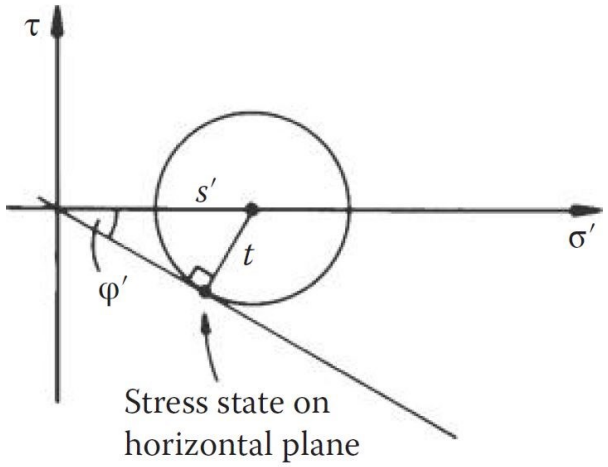

Figure 2.21 Mohr circle for the stress state assuming a horizontal shear plane from Powrie (2014).

The more realistic assessment of the stress state in the shearbox could be made by assuming that principle stresses are coincident with the directions of principle plastic strain *increments* (Rowe, 1969; Jewell and Wroth, 1987) resulting in the Mohr circle of Figure 2.22.

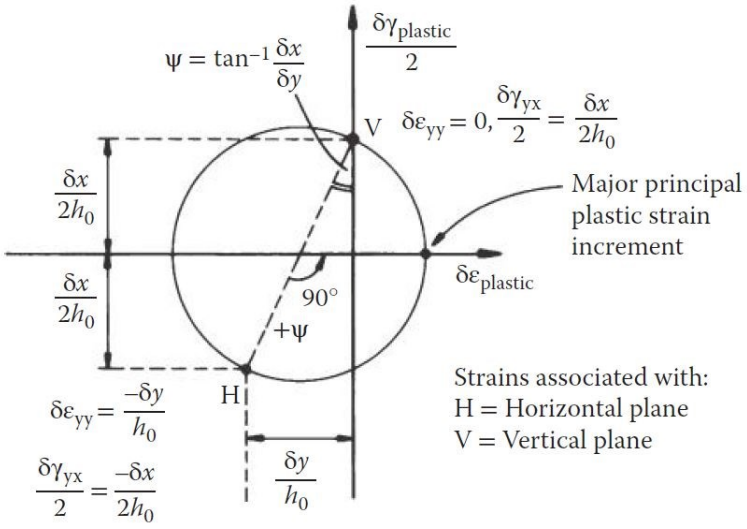

Figure 2.22 Mohr circle of plastic strain increment for a shearbox test from Powrie (2014).

Powrie (2014) details and shows mathematically that the angle of friction from the conventional interpretation relates to the alternate plane strain interpretation by:

$$sin\phi_{ps} = tan\phi_{ds} \qquad (Eq.2.30)$$

ϕ_{ps} = plane strain friction angle

ϕ_{ds} = conventional direct shear friction angle

Table 2.5 summarises the implications of *Eq* 2.30. Using the conventional approach to assessing the stress state in the shear box is likely to underestimate the angle of friction with the discrepancy increasing as the strength increases. Jewell and Wroth (1987) show that it is insensitive to angle of dilation. Powrie (2014) counsels for erring on the side of caution, as is the established approach in geotechnics. In pipeline geotechnics, however, the conservative approach varies between overestimating and underestimating soil and interface friction depending on the limit state under consideration. A single conservative value does not exist. For the purpose of this work the conventional approach to determining the stress state was adopted to be aligned with common industry practice, and to aid in the comparison of results with literature and published design standards.

Table 2.5 comparison of ϕ_{ps} and ϕ_{ds}

ϕ_{ps}	ϕ_{ds}	ϕ_{ps} / ϕ_{ds}
20	18.9	1.06
25	22.9	1.10
30	26.6	1.15
35	29.8	1.22

2.3.4 Flow rules

Measurements in a simple shear apparatus (SSA) and direct shear apparatus (DSA) have shown that at peak state the axes of principle stress and strain are coaxial (Cole, 1967; Stroud, 1971; Dyer, 1986). This assumption allows the measured soil friction angles (ϕ) in peak and ultimate states to be related to one another via the derived angle of dilatancy (ψ). The term *flow rule* is used to describe the relationship between dilatancy (a quasi-proxy for volume change) and soil friction angle. Lings and Dietz (2004) draws attention to the three flow rules which have gained most favour when describing sands. The first, from Taylor (1948), introduces the sawtooth model and imagines a soil grain being forced to over-ride its neighbours similar to were it being forced up the slope of a saw tooth in order to override the next grain. The angle of the incline on the sawtooth is equivalent to the measured soil dilatation angle and the work-done in achieving it manifests as the additional peak strength that densely packed soils mobilise in the initial stages.

$$tan\phi_{ds} = sin\phi_{cs} + tan\psi \qquad (Eq. 2.31)$$

Rowe (1962) devised a flow rule to consider plane-strain conditions:

$$sin\phi_{ps} = \frac{sin\phi_{cs} + sin\psi}{1 + sin\phi_{cs} \cdot sin\psi} \qquad (Eq. 2.32)$$

Bolton (1986) also developed a flow rule based on empirical observations taking the form:

$$\phi_{ps} = \phi_{cs} + 0.8\psi \qquad (Eq. 2.33)$$

Lings and Dietz (2004) showed that in their winged direct shear apparatus (WDSA, discussed later) both Bolton's (1986) empirical flow rule and a flow rule based on a Davis/Rowe framework designed to eliminate ϕ_{peak} and that is internally consistent between each cardinal parameter, were appropriate (Dietz, 2000). The latter Davis/Rowe framework showed the best fit to their data.

2.4 Interface shear testing

To measure the shear strength of a soil-surface interface it is necessary to measure the force that is required to cause or resist shear displacement between the soil and surface. Numerous apparatus have been developed or modified to meet such a requirement.

2.4.1 Direct shear apparatus

The direct shear apparatus when used for soil testing forces displacement along a horizontal plane within an included soil sample. The sample is contained within a split box which, when the upper and lower halves displace relative to one another, causes a shear band to form along the plane of the split. The force required to resist movement in the top half converts to shear stress using the known shear area dimensions of the shearbox. This arrangement can be easily adapted for interface shear testing by replacing one half of the box with a solid material. The shear plane then forms at the interface between the solid and particulate components of the shear box. Potyondy (1961) first systematically studied interface friction in the direct shear apparatus by replacing the lower half with a solid piece of steel, concrete, or wood, and depositing the soil on top. Other notable works adopting this methodology, albeit with different combinations of materials, include Butterfield and Andrawes (1972), Lehane *et al*. (1993), and Lings and Dietz (2005). Uesugi and Kishida (1986a) used a simple shear apparatus in a similar fashion. The general arrangement of a typical direct shear apparatus is shown in Figure 2.23 from Lings and Dietz (2004). It can be easily envisaged that replacement of the lower frame, which remains fixed in place relative to the shear carriage, with a block of some other material is straight forward to accomplish. Figure 2.24b after Uesugi and Kishida (1986b) shows how such an arrangement in the shear carriage might look and compares the

nature of the shear deformation within the soil sample between the direct shear apparatus and their simple shear apparatus.

The modern direct shear apparatus is displacement-controlled so is able to mobilise both peak and ultimate shear strengths and allows measurement of changes in sample height during testing. Total displacement is limited (typically to a maximum of approximately 15% of the shearbox length) so this method is not suited to continuous large-displacement shearing. However, cyclic test modes are easily accommodated and shearing occurs in a single plane with respect to the test surface and soil.

Owing to the simplicity of the direct shear apparatus (DSA), its use is widespread in the investigation of interface shear response. Various researchers have investigated the thickness the soil-surface interaction zone and determined shear zones of 6, 5 to 8, or 2 to 5 particle diameters in width (Nedderman and Laohakul, 1980; Yoshimi and Kishida, 1981a; Gudelus and Tejcham, 1988) which are all of similar magnitudes and fit well within the kinematic of the direct shear apparatus.

In some ways analogous to the direct shear apparatus is the Cam-shear device (Ganesan *et al*., 2013) which has a circular specimen sliding above a fixed surface in a similar fashion to an interface shear box in the direct shear apparatus. Like the DSA, the Cam-shear device has a controlled rate of displacement and the apparatus is relatively simple. However, is has limited horizontal displacement range and is unable to measure pore pressure.

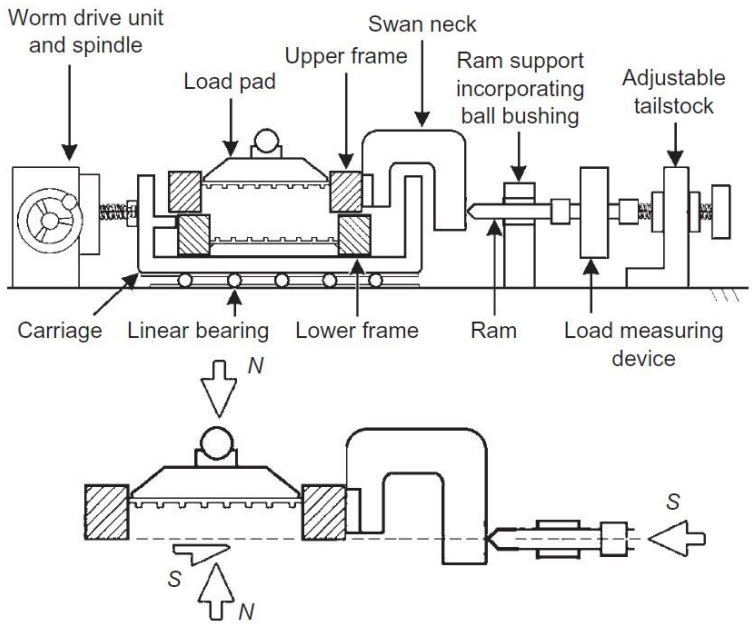

Figure 2.23 General arrangement and free-body diagram of the conventional direct shear apparatus (from Lings and Dietz, 2004).

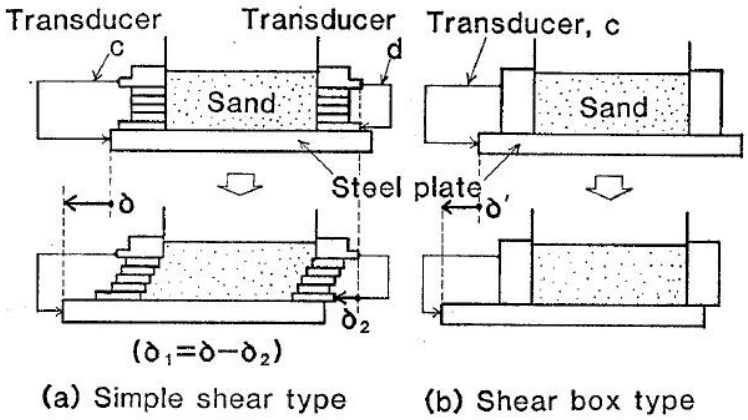

Figure 2.24 Comparison between interface test arrangements for (a) interface simple shear and (b) interface direct shear from Uesugi and Kishida (1986b).

The direct shear apparatus can adopt two loading modes, either adopting a constant normal load or by maintaining a constant normal stiffness. Constant normal load (CNL) uses a simple dead weight on a load hanger to apply a uniform load to the top of the sample and which remains constant throughout the test. CNL is the conventional direct shear arrangement. Boundary conditions in CNL testing are lateral confinement by the edges of the box and a constant vertical confining stress imparted by the deadload applied to the top cap. However, in some situations it may be advantageous to maintain a constant normal stiffness (CNS), which has applications in pile design where constant stiffness is more representative of the in-situ conditions at the soil-pile interface. In CNS conditions, the soil sample is still confined laterally by the shearbox, but the vertical confining stress is modulated through the test such that the stiffness of the sample remains constant. CNS testing can be applied to both soil testing (e.g. Ooi and Carter, 1987), and to interface testing (e.g. Porcino *et al*. 2003).

2.4.2 Ring shear apparatus

Ring shear devices adopt an anulus-shaped chamber in which a soil sample is prepared which means the soil sample has no edges in the circumferential direction allowing limitless displacement shearing. Bishop *et al*. (1971) first developed a ring shear device (Figure 2.25) which was later simplified by Bromhead (1979) (Figure 2.26) but the arrangement is still more complex than a direct shear apparatus.

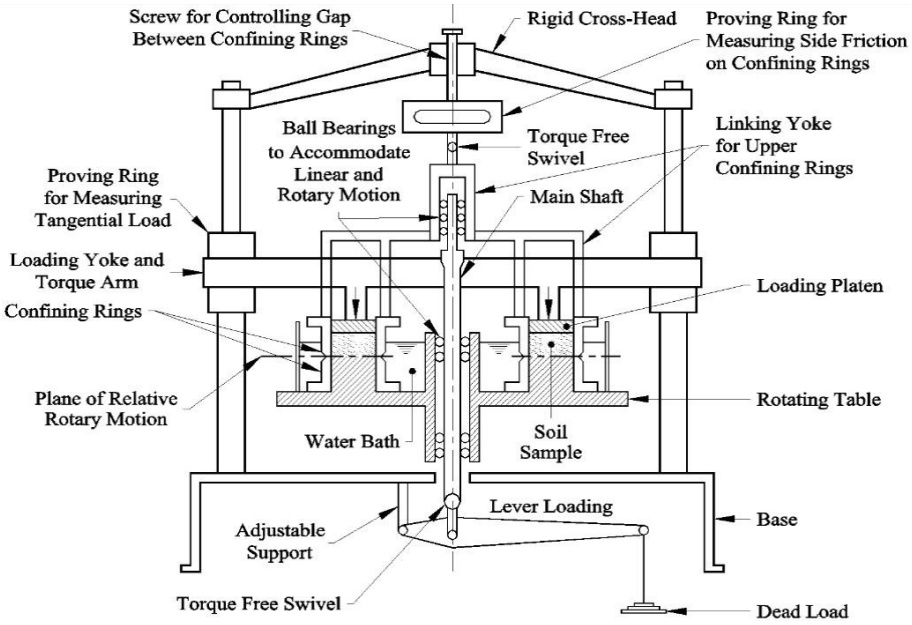

Figure 2.25 Schematic cross sectional view of the Bishop *et al*. (1971) ring shear apparatus from Ramsey *et al*. (1998).

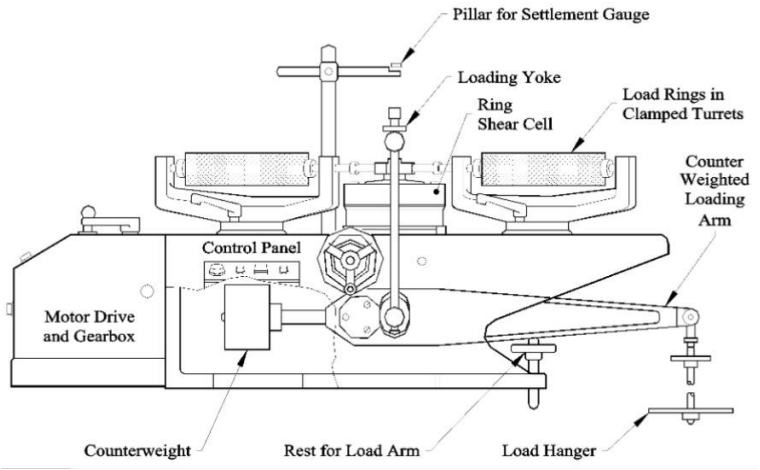

Figure 2.26 Schematic side view of the Bromhead (1979) simple ring shear apparatus from Ramsey *et al*. (1998).

Shearing along the horizontal plane through the middle of the sample is achieved by rotating one half of the ring which allows for continuous large displacement sample shearing. The ring shear apparatus is best suited to applications where large-displacements are expected including at interfaces between soil and solid materials, or where residual strengths are of interest.

Similar to the direct shear apparatus, one half of the ring shear can be replaced with a solid surface to test the shear strength at the interface. Such methods, or analogous techniques, are widely used for interface testing of both cohesive (e.g. Lupini *et al.,* 1981; Tika-Vassilikos, 1991) and granular soils (e.g. Yoshimi and Kishida 1981a; Quinteros *et al*., 2017).

Similar in nature to the ring shear device is the Cam-Tor device (Kuo *et al*., 2015; De Brier *et al*., 2016) which instead has a circular interface rotating under a fixed specimen. The Cam-Tor has less machine friction than ring shear, and smaller in-tact samples can be used, but there is significantly greater strain-rate variation radially across the specimen than in ring shear.

2.4.3 Tilt-table testing

A tilt-table is an apparatus which allows a surface specimen (or indeed a model structure such as a length of pipe) to be placed on a surface which can be inclined. Normal loads can be applied and the experiment suitably instrumented with the key output parameter being the angle of inclination of the table at the point where shearing occurs and the object or specimen slides down the table. A schematic diagram of a tilt-table test showing a pipe coating and clay soil interface is shown in Figure 2.27. Tilt-table testing has been extensively used in the investigation of geosynthetic interface strengths (e.g. Lopes *et al.,* 2001; Narejo, 2003) and has also gained common usage as a method of investigating interface friction for flowlines and pipelines (e.g. Pedersen *et al.,* 2003; Najjar *et al*., 2007; Randolph and Gourvenec, 2011; Houhou *et al*., 2020).

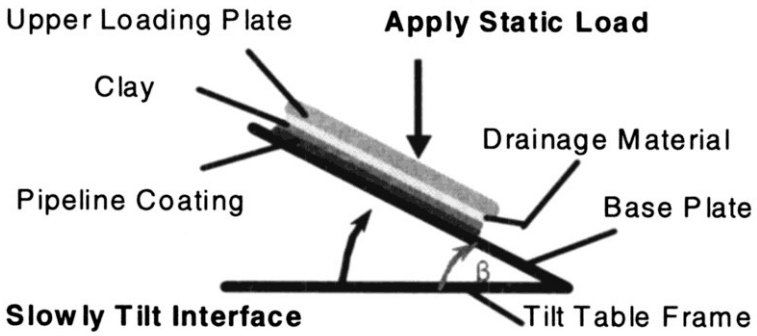

Figure 2.27 Schematic diagram of a tilt-table interface test from Najjar *et al*. (2007).

Tilt-table testing allows for determination of an angle at which sliding begins to occur but they are difficult to instrument so the range of possible parameters is limited when compared to direct or ring shear alternatives. However, the possibility for using models of the structure in question potentially allows for geometric effects to be studied, such as pipe curvature at the interface contact.

2.4.4 Pull-out test

Prior to the use of polymers in rigid form in offshore and pipeline engineering, their primary use in geotechnical engineering was in the form of flexible geotextile. The pull-out test is a commonly used method for determining the pull-out resistance of a geomembrane or geotextile (Yogarajah and Yeo, 1994) when sandwiched in a host soil and under a confining load. The pull-out test also includes a passive resistance component so the output is defined in terms of soil-membrane pull-out interaction coefficient, or in terms of an effective friction coefficient (Negussey, 1989; Mirzaalimohammadi *et al*., 2019). Pull-out test apparatus can vary in specific detail depending on the type of material being tested, but an example of a pull-out test rig is presented in Figure 2.28 from Işık and Gürbüz (2018). The geomembrane or geocell is sandwiched in the test soil and confined between two plates with a confining stress applied. The force required to retract the test material is measured and a friction coefficient can be determined.

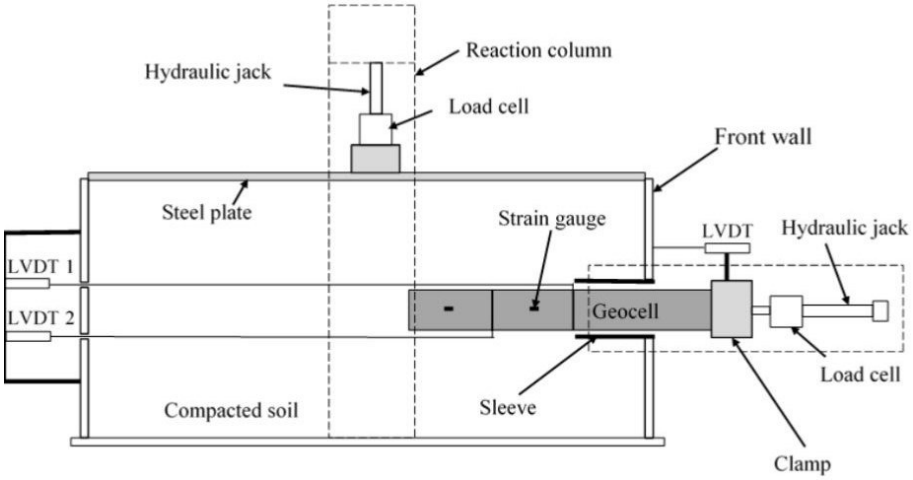

Figure 2.28 Schematic diagram of a pull-out test apparatus from Işık and Gürbüz (2018).

2.4.5 Friction sleeve test

In addition to the laboratory techniques discussed, reliable in-situ methods are always desirable to eliminate sampling disturbance and to test under the real and relevant stress conditions. To this end a multi-sleeve friction tool was developed by Frost and DeJong (2001) and DeJong and Frost (2002) which attaches behind a conventional CPT cone and comprises of four zones of different surface roughness from which in-situ determination of soil-surface friction coefficient can be made. A drawing of the arrangement is shown in Figure 2.29 from Frost and DeJong (2005).

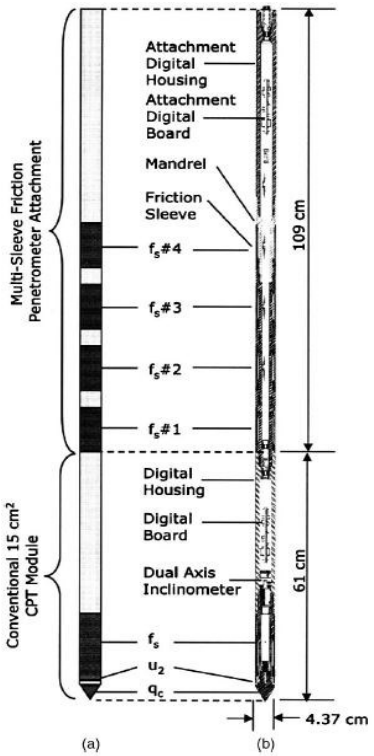

Figure 2.29 Multi-sleeve friction penetrometer (a) schematic and (b) design detail from Frost and DeJong (2005) after DeJong and Frost (2002).

2.4.6 Interface test mode

Numerous apparatus and combinations of surface materials and soil have been tested by many researchers. However, in the case of direct shear and ring shear apparatus, interface testing can be further split into two modes; surface-over-soil and soil-over-surface testing, also referred to as Type-A and Type-B testing (Subba Rao *et al*., 1998) though for clarity they shall be referred to by their full descriptors. Schematic diagrams depicting the two modes are presented in Figure 2.30. Disagreements in the literature relating to test mode principally relate to the mobilisation of peak strengths and the influence of density on shear strengths.

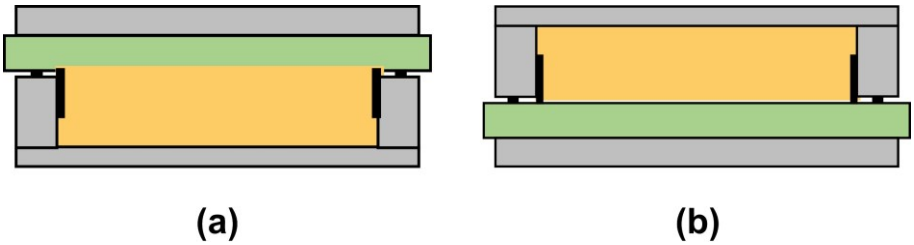

Figure 2.30 Schematic representation of (a) Type-A surface-over-soil configuration and (b) Type-B soil-over-surface configuration.

Density

Unlike soil-only tests where ultimate strength is independent of density, its influence on interface strength is not settled in the literature with further disagreement between surface-

over-soil and soil-over-surface test modes. Butterfield and Andrawes (1972) established that interface friction had a dependence on the density of the soil and Acar *et al*. (1982) found that the interface efficiency (the ratio between interface strength and equivalent soil-only strength) was independent of relative density though their work only included one soil and surface whose properties are both unknown. Jardine *et al*. (1993) and Porcino *et al*. (2003) found that in soil-over-surface sand-steel and sand-aluminium interfaces respectively, that with different roughness the critical state interface strength was independent of density but reported increasing peak strengths with density consistent with soil-only tests. Similarly, in a surface-over-soil configuration Yoshimi and Kishida (1981a) and Noorany (1985) found using a ring torsion apparatus and direct shear apparatus respectively with steel-soil interfaces that ultimate strengths were independent of density.

Peak strengths

Though Jardine *et al*. (1993) and Porcino *et al*. (2003) observed that ultimate shear strengths were independent of sample density, there was an increasing peak strength with density which is consistent with equivalent soil behaviour. Subba Rao *et al*. (1998) observed that maximum interface shear strength from surface-over-soil configurations is analogous to the ultimate shear strength from soil-over-surface configurations while the latter is also able to mobilise peak shear strengths. Uesugi and Kishida (1986a) offer an explanation related to disturbance of the upper surface when samples are prepared in surface-over-soil type tests. In soil-over-surface tests soil is placed onto the surface specimen ensuring good soil to surface contact which remains undisturbed before testing. However, in the case of surface-over-soil tests the surface is placed onto the soil sample which necessarily disturbs the upper layers of grains and forces localised rearrangement to accommodate the emplaced surface texture. In this way the soil-surface shear zone has already been disturbed and pre-sheared so interface stress response is limited to an ultimate strength condition.

The general pattern in the literature appears to be that for soil-metal interfaces there is little difference in the ultimate shear strength between the two interface test configurations and that is it independent of sample initial density. Additionally, surface-over-soil configurations are only able to mobilise an ultimate strength as peak-postpeak behaviour is a feature only of soil-over-surface arrangements if there is sufficient surface texture to induce dilation.

Polymers

O'Rourke *et al.* (1990) observed that interfaces comprising polymers tested in soil-over-surface configuration did experience enhanced maximum interface shear strength with increased sample density, just as in sand-steel interfaces. However, the response of smooth

polymer interfaces is such that the peak and ultimate shear strengths are analogous so the increased strength manifests also as an increase in the ultimate shear strength, contrary to the findings of the authors working with sand-steel. It could be assumed that interface testing of polymers in surface-over-soil configuration would follow the pattern of steel interfaces and achieve an ultimate strength independent of density.

2.5 Interface shear mechanics

The mechanics of shearing in interface zones and the interaction between soil grains and surfaces is multifaceted and depends in varying degrees on the components discussed previously. Potyondy (1961) first carried out a systematic investigation of interface behaviour for various soils and construction materials and established the idea of interface efficiency, or the ratio between the interface strength and the equivalent soil-only strength. Butterfield and Andrawes (1972) and Acar *et al*. (1982) later carried out studies investigating other pertinent parameters such as relative density and stress level.

Numerous studies have been conducted investigating polymer interfaces, particularly with respect to geomembranes (e.g. Ingold, 1982; Saxena and Wong, 1984; Negussey *et al*., 1989; Williams and Houlihan, 1987; Dove and Frost, 1999). O'Rourke *et al*. (1990) investigated a range of polymers with reference to their application in pipeline coating materials. Common to polymer interface investigation findings is their relatively low angles of shearing resistance compared to steel or concrete interfaces. The various inter-related factors contributing to interface shear mechanics are discussed.

2.5.1 Hardness

Surface hardness is more usually considered for "softer" more deformable materials such as polymers rather than "harder" materials like metals or concrete where other properties are considered to be more dominant. Measurement of surface hardness of a polymer is most typically carried out with a Shore durometer; in the field of interface testing this is best exemplified in O'Rourke *et al*. (1990). A durometer contains a preloaded spring and actuation of the protruding indentor compresses it which converts linearly to a scale from which a reading can be taken. The greater the compression of the spring during indentation the greater the hardness of the surface. Different durometers exist applicable to different ranges of measurement where spring stiffness and indentor tip shape vary. Mix and Giacomin (2011) thoroughly discuss durometry in the context of polymers and proposed a non-dimensional factor to define mechanical indentability, M_i, based on Young's Modulus determined from the durometer test such that surfaces measured with different apparatus may be directly

compared. However, in the literature polymers applicable to pipelines fall within the useful range of a single scale, Shore D, and its use is commonplace so it is sufficient to simply quote the Shore D reading directly from the instrument. The Shore D durometer consists a 30° cone with diameter 1.4 mm and 2.54 mm extension and functions simply by pressing the indentor into the surface and reading the value directly from an analogue dial gauge.

O'Rourke *et al*. (1990) carried out a systematic investigation into the relationship between interface strength and the hardness of various polymers adopting Shore D to quantify hardness. Their findings are best shown as in Figure 2.31 which compares interface efficiency and polymer hardness.

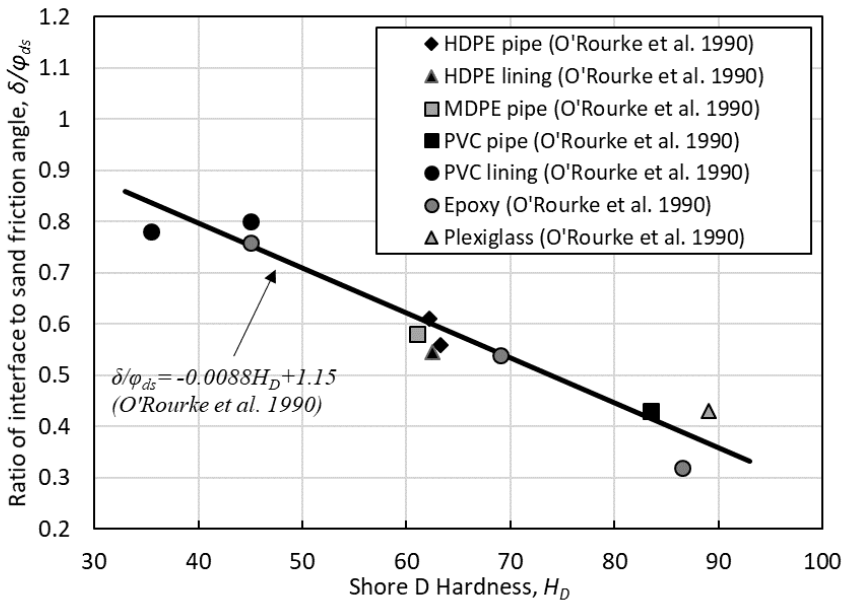

Figure 2.31 Interface efficiency and surface hardness after O'Rourke *et al*. (1990).

O'Rourke *et al.* (1990) demonstrated a clear dependency of interface strength on surface hardness for polymers. The context of their investigation was pipelines and coating materials but polypropylene, the subject of this thesis, was not included – perhaps because its use in this application is relatively recent. For reference, the polypropylene specimens available for use in this research had a hardness in the ranging of 70-75 Shore D which will be discussed later.

2.5.2 Surface texture

In addition to the mechanical properties of a surface, the shape and topography of the surface texture plays a key role in controlling shear behaviour at the interface. Broadly speaking, surface texture can be broken down into form, waviness, and roughness components whose

net profile makes up the surface. There is no set distinction between features of form, waviness, and roughness as it depends on the application or relationship to adjacent materials. Figure 2.32a shows a schematic representation of surface form, waviness, and roughness to illustrate the distinctions. Each feature type has the same amplitude but manifests as a very different surface texture. The overall net surface shape combines these different features to give a surface texture schematically shown in Figure 2.32b.

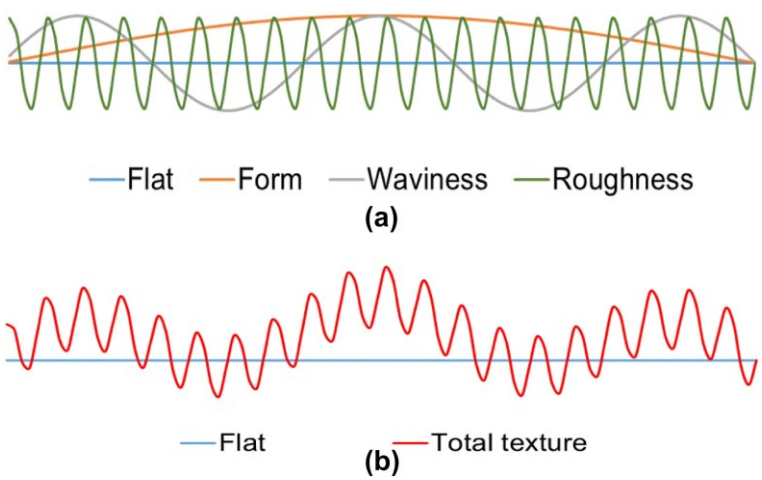

Figure 2.32 Schematic representation (not to scale) of (a) surface, form, waviness, and roughness and (b) total net surface texture.

Surface texture can be measured through profilometry which typically converts vertical movements of a stylus tip traversing a surface into a digital file containing ordinates defining the two-dimensional surface profile. Profilometry is a widely used technique in the field of tribology and has been used extensively for measurement of surface textures during interface investigations e.g. Dove and Frost (1999), Dove and Jarrett (2002), Lings and Dietz (2005), Han *et al.* (2018) among many others.

In recent years improvements in technology have allowed the development of alternative techniques for measuring surface texture. Optical methods using focus variation offer an alternative to dragging a stylus tip across a surface to measure its topography. To the author's knowledge this technique has not previously been used in application to soil-structure interfaces and soil mechanics and the equipment available at University of Bristol comes from the world of composite materials research and aerospace engineering. Traditional stylus-tipped contact profilometry methods have been widely used on steel surfaces because the dominant research interest has been steel pipelines and piles. However, the focus of this thesis is on the softer polypropylene coatings and there is a concern that a hard stylus tip could cause damage to a surface and destroy asperities (Conroy and Armstrong, 2005; Slade and Yip, 2005; Lee, 2013), thereby under-measuring surface topography. Non-contact optical methods scan a surface and use focus-variation and computer algorithms to convert the

information into a three-dimensional surface from which the chosen texture parameters may be extracted. These competing methods are tested and discussed as part of this thesis.

2.5.3 Roughness (ISO 4288:1998)

In contrast to “softer” surfaces like polymers which are prone to indentation and are generally categorised as smooth with a negligible component of surface texture contributing to interface mechanics, “harder” surfaces like metals are typically described in terms of various surface texture parameters. The most relevant surface texture descriptor is surface roughness with two parameters in most common usage, R_a and R_{max}, the average roughness and maximum roughness, respectively. R_a and R_{max} are schematically demonstrated in Figure 2.33. R_a is the arithmetic mean average of deviations from the centre line of a profile whereas R_{max} is the single largest measured amplitude feature.

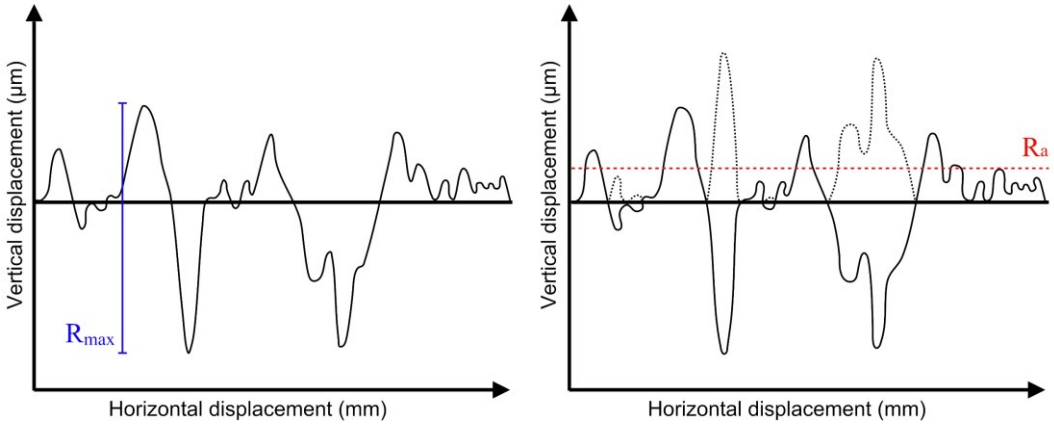

Figure 2.33 Representation of R_{max} and R_a from a digitised trace of a real surface.

Traditionally the techniques for measurement of surface texture and determining roughness were developed from the need to assess surface finishes as a result of industrial processes such as polishing and machining of metals. ISO 4288:1998 Geometric Product Specifications (GPS) is the relevant standard for determination of surface finish roughness parameters and provide guidelines for the selection of the appropriate filters to isolate roughness from form and waviness components. Three terms are important here: the evaluation length, which is the total length of the profile, the sampling length, which is a subset of the evaluation length, and the L_c filter cut-off which isolates undesirable long wavelength information from the results. Selection of the appropriate L_c filter according to ISO 4288:1998 depends largely on the nature of the surface texture and whether it can be characterised as a periodic or non-periodic profile. Non-periodic profiles seem to require the roughness to be known before selecting the appropriate measurement parameters used to determine the roughness in the first place,

which is problematic. Another complication arises when there is a conflict between the R_z and R_a determinant if the surface parameters fall into different categories. Further stipulations of ISO 4288:1998 govern the choice of sampling length which should be equal to the L_c cut-off length. The evaluation length must be equal to five times the sampling length. The recommended measurement parameters are summarised in Table 2.6. The *RSm* term for periodic profiles can be thought of as analogous to the wavelength of a surface texture, and the R_z term is the average of successive R_t values over the evaluation length. R_t is similar to R_{max}.

Table 2.6 Recommended measurement parameters according to ISO 4288:1998

Periodic Profiles	**Non-Periodic Profiles**		**Cut-off**	**Roughness Sampling Length**	**Roughness Evaluation Length**
RSm (mm)	R_z (μm)	R_a (μm)	L_c (mm)	L_r (mm)	L_n (mm)
0.013 – 0.04	<0.1	<0.02	0.08	0.08	0.40
0.04 – 0.13	0.1 – 0.5	0.02 – 0.1	0.25	0.25	1.25
0.13 – 0.4	0.5 – 10	0.1 – 2.0	0.80	0.80	4.00
0.4 – 1.3	10 – 50	2 – 10	2.50	2.50	12.50
1.3 – 4.0	>50	10 - 80	8.00	8.00	40.00

Due to the provenance of profilometry as a tool for assessing surface finishes from a manufacturing process it may not be surprising that determination of roughness in this way is not best suited to characterising the roughness pertinent to interaction between continuum and particulate media such as at surface-soil interfaces. ISO 4288:1998 deals with the surface in isolation and does not account for the interaction with soil or consider the notion of an effective roughness.

2.5.4 Relative roughness

It has long been recognised that roughness in itself is not a particularly useful parameter as the impact on shearing behaviour is related also to the grain size because the effective roughness is a product of meshing between grains and the surface. Yoshimi and Kishida (1981b) first proposed the term R_n for normalised roughness as the measured roughness divided by the mean grain size giving:

$$R_n = R_{max}/D_{50} \qquad (Eq. 2.34)$$

Kishida and Uesgui (1987) further refined the term by obtaining the roughness over a profile length equal to D_{50} instead of the more accepted L = 2.5 mm which better captured the

relationship between grain size, roughness, and the length over which soil-surface interaction actually takes place. Using normalised roughness in this way they showed a reasonable linear relationship between interface shear strength and roughness. The concept of normalised roughness determined in this way is shown schematically in Figure 2.34.

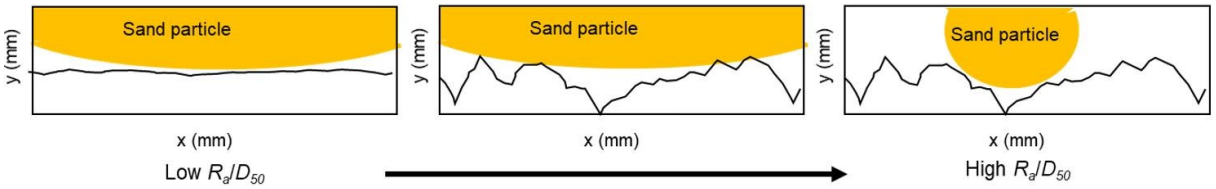

Figure 2.34 Conceptualisation of relative roughness.

Relationships between granular media and continuum surfaces of varying roughness have considerable precedent. Uesugi and Kishida (1986b) used Toyoura sand, and Paikowski *et al*. (1995) used glass beads to establish the notion of a fully smooth, fully rough, and an intermediate zone in the relationship between normalised roughness and interface shear strength. Their findings are summarised in Figure 2.35 from Lings and Dietz (2005). The discrepancy between the two trends is likely related principally to angularity effects.

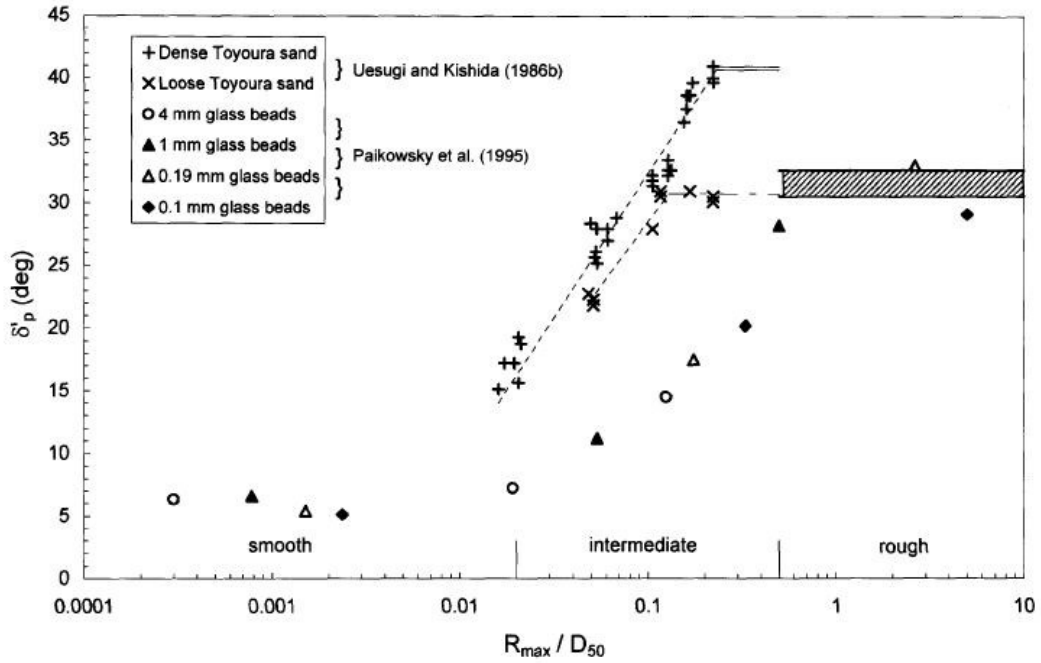

Figure 2.35 Peak interface friction and normalised roughness after Uesugi and Kishida (1986b) and Paikowsky *et al*. (1995).

Interface friction angles in the fully rough zone were found to be analogous to the equivalent soil-only strength. Jardine *et al.* (1993) and Subba Rao *et al.* (1998) adopted a similar methodology but used R_a instead of R_{max} and fitted S-shaped curves to data plotted also on semi-logarithmic plots as in Figure 2.36.

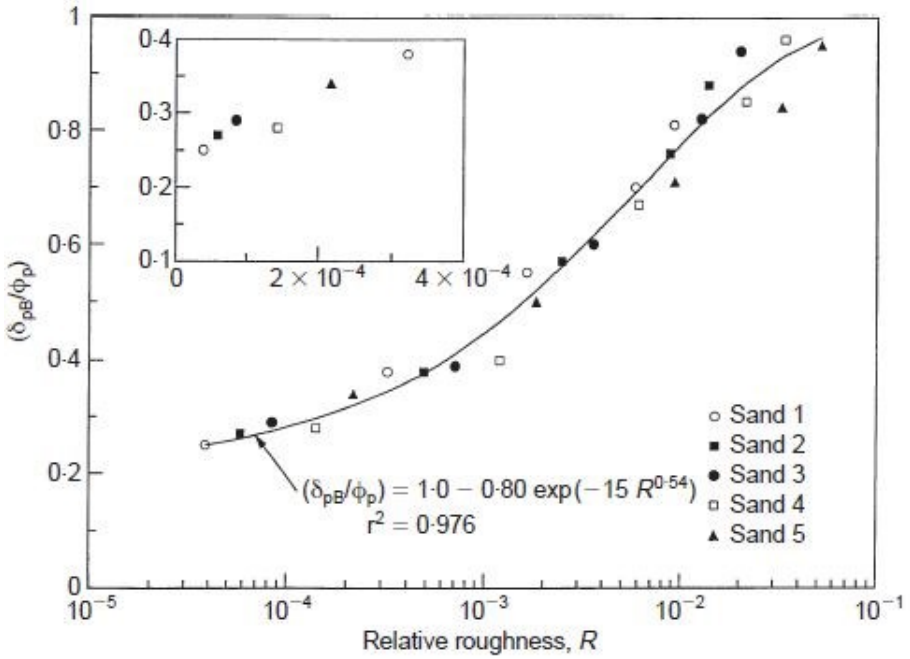

Figure 2.36 Variation in interface efficiency with relative roughness from Subba Rao *et al*. (1998).

Yoshimi and Kishida (1981a) first showed dilative behaviour of interfaces and Dove and Jarrett (2002) went on to show that interfaces with both “harder” metallic and “softer” geosynthetic surfaces exhibited non-dilative and dilative behaviour corresponding to the “smooth” and “rough” zones previously discussed. Lings and Dietz (2005) carried out a study of interface roughness using a range of different sand types and techniques to create surfaces of varying roughness. They established that greater normalised roughness leads to increasing dilatancy and commensurately greater peak interface shear strengths. They found that both R_{max} and R_a were effective when normalised by D_{50} in distilling interface strength-roughness into a unique relationship. Dietz and Lings (2006) extended the work to include the post-peak or ultimate strength of interfaces along the same lines. Relationships for sand-steel peak and postpeak interface strength and normalised roughness are shown in Figure 2.37 after Lings and Dietz (2005) and Dietz and Lings (2006).

To the author’s knowledge, there is no precedent for establishing analogous relationships between rigid polymer surfaces as applicable to pipeline coatings, and their surface texture and, with the notable exception of O’Rourke *et al.* (1990). The majority of work on polymers revolves around flexible geosynthetics and membranes. Dove *et al*. (1997) investigated the interface shear strength of roughened geomembranes and sand and found that at the lowest stress level they tested, 50 kPa, the secant angles of friction ranged between 20° and 42° for peak (although relative densities are not given) and 18° and 30° for residual conditions.

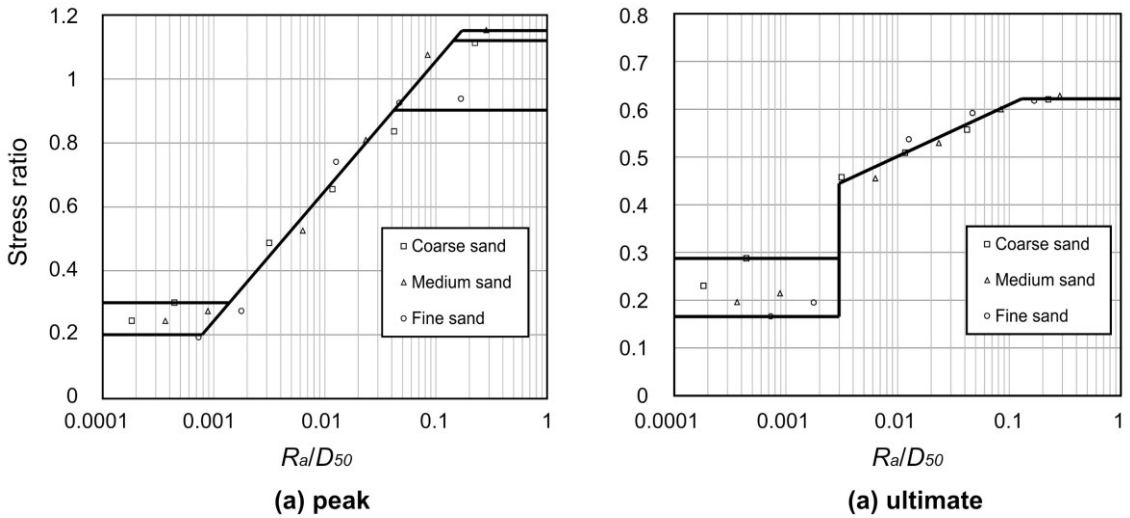

Figure 2.37 Sand-steel interface stress ratio and relative roughness for (a) peak and (b) postpeak (ultimate) condition after (a) Lings and Dietz (2005) and (b) Dietz and Lings (2006).

2.5.5 Grain kinematics

On hard surfaces such as concrete and steel, grains are thought to shear across the surface through sliding and any rotations are caused by the interaction between surface asperities and neighbouring soil grains. However, polymers are relatively smooth so surface asperities do not feature sufficiently to influence the mode of grain motion across the surface. O'Rourke *et al*. (1990) recognised that the mechanism of shear transfer and grain dynamics across the surface played a role in the relationship between surface hardness and shear strength shown in Figure 2.31. Scanning electron microscope (SEM) photos of post-shearing surfaces revealed a striated appearance for harder surfaces and a pockmarked appearance for softer surfaces. Striations were considered to have been caused by grains sliding and scratching the surface and pockmarking caused by grains rolling and localised stress concentrations at grain asperities causing indentation of the surface. The processes are illustrated in Figure 2.38 from O'Rourke *et al*. (1990). It can be easily envisaged that grain indentation and rolling requires more energy than simple sliding, hence the inverse relationship between interface strength and polymer hardness.

Interface strength failure envelopes in terms of shear and normal stress are typically constructed as straight lines passing through the origin. However, Dove and Frost (1999) noted that in fact the failure envelope is slightly concave upward caused by curvature at higher normal stresses and flattening at lower stress (in the range of up to 350 kPa normal stress). Two components are known to contribute to the force required to promote shearing, an adhesion component and a ploughing (or plastic deformation of the surface) component (Shooter and Tabor, 1952; Bowden and Tabor, 1956; Adamson, 1982; Briscoe, 1992). The

adhesion and ploughing components are shown schematically in Figure 2.39 from Dove and Frost (1999) after Briscoe (1992).

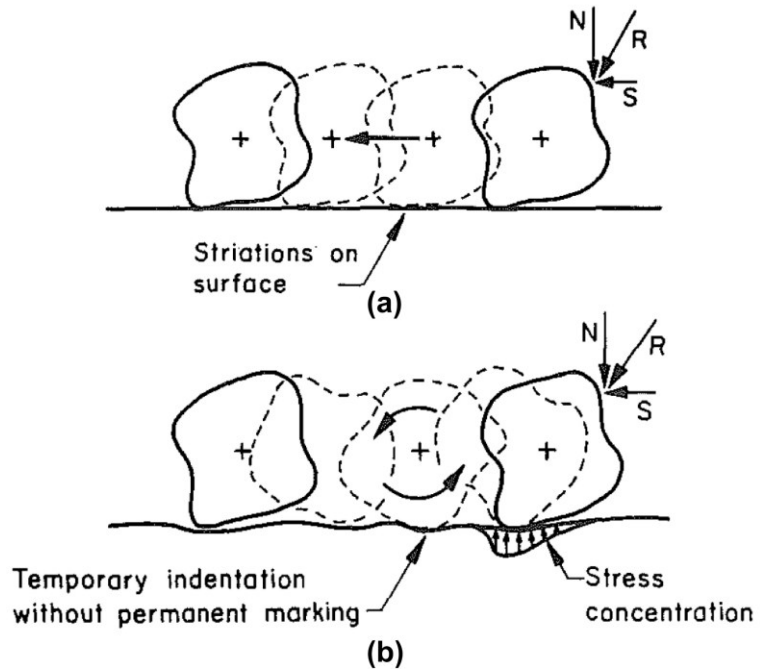

Figure 2.38 Schematic representation of (a) grain sliding and (b) grain rolling from O'Rourke *et al*. (1990).

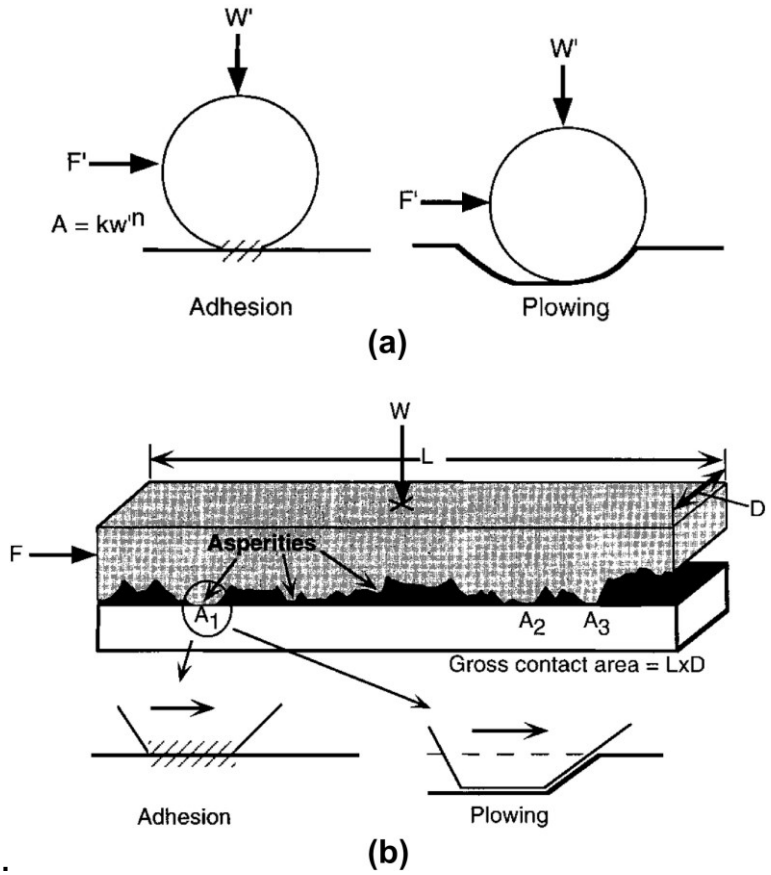

Figure 2.39 Interface frictional adhesion and ploughing for (a) single point and (b) multiple asperities from Dove and Frost (1999) after Briscoe (1992).

The adhesion factor is related to the shear strength of the material and the ploughing component related to the bulk strength of the material. The ploughing term becomes significant where there is a large discrepancy between the hardness of the two shearing materials as in the case of a predominantly quartz-based sand sliding across a polymer surface. Shooter and Tabor (1952) showed that ploughing results in higher friction than sliding alone due to the energy required to push through the counterface material. It is not surprising then that if softer materials precipitate greater grain ploughing then the overall shear resistance is greater which is precisely what O'Rourke *et al.* (1990) demonstrated to be the case. Further, given the ploughing term is related to indentation and the bulk strength of the surface material it is also not surprising that failure envelopes for polymer interfaces are concave upward at higher normal stress. Greater normal stress leads to greater indentation and, therefore, an increase in overall resistance to sliding.

However, at low normal stress (e.g. less than 50 kPa) Dove and Frost (1999) observed that there was an enhancement to polymer shear strength with lower stress level. Their experimental campaign yielded the relationship shown in Figure 2.40. They theorised that for a given patch of soil-surface contact, an increasing number of particles would be pressed into the surface as the normal stress increased. The result is a greater number of soil-surface contacts giving a lower contact stress at each point and, therefore, mobilising less shear resistance. This phenomenon occurs at stresses low enough that grain indentation and ploughing mechanics become significant as has been discussed, and shear resistance rises again. The nature and stress level at which the transition occurs is likely to depend on the hardness ratio between soil and surface.

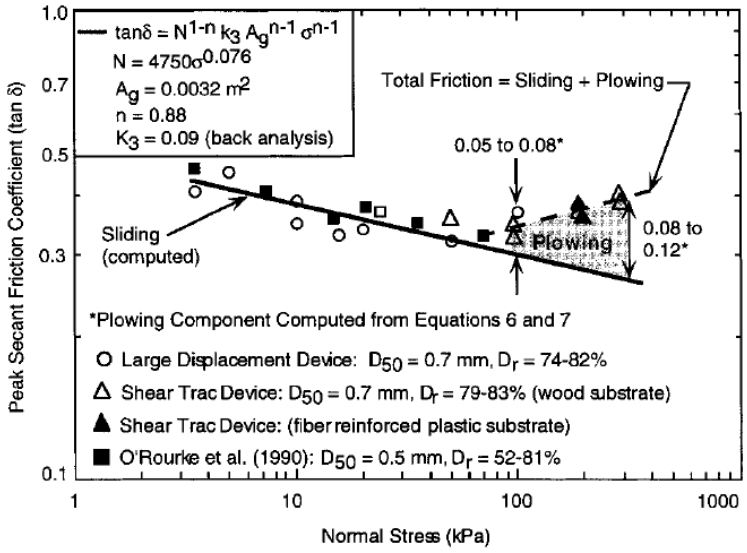

Figure 2.40 Smooth HDPE geomembrane-Ottawa Sand interface shear strength and mechanisms after Dove and Frost (1999).

2.5.6 Coupled hardness and roughness

Both hardness and roughness are known to influence the shear strength of interfaces. Frost *et al*. (2002) developed a coupled model using Discrete Element Modelling (DEM), and validated against experimental results, to predict peak and residual (ultimate) interface strengths based on surface hardness and roughness. Their model outputs are shown in Figure 2.41. The hardness scale used here is an equivalent hardness based on the Brinell scale and converted to a particle-continuum friction coefficient to mimic the hardness mechanic in the DEM. Figure 2.41 is illuminating in terms of examining the interaction of roughness and surface hardness and shows that the effect of hardness is far more pronounced where roughness is low. When roughness increases, dilation occurs which enhances the peak strength, and the residual (ultimate) strength is then mobilised along a soil-soil shear band above the surface mitigating any mechanical property the surface may have.

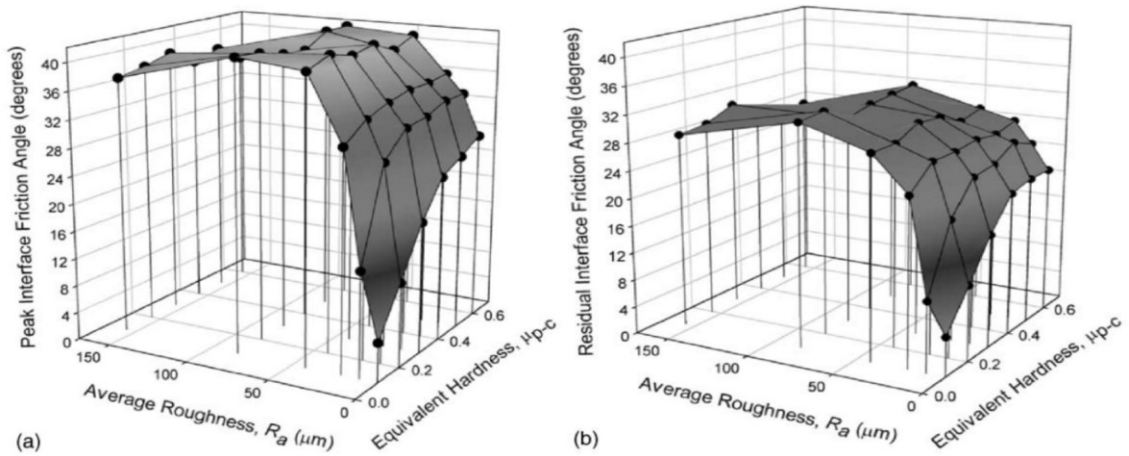

Figure 2.41 Relationship between surface roughness, hardness, and interface friction from DEM with uniform grain size for (a) peak and (b) residual (ultimate) conditions after Frost *et al*. (2002).

2.5.7 Interface flow rules

Flow rules relating peak shear strengths to critical state strength and volumetric behaviour through the use of dilatancy during shearing have been discussed for soils. Flow rules have also been proposed to perform a similar function for interfaces. Lings and Dietz (2005) proposed a flow relation for sand-steel interfaces echoing the simple saw-tooth model of dilation where any increase in strength above the ultimate condition is entirely from dilation:

$$\delta_{peak} = 25° + \xi_{peak} \qquad (Eq. 2.35)$$

where:

δ_{peak} = peak interface angle of friction

ζ_{peak} = peak angle of interface dilation

The flow relation is related to the roughness of the surface and is determined empirically where 25° is the interface angle of friction at which dilation becomes non-zero and begins to contribute to additional strength. This is in contrast to flow rules discussed previously for soil-only where flow rules relate the ultimate strength to the peak strength and is unique to each test and internally consistent. It may, therefore, be expected that an interface flow relation framed in this way is unique to a particular surface.

A study of sand and glass bead interfaces with woven geotextile and angular sand with steel by Afzali-Nejad *et al*. (2017) suggests that for dilative interfaces, a flow rule relating peak to residual strength by approximately the dilation angle as per Taylor's (1948) original model, is still appropriate. Their relation suggests that close, or even slightly more than, the full magnitude of dilation contributes to the mobilisation of peak strengths:

$$\delta_{peak} = \delta_{res} + 1.05\xi_{peak} \qquad (Eq. 2.35)$$

where:

δ_{res} = residual interface angle of friction

2.6 Enhanced interface shear strength

Numerous studies impose the equivalent soil strength as an upper limit on interface strength, so called "$\delta = \phi$ conditions" (e.g. Uesgui and Kishida, 1986a; Subba Rao *et al*., 1998; Dove and Jarrett, 2002; Lings and Dietz, 2005; Dietz and Lings, 2006). However, some studies also posit that "$\delta > \phi$ conditions" are possible when surfaces have extreme profiles of roughness (e.g. Irysam and Hryciw, 1991; Hryciw and Irysam, 1993; Frost and DeJong, 2005; Hebeler *et al*., 2015). Although there are differences in test methodology, loading conditions, and application, the key distinguishing feature is the nature of the surface texture in question. Surfaces can be considered to have a randomised texture or a structured texture, the difference relating to whether the surface asperities and textural components become clogged with soil or not (Martinez and Frost, 2017). Clogged surfaces refer to surfaces where the texture becomes infilled with soil grains which remain immobile and do participate further in

the soil-surface shear interaction. Where surfaces become clogged "$\delta = \phi$ conditions" prevail imposing an upper limit on interface shear strength equal to the equivalent soil strength. Non-clogging surfaces allow soils grains to remain participant in soil-surface interaction during shearing and the formation of passive wedges is thought to contribute to the potential for "$\delta > \phi$ conditions". The phenomena of clogging and passive resistance in this context is illustrated in Figure 2.42 from Martinez and Frost (2017).

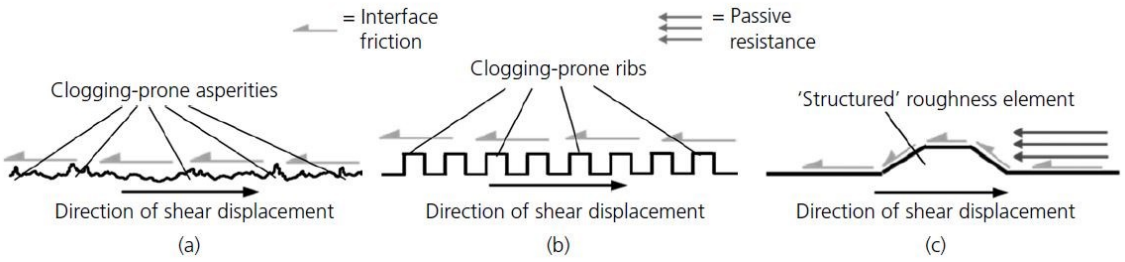

Figure 2.42 Load transfer mechanism during shear against surfaces of (a) random, (b) ribbed, and (c) structured roughness form from Martinez and Frost (2017).

Straight forward techniques such as sandblasting of surfaces, particularly metallic ones, are easy to accomplish and were used to great effect by Lings and Dietz (2005). They also resorted to gluing grains of sand to steel plates to achieve a fully rough response, although this can probably not be considered to be a truly rough soil-surface interface, but rather mimicking the soil-soil condition. Such interfaces fall within the category of randomised, clogging-prone surfaces shown in Figure 2.42.

Irsyam and Hryciw (1991) and Hryciw and Irsyam (1993) carried out studies on surfaces with a ribbed texture of various spacing and geometries with the average approach angle of the asperity directly linked to the dilation angle and strength of the soil, though limited to an upper bound equal to the equivalent soil-only angle of dilation. Dove and Jarrett (2002) carried out an extensive investigation of structured roughness interfaces and found the interface efficiency depended also on the asperity height (normalised by the soil grain size) and the asperity spacing. Dependent on spacing and angle of asperities, these interfaces may be either the clogging-prone or non-clogging structures shown in Figure 2.42.

An additional perspective on these considerations is the potential for surface textures which mobilise variable interface shear strength depending on the direction of displacement. Martinez *et al*. (2019) and Stutz *et al*. (2019) explored such a possibility with snake-skin inspired surface textures which were able to mobilise up to 225% greater skin friction in piles, and a stress ratio difference in the region of 0.4 in interface shear box testing, in one direction compared with the reverse. It can be imagined how such a technology might be beneficial in application to pipelines where low pipe-soil friction leaves a pipeline susceptibly to walking

where asymmetric pipe-soil friction could promote return to an initial position. Similarly, asymmetric interface friction could be used to inhibit walking but un-constrain buckling.

2.7 Cyclic Interface testing

Cyclic effects are an important extra dimension to many offshore projects. In the case of pipelines, repeated start-up and shut down cycles can lead to cyclic movement, axially which can lead to pipeline walking, or laterally which can lead to further embedment or build-up of soil berms. Additionally, cyclic loading of an interface can cause evolution of the surface particularly in terms of roughness, and lead to changes in interface shear strength.

Fakharian and Evgin (1997), using constant normal stiffness in simple shear, and DeJong *et al*. (2003), using a modified direct shear apparatus and Particle Image Velocimetry PIV (White *et al*., 2001), both found that interface strength for hard metallic surfaces reduced with increasing cycle number. DeJong *et al*. (2003) found reductions in shear strength of between approximately 20 and 50% with their uncemented test sands and observed that the thickness of the shear band increasing with more cycles. As these experiments were conducted with steel or aluminium coated with sand, surface evolution is likely to have been a minor factor in any strength evolution. There is limited directly applicable element-scale research for rigid polymer surfaces, the majority of polymer testing being related to geotextiles and geomembranes (e.g. Vieira *et al*., 2013; Wang *et al*., 2016). In contrast to pipe coatings, those materials are flexible or gridded, and they are designed to improve soil stiffness which was confirmed by those authors.

Large-scale cyclic tests of plastic-coated steel pipes and polyethylene pipes were carried out by Kobayashi *et al*. (1995) and Bilgin and Stewart (2009) respectively. They tested buried pipes and found axial shear strength reduced by 70 to 75% over 10 cycles (equivalent to about 1000 mm cumulative displacement). Though not cyclic, similar levels of strength reduction (~60%) were reported by Dove *et al*. (2006) with HDPE sheet when testing a single particle-surface contact with continuous large displacement using a pin-on-disk tribometer. They attributed the reduction in strength to the incremental removal of material leading to a subtle increase in contact area that in turn led to lower localised contact stress and hence reduced shearing resistance.

2.8 Summary

The literature relevant to pipeline geotechnics, pertinent soil mechanics, and existing work on the subject has been reviewed. Some particular gaps have been identified and provide the motivation for this work.

- Soil mechanics and pipeline geotechnics is multi-facetted with often competing effects and requirements for the safe design of high-pressure high-temperature pipelines offshore.
- Both drained and undrained conditions prevail at pipe-soil interfaces and in the surrounding soils into which pipes become embedded and understanding of the behaviour of pipes in those conditions when subject to both axial and lateral loads is key.
- In the case of pipes laid on clay soils, undrained behaviour and embedment within clay berms has attracted far more attention. The soil and interface mechanics of pipes laid on clay soils though is primarily concerned with the nature of the soil response rather than at the interface of pipe and soil.
- In the case of pipes laid on granular soils, where drained conditions dominate both axially and laterally, the interface behaviour and frictional coefficient between pipe coating and soil is key to determining the shear response.
- Despite the prevalent use of polypropylene as a pipe coating technology and the widespread presence of granular soils in some basins, there is a paucity of information in the literature providing characteristic values or a methodology for predicting pipe-soil interface friction for polypropylene coated pipes and sandy seafloors. There is wide-spread precedent for establishing relationships between interface shear strengths of various materials and various parameters (hardness, roughness, angularity, strain rate/pore water pressure, etc). However, to the author's knowledge nothing exists to allow engineers to make a prediction of pipe-soil interface friction coefficient for polymer-soil interfaces using easily obtainable parameters a designer would have access to already.
- There is a paucity of interface shear strength data relating to polypropylene pipeline coatings (including specifically relating to granular soil substrates).
- There is a lack of a usable relationship between surface texture, commonly established soil properties, and stress level to predict polypropylene-soil interface friction.
- There is some room for establishing the best methodology for quantifying the surface topography and texture of relatively soft surfaces.

3 Materials and Methodology

This chapter details the materials, test methodology, and test apparatus used for the research in this thesis. First is an examination of seven different test sands with index characteristics and soil properties. Next are methods for characterising surfaces including a discussion on the relative merits of two different profilometry techniques with reference to relevant industry standards. The final part of this chapter deals with the sample preparation and test methodologies including discussion about pertinent test parameters, determination of test outputs, and checking reliability of the apparatus.

3.1 Granular materials

Seven different granular soils were used for this research. They are detailed below and some index properties for each test soil are summarised in Table 3.1. A visualisation of soil grain angularity descriptors is shown in Figure 3.1 to aid the reader with understanding the nature of the test soils. Photographs of the general appearance of the soils and macro images of the soil grains are presented in Figure 3.2 and Figure 3.3.

- Lowestoft Gravel is dredged material from East Lowestoft Cargo in the North Sea and bulked out with approximately 30% crushed quartz-rich aggregate in the laboratory. Grains are angular to sub-angular and vary in shape from elongate and tabular to more spherical grains.
- Leighton Buzzard 14-25 (known also as Fraction B in the literature) is extracted from sand quarries near the town of Leighton Buzzard, Bedfordshire, UK, and is characterised as subangular to subrounded with grains of medium to high sphericity. Leighton Buzzard is well known in the literature including the offshore sector and pipelines (e.g. White *et al.*, 2008; Bransby and Ireland, 2009).
- Hostun Sand is an industrially produced silica sand which is manufactured by crushing and grinding of source materials and is characterised by angular to subangular grains of medium to high sphericity. Hostun Sand has been widely used in the literature including for offshore applications (e.g. Foray *et al.*, 1993).
- Redhill Sand is sieved silica sand characterised by subangular to subrounded grains with medium to high sphericity which has some precedent for use in application to the offshore sector (e.g. Kelly *et al.,* 2004) due to its similarity to some marine sands.
- Soil S0 was formulated in the laboratory using a combination of silica sand dredged from the North Sea, a uniform belgian silica sand, and some silica silt. S0 is

characterised by generally subangular to subrounded medium to high sphericity grains.

- Soil S15 is the same as Soil S0 but with additional soil grains that are retained on a 0.4 mm aperture sieve added such that the final soil has a coarse fraction content of 15%.
- Soil S35 is like S15 but instead contains 35% coarse grains that are retained by a 0.4 mm aperture sieve.

Table 3.1 Index characteristics for each test soil

	Lowestoft Gravel	Leighton Buzzard	Hostun Sand	Redhill Sand	S0	S15	S35
ρ_{max} (Mg/m^3)	1.71	1.73	1.64	1.65	1.56	1.69	1.81
ρ_{min} (Mg/m^3)	1.37	1.44	1.33	1.30	1.39	1.51	1.62
e_{max}	0.94	0.84	1.00	1.04	0.90	0.76	0.64
e_{min}	0.55	0.53	0.62	0.61	0.70	0.57	0.47
D_{50} (mm)	1.59	0.88	0.35	0.17	0.24	0.25	0.32
C_u	1.88	1.44	1.71	2.22	2.79	3.22	3.69
C_c	1.00	1.00	0.90	1.17	1.28	1.23	1.10
G_s	2.65	2.65	2.65	2.65	2.65	2.65	2.65
Ratio of soil sample height to soil D_{50} during direct and interface shear tests							
Direct shear	31	57	143	294	208	200	156
Interface	16	28	71	147	104	100	78

It was previously discussed that shear bands in the direct shear apparatus can be expected to be between 2 and 8 particle diameters so the ratio between the sample height being tested and the D_{50} of the test soil is important. This information is included in Table 3.1 and assumes a direct shear soil sample height of 50 mm, reducing to 25 mm during interface tests. It is clear that with each test soil the ratio is sufficient that formation of shear bands is unlikely to be impeded.

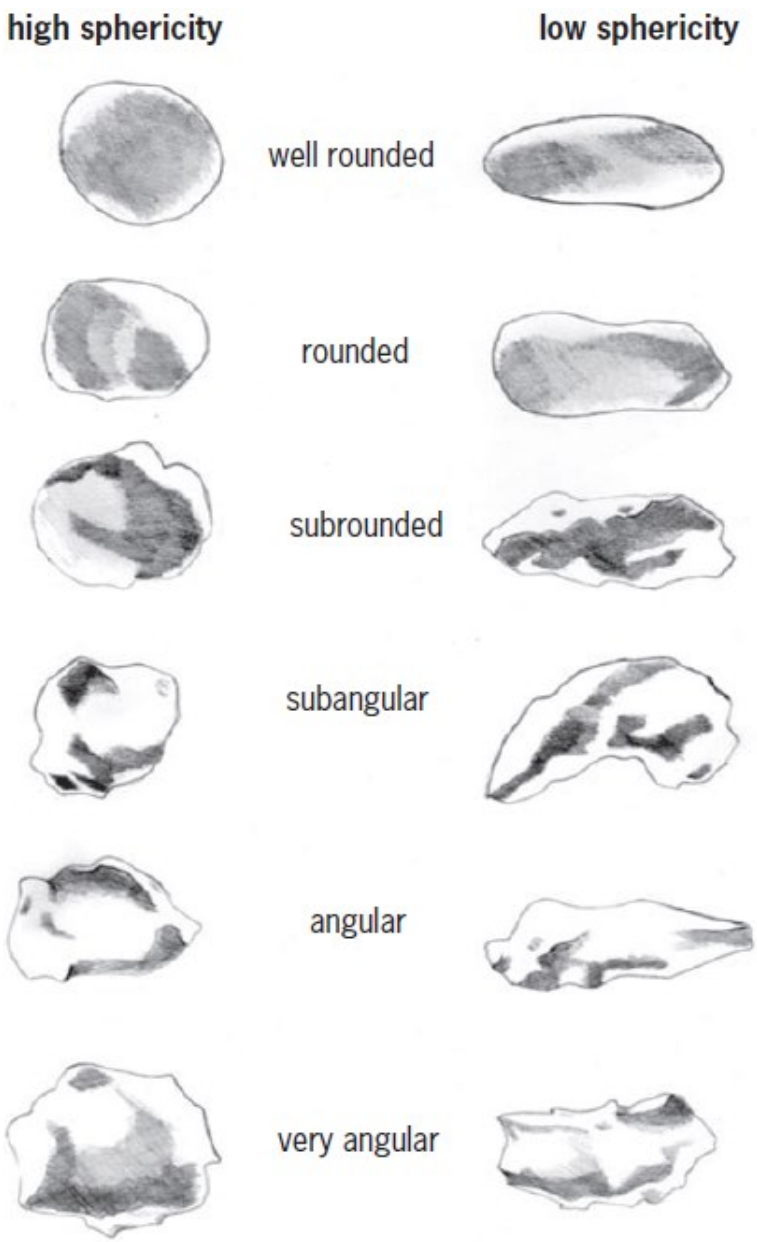

Figure 3.1 Graphical representation of soil grain shapes after Norbury (2010).

(a) Lowestoft Gravel

(b) Leighton Buzzard

(c) Hostun Sand

(d) Redhill Sand

(e) S0

(f) S15

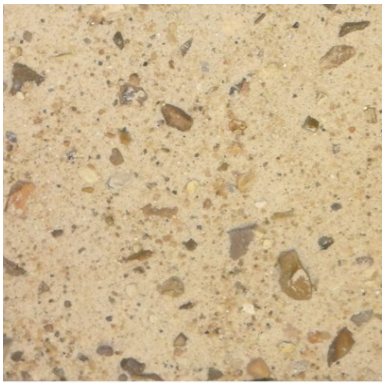

(g) S35

Figure 3.2 Photographs showing the general appearance of each test sand and gravel fractions used to make S0, S15, and S35 soils.

(a) Lowestoft Gravel

(b) Leighton Buzzard

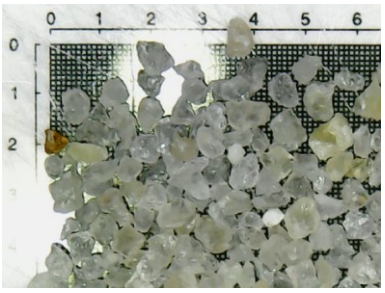

(c) Hostun Sand

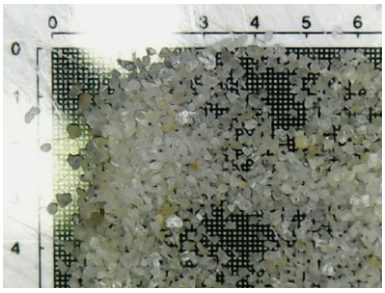

(d) Redhill Sand

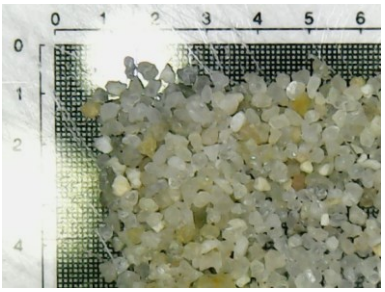

(e) S0 (also base for S15, S35)

Figure 3.3 Close-up microscope photos of grains from each test soil.

3.1.1 Soil classification

Various soil classification tests were carried out including particle size distribution, particle density, minimum and maximum void ratios.

Particle size distribution

Particle size distribution of soils was determined following the dry sieving method set out in British Standard BS1377 Part 2 (BSI, 1990a). Dry sieving was selected because the soils were predominantly sand-sized or above and where there is a small silt component it was added in to prepare a mixture of specific distribution, so the percentages were known. Particle size distributions (PSD) for each test sand are detailed in Table 3.2 and displayed graphically in Figure 3.4 along with the typical spread of granular soils PSD in the North Sea indicated by the grey shadow after Milewski *et al*. (2019). The test soils used for the majority of this research (LG, LB, HS, RH) are more uniform than would typically be found on the seafloor, but they ought nonetheless to serve as a practical representation for testing purposes.

Table 3.2 Particle size distribution by percentage passing for each test soil

Sieve aperture (mm)	Lowestoft Gravel	Leighton Buzzard	Hostun Sand	Redhill Sand	S0	S15	S35
10.000	100.000	100.000	100.000	100.000	100.000	100.000	100.000
6.700	100.000	100.000	100.000	100.000	100.000	98.100	93.700
5.000	100.000	100.000	100.000	100.000	100.000	96.400	86.500
2.000	72.055	100.000	100.000	100.000	100.000	91.800	76.400
1.180	21.625	99.785	100.000	100.000	100.000	90.400	74.800
0.800	1.800	32.975	100.000	100.000	100.000	87.600	66.500
0.600	0.910	1.005	98.690	99.980	100.000	86.500	65.200
0.425	0.330	0.115	69.210	99.885	99.700	84.400	63.600
0.212	0.015	0.065	4.460	85.865	39.500	38.600	29.100
0.150	0.005	0.065	0.595	36.470	18.000	19.400	13.500
0.063	0.005	0.065	0.065	0.140	2.300	3.800	4.500
Tray	0.000	0.000	0.000	0.000	0.000	0.000	0.000

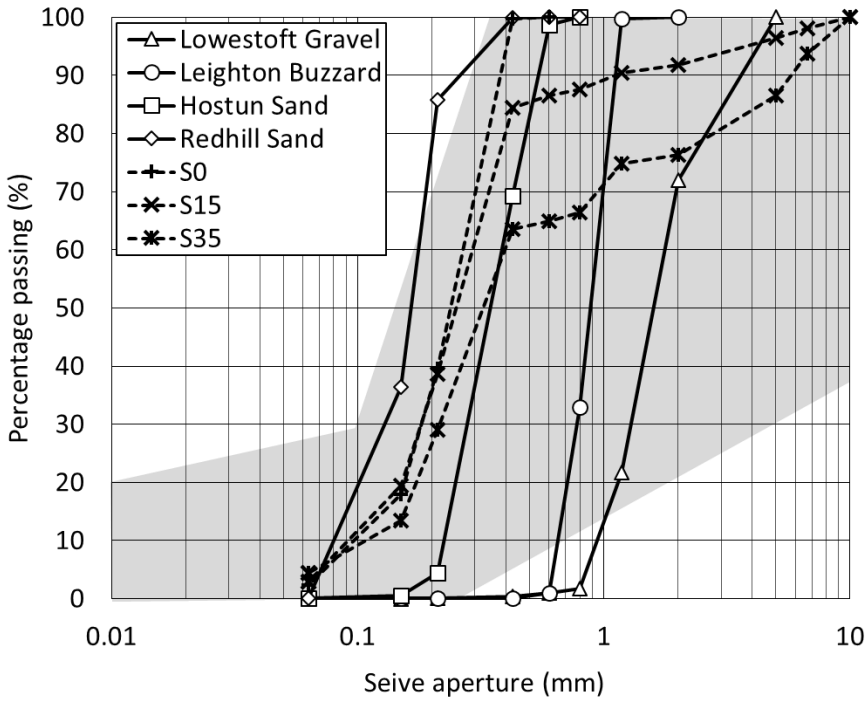

Figure 3.4 PSD for granular test soils with the grey shadow indicating the typical spread of PSD for granular soils sampled across the North Sea after Milewski *et al*. (2019).

Particle density

Particle density of soil grains is required to determine the specific gravity as this forms an important part of calculating appropriate sample masses for testing at a later stage. Particle density was determined following British Standard BS1377 Part 2 (BSI, 1990a) and is converted to specific gravity by multiplying by acceleration due to gravity, *g*. The results are included in Table 3.1.

Minimum and maximum void ratio

Minimum and maximum void ratio was calculated from the maximum and minimum density of each test soil determined according to British Standard BS1377 Part 4 (BSI, 1990b). The maximum and minimum density and minimum and maximum void ratio for each soil is included in Table 3.1.

3.2 Polypropylene pipe coating specimens

27 polypropylene pipe coating specimens were acquired from an industry partner and was prepared at their in-house testing facility. Coating materials were removed from already manufactured steel pipes by heating to soften the bonding resin and prying them free. Specimens were cut to size and flattened by placing under 20 kg of mass and heating to approximately 160°C until the curvature had been removed. Typical examples of the coating specimens extracted from pipes are shown in Figure 3.5. These surface specimens are designated type “T” and interface tests on them are labelled as such.

Specimens can be qualitatively described as being smooth , and their roughness’ generally fall in the range of 0.3 to 1.0 μm, though further quantitative assessments and analysis are discussed later. Some of the surface specimens feature a seam across their face, artefacts of manufacturing associated with the finite width of polypropylene extrusion as it wraps around the pipe. Where present, the surface seams run at 81° to the direction of shearing. No test specimen was inscribed with more than a single seam, and some not at all. Other manufacturing artefacts include prolate hemispheroidal protrusions up to three millimetres diameter present on many of the specimens, although the number, position, and clustering of such features varies considerably. There are also other signs of imperfection such as subtle undulations and indentation which are the result of handling and transportation. Such features are common and are likely to be present in real-world application.

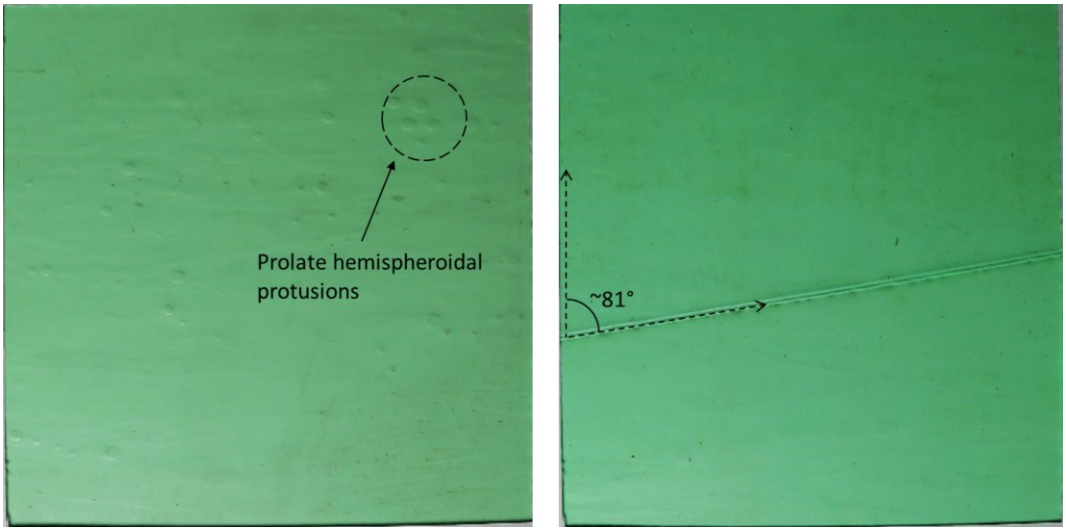

Figure 3.5 Photographs of typical real polypropylene coating specimens showing examples with, and without a seam.

3.3 Surface hardness

The hardness of ten surface specimens was characterised using a durometer measuring on the Shore D scale. Tests were conducted at ambient conditions in the laboratory, temperature-controlled between 20-22°C, in which the surface specimens had been equilibrating for more than one week. Each of the surface specimens was subjected to four hardness measurements. Figure 3.6 shows the durometer in use. The mean and standard deviation of the ten Shore D harness measurements was 70 and 0.9, respectively.

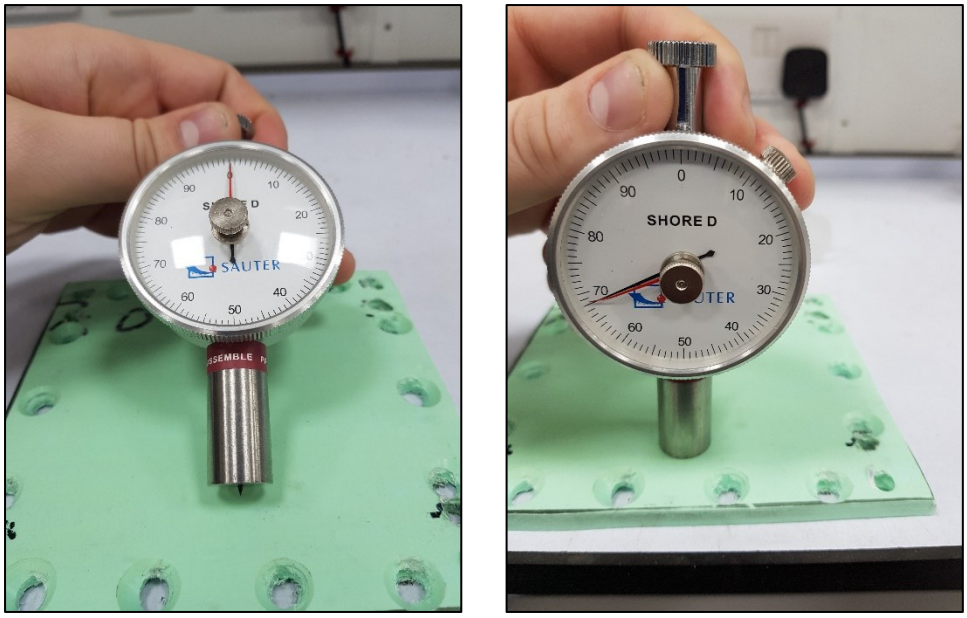

Figure 3.6 Durometer in use measuring surface hardness

3.4 Surface topography measurement

Two methods of measuring surface topography through profilometry were adopted in the initial phases of the research because the difference in approaches posed questions over the most appropriate technique with relatively soft polymer surfaces. The hard stylus tip of traditional profilometers posed a potential problem when applied to softer surfaces like polymers instead of surfaces like steel. The concern was that asperities and extreme features may be damaged or removed by the hard stylus tip ploughing through them resulting in an underestimation of the surface texture parameter. Use of non-contact techniques avoids this problem as there is no physical contact between surface and measuring apparatus.

3.4.1 Contact profilometry

The surface topography of the 27 pipe coating surfaces was recorded and digitised using a Taylor Hobson Form Talysurf 50 profilometer (referred to hereafter simply as “Talysurf” for brevity). The stylus of this instrument consists of a 2 mm conical diamond applying a contact force less than 1 mN and capable of 8 nm resolution. When conducting a measurement, the stylus was first lowered onto a surface specimen and then displaced horizontally over a traverse length of 50 mm. Every 0.5 μm the vertical position of the stylus was recorded. A template like that shown in Figure 3.7 was used to orchestrate the profilometry schedule. A total of ten traverses of the profilometer were used to characterise a surface: five running parallel to the direction of shearing (X), and five running perpendicular (Y). The template was positioned on top of the surface specimen while the stylus of the profilometer was lowered into position. In this way the starting point of each profilometer traverse was controlled (to ± 1 mm) and the traverse could be made to run near-parallel to the edges of the specimen. The topography of each surface specimen was recorded before testing and after each test.

A second order Butterworth filter was used to separate the topography’s long wavelength characteristic (the form), medium wavelength characteristic (the waviness), and short wavelength characteristic (the roughness). The cut-off wavelength between form and waviness was taken as 8 mm, and between waviness and roughness as 0.25 mm. With these parameters, any residual bow or twist remaining from ineffectiveness of the surface specimen flattening procedure was apparent in the form, and both seams and bubbles were apparent predominantly in the waviness.

The parameter used to quantify the profiles was the arithmetic-mean deviation of the profiles from their centre lines as previously discussed in Chapter 2. To better account for the effect of the relationship between grain size and surface topography the 50 mm long profiles were subdivided into gauge lengths of 0.284 mm each (the mean D_{50} value for soils S0, S15, and S35 used in this part of the investigation). Profilometry discussion is in Chapter 4.

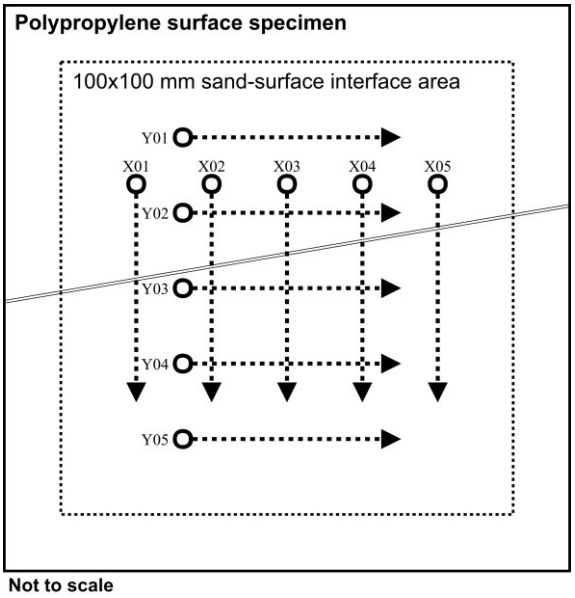

Figure 3.7 Schedule of Talysurf profilometry

3.4.2 Non-contact profilometry

Surface specimens were imaged using a focus variation method, an optical 3D measurement technique achieved by an Alicona InfiniteFocus digital microscope (shown Figure 3.8 and hereafter referred to simply as “Alicona” for brevity). The method integrates the small depth of field associated with an optical microscope, vertical (Z) scanning of the microscope lens and horizontal (X and Y) scanning of the underlying specimen. The resolution of the Alicona device is dependent on the magnification provide by the utilised lens. Here, a magnification of 10x was adopted rendering the vertical resolution as 250 nm.

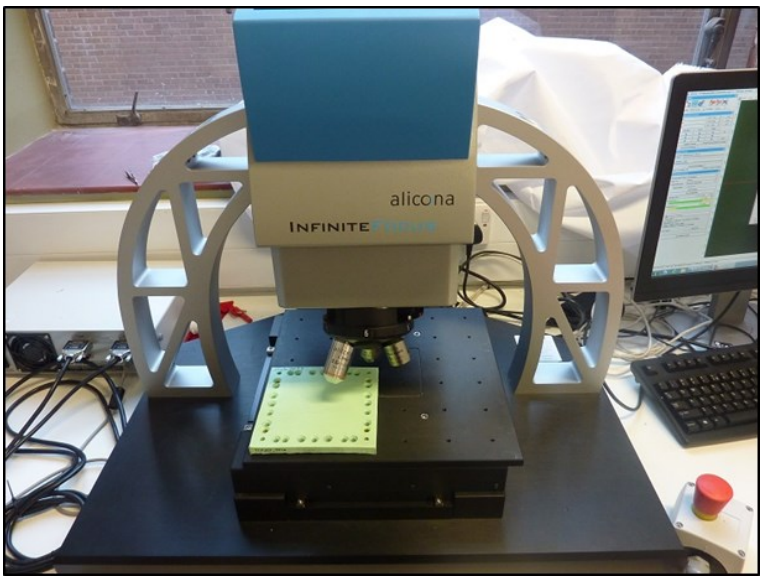

Figure 3.8 Alicona InfiniteFocus machine

Typical examples of processed surfaces from an Alicona scan are presented in Figure 3.9. The shearing direction is from the bottom left to the top right of the images and there is clear damage caused during shear visible in the form of straight parallel striations and a larger gouge. Surface topography and roughness characteristics can be extracted from these data and analysis facilities built-in to the processing software determines the parameter of interest from a user-specified profile drawn across the 3D surface.

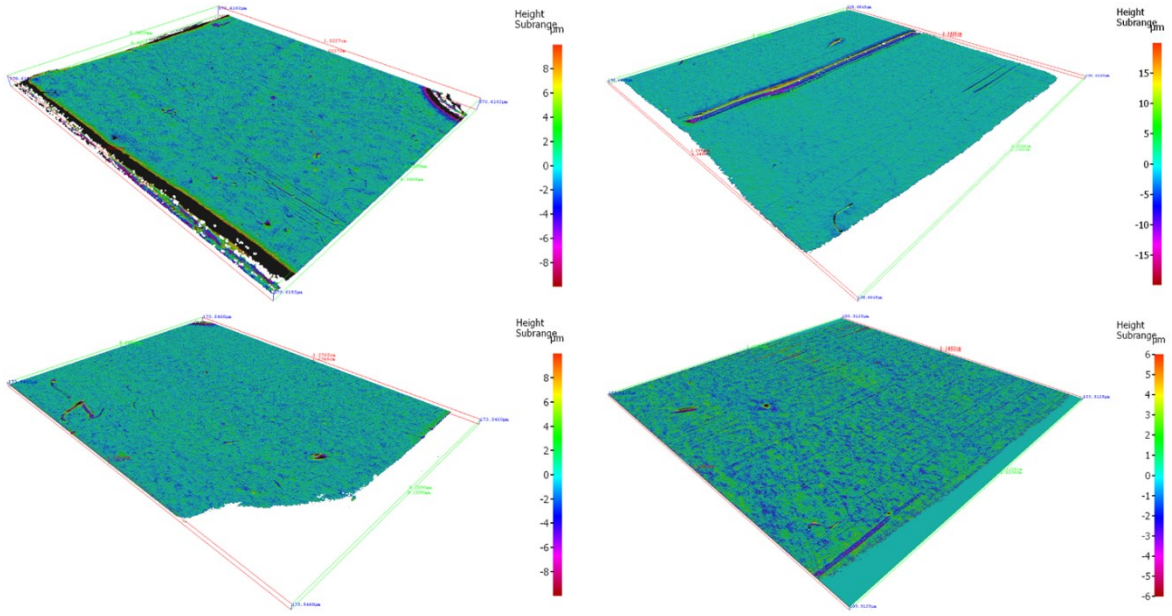

(a) after **(b) after**

Figure 3.9 Typical processed surface image outputs from Alicona (a) before shearing and (b) after shearing.

3.5 Experimental apparatus

The direct shear apparatus (DSA) is a stalwart of methods available for testing the strength of soils, particularly granular soils like sand or fine gravel. Direct shear is induced when shear stresses are generated within a specimen by the direct action of forces trying to slice through it rather than those generated by compression or torsion. Many devices used to test soil strength make use of this method (e.g. vane test, ring shear test, simple shear test) but the name is given directly to one particular test arrangement. The ubiquitously named Direct Shear Apparatus comprises a laterally constrained soil sample inside a horizontally split box where one half of the box is forced to translate relative to the other at a constant rate. The force required to restrain the stationary half is measured and thus shear forces can be measured.

The Winged Direct Shear Apparatus available at University of Bristol was chosen because its reliability and quality of results has considerable precedent in the literature (e.g.

Lings and Dietz, 2004; Lings and Dietz, 2005; Dietz and Lings, 2006; Ibraim and Fourmont, 2007) and allowed easy modification for interface testing.

3.5.1 The conventional Direct Shear Apparatus

Though the precise arrangement and look of a complete direct shear apparatus may vary according to manufacturer, they all work in the same way. A hollow squared box, split along its central plane in the horizontal orientation, is formed of an upper and lower frame which when secured together, and with top and bottom plates added, make a box. The upper and lower frames are secured with bolts in opposing corners passing through the upper and lower frame. The remaining corners contain threaded holes in the upper frame to allow a grub screw to protrude from the bottom of the upper frame and push against the lower frame to support the formation of a gap between the two frames. The lower plate of the box, making the floor, is held in place with four supporting pins protruding from the inside of the lower frame. The box is completed with the placement of the upper plate, formed with a conical receiver on top for applying the load, and is called the load pad.

Once the soil sample is included and the box complete it is seated in a shear carriage and secured in place so that the carriage and shearbox lower frame move as one. The load carriage itself is deeper than the shearbox is high to allow for saturation of included samples. The carriage is supported on bearings to allow unimpeded longitudinal motion and displacement is controlled during the test by a worm drive imposing a fixed rate of displacement. Before the test is commenced the upper and lower frames are unbolted to allow relatively displacement between them. The upper frame is connected via a swan-neck to a reaction frame and load cell which is able to measure the force required to restrain the upper half of the box as the lower half translates. A schematic taken from Lings and Dietz (2004) was presented in Chapter 2 as Figure 2.23.

3.5.2 Improvements to the Direct Shear Apparatus

A number of improvements to the archetypal design have been made in recent decades in response to weaknesses identified in the conventional apparatus. A dominant problem of the archetypal DSA is for the load cap, which is free to move during testing, to rotate over the course of the test which is generally accepted to be indicative of non-uniformity and renders test results potentially unreliable. Rotations are more prevalent under lower normal loads (Hvorslev, 1939) which is of concern when investigating at the low stresses relevant to pipelines, and Wernick (1979) noted that counter-rotations may also occur leading to further repeatability concerns. Lings and Dietz (2004) discussed at length the relative merits of

various researcher's attempts to tackle the problem of top cap rotation through either enforced (Wernick, 1979; Shibuya *et al*., 1997) or induced methods (Jewell and Wroth, 1987; Jewell, 1989). Enforced methods attempt to physically prevent rotations whereas induced methods seek the same net effect but without restricting movement. Shibuya *et al*. (1997) found that enforced restraints necessarily meant grains moving past the internal walls of the shearbox leading to unreliable results. Their solution was to lubricate the walls and use a load cell at the base of the shearbox but this makes for a complicated test procedure and a potentially cluttered apparatus.

The simpler, more elegant, solution proposed by Jewell and Wroth (1987) and Jewell (1989) is to secure the load cap within the upper frame in a so-called symmetrical arrangement. The symmetrical arrangement reduces rotation of both the upper frame and the load pad, unbalanced moments are reduced, and the included sample becomes less distorted.

3.5.3 Winged Direct Shear Apparatus

The DSA available in the geomechanics laboratory at University of Bristol Department of Civil Engineering is a WF-25300 manufactured by Wykeham Farrance (general arrangement shown in Figure 3.10). The normal load is applied to the top of the load cap by a pin seated in a conical receiver. The loading mechanism is by a dead load with a 1:10 lever arm which is counterbalanced to ensure constant loading even as changes in sample height move the level arm.

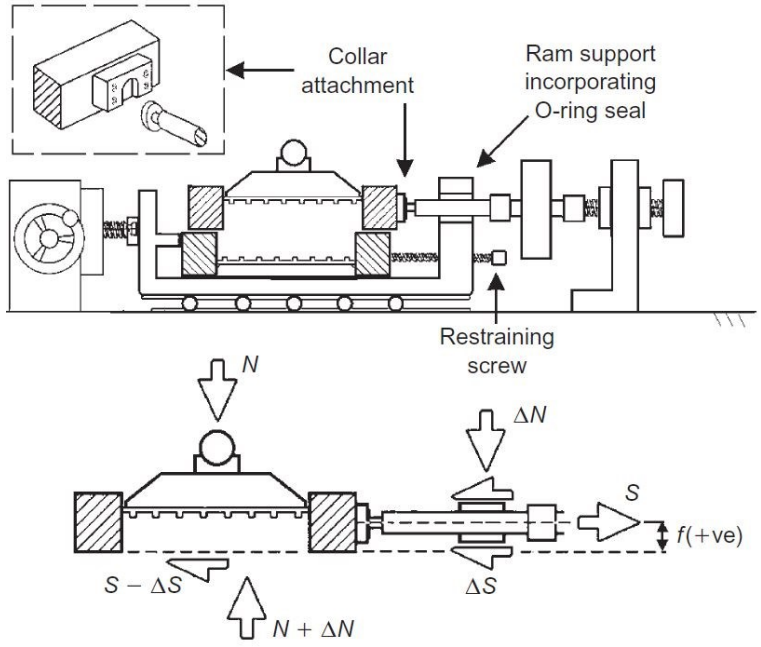

Figure 3.10 General arrangement and free-body diagram of the Wykeham Farrance WF-25300 (from Lings and Dietz, 2004).

It differs slightly from the archetype in that in place of a swan neck, the shear load ram instead passes directly through the wall of the carriage and connects to the upper frame with a collar. As a result of this different arrangement the line of thrust is no longer the same as the central plane, the collar attachment restricts vertical displacement so an effective extra vertical reaction load is applied to the upper frame, and horizontal loads can be inaccurate due to friction in the seals around the ram as it passes through the carriage. These drawbacks can lead to rotations of the upper frame leading to eccentric loading and distortion of normal and shear forces from measured values. Similar undesirable effects are also present in the archetypal arrangement due to the weight of the swan neck imposing clockwise moments on the upper frame so neither arrangement is without flaws.

To counter the drawbacks of the arrangements discussed, Lings and Dietz (2004) presented the Winged Direct Shear Apparatus (WDSA), as shown in Figure 3.11, modified from the WF-25300. A pair of wings was attached to the sides of the upper frame. The loading ram is then connected to the wings via ballraces which sit in a channel on the outside face of the wings allowing unimpeded vertical movement of the upper frame without influencing the horizontal load or imposing any reaction force during displacement. In addition, as shown in Figure 3.11a, the point of application of the load is now close to the centre of the shearbox and the central plane with linear bearings to ensure freedom of longitudinal movement which keeps the load arms horizontal.

In addition to the modifications to the apparatus and loading mechanism, the shearbox itself is modified to have a more comprehensive arrangement of securing bolts and grub screws. In place of just two bolts at opposing corners to secure the shearbox halves together, there is now a bolt at each corner. Similarly, in place of two grub screws at the alternate opposing corners used to create a gap between the frames, there is now one at each corner. Stub bolts in both the upper and lower frames allow the top and bottom plates to be fixed in place to achieve the symmetrical test arrangement recommended by Jewell and Wroth (1987) and Jewell (1989). The comprehensive arrangement of bolts and features of the modified shearbox is presented in Figure 3.12 from Lings and Dietz (2004).

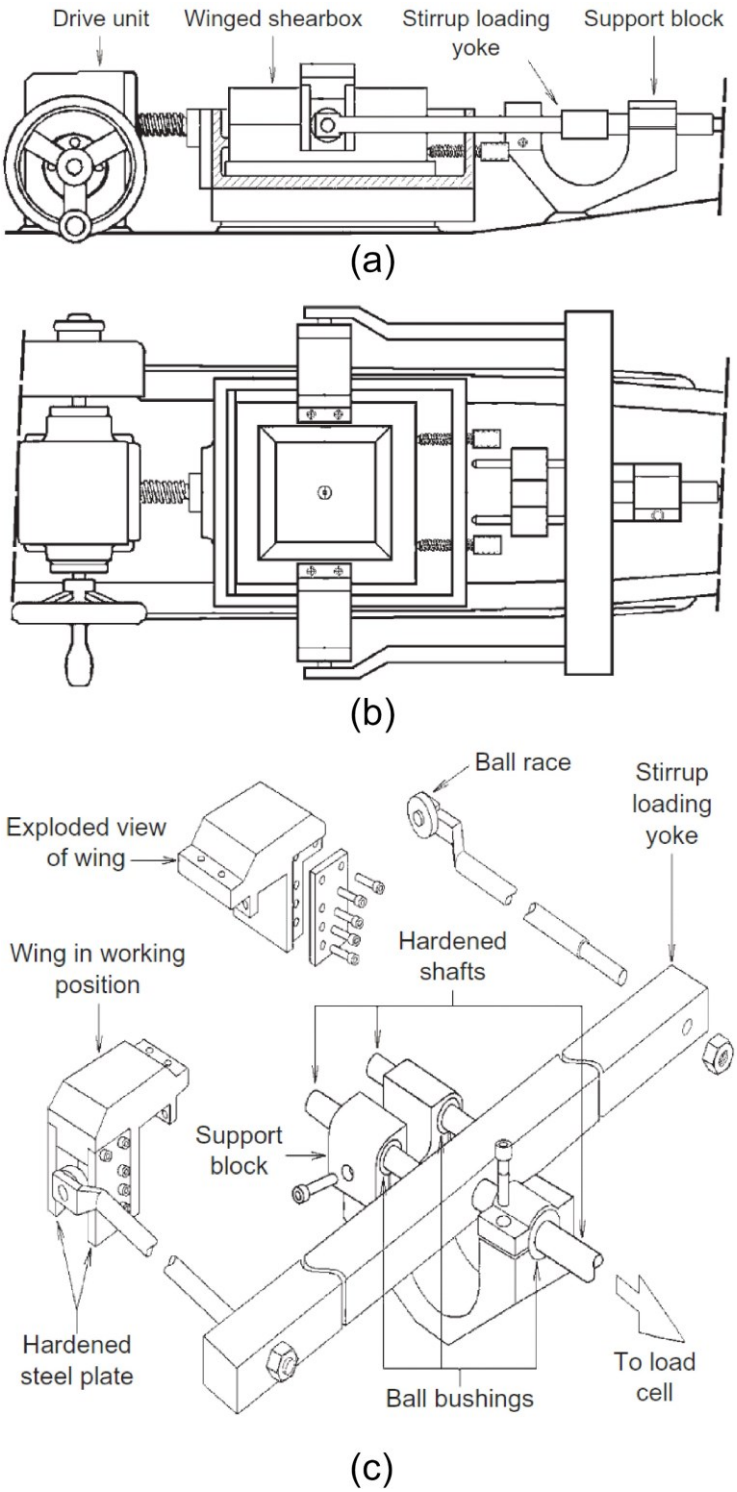

Figure 3.11 The winged direct shear apparatus: (a) section, (b) plan, (c) perspective (from Lings and Dietz, 2004).

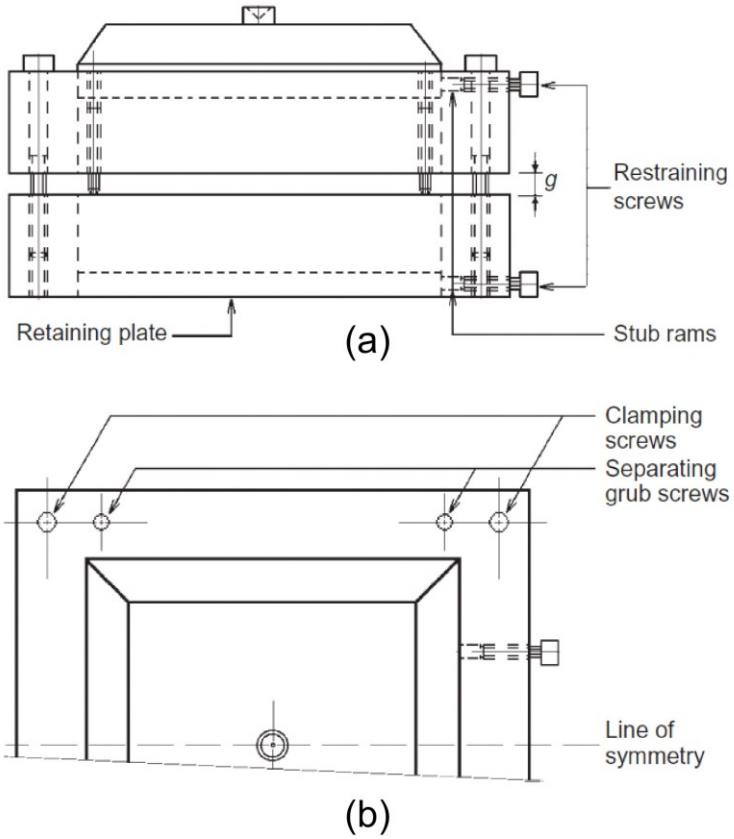

Figure 3.12 The winged direct shear apparatus shearbox (a) elevation, (b) plan (from Lings and Dietz, 2004).

Reliable interpretation of direct shear test data is contingent on the accurate appraisal of the forces acting on the horizontal split plane of the shearbox. The WDSA and the adopted test methodology have been designed to enable robust measurement of shear loads and reliable estimation of the applied normal load. Considering the measurement of the shear load, the deployed load measuring device is of an appropriate range for the applied magnitudes of normal load and the strength characteristics of the test materials. In addition, the load measuring device is held in a horizontal position using ball bushes to ensure that frictional burdens through the supports are minimal. Considering the estimation of the normal load, the WDSA works to minimise parasitic loads – reaction forces that are developed when the natural motion of the upper shearbox components is inadvertently impeded, indeterminately modifying the normal load that is applied across the horizontal split plane of the shearbox. Parasitic loads arise when the upper frame contacts the lower frame during testing, either directly or indirectly via extruded granular material, or when the application of shear load is via a connector capable of offering constraint to motion. The application of shear load in the WDSA is via ballraces to ensure minimal resistance is offered to the upper half of the apparatus. In addition, unwanted load paths between the upper and lower frames are prevented by installing a sizeable gap between these components and preventing sample extrusion using rubber edging. Finally, during testing the upper frame is rigidly secured to the load pad in a symmetrical arrangement

preventing any untoward interference between these closely fitting and otherwise counter-rotating components. The WDSA and the adopted test method prevent the incidence of parasitic loads so that the loading on the horizontal split plane is either robustly measured or reliably estimated.

3.5.4 Interface testing adaptation

An interface load pad was designed and manufactured specifically to facilitate surface-over-soil testing in the WDSA. The interface load pad replaces the upper frame and load pad of the shearbox (i.e. the top half of Figure 3.12a) and is shown schematically in Figure 3.13 and photographically in Figure 3.14.

The surface specimen bolts to the underside of the interface load pad using 14 perimeteral M5 countersunk bolts tightened so that their heads are recessed within the surface specimens to give a flat surface. Viewed from the topside, the interface load pad replicates both the mounting points for the shearbox wings and the arrangement of separating grub screws and clamping screws to pre-set the gap as found on the upper-frame of the shearbox. A conical seat to accept the load hanger was located centrally in the uppermost horizontal surface so that the vertical normal load could be applied.

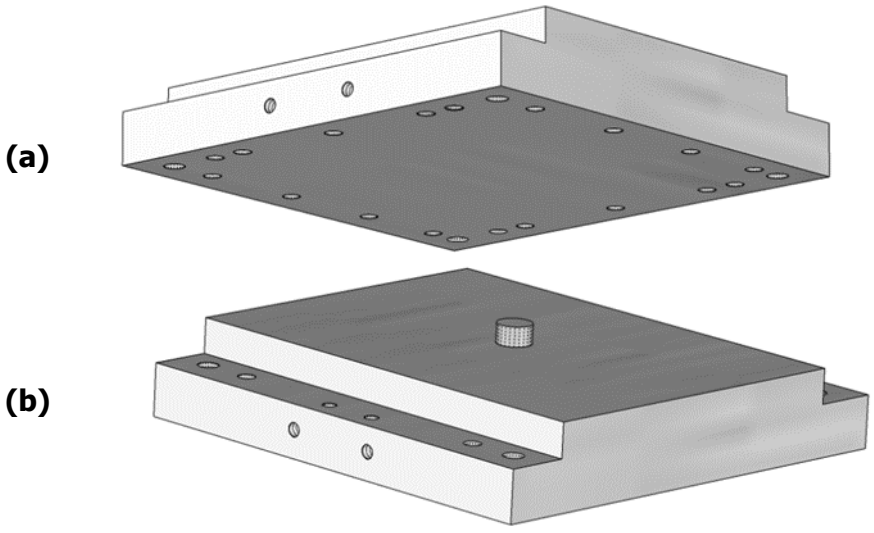

Figure 3.13 Modified load pad for surface-over-soil interface testing: (a) underside, (b) topside.

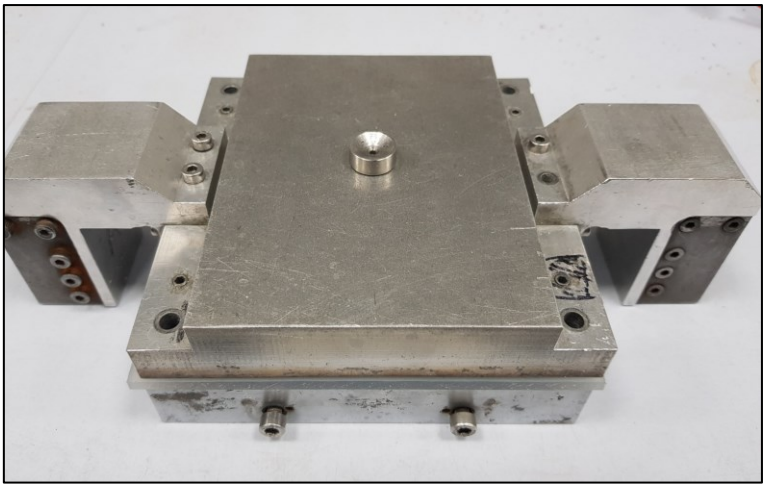

Figure 3.14 Photograph of the interface load pad with wings attached in the interface test arrangement.

Fixing a surface to the underside of the interface load pad results in a largely flat specimens, which is not representative of the real condition of curved pipe in contact with the soil. Contact stresses around the embedded arc of the pipe vary and thus the axial resistance in the pipe system is typically modelled using the *equivalent* friction coefficient (Bruton *et al*., 2009). These issues are not unique to pipelines; much interface work with steel is related to pile design which also simplifies a curved interface contact to a flat surface in the shear box. None the less, use of flattened surfaces in the interface shear box has an established precedent so comparison of results with the literature is straight-forward. However, the most robust methodology might involve validation and comparison of results with large-scale tests adopting pipe sections with realistic curvature and embedment.

3.5.5 Instrumentation

Measurements taken during a direct shear and interface test include:

- the carriage displacement, which corresponds closely to the relative motion between the two halves of the shearbox or on the interface.
- the force required to restrain the upper portion of the apparatus while the lower portion translates horizontally.
- the vertical displacement of the load pad.
- the rotation of the load pad.

The positions of instrumentation are illustrated in Figure 3.15 and Figure 3.16 . Rectilinear motion was recorded using a collection of Linear Variable Differential Transducers (LVDTs).

The LVDT bodies were clamped at fixed mounting locations on the DSA with their spindles contacting the translating parts. A single LVDT was used to monitor horizontal carriage displacement. Three LVDTs were used to monitor vertical motion of the upper half of the shearbox: one centrally to provide the vertical displacement, and two off set along the axis of shear displacement to provide the rotation. The horizontal force required to restrain the upper portion of the apparatus was measured using a 500 Newton capacity S-Type load cell positioned in line with the load restraint system. The sensors were selected so that during testing they were exercised over a sizable proportion, and across the middle, of their range.

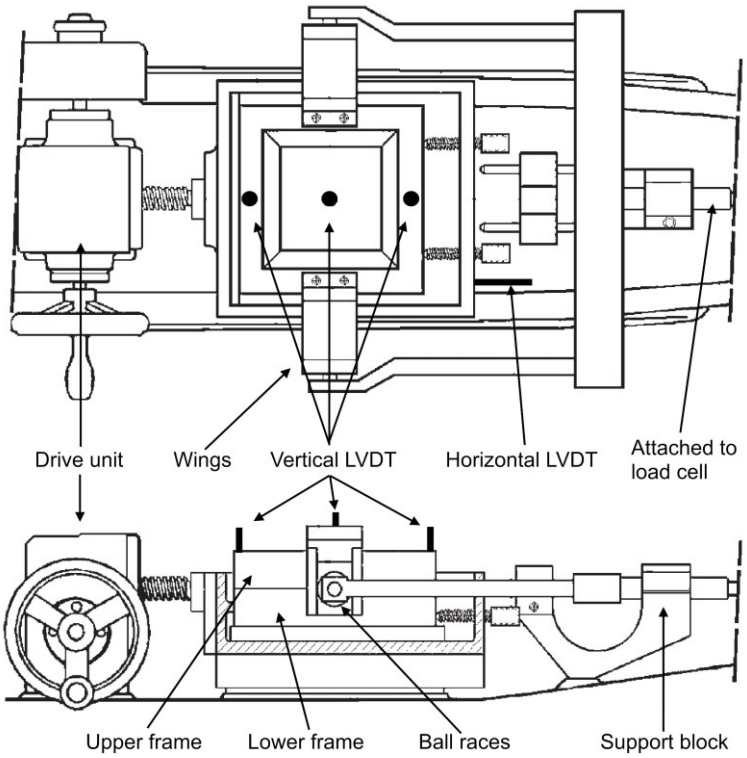

Figure 3.15 Schematic diagram of instrumentation positions on the WDSA.

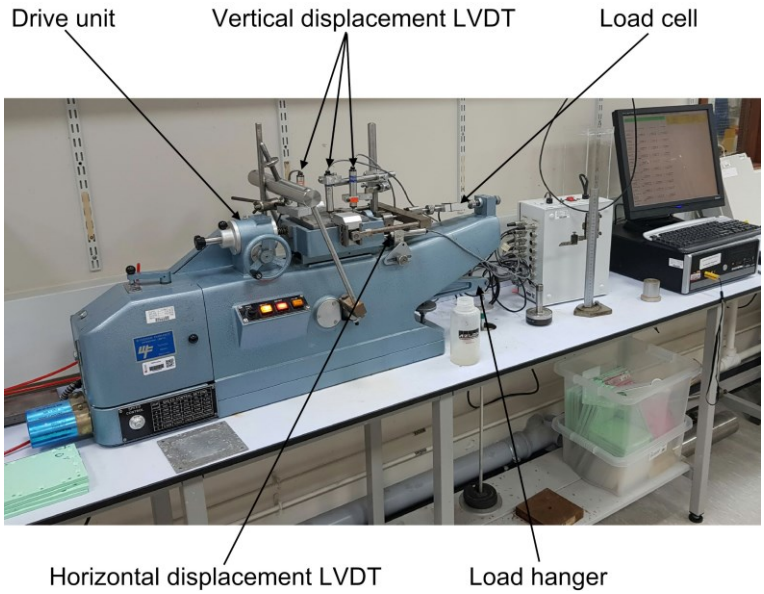

Figure 3.16 The Winged Direct Shear Apparatus in operation with instrumentation labelled.

3.5.6 Calibration and resolution

Before testing began all the LVDTs (Linear Variable Differential Transformers) and the load cell were calibrated to ensure that their actuation properly converted from volts to millimetres or kilonewtons as appropriate. LVDTs were calibrated by clamping them in a micrometer and recording the output voltage in the data logger at 1 mm intervals. The load cell was calibrating using a Budenberg deadweight tester to apply a precisely known load to the load cell in multiple stages with the output voltage recorded at each stage. Calibration lines are presented graphically in Figure 3.17 including the calibration factors inset.

In addition to calibration it was necessary to establish both the resolution and precision of the instrumentation. The four LVDTs and the load cell were left unloaded and logged for 60 minutes to record any drift. Converted values (from voltage in which the instrumentation measures) and any drift over the 60 minutes is shown in Figure 3.18. Resolution and precision are demonstrated in Figure 3.18a. Resolution is the converted step size in output measurement for any individual drift increment and precision is the maximum amplitude of the drift over the 60 minute monitoring period.

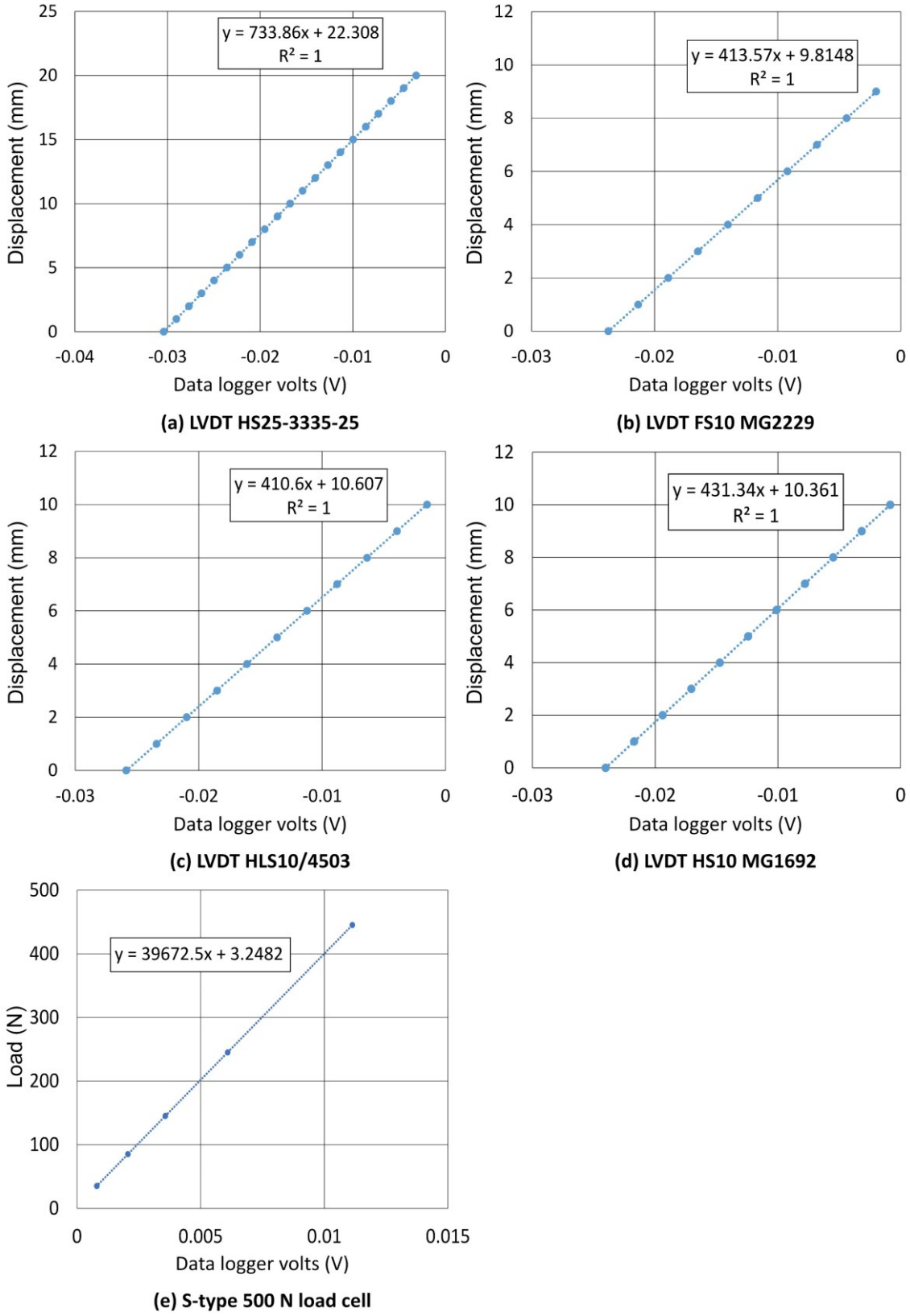

Figure 3.17 Calibration graphs for LVDTs to measure (a) horizontal displacement, (b) central vertical displacement, (c) vertical displacement proximal to the load cell and (d) distal to the load cell, and (e) the load cell itself.

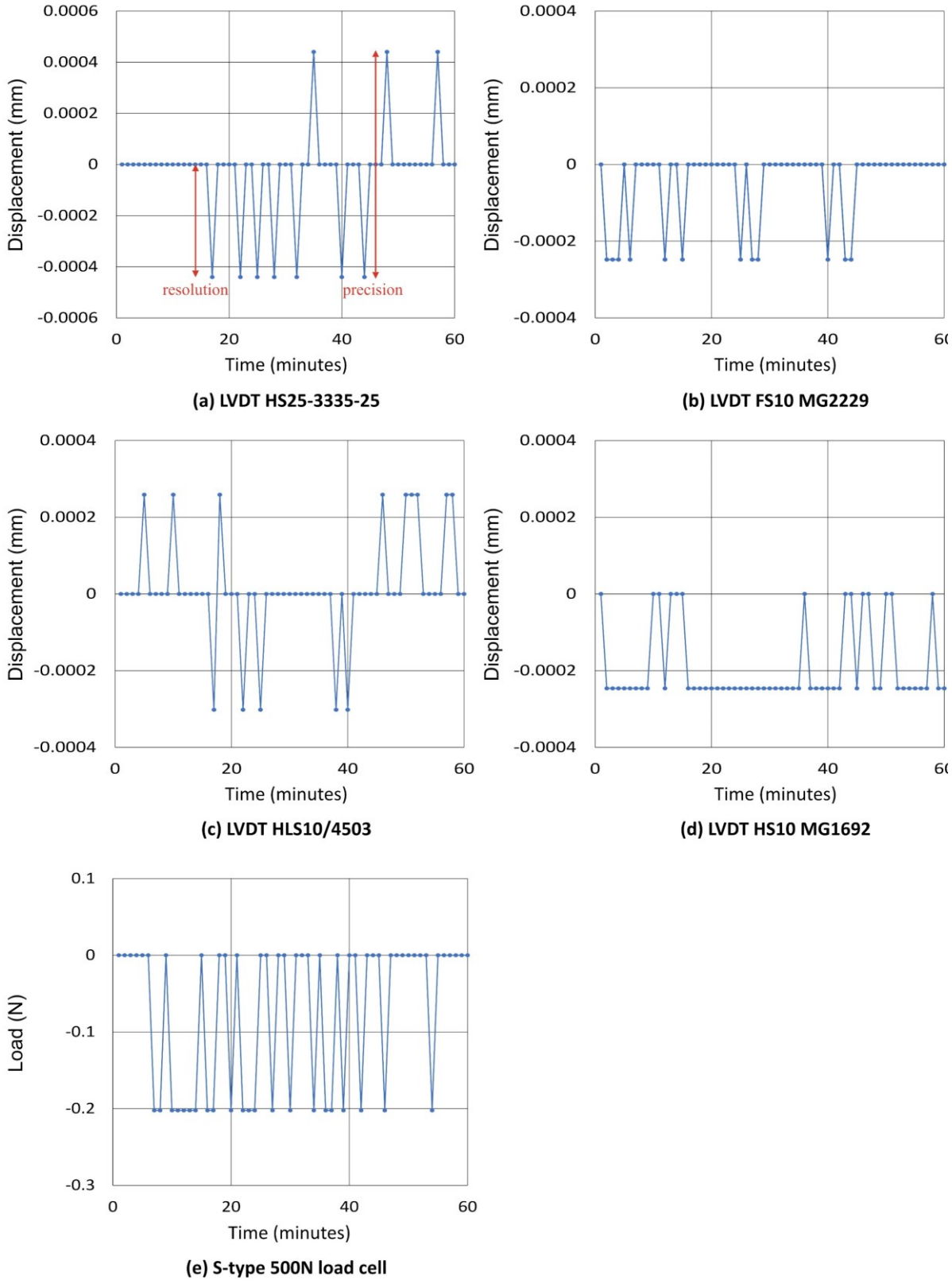

Figure 3.18 Drift over 60 minutes for LVDTs measuring (a) horizontal displacement, (b) central vertical displacement, (c) vertical displacement proximal to the load cell and (d) distal to the load cell, and (e) the load cell itself.

3.6 Sample preparation

A critical component of laboratory testing is sample preparation and this is also true for direct shear testing where sample density plays such a key role in prescribing shear response. A method often used in preparation of samples for various laboratory tests comprising granular soils is air pluviation (or raining of grains) into the sample container. A second method is the dry deposition method detailed in Miura *et al.* (1997) which has been adopted by the Japanese Geotechnical Society as the standard method to determine the maximum void ratio of a granular material.

Pluviation involves the raining of granular soil samples into the test container and theoretically results in a specimen of uniform density. Unwanted consequences of pluviation are that the resulting soil upper surface may not be level and it can be untidy from sample missing the container. Miura and Toki (1982) developed a method for preparing granular soil samples for use in triaxial testing. They built a piece of equipment called a Multiple Sieving Pluviation Apparatus (MSP) which consisted of a Perspex cylinder encasing seven square-holed sieves of varying apertures and sample dispensed from a conical hopper at the top. The rate of sand dispensing from the hopper was controlled by varying the nozzle aperture diameter and sieves were the same size apart from the first which was smaller. They tested a range of grain sizes and uniformity coefficients.

It is intuitive to think that the resulting density of the sample through pluviation would be related to the fall height, however, Miura and Toki (1982) showed that specimen density is relatively insensitive to the fall height but rather depends on the rate of sample dispensing from the hopper. That rate is controlled by the hopper nozzle aperture. Changing fall height from 300 mm to 700 mm results in a change in density of 3%. Conversely a nozzle diameter of 7 mm could achieve a relative density of over 100% compare to a nozzle diameter of 32 mm which could only achieve 25%. The primacy of nozzle diameter over fall height for controlling density was also earlier noted by Mullilis *et al*. (1975) where specimens were pluviated through both air and water.

An attempt was made to follow the work of Miura and Toki (1982) and construct a MSP apparatus to fit the direct shear box frame used in this research to ensure uniformity of soil sample density where the relative density of the resulting sample could be controlled. However, the apparatus could not be made to work satisfactorily for this research. The potential benefits of an MSP system over the more traditional dry deposition method did not warrant spending the extended time it would have required to perfect it, assuming it came to fruition, to the detriment of testing and addressing the key research questions.

Instead, the dry deposition method suggested by Miura *et al*. (1997) and adopted by the Japanese Geotechnical Society as the method of obtaining the maximum void ratio, was

adopted. The method involves simply pouring dry sample into the container with a funnel ensuring that the funnel tip is gently raised so that soil slowly and steadily falls out and into a conical heap. Allowing grains to roll down the slope with minimal energy encourages them to settle into their loosest configuration with angle of repose being equal to the ultimate angle of friction. Once deposited, samples could be uniformly densified using an aluminium plate and vibrating device to the appropriate test density. All tests are undertaken water saturated with water at ambient laboratory temperature.

3.6.1 Direct shear soil tests

1. The two halves of the shear box are assembled and a set of protruding grub screws within the upper portion of the shearbox used to set the required gap between the lower and upper frames (Figure 3.19a).The height of the box is measured at its four corners using callipers with an accuracy of 0.01 mm.
2. Rubber strips of 1 mm thickness are placed against the four sides of the box to limit sample extrusion through the gap during preparation and shearing (Figure 3.19b).
3. A precise mass of soil is gently poured with a funnel to form a conical heap within the central part of the box following the procedure of Miura *et al.* (1997) (Figure 3.19c).
4. The material is then spread to achieve a flat uppermost surface (Figure 3.19d). The top plate is placed and gently vibrated until a target sample height is achieved (Figure 3.19e). The top plate then is secured within the upper frame of the shearbox (to create a symmetrical test arrangement) and the height of the sample is measured at its four corners (Figure 3.19f).
5. The box is gently inserted in the DSA shear carriage and the load cap put in position (Figure 3.19g). The sample is saturated by gently flooding the shearbox (Figure 3.19h) and all restraining screws that fix and maintain the gap between the two halves of the shearbox are removed. The normal load is applied to the conical seat positioned centrally on the uppermost surface of the load pad.

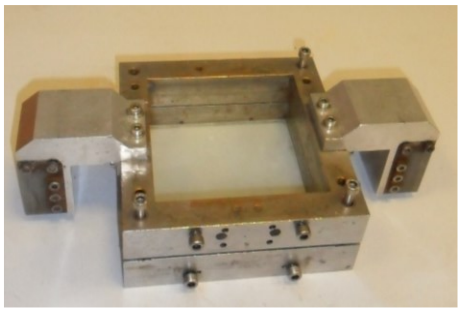

(a) Assembly of direct shear box

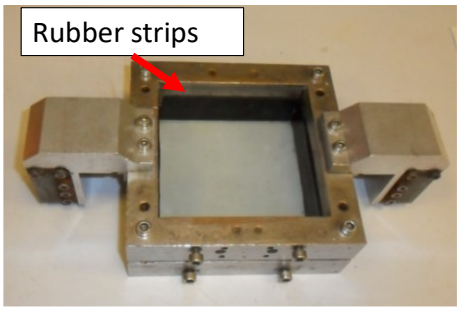

(b) Placement of rubber strips

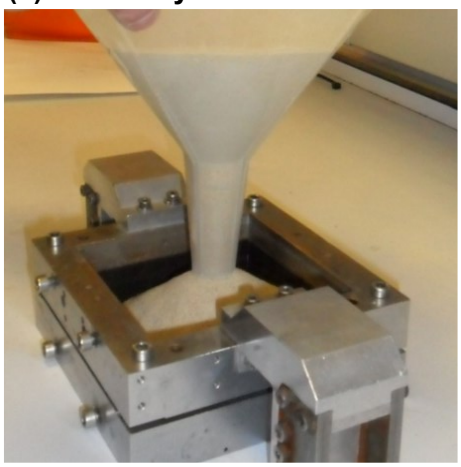

(c) Sample deposition

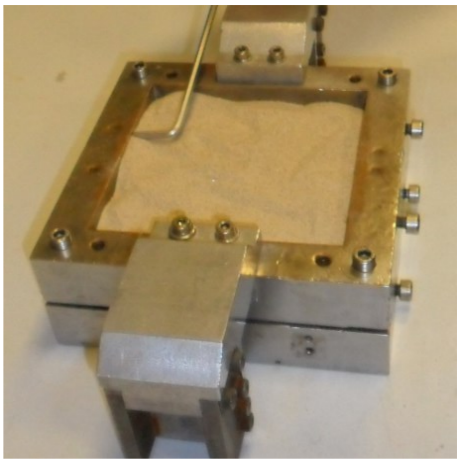

(d) Levelling of the sample

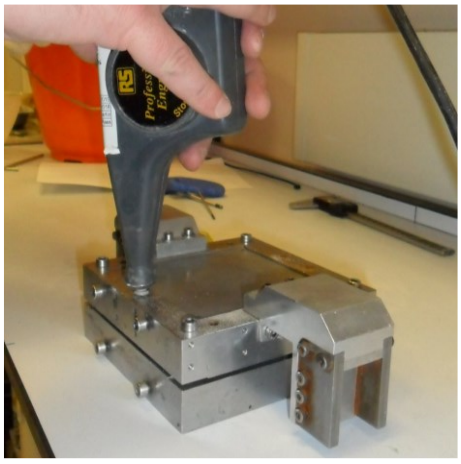

(e) Sample densification

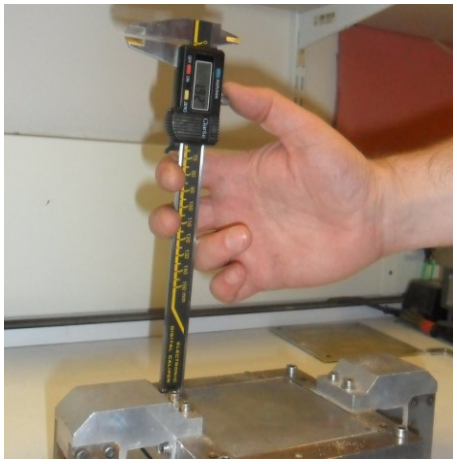

(f) Measuring height of sample

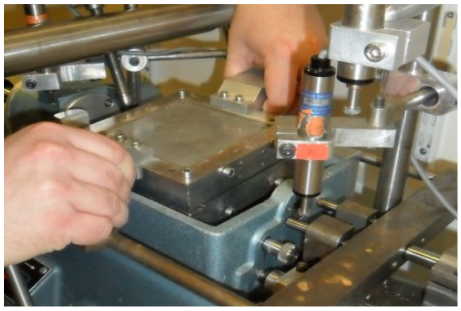

(g) Transfer of sample to the apparatus

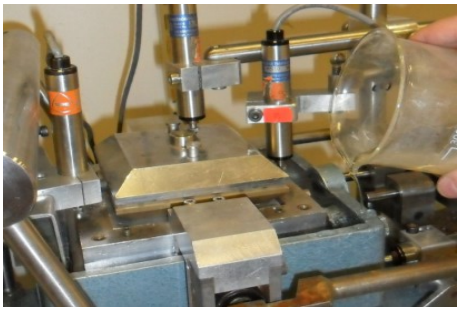

(h) Saturation of the sample

Figure 3.19 Method of preparation for direct shear tests

It is worth writing a note on the placement of the rubber edging strips. It may be intuitive to think that such edging may compromise the correct quantification of shear stresses in the soil through some interference by the rubber. However, Lings and Dietz (2004) carried out a parametric study on the use of rubber edging in their development of the WDSA and did not find it compromised results. The use of such edging follows earlier works by Al-Douri and Poulos (1992) and Shibuya *et al*. (1997). Al-Douri and Poulos (1992) noted a negligible (in fact, unmeasurable) effect of the edging during testing.

3.6.2 Interface tests

In order to maintain a realistic approximation of pipes resting on the seabed, and mindful of Uesugi and Kishida's (1986a) explanation on upper grain layer disturbance, a novel preparation technique was adopted for interface tests. Usually surface-over-soil tests are prepared with the surface specimen being placed onto the sand, however, in the present work the sand is placed onto the surface specimen and then inverted to the correct orientation. Such a technique ensures better soil to surface contact, similar to soil-over-surface testing, and minimises any sample disturbance in the interface shear zone. The interface test sample preparation procedure has been designed to ensure uniform contact between the constituent materials of the interface (i.e. the soil and the surface) and to avoid any inadvertent pre-shearing of the interface prior to testing. The sample fabrication procedure followed the steps described below:

1. The polypropylene surface is secured to the interface load pad. The lower frame of the shearbox is secured at the required height above the surface specimen using a system of protruding grub screws (Figure 3.20a). The height of the sample at the four corners of the box is measured using callipers with an accuracy of 0.01 mm. Rubber strips of 1 mm thickness are placed against the four the sides of the box to limit sample extrusion (Figure 3.20b)
2. An extension to the box is placed to avoid any spilling of the material during the next stage. A predetermined mass of material is poured in the box according the dry deposition method by Miura *et al*. (1997) (Figure 3.20c).
3. The top surface of the granular material was first levelled and then gently vibrated to achieve a target sample height (Figure 3.20d).
4. The extension of the box is removed, and the excess material is gently scraped off with a flat metal edge object to obtain a flat surface (Figure 3.20e). Depositing the sample in this way places the portion of the sample liable to disturbance by the scraping process remotely from the surface specimen. Moreover, uniform soil-surface contact

is achieved as any variation in the form of the surface specimen that remains after it has been secured to the interface load pad is automatically accommodated by the soil sample. Any excess material outside the box is carefully cleaned with a suction device (Figure 3.20f) and an aluminium retaining plate is secured to what will become the base of the shearbox (Figure 3.20g).

5. The mass of sand within the sample is next determined by weighing on a scale (Figure 3.20h). If the sample does not possess the required density, steps two to five of this sequence are repeated with an amended mass of soil poured in the box. The box is smoothly but decisively inverted, a manoeuvre taking less than 1 second, and then carefully inserted in the direct shear apparatus (Figure 3.20i). The sample is saturated by gently flooding the shearbox (Figure 3.20j) and all restraining are removed before the load is applied.

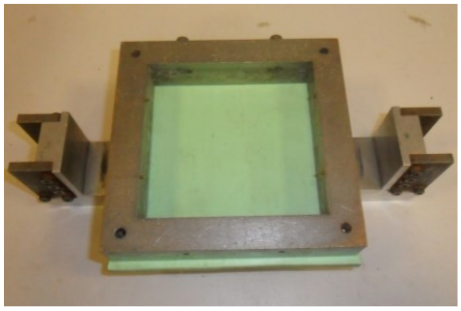

(a) Inverted assembly of surface and lower half

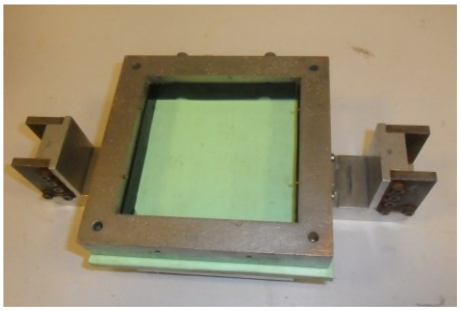

(b) Placing rubber curtain covering the gap

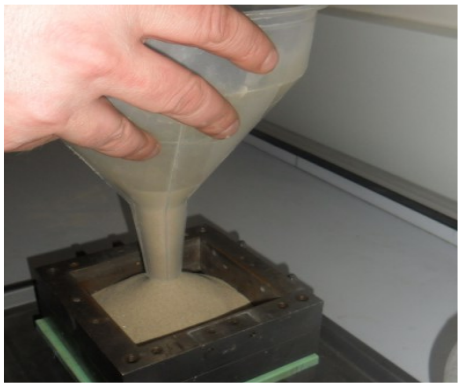

(c) Sample deposition

(d) Sample densification

(e) Sample levelling

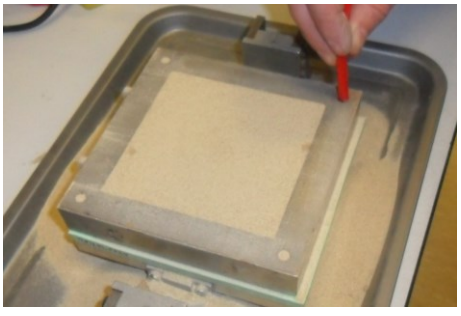

(f) Removing excess material

(g) Fixing lower retaining plate

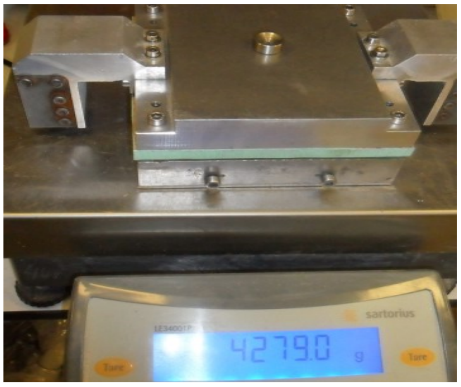

(h) Inverting box and measuring the mass

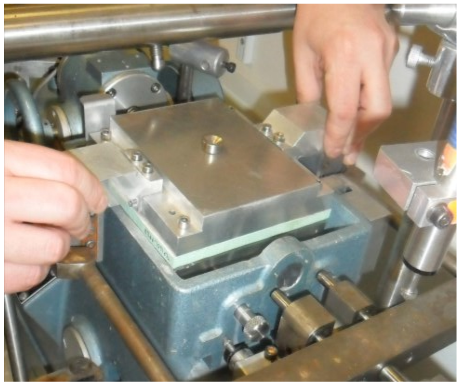

(i) Transferring the box to the shear carriage

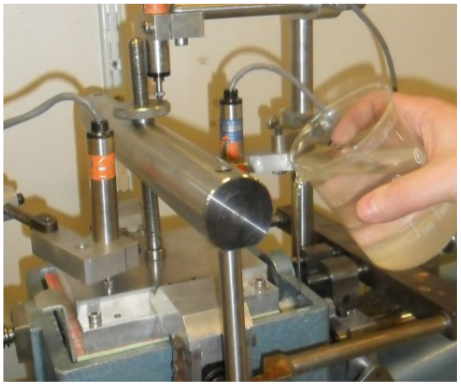

(j) Saturation of the sample

Figure 3.20 Method of preparation for interface shear tests

For additional clarity, the process of preparing interface tests is illustrated schematically in Figure 3.21. The typical time frame to complete the transition from step (e) to (f) is within 1 second. It is recognised that inverted the sample in this way is not ideal for maintaining perfect sample integrity. However, the benefits of ensuring a better, less disturbed, contact between soil and surface were considered to outweigh the drawbacks of this disruptive manoeuvre.

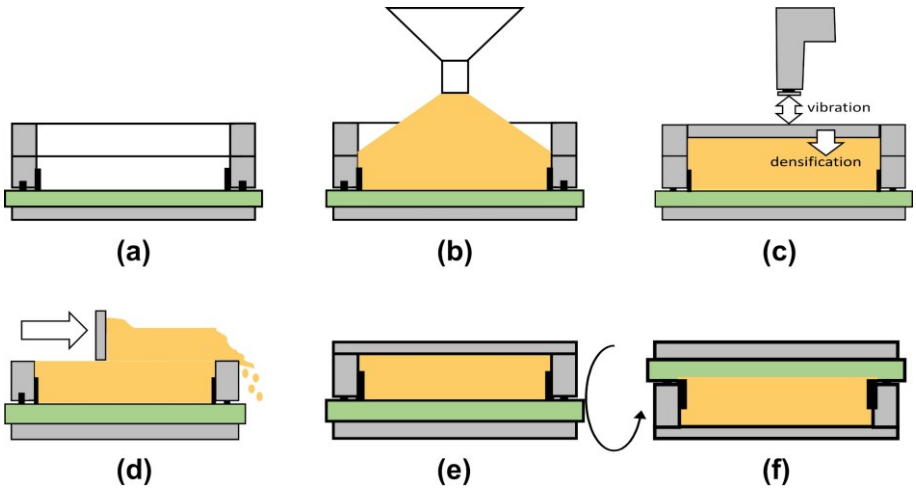

Figure 3.21 Schematic illustration of interface test sample preparation.

3.6.3 Relative density of soils

Relative density is a useful parameter to describe density of soil samples rather than the use of absolute densities and is a crucial part of sample preparation. It relates the density of a sample to its theoretical minimum and maximum which means that soils of equivalent relative density ought to exhibit analogous stress-dilatancy and peak-postpeak behaviour. Relative density is defined:

$$D_r = \frac{e_{max} - e}{e_{max} - e_{min}} \qquad Eq.\,3.1$$

where:
D_r = relative density
e_{max} = maximum void ratio
e_{min} = minimum void ratio

Determination of the required mass of soil for each direct shear test was carried out by rearranging the above equation and following the below steps:

$$e = D_r(e_{max} - e_{min}) - e_{max} \qquad Eq.\,3.2$$

$$e = \frac{V_t - V_s}{V_s} \qquad Eq.\,3.3$$

$$V_s = \frac{V_t}{1 + e} \qquad Eq.\,3.4$$

$$M_s = G_s \cdot V_s \qquad Eq.\,3.5$$

where:
V_t = total volume (m^3)
M_s = mass of solids (g)
G_s = specific gravity

3.7 Testing procedure

Once the test sample had been prepared according to the steps previously detailed, and the shearbox seated in the shear carriage, the following steps describe the test procedure.

1. The shearbox is placed into the shear carriage and secured in place using thumbscrews to clamp the box in.

2. The load hanger is levelled and the loading arm swung over the top of the shearbox and seated in the conical receptor attached to the top. Care is taken that no load is applied to the shearbox.
3. Three vertical LVDTs are put in position, one centrally, and one at the leading and trailing edge of the upper frame or interface pad. A fourth LVDT outside the shear carriage measures horizontal displacements. With all LVDTs in place the initial position of the central vertical LVDT is recorded.
4. The carriage is gently flooded allowing sufficient time, and topping up as necessary, for the whole soil sample to become saturated.
5. The grub screws which are maintaining the gap between upper and lower frames are gently removed ensuring no downward pressure is inadvertently applied.
6. The normal load is gently applied to the sample
7. The bolts keeping the upper and lower frame aligned are gently removed and the reading for the central vertical LVDT recorded again to determine how much settlement has occurred during saturation and loading.
8. Finally, the test can begin and the drive unit imposes a constant rate of displacement on the shear carriage while the upper frame or interface load pad is held in place with the resistance to move measured by the load cell.

3.7.1 Area correction

A consideration worthy of brief comment is the effect of reducing soil shear area as the frames of the shearbox displace relative to one another. In the initial arrangement the upper and lower shearbox frames are aligned forming a square contact area when viewed in plan. As the lower half displaces relative to the top half, the sample becomes split along a plane coaxial with the direction of relative displacement. As displacement of frames progresses the initial shear area of soil to soil contact progressively reduces and is replaced at the overlap between frame and soil with an interface friction instead. The phenomenon is illustrated in Figure 3.22.

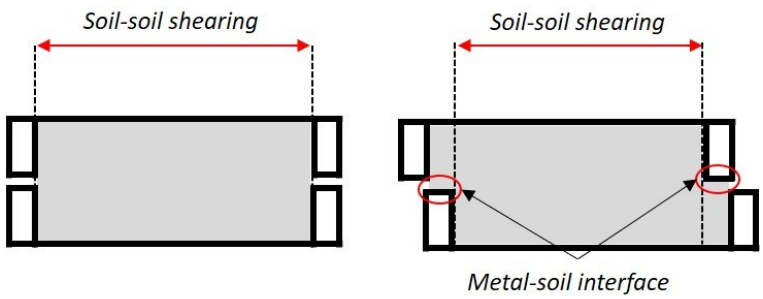

Figure 3.22 Schematic illustration of reducing shear area during DSA testing.

The reducing area of the shear area has implications for calculation of the shear stress and a correction can be made to take this into account. Shear stress would be calculated:

$$\tau = \frac{T - \sigma_n \cdot \delta_{ss} \cdot dl}{A_s - d \cdot l} \qquad Eq.\,3.6$$

where:

T = force measured by the load cell (kN)

σ_n = normal stress (kPa)

δ_{ss} = sand-steel interface angle of friction

d= horizontal shear displacement (m)

l = internal width of the shearbox (m)

A_s = cross sectional area of the shearbox (m^2)

3.7.2 Frame gap size

Lings and Dietz (2004) studied the impact of gap size between upper and lower frames to corroborate the reported findings of Nakamaru *et al*. (1995) and Shibuya *et al.* (1997) who found that shear strengths associated with smaller gaps were 10% higher than with larger openings (Kuwano, 1999). Lings and Dietz (2004) came to a similar conclusion, finding that increasing gap size generally led to lower peak strengths and reduced peak dilatancy and also increase top cap rotation. They observed a plateau in their data at a gap size of approximately 2 to 4 mm. They also reported that adopting a ratio of gap size to grain size, with gap size being at least $5 \cdot D_{50}$, also eliminated the need for apply the area correction. Discounting the area correction is based on empirical observations from their data which shows ultimate strengths remaining stable suggesting that reducing area was not influencing the strength anymore. In the case of interface testing the surface sample is oversized so the soil-surface contact area remains constant regardless of relative displacements so gap size and area correction considerations become redundant.

It became apparent during testing that adopting a gap size of $5 \cdot D_{50}$ was not practical across all sand types. In the case of Lowestoft Gravel, it would have results in a gap of 8 mm, and in the case of Redhill Sand of approximately 0.7 mm, both of which result in poor quality tests due to excessive settlements or unstable upper frames. Therefore, all tests were conducted with a gap size of 4 mm. A further advantage of preinstalling a gap between the box halves was that the otherwise-systemic effect of box friction, or corruption of results by contact between upper and lower frame during shearing, was entirely negated. In the event that the frames did come into contact, the test was treated as a failure as the results were then

unreliable. Such events were rare but clearly discernible by a sudden plateauing in vertical displacement data or by an unexpected upward trend in shear force measured by the load cell.

3.7.3 Determination of test parameters

Normal stress

The normal stress is generated by application of a load directly to the top of the shearbox. The load hanger assembly and mechanisms for transferring the load to the sample are counter-balanced and in equilibrium such that the mechanism itself does not impart any additional load. In addition to the masses placed on the load hanger, the mass of the top half of the shear box, including the top half of the soil sample that is above the shear plane, needs to be considered. With the masses summed they are multiplied by the acceleration due to gravity, *g*, to give the normal load. The average normal stress across the shear plane is the normal load divided by the shear plane area, which here is approximately 100 mm square. All tests were carried out under constant normal load.

$$\sigma_n = \frac{N}{A_s} \qquad (Eq. 3.7)$$

where:

N = normal load (kN)

Shear stress

The shear load required to restrain the upper half of the shearbox as the lower half translates beneath it is measured by a load cell. The load cell is calibrated directly into a load output. It has been discussed that there is no requirement for an area correction to account for the reducing shear area due to the size of the pre-installed gap between shear box halves. Therefore, for soils tests and interface tests where the surface specimen is oversized anyway so the shear area remains constant, the shear stress is calculated simply by dividing the shear load by the cross-sectional area of the shear plane:

$$\tau = \frac{T}{A_s} \qquad (Eq. 3.8)$$

Rotation

Rotation of the top cap can be indicative of a compromised test, often related to poor sample preparation or reaction loads generated in the apparatus, so it is worthwhile measuring this phenomenon. Rotations were measured by the placement of two LVDTs, one at the leading

and one at the trailing edge of the upper shear box half. Differential vertical displacement between the two ends is indicative of rotation and the angle of that rotation calculated in degrees. Acceptable rotations for a shear test are less than 2° although Lings and Dietz (2004) show that in the WDSA rotations do not have a significant effect on determination of cardinal parameters.

Dilatancy

Dilatancy is the phenomenon realised when densely packed grains are forced to over-ride their neighbours in order to unlock to facilitate shearing. Dilatancy was measured as the average value across the shear area and can be thought of as the maximum gradient on the vertical displacement curve during shearing. Dilatancy at any one point in the test was determined from the preceding eight sampling intervals approximately equal to 0.20 mm of horizontal displacement. The centrally placed LVDT was used for the calculation:

$$tan\psi = \frac{\Delta v}{\Delta h} \qquad (Eq. 3.9)$$

where:

ψ = angle of dilation

Δv = change in vertical position (m)

Δh = change in horizontal position (m)

3.7.4 Determination of derived parameters

The most commonly used formats for expressing the strength of soils or geomaterials is either as a ratio of the shear to normal stress (analogous to a friction coefficient) or converted to a friction angle which relates the shear resistance offered to the normal stress imposed. Relevant parameters can be evaluated from the experimental data as follows:

$$tan\phi_{peak} = \tau_{peak}/\sigma_n \qquad Eq. 3.10$$

$$tan\phi_{ult} = \tau_{ult}/\sigma_n \qquad Eq. 3.11$$

$$tan\psi_{peak} = \left(\frac{\Delta_z}{\Delta_x}\right)_{max} \qquad Eq. 3.12$$

Where:

ϕ_{peak} = peak angle of friction

ϕ_{ult} = ultimate angle of friction

ψ_{peak} = maximum angle of dilatancy

Δ_x = incremental shear displacement (m)

Δ_z = incremental vertical displacement (m)

In the case of interfaces, ϕ is substituted with δ and ψ with ζ but they are determined in the same way using equivalent measured parameters from interface test results.

3.7.5 Repeatability

Some repeatability tests were conducted to check that the outputs from the apparatus could be trusted and relied upon to give consistent results. Leighton Buzzard sand was selected for three soil repeatability tests, prepared in the same way at a relative density of 60% and a normal stress of ~25 kPa with a shearing rate of 0.8 mm/min. Shear stress, stress ratio, and vertical displacement plots are presented in Figure 3.23. The plots show excellent agreement with one another with secant peak and ultimate angles of friction of 37.4°, 37.9°, 38.0° and 30.2°, 29.2°, 29.0°, respectively. Vertical displacements also show good agreement with peak measured dilatancy of 12.6°, 13.7°, 12.4° also showing acceptable agreement.

Three interface repeatability tests were also conducted using Soil S0 at 15% relative density and a normal stress of ~35 kPa. Similar to soil, result plots are presented in Figure 3.24. Peak and ultimate secant angles of friction are 19.9°, 19.8°, 20.9° and 19.2°, 18.8°, 19.6° respectively which shows a similar level of variability to the soil-only tests and shows good repeatability for the WDSA for testing both soils and interfaces with both loose and dense soil samples.

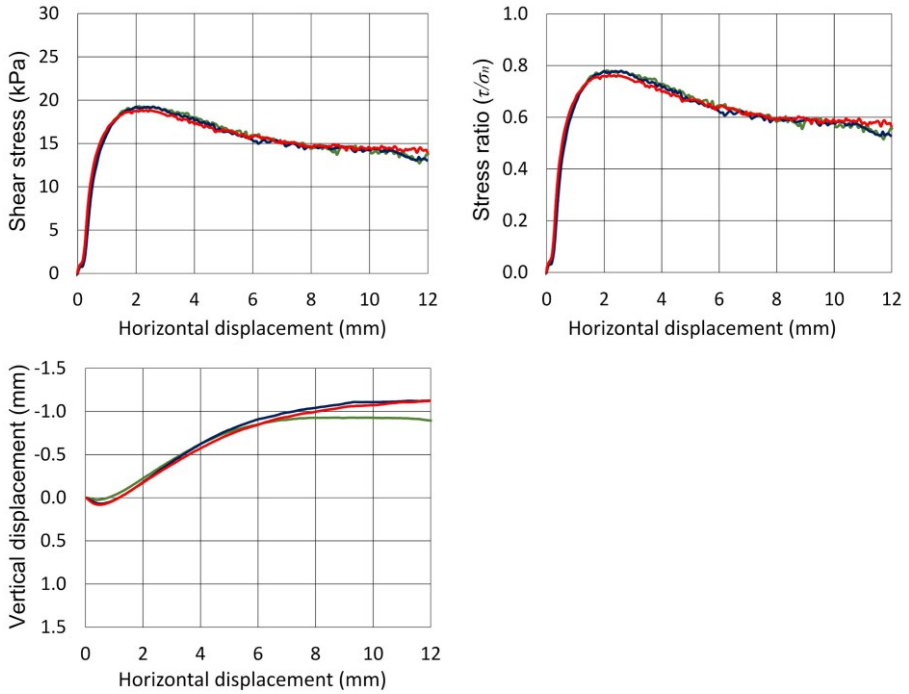

Figure 3.23 Three direct shear tests with Leighton Buzzard prepared in the same way at ~60% relative density and ~25 kPa confining stress.

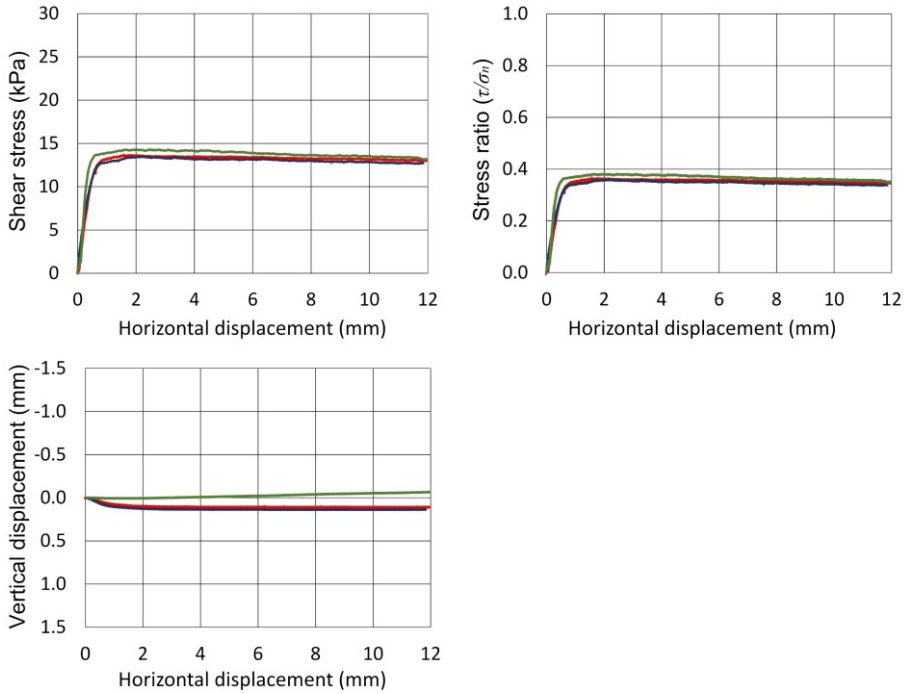

Figure 3.24 Three interface tests with Soil S0 prepared in the same way at 15% relative density and ~35 kPa confining stress.

3.8 Summary

This chapter has reviewed the materials and methods used for the research in this thesis.

- Seven different test sands were introduced, some of which have precedent in the literature for this use, and others which were selected to give a suitable spread in granulometry.
- Polypropylene pipe specimens were provided by an industrial partner and have been shown to have a variable surface topography but a consistent hardness and some have other surface features such as seams or other manufacturing artefacts.
- Two methods of measuring and quantifying surface topography and texture were discussed, a conventional contact method and an optical non-contact method which could be a preferably option on relative soft surfaces.
- The Winged Direct Shear Apparatus was adopted for soil and interface shear strength testing as there is good precedent in the literature for providing high quality results in both of these applications. Repeatability tests discussed in this chapter show that it is able to do so consistently.
- The WDSA was modified to accept an interface load pad in place of its upper frame, to which a surface specimen could be secured. The apparatus was instrumented to record horizontal displacement, vertical displacement in three places, and the shear load during testing.
- Instrumentation was calibrated and checked for electrical drift and the results show strong linear relationships between actuation and measurement outputs with excellent resolution and precision.
- A novel sample preparation procedure was adopted for interface tests. Testing was carried out in a surface-over-soil configuration but to ensure good soil to surface contact samples were prepared upside down. Soil was poured onto the upturned surface, densified as appropriate and then gently but decisively inverted before placement into the shear carriage. The key benefit of this methodology is that any sample disturbance during inversion ought to occur away from the soil-surface contact, and the interface zone does not pre-shear whilst maintaining a surface-over-soil test configuration.

4 Shear Response of Polypropylene Pipe Coatings

It was shown in Chapter 2 that there is a paucity of information available in the literature that characterises or provides a database of values for estimating interface shear strength of polypropylene pipe coatings with granular seafloor soils. The principle aim of this chapter is to provide data and a framework for determination of interface friction coefficients between polypropylene pipe coatings and granular seafloor soils. In pursuit of this aim a number of factors were investigated including gravel content of soils with a similar D_{50}, soil mean average grain size, interface shearing displacement rate, the effect of surface manufacturing artefacts, stress level, and soil density. The reader should be mindful of earlier observations about the nature of the test soils and pipe specimens. There is some variability in the angularity of test soils which is an uncontrolled variable. Just as more angular soil grains lead to an increased soil strength, interface shear strengths are susceptible to analogous increases. The interface results should also be viewed with the knowledge that the pipe specimens are generally smooth in nature.

The first section of this chapter deals with soils of varying gravel content and looks also at displacement rate effects and whether the seams that are present on some specimens have any effect. The second part looks at the impact of changing soil mean grain size. The third part of the chapter measures the evolution of surface texture from before to after interface testing including discussion on the most appropriate method for measuring surface textures. Finally, the results are compared with existing literature and the conclusions made throughout the chapter are summarised.

More detailed plots than are included here are presented in Appendices B1 and C1 and all the raw test data is contained in the data pack on an SD card attached to this thesis.

4.1 Preliminary testing

Before the main investigation could begin there were some variables which needed assessing in order that meaningful analysis of the results could take place. The first was to determine if there was any rate effect, and the second to determine if the presence of surface seams (a manufacturing artefact) had any impact as they were an unavoidable presence on a number of specimens.

4.1.1 Influence of displacement rate

Two displacement rates were tested, approximately 0.8 mm/min and approximately 0.2 mm/min. The reason for carrying out these tests is that some of the finer soils contain some

silt and although drained conditions were expected to prevail, it was necessary to be sure. Ten interface tests with soil S0 were conducted at a displacement rate of 0.2 mm/min and 10 tests at 0.8 mm/min. Soil S0 was chosen as it amongst the finest of the soils used in this research so most susceptible to excess pore water pressure generation. Table 4.1 lists the interface tests and cardinal parameters for this work. The $D_{r\ fab}$ and $D_{r\ con}$ are the soil sample relative densities as fabricated and post consolidation after the application of the normal load and represents the relative density at the start of shearing. The same applies to e_{fab} and e_{con} with regard to the sample void ratio. The peak shear stress, τ_{peak}, is the maximum shear stress recorded during the test and the ultimate shear stress, τ_{ult}, is the average shear stress between 10 mm and 12 mm of horizontal displacement. For each soil, two nominal relative densities were tested (D_r approximately 15% and 70%) at five levels of vertical confining stress (σ_n approximately 2, 5, 10, 20, 35 kPa). For soil tests a three part naming convention has been adopted to uniquely identify each test consisting of a soil type reference [S0, S15, S35], a density reference [L (for loose), D (for dense)], and a nominal stress level reference [2, 5, 10, 20, 35 (kPa)]. The displacement rate is given at the end of each test reference. Figure 4.1 shows their shear response and volumetric behaviour with 0.2 mm/min in darker colours and 0.8 mm/min in paler shades. Figure 4.2 shows the shape of their failure envelopes.

A note needs to be made on relative densities detailed with negative values. This arises because the maximum void ratio of soils was determined according to BS 1377-2:1990 but the method of sample preparation sometimes resulted in soil samples adopting an even looser configuration. In these instances, the calculated relative density is negative. A few tests, limited to loose samples, show large changes in relative density between the as fabricated condition and after consolidation from application of the normal load. Between these points, three things occur which are likely to contribute to this. The first is when the samples are flipped over, which disproportionately impacts loose samples as grain are less tightly packed allowing for more movement and settlement. The second is during saturation which consistently led to an initial phase of sample settlement through the testing campaign to less or greater degrees, with finer soils being more susceptible. Lastly, application of the load generally caused the greatest degree of settlement. For the worst case change in relative density in Table 4.1, from D_r -33.5 to +11.3, the equivalent approximate sample settlement is 1.2 mm from an initial sample height of approximately 29 mm. Tests with such large settlements became fewer as the campaign progressed as more experience led to improvements in sample quality.

Table 4.1 S0 interface displacement rate effect tests

Test reference	σ_n (kPa)	$D_{r\ fab}$ (%)	$D_{r\ con}$ (%)	e_{fab}	e_{con}	τ_{peak} (kPa)	τ_{ult} (kPa)	τ_{peak}/σ_n	τ_{ult}/σ_n
S0_L02_T(0.2)	2.26	14.9	31.6	0.871	0.838	1.01	0.96	0.45	0.42
S0_L05_T(0.2)	5.89	16.7	31.4	0.869	0.838	2.04	1.93	0.35	0.33
S0_L10_T(0.2)	12.01	14.9	41.5	0.871	0.818	4.03	3.89	0.34	0.32
S0_L20_T(0.2)	22.22	14.2	44.3	0.871	0.812	8.09	7.87	0.36	0.35
S0_L35_T(0.2)	37.54	14.9	48.4	0.871	0.804	13.62	13.08	0.36	0.35
S0_D02_T(0.2)	2.27	70.1	77.3	0.761	0.746	1.00	0.95	0.44	0.42
S0_D05_T(0.2)	5.9	71.0	75.3	0.759	0.750	2.24	2.14	0.38	0.36
S0_D10_T(0.2)	12.03	70.5	78.3	0.760	0.744	4.67	4.41	0.39	0.37
S0_D20_T(0.2)	22.24	70.8	90.0	0.760	0.721	8.65	8.26	0.39	0.37
S0_D35_T(0.2)	37.56	70.1	87.7	0.761	0.726	14.45	13.94	0.38	0.37
S0_L02_T(0.8)	2.26	-4.3	17.1	0.910	0.867	0.93	0.90	0.41	2.26
S0_L05_T(0.8)	5.89	4.6	23.7	0.892	0.854	2.41	2.37	0.41	5.89
S0_L10_T(0.8)	12.01	-14.8	19.8	0.931	0.861	4.14	3.91	0.35	12.01
S0_L20_T(0.8)	22.22	-33.5	11.3	0.968	0.878	7.96	7.39	0.36	22.22
S0_L35_T(0.8)	37.54	-29.1	10.5	0.959	0.88	14.3	13.39	0.38	37.54
S0_D02_T(0.8)	2.27	70.3	77.6	0.76	0.746	1.08	1.04	0.47	2.27
S0_D05_T(0.8)	5.90	68.7	80.3	0.764	0.740	3.00	2.93	0.51	5.90
S0_D10_T(0.8)	12.03	60.1	74.7	0.781	0.752	5.19	4.80	0.43	12.03
S0_D20_T(0.8)	22.24	47.8	73.7	0.805	0.754	8.85	8.60	0.40	22.24
S0_D35_T(0.8)	37.56	41	69.4	0.819	0.762	14.45	12.68	0.38	37.56

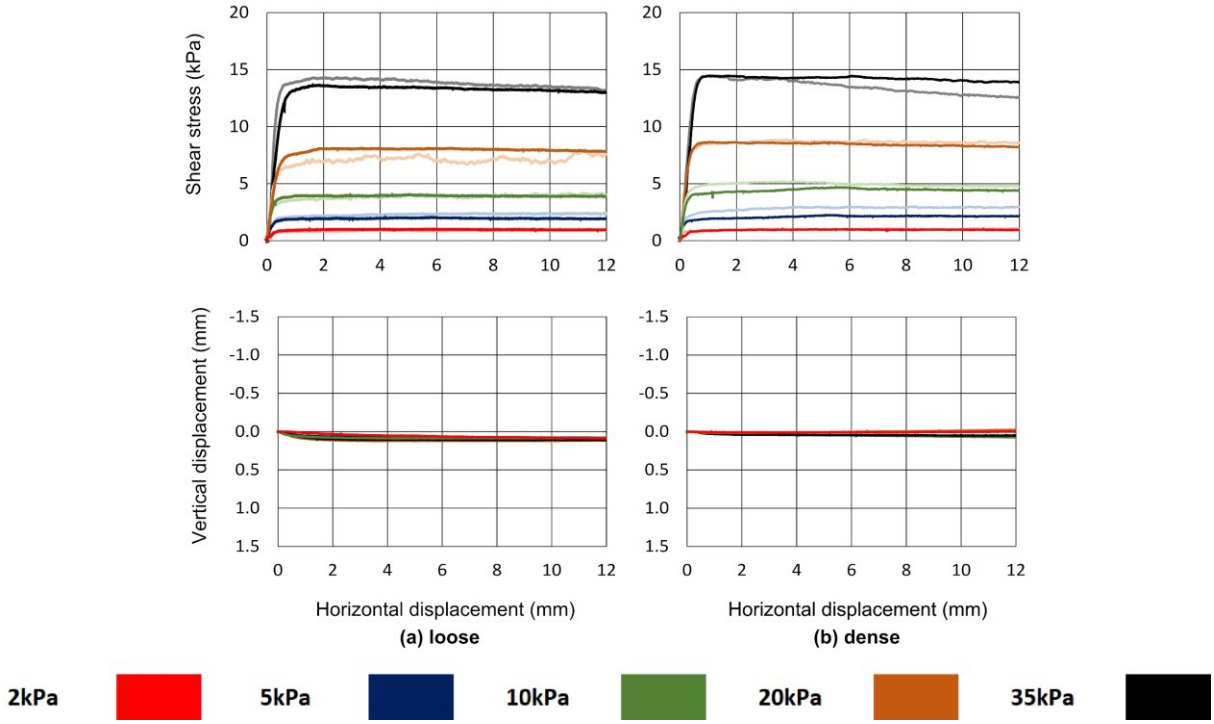

Figure 4.1 Interface shear stress and vertical displacement response with sand S0 at 0.2 mm/min (darker shades) and 0.8 mm/min (paler shades) horizontal displacement rate (a) loose and (b) dense sample.

Figure 4.2 shows that there is a slight variation in the shape of the failure envelope, however the shear strengths are very similar. Dense peak and ultimate, and loose ultimate strengths at 0.2 mm/min are 21.1°, 20.4°, 19.2° compared to 0.8 mm/min with 21.5°, 19.6°, and 19.3° respectively. Therefore, the displacement rate was not considered to have any significant effect on the results and that at 0.8 mm/min the finer test soils would still behave as a drained soil. These rate effect results confirm existing literature on the topic. Hungr and Morgenstern (1984) and Sassa (1985) found that the residual shear strength of granular soils was not effected by shearing rate, and Lemos *et al*. (1985) reported that soils with less than 5% clay content were not affected by the shearing rate. Therefore, 0.8 mm/minute was adopted for convenience, and is broadly in line with Bolton's (1991) suggestion that 1 mm/min is appropriate for sands.

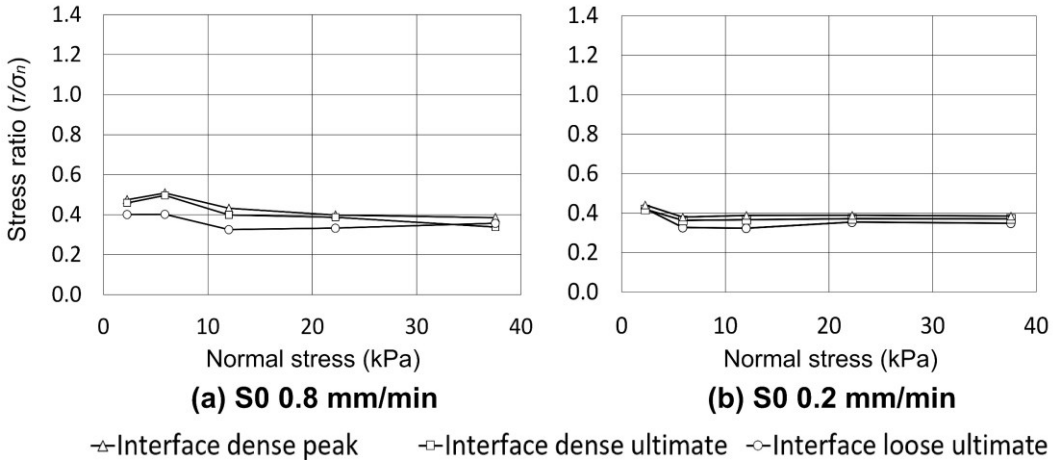

Figure 4.2 Comparison of S0 strength envelopes at horizontal displacement rate of (a) 0.8 mm/min and (b) 0.2 mm/min.

4.1.2 Influence of surface seams

Some surface specimens are inscribed with a surface seam which is an artefact of the manufacturing process where the polypropylene is extruded and wrapped around the pipe in a strip. Figure 4.3 shows a length of pipe coating where the seams are clearly visible between adjoining strips of polypropylene.

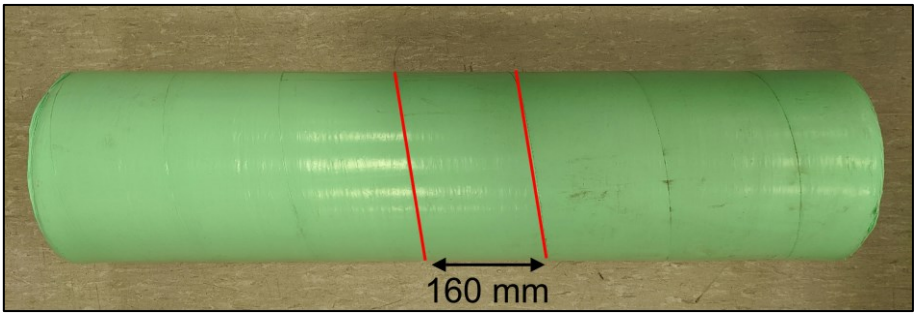

Figure 4.3 Length of polypropylene pipe coating.

Seams run at approximately 81° to the shearing direction of surface specimens where present and no surface had more than a single seam. Due to the presence of surface seams on some of the test surfaces it was necessary to assess their influence on interface shear response. Ten interface tests with soil S0 were conducted to establish what, if any, effect the presence of a surface seam had on the interface shear response. Table 4.2 lists these interface tests and cardinal parameters and Figure 4.4 shows their shear response and volumetric behaviour. Tests with the “uS” signifier mean surface without a seam, and “S” indicates a seam is present.

Table 4.2 S0 interface test on seamed and unseamed surfaces

Test reference	σ_n (kPa)	$D_{r\ fab}$ (%)	$D_{r\ con}$ (%)	e_{fab}	e_{con}	τ_{peak} (kPa)	τ_{ult} (kPa)	τ_{peak}/σ_n	τ_{ult}/σ_n
S0_D02_T(uS)	2.06	70.1	77.2	0.761	0.747	1.01	0.99	0.49	0.48
S0_D05_T(uS)	5.13	70.0	79.7	0.761	0.742	2.16	2.13	0.42	0.42
S0_D10_T(uS)	11.26	70.1	82.3	0.761	0.736	4.48	4.34	0.40	0.39
S0_D20_T(uS)	21.49	70.1	84.7	0.761	0.732	8.36	7.84	0.39	0.36
S0_D35_T(uS)	36.83	70.1	91.2	0.761	0.719	13.55	12.40	0.37	0.34
S0_D02_T(S)	2.06	63.9	70.2	0.773	0.761	1.02	1.00	0.50	0.49
S0_D05_T(S)	5.13	70.1	80.6	0.761	0.740	2.17	2.12	0.42	0.41
S0_D10_T(S)	11.26	59.4	75.3	0.782	0.750	4.24	4.18	0.38	0.37
S0_D20_T(S)	21.49	70.2	85.7	0.761	0.730	8.04	7.93	0.37	0.37
S0_D35_T(S)	36.83	70.1	95.7	0.761	0.710	13.62	13.29	0.37	0.36

Figure 4.4 presents the shear response and volumetric behaviour of these tests. Both show a similar elastic-perfectly plastic response. There is a subtle tendency for the surface without a seam to exhibit a slight downward trend in shear stress over the course of the test.

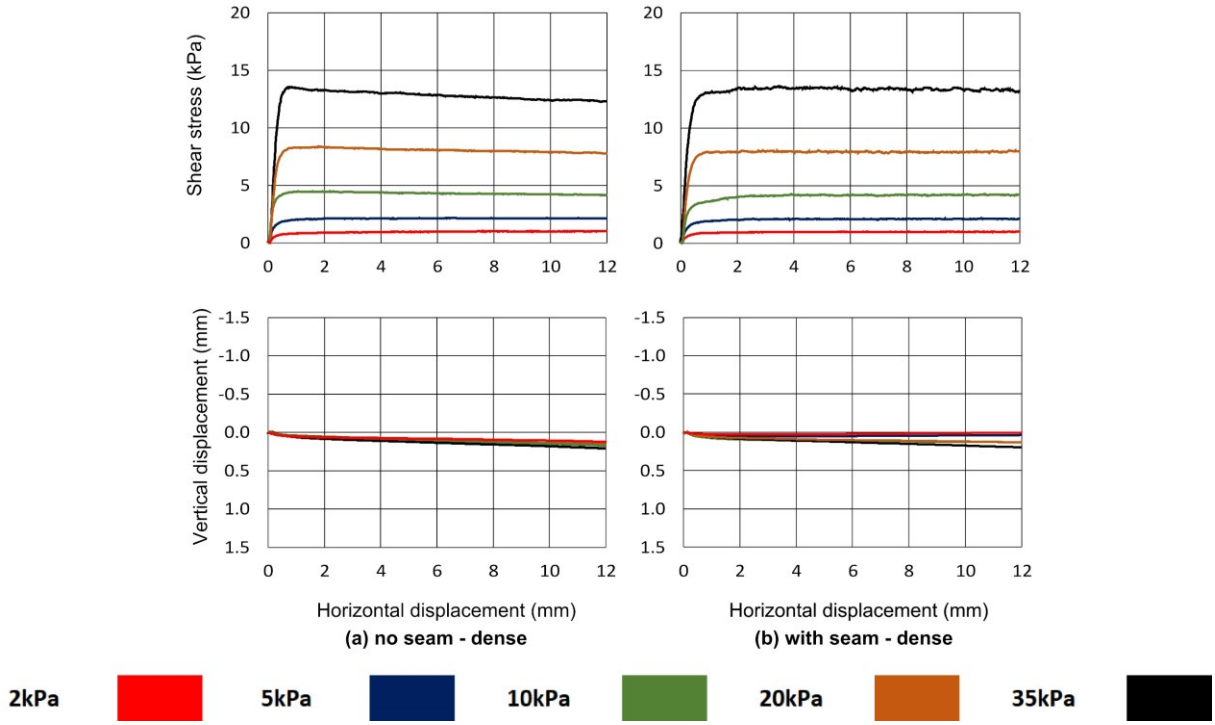

Figure 4.4 "T" interface shear stress and vertical displacement response with sand S0 for a surface specimen (a) without and (b) with a seam present.

Figure 4.5 presents the shear to normal stress ratios. The lines plot almost on top of each other indicating both that the peak and ultimate strengths are analogous and that strengths are comparable between the two. Peak and ultimate angles of friction for seamed and

unseamed interfaces are 20.4° and 20.0°, and 20.6° and 19.2° respectively indicating there is a negligible impact on interface strength from the presence of a seam. Therefore, the presence or absence of seams on test specimens can be disregarded as a variable of concern. In any case, only a select few tests involving soils S0, S15, and S35 with "T" surfaces are affected.

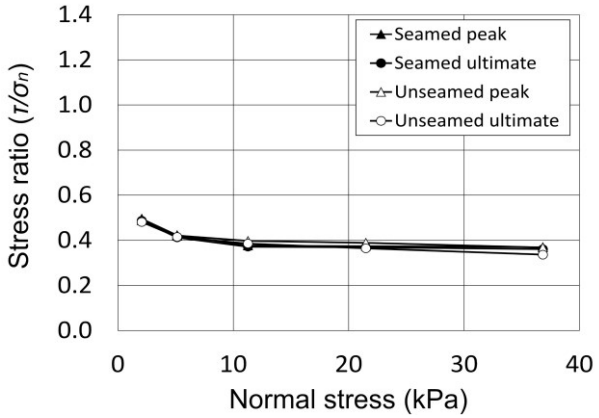

Figure 4.5 Peak and ultimate stress ratio for seamed and unseamed surface specimens.

4.2 Soil gravel content

Three test soils were fabricated in the laboratory to conduct the investigation into the effect of gravel content on interface shear response. The soils are named S0, S15, and S35 and their composition and provenance is discussed in Chapter 3. Soils S0, S15, and S35 are comprised of 0%, 15%, and 35% grains retained on a 0.4 mm aperture sieve respectively whilst attempting to maintain similar D_{50} mean average grain size across each soil. The formulation of these soils was chosen to be analogous to typical granular soils at the finer end of the range found in the North Sea (Milewski *et al.*, 2019), although the grading curve may not be representative as these can be very variable. Thirty soil-only direct shear tests were carried out to determine their shear response and 50 interface tests were carried out to test their interface shear response.

4.2.1 Soil tests

Table 3.1 lists the soil-only tests with soils S0, S15, and S35 and includes some cardinal parameters. The definitions for the table column headings are the same as defined previously in this chapter and tests adopt an analogous naming system with the omission of a surface specimen reference in the case of soil-only tests. Peak dilatancy data is included (Ψ) presented in degrees. Shear response and volumetric behaviour plots are presented in Figure 4.6. Each series of tests exhibits behaviour consistent with classical soils mechanics. For

dense sample tests peak strengths are mobilised in the early stages that coincide with the maximum rates of dilation. As dilation rates fall so do shear resistances until a near-constant ultimate state is mobilised. Loose sample tests exhibit a monotonic increase of shear resistance to a near-constant ultimate state accompanied by generally lower or no dilation.

Table 4.3 S0, S15, and S35 soil direct shear tests

Test reference	σ_n (kPa)	$D_{r\,fab}$ (%)	$D_{r\,con}$ (%)	e_{fab}	e_{con}	τ_{peak} (kPa)	τ_{ult} (kPa)	τ_{peak}/σ_n	τ_{ult}/σ_n	Ψ $\Delta v/\Delta h$
S0_L02	2.87	15.6	21.0	0.870	0.859	1.84	1.76	0.64	0.61	-
S0_L05	5.94	8.4	14.9	0.884	0.871	3.92	3.82	0.66	0.64	-
S0_L10	11.91	6.1	30.2	0.889	0.841	8.04	7.11	0.68	0.60	-
S0_L20	22.13	-0.2	14.6	0.901	0.872	14.48	13.30	0.65	0.60	-
S0_L35	37.45	0.5	28.5	0.900	0.844	24.99	23.43	0.67	0.63	-
S0_D02	2.89	67.1	69.1	0.767	0.763	3.62	2.06	1.25	0.71	0.43
S0_D05	5.26	64.0	74.0	0.773	0.753	5.51	3.74	1.05	0.71	0.32
S0_D10	11.49	62.3	73.3	0.776	0.754	9.70	7.51	0.84	0.65	0.22
S0_D20	22.14	55.5	73.1	0.790	0.755	17.28	13.44	0.78	0.61	0.18
S0_D35	37.46	62.3	84.1	0.776	0.733	29.26	23.27	0.78	0.62	0.23
S15_L02	2.90	16.8	21.2	0.729	0.721	2.32	2.02	0.80	0.70	-
S15_L05	5.28	11.0	27.2	0.740	0.710	3.60	3.54	0.68	0.67	-
S15_L10	11.19	15.3	18.6	0.732	0.726	7.49	7.14	0.67	0.64	-
S15_L20	22.15	8.7	9.3	0.745	0.743	15.21	15.15	0.69	0.68	-
S15_L35	37.48	8.7	11.0	0.745	0.740	24.30	23.93	0.65	0.64	-
S15_D02	2.92	69.5	73.6	0.630	0.622	3.26	2.32	1.12	0.79	0.33
S15_D05	5.29	60.5	63.3	0.647	0.641	5.13	4.68	0.97	0.88	0.25
S15_D10	11.95	61.5	70.1	0.645	0.628	10.69	8.29	0.89	0.69	0.28
S15_D20	22.16	54.8	76.2	0.657	0.617	18.51	14.23	0.84	0.64	0.27
S15_D35	37.46	61.1	73.9	0.646	0.621	30.53	24.73	0.82	0.66	0.22
S35_L02	2.91	-7.2	3.2	0.652	0.634	2.45	2.03	0.84	0.70	-
S35_L05	5.29	1.4	0.2	0.637	0.639	3.69	3.42	0.70	0.65	-
S35_L10	11.95	-9.0	15.5	0.655	0.613	8.94	8.84	0.75	0.74	-
S35_L20	22.16	-15.8	3.0	0.667	0.635	14.77	14.37	0.67	0.65	-
S35_L35	37.49	-19.5	11.8	0.673	0.620	24.59	24.10	0.66	0.64	-
S35_D02	2.95	52.1	48.8	0.550	0.556	3.47	2.50	1.18	0.85	0.41
S35_D05	5.32	52.1	54.7	0.550	0.545	4.89	3.45	0.92	0.65	0.20
S35_D10	11.99	64.4	68.9	0.529	0.521	11.16	7.78	0.93	0.65	0.28
S35_D20	22.20	51.4	65.2	0.551	0.527	18.20	16.12	0.82	0.73	0.17
S35_D35	37.52	49.4	77.6	0.555	0.506	27.65	24.25	0.74	0.65	0.29

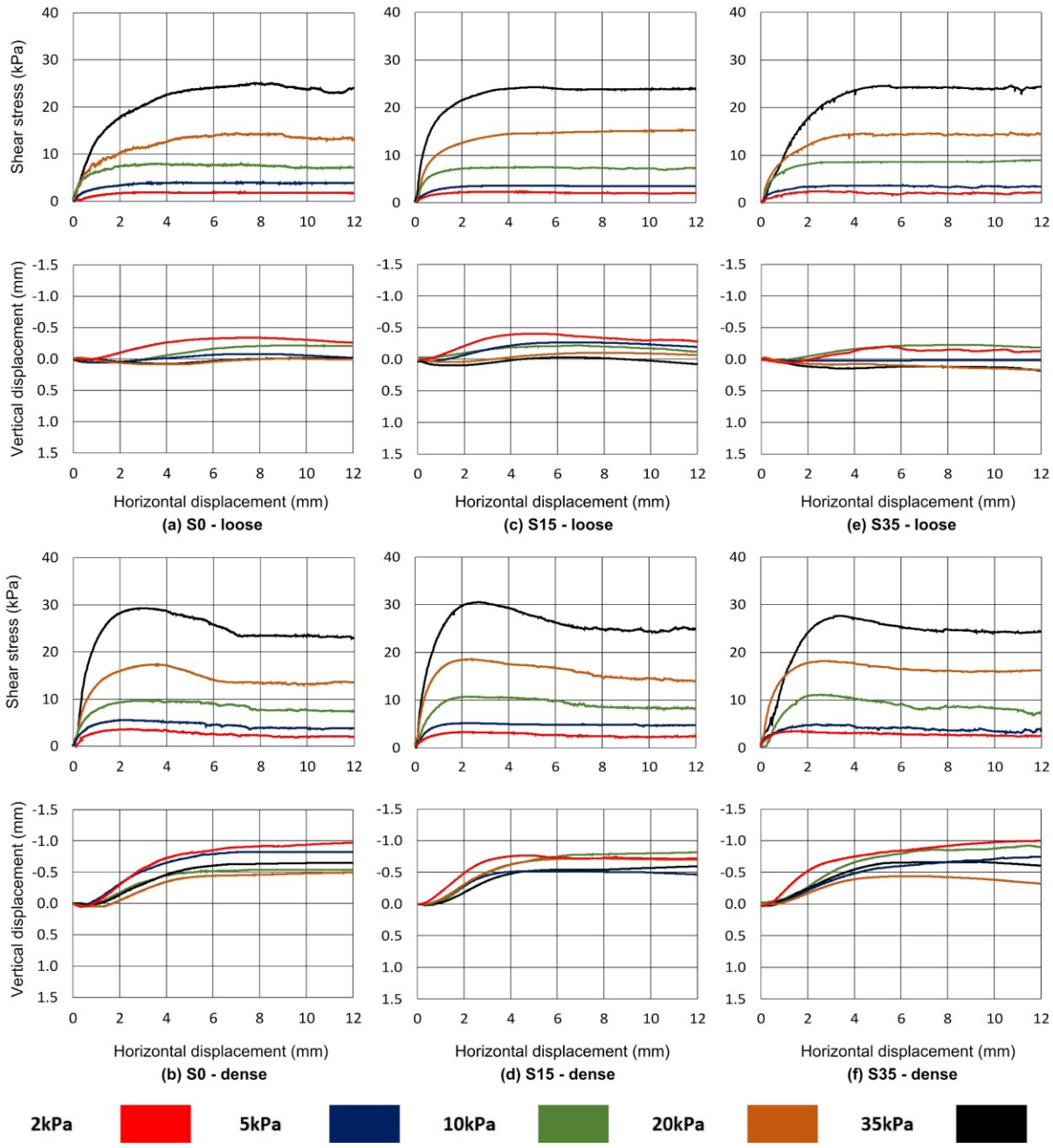

Figure 4.6 Soil-only shear stress and vertical displacement response with (a,b) S0, (c,d) S15, and (e,f) S35.

Strength envelopes for soils S0, S15, and S35 are presented in Figure 4.7. The angle of friction, ϕ, for each soil is calculated from the tangent of the slope. Due to the very low stresses involved the failure envelopes are forced through the origin for calculation of ϕ. Presented in Figure 4.7 in terms of the ratio between shear and normal stress it is obvious that failure envelopes are nonlinear, particularly in the case of the peak strengths which is consistent with the known behaviour of geomaterials (e.g. Sture *et al.*, 1998; Fannin *et al.*, 2005; Chakraborty and Salgado, 2010).

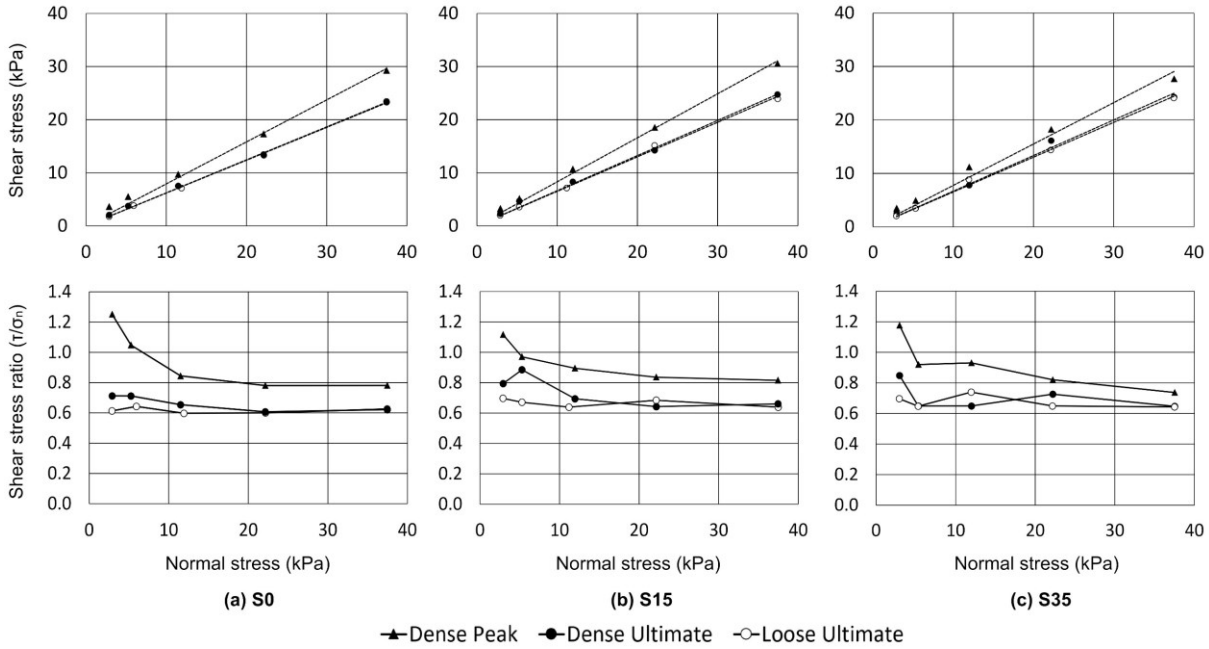

Figure 4.7 Strength envelopes in terms of shear stress and shear to normal stress ratio for soils (a) S0, (b) S15, and (c) S35.

Angles of friction in each condition, loose and dense ultimate, and dense peak, are summarised in Table 4.4 and it can be seen that loose and dense ultimate strengths show good agreement, within a maximum of 0.6°, as is expected. There is a tendency for the soils with greater gravel content to mobilise a slightly greater ultimate shear strength, an increase of 1.4° and 1.8° for loose and dense soils respectively between soils S0 and S35 which is consistent with the trend identified by Simoni and Houlsby (2006). These increases in strength may be related to the contribution of more angular gravel grains to the overall soils net average angularity. The peak strengths of dense samples do not follow the same pattern but this may be explained by the sensitivity of peak strengths to initial sample density. It can be seen from Table 4.3 that initial and post-consolidation sample relative densities for tests with soil S35 were lower than for soils S0 and S15 which is likely to have resulted in a lower peak strength being mobilised.

Table 4.4 S0, S15, and S35 soil angles of friction

Soil ϕ	Loose ultimate (°)	Dense peak (°)	Dense ultimate (°)
S0	31.7	38.3	31.9
S15	33.0	39.7	33.5
S35	33.1	37.8	33.7

4.2.2 Interface tests

Table 4.5 lists the interface tests with soils S0, S15, and S35 and includes some cardinal parameters which are defined as previously discussed. Peak dilatancy data is not provided for tests where it was negligible or absent due to the difficulties in extracting a robust rate of change in vertical position from the data. Shear response and volumetric behaviour plots for "T" interfaces with soils S0, S15, and S35 are presented in Figure 4.8.

Table 4.5 "T" interface tests with soils S0, S15, and S35

Test reference	Surf.	σ_n (kPa)	$D_{r\ fab}$ (%)	$D_{r\ con}$ (%)	e_{fab}	e_{con}	τ_{peak} (kPa)	τ_{ult} (kPa)	τ_{peak}/σ_n	τ_{ult}/σ_n
S0_L02_T	PP26	2.26	-4.3	17.1	0.910	0.867	0.93	0.90	0.41	0.40
S0_L05_T	PP22	5.89	4.6	23.7	0.892	0.854	2.41	2.37	0.41	0.40
S0_L10_T	PP25	12.01	-14.8	19.8	0.931	0.861	4.14	0.00	0.35	0.33
S0_L20_T	PP24	22.22	-33.5	11.3	0.968	0.878	7.96	7.39	0.36	0.33
S0_L35_T	PP27	37.54	-29.1	10.5	0.959	0.880	14.30	13.39	0.38	0.36
S0_D02_T	PP09	2.27	70.3	77.6	0.760	0.746	1.08	1.04	0.47	0.46
S0_D05_T	PP04	5.9	68.7	80.3	0.764	0.740	3.00	2.93	0.51	0.50
S0_D10_T	PP03	12.03	60.1	74.7	0.781	0.752	5.19	4.80	0.43	0.40
S0_D20_T	PP02	22.24	47.8	73.7	0.805	0.754	8.85	8.60	0.40	0.39
S0_D35_T	PP01	37.56	41.0	69.4	0.819	0.762	14.45	12.68	0.38	0.34
S15_L02_T	PP18	2.28	5.9	14.1	0.750	0.734	0.87	0.86	0.38	0.38
S15_L05_T	PP23	5.9	5.9	32.7	0.750	0.699	2.41	2.30	0.41	0.39
S15_L10_T	PP21	12.03	12.4	28.0	0.738	0.708	4.75	4.57	0.39	0.38
S15_L20_T	PP19	22.24	-22.0	14.1	0.803	0.734	7.83	7.69	0.35	0.35
S15_L35_T	PP17	37.56	-11.4	15.1	0.783	0.732	12.80	12.39	0.34	0.33
S15_D02_T	PP09*	2.29	71.5	74.5	0.626	0.620	1.28	1.24	0.56	0.54
S15_D05_T	PP11*	5.92	74.9	82.1	0.620	0.606	3.37	3.29	0.57	0.56
S15_D10_T	PP16	12.04	68.2	74.6	0.626	0.620	4.99	4.93	0.41	0.41
S15_D20_T	PP13*	22.26	56.5	75.4	0.654	0.619	11.69	11.50	0.53	0.52
S15_D35_T	PP26*	37.58	57.0	69.4	0.653	0.608	16.00	14.67	0.43	0.39
S35_L02_T	PP13	2.29	15.7	25.7	0.613	0.596	0.87	0.83	0.38	0.36
S35_L05_T	PP08	5.92	3.8	33.7	0.633	0.582	2.26	2.19	0.38	0.37
S35_L10_T	PP14	12.04	3.1	21.5	0.635	0.603	4.79	4.65	0.40	0.39
S35_L20_T	PP15	22.25	-11.3	23.1	0.660	0.600	8.56	7.91	0.38	0.36
S35_L35_T	PP07	37.58	-6.3	31.4	0.651	0.586	13.68	13.34	0.36	0.36
S35_D02_T	PP11	2.3	59.6	64.4	0.537	0.529	1.11	1.07	0.48	0.47
S35_D05_T	PP05	5.93	68.2	82.2	0.522	0.498	3.15	3.06	0.53	0.52
S35_D10_T	PP12	12.06	67.5	73.0	0.523	0.514	5.39	5.25	0.45	0.44

Table 4.5 "T" interface tests with soils S0, S15, and S35

Test reference	Surf.	σ_n (kPa)	$D_{r\ fab}$ (%)	$D_{r\ con}$ (%)	e_{fab}	e_{con}	τ_{peak} (kPa)	τ_{ult} (kPa)	τ_{peak}/σ_n	τ_{ult}/σ_n
S35_D20_T	PP10	22.27	52.1	69.7	0.550	0.519	9.56	8.95	0.43	0.40
S35_D35_T	PP06	37.59	54.1	76.0	0.546	0.509	16.54	16.26	0.44	0.43

*Due to a shortfall in the required number of surface specimens, four were subjected to two interface tests. The second test of these cases is indicated by an asterisk (*) following the surface reference. The effect of the former test on subsequent data was minimised by selecting for retest only those surface specimens that had experienced low levels of normal stress.

For both dense and loose samples tests there is a rapid increase in shear stress until a plateau is reached at a horizontal displacement of less than 0.5 mm. From then on, the shear stress remains largely stable until the end of the test. Shear response may be generally described as elastic-perfectly plastic. In both dense and loose sample tests there is little vertical displacement. In general samples tend to maintain a constant volume or are slightly contractile irrespective of sample density.

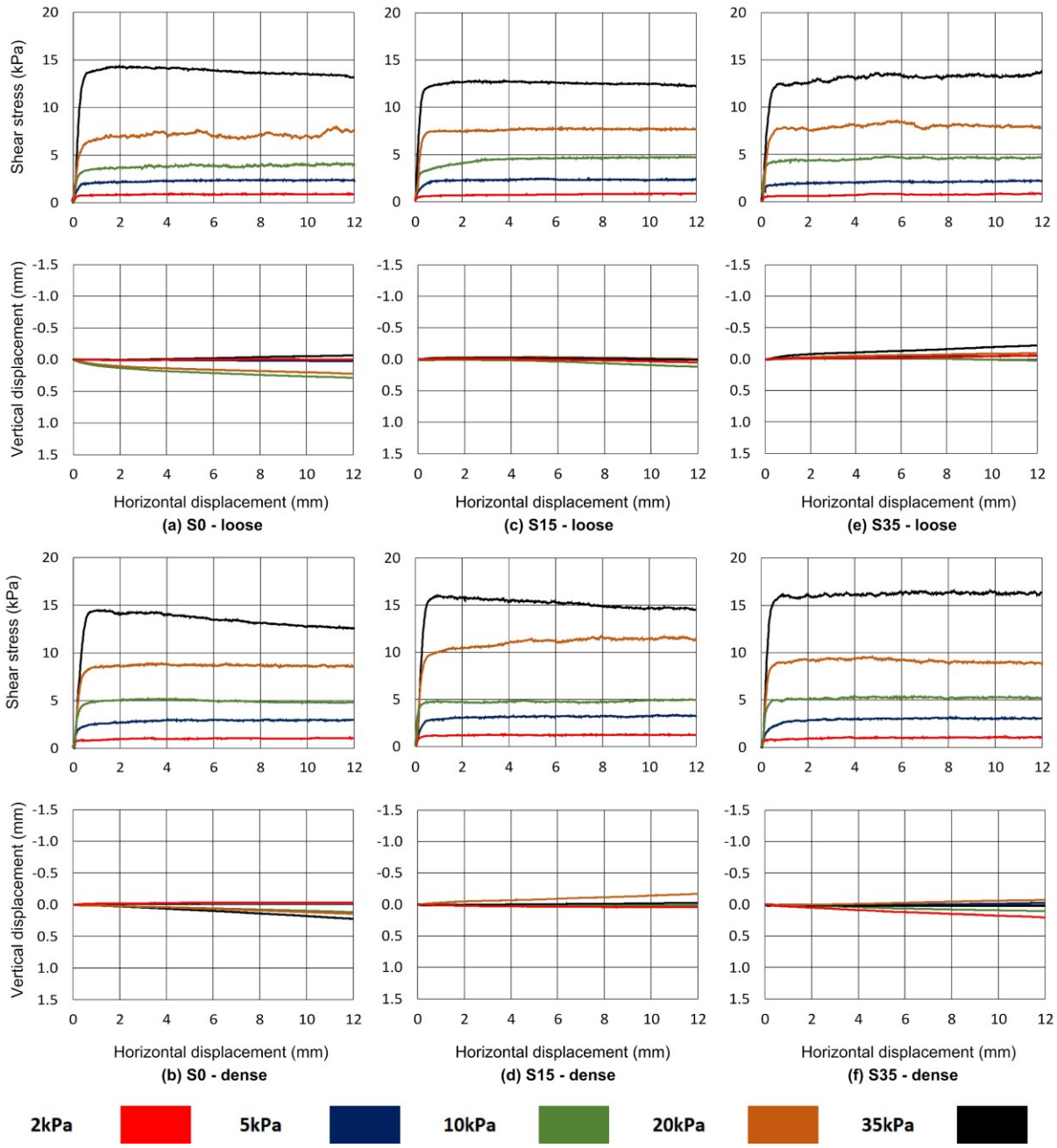

Figure 4.8 "T"-type interface shear stress and vertical displacement response with (a,b) S0, (c,d) S15 and (e,f) S35.

Strength envelopes for pipe coating interface tests with soils S0, S15, and S35 are presented in Figure 4.9 as shear to normal stress ratio alongside those of the soil-only tests. It is clear to see that interface strengths are significantly lower than their equivalent soil-only strength. Strength envelopes still have a subtle nonlinearity analogous to that seen in the ultimate condition of the soil tests. Peak strengths are not observed, even in dense tests, which is consistent with the findings of other authors that worked with smooth polymers (e.g. O'Rourke *et al.*, 1990).

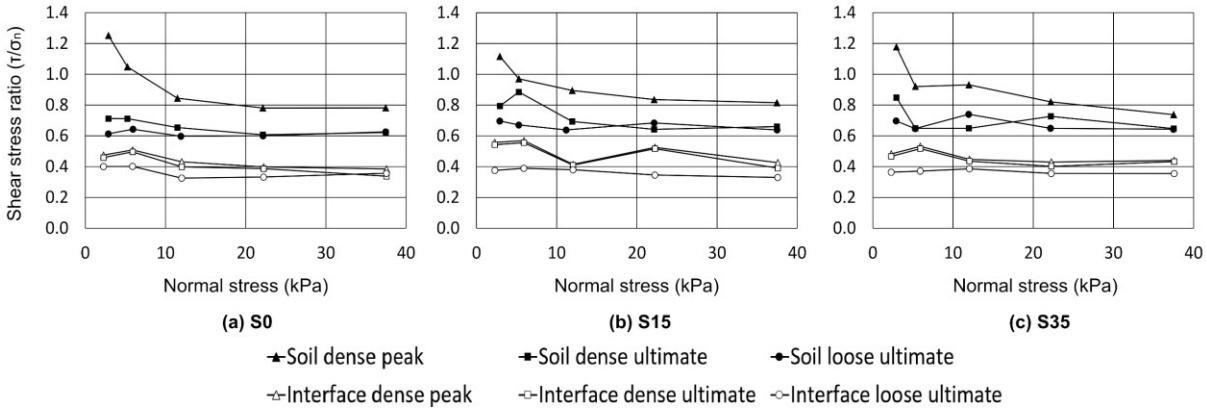

Figure 4.9 Strength envelopes as shear to normal stress ratio for interface tests (a) S0, (b) S15, and (c) S35.

Similar to soil tests, the interface shear strengths are distilled into interface angles of friction, which are summarised in Table 4.6. Contrary to soil tests, the peak and ultimate strengths for dense soils are similar while there is a much greater difference between the ultimate strengths of loose and dense tests. Dense sample interface tests were up to 4.3° stronger than their loose sample equivalents. A dependence on density for polypropylene interface ultimate strength corroborates the findings of O'Rourke *et al.* (1990) but is contrary to the observed behaviour of metal interfaces (Yoshimi and Kishida, 1981b; Noorany, 1985; Jardine *et al*., 1993; Porcino *et al.,* 2003). Just as evolution of the number of soil-surface contacts at the interface changes with stress level (Dove and Frost, 1999) so too would they in relation to the sample density. When greater numbers of particles contact the surface, the contact stress per particle reduces for a given normal stress. As is seen from nonlinear soil and interface strength envelopes, with greater strength toward lower stress level, it may be that the localised reduction in contact stress from a greater number of particle contacts in dense samples, causes the modest strength enhancement.

Table 4.6 S0, S15, and S35 interface friction angles

Interface δ	Loose ultimate (°)	Dense peak (°)	Dense ultimate (°)
S0	19.3	21.5	19.6
S15	18.7	24.3	23.0
S35	19.7	23.7	23.1

4.3 Soil mean grain size

In addition to the effect of gravel content on interface response, the effect of soil mean grain size was also investigated. To this end, 40 soil-only direct shear tests were carried out to establish their normal behaviour, and 40 interface tests conducted to evaluate their effect on shear response of polypropylene pipe coatings.

4.3.1 Soil tests

Figure 4.10 lists and provides cardinal parameters for the soil-only tests involving Lowestoft Gravel, Leighton Buzzard, Hostun Sand, and Redhill Sand. The naming convention follows the same pattern as previously with a soil type reference [LG, LB, HS, RH], a density reference [L (for loose), D (for dense)], and a nominal stress level reference [2, 5, 10, 20, 35 (kPa)]. Shear response and volumetric behaviour plots for the tests listed in Table 4.7 are presented in Figure 4.10. Similar to the other soil-only tests, they exhibit behaviour that is consistent with classical soil mechanics and show clear stress-dilatancy for dense soil tests and contractile behaviour for loose soil tests. Both peak and ultimate states are present in dense tests while loose tests only mobilise an ultimate strength.

Table 4.7 LG, LB, HS, and RH sand direct shear tests

Test reference	σ_n (kPa)	$D_{r\,fab}$ (%)	$D_{r\,con}$ (%)	e_{fab}	e_{con}	τ_{peak} (kPa)	τ_{ult} (kPa)	τ_{peak}/σ_n	τ_{ult}/σ_n	Ψ $\Delta v/\Delta h$
LG_L02	2.89	22.1	27.2	0.854	0.834	2.46	2.27	0.85	0.79	-
LG_L05	5.31	16.3	19.8	0.876	0.863	3.98	3.78	0.75	0.71	-
LG_L10	11.39	19.7	24.5	0.863	0.844	8.02	7.12	0.70	0.63	-
LG_L20	21.62	24.6	32.0	0.844	0.815	14.88	13.75	0.69	0.64	-
LG_L35	36.96	25.3	34.7	0.841	0.805	24.22	23.02	0.66	0.62	-
LG_D02	2.93	53.7	56.4	0.730	0.720	3.02	2.26	1.03	0.77	0.28
LG_D05	5.34	60.2	62.0	0.705	0.698	5.05	3.68	0.94	0.69	0.29
LG_D10	11.42	62.7	67.3	0.695	0.678	10.59	7.34	0.93	0.64	0.28
LG_D20	21.65	52.0	62.9	0.737	0.695	17.85	13.87	0.82	0.64	0.23
LG_D35	37.00	60.9	69.5	0.703	0.669	29.88	22.16	0.81	0.60	0.26
LB_L02	2.89	19.1	29.4	0.781	0.749	2.24	1.99	0.77	0.69	-
LB_L05	5.31	21.9	27.6	0.772	0.754	3.72	3.51	0.70	0.66	-
LB_L10	11.38	21.2	29.1	0.774	0.750	7.73	7.08	0.68	0.62	-
LB_L20	21.61	20.2	45.8	0.777	0.698	14.75	12.56	0.68	0.58	-
LB_L35	36.96	26.7	44.0	0.757	0.704	23.93	22.10	0.65	0.60	-
LB_D02	2.92	70.4	71.2	0.622	0.619	2.84	2.12	0.97	0.73	0.33
LB_D05	5.34	63.2	64.6	0.644	0.640	5.14	3.34	0.96	0.63	0.31
LB_D10	11.41	61.4	74.7	0.650	0.608	9.53	7.10	0.83	0.62	0.25
LB_D20	21.64	70.3	76.0	0.622	0.604	17.94	12.44	0.83	0.57	0.27
LB_D35	36.99	70.6	85.1	0.621	0.576	31.08	21.54	0.84	0.58	0.28
HS_L02	2.86	9.1	19.2	0.965	0.927	2.73	2.04	0.96	0.71	-
HS_L05	5.27	17.4	24.4	0.934	0.907	4.58	3.77	0.87	0.72	-
HS_L10	11.35	11.5	26.0	0.956	0.901	8.74	7.19	0.77	0.63	-
HS_L20	21.58	13.9	31.1	0.947	0.882	15.99	14.00	0.74	0.65	-

Table 4.7 LG, LB, HS, and RH sand direct shear tests

Test reference	σ_n (kPa)	$D_{r\,fab}$ (%)	$D_{r\,con}$ (%)	e_{fab}	e_{con}	τ_{peak} (kPa)	τ_{ult} (kPa)	τ_{peak}/σ_n	τ_{ult}/σ_n	Ψ $\Delta v/\Delta h$
HS_L35	36.92	18.3	32.4	0.930	0.877	25.91	22.97	0.70	0.62	-
HS_D02	2.88	57.4	57.7	0.782	0.781	3.00	2.13	1.04	0.74	0.31
HS_D05	5.30	54.7	55.5	0.792	0.789	5.21	3.74	0.98	0.71	0.30
HS_D10	11.38	59.2	60.8	0.775	0.769	10.49	7.25	0.92	0.64	0.27
HS_D20	21.61	62.5	69.5	0.763	0.736	18.67	12.77	0.86	0.59	0.28
HS_D35	36.95	55.8	60.5	0.788	0.770	29.75	22.86	0.81	0.62	0.24
RH_L02	2.85	19.2	30.2	0.957	0.910	2.76	1.86	0.97	0.65	-
RH_L05	5.27	23.4	39.6	0.939	0.870	4.05	3.67	0.77	0.70	-
RH_L10	11.34	25.3	40.7	0.931	0.865	8.25	7.26	0.73	0.64	-
RH_L20	21.57	24.8	46.0	0.933	0.842	15.45	13.45	0.72	0.62	-
RH_L35	36.92	23.0	44.7	0.941	0.848	25.70	23.17	0.70	0.63	-
RH_D02	2.88	64.3	64.7	0.764	0.762	3.00	2.16	1.04	0.75	0.27
RH_D05	5.30	62.1	66.7	0.773	0.753	4.97	3.58	0.94	0.68	0.30
RH_D10	11.37	66.6	70.2	0.754	0.738	9.66	7.52	0.85	0.66	0.25
RH_D20	21.61	61.8	70.4	0.774	0.737	17.73	14.07	0.82	0.65	0.21
RH_D35	36.95	60.8	67.3	0.779	0.750	27.74	24.26	0.75	0.66	0.19

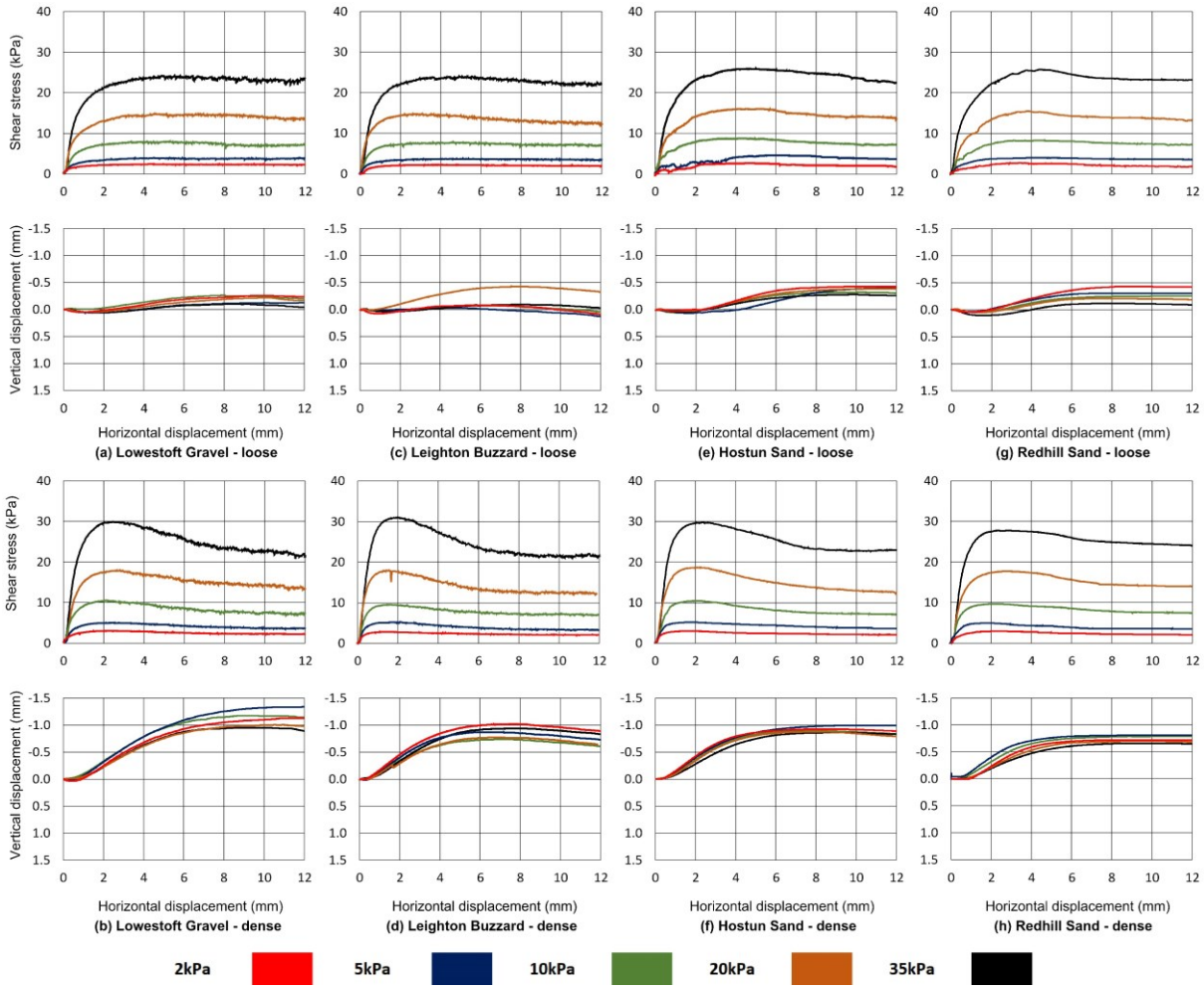

Figure 4.10 Soil-only shear stress and vertical displacement response with (a,b) Lowestoft Gravel, (c,d) Leighton Buzzard, (e,f) Hostun Sand, and (g,h) Redhill Sand.

Strength envelopes for soils LG, LB, HS, and RH are presented in Figure 4.11. Just as for the other three soils previously discussed, strength envelopes are forced through the origin for calculation of ϕ. Failure envelopes are nonlinear with a clear increase in strength towards very low normal stresses across all strength states, loose and dense ultimate, and dense peak. Angles of friction in each condition, loose and dense ultimate, and dense peak, are summarised in Table 4.8. There is good agreement between loose and dense ultimate strengths, typically within 0.9° except Hostun Sand which varies by 1.7°. In each case peak strengths manifest as a significantly greater angles of friction.

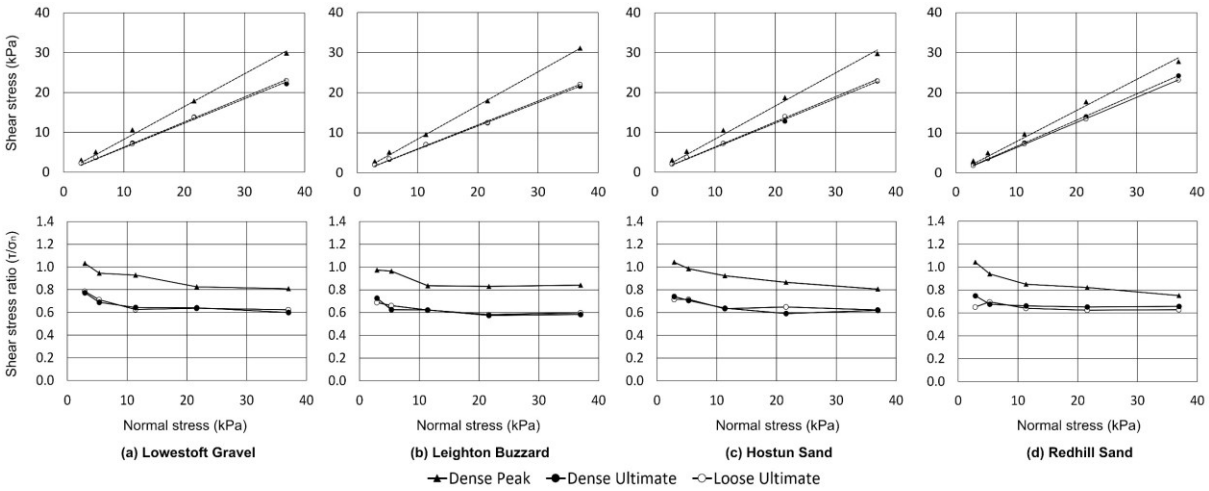

Figure 4.11 Strength envelopes in terms of shear stress and shear to normal stress ratio for soils (a) Lowestoft Gravel, (b) Leighton Buzzard, (c) Hostun Sand, (d) Redhill Sand.

Table 4.8 LG, LB, HS, and RH soil friction angles

Soil ϕ	**Loose ultimate (°)**	**Dense peak (°)**	**Dense ultimate (°)**
Lowestoft Gravel	32.6	40.5	32.8
Leighton Buzzard	30.7	40.0	30.5
Hostun Sand	33.0	41.5	31.3
Redhill Sand	32.2	39.9	33.3

4.3.2 Soil stress dilatancy

Soil tests exhibit classical stress dilatancy in dense sample tests and Bolton's (1986) flow rule for sands, derived empirically and from Rowe (1962), may be used to evaluate the relationship between the ultimate and peak shear strength:

$$\phi_{Bolton} = \phi_{ult} + 0.8\psi \qquad Eq.\,4.1$$

The comparison between the experimental measurements of ϕ_{peak} and ϕ_{Bolton} is shown graphically in Figure 4.12 where a perfect agreement would manifest as a 1:1 relation (indicated by the dashed straight line showing parity). The agreement between experimental data and that predicted by Bolton's (1986) flow rule (grey shapes in Figure 4.12) is not good as there is tendency for it to over-predict peak shear strengths in relation to those measured in the test. A better agreement with measured values is obtained by using 0.55 in place of 0.80 to factor the contribution of dilatancy. A possible explanation for the discrepancy is that Bolton (1986) used data from a variety of sources to support his empirical relationship for plane strain conditions and the stress level of tests used to confirm it was 300 kPa, far in excess of the stress levels used here. Jewell (1989) observed that relationships between

ultimate and peak strengths with respect to angles of dilation diverge and become less reliable at low stresses.

A further aspect when considering the apparent under-measuring of peak strengths is the boundary condition at the edge of the shearbox. In the current test arrangement, the shearbox is constructed with an initial 4 mm gap between the upper and lower frame, which means that soil at the edges of the shear plane are not laterally confined. It was previously said that the rubber edging placed to prevent sample extrusion has a negligible effect on the measured shear force, so by extension it cannot be considered to perform any meaningful confining function. That the soil does not spill out of the box suggests some soil arching may be present and the shear load may not be distributed across the full extent of the shear area. The corollary is that the real peak shear stress may be greater than determined by assuming the whole shear area participates equally in mobilising the shear resistance.

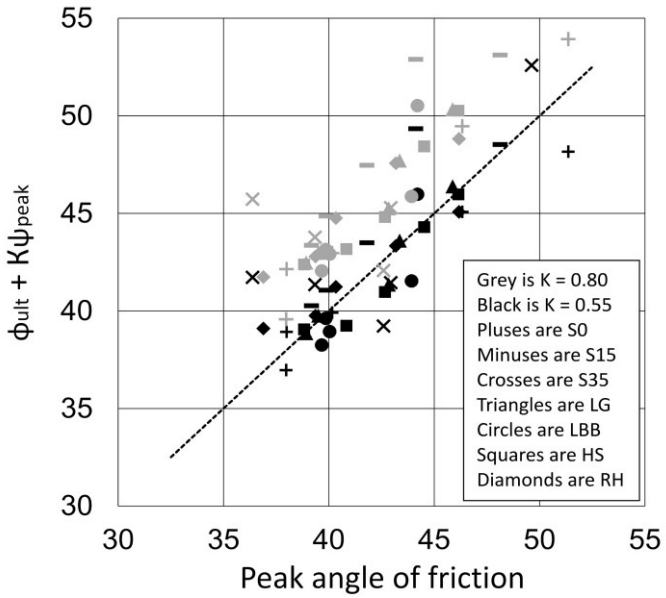

Figure 4.12 Measured ϕ_{peak} compared to $\phi_{Bolton} = \phi_{ult} + K\psi_{peak}$ with K=0.8 (grey shapes) and K=0.55 (black shapes).

4.3.3 Interface tests

As before, interface tests follow the same test reference convention with an additional surface type signifier. Table 4.9 lists tests and cardinal parameters of interest. A single surface specimen was used for each set of tests with a given test soil in order to mitigate the effects of variable surface specimens and improve the reliability of the results. The surface specimens used were PP22, PP21, PP23, PP18 for soils LG, LB, HS, and RH, respectively. To mitigate the impact of each test on the surface, tests were conducted in order of increasing stress level and loose sample tests before dense.

A very few tests did not reach 12 mm horizontal displacement and in these instances the ultimate shear stress is the average of the last 2 mm of recorded horizontal displacement. Where this has occurred the difference in result would likely have been negligible.

Table 4.9 "T" interface tests with soils LG, LB, HS, and RH

Test reference	σ_n (kPa)	$D_{r\ fab}$ (%)	$D_{r\ con}$ (%)	e_{fab}	e_{con}	τ_{peak} (kPa)	τ_{ult} (kPa)	τ_{peak}/σ_n	τ_{ult}/σ_n
LG_L02_T	2.08	37.5	47.1	0.794	0.756	0.74	0.72	0.35	0.35
LG_L05_T	5.15	37.6	40.5	0.793	0.782	1.34	1.29	0.26	0.25
LG_L10_T	11.29	37.4	47.1	0.794	0.756	2.46	2.14	0.22	0.19
LG_L20_T	21.51	29.2	48.7	0.826	0.750	4.61	4.26	0.21	0.20
LG_L35_T	36.85	25.5	41.4	0.840	0.778	8.22	7.50	0.22	0.20
LG_D02_T	2.08	84.5	84.5	0.610	0.610	0.82	0.73	0.39	0.35
LG_D05_T	5.15	83.9	83.9	0.613	0.613	1.68	1.30	0.33	0.25
LG_D10_T	11.29	82.6	82.9	0.618	0.617	3.94	3.42	0.35	0.30
LG_D20_T	21.51	78.0	80.0	0.636	0.628	5.00	4.15	0.23	0.19
LG_D35_T	36.85	74.4	76.1	0.650	0.643	8.30	7.68	0.23	0.21
LB_L02_T	2.02	-1.8	22.2	0.845	0.771	0.63	0.61	0.31	0.30
LB_L05_T	5.09	-1.4	20.7	0.844	0.776	1.25	1.20	0.25	0.24
LB_L10_T	11.23	22.9	56.6	0.769	0.665	2.29	2.18	0.20	0.19
LB_L20_T	21.45	22.0	54.0	0.772	0.673	3.75	3.30	0.18	0.15
LB_L35_T	36.79	15.3	53.8	0.793	0.673	6.53	6.19	0.18	0.17
LB_D02_T	2.02	77.2	80.7	0.601	0.590	0.79	0.76	0.39	0.38
LB_D05_T	5.09	77.6	83.7	0.599	0.581	1.45	1.37	0.28	0.27
LB_D10_T	11.23	79.4	81.8	0.594	0.586	2.69	2.28	0.24	0.20
LB_D20_T	21.45	75.6	83.7	0.606	0.581	3.82	2.97	0.18	0.14
LB_D35_T	36.79	72.9	87.8	0.614	0.568	7.47	5.96	0.20	0.16
HS_L02_T	2.10	17.0	30.3	0.936	0.885	0.83	0.82	0.40	0.39
HS_L05_T	5.16	16.2	35.4	0.938	0.866	2.09	2.04	0.40	0.40
HS_L10_T	11.30	16.9	39.5	0.936	0.850	3.98	3.93	0.35	0.35
HS_L20_T	21.52	15.7	39.2	0.940	0.851	7.80	6.97	0.36	0.32
HS_L35_T	36.86	15.3	43.6	0.942	0.834	13.00	11.77	0.35	0.32
HS_D02_T	2.10	70.1	71.0	0.734	0.730	0.96	0.94	0.46	0.45
HS_D05_T	5.16	70.3	70.7	0.733	0.731	2.09	2.02	0.40	0.39
HS_D10_T	11.30	70.2	75.4	0.733	0.714	4.49	4.27	0.40	0.38
HS_D20_T	21.52	69.8	75.5	0.735	0.713	8.47	7.68	0.39	0.36
HS_D35_T	36.86	70.5	83.6	0.732	0.682	15.25	13.25	0.41	0.36
RH_L02_T	2.05	18.1	41.0	0.962	0.864	0.89	0.78	0.43	0.38
RH_L05_T	5.11	15.5	38.2	0.973	0.876	2.21	1.54	0.43	0.30

Table 4.9 "T" interface tests with soils LG, LB, HS, and RH

Test reference	σ_n (kPa)	$D_{r\ fab}$ (%)	$D_{r\ con}$ (%)	e_{fab}	e_{con}	τ_{peak} (kPa)	τ_{ult} (kPa)	τ_{peak}/σ_n	τ_{ult}/σ_n
RH_L10_T	11.25	18.9	46.4	0.959	0.841	4.19	3.87	0.37	0.34
RH_L20_T	21.47	17.3	45.9	0.965	0.843	6.73	6.48	0.31	0.30
RH_L35_T	36.81	18.2	56.7	0.962	0.796	12.43	11.98	0.34	0.33
RH_D02_T	2.05	70.1	70.2	0.739	0.738	1.18	1.04	0.58	0.51
RH_D05_T	5.11	70.0	72.9	0.739	0.726	2.10	2.07	0.41	0.41
RH_D10_T	11.25	70.4	78.1	0.737	0.704	3.89	3.51	0.35	0.31
RH_D20_T	21.47	69.4	77.3	0.742	0.708	7.36	7.12	0.34	0.33
RH_D35_T	36.81	70.6	77.1	0.736	0.708	11.44	11.33	0.31	0.31

Shear response and volumetric behaviour for these interface tests are presented in Figure 4.13. Similar to before, they show a generally elastic-perfectly plastic type response with negligible vertical displacement change throughout the test. There is little to distinguish between the behaviour of dense sample and loose sample tests.

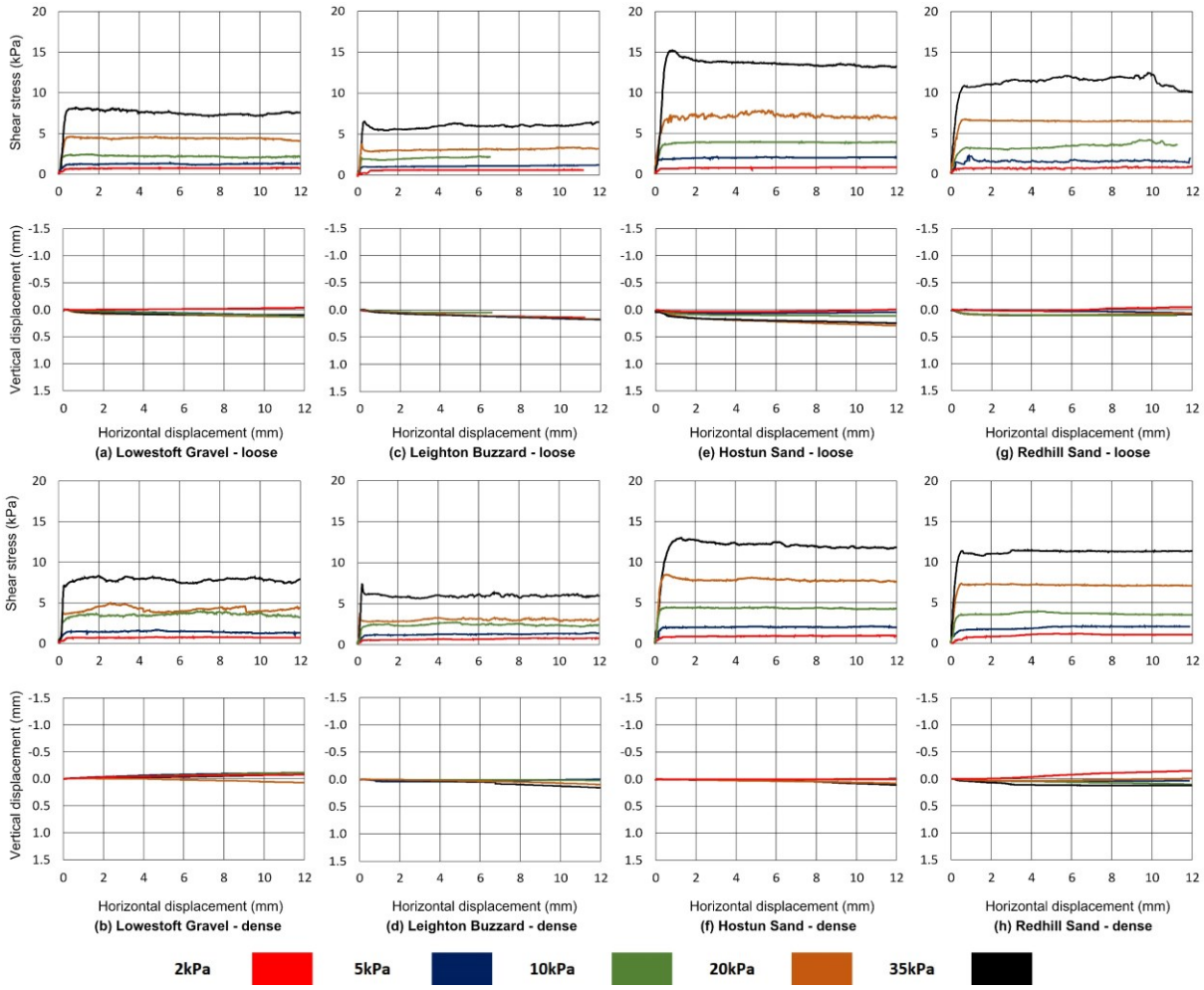

Figure 4.13 "T" interface shear stress and vertical displacement response with (a,b) Lowestoft Gravel, (c,d) Leighton Buzzard B, (e,f) Hostun Sand, and (g,h) Redhill Sand.

Figure 4.14 presents failure envelopes for these interface tests compared to their equivalent soil-only failure envelopes. As for the other three test soils, interface strengths are far lower than soil strengths though the shape of their failure envelopes are similar with a nonlinear trend for enhanced shear strengths are lower stress levels. In the case of interfaces, Dove and Frost (1999) provided a theoretical explanation for such an increase based on the evolution of the contact area and stress between particles and the counterface, suggesting a power law decrease of interface friction angle with increasing stress level.

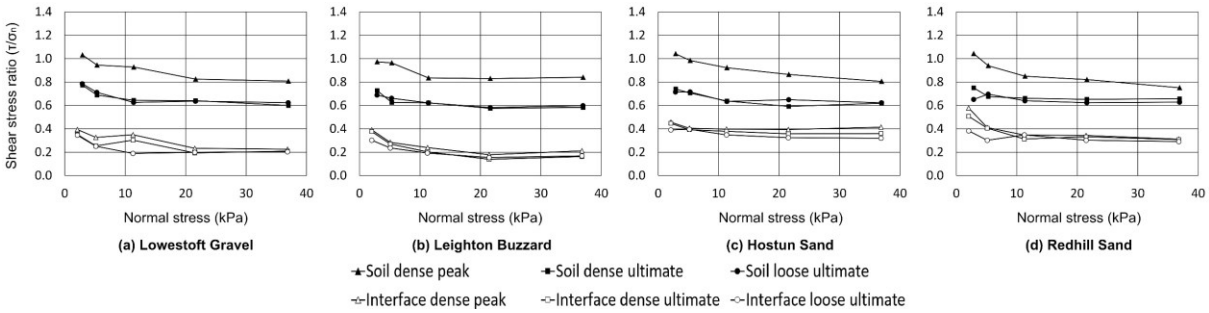

Figure 4.14 Strength envelopes as shear to normal stress ratio for interface tests (a) Lowestoft Gravel, (b) Leighton Buzzard, (c) Hostun Sand, and (d) Redhill Sand.

4.4 Interface efficiency

Interface efficiency is a useful term to quantify how effective a surface is at mobilising the equivalent soil-only strength. It is defined as the ratio between the interface strength and the soil strength. Because stress level influences the measured strength and the stress levels vary subtly between soil and interface tests, interface efficiency is only addressed in terms of the ratio of the interface friction angle to the soil friction angle. Table 4.10 details the efficiency of the polypropylene pipe coatings with respect to the various test soils. They range between an average value of 0.30 and 0.64 with a reasonable general trend for the coarser soils (Lowestoft Gravel and Leighton Buzzard) to be less efficient than the finer ones such as S0, S15, S35, Hostun, and Redhill Sand. The reason that finer soils are better able to mobilise their strength at the interface was discussed in Chapter 2. For finer soils result their effective roughness is greater leading to better engagement with surface asperities and textures that in turn promotes greater frictional resistance. The relationship with surface texture will be elaborated on later.

Table 4.10 Summary of interface efficiencies (δ / ϕ)

Sand type	*Loose ultimate*	*Dense peak*	*Dense ultimate*	*Average*
S0	0.61	0.56	0.61	0.59
S15	0.57	0.61	0.69	0.62
S35	0.60	0.63	0.69	0.64
Lowestoft Gravel	0.36	0.34	0.38	0.36
Leighton Buzzard	0.31	0.28	0.30	0.30
Hostun Sand	0.56	0.56	0.63	0.58
Redhill Sand	0.55	0.47	0.53	0.52

4.5 Surface texture evolution

It is known from the literature that shear of soils against softer surfaces leaves surface damage (e.g. O'Rourke *et al.*, 1990) so quantifying the scale of surface evolution is a key consideration. Quantified average form (F_a), waviness (W_a) , and roughness (R_a) parameters are presented

in Figure 4.15 for both the X and Y directions in both pre-test (crosses) and post-test (pluses) condition for interface tests with soils S0, S15, and S35 only. Description and a schematic representation of form, waviness, and roughness can be found in Chapter 2. Arithmetic average magnitudes are calculated by the same equation with the distinction between form, waviness, and roughness controlled only by the L_c cut-off filter:

$$Average\ texture\ component = \frac{1}{n}\sum_{i=1}^{n}|y_i| \qquad Eq.\ 4.5$$

In which n are ordered, equally spaced (every 0.5 μm) points along a surface trace and y_i is vertical distance from mean line to the i^{th} data point. The cut-off filters between form and waviness, and waviness and roughness are 8.00 mm and 0.25 mm, respectively. At this stage of the investigation the Alicona non-contact profilometer was not available for use but the Talysurf methodology is sufficient for drawing comparisons between pre- and post- data topography. Data points represent the mean of deviations of each gauge length. A comprehensive table of results and measurements is included in Appendix A1.

There is a significant variation in surface topography across the range of specimens. In the pre-test condition the coefficients of variation (the ratio of the standard deviation to the mean) for form, waviness, and roughness of a specimen are typically 19%, 19%, and 11% in the X direction and 32%, 33%, and 13% in the Y direction respectively. Across the whole group of surfaces the coefficients of variation rise to 31%, 34%, and 19% in X and 80%, 20%, and 13% in the Y direction for form, waviness, and roughness, respectively. Surface variability across the whole group is much greater than across individual specimens suggesting that the full heterogeneity of topography inherent to this coating material is not captured by individual 140 mm by 140 mm square specimens.

It is necessary to note that the form and waviness are not particularly useful parameters in this situation due to the relative scales of interaction between the soil grains and surface. Surface specimens were prepared from manufactured pipes with specimens flattened for interface testing so the form measurement is not instructive about real pipes, nor is it instructive of the sample when tested because by tightly securing the surface to the interface load cap the specimens are further flattened and form further distorted. Further related to these considerations is the relatively high variability in the form measurements which can be attributed to imperfections and inconsistencies in the surface specimen flattening process.

Although the magnitude of form, waviness, and roughness is of similar order of magnitude, the waviness is generally greater than form or roughness. The greater magnitudes

of waviness are associated with surface specimens which include a surface seam. The influence of the surface seam on characterisation of surfaces and interface shear strengths will be discussed later. The magnitude of topography parameters in the X direction (i.e. parallel to the axis of interface shear direction) generally exceed those in the Y direction. In numerous instances there is a discrepancy between the pre- and post-test parameter magnitude of varying amounts, which in some instances is explained by minor deviations in the starting point and alignment of each profilometer traverse. Others are not easily explained and the assumption is that shearing has modified the surface texture.

To quantify the degree to which topography parameters may have been modified during interface shearing the differences between pre-test and post-test parameters are calculated as percentages. Figure 4.16 presents the calculated differences for each parameter against test soil (Mix 1 = S0, Mix 2 = S15, Mix 3 = S35), stress level, and soil sample relative density. Lines of best fit (solid lines) are drawn through the data to help reveal any underlying trends and coefficients of variation (dashed lines) are shown to try and show the overall variability.

Figure 4.16 shows that for form and waviness, the effect on surface topography remains within the bounds of the inherent variability across each stress level, relative density, and soil type. For roughness also, in most cases the effect remains within the bounds of inherent variability. The exception is the roughness parameter in the Y direction (perpendicular to shearing direction) with stress level indicating that higher stress level leads to greater surface damage which is related to greater indentation of the polypropylene surface.

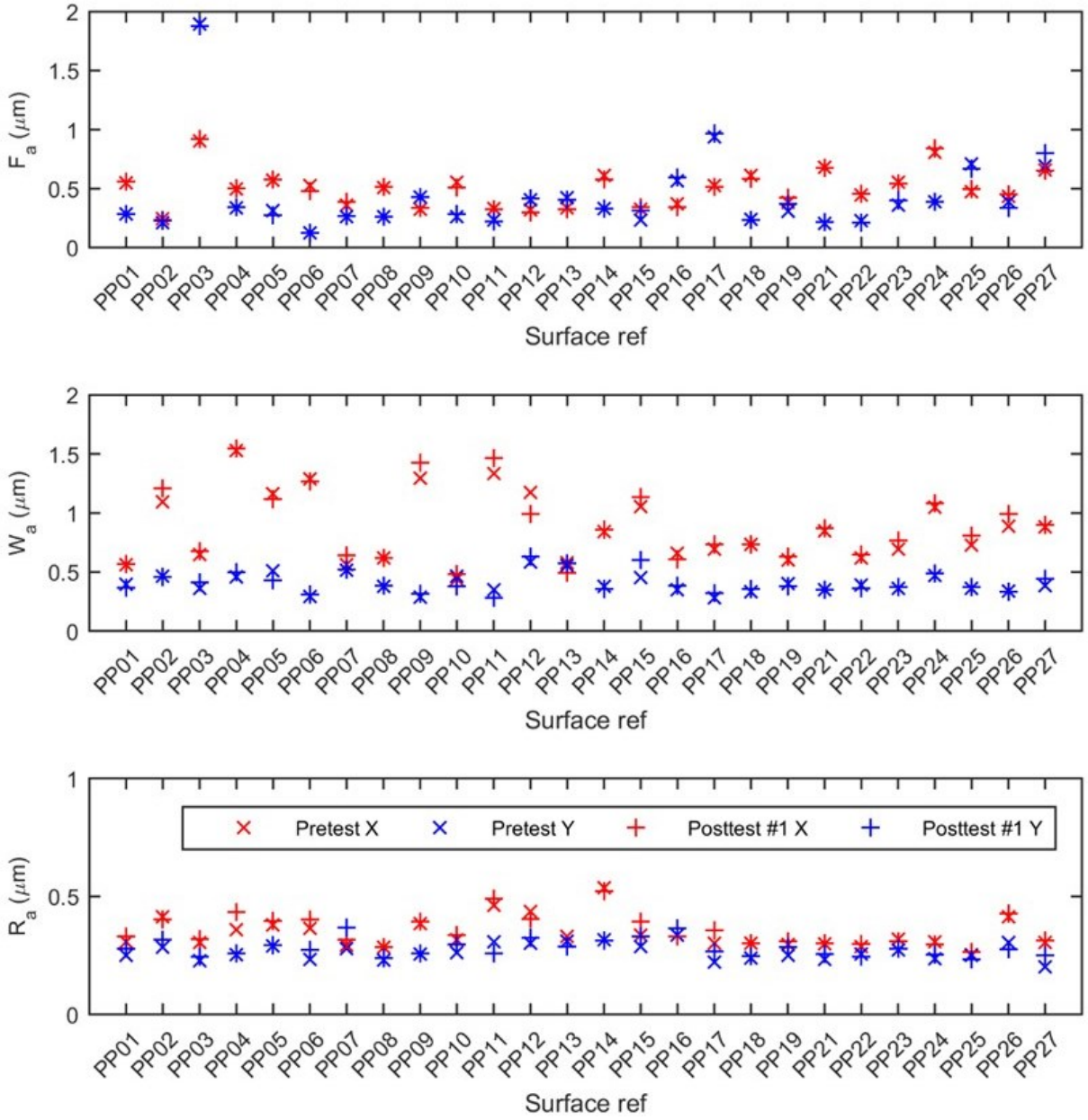

Figure 4.15 Quantified roughness parameters pre- and post- interface test with soils S0, S15, and S35. PP labels on the x-axis refer to individual surface specimens.

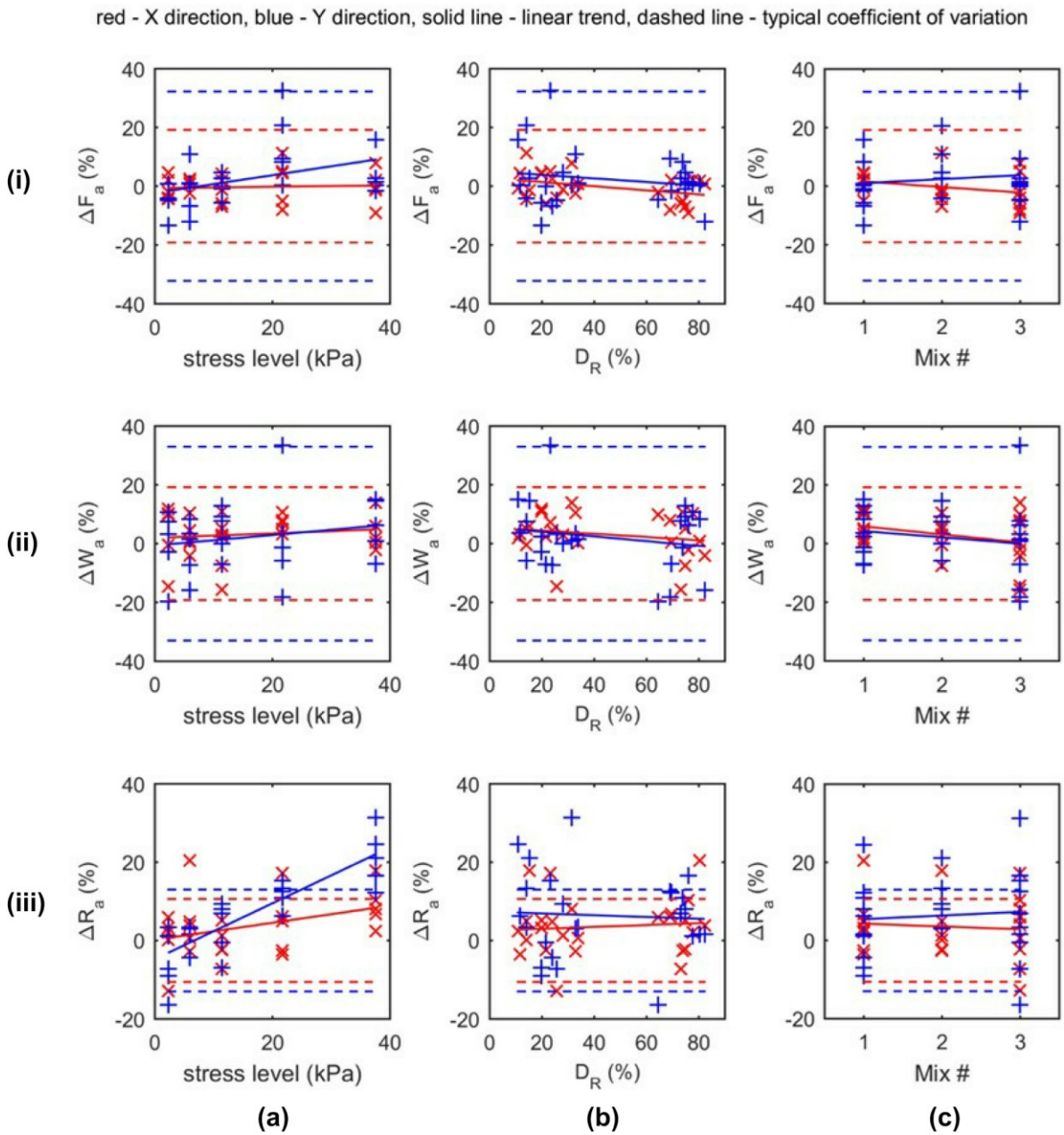

Figure 4.16 The influence of (a) stress level, (b) relative density and (c) mix type of an interface test on the resultant surface specimen (i) form, (ii) waviness, and (iii) roughness (Mix 1 = S0, Mix 2 = S15, Mix 3 = S35).

4.5.1 Evaluation of profilometry methods

At a later stage, the Alicona non-contact method became an option so four of the surfaces measured by Talysurf were also measured by the Alicona. The Alicona uses a microscope to digitally image a surface in three-dimensions using focus variation algorithms in the processing software to assign co-ordinates in x, y, and z directions to map a surface profile. From this surface, profiles can be extracted and the appropriate texture parameters determined within the accompanying software. A 10 mm x 10 mm area was scanned - larger areas were problematic due to the extended time that the process takes, even small areas take several hours to scan so scanning every surface was impractical. At time of measurement the surfaces had already been subjected to at least one shear test so specimens were instead measured around the perimeter where no surface damage had occurred. The L_c cut-off filter was set to 0.25 mm, similar to the measurement from the Talysurf to distinguish between waviness and roughness. Computer-generated post-processing images from the Alicona are shown in Figure 4.17.

In each case there is a set of visible parallel striations in the post-shearing images which are not seen pre-shearing, including examples of gouges where grains have ploughed through the surface. The relationship between surface wear and extraction of a surface profile is shown in Figure 4.18. Comparison of R_a from Talysurf and Alicona profilometry is presented in Table 4.11 where it is clear that non-contact methods return greater values of R_a. Both methods used have resolutions far in excess of the measured values (250 nm and 8 nm for the Alicona and Talysurf respectively), which suggests that it is not measurement resolution influencing the result unduly. The finer resolution of the Talysurf also means that the discrepancy in results is unlikely to be caused by the measuring resolution as it is expected that finer resolution would yield a greater roughness, the opposite of what is seen.

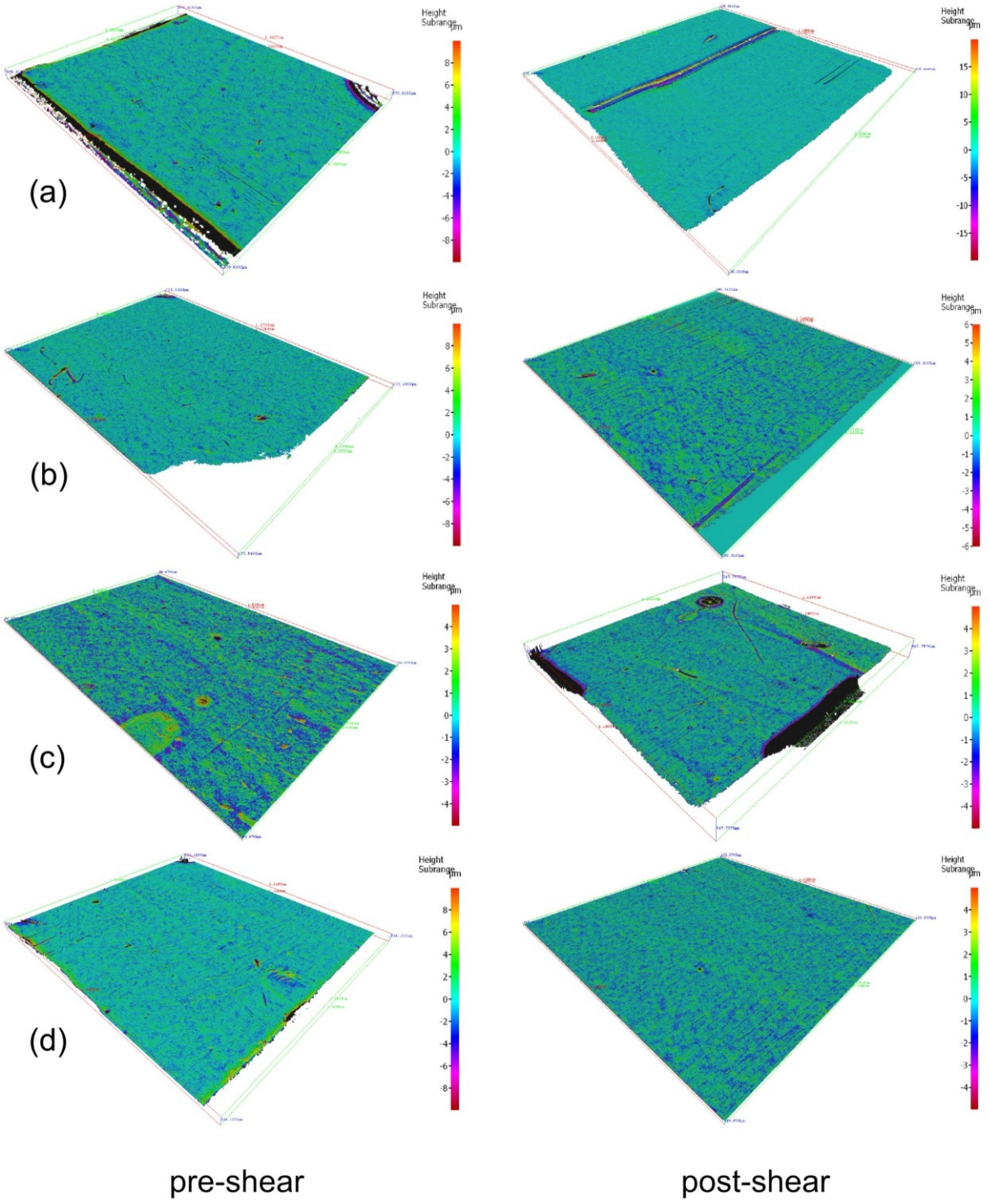

Figure 4.17 Alicona post-processing imaging of polypropylene surfaces pre-shearing at the sample periphery and post-shearing in the central area for (a) Lowestoft Gravel, (b) Leighton Buzzard, (c) Hostun Sand, and (d) Redhill Sand.

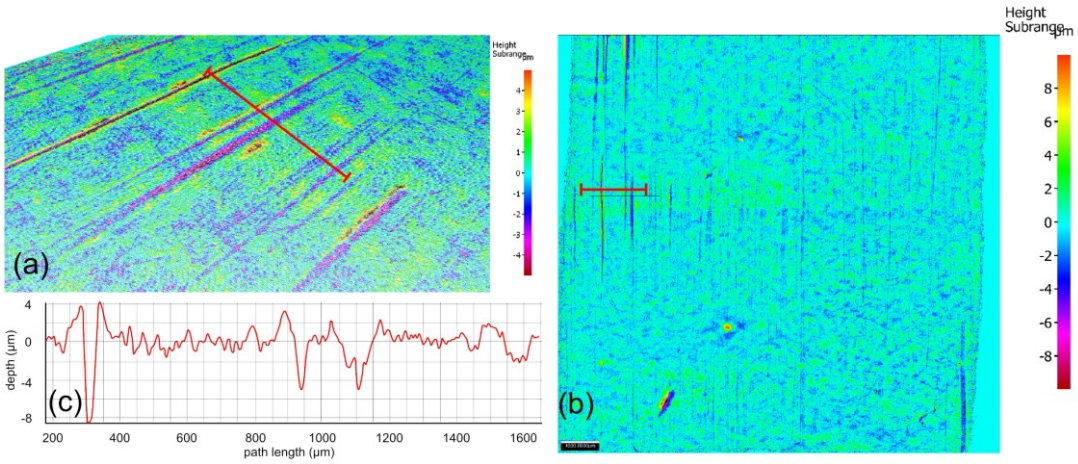

Figure 4.18 Alicona imaging of wear scars inscribed in surface PP21 tested with Leighton Buzzard: (a) orthographic projection, (b) plan view, (c) surface profile perpendicular to direction of shear displacement.

Table 4.11 R_a from Talysurf and Alicona

Surface	Talysurf R_a (µm)	Alicona R_a (µm)	Difference (µm)	Difference %
PP22	0.454	0.785	0.331	73%
PP21	0.392	0.724	0.332	85%
PP23	0.445	0.849	0.414	93%
PP18	0.499	1.075	0.576	115%

Profilometry techniques were historically developed to measure the surface texture and roughness of hard materials like steel and to evaluate the quality of other metal surface finishes. Even with the relative hardness of steel, the profilometer diamond tip is harder, and surface damage of metals is known to occur (Whitehouse, 2000). Therefore, for materials which are much softer and more prone to indentation such as polymers including polypropylene, there was a concern that the diamond-tipped stylus could be indenting and ploughing through asperities leading to reporting of lower values of R_a than were true. Use of the Alicona non-contact methodology appears to support this suspicion as higher values of R_a are reported. Therefore, it was considered that the Alicona non-contact method provided a more reliable way of quantifying and characterising surface roughness of polypropylene surfaces.

As it has been shown that Alicona surface texture values are likely to be greater than those measured previously by Talysurf, some comment on the preceding discussions involving surface texture is required. That the Talysurf appears to have been under-measuring asperities does not detract from the overall trends that those data have revealed, it is most likely that just the absolute magnitudes are suppressed. The trend for surface roughness to evolve beyond inherent variability in response to only stress level and perpendicular to the shearing direction is not called into question by these revelations. However, it is worth

recognising that if the stylus tip is indeed causing its own damage to the surface as is suspected, then this may be masking surface wear at lower stress levels. Equally, when considering the roughness of a surface that is relevant to interface mechanics, it is the roughness parallel to the shearing direction that is key and this parameter does not increase outside of the inherent surface variability in response to any test variable.

It has been shown that Alicona profilometry is the better tool, so all further analysis involving the texture of surfaces is conducted using values determined this way. The Talysurf will still be used for characterising variability where there are a large number of surfaces for expedience but detailed analysis adopts the Alicona methodology.

4.6 Comparison with the literature

It is useful to compare the data with existing data and trends in the literature. The principal surface attributes contributing to shear response are the surface hardness and the surface texture.

4.6.1 Hardness

The hardness of polymers is a key controlling parameter on shear response and interface strength. O'Rourke *et al*. (1990) identified a relationship between the hardness of polymers and their interface efficiency which is shown again in Figure 4.19. O'Rourke *et al*. (1990) reports the test sand (Ottawa Sand) to have a D_{50} of 0.4 mm, the confining stress to have been 20.7 kPa, and an absolute density of between 16.5 and 17.0 kN/m^3. The relative density is not given but is likely to be dense as the quoted absolute density is in the upper range of densities typical for dry sands.

The interface efficiency for each test sand with the polypropylene pipe coatings from Table 4.10 for dense soil tests only is also shown in Figure 4.19. There is considerable scatter in the data when compared to the trend line and the other data points that inform it. The tendency for finer grained soils to be more efficient in mobilising their shear strength at the interface is highlighted again in this figure. However, angularity effects also likely play a role which may explain variations in the precise order for increasing strength with decreasing grain size. The finer sand options, S0, S15, S35, HS, and RH, all lie in the range that is within the scatter of O'Rourke *et al*.'s (1990) original data. LG and LB sands being less efficient is explained by their lower effective roughness. Given that finer soils mobilise a greater shear strength, related to their effective roughness, it might be expected that the trend line in Figure 4.19 would move vertically up or down in response to changes in the surface roughness for a given soil. Surface roughness effects are discussed later.

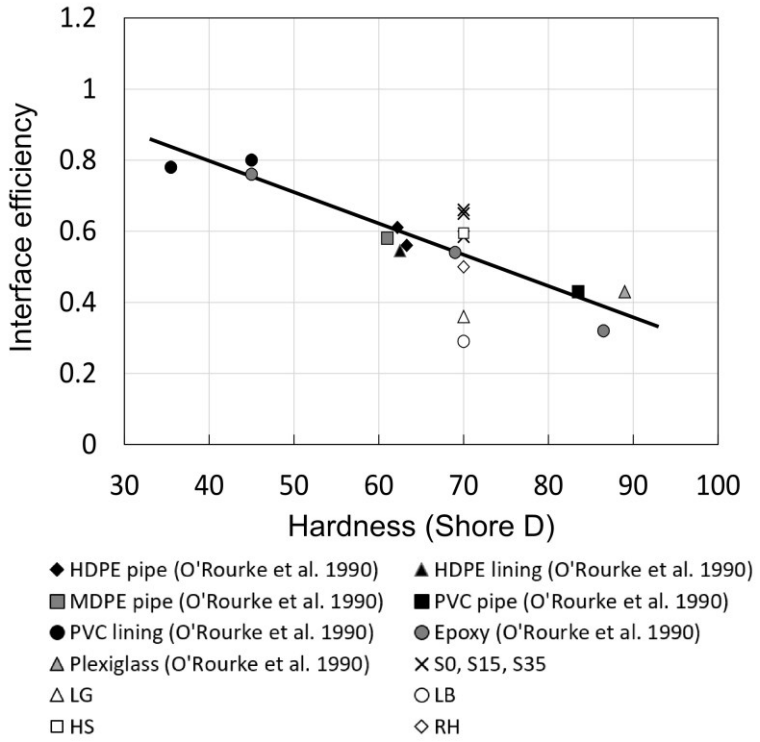

Figure 4.19 Interface efficiency for each soil type compared to the data and trend established by O'Rourke *et al*. (1990).

4.6.2 Grain kinematic

Dove and Frost (1999) proposed the term load index which is the slope of the log normal stress log shear strength relationship for the data presented in Figure 4.20 for each test sand. Just two trend lines are included as an example, for S0 and LB. The load indices for each line are summarised in Table 4.12, also including the R^2 showing the goodness of the fit. Dove and Frost (1999), building on Shooter and Tabor (1952), suggest that a load index of less than the theoretical maximum of 1.0 is indicative of sliding and any value over 1.0 most likely indicates a transition to a rolling shear mechanism. The results determined here suggest sliding dominates which agrees with the previously discussed lack of vertical displacement and the linear wear scars seen in the Alicona scans.

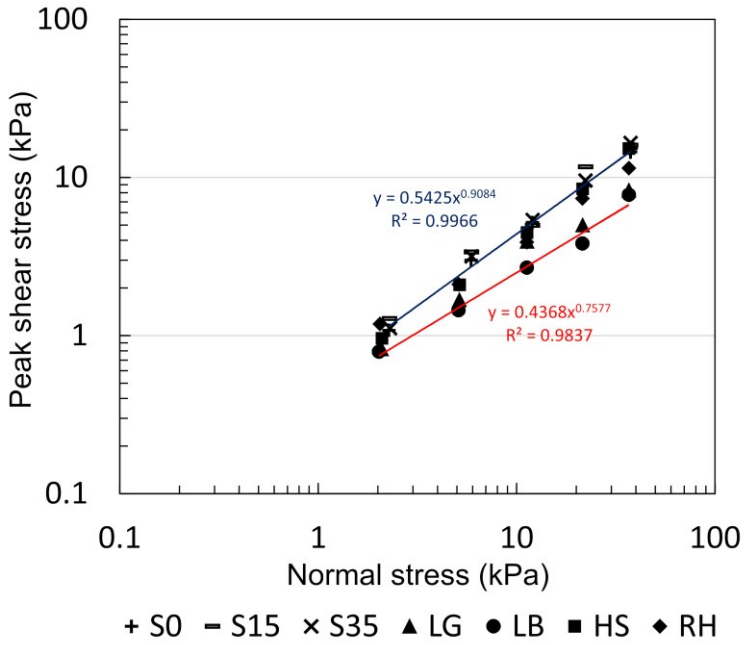

Figure 4.20 Determination of load index, *n*, after Dove and Frost (1999).

Table 4.12 Load index from Figure 4.20

Soil	Load index, *n*	R^2
S0	0.91	0.99
S15	0.91	0.99
S35	0.94	0.99
LG	0.80	0.99
LB	0.76	0.98
HS	0.96	0.99
RH	0.80	0.99

4.6.3 Stress level

It was discussed previously that the strength envelopes in this work are nonlinear with a tendency for reduced strengths at greater normal stress which corroborates the findings of other authors such as Dove and Frost (1999). Their work identified the generalised trend in peak shear strength for smooth polymer interfaces and Ottawa 20/30 sand shown in red in Figure 4.21. Factors affecting the shape of the relationship include the hardness of the surface which influences ploughing, and particle angularity with Dove and Frost (1999) finding that more angular grains mobilised greater shear resistance.

The relationship generally shows a decreasing shear strength with increasing normal stress. Dove and Frost (1999) provided an explanation for reduced friction coefficient with increasing stress level which is related to the evolution of the number of grain-surface contacts as stress level increases. When more grains are pressed against the surface by higher stress the number of contact points increases which means that the average stress per contact point

reduces leading to an overall reduction in shear strength. At a certain point, the interface becomes saturated with grain-surface contacts and no further reduction in strength occurs. In the case of hard surfaces, the interface shear strength remains constant from this point as grains do not cause indentation of the surface and no grain ploughing occurs. The solid line in Figure 4.21 represents such theoretical behaviour. The data from the present study broadly follow a similar pattern of behaviour to that of Ottawa 20/30 sand in Dove and Frost (1999) shown in Figure 4.21. The discrepancy in strength and slope is readily explained by grain size and angularity effects as has been discussed here previously and agrees with their own observations.

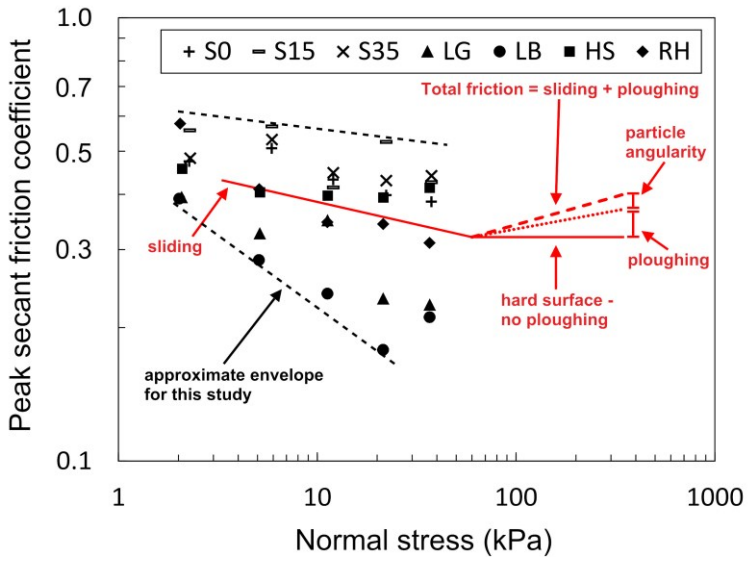

Figure 4.21 Relationship between peak interface secant friction coefficient (peak shear stress ratio) and normal stress including the relationship between sliding and ploughing components after Frost *et al*. (2002) and Martinez (2015).

4.6.4 Surface roughness

In addition to hardness and stress level, the roughness of the surface texture is the third key parameter for controlling the interface shear response. The roughness of surfaces investigated here lies at the lower end of the scale (~0.5 to 1.0 μm) of the coupled model developed by Frost *et al*. (2002) that was discussed in Chapter 2. At such low levels of roughness, the hardness was the more dominant parameter because roughness was insufficient to engender any dilation. However, their model does not include relative roughness and this is the more useful parameter to account for the meshing effect of soil grains and surface texture.

Relative roughness parameters, discussed previously, can be formulated using either average or maximum values (Jardine *et al.,* 1993; Uesugi and Kishida, 1986) and for surfaces like steel both are effective (Lings and Dietz, 2005). Steel surfaces tend to have generally

uniform distributions of roughness and surface texture, particularly those the subject of interface research. However, the pipe coatings investigated here and in their real-world application may contain individual large-amplitude features such as seams which are artefacts of the manufacturing process, but which are not representative of the whole surface. Soil grain angularity effects are likely to contribute and obscure the detail of trends relating interface strength to soil grain size.

For sand-steel interfaces Lings and Dietz (2005) revealed a unique relationship between interface shear strength and relative roughness parameters (Figure 4.22) using the same apparatus (albeit in a different test mode) to that used for this work. Three zones were identified corresponding to non-dilatant shearing, fully dilatant shearing, and a transition zone. Figure 4.22 plots the peak and ultimate interface strength of each soil against both expressions of relative roughness parameters. Using R_{max} suggests the interface strengths plot toward the upper end of the dilatancy transition zone which suggests a significant degree of soil dilation during shearing and peak-postpeak behaviour but this is not seen in the data. Conversely, using R_a plots the data much closer to the trend identified by Lings and Dietz (2005) and Dietz and Lings (2006) and places the results at the bottom end of the transition suggesting little or no dilative behaviour which is supported by the data presented previously. They note that with their steel surfaces there was very little surface waviness or form which rendered R_a and R_{max} of similar magnitude with both options being viable for establishing a relationship between surface roughness and interface shear strength. However, examination of Figure 4.15 and comparison between the panels, suggests that pipe coating specimens have a much greater bandwidth with surface topography featuring a combination of form, waviness, and roughness such that average parameters are the more appropriate metric.

In addition to considerations about the relative contributions of surface form, waviness, and roughness, it must also be noted that surfaces which include a manufacturing artefact like a seam are likely to have exaggerated R_{max} values. It has been shown previously that interface shear response between surfaces including a seam and those without, is negligible. For these reasons, their presence can be discounted and use of R_a provides a better method of reducing their impact on surface roughness measures. Selection of the appropriate surface topography quantifier is discussed in more details in Chapter 5 where enhanced textures are investigated and bandwidth considerations become more pressing.

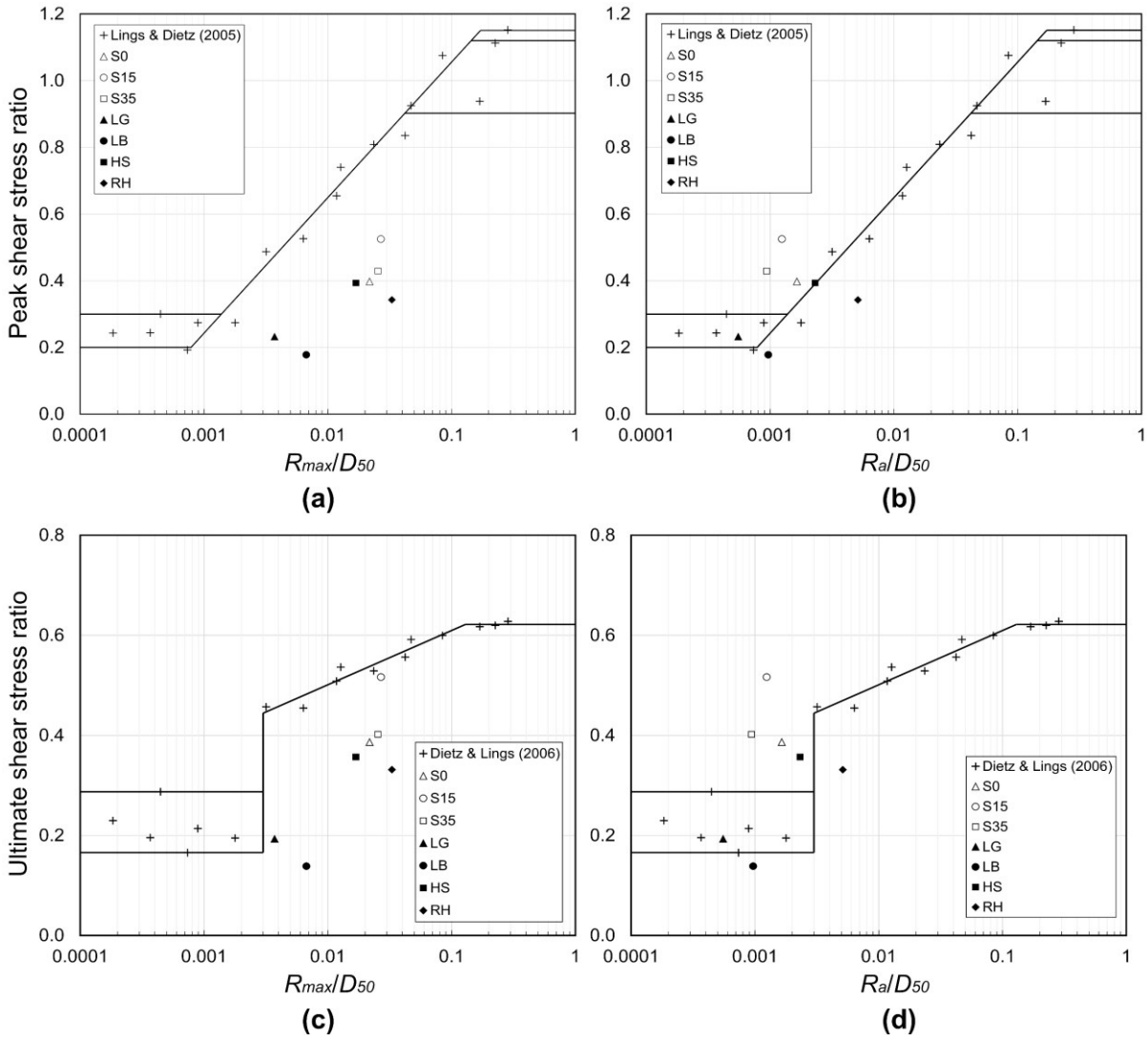

Figure 4.22 Peak stress ratio with (a) R_{max}/D_{50} and (b) R_a/D_{50} with data for sand-steel interface after Lings and Dietz (2005) and ultimate stress ratio with (c) R_{max}/D_{50} and (d) R_a/D_{50} after Dietz and Lings (2006) at ~25 kPa σ'_n and D_r 70-90%.

4.6.5 Industry standards and design considerations

The experimental investigations undertaken in this chapter have revealed a wide range of interface friction coefficients for polypropylene and sandy seafloor soils. They fall in the range of 0.15 to 0.55. In terms of interface efficiency, the surfaces tested under these conditions mobilised, on average, between 30% and 65% of their equivalent soil-only strengths. These findings conflict with the available standards and design guidance. DNVGL Recommended Practice F109 (DNVGL, 2017a) recommends a constant friction factor of 0.60 for sand-concrete interfaces but makes no allowance for other surface coating materials or other variables and instead leaves such decisions to the designer to interpret. The British Standard Code of Practice for Subsea Pipelines (BSI, 2016) recommends friction coefficients in the

range of 0.55 – 1.20 for subsea pipelines on North Sea sands (Milewski *et al*., 2019) and the guidance does not make any distinction based on the roughness of the pipeline in question.

The friction coefficients recommended by industry guidance are at the upper bound of values presented in this chapter and in some cases industry guidance values are more than double this upper estimate. No distinction is made in these standards for surface properties like hardness or roughness. It is likely that the suggested values are appropriate for concrete-coated pipes which are very rough. However, the work presented here has demonstrated that those recommendations are wholly unsuitable for polypropylene (or other smooth coating technologies) and would lead to considerable overestimation of pipe-soil interface friction. Such overestimations would have serious ramifications for pipeline global stability and buckling considerations.

4.7 Conclusions

This chapter has presented an extensive campaign of soil and interface tests to establish the shear response and shear strength of typical polypropylene pipe coatings and a range of granular materials. The tested soils were chosen to test the impact of changes in coarse fraction content and the effect of changes in mean grain size. A number of observations and conclusions were drawn which are summarised:

- The interface response of all soils with these relatively smooth polypropylene pipe coatings is best characterised as elastic-perfectly plastic with little or no associated changes in sample height (no dilation or contraction).
- Greater coarse fraction content in soils results in greater mobilised shear strengths with an increase of up to 1.8° from 0% to 35% coarse fraction in interface tests.
- There is a dependence of the ultimate interface shear strength on the soil sample density with dense soil tests mobilising up to 4.6° greater angle of friction.
- The displacement rate of interface shear was demonstrated to have negligible impact on interface shear strength or vertical displacement behaviour supporting the contention that drained conditions dominate in the circumstances tested here.
- The efficiency of the surfaces at mobilising the equivalent soil-only strength varied considerably according to the grain size of the tested soil. The range was between averaged values of 0.30 and 0.64 with greater efficiency observed in finer grained soils. This trend is easily understood when considered in light of the effective roughness at the interface varying according to grain size.
- It was shown that shearing at the interface was able to modify the surface topography with greater stress levels resulting in an increase in surface roughness post-test which

raises interesting questions about the surface evolution and interface strength under cyclic conditions which is the subject of Chapter 6.

- It was shown that the results are in reasonable agreement with existing literature with respect to surface parameters such as hardness and roughness and that selection of average surface roughness parameters is most appropriate for pipe coatings which have high bandwidth textures.
- In contrast to existing industry standards and guidance, this chapter recommends the use of friction coefficients in the range of 0.15 to 0.55 for selection of appropriate pipe-soil interface friction factors with typical polypropylene coatings. However, for more specific values appropriate interface shearbox testing is required as other variables such as grading, angularity, stress level, and surface roughness and hardness, are influential.

In light of the far lower interface shear strengths mobilised by polypropylene compared to published values, there is potential benefit to enhancing the shear strengths of these surfaces to bring them into line with those values and provide a greater range of usable friction coefficients. Doing so may provide pipeline designers with some additional tools for managing pipe-soil friction coefficients and invites the possibility of prescribing the friction to meet design requirements.

5 Enhanced Polypropylene Textures

It was shown in Chapter 4 that interface strength depends in part on soil average grain size which is explain by the concept of effective and normalised roughness. Rougher surfaces are known to lead to greater interface shear strengths in a range of materials, and the same is expected of polypropylene. Therefore, there may be a benefit to pipeline engineers in being able to modify surface textures to suit their design requirements.

This chapter details the methods involved in producing a range of enhanced surface textures, how they are characterised, and their shear response. A wide-ranging discussion follows on the nature of their shear response in comparison with the literature and with reference to classical soil mechanics, and a unique relationship is derived to allow pipeline engineers to make predictions of polypropylene-soil interface friction coefficients.

More detailed plots than are included here are presented in Appendices C2, C3, C4, and C5 and all the raw test data is contained in the data pack on an SD card attached to this thesis.

5.1 Polypropylene surface types

Four additional polypropylene surface types were produced to cover a wide range of surface textures. Three have textures greater than the type “T” polypropylene pipe specimens examined previously, and one is smoother. The additional surface types are referred to as virgin polypropylene sheet (type “V”), engraved (type “E”), sandblasted (type “S”), and pressed (type “P”) and their production and detail is described below. For brevity, the surfaces will generally be referred to by their type letter (V, T, E, S, P) rather than their full names.

5.1.1 Virgin polypropylene

Polypropylene sheet was purchased from a material stock merchant to ensure a uniform homogenous stock of material from which enhanced texture specimens could be produced. The polypropylene sheet was simply cut to size as flattening was not required. Hardness of the pristine sheet was approximately 70 Shore D at ambient laboratory temperatures of between 20°C and 22°C. These unmodified surface specimens are designated type “V” and interface tests on them are labelled as such. Pristine surfaces could not be satisfactorily photographed due to the smoothness and reflective nature of the surface.

5.1.2 Engraved specimens

Virgin polypropylene sheet specimens were engraved using a Trotec Speedy100 laser engraver to enhance the surface texture. The engraving process resulted in the formation of melt zones rather than ablation – a feature of this combination of equipment and material – but it was still effective. The engraved pattern consisted of 2 mm circles immediately adjacent to one another with subsequent rows offset by half a diameter. The equipment used is shown in Figure 5.1 and a schematic representation of the engraved pattern is presented in Figure 5.2. These surface specimens are designated type “E” and interface tests on them are labelled as such. An oblique view across an engraved surface is shown in Figure 5.3.

Figure 5.1 Trotec Speedy100 laser engraver used to engrave polypropylene “E” specimens.

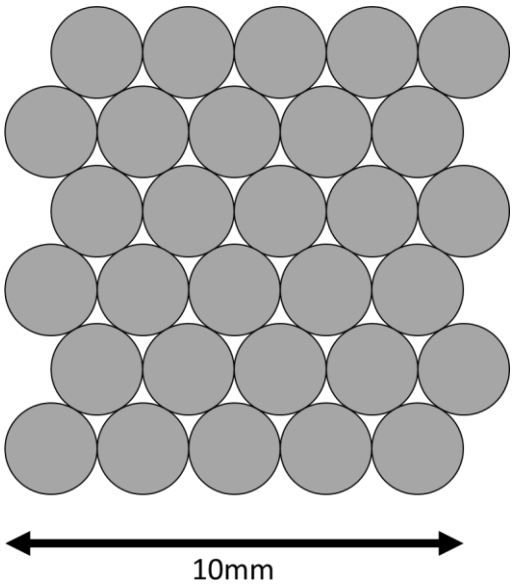

Figure 5.2 Schematic diagram of the laser engraved pattern.

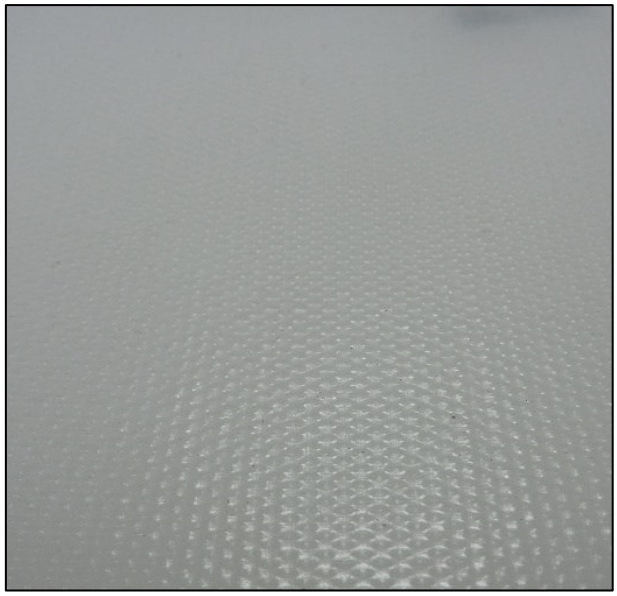

Figure 5.3 Oblique view across the surface of an engraved specimen.

5.1.3 Sandblasted specimens

To further enhance surface texture, engraved specimens were subjected to sandblasting using Leighton Buzzard sand as the abrasive. Each sample was subjected to the same number of passes with the gun and from the same distance to ensure as uniform and repeatable a process as possible. The blasting cabinet used for the sandblasting process is shown in Figure 5.4. An oblique view across an engraved surface is shown in Figure 5.5 and these samples are designated type “S”.

Figure 5.4 Sandblasting cabinet.

Figure 5.5 Oblique view across the surface of a sandblasted specimen.

5.1.4 Pressed specimens

Polypropylene specimens for pressing were obtained from an industrial pipeline coatings manufacturer and prepared in the laboratory. Sections of coating were initially cut to size and then flattened under 20 kg of mass at approximately 160°C to remove any curvature. A steel plate of similar dimensions to the surface specimens was machined with a knurled surface comprising tetrahedral protrusions 3 mm in height with slope angles of 45°. The knurled steel plate and surface specimens were heated to approximately 180°C to soften the polypropylene to the brink of liquefying; Shore D hardness was reduced from approximately 70 to between zero and five. When sufficiently softened, surface specimens were sandwiched between the two heated steel plates, one smooth to act as a base and the knurled plate on top, and a load of 10,000 kg applied using a hydraulic jack. The knurled surface of the plate pressed into the polypropylene specimens is represented in Figure 5.6 and an oblique view across a specimen is shown in Figure 5.7. These specimens were designated type “P”.

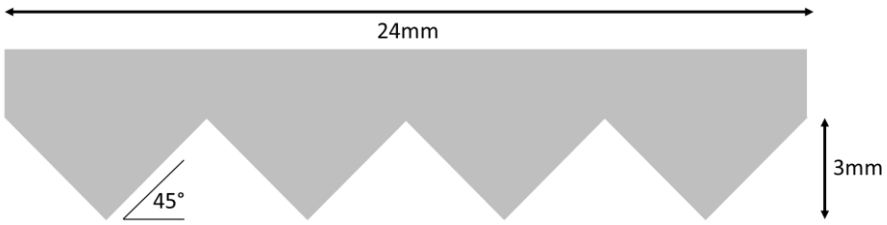

Figure 5.6 Schematic representation of a section of the knurled surface used to impress the polypropylene specimens.

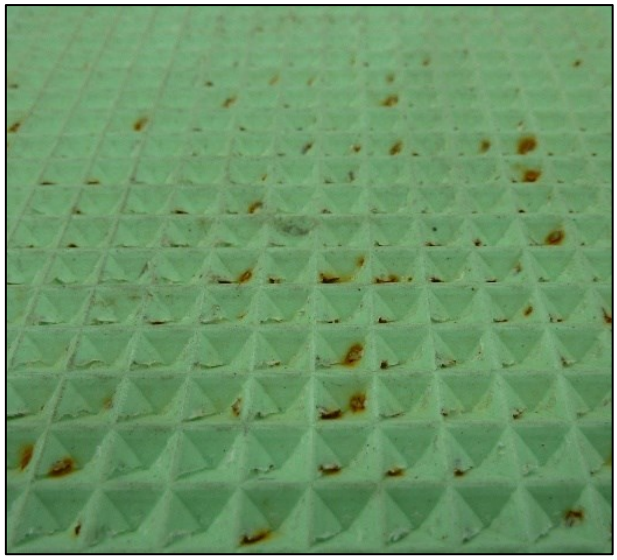

Figure 5.7 Oblique view across the surface of a pressed specimen.

5.2 Texture characterisation

It was necessary to properly characterise the surfaces to generate a reliable average value to describe each specimen type. Due to the extended time required for Alicona scans (sometimes up to three hours for a single trace or two days for a whole surface compared to a few minutes for a Talysurf profile) it was not feasible to adopt the Alicona methodology for all required profilometry. Availability of equipment and other users also precluded extended use of the equipment for long periods of time. To properly characterise the surface types whilst making efficient use of resources the “E” and “S” surface types, which had greatest inherent variability, were subjected to a campaign of Talysurf contact profilometry to determine the variability across the whole set and also across a single individual surface. A smaller subset of typical examples was then measured with the Alicona to obtain the most appropriate roughness values.

To determine variability, a single 25 mm traverse was made parallel to the shearing direction on all “E” and “S” surfaces (longer traverses were not possible due to the curvature in the specimen caused by the heating effect of laser engraving – this was not an issue during testing as bolting the surface to the interface load pad flattened it out). Then, a typical example of each was selected for a further four traverses to determine variability across individual specimens. This methodology was not applied to “V” surfaces due their pristine nature and extreme homogeneity, or to “P surfaces because only a single specimen was used for every test so the texture was measured directly with the Alicona. Additionally, the magnitude of the surface texture of “P” specimens precludes use of the Talysurf due to the range of movement possible on the stylus arm. For the purposes of determining variability across specimens the L_c filter was set to 8 mm and the results are presented in Table 5.1 including those of “T”

surfaces from Chapter 4. Manipulation and appropriate use of L_c filter will be discussed later. Surface roughness results are broken down by surface specimen in Appendix A1.

Table 5.1 Variability of surface roughness

Surface Type	R_a / St. Dev. (μm)	R_{max} / St. Dev. (μm)
T total	0.3 / 0.1	5.9 / 1.6
T individual	0.3 / *	unavailable
E total	12.714 / 2.755	69.268 / 10.568
E individual	10.373 / 0.376	59.983 / 3.790
S total	35.238 / 11.412	198.987 / 52.423
S individual	36.048 / 8.759	193.839 / 31.338

*standard deviation is within a rounding error so not reported

In general, the absolute standard deviation is greater for rougher surfaces though the difference becomes less stark when considered in percentage terms. Standard deviations vary between ~15% and 33% with no clear relationship to surface type or roughness.

5.2.1 Texture and L_c filter length

There is considerable precedent in the literature for the use of roughness parameters to describe interface surface texture but this neglects any influence of waviness or form and imposes artificial limits on the wavelength of pertinent features. Figure 5.8 clearly shows that when considering the x-axis scale and the range of grain sizes in this study (0.17 to 1.59 mm), that both roughness and waviness are likely to have controlling effects on soil-surface interaction. Therefore, such distinctions are disregarded and instead surfaces are considered only in terms of their overall texture, T, to avoid confusion with existing terms. Surface parameters have a variety of metrics but the two most often used are the arithmetic mean average of absolute deviations from the centre line, T_a, or the maximum absolute deviation, T_{max}, analogous to Jardine *et al.* (1993) and Uesugi and Kishida (1986) respectively.

To capture the best possible measurement of surface roughness each surface type was measured by the Alicona non-contact profilometry method using an evaluation length of 50 mm. The determined T_a and T_{max} varies with the cut-off filter, L_c, and the average values for each surface type are summarised in Table 5.2. Individual measurements are included in Appendix A1.

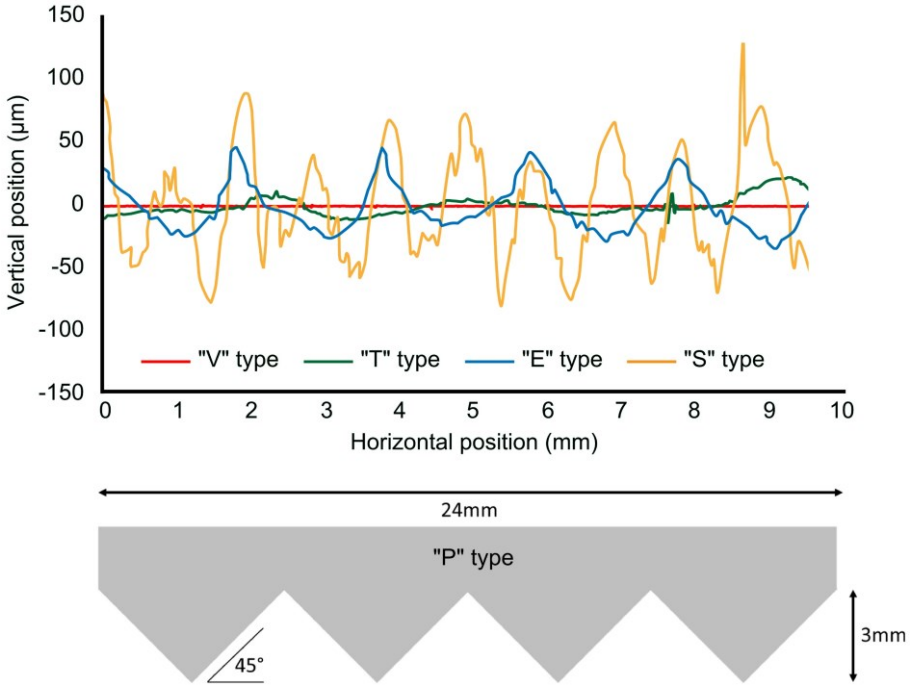

Figure 5.8 Schematic representation of surface specimen profiles with exaggerated vertical scale.

Table 5.2 Summary of roughness (μm) and L_c filter

	L_c filter length (mm)				
Surface	**8.00**	**2.50**	**0.80**	**0.25**	**0.08**
T_a					
V	0.0610	0.0500	0.0433	0.0332	0.0192
T	3.3478	1.2879	0.9123	0.8043	0.5803
E	11.9229	8.2679	2.7986	1.6452	1.2152
S	39.1212	30.9658	12.3907	4.5243	1.7768
P	364.0075	63.7547	14.8103	5.6708	2.2617
T_{max}					
V	3.2223	3.1792	3.1145	2.8326	2.1965
T	38.1308	23.2552	17.1759	10.6196	5.5159
E	71.9259	54.8721	33.8088	18.7413	11.6534
S	177.6979	165.7929	123.1585	55.0586	21.1320
P	unavailable				

In Figure 5.9 the variation of T_a with different L_c cut-offs for each surface type is shown graphically. Although measured T_a varies according to L_c and surface type, there is a clear distinction between the five surface types and overall distinctions in texture are clear when shown on a log-log scale. Where available, T_{max} values are presented in the right-hand panel of Figure 5.9. It is clear from the figure that correct selection of the L_c parameter is key due to the large variation in surface texture value.

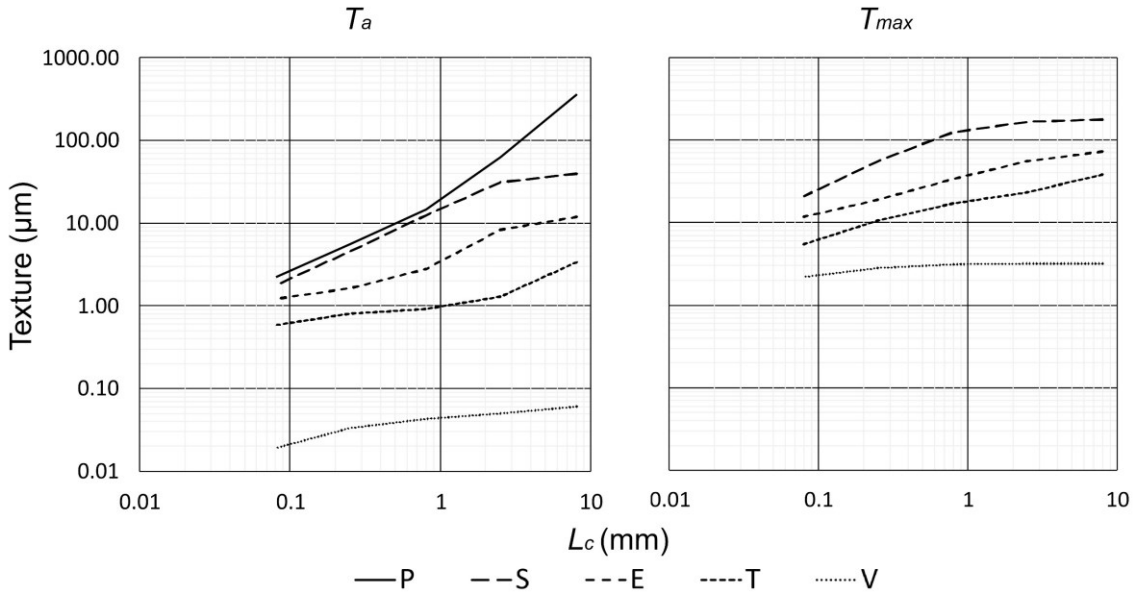

Figure 5.9 Change in T_a with long wavelength cut-off filter, L_c

5.2.2 Relative texture

It is well recognised that the effective texture of an interface surface is affected by particle size of the interface soil and as such is commonly quantified using a measure of relative parameters as in Uesugi and Kishida (1986). Such parameters recognise that the degree of engagement or meshing between a granular material and a surface, and hence the shear resistance offered, is dependent on the relative size of particles in relation to the magnitude of the surface texture. A given surface appears to have a greater texture to a finer grained soil. Relative parameters quantify the degree of meshing by expressing the surface texture as a proportion of mean particle diameter giving the parameter of interest:

$$T_{relative} = T_a/D_{50} \qquad Eq.6.1$$

In addition to normalising texture by the grain size it is also necessary to consider the scale over which it is measured. Uesugi and Kishida (1986) limited their scope to roughness and measured over a length equal to D_{50} so that large asperities that a longer profile might have picked up would not be counted as it would not have affected the particles in question. Surfaces considered in this research have a much wider bandwidth, including features traditionally referred to as roughness, waviness, and form, so Uesugi and Kishida's (1986) philosophy is applied to surface texture as previously defined. It is necessary to consider the surface texture at the appropriate wavelength, an effect Uesugi and Kishida (1986b) achieved by measuring their surface over a length equal to D_{50}. In the current work the same effect is more easily achieved by manipulation of the cut-off filter, L_c. Figure 5.9 shows that as the

magnitude of the (high-pass) filter, L_c, decreases, progressively more long-wavelength information is removed from the surface profile resulting in lower magnitudes of texture. Having defined the relationship for relative texture in *Eq. 6.1*, setting $L_c = D_{50}$ achieves a similar effect as Uesugi and Kishida (1986) intended and reveals the appropriate T_a for any test sand in question for a given surface. It is recognised that it may not always be possible to set the L_c filter to a specific value equal to D_{50}. However, charts similar to those in Figure 5.9 can be easily produced and the appropriate roughness determined by reading from the graph. Table 5.3 summarises the appropriate roughness according to soil and surface type using $L_c = D_{50}$ and with values determined as per ISO 4288:1998 included for comparison.

Table 5.3 Summary of L_c=D_{50} texture, T_a, and ISO 4288 roughness, R_a (µm)

Soil / Surface Type	"V"	"T"	"E"	"S"	"P"
S0	-	0.79	-	-	-
S15	-	0.81	-	-	-
S35	-	0.82	-	-	-
Lowestoft Gravel	0.05	0.88	6.44	18.55	44.20
Leighton Buzzard	0.04	0.85	2.91	13.70	18.00
Hostun Sand	0.04	0.81	1.78	6.20	7.20
Redhill Sand	0.03	0.82	1.35	3.15	4.00
ISO 4288 (R_a)	0.04	0.91 / 1.29	11.92	39.12	364.01

Table 5.3 shows considerable variation between the appropriate roughness according to ISO 4288:1998 and according to the novel methodology, particularly as the surface texture increases. The latter approach has been adopted as the most suitable methodology for assessing the appropriate texture magnitude at particulate-continuum interfaces as it considers both the soil and the surface together rather than just the surface is isolation. It is interesting to note that the range of L_c values recommended by ISO 4288:1998 (0.08, 0.25, 0.8, 2.5, 8.0 mm) broadly covers the grain size range for sand. This is not likely to be intentional as the standard is not designed to consider soil-surface scenarios, but it means that the proposed technique adopted in this work is within the range and applicability of existing standards.

Table 5.4 summarises the appropriate relative texture for each sand-surface combination adopting the novel approach. Measurement of texture in this way is easily achievable by a test house as it requires only standard profilometry tools and process so it is not anticipated that there would be any inhibitor to take up and adoption of this methodology.

Table 5.4 Summary of relative texture, T_a/D_{50}

Soil / Surface Type	"V"	"T"	"E"	"S"	"P"
S0	-	0.00330	-	-	-
S15	-	0.00319	-	-	-
S35	-	0.00253	-	-	-
Lowestoft Gravel	0.00003	0.00055	0.00405	0.01167	0.02779
Leighton Buzzard B	0.00005	0.00097	0.00331	0.01557	0.02046
Hostun Sand	0.00010	0.00231	0.00509	0.01771	0.02057
Redhill Sand	0.00016	0.00513	0.00844	0.01969	0.02500

5.3 Interface test results

The following subsections detail the interface tests carried out and present shear and volumetric responses. Results tables adopt the same nomenclature as in previous chapters. The $D_{r\ fab}$ and $D_{r\ con}$ are the soil sample relative densities as fabricated and post consolidation after the application of the pertinent normal load and represents the relative density as at the start of shearing. The same applies for e_{fab} and e_{con} with regard to the sample void ratio. The peak shear stress, τ_{peak}, is the maximum shear stress recorded during the test and the ultimate shear stress, τ_{ult}, is the average shear stress between 10 mm and 12 mm of horizontal displacement. For each surface, two nominal relative density were tested (D_r approximately 15% and 70%) at four levels of vertical confining stress(σ_n approximately 2, 5, 15, 20 kPa). For interface tests a four part naming convention has been adopted to uniquely identify each test consisting of a soil type reference [LG, LB, HS, RH], a density reference [L (for loose), D (for dense)], and a nominal stress level reference [2, 5, 15, 20 (kPa)]. Test references end with the surface type reference.

5.3.1 Virgin polypropylene interface results

Table 5.5 summarises tests carried out on virgin polypropylene sheet specimens. Twenty-eight tests were carried out on virgin polypropylene surfaces. Loose sample tests are not reported for Redhill Sand due to excessive sample consolidation such that the upper and lower frame came into contact during, which compromised the quality of the data beyond any useful meaning.

Shear response and volumetric behaviour plots for "V" interfaces are presented in Figure 5.10. For dense sample tests there is a steady increase in shear stress until a plateau is reached at a horizontal displacement of less than 0.5mm. From then on, the shear stress remains largely stable until the end of the test. Shear response may be generally described as elastic-perfectly plastic. There is little vertical displacement observed. In general samples

tend to maintain a constant volume through the test. It can be seen from panel *(a)* that the test for Lowestoft Gravel in loose condition is somewhat unreliable.

Table 5.5 Summary of "V" virgin interface tests

Test reference	σ_n (kPa)	$D_{r\ fab}$ (%)	$D_{r\ con}$ (%)	e_{fab}	e_{con}	τ_{peak} (kPa)	τ_{ult} (kPa)	τ_{peak}/σ_n	τ_{ult}/σ_n
LG_L02_V	1.96	15.0	32.7	0.881	0.813	0.39	0.35	0.20	0.18
LG_L05_V	5.03	15.1	35.4	0.881	0.802	0.82	0.53	0.16	0.11
LG_L10_V	10.14	15.1	36.2	0.881	0.799	1.60	1.17	0.16	0.12
LG_L20_V	20.37	15.1	36.7	0.881	0.797	3.76	3.34	0.18	0.16
LG_D02_V	1.96	70.1	68.5	0.667	0.673	0.54	0.50	0.28	0.25
LG_D05_V	5.03	70.0	72.1	0.667	0.659	1.07	0.95	0.21	0.19
LG_D10_V	10.14	70.0	69.0	0.667	0.671	2.03	1.78	0.20	0.18
LG_D20_V	20.37	70.0	70.4	0.667	0.666	4.32	3.95	0.21	0.19
LB_L02_V	1.96	15.0	37.8	0.793	0.723	0.31	0.28	0.16	0.15
LB_L05_V	5.03	18.8	34.3	0.782	0.734	1.00	0.96	0.20	0.19
LB_L10_V	10.14	15.3	39.8	0.793	0.717	3.01	2.94	0.30	0.29
LB_L20_V	20.36	15.0	38.6	0.793	0.720	4.32	3.44	0.21	0.17
LB_D02_V	1.96	70.0	70.3	0.623	0.622	0.65	0.62	0.33	0.32
LB_D05_V	5.03	70.0	73.4	0.623	0.612	1.25	1.12	0.25	0.24
LB_D10_V	10.14	70.1	75.1	0.623	0.607	2.20	1.856	0.22	.018
LB_D20_V	20.36	70.0	73.3	0.623	0.613	4.19	3.14	0.21	0.15
HS_L02_V	1.96	15.0	33.1	0.943	0.874	0.51	0.49	0.26	0.25
HS_L05_V	5.02	15.1	35.8	0.943	0.864	1.53	1.49	0.31	0.30
HS_L10_V	10.14	15.1	35.2	0.943	0.866	3.52	3.43	0.35	0.34
HS_L20_V	20.36	15.0	38.1	0.943	0.855	6.99	6.41	0.34	0.31
HS_D02_V	1.96	70.0	69.6	0.734	0.736	0.80	0.79	0.41	0.40
HS_D05_V	5.02	70.1	72.3	0.734	0.725	1.74	1.71	0.35	0.34
HS_D10_V	10.14	70.1	72.1	0.734	0.726	3.70	3.63	0.36	0.36
HS_D20_V	20.36	70.1	73.6	0.734	0.720	8.24	7.40	0.40	0.36
RH_D02_V	1.95	70.1	71.4	0.739	0.733	0.68	0.67	0.35	0.34
RH_D05_V	5.02	70.0	71.9	0.739	0.731	1.49	1.47	0.30	0.29
RH_D10_V	10.13	70.1	72.8	0.739	0.727	2.82	2.79	0.28	0.28
RH_D20_V	20.36	70.0	77.9	0.739	0.705	4.96	4.93	0.24	0.24

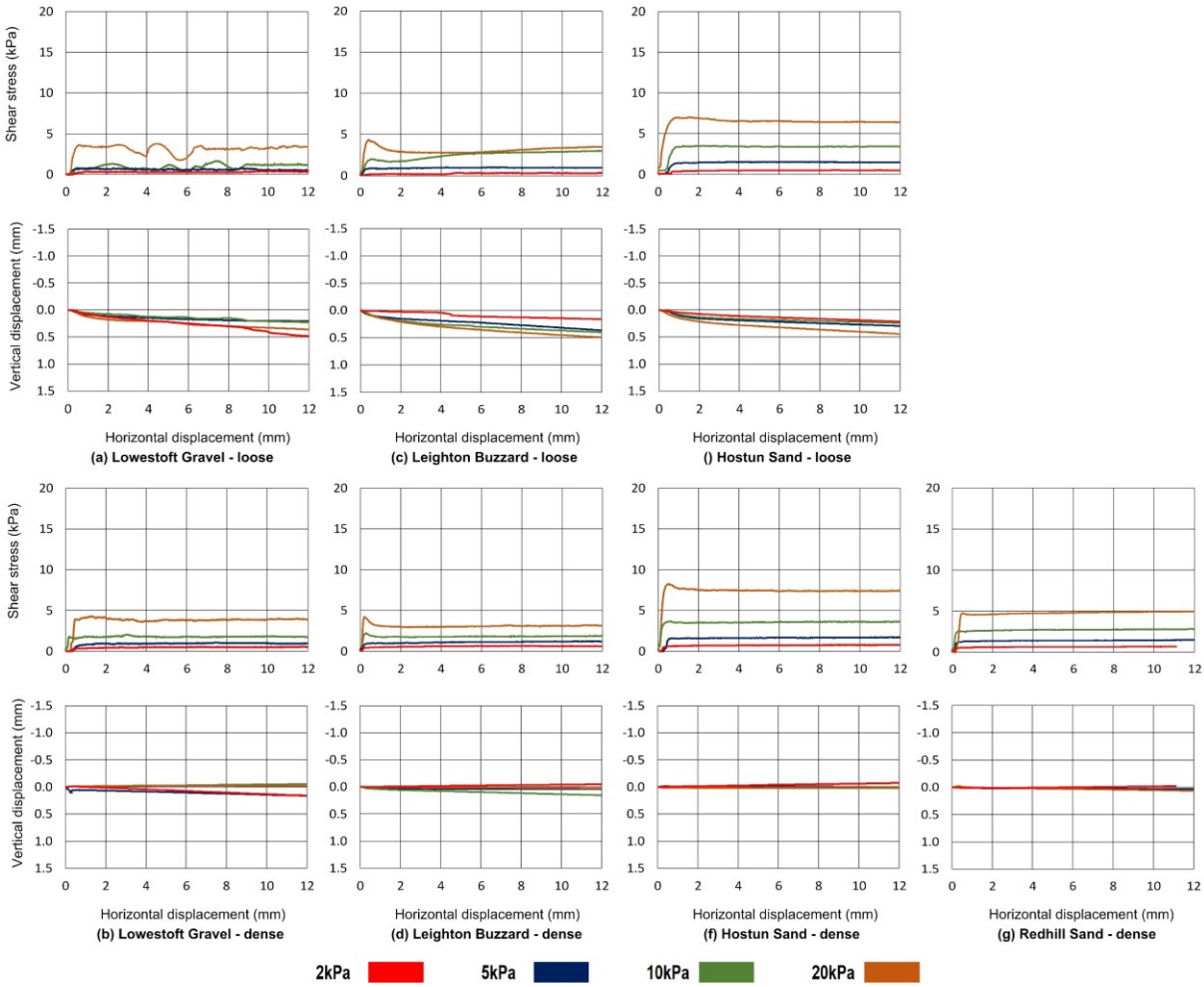

Figure 5.10 "V" interface shear stress and vertical displacement response with (a,b) Lowestoft Gravel, (c,d) Leighton Buzzard B, (e,f) Hostun Sand, and (g) Redhill Sand.

5.3.2 Engraved interface results

Table 5.6 summarises tests carried out on engraved polypropylene sheet specimens. Thirty-two tests were carried out on engraved polypropylene surfaces. Dilatant tests include the peak dilatancy derived from the vertical and horizontal displacement test data. Where dilation was absent or negligible no data is provided due to the difficulty in making a robust determination from the data.

Shear response and volumetric behaviour plots for "E" interfaces are presented in Figure 5.11. Similar to the "V" tests for both dense and loose samples tests there is a steady increase in shear stress until a plateau is reached at a horizontal displacement of less than 0.5 mm. From then on, the shear stress remains largely stable until the end of the test. Shear response may be generally described as elastic-perfectly plastic. Dense samples tests exhibit very limited volumetric behaviour and remain largely static but loose sample tests show an overall trend for steady sample contraction throughout the duration of the test.

Table 5.6 Summary of "E" engraved interface tests

Test reference	σ_n (kPa)	$D_{r\ fab}$ (%)	$D_{r\ con}$ (%)	e_{fab}	e_{con}	τ_{peak} (kPa)	τ_{ult} (kPa)	τ_{peak}/σ_n	τ_{ult}/σ_n	Ψ $\Delta v/\Delta h$
LG_L02_E	1.95	15.1	28.3	0.881	0.830	0.89	0.86	0.45	0.44	-
LG_L05_E	5.02	15.1	27.3	0.881	0.833	1.89	1.80	0.38	0.36	-
LG_L15_E	15.25	15.0	33.0	0.881	0.811	5.61	5.31	0.37	0.35	-
LG_L20_E	20.36	15.1	37.4	0.881	0.794	6.86	6.51	0.34	0.32	-
LG_D02_E	1.95	70.1	70.1	0.667	0.667	0.97	0.90	0.50	0.46	0.06
LG_D05_E	5.02	70.0	70.3	0.667	0.666	2.00	1.94	0.40	0.39	0.02
LG_D15_E	15.25	70.0	70.2	0.667	0.666	5.77	5.45	0.38	0.36	0.02
LG_D20_E	20.36	70.1	71.7	0.667	0.660	7.87	7.36	0.39	0.36	0.02
LB_L02_E	1.95	15.0	34.2	0.793	0.734	0.82	0.75	0.42	0.38	-
LB_L05_E	5.02	15.1	34.7	0.793	0.732	1.69	1.58	0.34	0.31	-
LB_L15_E	15.25	15.0	42.7	0.793	0.708	4.92	4.53	0.32	0.30	-
LB_L20_E	20.36	15.0	39.6	0.793	0.717	6.09	5.92	0.30	0.29	-
LB_D02_E	1.95	70.1	71.9	0.623	0.617	0.99	0.96	0.51	0.49	0.02
LB_D05_E	5.02	70.0	74.5	0.623	0.609	2.08	2.01	0.41	0.40	0.01
LB_D15_E	15.25	70.1	76.4	0.623	0.603	5.68	5.34	0.37	0.35	0.01
LB_D20_E	20.36	70.1	76.6	0.623	0.602	7.45	7.07	0.37	0.35	0.00
HS_L02_E	1.95	15.1	32.0	0.943	0.878	0.95	0.92	0.49	0.47	-
HS_L05_E	5.02	15.1	34.2	0.943	0.870	2.29	2.24	0.46	0.45	-
HS_L15_E	15.25	15.1	49.1	0.943	0.814	6.20	6.12	0.41	0.40	-
HS_L20_E	20.36	15.1	38.8	0.943	0.853	8.50	8.25	0.42	0.41	-
HS_D02_E	1.95	70.0	72.1	0.734	0.726	1.14	1.11	0.58	0.57	0.03
HS_D05_E	5.02	70.1	74.2	0.734	0.718	2.61	2.53	0.52	0.50	0.02
HS_D15_E	15.25	70.1	77.3	0.734	0.706	7.83	7.45	0.51	0.49	0.03
HS_D20_E	20.36	70.0	73.7	0.734	0.720	10.32	9.85	0.51	0.48	0.05
RH_L02_E	1.95	15.7	42.6	0.973	0.857	0.92	0.90	0.47	0.46	-
RH_L05_E	5.02	15.7	41.9	0.972	0.860	1.97	1.92	0.39	0.38	-
RH_L15_E	15.25	15.0	44.3	0.975	0.850	5.99	5.91	0.39	0.39	-
RH_L20_E	20.36	15.1	46.7	0.975	0.839	7.53	6.46	0.37	0.32	-
RH_D02_E	1.95	70.0	71.4	0.739	0.733	1.02	1.01	0.52	0.52	-
RH_D05_E	5.02	70.1	73.2	0.739	0.725	2.25	2.19	0.45	0.44	-
RH_D15_E	15.25	70.1	75.0	0.739	0.717	6.48	6.32	0.42	0.41	-
RH_D20_E	20.36	70.1	72.2	0.739	0.730	8.99	8.95	0.44	0.44	-

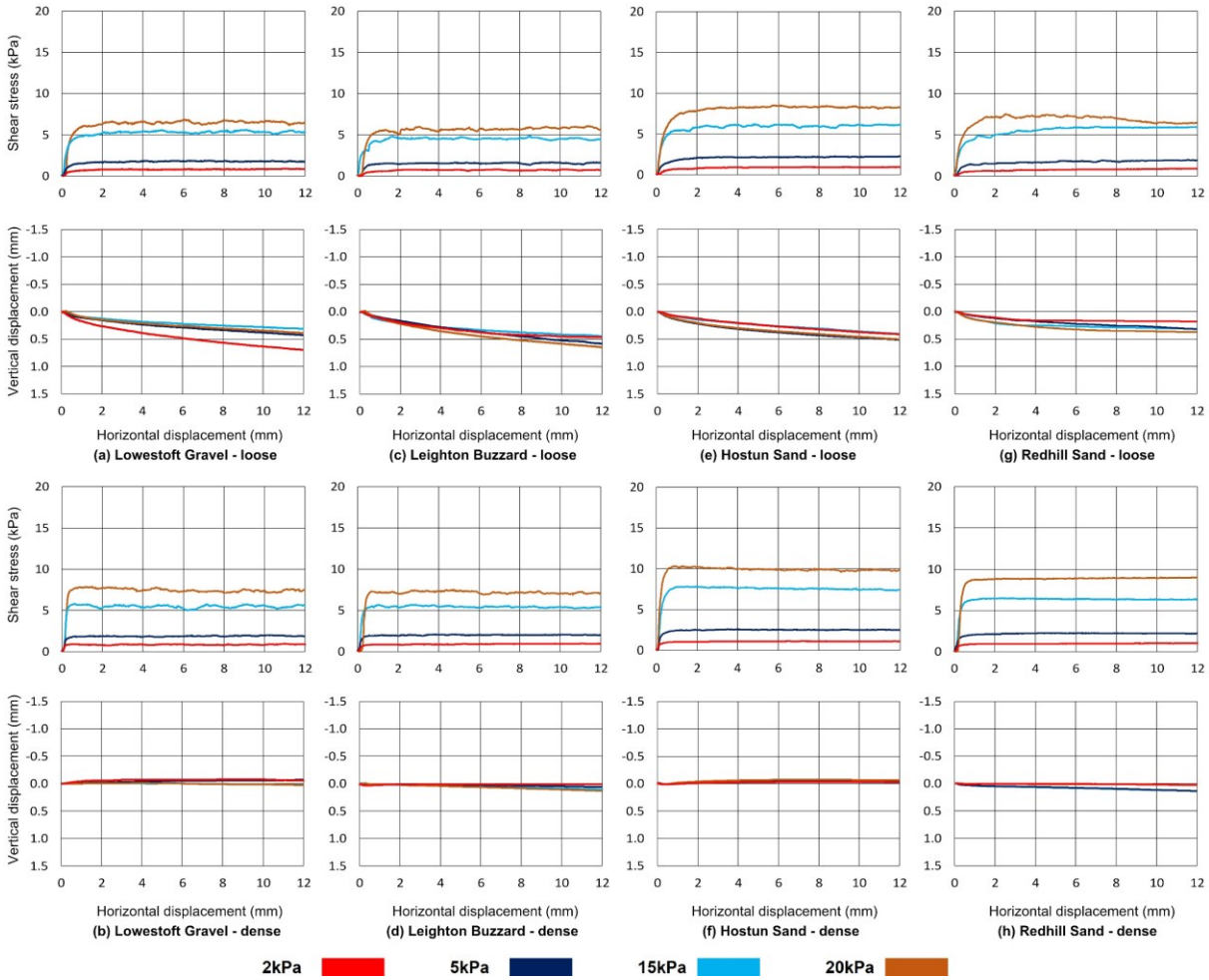

Figure 5.11 "E" interface shear stress and vertical displacement response with (a,b) Lowestoft Gravel, (c,d) Leighton Buzzard B, (e,f) Hostun Sand, and (g,h) Redhill Sand.

5.3.3 Sandblasted interface results

Table 5.7 summarises tests carried out on sandblasted polypropylene sheet specimens. Twenty-eight tests were carried out on sandblasted polypropylene surfaces. Shear response and volumetric behaviour plots for "S" interfaces are presented in Figure 5.12. In contrast to "V" and "E" (and "T" from Chapter 4) interface tests, "S" interfaces exhibit behaviour much more similar to a soil test. Dense tests mobilise an initial peak shear stress accompanied by concurrent dilation which as it subsides corresponds to a gradual reduction in shear strength to a stable ultimate magnitude. Loose tests mobilise only an ultimate strength and generally see a tendency for slight sample contraction.

Table 5.7 Summary of "S" sandblasted interface tests

Test reference	σ_n (kPa)	$D_{r\ fab}$ (%)	$D_{r\ con}$ (%)	e_{fab}	e_{con}	τ_{peak} (kPa)	τ_{ult} (kPa)	τ_{peak}/σ_n	τ_{ult}/σ_n	Ψ $\Delta v/\Delta h$
LG_L02_S	1.95	15.0	25.9	0.881	0.839	1.27	1.15	0.65	0.59	-
LG_L05_S	5.02	15.1	26.6	0.881	0.836	3.34	3.10	0.66	0.62	-
LG_L15_S	15.25	15.1	31.8	0.881	0.816	9.25	8.93	0.61	0.59	-
LG_L20_S	20.36	15.0	37.8	0.881	0.793	10.89	10.57	0.53	0.52	-
LG_D02_S	1.95	70.0	68.8	0.667	0.672	1.43	1.16	0.73	0.60	0.17
LG_D05_S	5.02	70.0	68.5	0.667	0.673	3.44	2.89	0.69	0.58	0.15
LG_D15_S	15.25	70.0	70.5	0.667	0.665	10.86	9.18	0.71	0.60	0.19
LG_D20_S	20.36	70.0	79.1	0.667	0.632	12.98	10.55	0.64	0.52	0.14
LB_L02_S	1.95	15.1	34.2	0.793	0.734	1.26	1.20	0.64	0.62	-
LB_L05_S	5.02	15.1	34.3	0.793	0.734	2.81	2.75	0.56	0.55	-
LB_L15_S	15.25	15.1	39.0	0.793	0.719	8.49	8.20	0.56	0.54	-
LB_L20_S	20.36	15.1	39.8	0.793	0.717	11.39	11.04	0.56	0.54	-
LB_D02_S	1.95	70.0	72.5	0.623	0.615	1.46	1.20	0.75	0.62	0.15
LB_D05_S	5.02	70.0	72.9	0.623	0.614	3.73	2.91	0.74	0.58	0.19
LB_D15_S	15.25	70.1	76.0	0.623	0.604	11.33	8.42	0.74	0.55	0.18
LB_D20_S	20.36	70.1	73.8	0.623	0.611	15.36	11.40	0.75	0.56	0.21
HS_L02_S	1.95	15.1	30.3	0.942	0.885	1.14	1.12	0.58	0.57	-
HS_L05_S	5.02	15.0	37.8	0.943	0.856	3.00	2.90	0.60	0.58	-
HS_L15_S	15.25	15.0	37.0	0.943	0.859	8.41	8.28	0.55	0.54	-
HS_L20_S	20.36	15.5	46.7	0.941	0.823	11.93	11.82	0.59	0.58	-
HS_D02_S	1.95	70.0	71.5	0.734	0.728	1.90	1.40	0.97	0.72	0.24
HS_D05_S	5.02	70.0	70.4	0.734	0.733	4.30	3.45	0.86	0.69	0.25
HS_D15_S	15.25	70.0	74.2	0.734	0.718	11.43	9.17	0.75	0.60	0.18
HS_D20_S	20.36	70.0	75.3	0.734	0.714	14.63	12.60	0.72	0.62	0.14
RH_L02_S	1.95	15.8	39.6	0.972	0.870	1.04	1.00	0.53	0.51	-
RH_L05_S	5.02	16.4	46.2	0.969	0.841	2.76	2.66	0.55	0.53	-
RH_L15_S	15.25	15.8	45.6	0.972	0.844	7.78	7.59	0.51	0.50	-
RH_L20_S	20.36	17.2	48.4	0.966	0.832	9.80	9.15	0.48	0.45	-
RH_D02_S	1.95	70.0	71.4	0.739	0.733	1.43	1.28	0.73	0.65	0.12
RH_D05_S	5.02	70.1	73.6	0.739	0.724	3.25	2.84	0.65	0.57	0.11
RH_D15_S	15.25	70.0	74.1	0.739	0.721	9.93	8.84	0.65	0.58	0.09
RH_D20_S	20.36	70.0	74.2	0.739	0.721	13.78	12.10	0.68	0.59	0.11

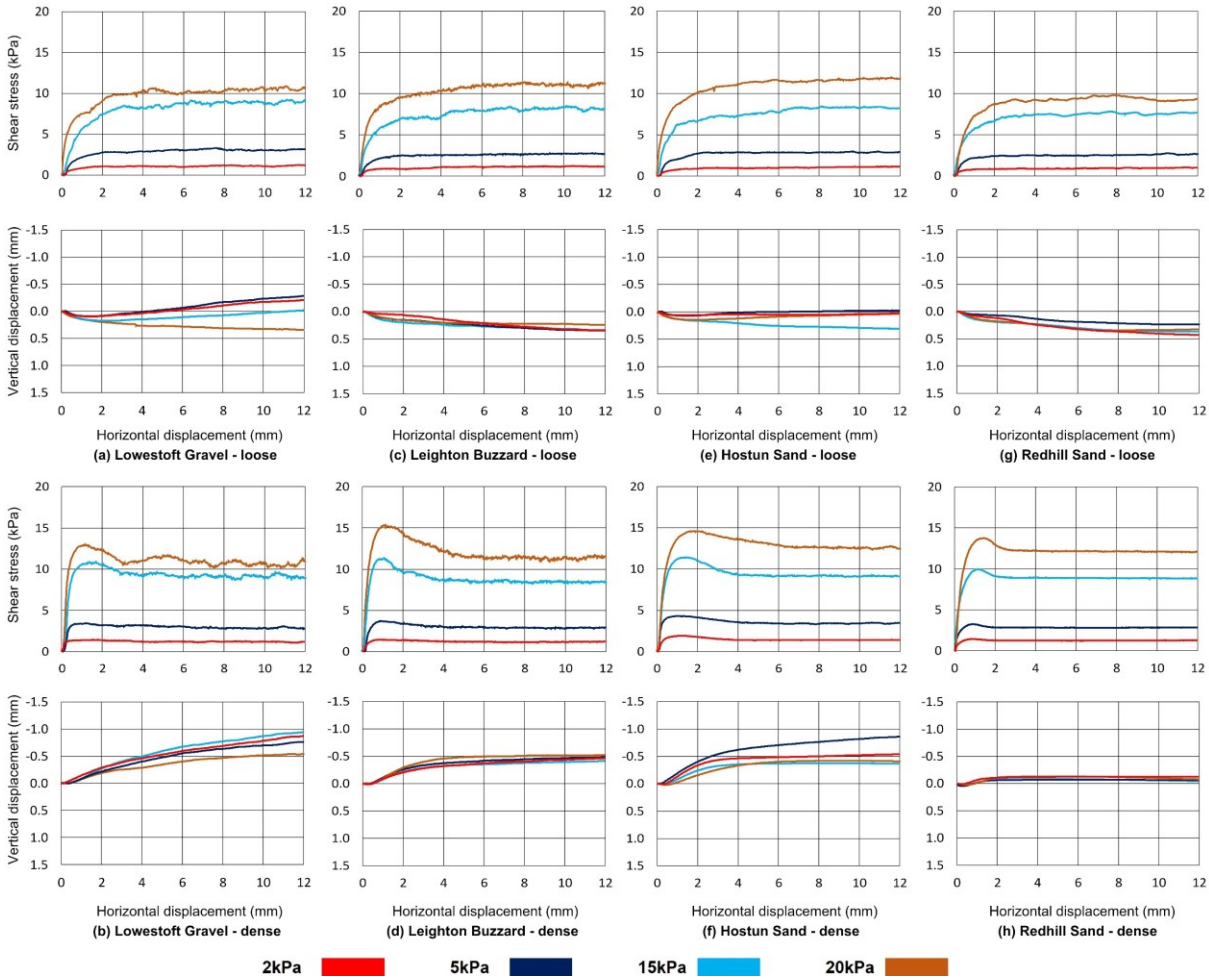

Figure 5.12 "S"-type interface shear stress and vertical displacement response with (a,b) Lowestoft Gravel, (c,d) Leighton Buzzard B, (e,f) Hostun Sand, and (g,h) Redhill Sand.

5.3.4 Pressed interface results

Table 5.8 summarises tests carried out on pressed polypropylene surfaces. Twenty-four tests were carried out on pressed polypropylene surfaces but loose sample tests are not reported for Lowestoft Gravel or Redhill Sand as reliable data could not be acquired. Large sample settlements caused the upper and lower frames to contact which compromised the test results. Shear response and volumetric behaviour plots for "P" interfaces are presented in Figure 5.13. Similar to "S" interfaces, "P" test results exhibit clear stress-dilatancy behaviour with dense sample tests mobilising a peak shear stress concurrently with maximum rates of dilation which both settle to a constant ultimate magnitude.

Table 5.8 Summary of "P" pressed interface tests

Test reference	σ_n (kPa)	$D_{r\ fab}$ (%)	$D_{r\ con}$ (%)	e_{fab}	e_{con}	τ_{peak} (kPa)	τ_{ult} (kPa)	τ_{peak}/σ_n	τ_{ult}/σ_n	Ψ $\Delta v/\Delta h$
LG_D02_P	1.95	70.0	70.0	0.667	0.667	1.87	1.45	0.96	0.74	0.19
LG_D05_P	5.02	70.0	70.5	0.667	0.665	4.16	3.46	0.83	0.69	0.23
LG_D15_P	15.25	70.1	71.3	0.667	0.662	11.76	9.83	0.77	0.65	0.19
LG_D20_P	20.36	70.0	71.5	0.667	0.661	16.26	12.73	0.80	0.63	0.23
LB_L02_P	1.95	15.1	30.6	0.793	0.745	1.18	1.14	0.60	0.59	-
LB_L05_P	5.02	15.0	34.5	0.793	0.733	2.79	2.66	0.56	0.53	-
LB_L15_P	15.25	15.1	36.9	0.793	0.726	9.33	9.16	0.61	0.60	-
LB_L20_P	20.36	15.9	37.8	0.791	0.723	12.83	12.38	0.63	0.61	-
LB_D02_P	1.95	70.1	70.2	0.623	0.623	1.88	1.38	0.96	0.71	0.22
LB_D05_P	5.02	70.1	72.0	0.623	0.617	3.97	3.28	0.79	0.65	0.18
LB_D15_P	15.25	70.0	72.3	0.623	0.616	12.04	9.47	0.79	0.62	0.21
LB_D20_P	20.36	70.1	72.0	0.623	0.617	15.76	12.43	0.77	0.61	0.19
HS_L02_P	1.95	15.1	36.4	0.943	0.862	1.18	1.14	0.60	0.59	-
HS_L05_P	5.02	15.1	33.6	0.943	0.872	2.87	2.74	0.57	0.55	-
HS_L15_P	15.25	15.1	37.5	0.943	0.858	9.13	8.87	0.60	0.58	-
HS_L20_P	20.36	15.0	39.7	0.943	0.849	11.87	11.67	0.58	0.57	-
HS_D02_P	1.95	70.1	70.2	0.734	0.733	1.86	1.46	0.96	0.75	0.22
HS_D05_P	5.02	70.0	71.4	0.734	0.729	3.91	3.11	0.78	0.62	0.18
HS_D15_P	15.25	70.1	74.2	0.734	0.718	11.48	9.48	0.75	0.62	0.17
HS_D20_P	20.36	70.0	73.2	0.734	0.722	15.46	12.78	0.76	0.63	0.18
RH_D02_P	1.95	70.0	71.9	0.739	0.731	1.55	1.36	0.79	0.69	0.09
RH_D05_P	5.02	70.0	72.9	0.739	0.727	3.45	3.07	0.69	0.61	0.09
RH_D15_P	15.25	70.1	73.2	0.739	0.725	10.60	9.23	0.70	0.61	0.13
RH_D20_P	20.36	70.0	76.8	0.739	0.710	13.99	12.06	0.69	0.59	0.09

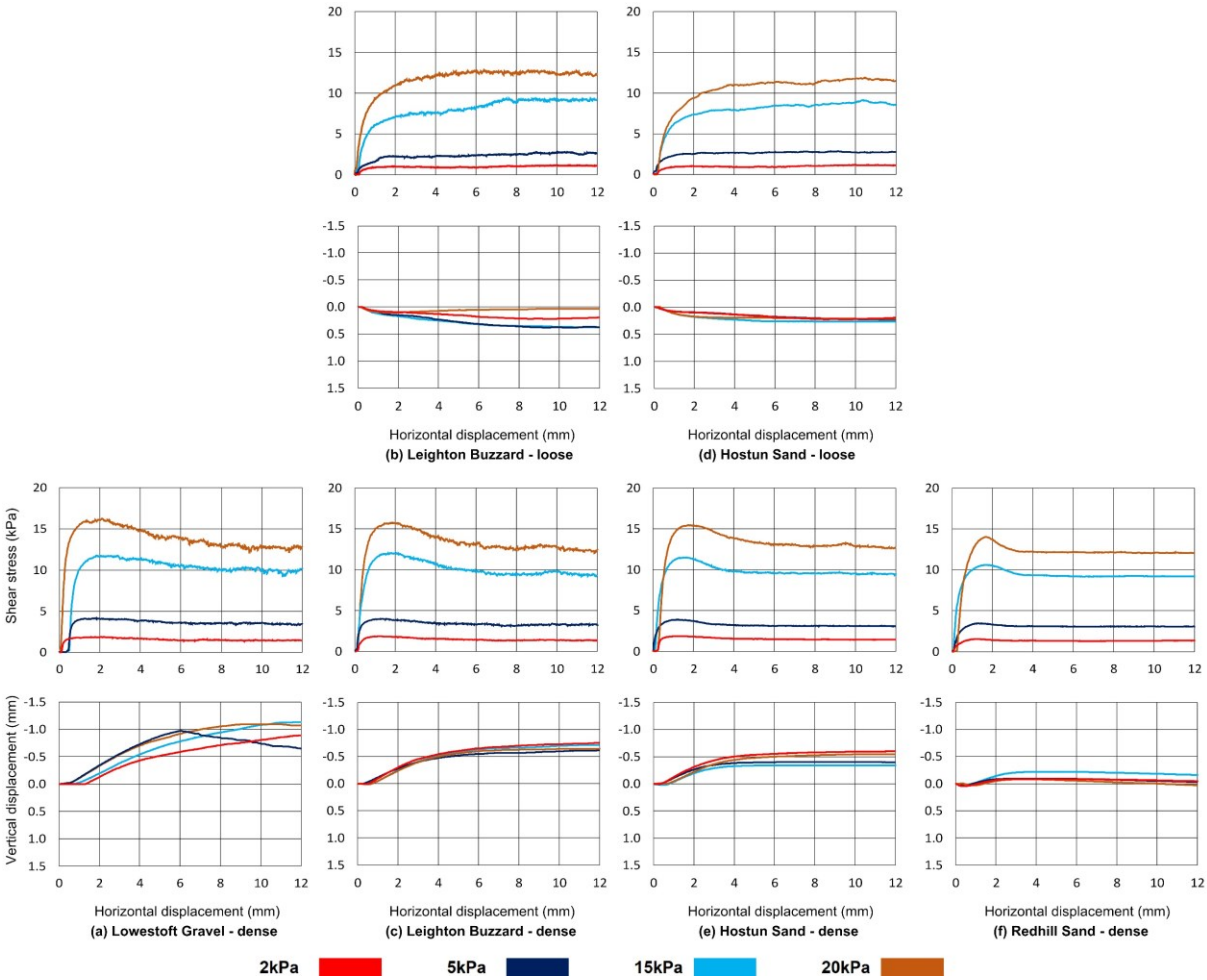

Figure 5.13 "P" interface shear stress and vertical displacement response with (a) Lowestoft Gravel, (b,c) Leighton Buzzard B, (d,e) Hostun Sand, and (f) Redhill Sand.

5.3.5 Failure envelopes

Figure 5.14, Figure 5.15, Figure 5.16, and Figure 5.17 present the failure envelopes in terms of shear to normal stress ratio, for Lowestoft Gravel, Leighton Buzzard, Hostun Sand, and Redhill across each surface type (including "T" surfaces from Chapter 4 which will feature as part of all future discussion). There is a steady increase in interface shear strength from surfaces of lesser to greater texture across each strength condition. Interface friction angles for each surface and soil combination are summarised in Table 5.9 including those of their respective soil only tests and also S0, S15, and S35 from Chapter 4 for reference.

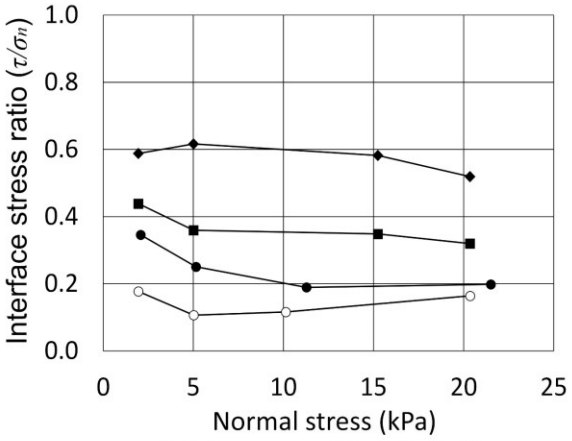

(a) Loose ultimate LG

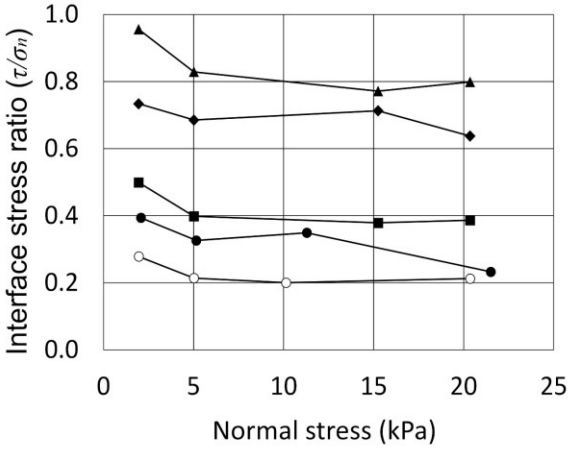

(b) Dense peak LG

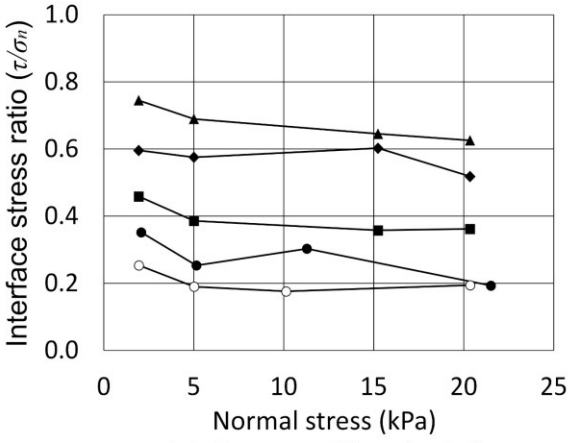

(c) Dense ultimate LG

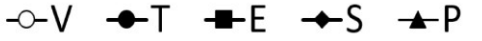

Figure 5.14 Lowestoft Gravel interface shear failure envelopes

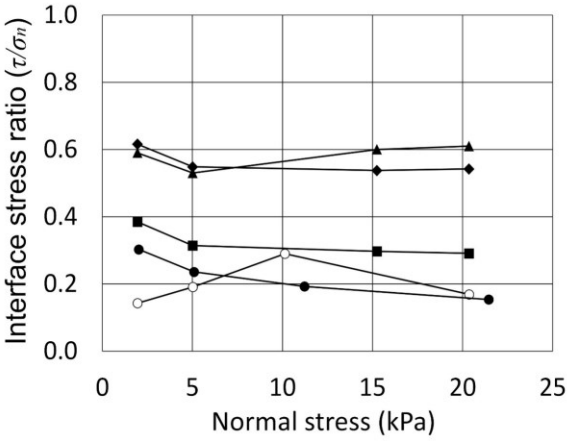

(a) Loose ultimate LB

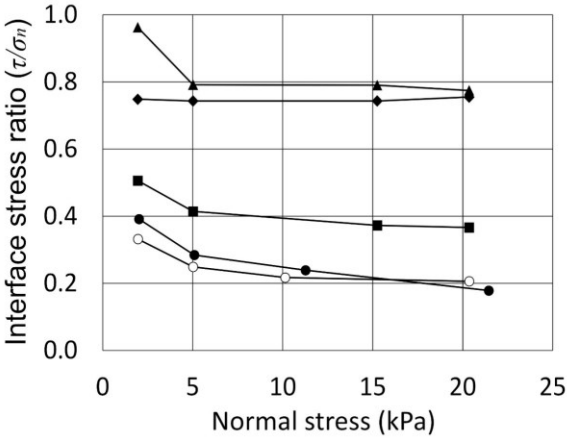

(b) Dense peak LB

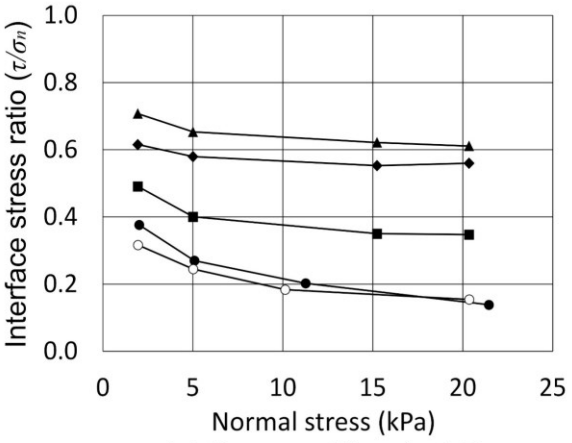

(c) Dense ultimate LB

Figure 5.15 Leighton Buzzard interface shear failure envelopes

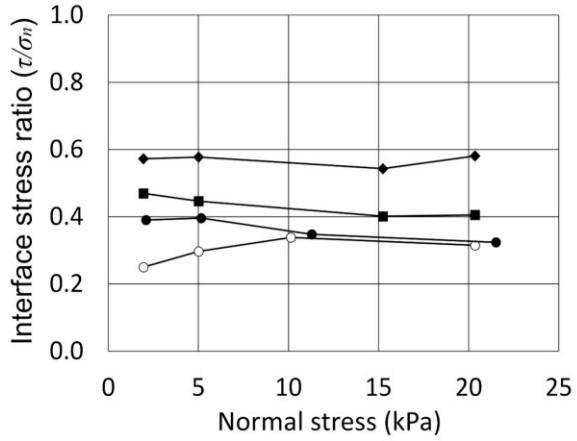

(a) Loose ultimate HS

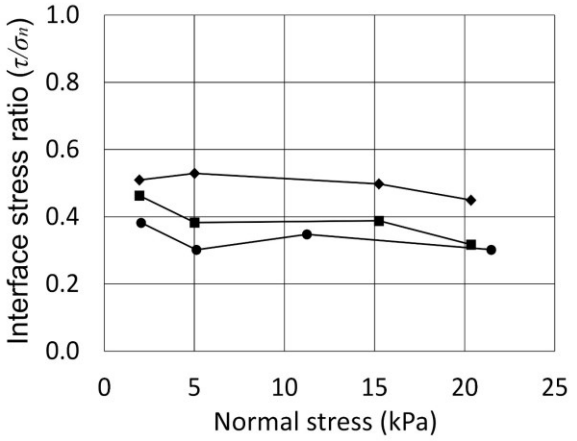

(a) Loose ultimate RH

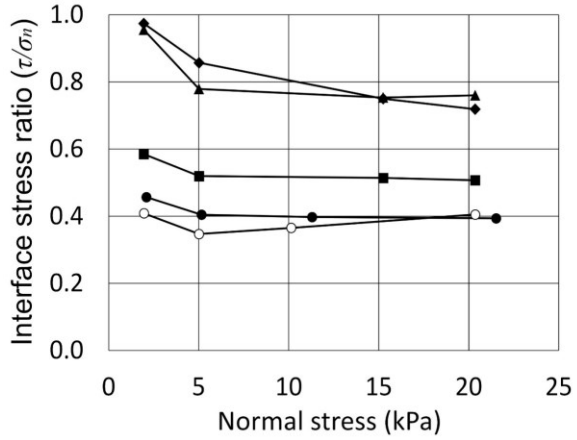

(b) Dense peak HS

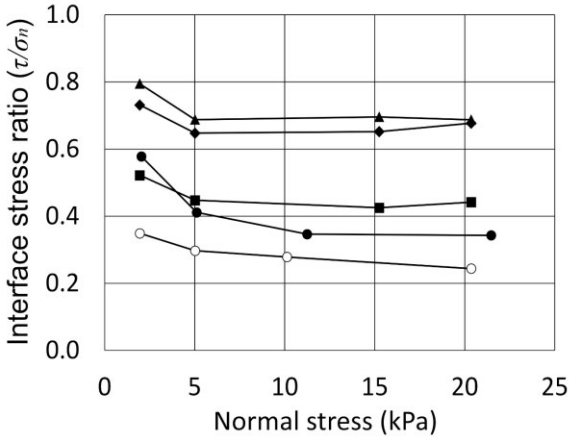

(b) Dense peak RH

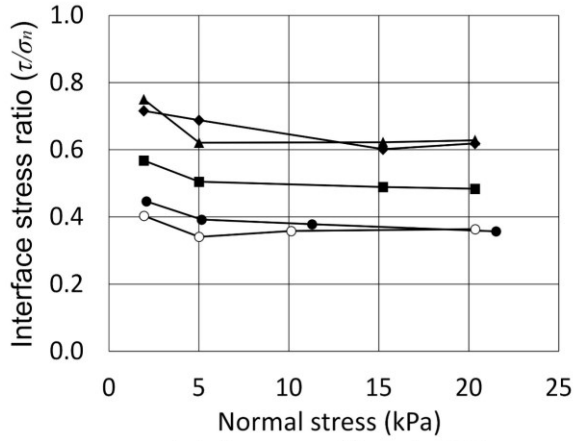

(c) Dense ultimate HS

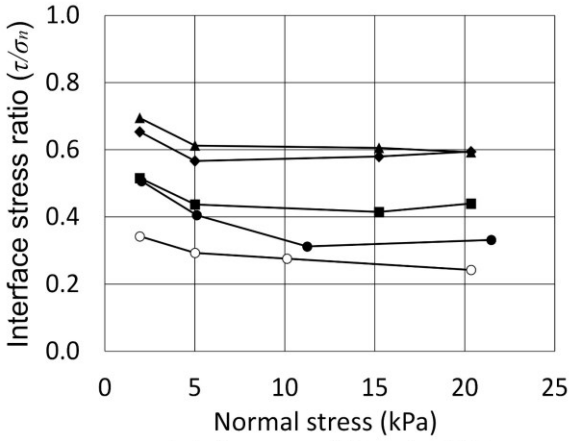

(c) Dense ultimate RH

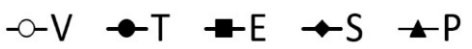

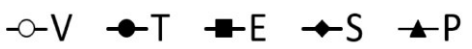

Figure 5.16 Hostun Sand interface shear failure envelopes

Figure 5.17 Redhill interface shear failure envelopes

Table 5.9 Summary of angles of friction

Test	Loose ultimate	Dense peak	Dense ultimate
Soil ϕ			
S0	31.7	38.3	31.9
S15	33.0	39.7	33.5
S35	33.1	37.8	33.7
Lowestoft Gravel	32.6	40.5	32.8
Leighton Buzzard	30.7	40.0	30.5
Hostun Sand	33.0	41.5	31.3
Redhill Sand	32.2	39.9	33.3
Pipe coating (T) δ			
S0	19.3	21.5	19.6
S0 (at 0.2 mm/min)	19.2	21.1	20.4
S15	18.7	24.3	23.0
S35	19.7	23.7	23.1
Lowestoft Gravel	11.4	13.4	12.0
Leighton Buzzard	9.5	11.4	9.2
Hostun Sand	17.9	22.2	19.8
Redhill Sand	17.8	17.9	17.5
Virgin (V) δ			
Lowestoft Gravel	8.7	11.9	10.8
Leighton Buzzard	10.9	11.9	9.4
Hostun Sand	17.6	21.5	19.9
Redhill Sand	-	14.2	14.1
Engraved (E) δ			
Lowestoft Gravel	18.4	21.1	19.9
Leighton Buzzard	16.4	20.4	19.3
Hostun Sand	22.1	27.0	26.0
Redhill Sand	19.0	23.6	23.3
Sandblasted (S) δ			
Lowestoft Gravel	28.6	33.7	28.8
Leighton Buzzard	28.4	36.9	29.2
Hostun Sand	29.6	36.4	31.6
Redhill Sand	25.1	33.7	30.5
Pressed (P) δ			
Lowestoft Gravel	-	38.4	32.4
Leighton Buzzard	31.1	38.0	31.7
Hostun Sand	29.9	37.2	32.1
Redhill Sand	-	34.6	30.9

5.4 Interface efficiency

The concept of interface efficiency, how much of the equivalent soil strength could be mobilised at a given interface, was discussed previously in Chapter 4. The results presented there are expanded in Table 5.10 to include the new results from enhanced textures with average values summarised in Table 5.11. Not surprisingly, given the trend for greater shear strength from surfaces of greater texture, interface efficiencies also increase with enhanced surface textures.

Table 5.10 Summary of interface efficiencies δ / ϕ

Surface / Sand type	*Loose ultimate*	*Dense peak*	*Dense ultimate*
Virgin sheet (V)			
Lowestoft Gravel	0.27	0.30	0.34
Leighton Buzzard	0.35	0.30	0.31
Hostun Sand	0.55	0.54	0.63
Redhill Sand	-	0.38	0.42
Pipe coating (T)			
S0	0.61	0.56	0.61
S1	0.57	0.61	0.69
S35	0.60	0.63	0.69
Lowestoft Gravel	0.36	0.34	0.38
Leighton Buzzard	0.31	0.28	0.30
Hostun Sand	0.56	0.56	0.63
Redhill Sand	0.55	0.47	0.53
Engraved (E)			
Lowestoft Gravel	0.57	0.53	0.63
Leighton Buzzard	0.53	0.51	0.64
Hostun Sand	0.69	0.68	0.82
Redhill Sand	0.59	0.62	0.70
Sandblasted (S)			
Lowestoft Gravel	0.89	0.85	0.91
Leighton Buzzard	0.92	0.92	0.96
Hostun Sand	0.92	0.92	1.00
Redhill Sand	0.78	0.89	0.92
Pressed (P)			
Lowestoft Gravel	-	0.97	1.03
Leighton Buzzard	1.01	0.95	1.04
Hostun Sand	0.93	0.94	1.01
Redhill Sand	-	0.91	0.93

Table 5.11 Average interface efficiency δ / ϕ

Surface	S0	S15	S35	LG	LBB	HS	RH
V	-	-	-	0.30	0.32	0.57	0.40
T	0.59	0.62	0.64	0.36	0.30	0.58	0.52
E	-	-	-	0.58	0.56	0.73	0.64
S	-	-	-	0.89	0.94	0.94	0.86
P	-	-	-	1.00	1.00	0.96	0.92

Values from Table 5.11 (excluding soils S0, S15, and S35) are plotted in Figure 5.18 which shows the change in interface efficiency with increasing surface texture more clearly. The data in each panel are the same, presented on a natural and semi-log scale. Each sand type shows a similar trend and the black line is an approximated average showing the general trend across all sand types. It is identical across both panels. As interface efficiency approaches 1.0 there is a reducing benefit from any additional surface texture. It may be envisaged that as the magnitude of texture increases, the surface texture increasingly meshes with grains sufficiently well to provoke the formation of a shear band in the soil above the surface suggesting that the equivalent soil-only strength imposes an upper limit on interfacial strength. Surfaces that have randomised roughness (analogous to texture) have been shown to be limited in their maximum shear strength to the equivalent internal soil strength (Uesugi and Kishida, 1986; Subba Rao *et al.,* 1998; Dove and Jarrett, 2002). Martinez and Frost (2017) note that surfaces comprising periodic features which do not become clogged by particles during shearing may mobilise interface strengths greater than the equivalent soil-soil strength by the generation of passive resistances. The surfaces in this research are of a random, non-periodic nature, that are prone to clogging so such enhanced strengths are not applicable.

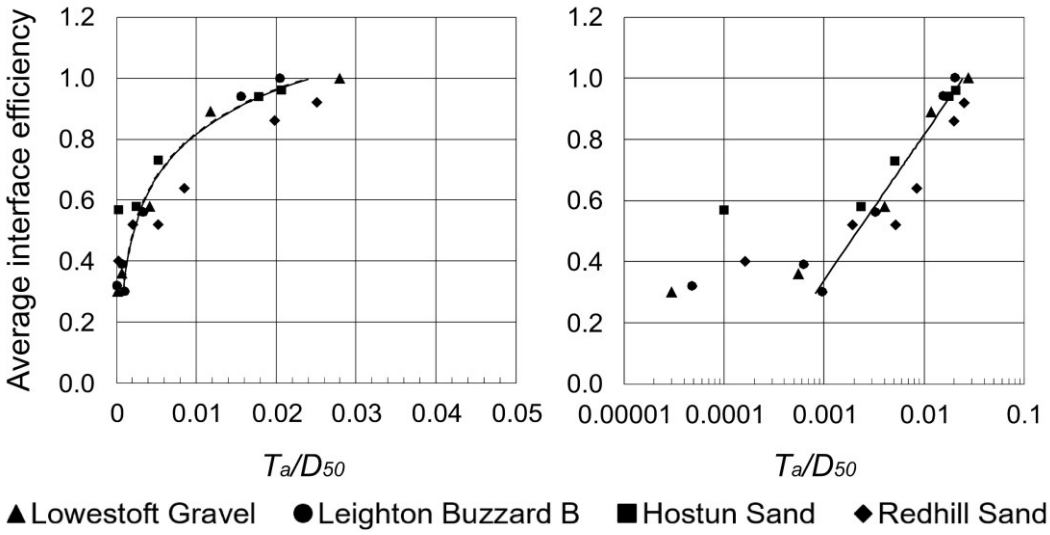

Figure 5.18 Average (loose and dense ultimate and dense peak) interface efficiency variation with relative texture.

5.5 Comparison with the literature

The data for enhanced texture surfaces are compared here with existing literature with regards to surface hardness and surface texture (analogous to roughness in the literature).

5.5.1 Hardness

Just as in Chapter 4, some results for interface efficiency are plotted against the relationship identified by O'Rourke *et al*. (1990) in Figure 5.13. The closest analogous test results (Hostun Sand at 20 kPa in dense state) are plotted for comparison. The roughness of O'Rourke *et al*.'s (1990) surfaces are not known but are assumed to be relatively smooth, therefore, "V" and "T" surfaces are plotted together as most likely to be comparable. They show reasonable agreement to the fit and the error is similar to the other data informing the fit. It is worth noting that Hostun Sand is angular whereas Ottawa Sand is subrounded. Hostun Sand is also finer than Ottawa Sand and it has been shown in Figure 5.18 that this would likely result in a greater efficiency. "E", "S", and "P" results are also included for comparison and shows clearly that the texture has an effect at least as great as surface hardness as the range between minimum and maximum efficiency for the present data for polypropylene is to similar between O'Rourke *et al*.'s (1990).

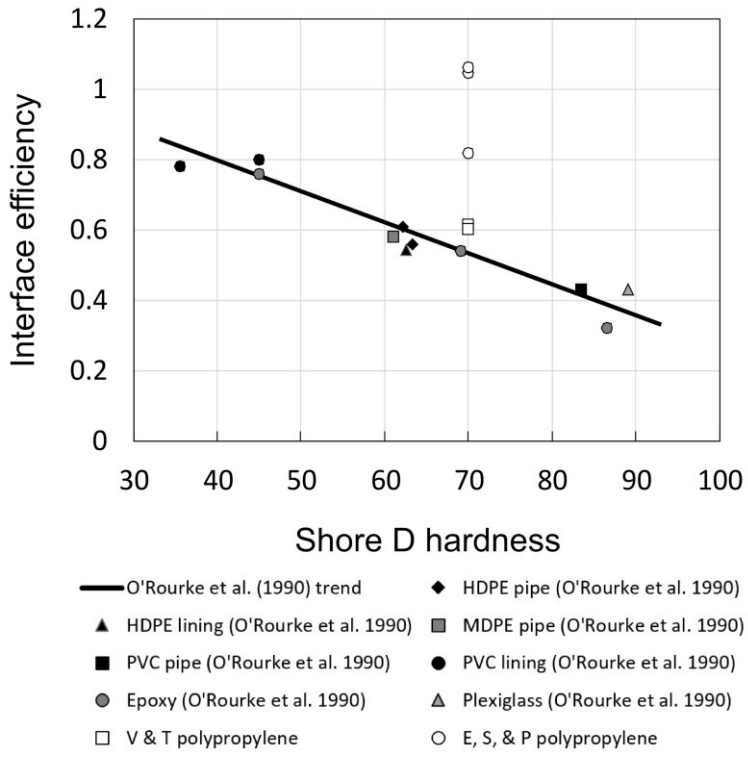

Figure 5.19 Relationship between polymer hardness and interface efficiency in dense soil condition at ~20 kPa normal stress.

5.5.2 Surface texture

Interface efficiency can be compared to the work of Dove *et al*. (1997) as they identified trends between roughness of geomembranes and interface strength with various granular soils. At 50 kPa normal stress (their lowest stress level) they report interface efficiency ranging between 0.5 and 1.0 for peak strength, and 0.5 and 0.9 for residual (ultimate) strength. Their work adopts a stereological approach to characterising roughness and parallels between that and the present methodology cannot easily be drawn. However, their upper ranges broadly agree with the current work although here the ultimate condition is slightly more efficient than the peak. Perhaps owing to the pristine nature of the smoothest surfaces examined here, and large grain sizes of some test sands, the lower bound for the potential efficiency is lower giving a wider overall range.

It is perhaps more useful to compare the relationship between efficiency and texture with the relationship identified by Lings and Dietz (2005) and Dietz and Lings (2006) as their work utilised the same apparatus as in the present work, the Winged Direct Shear Apparatus. There are some important differences between their work and the present work though in addition to the materials used. A notable difference is the interface testing configuration which here is surface-over-soil, opposite to their work. Their work looked at steel surfaces rather than much softer polypropylene which can have a considerable impact. Furthermore, the textures generated in this work are real textures of the surface in question. The work of Lings and Dietz (2005) and Dietz and Lings (2006) required sand grains to be adhered to steel plates in order to create surfaces of high roughness. Such a technique results in shearing analogous to soil-soil conditions. The present work is able to generate similar levels of surface texture but the contact in the shear zone remains grain to surface. Such a distinction is important due to differences in relative hardness and the nature of particle-continuum shearing compared to particle-particle shearing. The distinction is likely to be less important where a textured surface is fully clogged as in that case shearing is sand-sand in any case. In intermediate texture where there is a transition from sliding to fully clogged surfaces the difference may be more important.

Despite the significant differences in testing method, material, and roughening technique, Figure 5.20 shows that the relationship between relative texture and interface efficiency is reminiscent of the relationship identified by Lings and Dietz (2005) and Dietz and Lings (2006). There is some scatter and an obvious outlier but the present data can be said to compare favourably with the literature here in respect of generalised behaviour. It should be noted that the grey dashed lines representing Lings and Dietz (2005) and Dietz and Lings (2006) data used R_a instead of T_a and their surfaces had much lower bandwidth of surface

topography. This difference may also be the cause of the discrepancy in the detail of the shape of the relationship.

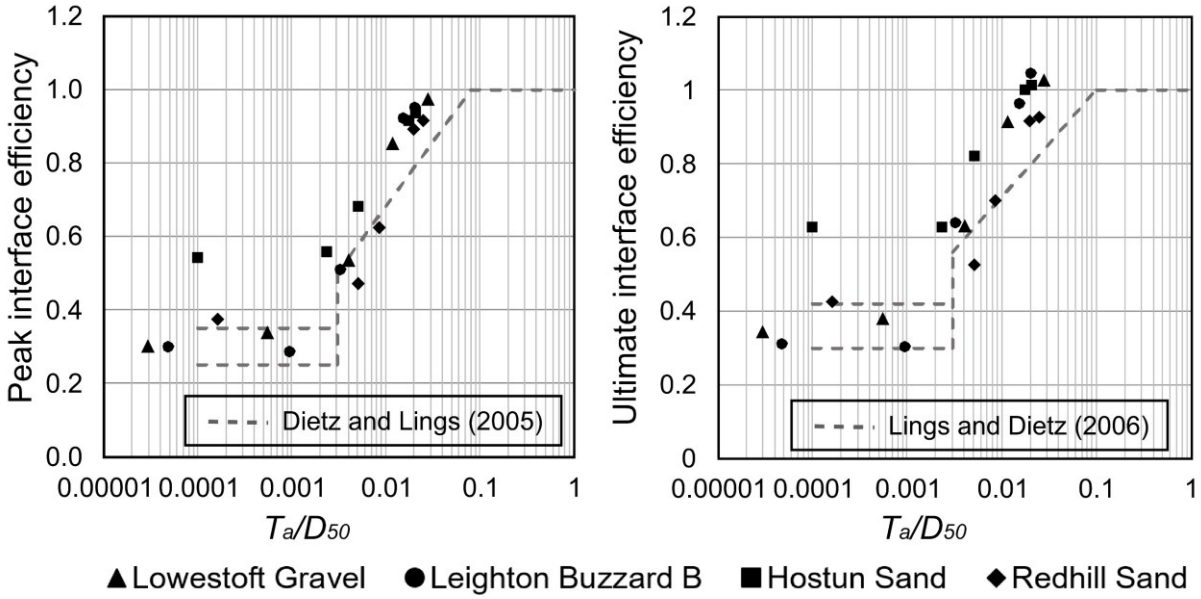

Figure 5.20 Relationship between surface roughness and interface efficiency in dense soil condition at ~20 kPa normal stress.

5.6 Stress dilatancy

Some interface tests exhibited dilative and peak-postpeak behaviour indicative of stress-dilatancy, so it follows that Bolton's (1986) expression relating peak to ultimate states and dilation may be modified to evaluate the behaviour of dilative interface tests assuming that they abide by equivalent laws:

$$\delta_{peak} = \delta_{ult} + \text{K} \cdot \zeta_{peak} \qquad Eq.\,6.2$$

Where:

δ_{peak} = peak angle of interface friction

δ_{ult} = ultimate angle of interface friction

ζ_{peak} = maximum angle of interface dilatancy

The comparison between the experimental measurements for "E", "S", and "P" surface specimens and the expression reworked from Bolton (1986) is presented in Figure 5.21a where a perfect agreement would manifest as a 1:1 relation (indicated by the dashed straight line showing parity). The grey data points follow Bolton's expression using his original dilatancy coefficient of 0.8. At lower δ_{peak} there is good agreement because dilation is zero,

but when dilation starts to play a role a clear divergence develops. Just as for soil tests discussed in Chapter 4, using a coefficient of 0.8 does not give a good agreement. As before, using coefficient K=0.55 brings the data much closer to the idealised 1:1 line which suggests that for the present data at the stress levels investigated, the contribution of dilatancy to the peak strength is less than suggested by Bolton (1986) for sand only strength but it does match the findings of soils tested in this work. Figure 5.21b clearly demonstrates that as dilatancy increases the divergence between δ adapted from Bolton' (1986) expression using K=0.8 and K=0.55 increases. However, as noted in the previous discussion on this topic with soil-only tests, Bolton (1986) used a much higher stress level than used here to determine his relationship and Jewell (1989) observed that relationships between peak and ultimate states with respect to dilatancy become unreliable at low stresses. The boundary conditions and unconfined soil elements adjacent to the shearbox gap that were discussed for the soil only tests are applicable in this scenario too.

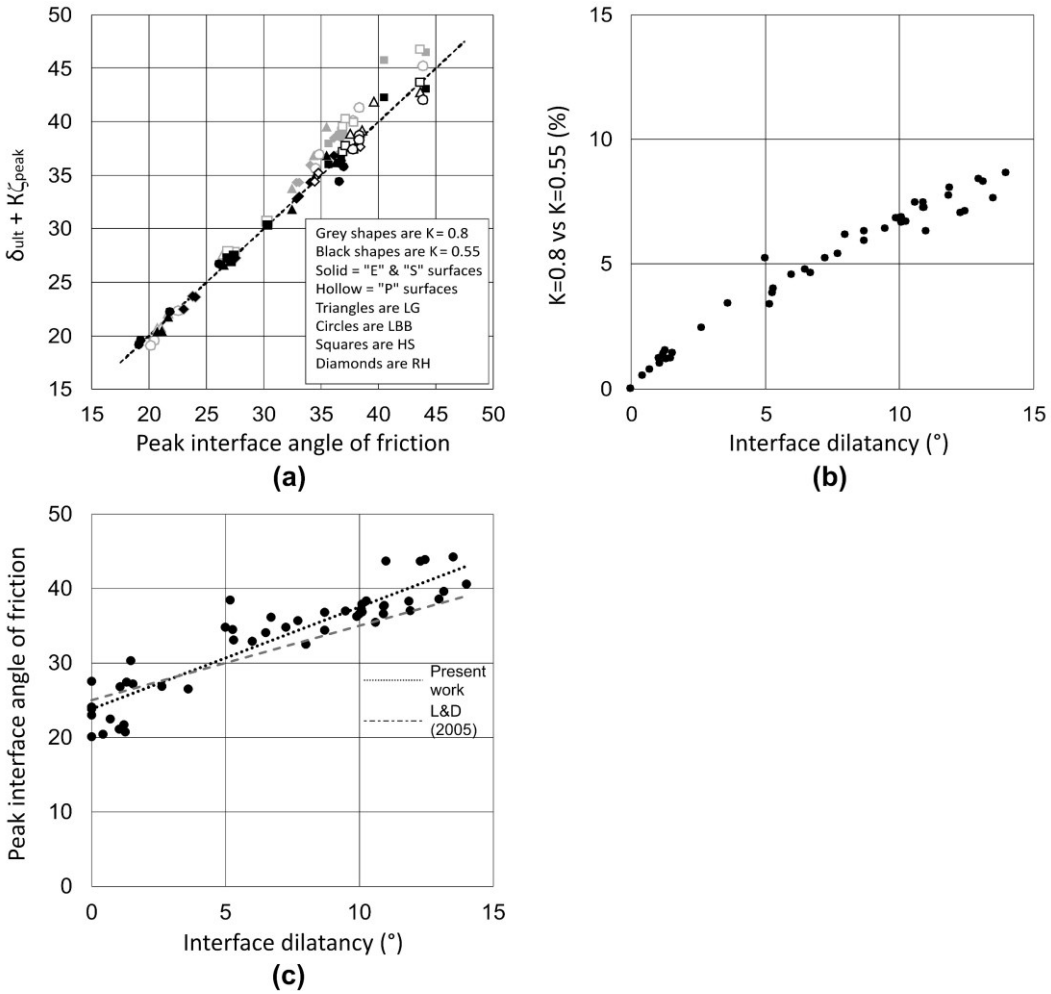

Figure 5.21 (a) (a) Measured δ_{peak} compared to $\delta_{peak} = \delta_{ult} + K \cdot \zeta_{peak}$, (b) comparison of difference between using variable K = 0.80 and K = 0.55 with interface dilatancy and (c) change in δ_{peak} with interface dilatancy.

An alternative flow rule for interfaces was determined by Lings and Dietz (2005) who found that for steel-sand interfaces the peak interface friction angle could be well approximated by the equation:

$$\delta_{ss} = 25° + \zeta_{peak} \qquad Eq.\,6.3$$

Where:

δ_{ss} = angle of interface friction for sand-steel

Figure 5.21c presents the peak shear strength of dilatant interfaces tests with their associated peak angle of interface dilatation. Although there is considerable scatter which means any conclusion from them should be treated with some caution, a linear best-fit through the data gives an intercept of 23.8°, although with a steeper gradient than the interface flow rule of Lings and Dietz (2005).

Dove and Jarrett (2002) and Lings and Dietz (2005) found that interface friction angles of aluminium and steel respectively, are enhanced by the full magnitude of their angles of dilation rather than only a portion of it as is suggested here. Interface shearing typically comprises two components, adhesive sliding and ploughing. Dove and Frost (1999) showed that the ploughing component is more significant for softer surfaces less able to resist indentation, and Shooter and Tabor (1952) showed that ploughing generates greater frictional resistance than adhesive sliding alone. Table 5.10 showed that the interface efficiency in the ultimate state is consistently greater than the peak state so it may be that ultimate strengths are being enhanced by grain ploughing resulting in an apparent lesser contribution of dilation toward the peak strength. Although not specifically investigated here it may be conjectured that the portion of dilatancy contributed to the peak strength of interfaces is related to the surface hardness. This is not entirely satisfactory though as the conventional view is that rougher surfaces provoke shearing in a shear band above the level of surface asperities which have become clogged with soil grains. In this scenario the mechanical surface properties should be of less relevance as they do not participate in shearing. Perhaps hardness yet plays a role though if asperities are damaged in the initial stages due to their relative softness such that peak strengths are reduced. Without further testing and analysis of surface texture before and after testing this is only conjecture.

5.7 Predicting interface friction coefficient

It may be a useful tool for the pipeline engineering community to be able to make an estimation of expected friction coefficients between pipe coatings and soil based on a small number of

input parameters. To that end, determination of a single usable expression to make such a prediction would be beneficial.

Using relative texture parameters can condense interface strength data close to a unique line with respect to roughness which can reveal unique relationships for a given interface. Given the nonlinear nature of strength envelopes the data and trends have been separated out by stress level to give the trends shown in Figure 5.22. It can be seen from both Figure 5.20 and Figure 5.22 that Hostun Sand is an outlier, plotting consistently more strongly than the other sands considered here. One explanation is that the sand itself is industrially manufactured by crushing and grinding and, therefore, is not a representative proxy of naturally occurring soils. Hostun Sand is discounted from consideration for determination of a relationship between interface strength and texture. Hostun Sand symbols in Figure 5.22 are hollow to highlight their omission from derivation of trend lines.

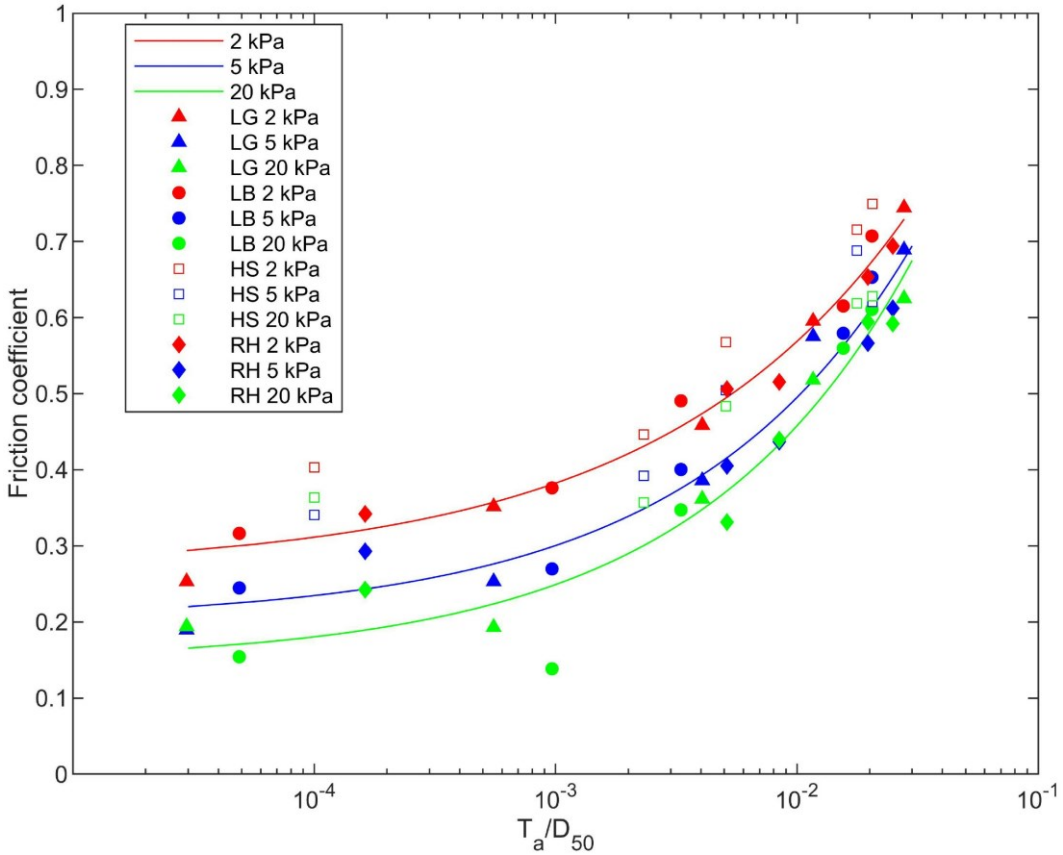

Figure 5.22 Friction factor (equivalent to the ultimate shear strength, τ/σ_n) and relative roughness for each soil type in the dense condition. Hollow shapes for Hostun Sand indicate they are omitted from curve fitting.

Each fitted curve in Figure 5.22 follows a power law relationship but the coefficients controlling the form of the curve vary subtly between stress levels. The largest difference is in the coefficient controlling the y-axis intercept. The relationship between surface texture and interface friction including stress level considerations is similar to that described by Meyer *et*

al. (2015) but with the omission of strain rate effects as pore pressure generation is not applicable to the sandy soils considered here. Coefficients defining the shape of the curves at each stress level (Figure 5.22) are averaged into a single approximation to predict the friction factor which is the sum of a texture component and stress component:

$$\mu = a \cdot \left(\frac{T_a}{D_{50}}\right)^b + c \cdot \left(\frac{\sigma_n}{\sigma_f}\right)^d + e \qquad Eq.6.4$$

Table 5.12 Coefficients and terms for interface strength roughness relationship

Coefficient	*Description*
μ	Interface friction coefficient
T_a	Average texture
D_{50}	Mean average grain size
σ_n	Normal stress
σ_f	1 kPa
a	2.40
b	0.45
c	0.25
d	-0.55
e	0.10

The key exponents in *Eq 6.4* explain the following phenomena. Coefficient *b* describes the power law relationship between the relative texture component of a surface, and the shear strength it is able to mobilise. Coefficient *c* accounts for the stress level with coefficient *d* describing the nonlinear relationship between strength and stress level. The term σ_f is simply a normalising factor to ensure the user adopts the correct units for their stress level. Coefficient *e* accounts for the non-zero strength of surfaces at the lowest roughness across these data.

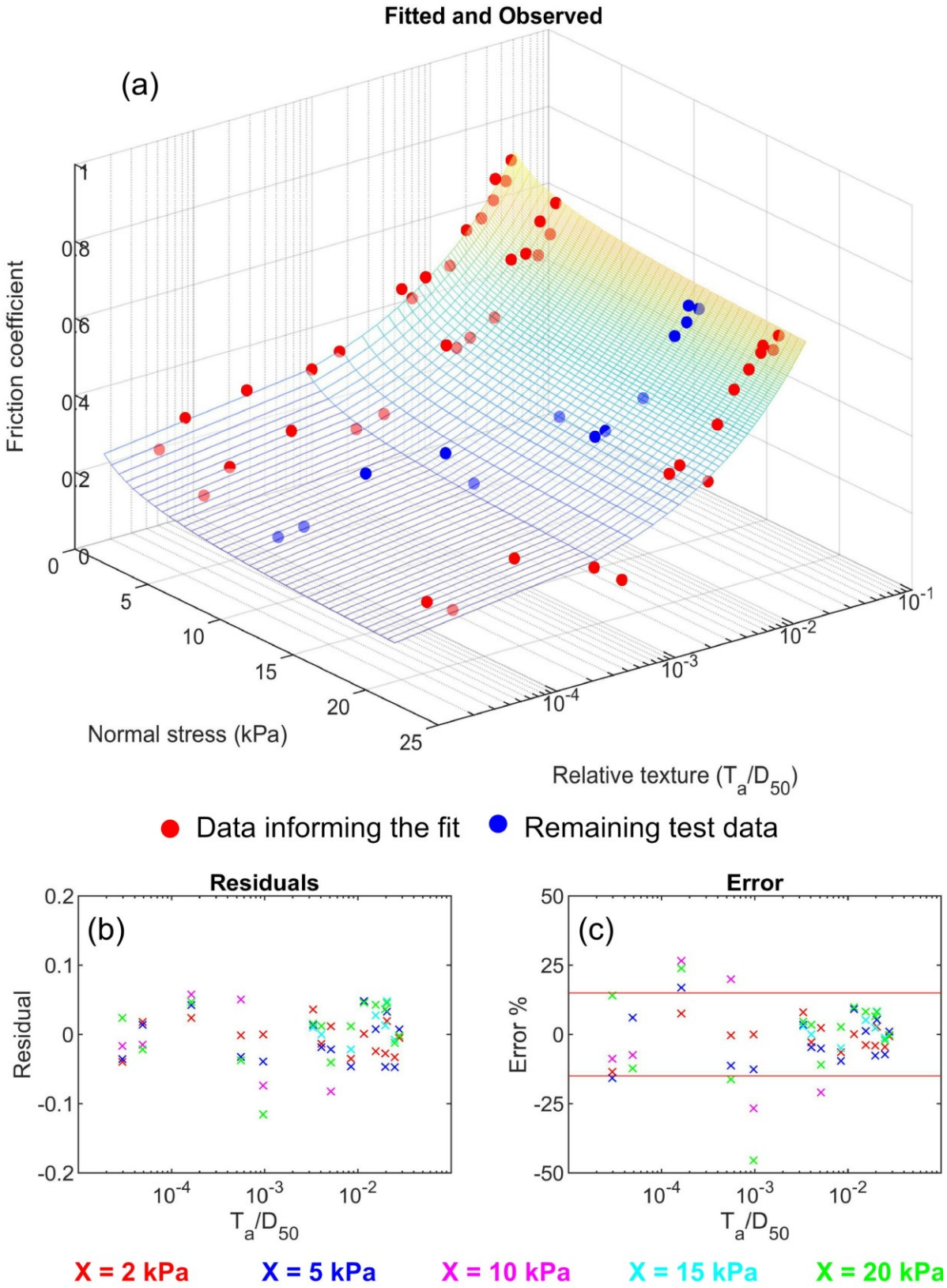

Figure 5.23 (a) graphical representation of the friction coefficient-surface roughness relationship varying with applied stress including plots of (b) residuals between the fitted and observed data and (c) error.

The expression is only valid up to a maximum relative texture (T_a/D_{50}) of 0.025 and has not been tested outside of the range of stress levels investigated in this work. The expression describes the 3D plane shown in Figure 5.23 with red points representing data used to derive the fit, and blue points are the remaining data included to help show the goodness of the fit. The residual and percentage error between the 3D plane described by the equation and the observed data at approximately 2, 5, and 20 kPa are also included. In general, there is a consistent level of friction coefficient residual error of less than 0.1 across the range. The error is stress level dependent with average error increasing from 4.2, to 7.8, to 11.2% from 2, to 5, to 20 kPa normal stress, respectively. The average percentage error across each stress level is 7.7% whilst most of the data fall within 15% error bounds at lower roughness and falls within 10% at higher roughness. Figure 5.18 shows that interface efficiency reaches 1.0 at approximately T_a/D_{50} = 0.025 so the plane in Figure 5.23 is truncated at this value as well. For the types of surfaces tested here the internal soil strength is expected to provide an upper bound to interface strength as previously discussed.

As previously mentioned, the results for Hostun Sand have been omitted from Figure 5.23 due to the difference in the nature of the soil, because the results have more scatter, and generally exhibit greater than anticipated strength at low roughness (illustrated in Figure 5.18). However, it is possible to fit the same expression as defined Figure 5.23 to the Hostun Sand results with only a minor modification to the *"e"* term in *Eq. 6.8*, assuming a value of 0.17 instead. The equation for the surface in Figure 5.23:

$$\mu = 2.40 \cdot \left(\frac{T_a}{D_{50}}\right)^{0.45} + 0.25 \cdot \left(\frac{\sigma_n}{1}\right)^{-0.55} + 0.10 \qquad Eq. 6.5$$

becomes:

$$\mu = 2.40 \cdot \left(\frac{T_a}{D_{50}}\right)^{0.45} + 0.25 \cdot \left(\frac{\sigma_n}{1}\right)^{-0.55} + 0.17 \qquad Eq. 6.6$$

The new 3D plane for Hostun Sand is presented in Figure 5.24 with the original 3D surface of *Eq. 6.5*, included in grey for comparison. Residuals and errors of 4.5, 6.1, and 10.8% for 2, 5, and 20 kPa normal stress respectively, with an average of 6.1% are comparable to the fits for the larger data set. Figure 5.24c shows the majority of the data falling within the same 15% error bounds as in Figure 5.23c.

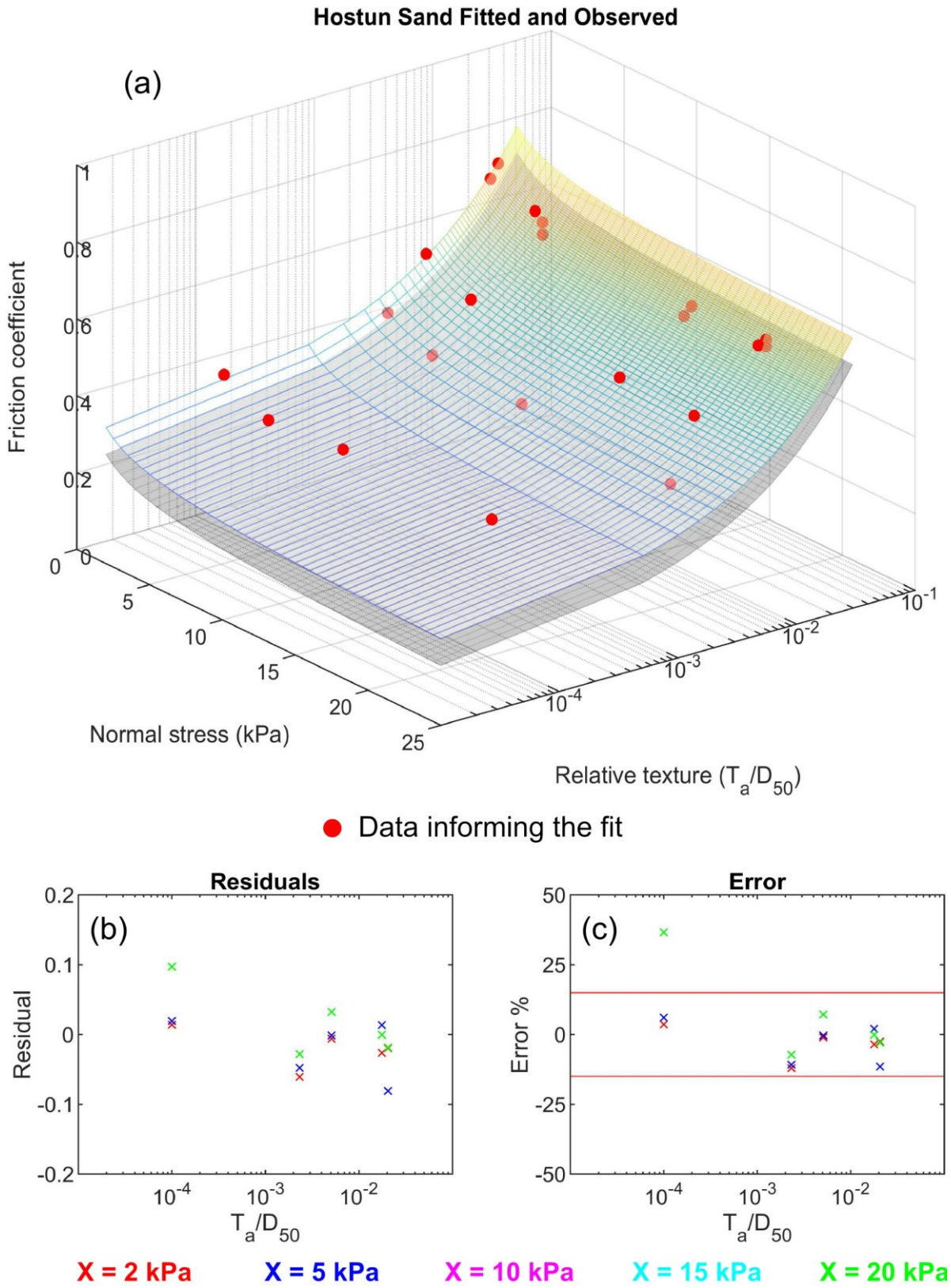

Figure 5.24 Hostun Sand relationship (a) graphical representation of the friction factor-surface roughness relationship varying with applied stress including plots of (b) residuals between the fitted and observed data and (c) error. The grey plane is from Figure 5.23 for easy comparison.

There are a number of other factors which are known to affect the interface shear response which have not been considered in this chapter such as soil particle angularity and soil grading. Surface hardness has also not been considered as all the test specimens have a comparable hardness, however, polymer hardness is sensitive to temperature so both the base material and its operating temperature are likely to affect the friction coefficient (Frost and Karademir, 2016). Just as modification of the "*e"* term for *Eq. 6.6* allows adequate prediction of the Hostun Sand interface friction with its different material properties, perhaps other factors such as surface hardness and soil grading can be accounted for by a similar simple modification. Coefficients *a* or *b,* which describe the shape of the relative texture component, may be subject to modification if the nature of the surface changes. For example, surfaces with a structured roughness, which it was previously discussed may include features generating passive resistance to shearing, may have a different texture-interface strength relationship.

5.8 Conclusions

This chapter has presented the results of a wide-ranging investigation into the interface shear response of polypropylene surfaces with enhanced textures. Four surface types of varying roughness were tested and discussed alongside the results from Chapter 4. Some significant findings were reported and some conclusions can be drawn.

- It has been demonstrated that it is possible to vary the peak strength (in terms of a friction coefficient) of polypropylene interfaces with sandy soils between approximately 0.15 and close to 1.0, and ultimate friction coefficients between 0.10 and 0.75 just through manipulation of the surface texture.
- Measurement of surface texture using traditional approaches has been shown to be unsuitable for surfaces which have wide bandwidth features – it is not enough to simply measure the roughness if there are waviness or form features which may also have an impact. Traditional approaches also fail to consider the phenomenon of soil-surface interaction and meshing of soil grains with the surface texture so a new approach has been proposed which addresses both of these shortcomings. A single choice of L_c cannot work for all soils.
- A novel methodology for determination of appropriate texture parameters was developed which involves setting the L_c filter in the profilometry software to equal the soil $D_{50.}$ Such an approach excludes surface features which are unlikely to effect the soil-surface interaction and accounts for the soil grain size and scale of interaction. Where this is not possible the same effect can be achieved by plotting various L_c values

and reading the appropriate texture term from the graph. Relative texture parameters can then be determined in the traditional way by normalising against soil mean grain size.

- Whilst smooth and less textured surfaces elicit elastic-perfectly plastic responses with limited or no dilation, as surface texture becomes greater there is a transition to elastoplastic shear responses engendering soil dilation or contraction and the mobilisation of both peak and ultimate states in the case of dense samples. Both peak and ultimate strengths are increased with greater surface texture.
- The relationship between peak strengths of dilatant interfaces and their ultimate strengths and peak dilatancy has been shown to be analogous to that of their soil only tests. However, the apparent contribution of dilatancy to peak strengths is reduced compared to literature relationships though the very low stress levels adopted in this work provide a likely explanation.
- A unique relationship has been identified between polypropylene surfaces examined here, stress level, and soil type. The relationship allows an engineer to make an estimate of polypropylene interface friction coefficient from the soil mean grain size, surface texture, and stress level – all readily available information in the pipeline engineering community.

6 Cyclic Interface Response

It has been well established in the literature and in this thesis that surfaces with greater roughness elicit a greater interface shear strength from a given soil and surface combination. It was shown in Chapter 4 that even a single interface test, equating to approximately 12 mm of displacement, was sufficient to modify the surface in such a way that the measured roughness measurably increased. Although a single interface test allows quantification of the shear strength and friction coefficient, it is not reflective of what occurs in the field. Over the life-cycle of a pipeline through repeated start up and shutdown routines, a pipe may displace multiple times in a cyclic fashion which leads to repeated shearing at the interface in multiple reverses. Secondly, cyclic testing is the only way to be able to mimic the large displacements seen in the field diameters in the direct shear apparatus. Given the propensity for surfaces to be damaged during shearing and that friction coefficient relates to surface roughness, it was necessary to investigate what effect cycling would have on interface shear response. After cyclic testing, surfaces were prepared again with a fresh soil sample to determine the reloaded shear response which is discussed in the second part of this chapter.

Two series of cyclic interface tests were conducted. The first using Soil S0, Leighton Buzzard, and Hostun Sand and polypropylene pipe coating specimens (type “T” surfaces), at a range of stress levels all in dense condition due to loose samples experiencing extreme settlements. The second series of tests used Leighton Buzzard on each surface specimen type to evaluate the impact of roughness on cyclic shear response. A more extensive campaign was not possible because of laboratory access restrictions in place due to the 2020 Covid-19 pandemic. More detailed plots than are included here are presented in Appendix D1 and all the raw test data is contained in the data pack on an SD card attached to this thesis.

A note is necessary on the term “ultimate strength” in this chapter. It is determined as previously, however, as the value varies from cycle to cycle, the term is a slight misnomer. However, for consistency and ease of discussion in the context of the preceding work, use of the term will continue. It is hoped the meaning and implication will be clear to the reader.

6.1 Pipe coating cyclic shear response

Seven cyclic interface tests were carried out on the polypropylene pipe coating specimens used in Chapter 4. Tests were conducted in dense condition because loose soil samples led to excessive cumulative settlements such that results became unreliable due to the shearbox frames coming into contact. Leighton Buzzard and Hostun Sand were tested at three stress levels, and soil S0 at only one stress level. Cyclic testing aimed for at least 100 individual traverses corresponding to approximately 1000 mm of total cumulative displacement.

Table 6.1 details the tests undertaken and some cardinal parameters. Shear stresses and stress ratios for the first and last traverse are included and full details for the stress ratio of each cycle can be found in Appendix D1. The nomenclature of cardinal parameters is repeated for reference. The $D_{r\,fab}$ and $D_{r\,con}$ are the soil sample relative densities as fabricated and post consolidation after the application of the pertinent normal load and represents the relative density as at the start of shearing. The same applies for e_{fab} and e_{con} with regard to the sample void ratio. Included also is $D_{r\,fin}$ and e_{fin} representing the *average* final sample condition at the end of the test. The peak shear stress, τ_{peak}, is the maximum shear stress recorded during the test and the ultimate shear stress, τ_{ult}, is the average shear stress of the last two mm of horizontal displacement for each cycle. For each surface, one nominal relative density was tested (D_r approximately 70%) at three levels of vertical confining stress(σ_n approximately 2, 10, 35 kPa). For interface tests a four part naming convention has been adopted to uniquely identify each test consisting of a soil type reference [S0, LB, HS], a density reference [D (for dense)], and a nominal stress level reference [2, 10, 35 (kPa)].

Table 6.1 Summary of pipe coatings cyclic interface tests

Test reference	σ_n (kPa)	$D_{r\,fab}$ (%)	$D_{r\,con}$ (%)	$D_{r\,fin}$ (%)	e_{fab}	e_{con}	e_{fin}	τ_{peak} (kPa)	τ_{ult} (kPa)	τ_{peak}/σ_n	τ_{ult}/σ_n
S0_D35_T-MR											
First traverse	36.80	-	70.0	-	-	0.623	-	15.59	13.89	0.42	0.37
Last traverse		-	-	73.0	-	-	0.733	13.46	12.39	0.36	0.33
LB_D02_T-MR											
First traverse	2.04	70.0	71.5	-	0.623	0.618	-	0.52	0.43	0.25	0.21
Last traverse		-	-	78.6	-	-	0.596	0.37	0.35	0.18	0.17
LB_D10_T-MR											
First traverse	11.24	70.0	75.8	-	0.623	0.605	-	2.32	2.02	0.21	0.19
Last traverse		-	-	86.7	-	-	0.571	2.02	2.01	0.18	0.18
LB_D35_T-MR											
First traverse	36.80	70.0	78.3	-	0.623	0.597	-	8.79	6.62	0.24	0.18
Last traverse		-	-	89.9	-	-	561	5.30	5.15	0.14	0.14
HS_D02_T-MR											
First traverse	2.09	70.1	71.8	-	0.734	0.727	-	1.01	0.92	0.48	0.44
Last traverse		-	-	78.6	-	-	0.701	0.88	0.86	0.42	0.40
HS_D10_T-MR											
First traverse	11.30	70.1	75.7	-	0.734	0.712	-	4.43	4.18	0.39	0.37
Last traverse		-	-	84.0	-	-	0.681	4.09	3.96	0.36	0.35
HS_D35_T-MR											
First traverse	36.86	70.0	75.3	-	0.734	0.714	-	16.54	14.74	0.45	0.41
Last traverse		-	-	89.3	-	-	0.661	15.45	13.64	0.42	0.37

Figure 6.1 presents the shear stress, stress ratio, and vertical displacement plots for the first and last cycle for Soil S0. As the test surface and sand is the same as in Chapter 4, the shear and volumetric responses are the same during the first traverse. There is a general trend for each cycle to mobilise slightly lower shear strength than the preceding cycle, the end result of which is shown in the last cycle curve in blue. Similarly, each cycle saw a gradual contraction in the sample until a relatively stable sample height was reached which is shown by the last cycle curve of the vertical displacement plots in all cases. It is tempting to look at the final relative density and void ratios in Table 6.1 and compare the value for each stress level between soils. However, the final void ratios detailed are necessarily averaged across the sample thickness and measured just from the settlement during the test and will not be representative of the void ratio along the shear plane. Therefore, no meaningful discussion can follow from these values other than to suggest that the final relative density determined in this way does not appear unreasonable suggesting that sample extrusion has not been excessive.

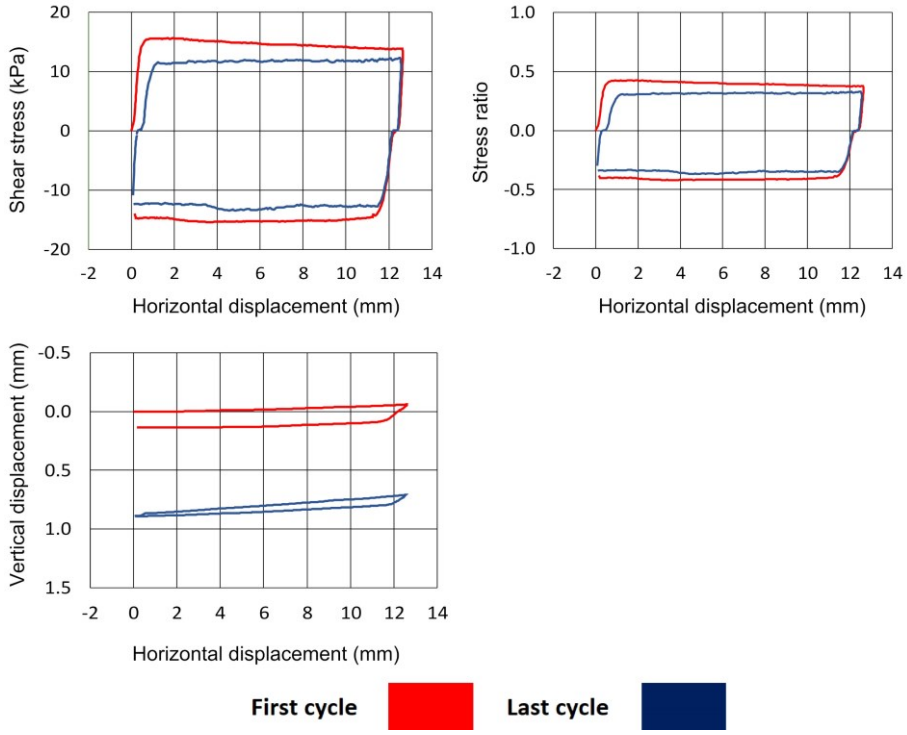

Figure 6.1 Pipe coating cyclic interface test results showing shear stress, stress ratio, and vertical displacement for soil S0 at ~35 kPa.

Shear and volumetric responses for the Leighton Buzzard and Hostun Sand tests at each stress level are presented in Figure 6.2 and Figure 6.3 respectively. Just as for Soil S0 there is a general trend for a reduction in shear strength mobilised with each cycle and, overall, the sample tends to contact. Greater normal stress leads to a greater degree of sample settlement during cycling and examination of the shear stress panels show a tendency to a slight initial maximum for the ~35 kPa normal stress tests.

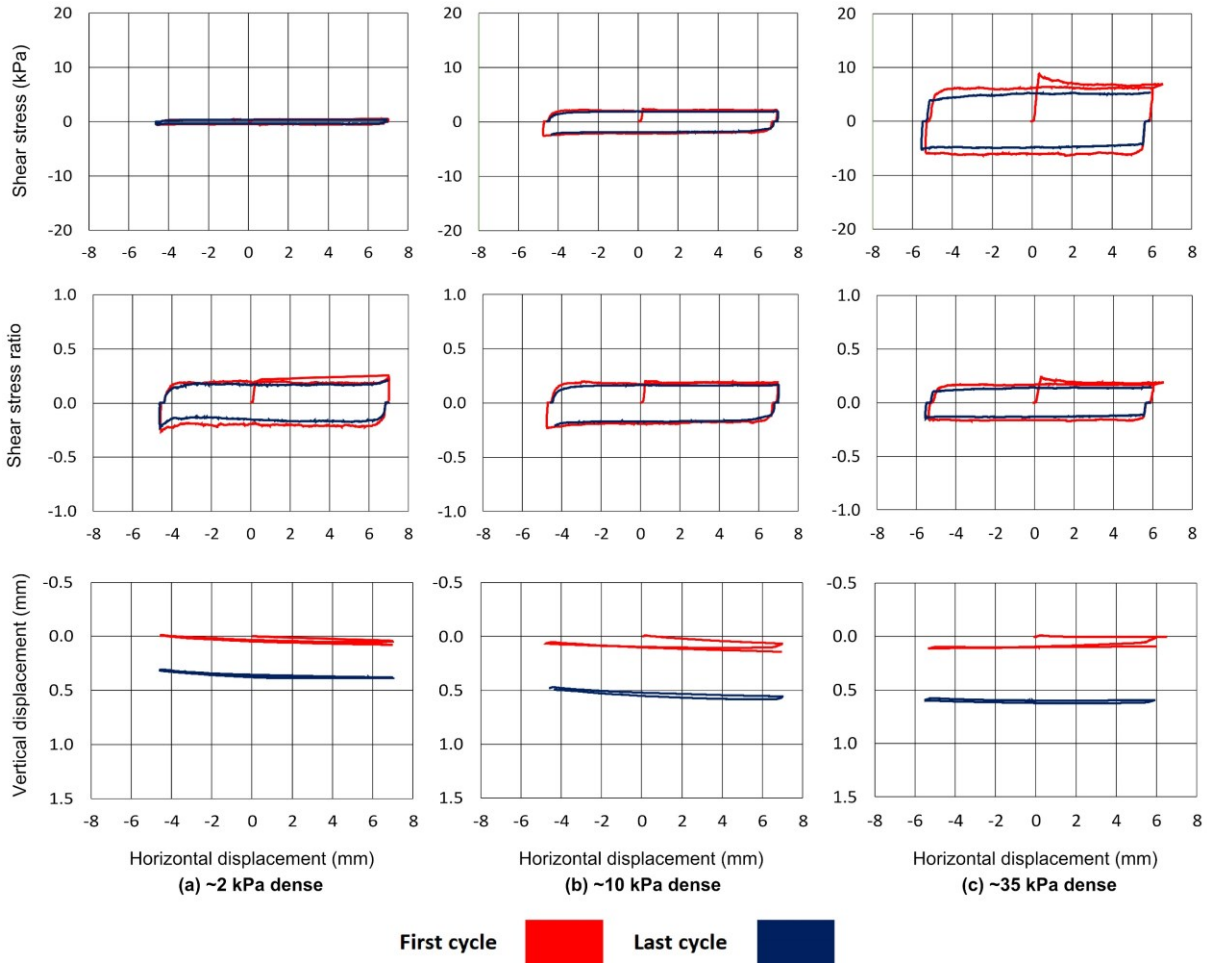

Figure 6.2 Pipe coating cyclic interface test results showing shear stress, stress ratio, and vertical displacement for Leighton Buzzard B at (a) ~2 kPa, (b) 10 kPa, and (c) ~35 kPa.

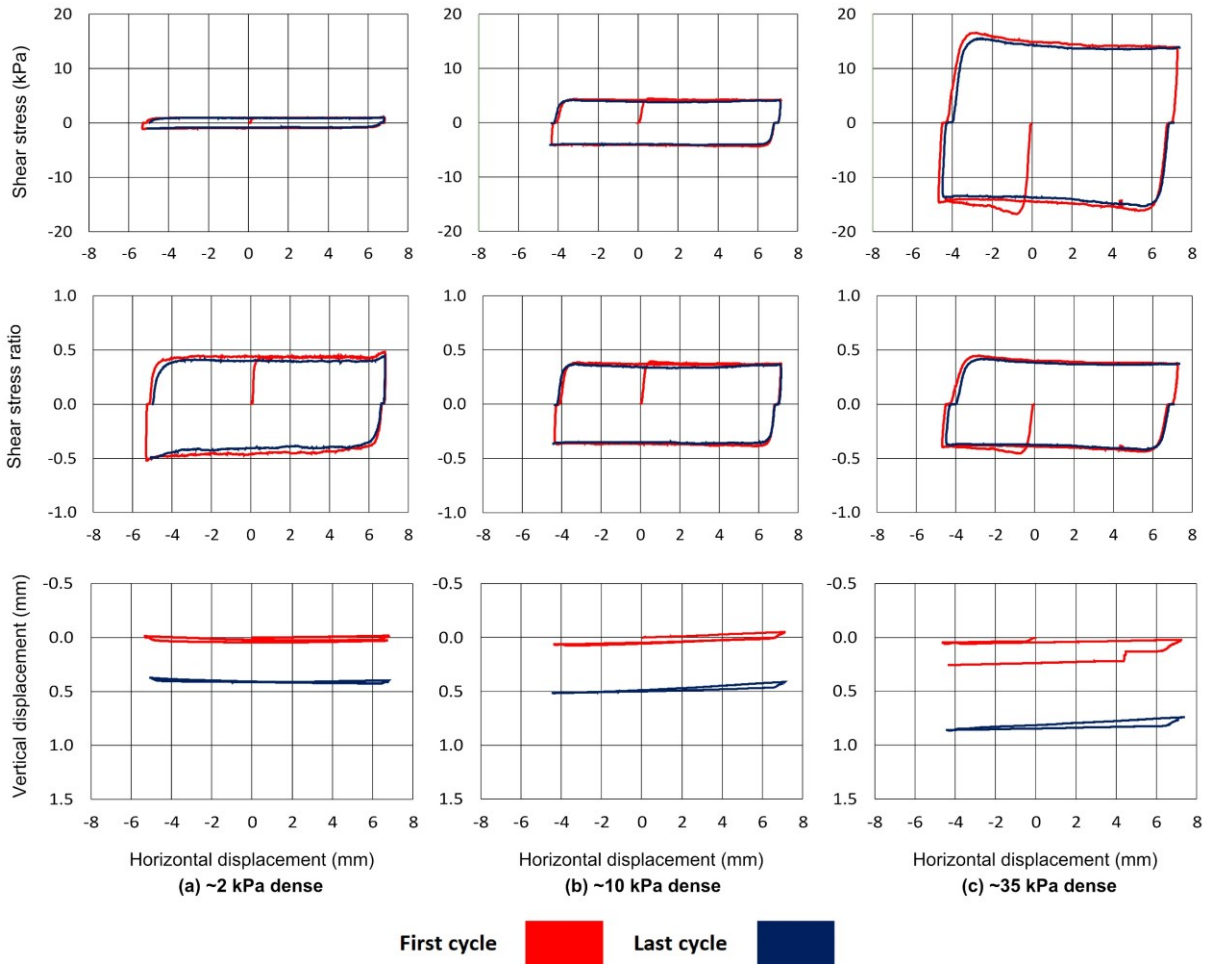

Figure 6.3 Pipe coating cyclic interface test results showing shear stress, stress ratio, and vertical displacement for Hostun Sand at (a) ~2 kPa, (b) 10 kPa, and (c) ~35 kPa.

6.1.1 Pipe coating strength evolution

Figure 6.4 shows the change in ultimate strength ratio for Soil S0 and the strength reduction is shown by normalising against the strength of the first cycle. Changes in the ultimate strength with successive cycles for Leighton Buzzard and Hostun Sand are presented in Figure 6.5 and Figure 6.6 respectively. In Figure 6.4, at approximately 30 and 75 traverses there are two notable jumps in the strength. This test was paused overnight and these jumps correspond to the restarts with soil creep suspected to explain them (although plastics are known to creep also so there may be complimentary effects occurring in tandem). Panel (c) shows the vertical position at the same point as the ultimate strength is measured. It is difficult to draw firm conclusions regarding the vertical displacement behaviour because it is not known how much is due to changes in the soil sample due and how much is caused by splaying of the rubber edging or sample extrusion during shearing.

Tests with Leighton Buzzard and Hostun Sand were continuous so there is no interruption to the ultimate stress ratio trend. In each test there is a rapid initial decrease in

strength up to the first 40 cycles before strengths settle at an approximately constant value of between 78% and 93% of the first cycle strength. The degree of reduction in strength appears to have some dependency on soil type, the finer S0 and Hostun Sand soils see lesser reductions than the coarser-grained Leighton Buzzard, though there are insufficient data to draw a firm conclusion. There does not appear to be any dependency on stress level as a control on degree of strength reduction, though there are also insufficient data to make a firmer conclusion about this. The results generally agree with DeJong *et al*. (2003) who used a comparable apparatus, albeit under Constant Normal Stiffness conditions, and found strength reductions of ~25% with similar size soils.

Figure 6.7 shows the change in sample settlement over the course of the cyclic tests at each stress level for Leighton Buzzard and Hostun Sand. Initially settlement is rapid but the rate reduces with successive cycles. Both soils show a broadly similar level of settlement with no clear distinction in behaviour between them. The main controlling factor seems to be stress level which is not unexpected. Greater normal stress leads to greater overall sample settlement though the shape of the settlement curves show a similar form in each case. As for the Soil S0 results, constant volume was not reached over the course of the test.

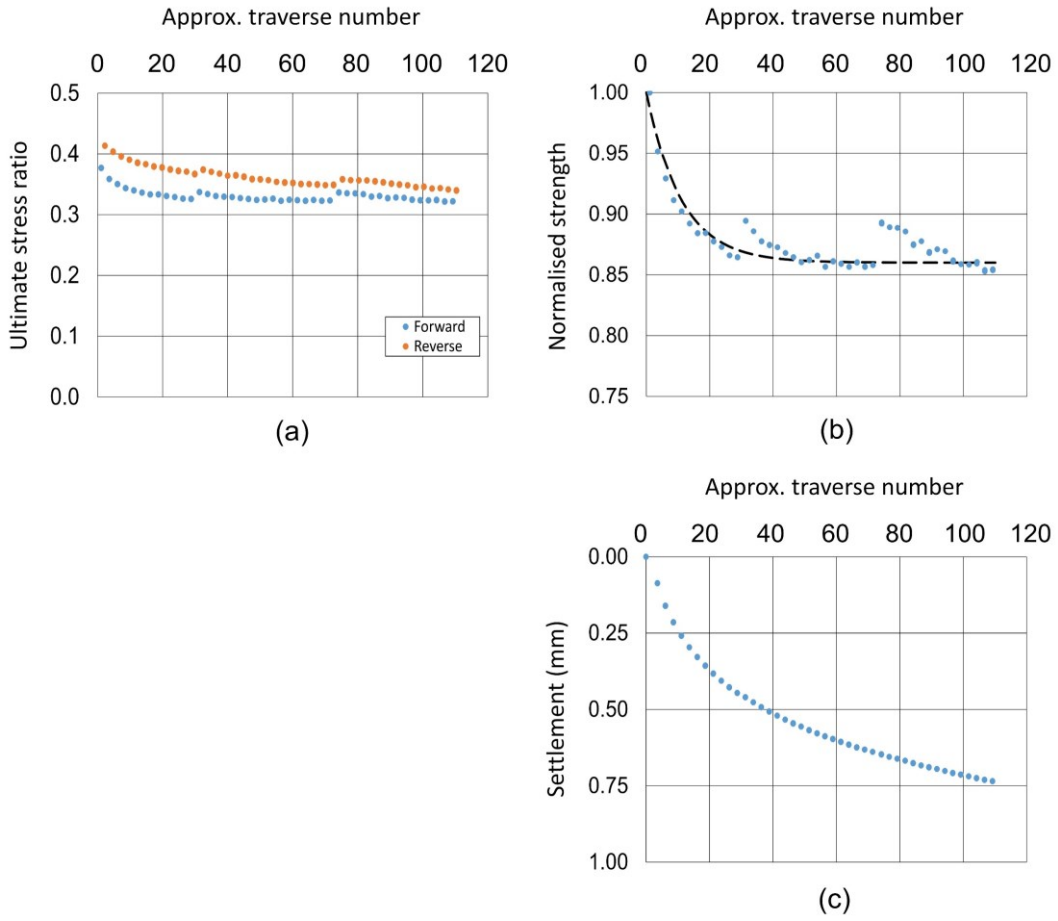

Figure 6.4 (a) Evolution in ultimate shear stress ratio for dense Soil S0 at 35 kPa and, (b) ultimate strength normalised against the first cycle strength, (c) settlement.

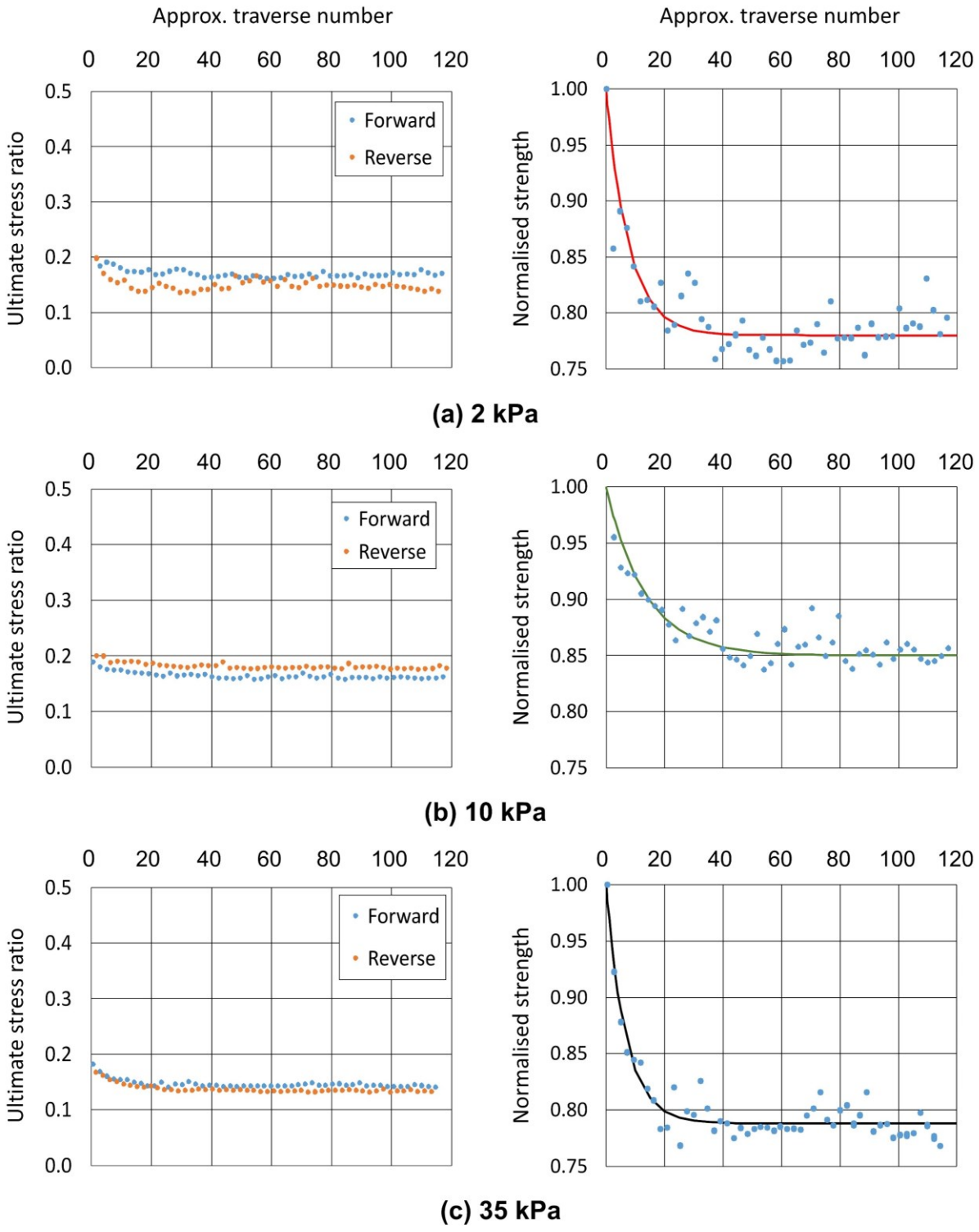

Figure 6.5 Evolution in ultimate shear stress ratio for dense Leighton Buzzard and ultimate strength normalised against the first cycle strength and best-fit curve to characterise the strength evolution at (a) ~2 kPa, (b) ~10 kPa, and (c) ~35 kPa.

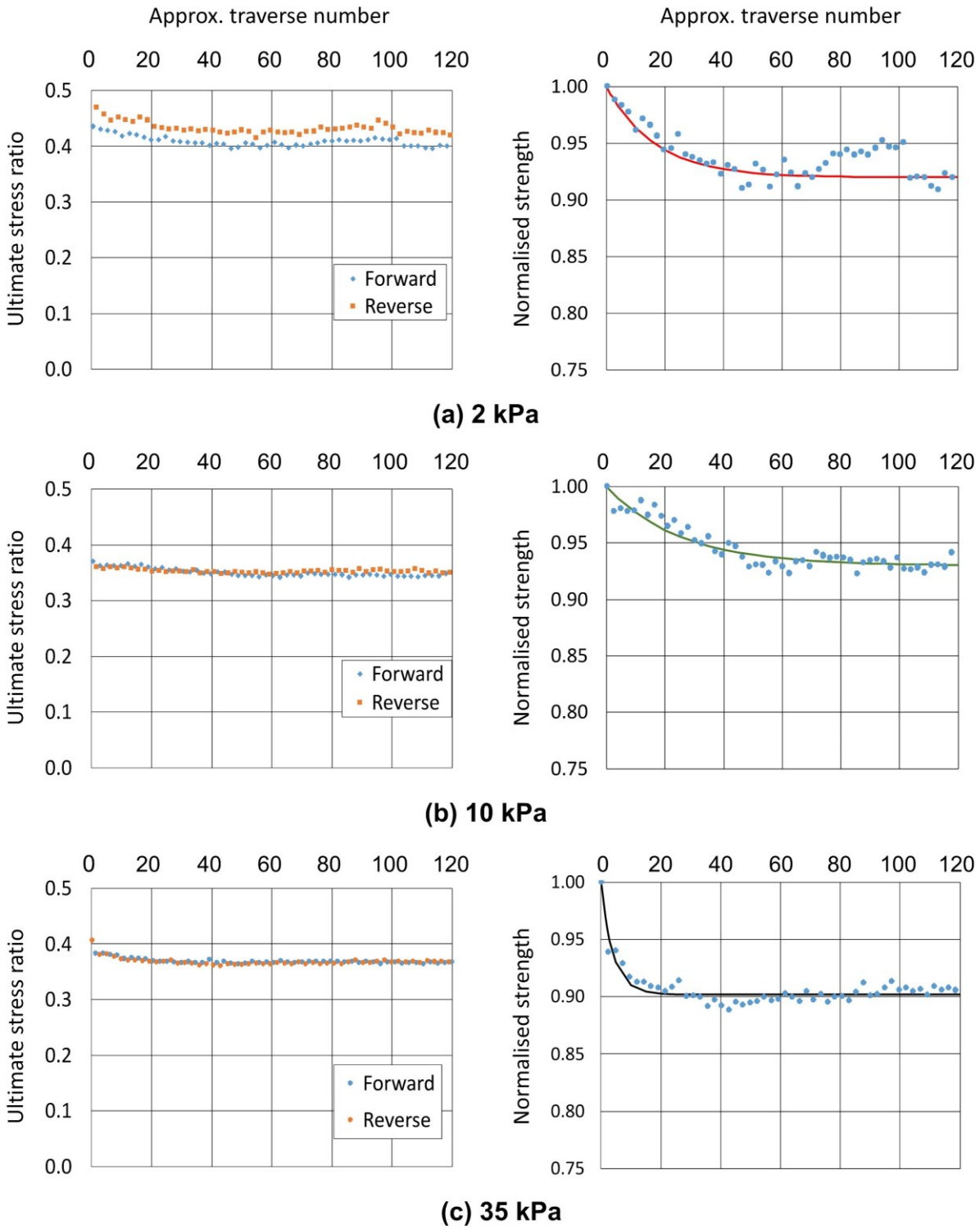

Figure 6.6 Evolution in ultimate shear stress ratio for dense Hostun Sand and ultimate strength normalised against the first cycle strength and best-fit curve to characterise the strength evolution at (a) ~2 kPa, (b) ~10 kPa, and (c) ~35 kPa.

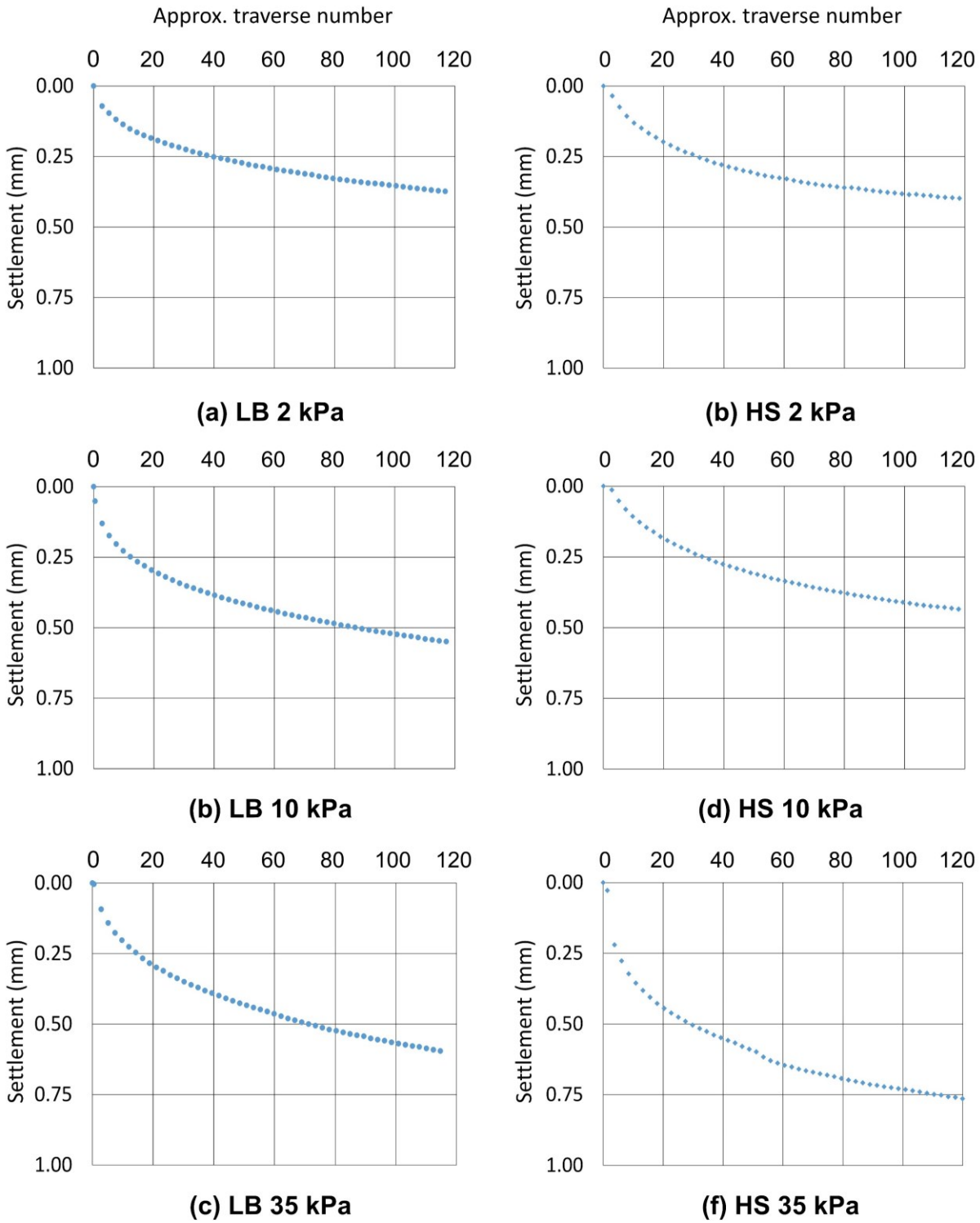

Figure 6.7 Sample settlement over cycling for Leighton Buzzard and Hostun Sand with "T" surface at 2, 10, and 35 kPa.

The trend for strength to reduce over the course of cycling is counter-intuitive in light of the established propensity for shearing to cause changes to surface roughness and for greater roughness to result in greater interfacial shear strengths. It must be remembered that in Chapter 4 it was discussed that roughness only increased after shearing perpendicular to the shear direction. Therefore, perhaps only limited changes in surface roughness occurred here in the direction parallel to shearing. Visual inspection of surfaces post testing reveals significant scarring with striations parallel to the direction of shearing and with a length similar to the shearing displacement. Given the lack of volumetric expansion or dilation, the shearing mechanism is consistent with O'Rourke *et al.*'s (1990) characterisation of grain sliding. In addition, as softer polymer surfaces are prone to grain ploughing (Briscoe, 1992; Dove and Frost, 1999). It can be envisaged that once ploughing has occurred and a striation formed, a path of relatively lower resistance has been created which is exploited and exacerbated during subsequent shearing cycles. In this way, along the path of individual striations or ploughing paths, roughness is lessened and the smoother paths result in an overall reduction in shearing resistance. This concept is visualised in Figure 6.8.

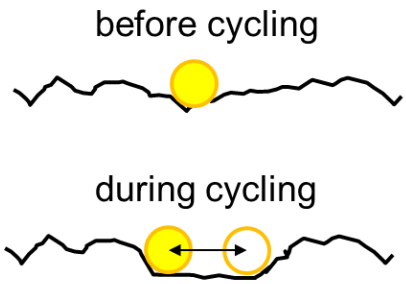

Figure 6.8 Schematic representation of local-smoothing effect during cyclic interface shearing.

Dove *et al*. (2006) also posited that as material is incrementally removed during ploughing, a groove is left through which the grain slides. Grains sliding through such a groove have a larger grain-surface contact area as the sidewalls are now also touching the grain, so the actual contact stress is reduced. Lower contact stress results in a lower overall mobilised shear stress.

The final normalised strength is plotted against the approximate traverse number at which the final strength becomes constant in Figure 6.9 in an attempt to establish if any relationship is revealed for pipe coatings. It may be tempting to see a relationship between the three points of Hostun Sand but the trend is not seen in the Leighton Buzzard points. Stress level does not appear to have a consistent effect, and nor does grain size as soil S0 is finer than both Leighton Buzzard and Hostun Sand. A more extensive campaign of laboratory

testing is required to determine if any relationships exist and to derive expressions to describe them.

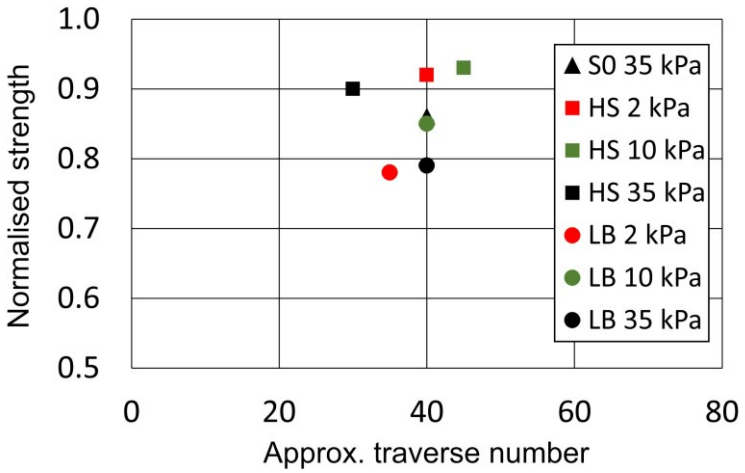

Figure 6.9 Final normalised strength and approximate traverse number at which final strength is reached.

6.2 Enhanced textures cyclic shear response

If surface damage causing striations and paths of localised lower resistance causes the reduction in shear strength with greater cycling, then it follows that such behaviour may be become less prominent as the surface roughness increases and as shearing progressively occurs in a shear band adjacent to the surface. Three cyclic interface tests were conducted on surfaces with the enhanced textures explored in Chapter 5 (type “E”, “S”). These tests are summarised in Table 6.2.

Table 6.2 Summary of enhanced textures cyclic interface tests

Test reference	σ_n (kPa)	$D_{r\ fab}$ (%)	$D_{r\ con}$ (%)	$D_{r\ fin}$ (%)	e_{fab}	e_{con}	e_{fin}	τ_{peak} (kPa)	τ_{ult} (kPa)	τ_{peak}/σ_n	τ_{ult}/σ_n
LB_D35_E-MR											
First traverse	34.96	70.2	80.2	-	0.622	0.591	-	11.71	10.80	0.33	0.31
Last traverse		-	-	98.3	-	-	0.535	14.96	14.61	0.43	0.41
LB_D02_S-MR											
First traverse	1.96	70.0	72.6	-	0.623	0.615	-	1.36	1.18	0.70	0.61
Last traverse		-	-	86.5	-	-	0.571	1.16	0.97	0.60	0.50
LB_D35_S-MR											
First traverse	35.70	70.5	77.8	-	0.622	0.599	-	21.38	18.13	0.60	0.51
Last traverse		-	-	98.6	-	-	0.534	17.46	17.07	0.49	0.48

Tests were also conducted on a type “P” surface but the test results are suspicious (included in Appendix D1 for reader interest) due to a malfunction in the equipment. A second attempt damaged the apparatus and broke the load cell (pictured in Figure 6.10). The reason for the failed test is not clear, but it is posited that significant dilatancy during the initial cycles lifted the surface such that the rubber edging was no longer able to contain the soil sample. As soil spilled out during successive cycles, excessive settlement cause the surface to touch the lower frame. It looks as if the switch, activated by the black tab, shown in Figure 6.10b was compromised during the test so the motor failed to change direction causing damage to the load cell. For these reasons, the direct shear apparatus in the current arrangement was deemed to be unsuitable for cyclic testing of highly dilatant surfaces.

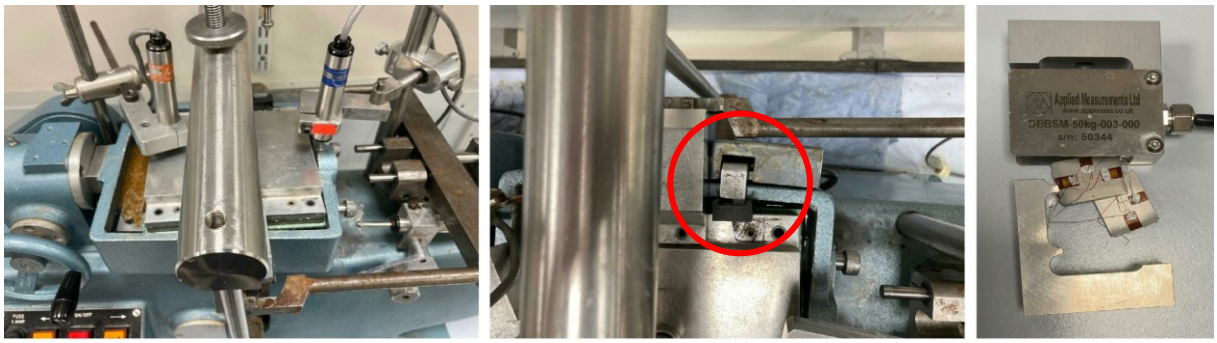

(a) (b) (c)

Figure 6.10 Pictures of the shear box apparatus damage form “P” surface cyclic testing (a) shear carriage, (b) multi-reverse switch and tab, (c) broken load cell.

Shear response results for the first and last cycle for “E” and “S” surfaces are presented in Figure 6.11. In contrast to the results for pipe coatings, the shear response in Figure 6.11a for type “E” surface shows the shear resistance increases between cycles with the last cycle mobilising greater shear strength than the first. In contrast, type “S” shown in panel (b) mimics the behaviour of the pipe coatings discussed previously with an overall reduction in strength between the first and last cycle. The first cycle also exhibits a peak and ultimate condition mirroring the shear response seen for these surfaces in monotonic testing in Chapter 5. In both cases there is an overall contraction of the sample throughout cycling, though the type “S” surface exhibits dilatant behaviour in the first cycle. The dilatancy effect diminishes over the initial cycles and tends to zero in tandem with the interface mobilising only ultimate strengths over progressive cycles.

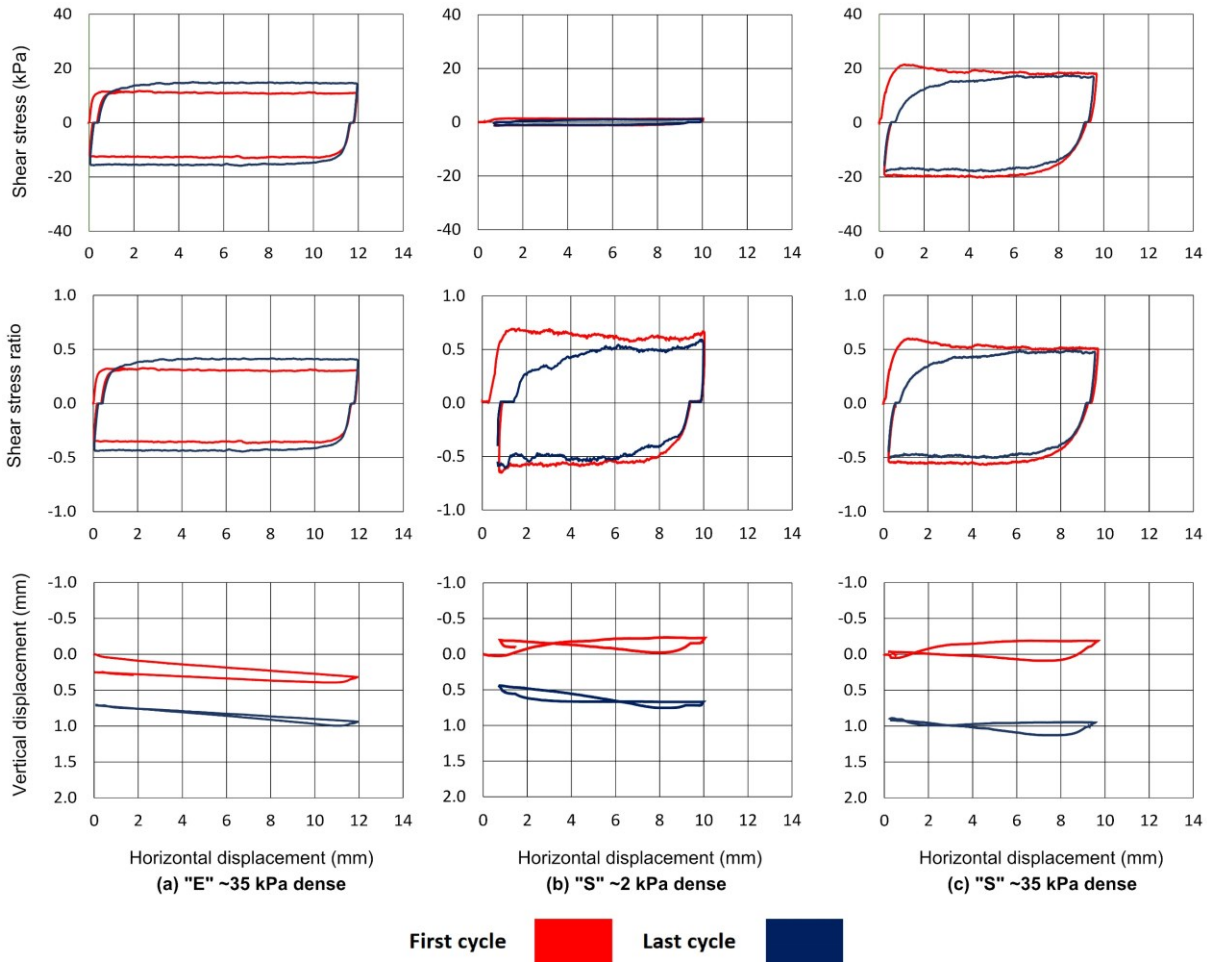

Figure 6.11 Enhanced textures cyclic interface test results showing shear stress, stress ratio, and vertical displacement for Leighton Buzzard B (a) type "E" 35 kPa, (b) type "S" 2 kPa, and (c) type "S" 35 kPa.

6.2.1 Enhanced textures strength evolution

The evolution in interface strength is quantified in Figure 6.12 where both absolute ultimate strength and normalised ultimate strength are shown with cumulative horizontal displacement. The results for pipe coating at ~35 kPa from Figure 6.5 are included for easy comparison. As was alluded to previously, the ultimate strength for the type "E" surface increases as the cumulative horizontal displacement increases which is at odds with the results seen previously for pipe coating specimens. The test was repeated to check this behaviour was correct. It is also at odds with the results for type "S" surface which exhibits a gradual reduction in strength. The shape of the generalised curve describing the reduction in strength is different from the pipe coating surfaces. The strength reduction is more gradual and does not appear to have reached a steady state over the cumulative displacement tested here. Similarly, the increasing strength of the "E" surface does also not appear to have reached a plateau. A possible explanation for the contrary behaviour of the "E" surface relates to how it was produced. From pristine polypropylene sheet, these specimens were textured using a laser engraver which

produced a patterned surface formed by localised melting and resetting. The resetting process produces what could be characterised as an un-worked surface. The “S” type surfaces, although starting out the same as type “E” were subsequently sandblasted creating a worked surface. “T” type surfaces, although smooth and originally extruded, were wrapped, pried free, heated, rolled, flattened, and transported so might also be described as worked. Surfaces were tested for hardness as detailed in Chapter 3, but did not experience any significant change before and after specimen preparation, remaining in the range of 70-75 Shore D. As the engineering properties of polypropylene can evolve with strain (e.g. Hirsch and Wang, 1991), whether the surface is worked or unworked may have an impact but this would need to be tested with further experimentation. Surfaces that have already experience large strains may be able to offer less resistance to grain ploughing and with on a downward trajectory.

Figure 6.13 shows the change in sample settlement at the end of each traverse. Compared to the pipe coating results, the enhanced “E” and “S” textures both show greater sample settlement with increasing number of cycles. Although the data set is limited, comparison of panels (a), (b), and (d) suggests that settlement is greater with greater surface texture though further testing would be needed to confirm it. The phenomenon could not be systematically investigated, but with rougher surfaces provoking more soil shearing and, therefore, precipitating greater soil structure collapse, this trend is not surprising. Looking at panels (c) and (d) suggests that the tendency for greater normal stress to result in greater settlement remains true for greater surface texture also.

Across the narrow range of cyclic tests conducted there does not appear to be a discernible trend or relationship between the surface type and the nature of strength evolution with cycling. Surfaces at both the smoother and rougher ends of the spectrum exhibit softening despite an intermediate roughness surface exhibiting hardening. Greater roughness surfaces are better able to engage soil grains in shearing and provoke formation of a shear band. Formation of a shear band leads to a more grains participating in shearing and volumetric changes rather than purely a narrow layer at the interface which explains the tendency for rougher surfaces to promote greater sample contraction (Sagitaningrum *et al.*, 2020).

The evolution of strength trends at ~35 kPa for “T”, “E”, and “S” surfaces are presented together in Figure 6.14. It is important to note that despite changes in strength over cycles, the benefit of using an enhanced texture surface remains as rougher surfaces maintain greater shear strengths all through cycling. The relationship between initial and final strengths is put into context with the monotonic testing results in Figure 6.15. The results fall in the range expected from the monotonic testing, with allowances made for the different stress level, which gives the expected lower initial strengths. Unfortunately, it was not possible to repeat measurements of surface texture for the surfaces used and it was not considered reasonable to speculate on the final texture value given the complex nature of soil-surface interaction.

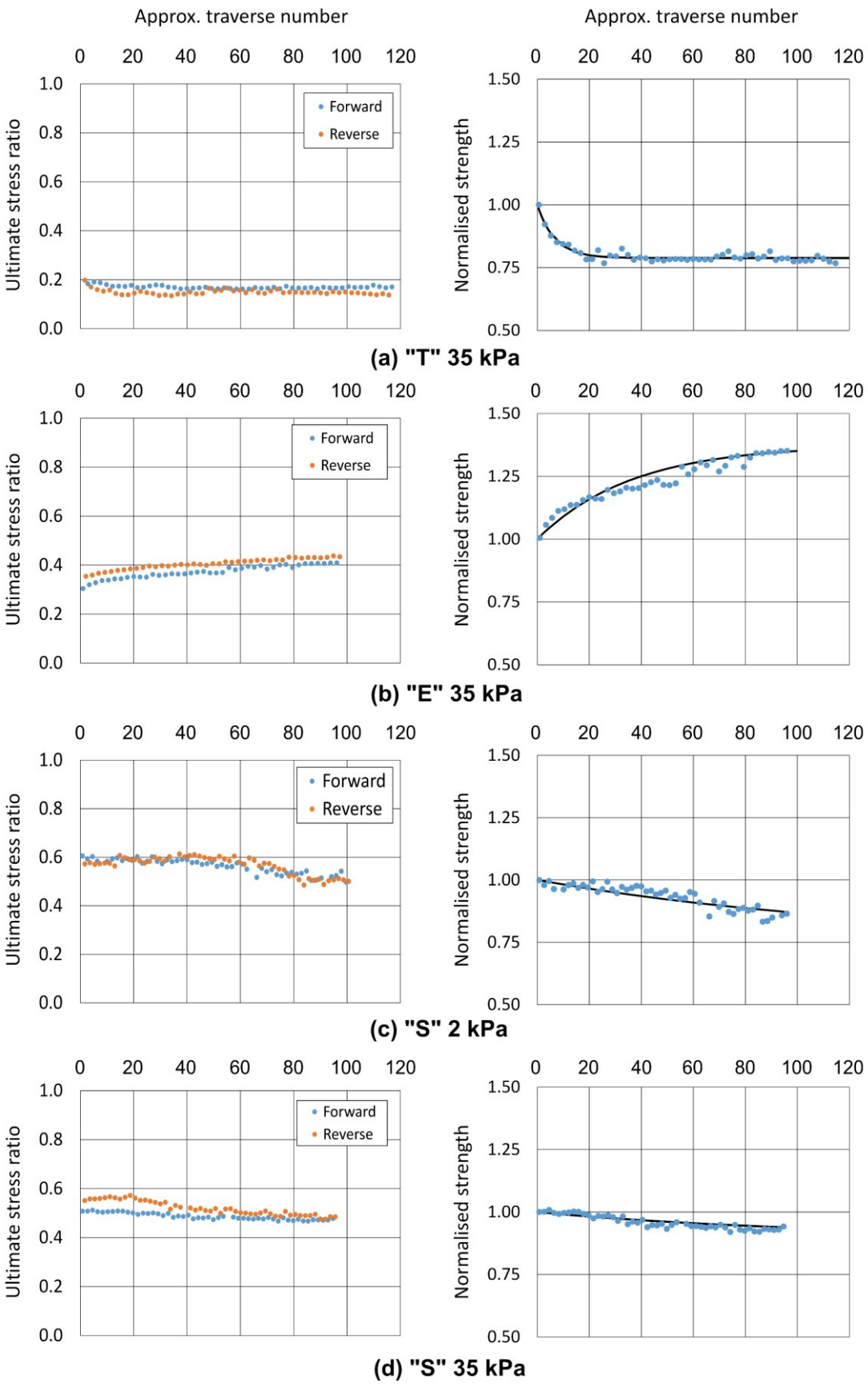

Figure 6.12 Evolution in ultimate strength and normalised strength for Leighton Buzzard for (a) "T" 35 kPa, (b) "E" 35 kPa, (c) "S" 2 kPa, (d) "S" 35 kPa.

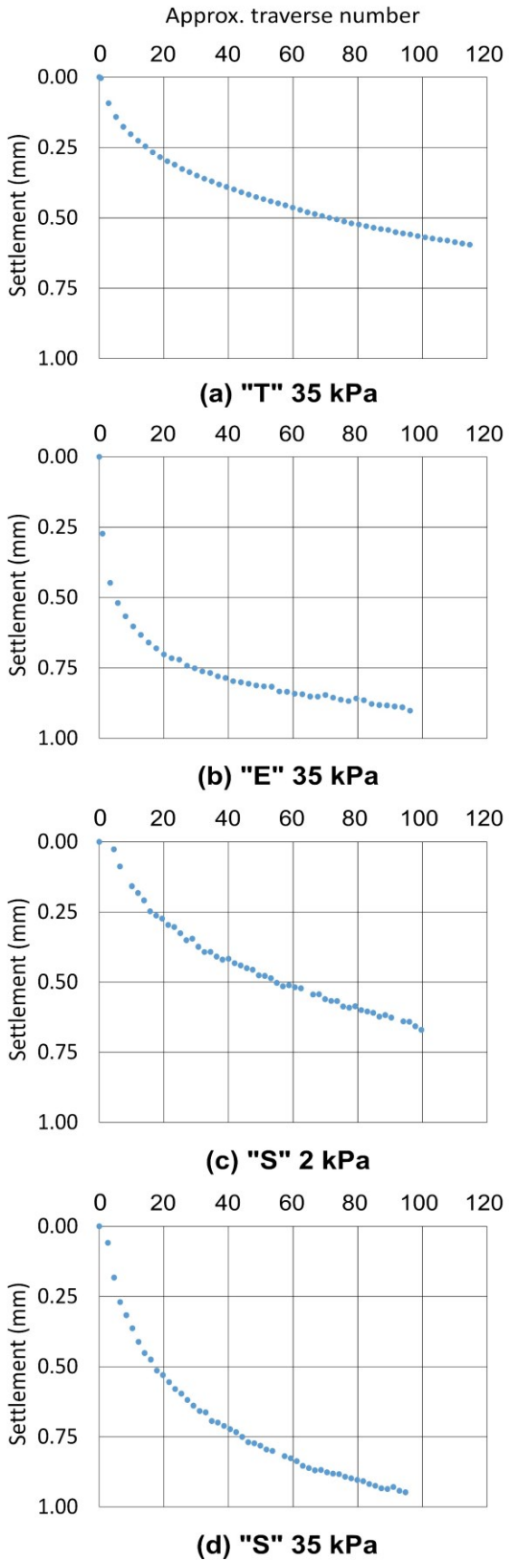

Figure 6.13 Sample settlement over cycling for Leighton Buzzard and Hostun Sand with "E" and "S" surfaces with "T" surface result at 35 kPa.

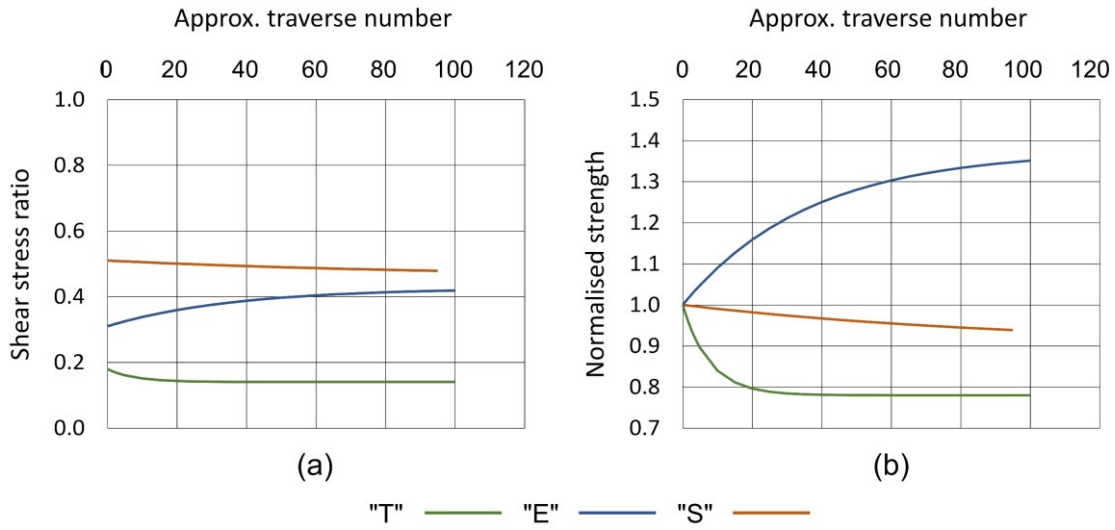

Figure 6.14 Evolution of normalised ultimate shear strength for Leighton Buzzard at ~35 kPa in (a) absolute strength and (b) normalised strength.

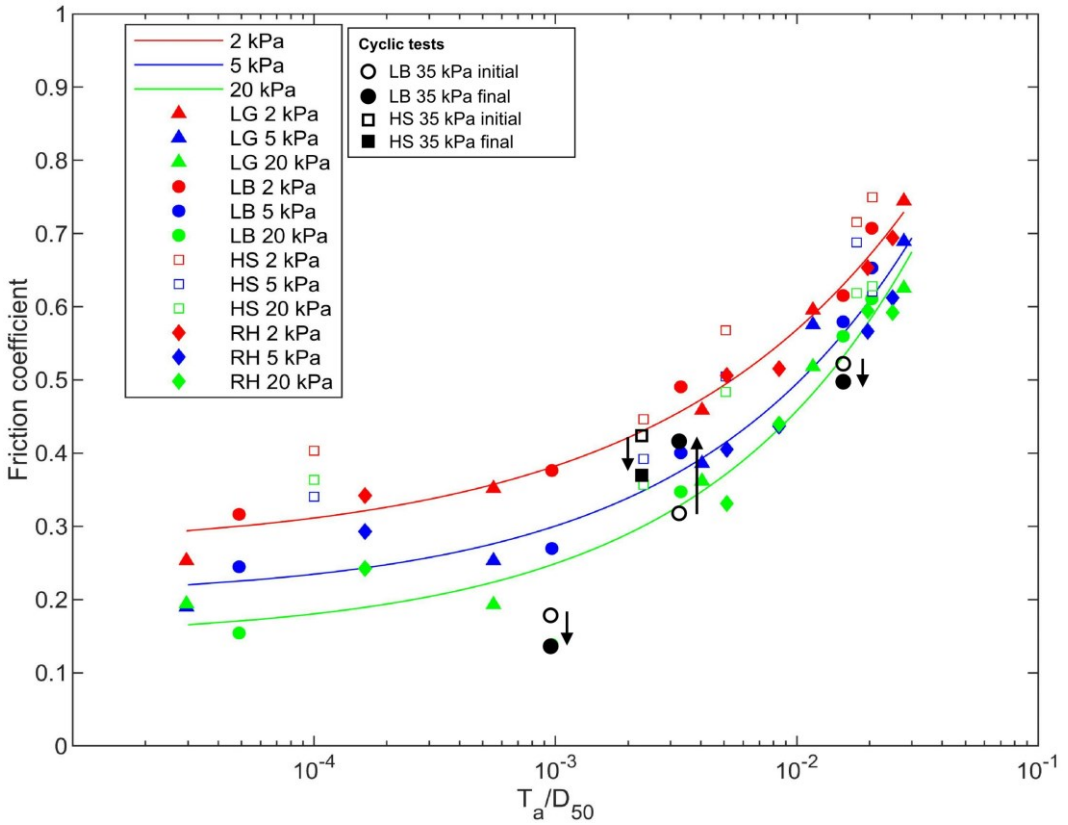

Figure 6.15 Change in friction factor (ultimate stress ratio) through cycling compared to monotonic strength.

6.3 Post-cyclic reloaded shear response

After cyclic testing each of the Leighton Buzzard and Hostun Sand tests were repeated monotonically using the same surface but with a freshly prepared soil sample to investigate if there was any increase in strength given that surfaces had sustained visible damage in the cycle test. Table 6.3 details the post-cyclic tests and shear responses are shown in Figure 6.16 to show the comparison between stress levels with Leighton Buzzard and Hostun Sand. Figure 6.17 shows the post-cyclic results of "T", "E", and "S" surfaces to compare surface texture effects. There is nothing remarkable about the nature of their shear responses that has not already been discussed previously in this thesis.

Table 6.3 Summary of post cyclic reloading interface tests

Test reference	σ_n (kPa)	$D_{r\ fab}$ (%)	$D_{r\ con}$ (%)	e_{fab}	e_{con}	τ_{peak} (kPa)	τ_{ult} (kPa)	τ_{peak}/σ_n	τ_{ult}/σ_n
LB_D02_T-pMR	2.10	70.1	70.4	0.623	0.622	0.72	0.59	0.34	0.28
LB_D10_T-pMR	11.30	70.0	72.2	0.623	0.616	2.88	2.40	0.26	0.21
LB_D35_T-pMR	36.87	70.1	78.4	0.623	0.597	7.50	6.28	0.20	0.17
HS_D02_T-pMR	2.09	70.1	70.2	0.734	0.733	1.04	1.00	0.50	0.48
HS_D10_T-pMR	11.29	70.1	74.8	0.734	0.716	5.04	4.37	0.45	0.39
HS_D35_T-pMR	36.85	70.0	79.0	0.734	0.700	16.35	13.83	0.44	0.38
LB_D35_E-pMR	35.70	70.0	77.8	0.623	0.599	15.93	15.21	0.45	0.43
LB_D35_S-pMR	35.70	70.0	76.2	0.623	0.604	20.68	17.84	0.58	0.50

The trends for reducing strength normalised for each stress level for both sands are compared in Figure 6.18 with the addition of a point representing the ultimate stress ratio as measured from the post cyclic reloaded test, again normalised to the strength of the first cycle. It is clear from Figure 6.18 that the post-cyclic ultimate shear strength is significantly greater than both the final last cycle strength and also the initial strength in the case of tests undertaken at ~2 kPa and ~10 kPa normal stress. Increases in strength over the first cycle strength of approximately 30% and 12% were observed with Leighton Buzzard at ~2 kPa and ~10 kPa, respectively. For Hostun Sand the increase was more modest, approximately 10% and 5% respectively for ~2 kPa and ~10 kPa. For both test sands at ~35 kPa the reloaded ultimate strength was greater than the final cyclic strength but approximately 6% and 3% lower than the initial ultimate strength for Leighton Buzzard and Hostun Sand, respectively.

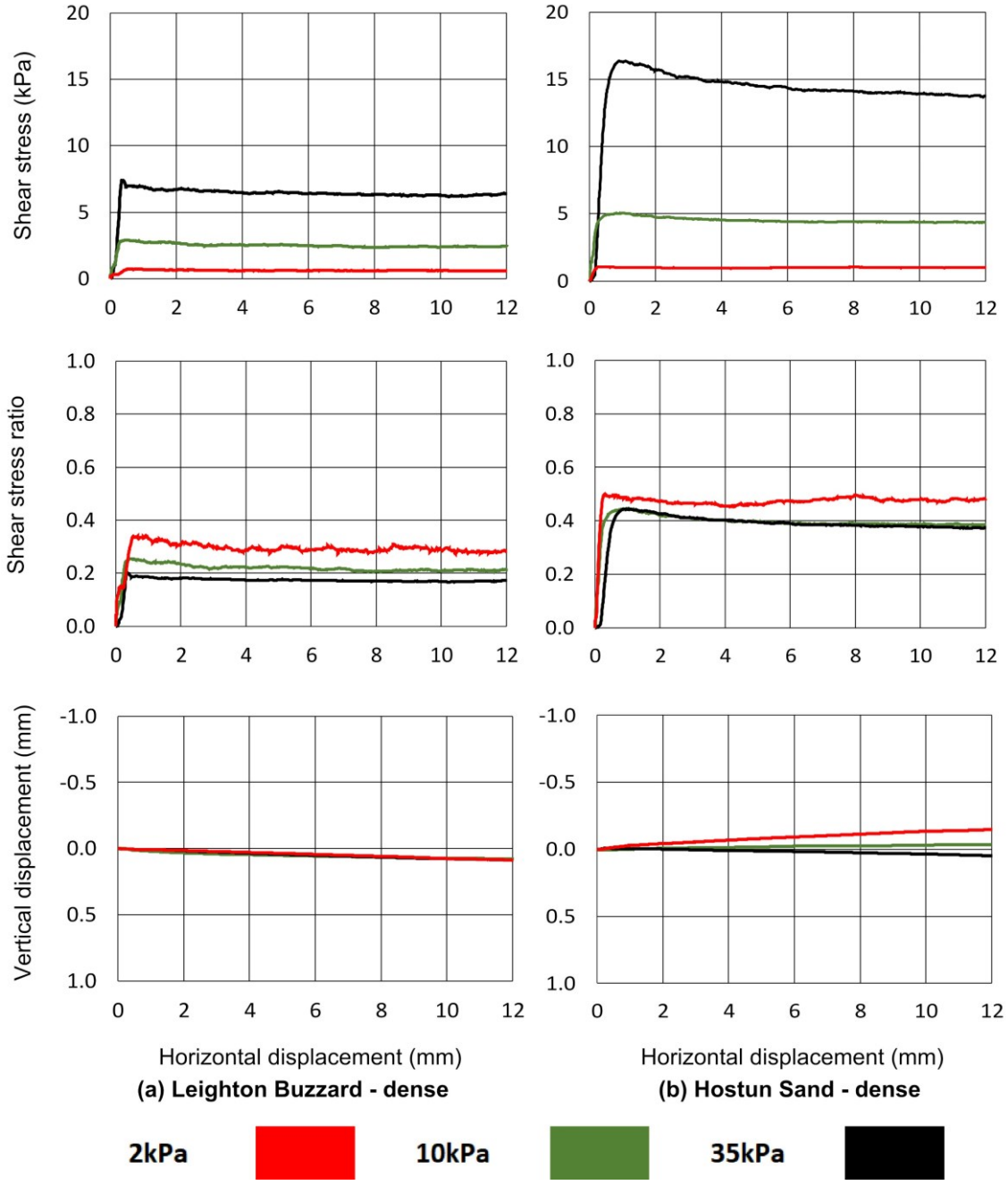

Figure 6.16 Post-cyclic interface test results showing shear stress, stress ratio, and vertical displacement for (a) Leighton Buzzard and (b) Hostun Sand at ~2 kPa, 10 kPa, and ~35 kPa.

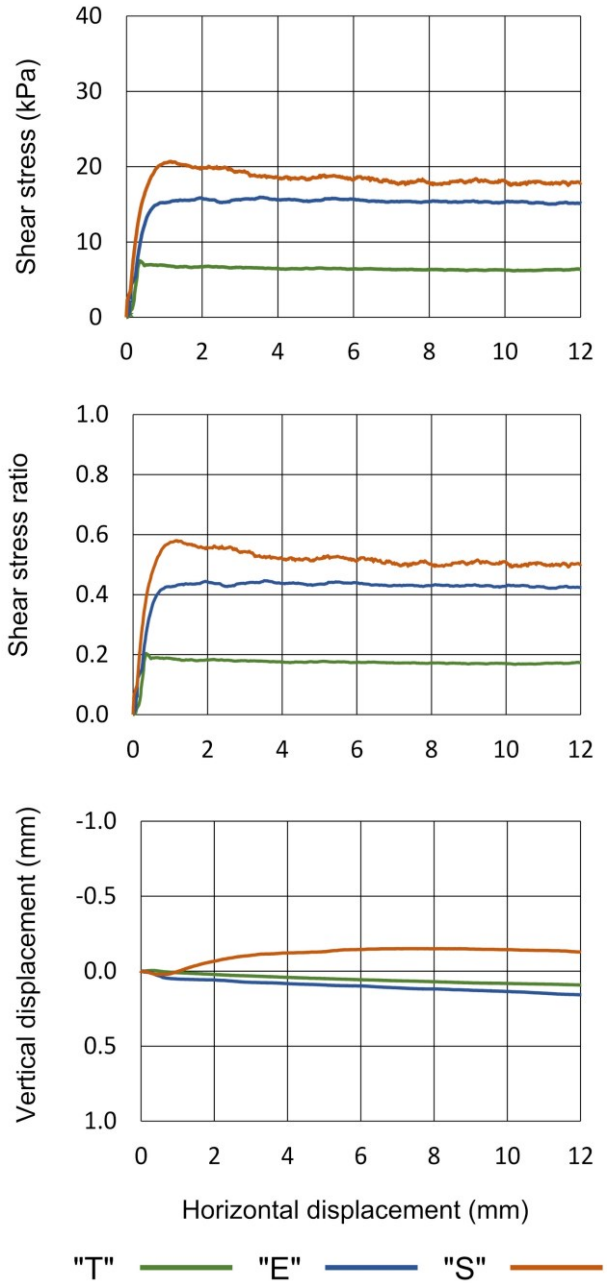

Figure 6.17 Post-cyclic interface test results showing shear stress, stress ratio, and vertical displacement with Leighton Buzzard for “T”, “E”, and “S” surfaces at ~35 kPa.

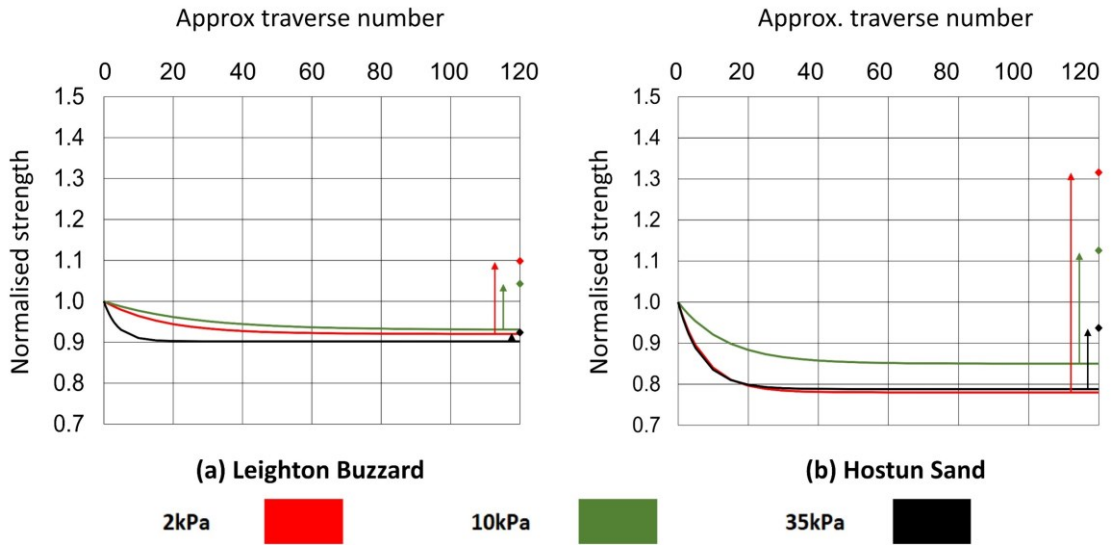

Figure 6.18 Evolution of normalised ultimate shear strength and post-cyclic reloaded interface ultimate shear strength with pipe coatings for (a) Leighton Buzzard and (b) Hostun Sand.

Figure 6.19 presents the reloaded strength in comparison to the evolution of the strength for "E" and "S" surfaces with the equivalent "T" test result included for easy comparison. The reloaded strength for the "S" surface is greater than the final strength but less than the initial strength which matches the behaviour of the "T" surfaces at this stress level. The "E" reloaded strength is also greater than the final strength by a similar margin and gives confidence that its behaviour is real in spite of it being contrary to the response of the other materials tested here. In the case of "E" surface, it is important to note the importance of the reloaded strength being greater (or at least as strong) as the final cyclic strength. Maintaining the greater strength after reloading would give confidence to a designer that the enhancement is not fleeting.

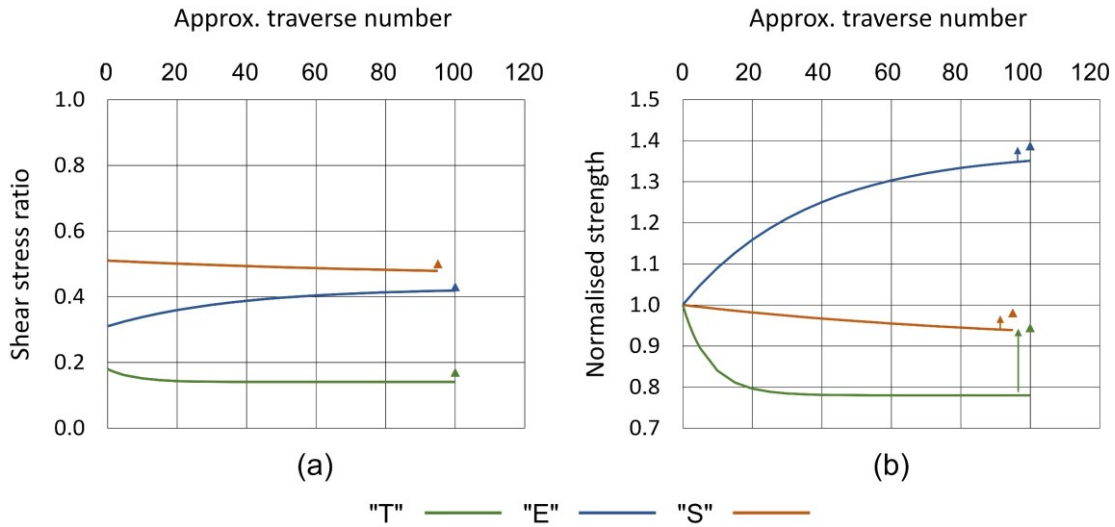

Figure 6.19 Comparison of strength evolution and post-cyclic reloaded interface ultimate shear strength with pipe coatings for Leighton Buzzard sand at ~35 kPa for (a) absolute strength and (b) normalised strength.

The increase in reloaded strength is possibly explained by the overall roughening effect that repeated cycling had on the surfaces. Although during cycling grains ploughed individual furrows leading to localised roughness, and therefore strength, reductions, when the interface test and soil sample is prepared from fresh such surface-soil grain arrangements are reset. The surface now appears to have a greater overall roughness and soil experiences greater resistance to shearing in-line with trends identified in earlier discussions. Unfortunately, the lack of post shearing roughness data means this is only conjecture and would benefit from further investigation.

6.4 Implications for design

There are significant design implications for cyclic hardening or softening of the interface shear response. It is important to remember that there are two orientations (axial and lateral) that need consideration in the case of pipelines. If a surface has been cycled laterally and experiences softening then progressive cycles lead to a gradual reduction in shear resistance leaving the pipe more prone to buckling. However, it may be that the formation of soil berms during cyclic displacement (Bruton *et al.*, 2007) would mitigate such effects through additional passive resistance.

Cyclic softening in the lateral direction creates wear scars perpendicular to the direction of motion, and it is theorised that localised reductions in roughness as grains become entrained in furrows is to blame, along with Dove *et al.*'s (2006) increasing contact area proposition. However, the axial shear resistance is perpendicular to these new wear scars and is likely to lead to an increased roughness and, therefore, increase shear resistance. Therefore, even as lateral resistance decreases, axial resistance in the same area may increase. This situation potentially leads to an increase in effective axial force in the pipeline as that is governed by the axial friction, whilst simultaneously lowering the lateral resistance to buckling. These competing phenomena are explored further with numerical studies in Chapter 7.

6.5 Conclusions

A limited campaign of cyclic interface tests was carried out on pipe coatings with Soil S0, Leighton Buzzard, and Hostun Sand. A range of stress levels and surface types was tested and all soil samples prepared were dense. After cycling, fresh samples were prepared and the test reset to measure the reloaded strength on the same surfaces. Some conclusions are drawn:

- In each case the initial traverse exhibited behaviour in keeping with the material responses seen previously in this thesis: elastic-perfectly plastic type for smoother surfaces evolving to elasto-plastic for more textured surfaces
- Through cycling up to at least 100 traverses the overall strength mobilised gradually reduced and was accompanied by overall sample contraction. Reductions in strength varied according to soil type but no other trend was identified within the limited range of tests undertaken. Average reduction in strength is between 7.5 and 25% and varies with no discernible trend according to grain size, stress level, or traverse number at which the reduction settles. The measured strength reductions are not, however, at odds with the literature. An exception to this trend is for “E” surfaces which, despite being an intermediate texture and not expected to behave differently, tended to harden by over 30% during cycling rather than soften. An explanation may be related to the nature of worked and unworked surfaces and requires further investigation.
- Reloaded tests with fresh soil samples on the same surfaces revealed significantly greater interface shear strengths, up to 30% in one instance, but the increase appeared to have some dependency on both soil type and stress level. In the case of the “E” surface, which increased strength over cycles, it is important to note that the increased strength was maintained in the reloaded test.
- It was posited that during cycling, individual grains, or groups of grains, became entrained in a furrow which then became smoother and smoother during repeated shearing. The local smoothening effect results in a lower localised roughness leading to the reduced interface shear strength. Reloading the surface reset the soil-surface contact and the new, apparently rougher, surface was able to mobilise a greater shear resistance.
- It would be of interest to assess the shear resistance of pipe coatings perpendicular to the direction of cyclic shearing to see what impact repeated wear scars would have in the other orientation. Such tests would have application where pipes move both laterally and axially, for example at buckle shoulders or feed-in zones.

To obtain a more comprehensive and robust view of the processes at work here it would be necessary to remeasure surfaces after cyclic shearing to quantify their surface roughness. However, the Alicona machine was not available for use at the required time due to maintenance and laboratory refurbishment. When it did later become available the 2020 global Covid-19 pandemic meant that access and use was no longer possible. The lack of profilometry after cyclic interface shearing is a notable omission from the investigation and is an avenue to consider in future work.

7 Application to Pipeline Engineering

The propensity for pipelines to undergo buckling that poses a risk to their structural integrity has led to a range of strategies for their optimal global stability design which have been discussed in the literature review of this thesis. The preceding chapters of this thesis have shown that the interface friction coefficient of polypropylene (and presumably other polymer coating technologies) can be controlled by modification of surface textures. In order to assess whether such an opportunity would be of practical use, a numerical investigation using finite element analysis was carried out. This chapter presents the results of numerical analysis of pipe performance parameters to demonstrate the implications of a potential range of friction coefficients using Abaqus, a general-purpose finite element programme, to model global buckling response.

7.1 Overview

Finite element analysis is a powerful tool for computer modelling structural behaviour under prescribed conditions and has been widely used for pipeline applications. A range of proprietary programs and numerical packages have been used for modelling of various pipeline problems over the last 40 years such as PIPLIN-III, PlusOne, PIPSOL, ABP, UPBUCK (Structural Software Development Inc., 1981; Andrew Palmer and Associates, 1995; Nixon, 1984; Klever *et al*., 1990).

Zhang and Tuohy (2002) conducted a global buckling analysis using commercially available finite element modelling programme ANSYS and showed that finite element programmes were a valuable tool for pipeline buckling analysis. Abaqus is a general-purpose finite element program which has capabilities key to pipeline applications. It incorporates pipe-type beam elements, pipe-soil interaction mechanisms, can accommodate large displacements and large model dimensions, and can accommodate highly non-linear behaviour. In recent years numerous researchers have used FE analysis to study global buckling and pipeline walking problems and Abaqus has gained common usage (e.g. Jukes *et al*., 2008; Jukes *et al*., 2009; Cumming *et al.,* 2009; Cumming and Rathbone, 2010; Jin *et al*., 2010; Bruton *et al*., 2011; Sun *et al.,* 2011; Liu *et al*., 2014; Chee *et al*., 2018).

Pipelines and soil may be modelled in various ways. 2D plane-strain models are typically used to do detailed investigations of pipe embedment and lateral displacement mechanics (e.g. Vanden Berghe *et al*., 2005; Wang *et al.,* 2010; Ansari *et al.,* 2014). Global buckling behaviour and consideration of the greater pipeline system is better modelled in 3D using a combination of shell, beam, and solid elements to variously model the pipe and soil

mass (e.g. Liu, *et al.,* 2014; Chee *et al*., 2018). Following these precedents, Abaqus was adopted for the finite element analysis in this research.

7.2 Abaqus finite element analysis

Finite element analysis (FEA) is a numerical approach to simulating problems relating to deformation of materials and determination of forces and displacements in the process. FEA works by discretising the geometry of the modelled problem into a large number of finite elements for which solutions are individually calculated in response to inputs. Such methods are able to robustly model a range of complex geotechnical problems such as foundation settlement, slope stability, and structural deformation with varying degrees of complexity.

Abaqus is a general purpose FEA program which excels at handling nonlinear responses from large displacements, nonlinear material properties, and boundary conditions like sliding, friction, and contact between model components. Abaqus also allows easy customisation of various mechanics through the integration of user-written subroutines.

7.2.1 Analysis methodology

In Abaqus, each load or action is applied through load steps allowing a sequential or simultaneous application of a variety of loads depending on what order they are applied in. Each load step is broken down to allow the loads to be applied in increments which can be defined by the user. For example, increments of 0.1 in a static analysis mean that 10% of the load is applied with each increment until it is fully applied. Abaqus can automatically adjust incrementation within user-defined limits if there is poor convergence.

The problems to be solved are expressed as partial differential equations (PDE) which FE programs solve using matrix equations which can be linear or nonlinear. To solve these equations, Abaqus can use implicit or explicit analysis. Implicit analysis generates solutions in a number of steps and is based on the solution from the previous step and each step is in equilibrium. Implicit solutions are also known as unconditionally stable and allow larger time-steps although this comes at a cost to computational efficiency for dynamic or nonlinear problems in larger or complex models.

Explicit analysis is used more commonly for dynamic problems which may involve accelerations, and only solves based on a later state of the model whilst disregarding the current state. In this way the later solutions do not depend on the equilibrium of early states and are said to be conditionally stable. Explicit analysis is more computationally efficient for dynamic problems or where there is large or complex nonlinearity, but the trade-off is a greater risk of errors carried forward through incrementations.

7.2.2 Solver algorithms

In static analysis, which comprises the majority of analyses appropriate for pipeline modelling in the absence of seismic loads, Abaqus uses the Newton-Raphson method for approximately determining the root of nonlinear functions. The method works by assuming that a nonlinear function can be approximated by a straight-line tangent to it. Unfortunately, if a nonlinear function has maxima and minima giving an undulating form, particularly when the solution required is close to zero, then this method becomes problematic due to the potential for tangents to return negative values in place of positive or vice versa.

The Newton-Raphson method also becomes problematic where a load-displacement response experiences snap-through or bifurcation, as may occur in the case of pipeline buckling, which results in a negative stiffness that a conventional matrix approach struggles to solve. The method modified from Riks (1979) (known as the Riks method or the arc length method) is an algorithm which allows effective solution in such cases by building on the Newton-Raphson method. The Riks method includes the load magnitude as an extra unknown and solves simultaneously for loads and displacements which means an additional term is required to measure progress toward the solution. The arc length along the static equilibrium path for load-displacement fulfils this role.

7.3 Pipe-soil finite element model

The purpose of the numerical analysis discussed in this chapter is to determine what effect on pipeline global stability and buckling variations in pipe-soil friction coefficient would have. These include stability parameters such as the axial effective force, pipe-end expansion, number and distribution of buckles, axial strain, and buckle curvature. To achieve this, it was necessarily to build a model that reliably approximated the relevant mechanics of a real high pressure-high temperature pipe resting on the seabed without overly complicating aspects of pipe-soil interaction that were of little consequence. For example, considerations such pipe embedment, the presence of soil berms, and wedging are simplified and their influence accounted for using linear and nonlinear springs as appropriate or surface-to-surface Coulomb friction penalties. It was not considered necessary to specifically model every mechanism at work for reasons of computational efficiency and to focus on the variables of interest. The scope, variables, and parameters of interest are comparable to the work of Chee *et al.* (2018) who modelled a 4880 m long pipeline laid on a hard, flat seabed with operating conditions of 200°C and 20,000 kPa internal pressure. This work adopts the same modelling approach and model geometry as their work such that useful comparisons can be made to existing literature including checking model efficacy.

7.3.1 Geometry of the problem

The model was constructed to represent a 4880 m long high pressure-high temperature pipeline with 0.3556 m outside diameter with a wall thickness of 0.0198 m, resting directly on a flat, level, seafloor. An overview of the model and cross-section through the pipe is shown in Figure 7.1. The pipe was assumed to have a submerged weight of 0.61 kN/m. Ambient conditions for temperature and pressure were assumed to be zero degrees and zero kilopascals with maximum operating conditions of 200°C and 20,000 kPa. The pipe steel had a Young's Modulus of 2.05×10^8 kPa with the idealised bilinear stress-strain relationship shown in Figure 7.2. The coefficient of linear thermal expansion, α, was 1.3×10^{-5}/°C. The model parameters are summarised in Table 7.1.

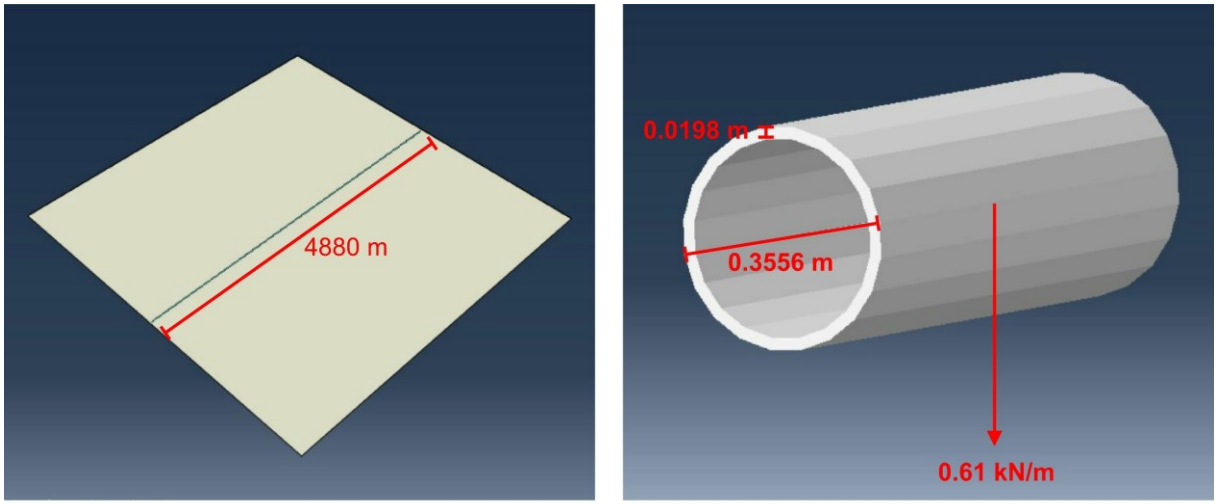

(a) plan view of the overall model (b) cross-section of the pipe section

Figure 7.1 (a) plan view of the pipe on the seabed and (b) cross-section of the pipe.

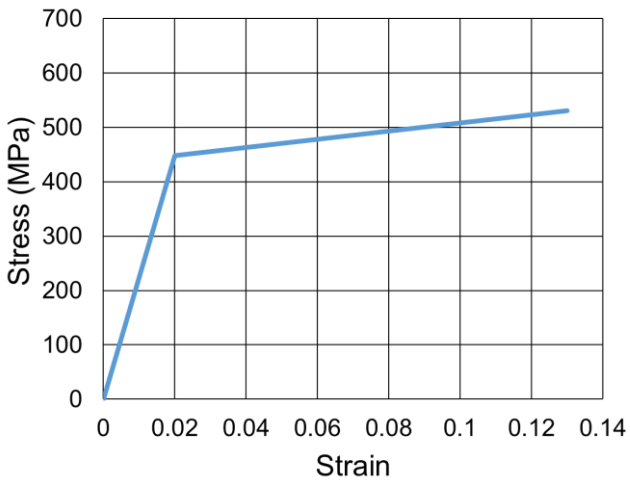

Figure 7.2 Idealised pipeline steel stress-strain relationship.

Table 7.1 Numerical modelling parameters

Parameter	Unit	Value
Pipe outside diameter, *OD*	m	0.3556
Pipe wall thickness, W_t	m	0.0198
Pipe submerged weight, W_s	kN/m	0.61
Pipeline total length, L_T	m	4880
Maximum operating temperature, T_{op}	°C	200
Ambient temperature, T_{amb}	°C	0
Maximum operating pressure, P_{op}	kPa	20,000
Pipeline steel Young's modulus, *E*	kPa	2.05e08
Coefficient of steel thermal expansion, α	1/°C	1.3e-05
Pipeline steel yield stress (bilinear)	MPa	448 / 530
Pipeline steel yield strain (bilinear)	-	0.02 / 0.13
Pipe-soil friction coefficient, μ	-	variable

7.3.2 Pipe model

The pipe was modelled with PIPE31H beam-type elements (Figure 7.3) which are 3D two-node linear pipe elements with 6 degrees-of-freedom at each node and numerical integration of the material response at 32 integration point around the circumference. The element uses linear interpolation and has a lumped mass distribution. Transverse shear deformation is allowed by a Timoshenko beam formulation and the hybrid formulation improves convergence where axial stiffness is much greater than bending stiffness. These formulations are particularly useful where the pipeline is likely to undergo large rotations when buckling. The pipe model was meshed to give 1 m length pipe elements.

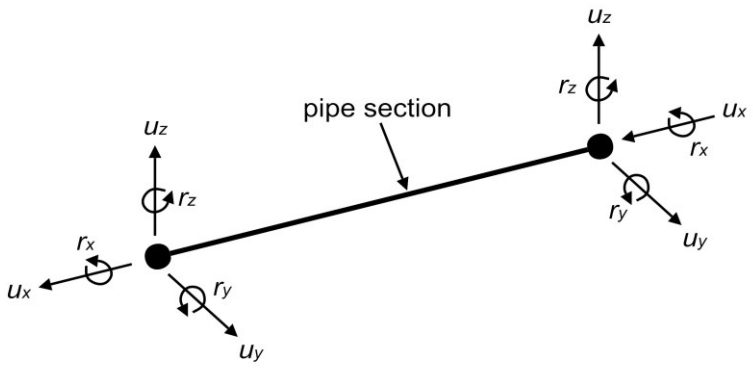

(a) 2 node pipe-beam element

Figure 7.3 Schematic representation of a PIPE31H element.

7.3.3 Seabed model

The seabed was modelled as a horizontal, flat, hard surface by using C3D20R elements with very high material property elastic stiffness and the whole element declared to be rigid. The C3D20R element is a general-purpose solid element, with 20 nodes and a reduced 2 x 2 x 2 integration scheme shown in Figure 7.4. The shape functions can be found in Lapidus and Pinder (1982).

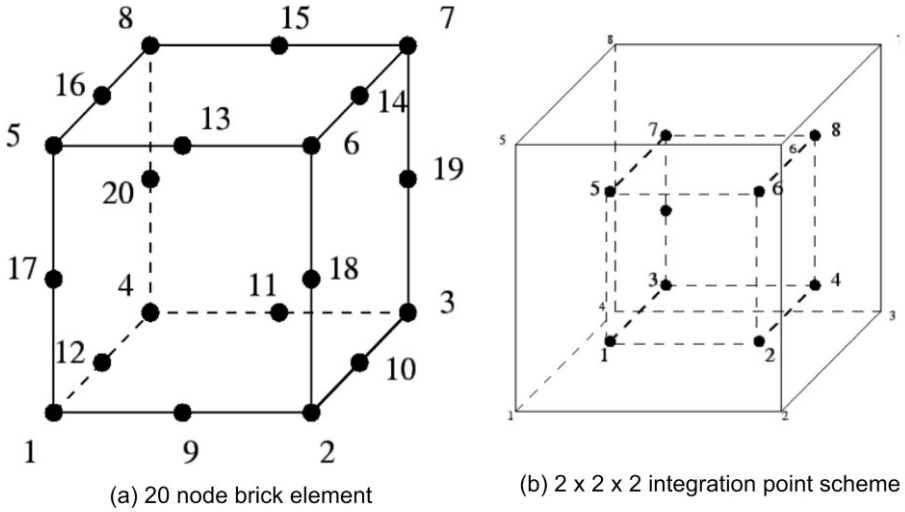

Figure 7.4 Schematic representation of a C3D20R element from Dhondt (2014).

7.3.4 Pipe-soil interaction

Contact pairs were used to model the interaction between pipe and seabed, using node-to-surface contact with the seabed as the master surface. Axial resistance was assumed to be constant with no enhanced initial resistance at breakout, and lateral resistance was assumed to have both breakout and residual resistances. Repeated from Chapter 2, the total horizontal resistance to pipe movement is defined as:

$$F_h = F_C + F_r \qquad (Eq.7.1)$$

$$F_C = \mu \cdot W_s \qquad (Eq.7.2)$$

where:

F_h = total soil horizontal resistance force

F_C = Coulomb frictional resistance

F_r = passive resistance

μ = friction coefficient

The Coulomb frictional resistance is assumed to be equivalent to the interface ultimate strength in terms of the ratio of shear to normal stress, or friction coefficient. The pipe weight is constant throughout the model, so only the friction coefficient, *μ,* needs to be specified. Coulomb friction was modelled using hard contact and friction penalty to relate the pipe weight to the available shear resistance. Where appropriate, the passive resistance component (to account for pipe embedment and soil berms) was modelled by using supplementary non-linear springs fixed to ground active over the appropriate initial displacements in the lateral direction only. Figure 7.5 shows a generalised schematic of the whole model including the different force-displacement models in use.

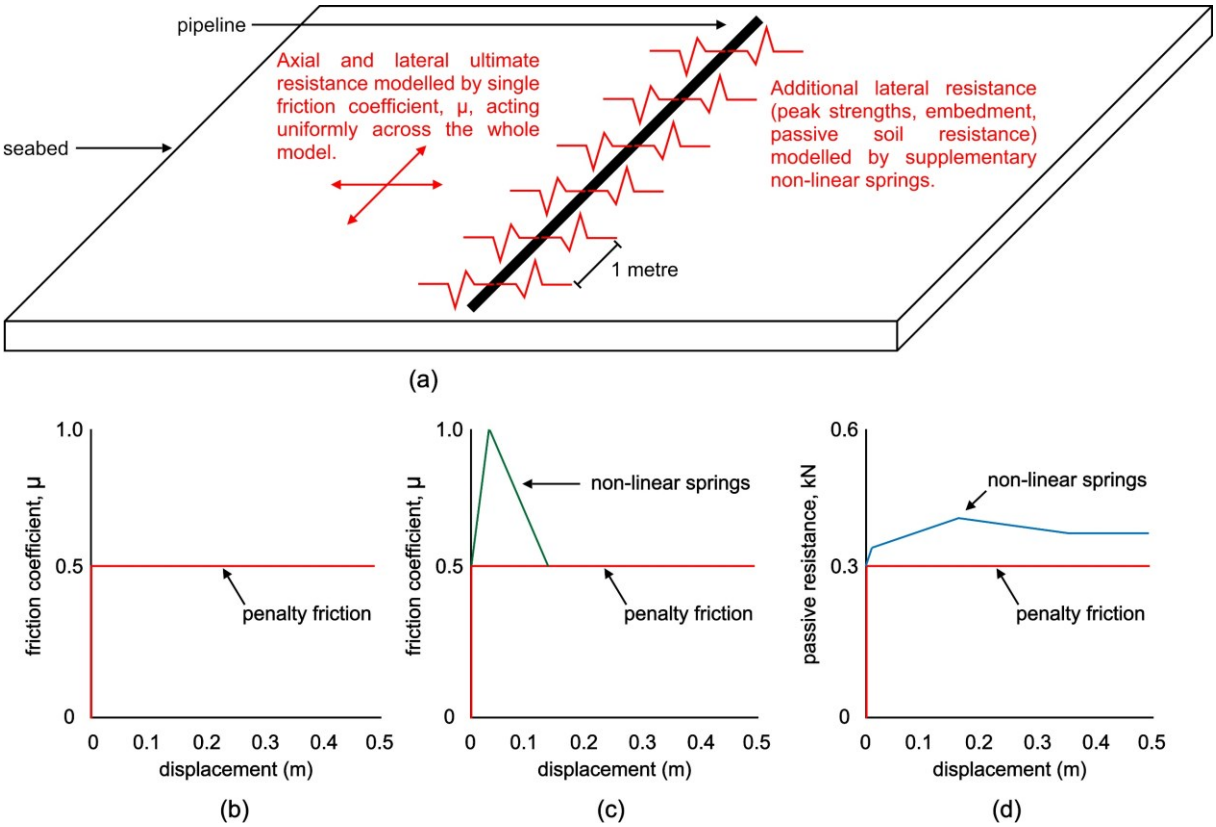

Figure 7.5 Schematic representation of the pipe-soil interaction model, (a) general arrangement, (b) Chee *et al*. (2018) axial resistance model, (c) Chee *et al*. (2018) lateral resistance model, (d) Verley and Sotberg (1994) lateral resistance model (in kN).

Initially an approximation of the force-displacement model of Chee *et al*. (2018) was used, summarised in Table 7.2, which was achieved by adopting $\mu = 0.5$ for all pipe-surface contacts (fulfilling the role of F_C in *Eq. 7.1*). This friction penalty (representative of Coulomb friction relating shear resistance to the normal load) represented the residual, large displacement, pipe-soil resistance acting both axially and laterally (Figure 7.5b). Later in this chapter the residual friction coefficient value is informed by the results of the interface shear tests of Chapter 4 and 5. In this scenario there is an additional initial breakout resistance of $\mu = 1.0$

over an initial mobilisation distance of 0.03 m which then reduces to the residual-only state by 0.15 m. In this work the initial breakout component (F_h in *Eq. 7.1*) is mimicked by nonlinear springs acting in the same orientation (laterally) with force-displacement responses equivalent to the extra resistance needed to result in the response shown in Figure 7.5c.

Table 7.2 Chee *et al*. (2018) model

Parameter	Unit	Value
Lat. breakout friction coefficient, μ:	-	1.0
Lat. breakout mobilisation distance:	m	0.03
Lat. residual friction coefficient, μ:	-	0.5
Lat. residual mobilisation distance:	m	0.15

Perhaps a more realistic model for passive soil resistance to model breakout caused is that used by Verley and Sotberg (1994) who derived analytical solutions from empirical data (previously discussed at length in Chapter 2 but summarised here for convenience). The Coulomb friction component (F_C in *Eq. 7.1)* remains unchanged, but the passive resistance component (F_h) instead takes the form shown in Figure 7.6.

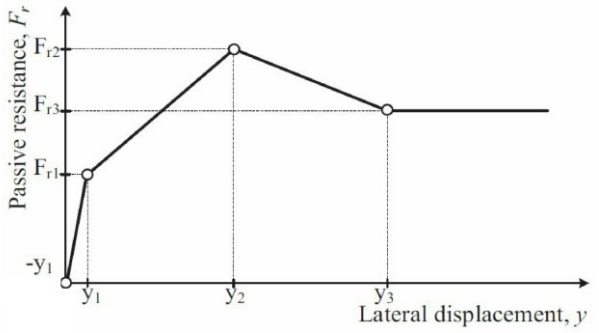

Figure 7.6 Verley and Sotberg's (1994) passive soil resistance model (after Youssef and Cassidy, 2014).

The mobilisation distances of each node in Figure 7.6. from Verley and Sotberg (1994) as being related to the pipe outside diameter (D) giving $y_1 = 0.2 \cdot D$, $y_2 = 0.5 \cdot D$, and $y_3 = 1.0 \cdot D$. The passive horizontal resistance ordinates are dependent on the force required to move the pipe horizontally which is a function of pipe embedment at each lateral position. Pipe embedment at each lateral displacement y_1, y_2, y_3 is first calculated. At y_1 it is assumed to be the same as initial embedment given by *Eq. 7.3* assuming drained conditions and soil submerged unit weight of 8 kN/m^3.

$$\left(\frac{z_i}{D}\right) = 0.037\left(\frac{\gamma_s \cdot D^2}{W_s}\right)^{-0.67} \qquad (Eq.7.3)$$

where:

z_i = pipe initial embedment (m)

D = pipe outside diameter (m)

γ_s = soil submerged unit weight (kN/m^3)

W_s = pipe submerged weight (kN/m)

However, analytical solutions like this typically underestimate pipe embedment due to other factors such as lay effects and the sea state which may increase the touch-down force. Therefore, pipe embedment was assumed to be 5% D though values up to 20% would not be inappropriate. Pipe penetration at breakout, z_2, which corresponds to lateral displacement y_2, is calculated:

$$\left(\frac{z_2 - z_i}{D}\right) = 0.23\left(\frac{\epsilon}{\gamma_s \cdot D^3}(K_s)^{-1}\left(\frac{y}{D}\right)^{-0.5}\right)^{0.31} \qquad (Eq.7.4)$$

$$K_S = \frac{\gamma_s \cdot D^2}{W_s} \qquad (Eq.7.5)$$

where:

y = pipe lateral displacement (m)

ϵ = energy (kN·m/m)

Residual pipe penetration, z_3, corresponding to lateral displacement y_3 is calculate by one of the following equations:

$$\left(\frac{z_2}{D}\right) \leq 0.1 \ldots\ldots\ldots\ldots\ldots \left(\frac{z_3}{z_2}\right) = 0.82 - \left(\frac{z_2}{D}\right) \qquad (Eq.7.6)$$

$$\left(\frac{z_2}{D}\right) > 0.1 \ldots\ldots\ldots\ldots\ldots \left(\frac{z_3}{z_2}\right) = 0.5 \qquad (Eq.7.7)$$

Using pipe penetrations calculate as above, the peak passive resistance force, F_{r2}, is given:

$$K_S \leq 20 \ldots\ldots\ldots\ldots\ldots F_{r2} = \gamma_s \cdot D^2(5 - 0.15K_s)\left(\frac{z_2}{D}\right)^{1.25} \qquad (Eq.7.8)$$

$$K_S > 20 \ldots\ldots\ldots\ldots\ldots F_{r2} = 2\gamma_s \cdot D^2\left(\frac{z_2}{D}\right)^{1.25} \qquad (Eq.7.9)$$

The residual passive force, F_{r3}, can be calculated simply by substituting z_3 into *Eq. 7.8 or Eq. 7.9* as appropriate. The passive resistance force in the elastic region, F_{r1} is assumed to be $0.3 \cdot F_{r2}$. When the nonlinear springs with the force-displacement response adopted from Verley and Sotberg (1994) are added to the underlying residual friction in the model, the net pipe-soil lateral resistance takes the form of Figure 7.5d with the values from Table 7.3.

Table 7.3 Verley and Sotberg (1994) model

Force		Displacement	
F_r1	0.13 kN	y1	0.01 m
F_r2	0.42 kN	y2	0.18 m
F_r3	0.35 kN	y3	0.36 m

7.3.5 Loading

The total submerged weight of the operational pipe was accounted for by applying a uniformly distributed line load to the pipe elements. Temperature was applied as a field to the pipe elements only, and the corresponding strain from changes in temperature calculated by Abaqus using the coefficient of linear thermal expansion (Table 7.1) assigned in the pipe element material properties. Initial temperature was assumed to be 0°C. Internal pipe pressure was applied directly to the pipe elements. External pressure has not been considered as it does not change during pipe operation. Both temperature and internal pressure loading occur simultaneously in one loading step and applied uniformly across the length of the pipe; no flow of oil or loading gradients have been included. Application of loading in this is not reflective of the actual conditions prevailing in the field as hot internal fluids will flow from the hot to cold end resulting in a) a distributed application of the load to the pipe over time, and a gradient from hot to cold end.

7.3.6 Assumptions

A number of assumptions were made in the model to aid simplicity, improve computational efficiency, and to focus on the pipe-soil friction coefficient as the variable of interest. The soil elements were declared to be hard, flat, and rigid to prevent any embedment or deformation of the contact surface and no provision was made for uneven seabed topography. Linear elastic springs acted laterally and axially on the pipe ends (Figure 7.7) with a spring stiffness of 100 kN/m to simulate typical resistance offered by end expansion spools as in Chee *et al*. (2018). The non-linear springs resisting lateral pipe movement acted with reference to the global coordinate system which means that in effect their directionality may not always be perfectly perpendicular to the pipe if the pipe deflects. This discrepancy was not considered

to be problematic as deviations from perfectly perpendicular were relatively small due to the length over which lateral deformations occur.

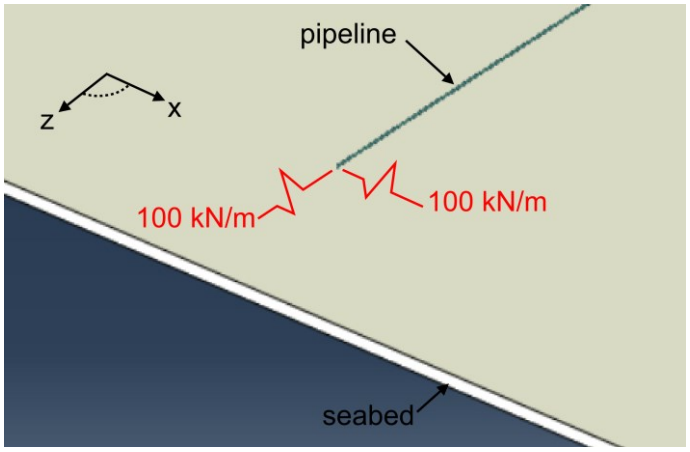

Figure 7.7 Schematic diagram of linear elastic springs at pipe ends to account for expansion spools.

7.3.7 Boundary conditions

The model was run in two steps, the first to apply the self-weight of the pipe and the second to simultaneously apply the pipe internal pressure and the temperature field to the pipe only. During application of the self-weight, boundary conditions were set to allow only a single degree of freedom in the vertical direction at the pipe ends. During the loading step, all boundary conditions were removed from the pipe such that the only forces acting on it were the pipe internal pressure load, strain generated by the temperature field, and the reaction forces of the springs modelling end expansion spools or soil response. No rotational springs were included at any point. The seabed element remained rigid during each stage.

7.4 Model mechanics test

Before fully building the model and expecting robust results it was necessary to check that the mechanics in the model were operating as expected. Two principal mechanics required attention; the force-displacement response of the pipe when subject to deformation, and the deformation and stress generated in the pipe elements by loading.

7.4.1 Force-displacement response

To check the force-displacement response was working as intended, a one metre section of model was tested with displacement control to determine the forces resisting movement. A one metre section of pipe element was forced to displace one metre axially and then in a second test, one metre laterally, illustrated in Figure 7.8. The reaction force provided by the

pipe-soil interaction (penalty friction plus nonlinear springs) was the output from these tests. The measured reaction force and mobilisation distance ought to match the input defining the pipe-soil resistance according to the parameters detailed in Table 7.2 and Table 7.3. Figure 7.9 shows the model outputs for the displacement-controlled test.

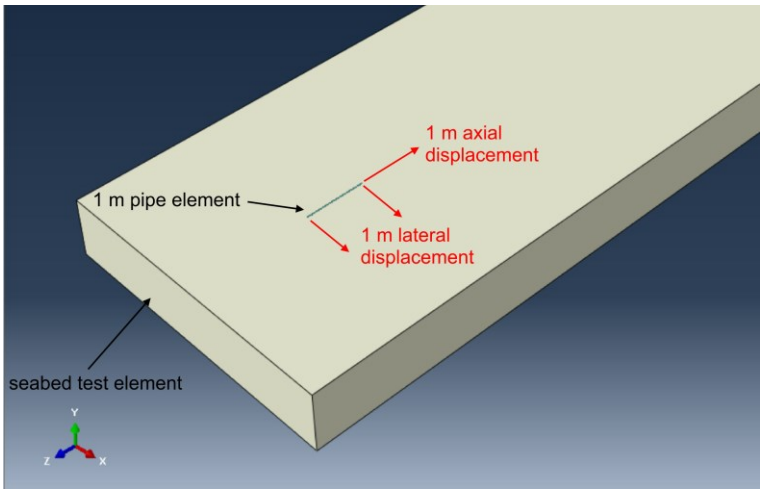

Figure 7.8 Schematic diagram of displacement control model mechanics test.

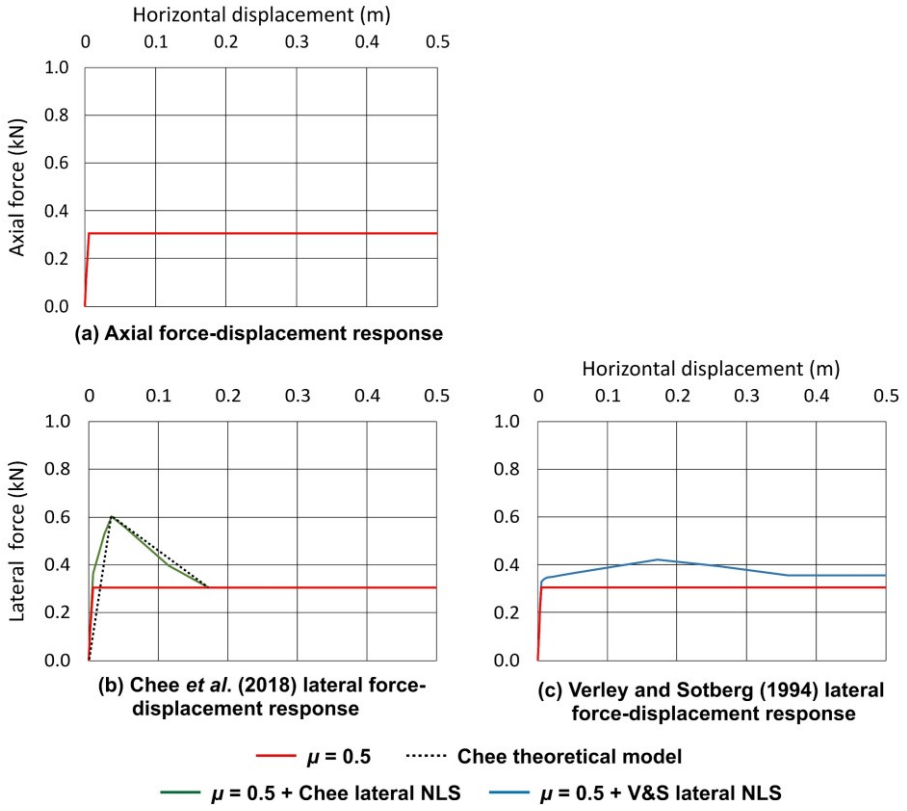

Figure 7.9 Displacement control element test results show lateral force-displacement outputs after (b) Chee *et al.*'s (2018) model and (c) Verley and Sotberg's (1994) model. (a) shows the axial force-displacement response which is common to both.

Comparison of the element test model outputs in Figure 7.9 and the theoretical models shown in Figure 7.5, there is excellent agreement with the input values from Table 7.2 and Table 7.3 particularly in the case of the Verley and Sotberg (1994) model. Chee *et al*.'s (2018) model is in terms of friction coefficient which, given the submerged pipe weight of 0.61 kN/m, corresponds well to the results in Figure 7.9 for lateral force of 0.305 kN and 0.610 kN for friction coefficients of 0.5 and 1.0 respectively. The force-displacement response output matches the input parameters for the relevant non-linear spring and pipe-soil penalty friction contact which gives confidence that the model and pipe-soil interaction mechanic is working as intended. Where there is a subtle difference, shown by the black dotted line in Figure 7.9b, it is because Chee *et al*.'s (2018) model adopts an elastic-plastic response, whereas the use of a simple penalty friction method in Abaqus to model the residual friction means this part of the response is rigid-plastic.

7.4.2 Pipe thermal strain

Thermal strain is generated by application of a temperature field to the pipe elements which have a thermal expansion coefficient assigned in their material properties. To test the generation of thermal strain a one metre long pipe section was subject to a temperature load in this way and the axial displacement measured to determine the strain. Thermal strain is calculated simply by:

$$\varepsilon_T = \alpha_t \cdot \Delta T_{op} \qquad Eq.7.10$$

where:
ε_T = thermal strain
α_t = coefficient of linear thermal expansion (1/C°)
ΔT_{op} = change in pipe operating temperature (°C)

The theoretical strain is 2.6000×10^{-3} and the strain from the Abaqus results was 2.6034×10^{-3} giving very good agreement.

7.4.3 Pipe effective axial force

To check that the force generated in the pipe wall was being modelled accurately, a short pipe section was fixed at both ends such that no expansion was possible and axial strain was fully constrained. First the pipe was subject to increasing pipe temperature loads with internal pressure constant at 0°C, and then the reverse with temperature kept at 0°C and increasing

internal pressure loads. The results for each test are compared in Figure 7.10 with the theoretical value by hand calculation and also combined together in terms of a percentage of the maximum operating load. The hand calculation for effective axial force is given:

$$S_{eff} = H - \Delta P_i \cdot A_i(1 - 2v) + E \cdot A_e \cdot \alpha_t \cdot \Delta T \qquad (Eq.7.11)$$

where:

S_{eff} = effective axial force (kN)

H = residual stress (kN)

P_i = pipe internal pressure (kPa)

A_i = pipe internal cross-sectional area (m^2)

v = Poisson ratio

E = Young's Modulus (kN/m^2)

A_e = pipe external cross-sectional area (m^2)

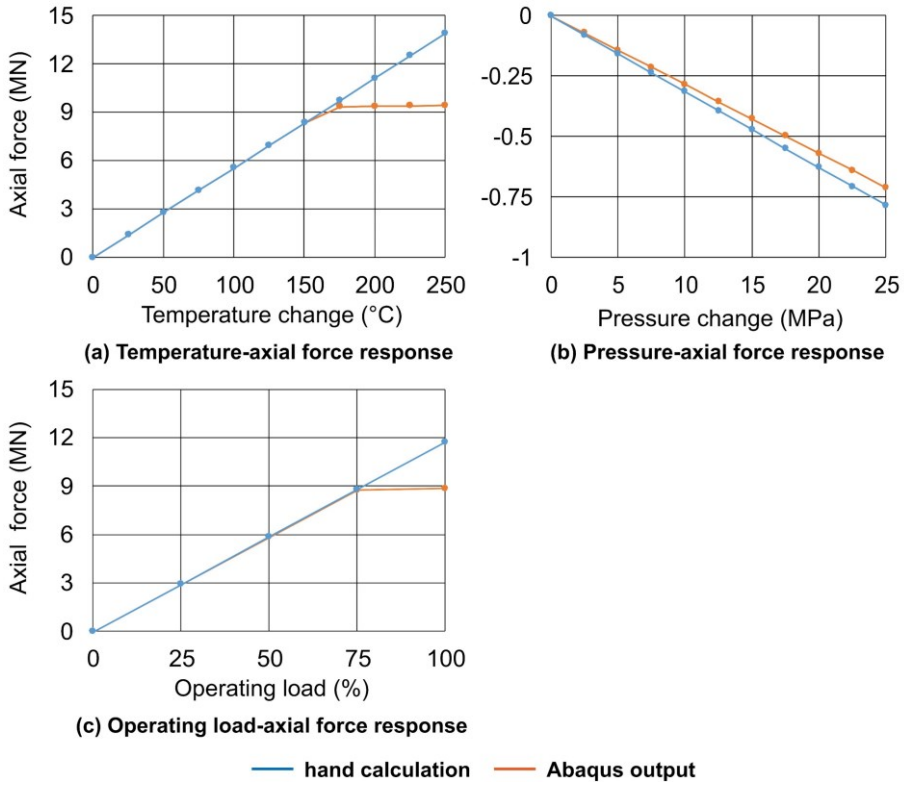

Figure 7.10 Axial force response to pipe pressure and temperature effects and comparison with hand calculation.

Operating load (%) in Figure 7.10c refers to the load generated by the equivalent percentage of the maximum pressure and temperature conditions. For example, 50% means the loading caused by 50% of the operating temperature and pressure detailed in Table 7.1. Figure 7.10 shows very good agreement between the hand calculated axial force in response to pipe

internal pressure and the output from Abaqus. The response to temperature is in perfect agreement up to approximately 150°C at which point there is a divergence resulting in a plateauing of axial force with any further temperature increase. A simple calculation from the steel pipe wall section area and the yield stress of steel from Table 7.1 gives the force required to cause yielding and transition to plastic deformation:

$$S_y = A_p \cdot f_y \qquad Eq.7.12$$

where:

S_y = yield force (kN)

A_p = pipe wall cross-sectional area (m^2)

f_y = yield stress (kPa)

The force required for yielding is ~9358 kN, very close to the plateau in axial force which averages ~9406 kN. These results give confidence that the model and mechanics in Abaqus are working as intended and giving reasonable and robust results. They also demonstrate that temperature is the primary driver in generating the effective axial force, with pressure effects a secondary component.

7.5 Benchmarking against Chee *et al*. (2018)

An initial model was built using the same approach as in Chee *et al*. (2018) and tested to replicate their results as a form of model validation. One important variation in the current work from that of Chee *et al*. (2018) is that in their work the friction contact between pipe and soil was modelled by a user-defined subroutine to allow bilinear (or trilinear) response varying between axial and lateral orientations. In contrast, the present study adopts a more straightforward method of applying a simple friction penalty to the pipe-soil contact which is equivalent to friction coefficient. The friction contact component can be considered to represent the ultimate (or residual) shear resistance of the Coulomb frictional component of soil lateral resistance as discussed previously. Any peak Coulomb friction and passive soil resistance is modelled with the application of supplementary non-linear springs with prescribed force-displacement responses.

Chee *et al.* (2018) tested four pipe geometries: perfectly straight pipe, perfectly predeformed pipe (PDP), imperfectly straight pipe, and imperfectly predeformed pipe. Predeformed pipe used the idea of pre-stressing the pipeline as it was laid in alternating directions to form a pipe geometry with subtle sinusoidal deflections away from its centre line. Figure 7.11 (from Chee *et al.*, 2018) shows the form of PDP pipe with lateral exaggeration to

highlight the shape. In reality the scale of as-laid and operational deviation from a straight line is much more subtle with sinusoid amplitudes of one pipe diameter (0.3556 m) and wavelength of 48.8 m. For PDP pipe, lateral positions along the pipeline relative to the straight is given by:

$$\Delta = \frac{\Delta_0}{2}\left[sin\left(\frac{2\pi x}{L_w}\right)\right] \qquad Eq.7.13$$

where:

Δ = lateral position along pipe (m)

Δ_0 = maximum lateral amplitude (m)

x = axial position along the pipeline (m)

L_w = wavelength (m)

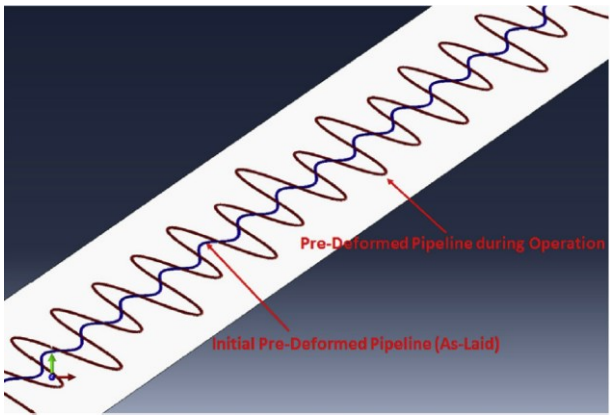

Figure 7.11 Exaggerated form of the PDP pipe to highlight the geometry after Chee *et al*. (2018).

Figure 7.12 compares the results from Chee *et al*. (2018) with the same conditions and loading in the present study and shows there is excellent agreement which gives confidence that the present model is working properly and is able to replicate results from the literature. Effective axial force builds up linearly for straight pipe with the gradient a function of the pipe-soil friction coefficient. Perfect PDP pipe follows a similar trend but plateaus at a much lower overall effective axial force as the thermal strain is accommodated by exacerbation of the predeformed geometry. Axial strain generated in the pipe and lateral deformations show the same behaviour and magnitude. Chee *et al*.'s (2018) results show a less uniform response compared to the present study. An explanation is not readily available though it may be explained by the difference in approach to modelling the pipe-soil interaction between the two studies.

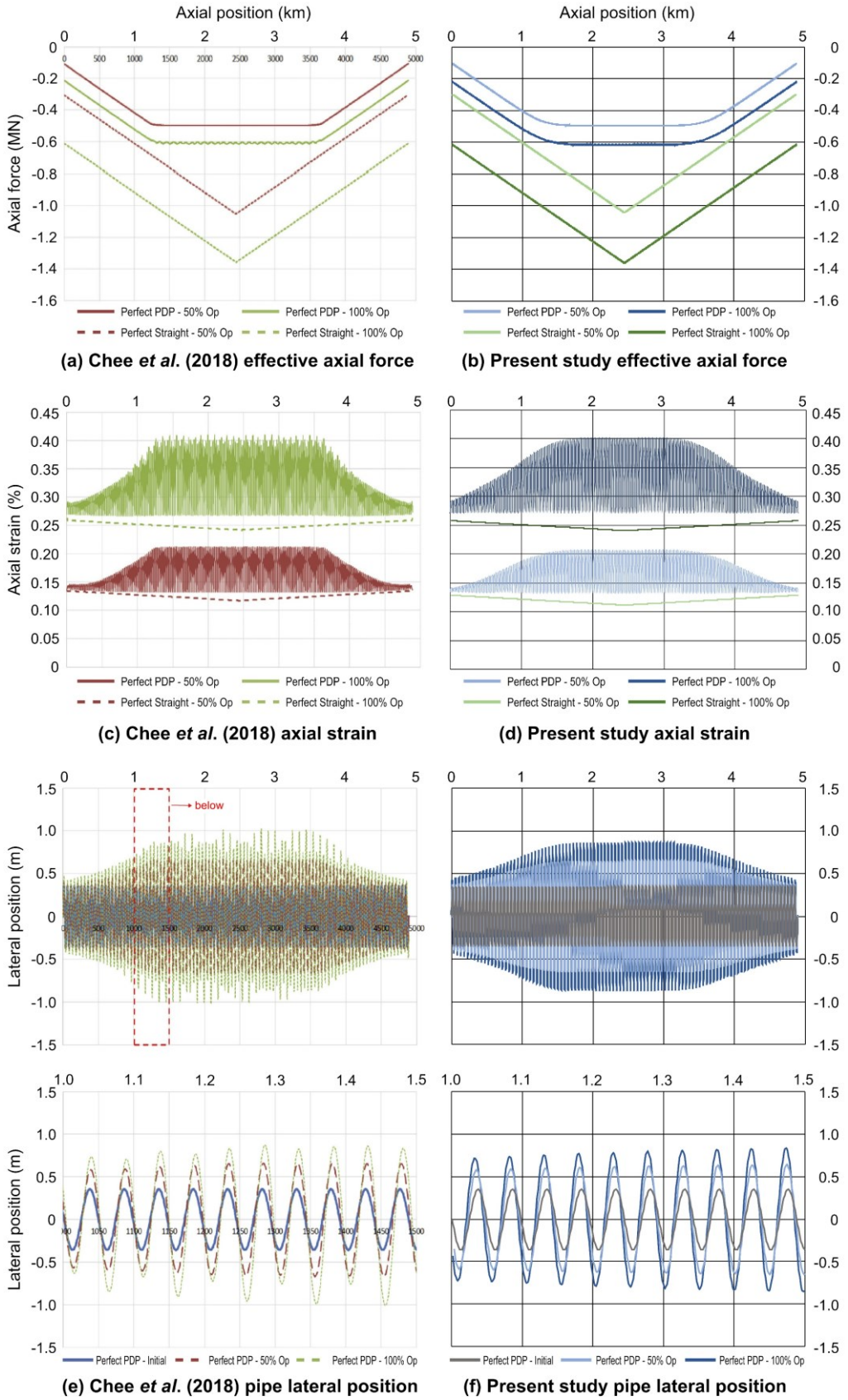

Figure 7.12 Comparison of results for straight pipe and perfect PDP (a, b) effective axial force, (c, d) axial strain, and (e, f) lateral deformation between the present study to those from the benchmark study of Chee *et al*. (2018).

In reality, pipe geometry will never be perfect. Even with the dubious assumption that the pipeline itself is perfectly homogenous, variation in seafloor topography and initial out-of-straightness from pipe laying is likely to lead to subtle geometric variations from the ideal. To capture this variability Chee *et al.* (2018) introduced randomised imperfections to the pipe as-laid geometry (note, not the pipe section or structural imperfections). Variations from the idealised perfect positions of up to ±0.1 m were assumed to occur along the pipe.

Imperfectly straight pipe was initially modelled as having a sine form defined by *Eq. 7.13* albeit with an amplitude of 0 to give a perfectly straight pipe at this first stage. Next, coordinates (position along the pipe, and lateral position) were determined as in *Eq. 7.13* but with the ω_0 now being amended to include random deviations of ±0.1 m from the ideal. Random number generation in Microsoft Excel was used to determine how much deviation from the ideal there would be at each position up to a maximum of ±0.1 m. The values were then averaged over each wavelength (48.8 m) such that each sine lobe was defined by a single equation to ensure a smooth pipe geometry. It was unreasonable to assume that everywhere along the pipe there would be geometrical imperfections so the distribution of deviations was filtered according to set criteria that also depended on the random numbers generated. This meant that both the magnitude and distribution of imperfections was randomised. The coordinates for perfect PDP and imperfect straight pipe used in this work are included in the data pack attached to this thesis on an SD card. It is not possible to directly compare the results for imperfect pipe geometries against those of Chee *et al.* (2018) because the geometries are essentially different.

7.6 Influence of residual friction coefficient

The three pipe geometries modelled here, perfect straight, perfect PDP, and imperfect straight were tested with varying residual pipe-soil friction coefficients modelled here by friction penalty. The nonlinear springs modelling the passive horizontal resistance and pipe embedment were kept constant throughout. Three residual friction coefficients were chosen for investigation which broadly cover the range identified in preceding chapters of this thesis: 0.25, 0.50, and 0.75. The net force-displacement responses used are shown in Figure 7.13 which shows the residual friction coefficient changing but the passive resistance component remaining constant between different scenarios.

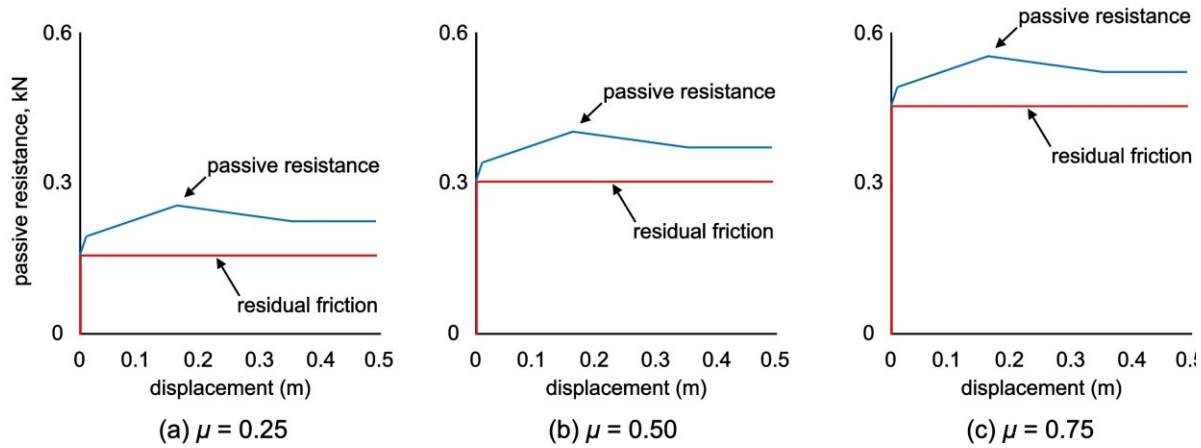

Figure 7.13 Force-displacement responses with friction coefficients of (a) 0.25, (b) 0.50, and (c) 0.75.

Figure 7.14 shows how rate of build-up and maximum effective axial force for straight pipe varies according to the friction coefficient. No buckles form as everything is in perfect equilibrium (of course this is not representative of real-world conditions but it illustrates the mechanisms at work). Axial displacement is linear with expansion uniform along the pipe. There is little difference in axial displacement across the three residual friction coefficients investigated.

Figure 7.15 shows that the maximum effective axial force for the perfect PDP pipe is the same regardless of friction coefficient and that lateral deformation is by way of exaggeration of the existing predetermined geometry. Axial displacements globally are much reduced compared to perfect straight pipe, though axial displacements at the feed-in to the buckle lobes are likely to be more widespread. Displacements also shows a much greater variation depending on the residual friction coefficient than perfect straight pipe.

In the case of imperfect straight pipe (Figure 7.16), a single buckle feature forms approximately at the centre of the pipe length. The effective axial force dramatically reduces as the stress is relieved and there is a large lateral deformation of the pipe. The magnitude of the buckle (and therefore the amount of stress relief) is larger for lower pipe-soil friction coefficients which is related to the buckle feed-in. Lower friction leads to less resistance to feed-in meaning more pipe is able to participate in buckling. Axial strain and pipe curvature are also presented, with data from perfect straight and PDP included for comparison. Higher residual friction leads to greater axial strain and greater curvature.

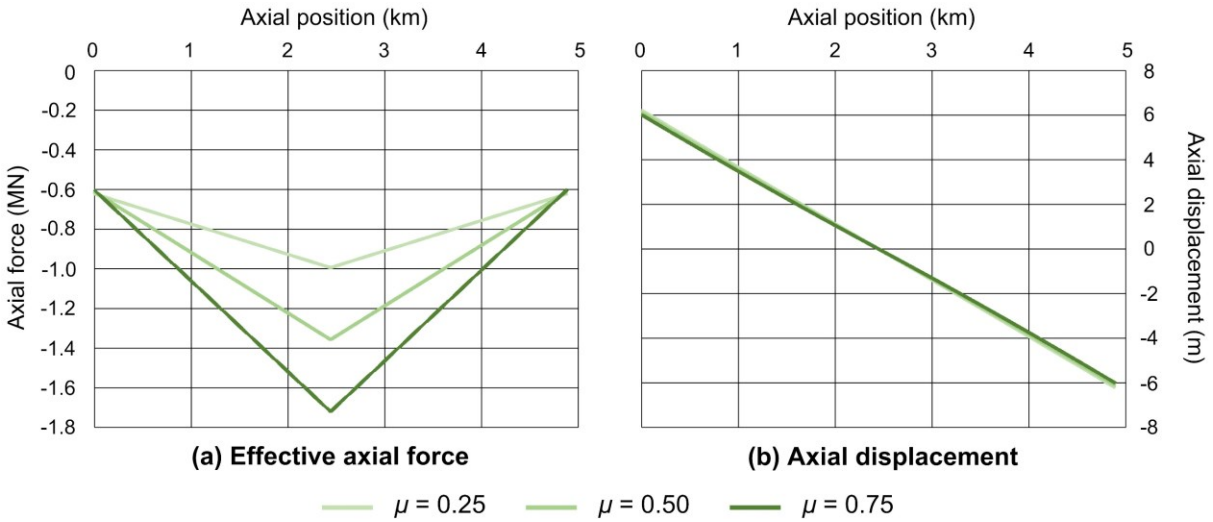

Figure 7.14 Perfect straight pipe effect of residual friction coefficient on (a) the build-up of effective axial force, (b) pipe axial deformation/end expansion.

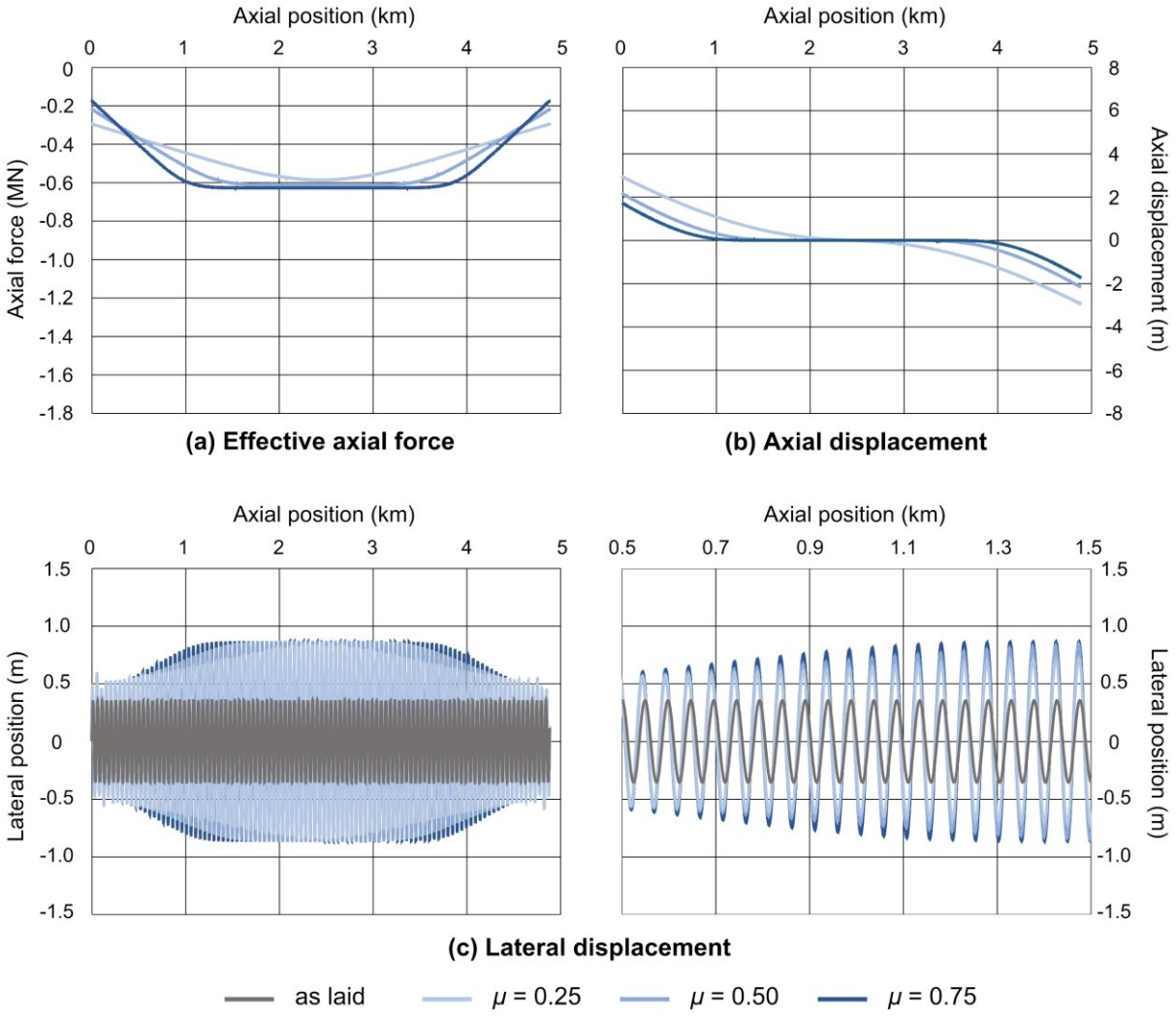

Figure 7.15 Perfect PDP pipe effect of residual friction coefficient on (a) the build-up of effective axial force, (b) axial, and (c) lateral deformation.

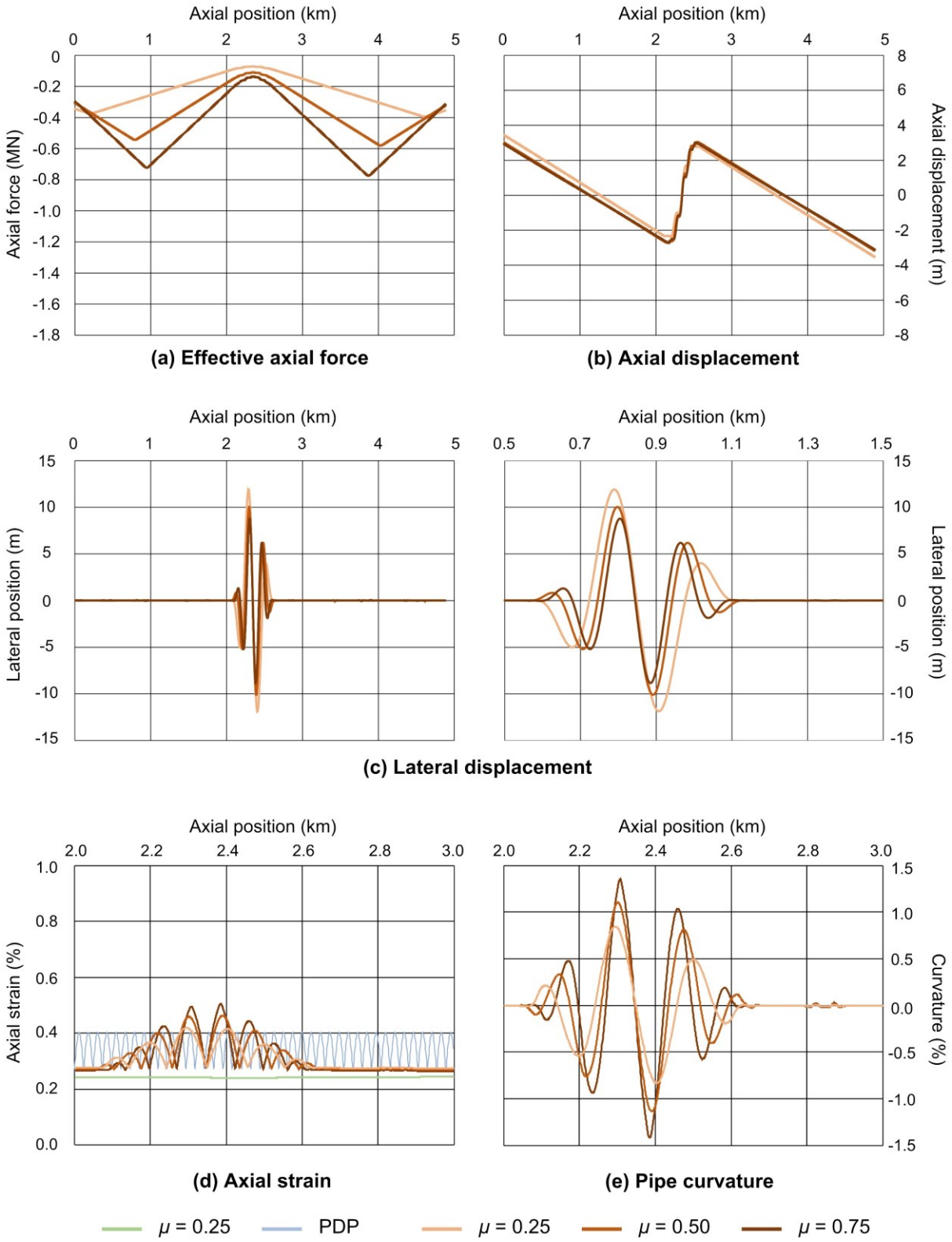

Figure 7.16 Imperfect straight pipe effect of residual friction coefficient on (a) the build-up of effective axial force, (b) axial, and (c) lateral deformation, (d) axial strain, and (e) pipe curvature.

In addition to lateral deformation and effective axial force in the pipeline, end expansion of the pipe is another stability response requiring consideration. Examination of the axial displacement panels from the preceding figures and Table 7.4 reveals that end expansion of the pipe varies with pipe-soil friction and it is more or less sensitive depending on the pipe geometry. Table 7.4 again shows good agreement between Chee *et al*. (2018) and the present study's results for pipe-soil friction of 0.50. In general pipe end expansion is greater with lower pipe-soil friction. The greatest variation in pipe end expansion is seen in the PDP pipe where effective axial force (and therefore strain) reached a fixed value across the central section of the pipeline. For other geometries, were the pipe longer and to become fully constrained, it is expected that there would be greater variation in pipe end expansion due to pipe-soil friction.

Table 7.4 Pipe end expansion

Pipe geometry	Chee *et al.* (2018) (μ = 0.5)	μ = 0.25	μ = 0.50	μ = 0.75
Perfect Straight	6.1 m	6.2 m	6.1 m	6.0 m
Perfect PDP	2.1 m	2.9 m	2.2 m	1.7 m
Imperfect Straight	unknown	3.5 m	3.1 m	3.0 m

Although greater residual friction leads to reduced pipe end expansion, a desirable outcome, it leads to greater effective axial forces which means buckle formation becomes more likely. When buckles do form, the amplitude is reduced with greater residual friction, however axial strains are greater and curvature is higher which may cause other structural problems. Lower residual friction results in buckles with a greater wavelength and less axial strain (also less axial force) resulting in lower curvature.

7.7 Differential pipe-soil friction

The differences in pipeline stability performance with different PSI friction and the potential for engineering surface texture during the manufacturing process invites the possibility of applying coatings with differential friction along the pipeline. Patterns of pipe coating or targeting control of friction where seabed conditions might otherwise be unfavourable, gives potential for pipeline global stability to be controlled in ways other than by use of secondary infrastructure. In this preliminary study, a number of arrangements for PSI friction varying along the length of the pipeline were modelled using the "imperfect straight" pipeline geometry.

7.7.1 Proportion of pipe subject to enhanced residual friction

Two avenues were investigated; the first starting with a pipe assumed to have a traditional smooth polymer coating with approximate residual friction coefficient of 0.25. Working from

the pipe ends toward the centre, progressively more of the pipe was assumed to have an enhanced residual friction coefficient of 0.75 corresponding to the enhanced textures tested in previous chapters. The passive soil resistance remains unchanged and is not affected by changes in the residual friction component. Six iterations of this process were tested and their pipe-soil interaction (PSI) regimes are presented schematically in Figure 7.17. They are labelled with approximate percentages of enhanced residual friction simply for ease of reference.

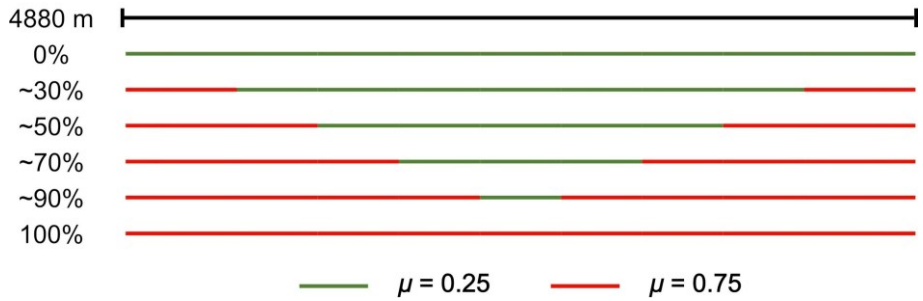

Figure 7.17 Distribution of increasing proportion of enhanced residual friction along pipe length from pipe ends.

Results from Abaqus showing the effective axial force, lateral and axial displacement, axial strain, and buckle curvature are presented in Figure 7.18. Generalised behaviour is similar to what has been previously discussed. Key output parameters are summarised in Table 7.5. Compared to the baseline scenario of a pipe that is smooth all the way along, adding some enhanced friction to the pipe ends gives an immediate improvement in the pipe end expansion reducing it from 3.1 m to 1.8 m in the scenario tested. Adding longer sections of enhanced residual friction does not lead to any increasing benefit, in fact the opposite. The use of a short section of high friction pipeline at the pipe ends whilst maintaining low friction across the rest to allow buckling, may be a useful alternative to physical infrastructure to reduce end expansion. There is also a benefit to the maximum buckle amplitude which, despite an initial increase, reduces to 8.9 m compared to 11.7 m in the initial condition. In the arrangements tested here, reducing end expansion comes at the cost of increased buckle amplitude. There is no discernible trend in terms of axial strain or buckle curvature other than all options being more onerous than the initial condition.

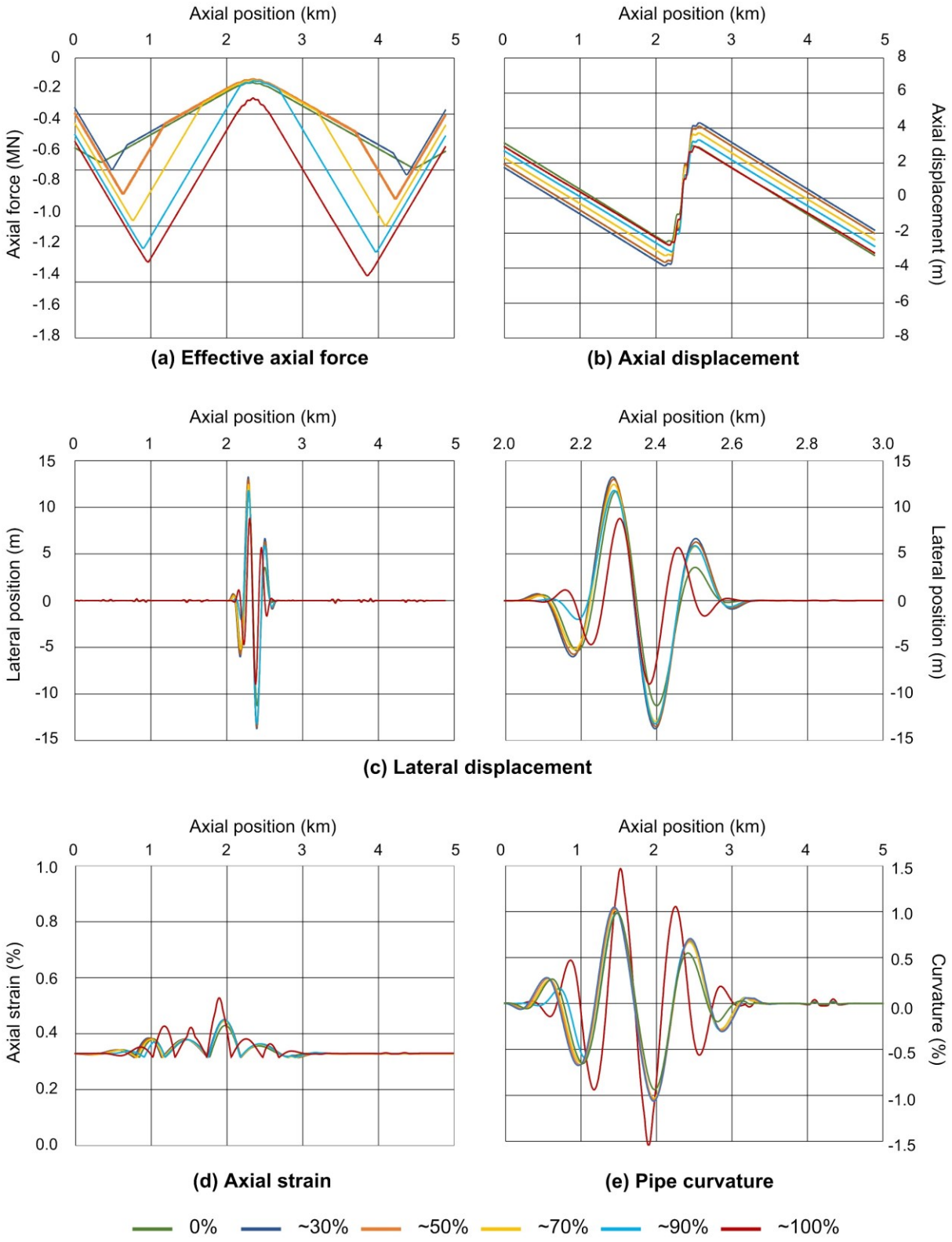

Figure 7.18 Distribution and magnitude of global stability parameters according to percentage of enhanced residual friction coefficient: (a) effective axial force, (b) lateral position, (c) axial displacement, (d) axial strain, (f) pipe curvature, with different PSI friction regimes varying along the pipe (e).

Table 7.5 Enhanced friction proportion output parameters

Enhanced amount	Average end expansion (m)	Number of buckles	Max. buckle amplitude (m)	Max. axial strain	Max. buckle curvature (%)
0%	3.2	1	11.7	0.429	0.984
~30%	1.8	1	13.7	0.450	1.063
~50%	2.0	1	13.5	0.448	1.052
~70%	2.4	1	13.0	0.449	1.033
~90%	2.7	1	13.2	0.450	1.057
~100%	3.1	1	8.9	0.528	1.547

7.7.2 Differential residual friction regimes

The second avenue for investigation of changing the residual friction is to apply a differential regime along the pipe length to see if the distribution or magnitude of instability features can be influenced. Five regimes were tested and they are shown schematically in Figure 7.19. The percentage component of enhanced friction (above 0.25) along the pipe varies between regimes (48.8, 51.2, 58.6, 41.0, 30.7% for regimes 1 to 5 respectively). Ideally the percentage of pipeline with enhanced friction would have remained the same but this was difficult to accomplish when accommodating mirrored arrangements such as in Regime 3 and 4 or with three different residual frictions as in Regime 5. As before, the passive horizontal resistance component remains unchanged regardless of variations in residual friction coefficient.

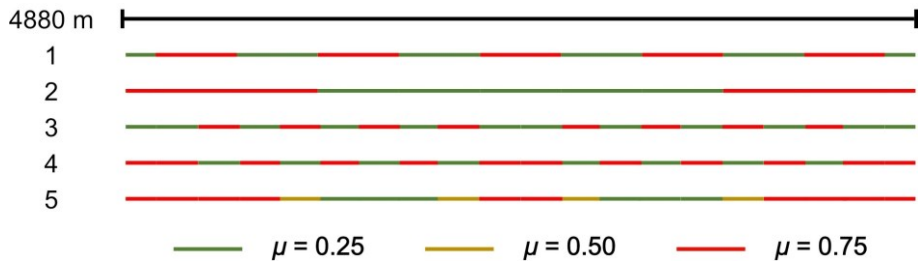

Figure 7.19 Differential residual friction regimes along pipe length.

Results of the differential residual friction tests are presented in Figure 7.20 and can be compared directly with the plots shown in Figure 7.16 and Figure 7.18 as the initial pipe geometries are identical. Figure 7.20 reveals a dramatic change in the distribution and magnitude of buckles formation. Similar to the single pipe-soil friction regime, configurations 2 and 3 result in a single buckle forming in the central part of the pipeline. Configurations 1, 4, and 5, where the mid-point of the pipe has a greater friction coefficient than elsewhere, lead to the formation of two buckles instead of one and they are distributed away from the mid-point by varying amounts depending on the detail of the particular friction regime.

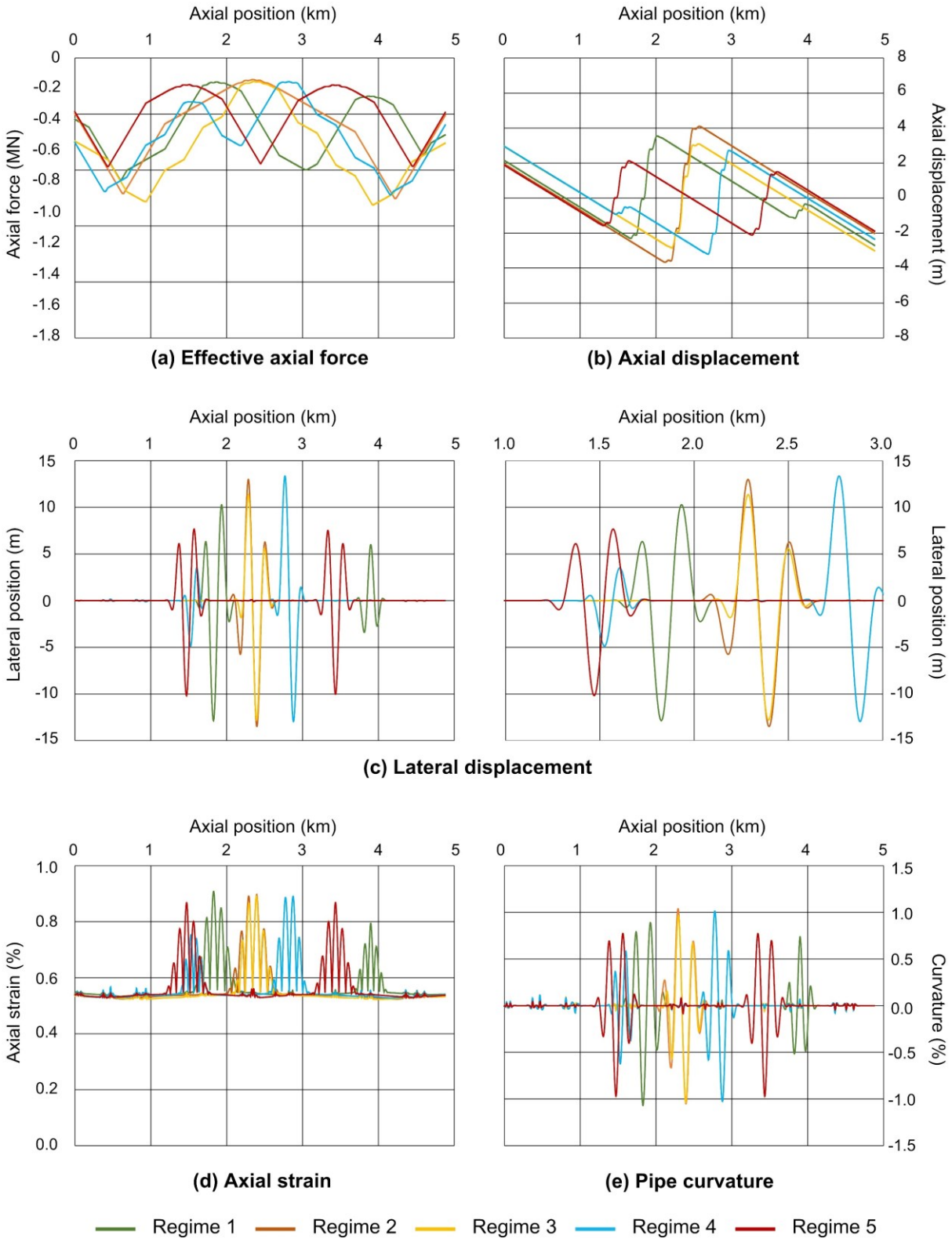

Figure 7.20 Distribution and magnitude of global stability parameters according to differential residual friction regimes: (a) effective axial force, (b) lateral position, (c) axial displacement, (d) axial strain, (f) pipe curvature, with different PSI friction regimes varying along the pipe (e).

Stability parameters from the model outputs are summarised in Table 7.6 although best appreciation of the results is from observing the relationship between the parameters shown in Figure 7.20. There is a wide range in the end expansion experienced by the pipes according to the residual friction regime with regime 2 and 5 performing best despite their buckle distribution varying significantly. However, examination of buckle amplitude shows regime 5 performs best and also experiences the lowest axial strain and buckle curvature. Regime 5 likely performs best here because of a combination of higher friction pipe-ends and the central high friction zone forcing the formation of two buckles rather than one. It was shown previously that pipes with a higher residual friction at the pipe end reduced average end expansion. It is also intuitive to think that as buckles form, axial strain is accommodated by the buckle and feed-in to the end-most buckle reduces end expansion. The phenomenon is shown in Figure 7.20b where regime 4 shows two buckles, one small at approximately 1.5 km and one much larger at approximately 2.8 km. The pipe end closer to the smaller buckle displaces axially by 3 m whereas the pipe end closer to the larger buckle displaces approximately 2.4 m despite this end being further from the buckle which means more expansion. Examination of regime 1 shows the same trend with axial end displacement of 2.2 m closer to the larger amplitude buckle and 2.7 m closer to the smaller one, also in spite of the asymmetric buckle position relative to their respective pipe ends.

It must be recognised that the effective axial force, which drives instability phenomena, is controlled in large part by the residual friction. Therefore, it would be prudent in future work to reassess the impact of differential residual friction regimes whilst keeping the overall proportion of the pipe subject to enhanced friction constant. In spite of this, these results demonstrate that formation of buckles can be influenced, and their location and proximity to pipe-ends directly effects the pipe end expansion.

Table 7.6 Differential residual friction output parameters

PSI regime	Average end expansion (m)	Number of buckles	Max. buckle amplitude (m)	Max. axial strain	Max. buckle curvature (%)
1	2.4	2	12.9	0.454	1.069
2	2.0	1	13.5	0.448	1.052
3	3.0	1	12.8	0.446	1.041
4	2.7	2	13.4	0.446	1.024
5	1.9	2	10.2	0.434	0.973

7.8 Implications for pipeline global stability design

Figure 7.21 is presented again from the beginning of this thesis. The results presented in this chapter have confirmed the already established nature of pipeline global buckling stability with changes in pipe-soil interface friction. It can be seen from Figure 7.21 that even without any

change to the surface coating, there may be significant changes to the residual friction coefficient due to the changing seafloor substrate and the relative texture relationship between grain size and coating texture discussed previously in this thesis. Techniques outlined in the experimental work and demonstrated in the numerical analysis work show that changes in seafloor substrate can be compensated for to ensure a consistent residual pipe-soil friction if desired. Equally, residual friction can be manipulated more generally to encourage or retard buckling according to the designer's preference.

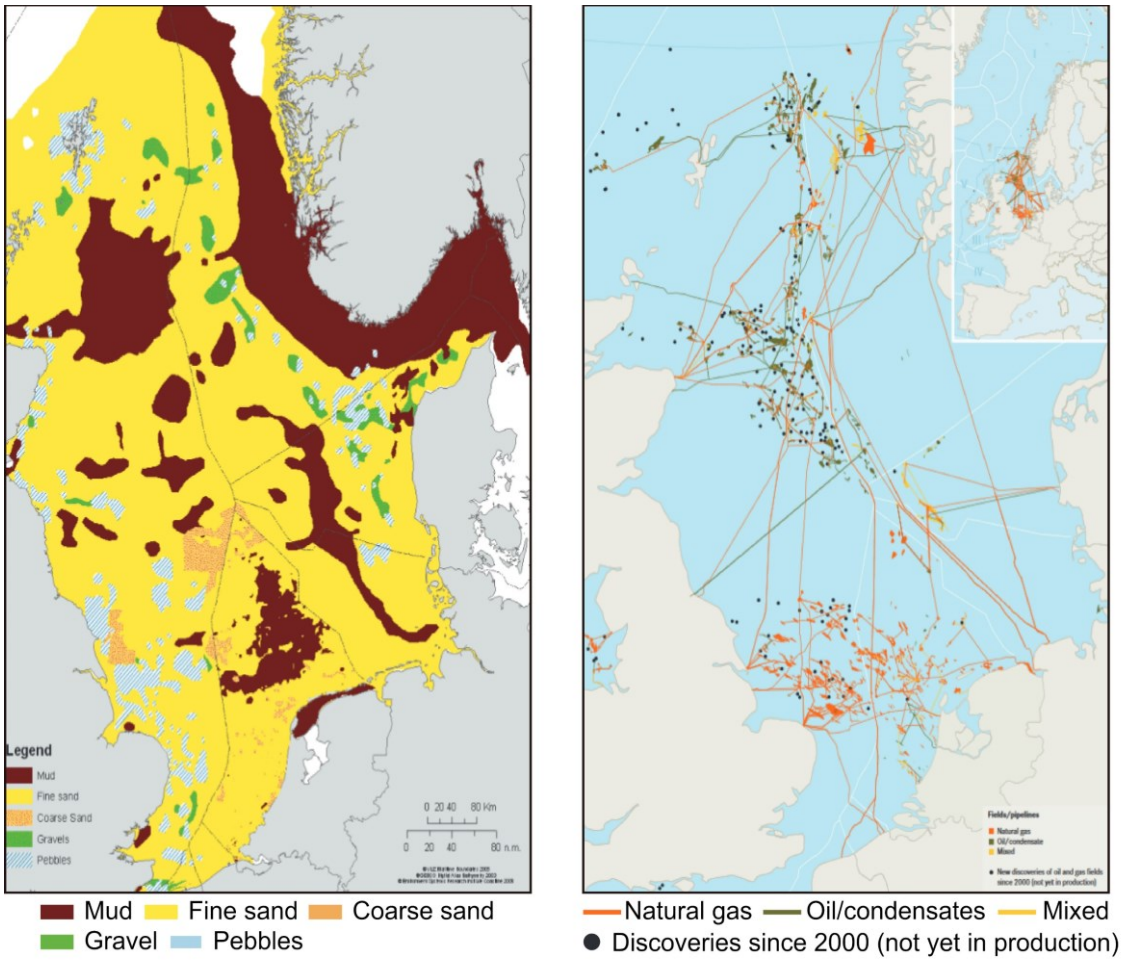

(a) Distribution of North Sea sediments **(b) Map of North Sea pipelines and fields**

Figure 7.21 (a) Distribution of seafloor sediments across the North Sea basin from MEFEPO (Paramor, 2009) and (b) distribution of pipelines and oil and gas fields in the North Sea from OSPAR (2010).

For more robust design using these techniques other real-world factors need to be considered such as seafloor topography, evolution of the pipe-soil contact area on mobile seabeds through scour, and cyclic effects from start-up and shut-down cycles. Real seabed topography is rarely flat and perfectly horizontal. Seabed gradients away from the pipeline cause localised reductions in the critical buckling force causing buckles to form preferentially in these areas.

Such localised effects may be prime candidates for enhanced residual friction if buckling is undesirable at that location.

In addition, seabeds may be mobile with scour changing pipe embedment and wedging over time depending on the local sediment transport regime. Figure 7.22 from Leckie *et al*. (2015) shows how over a four-year period the embedment, wedging, and area of pipe-soil contact can evolve significantly. In such cases both scenarios would need modelling as stability is likely to be affected.

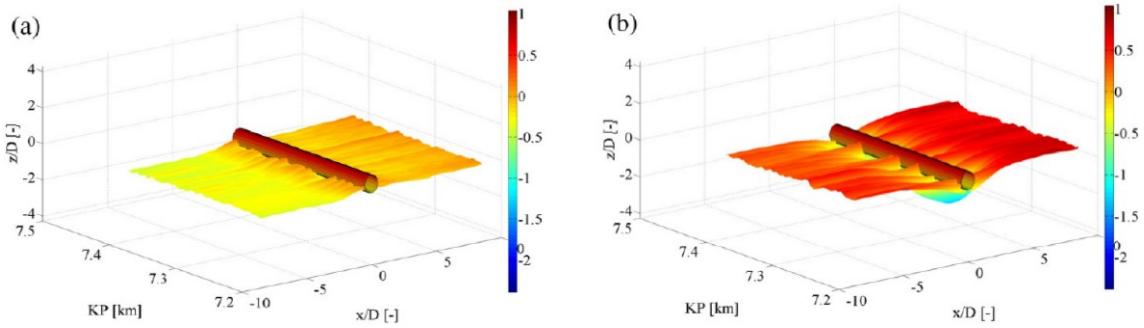

Figure 7.22 Change in seabed topography, scour, and pipe-soil contact (a) initially and (b) four years later from Leckie *et al*. (2015).

7.8.1 Relationship to SAFEBUCK JIP

The SAFEBUCK JIP, discussed in Chapter 2, developed design guidance to aid industry in the safe design of hot on-bottom pipelines susceptible to buckling. A key component to the design approach is to simplify the design by considering only an isolated buckle between virtual anchor points. When a pipeline buckles to relieve axial stress, the mid-point between two buckles is called a virtual anchor as it is about this point which the direction of axial strain changes from feeding in to one buckle to the next. This methodology is called VAS Analysis (Virtual Anchor Spacing Analysis). The design approach is centred around the Characteristic VAS which sets the maximum expected spacing along the pipe. Characteristic VAS is compared to the Tolerable VAS which is the point as which one of the design limit states is exceeded (Bruton and Carr, 2011).

Buckle formation depends on initial conditions such as out-of-straightness (OoS), modelled in the present analyses as the initially imperfectly straight pipe geometry, and lateral resistance. Closer VAS spacing implies less severe buckles but also reduces the likelihood of buckles forming at all so buckles may not form as intended. The SAFEBUCK JIP developed a probabilistic model (Cosham *et al*., 2009) to define an acceptable level of reliability for buckle formation and relies on the deployment of triggers to initiate buckling. Such triggers, discussed

in Chapter 2, include snake-lay, sinusoidal as-laid pipe geometry, sleepers to cause a vertical upset, or buoyancy modules to cause localised weight reduction.

It is anticipated that the manipulation of the pipe-soil residual friction coefficient through selection of an appropriate coating technology would be an additional tool available to pipeline engineers to trigger (or prevent) buckling and control pipeline VAS. Using enhanced texture pipe coating technologies ought to reduce installation costs as additional seabed infrastructure would no longer be required. It is envisaged the process of texturing coatings could be achieved on-shore prior to deployment or through a device onboard the vessel as the pipe is being laid.

7.9 Conclusions

This chapter has presented some numerical analyses of a 4880 m long pipeline laid on a hard, flat seabed, with pipe-soil interaction modelled through a combination of penalty friction and nonlinear springs to represent residual friction and passive soil resistance, respectively. The analyses were benchmarked against existing work in the literature adopting an analogous approach and the work here was able to replicate their results. Additional analysis was undertaken to investigate the impact of varying the residual pipe-soil friction coefficient according to the experimental results presented earlier in this thesis. Adopting a simple residual friction coefficient of varying magnitudes corresponding varied the pipeline buckling response, with greater friction leading to reduced pipe end expansion and buckle magnitudes but with greater curvature and axial strains experienced by the pipe.

Analyses were also undertaken where the pipeline residual friction was varied differentially along the pipe. The first approach enhanced the friction at pipe ends and additional iterations increased the proportion of pipeline with enhanced friction. The result was that the amplitude and wavelength of the single central buckle that formed was lessened but resulted in increased curvature and axial strain. However, if buckling was not the primary concern, but rather end expansion, the initial approach of enhancing the residual friction at just the pipe ends was able to reduce end expansion by nearly 44%.

The second approach to differential friction was to adopt a patterned approach where residual friction increased and decreased along the pipe. The result was that buckles were encouraged to form in areas of low friction (which reduced the local critical buckling threshold) and could influence the distribution of buckles. Such techniques could be used to encourage buckling away from areas where there would be a detrimental impact on the pipeline or adjacent infrastructure without recourse to additional measures like rock dump or concrete mattresses. Further benefit of pushing buckles closer to the pipe ends is that the buckle feed-

in reduces the length of pipe available for end expansion, with larger buckles drawing in more pipe.

It is anticipated that the manipulation of pipe-soil residual friction could be a viable technique for controlling the virtual anchor spacing that forms a central part of the SAFEBUCK Design Guidance for design of hot on-bottom pipelines. In addition to triggering buckling, such techniques can also be used to retard end expansion and may be effective in mitigating pipeline walking phenomena though this would be a topic for further research.

8 Conclusions

A wide-ranging campaign of experimental investigation and numerical analysis has been undertaken to understand the interface shear response of rigid polypropylene surfaces and granular soils and assess their design implications. Variables that have been investigated include soil grading and coarse fraction, density, surface texture, and stress level. Additional avenues of investigation included evolution of the surface texture during shearing, cyclic shear response, and the most appropriate methodology for determining surface texture parameters in this application. A study was also made into the impact on global pipeline stability of using enhanced surface textures, and a relationship defined to enable prediction of polypropylene interface shear strength with surface texture and stress level.

8.1 Profilometry

Two methods of measuring surface texture have been evaluated in this thesis. Contact methods, which make use of a stylus that traverses the surface and which is commonly used in industry, and a non-contact method using light and focal length variation. With relatively soft surfaces such as polypropylene, it was conjectured that a diamond tipped stylus might cause some indentation and under-measure asperities leading to a suppressed surface texture parameter value. It has been shown in this work that such a suspicion was valid as results from non-contact profilometry were approximately double that of the contact method on smooth surfaces. The recommendation is that with surfaces that are prone to indentation and damage, non-contact methods are better suited to obtaining reliable measurements.

8.2 Surface evolution

With surface topography characterised according to traditional components of roughness, waviness, and form, it has been demonstrated that wear caused by a single interface test did not change the surface texture parameter more than the variability already within specimens of pipeline coating material. The exception was the roughness parameter perpendicular to shear direction, suggesting that surface damage had been caused in the direction of shearing. The change in surface roughness was influenced only by increasing stress level.

In spite of evidence that interface shearing causes damage to surfaces, cyclic testing reaching up to at least 1000 mm of cumulative displacement did not precipitate a trend of progressively increasing interface strength for pipe coating specimens. It was conjectured that grains were causing localised smoothening leading to an overall reduction in strength. Reduced strength was also likely caused as the formation of wear scars gradually removed

material which increased the contact-area at the particle-surface interface leading to a reduction in contact stress. Upon resetting and preparing a fresh soil sample on the used surface, interface strengths were significantly enhanced, perhaps in response to the new overall rougher surface.

For the limited number of tests on enhanced texture surfaces, the more highly textured "S" surface also exhibited a trend for reducing shear strength with cycling, in contrast to the "E" surface which showed the opposite, with strengths increasing over cycling. In the case of "S" surfaces, when reloaded with a fresh sample, there was a subtle increase in strength similar to pipe coatings specimens. Reloading the "E" surface maintained the greater strength suggestive that the strength gain was not fleeting. Differences in the nature of the evolution of surface strength may be related to worked versus unworked polypropylene surfaces.

8.3 Surface texture characterisation

Due to the high bandwidth of topography features seen on surfaces used in this work, particularly where surfaces had enhanced textures, and the meshing relationship between soil and surface, traditional approaches of defining roughness, waviness, and form components in isolation were not appropriate. Therefore, a novel methodology was proposed that determined the appropriate surface texture parameter by setting the long-wavelength filter, L_c, to be equal to the D_{50} of the soil at the interface of interest. This procedure recognised the interaction and meshing of grains and surface texture and addressed the issue of appropriate scales of interaction during shearing. In addition, relative texture parameters (texture divided by soil D_{50}) were used to account for the interaction between grains and surface texture and determine the effective surface texture. Combined, these two methodologies result in a surface texture value that is unique to a given soil-surface combination and can be easily determined through existing laboratory techniques already widely used in industry and academia.

8.4 Interface shear response

A large number of interface tests were carried out and a number of parameters influenced the nature of the shear response and the measured shear strength.

Density

A trend throughout the data is that the mobilised ultimate shear strength is influenced by the density of the soil sample. Greater density leads to a noticeably greater shear strength which is a consistent feature of interface testing in the literature and is independent of other variables

tested here. The average difference between loose and dense ultimate strengths across the soil only tests is 0.3% but this rises to 10% in the interface tests though there is a significant variability and a wide range. Considered in terms of interface efficiency the trend is the same, with greater strength for dense over loose tests averaging 9.5%.

Stress level

In common with other granular geomaterials, the strength envelopes of sand-polypropylene interfaces are nonlinear. There is a significant increase in shear strength at very low stress level which is independent of other variables tested here. There is significant variability according to soil type and density but across each of these variables across all tests, the strength at 2 kPa normal stress is between 7.3 and 36.6% greater than at 20 kPa. The average value across all tests is 16.1%.

Soil grading

Increasing coarse fraction has the effect of slightly increasing the shear strength of soil. The same is true when considering the interface shear strength with the same soils. However, the soils tested here with enhanced coarse fractions also had a slightly larger D_{50} as a result, so the conflicting effect of reducing relative roughness and increasing coarse fraction may somewhat obscure any trends and underestimate the strength enhancement from coarser fractions.

Surface texture

Surface texture has the most dominant role in prescribing interface shear response within the scope of this work. The nature of the shear response changes from elastic-perfectly plastic with smooth surfaces to elastoplastic on more textured surfaces. Coincident with this evolution in shear response is the transition from non-dilative behaviour (regardless of density) to fully stress-dilatant behaviour for dense samples and sample contraction of loose samples. A modified version of Bolton's (1986) empirical flow rule satisfactorily describes the relationship between peak dilatancy and peak interface shear strength of dilatant surfaces at the stress levels investigated here (*Eq.8.1)*:

$$\delta_{peak} = \delta_{ult} + 0.55 \cdot \zeta_{peak} \qquad Eq.8.1$$

Similarly, there is a reasonable similarity to the interface flow rule of Lings and Dietz (2005). The contribution of dilatancy to peak strength varies slightly from steel interfaces but matches the relationship identified for soil in this work at the same stress levels. A possible explanation for the difference from steel behaviour is related to the relative softness of polypropylene which

encourages a greater degree of ploughing rather than sliding. More ploughing increases the underlying shear resistance such that dilatancy forms only a smaller part of the extra peak strength seen in dense tests. A further consideration is that the relationship between ultimate and peak strengths and dilatancy is known to become less reliable at very low stress levels.

As the surface changes from very smooth to highly textured, greater ultimate shear strengths are mobilised and peak strengths are increasingly mobilised as the surface texture becomes sufficient to engender dilatant behaviour. As the interface efficiency approaches 1.0 there is a diminishing increase in shear strength with any additional texture. Consistent with the literature in this area, reaching parity with the equivalent soil-only shear strength seems to impose an upper limit on interface shear strength of surfaces with randomised, non-structured, texture.

8.5 Predicting polypropylene interface friction

A relationship was identified between the relative texture of rigid polypropylene surfaces and interface friction coefficient. The relationship is assumed to be valid within the range of parameters tested in this thesis with a fixed upper bound at a relative texture of 0.025 at which point interface efficiency is assumed to be close to 1.0. Beyond this point no further increase in strength is expected without exploring structured surface textures making use of passive resistance features. The lower bound of the relationship identified here is at relative texture of $5x10^{-5}$. It is anticipated that the relationship holds for surfaces smoother than this but they have not been investigated here and likely fall outside the range applicable to most uses of rigid polypropylene coatings. The relationship varies also according to stress level due to the nonlinearity of interface strength envelopes in the range of stress levels investigated. The relationship is presented here again:

$$\mu = a \cdot \left(\frac{T_a}{D_{50}}\right)^b + c \cdot \left(\frac{\sigma_n}{\sigma_f}\right)^d + e \qquad Eq.8.2$$

Table 8.1 Coefficients and terms for interface strength roughness relationship

Coefficient	*Description*
μ	Interface friction coefficient
T_a	Average texture
D_{50}	Mean average grain size
σ_n	Normal stress
σ_f	1 kPa
a	2.40
b	0.45
c	0.25
d	-0.55
e	0.10

8.6 Pipeline global stability

A numerical analysis was undertaken to investigate the impact of interface friction coefficient regimes on global pipeline stability. The scope of the numerical modelling was narrow and limited to a single pipe of approximately 5 km length with a simplified seabed model and pipe-soil interaction model comprising contact friction penalty to model residual pipe-soil friction and nonlinear springs to model passive resistance and breakout.

The first series of analyses benchmarked the study against an existing study in the literature and gave results with excellent agreement across all measured parameters. Three geometries, perfectly straight, imperfectly straight, and perfectly pre-deformed, were tested with varying residual friction coefficients. The results showed that increasing residual friction lead to increased effective axial force but also reduced buckle amplitudes and wavelengths but with greater curvature and axial strains. End expansion was also reduced.

A second series of analyses was carried out where the proportion of the pipeline with enhanced residual friction (passive resistance was kept constant throughout) was incrementally increased to observe the effect on stability parameters such as buckle distribution, buckle magnitude, curvature, axial strain, and axial displacement at pipe ends. It was found that enhanced friction at just the pipe ends, with the remainder still under low friction conditions was able to reduce end expansion by over 40%.

A third series of analyses varied the distribution and proportion of enhanced friction along the pipe with five different regimes tested. It was found that positioning of higher friction sections could encourage formation of buckles away from certain areas and that provoking formation of buckles close to pipe ends could be effective in curtailing end expansion.

Manipulation of pipe-soil residual friction by specifying and manufacturing textured coatings has the potential to be a useful tool for pipeline engineers and designers.

8.7 Suggestions for further work

The trends and relationships revealed in this work have been illuminating but a number of avenues for further and future work have presented themselves. At a fundamental level it must be acknowledged that the relationship identified in this thesis was determined with sands of a narrow grading and that soils that are more widely – or gap – graded may have a different form. Similarly, soil grain angularity has not been considered and the lessons of Hostun Sand suggest that angularity is likely to play a role also. It is well known that surface hardness also has a large impact on interface friction. The fluids carried by pipelines can be in excess of 150°C, even as high as 200°C, and it seems likely that the external surfaces of some pipelines may experience elevated temperatures. Greater temperatures lower the hardness of polypropylene (and other polymers) so it is conceivable that the surface hardness, and therefore interface friction, may vary according to the pipe's external temperature. From an experimental perspective temperature effects on interface shear response, effect of soil grading on the interface strength to surface texture relationship and confirming the relationship with hardness by testing of other polymers with enhanced textures, are all avenues for further investigation. Some work in this area exists already (e.g. Bilgin and Stewart, 2009; Frost and Karademir, 2016) lending credence to the problem.

It should be recognised that although the direct shear apparatus is widely used for testing of interfaces, it is not an ideal representation of pipe-soil interfaces. Surface specimens in the direct shear apparatus are flat which does not reflect the true curvature seen in real applications. Work is already underway at University of Bristol to address this concern with the construction of the Experimental Pipe-Soil Interaction Testing Apparatus (ExψTA), pictured in Figure 7.10. This apparatus operates like a large scale shearbox where a real scale pipe section takes the place of the upper shearbox half. In this way the apparatus can measure the effective interface friction of pipes with realistic curvature and embedment at up to real scale.

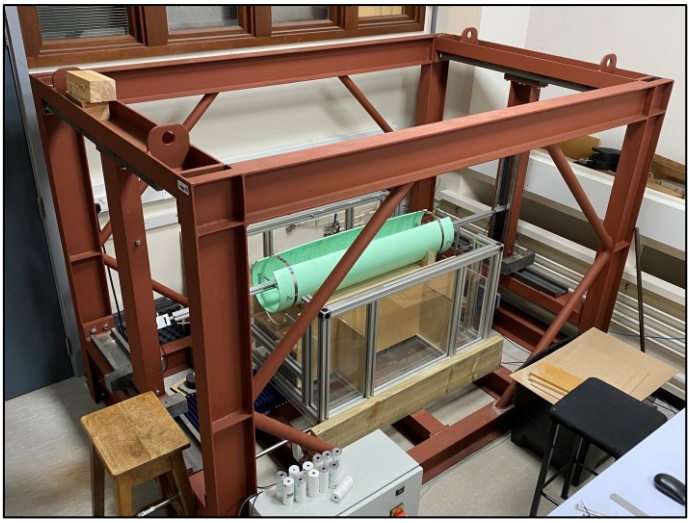

Figure 8.1 Experimental Pipe-Soil Interaction Testing Apparatus (ExψTA) designed and built at University of Bristol.

8.8 Concluding remarks

This thesis set out to comprehensively investigate the interface shear response of rigid polypropylene pipeline coatings at element level in the laboratory using equipment specifically designed to obtain the best possible quality data. It has been shown that the nature of polypropylene interface shear response with granular soils can be predicted and the body of data generated neatly compliments the existing literature. The ability to modify the interface friction coefficient and thereby influence the nature of pipeline global stability phenomena may be an attractive possibility in the field of pipeline engineering and it is hoped the work here will prove useful.

References

Acer, Y.B., Durgunoglu, H.T., Tumay, M.T. 1982. Interface properties of sand. *Journal of Geotechnical Engineering*, ASCE, 108 (4), pp.648-654.

Adamson, A.W. 1982. *Physical chemistry of surfaces*. Wiley, New York, USA.

Afzali-Nejad, A., Lashkari, A., Shourijeh, P.T. 2017. Influence of particle shape on the shear strength of sand-woven geotextile interfaces. *Geotextiles and Geomembranes*, 45 (1), pp.54-66.

Al-Douri, R.H., Poulos, H.G. 1992. Static and cyclic direct shear tests on carbonate sands. *Geotechnical Testing Journal*, 15 (2), pp.138-157.

Andrew Palmer and Associates, 1995. PlusOne Version 4.1 – Modelling of upheaval buckling of buried/trenched pipelines – Theoretical Manual, SAIC Ltd. London, England.

Ansari, Y., Kouretzis, G.P., Sheng, D. 2014. An effective stress analysis of partially embedded offshore pipelines: vertical penetration and axial walking. *Computers and Geotechnics*, 58, pp.69-80.

Bilgin, O., Stewart, H.E. 2009. Design guidelines for polyethylene pipe interface shear resistance. *Journal of Geotechnical and Geoenvironmental Engineering*, 135 (6), pp.809-818.

Bishop, A.W., Green, G.E., Gargo, V.K., Andersen, A., Brown, J.D. 1971. A new ring shear apparatus and its application to the measurement of residual strength. *Géotechnique*, 21 (2), pp.273-328.

Boëda, É., Bonilauri, S., Connan, J., Jarvie, D., Mercier, N., Tobey, M., Valladas, H., Sakhel, H.A. 2008. New evidence for significant use of bitumen in Middle Palaeolithic technical systems at Umm el Tlel (Syria) around 70,000 BP. *Paléorient*, 34 (2), pp.67-83.

Bolton, M.D. 1986. The strength and dilatancy of sands. *Géotechnique*, 2 (2), pp.113-116.

Bolton, M.D. 1991. *A Guide to Soil Mechanics*. Cambridge, United Kingdom.

Boukpeti, N., White, D.J. 2017. Interface shear box tests for assessing axial pipe-soil resistance. *Géotechnique*, 67 (1), pp.18-30.

Bowden, F.P., Tabor, D. 1956. *Friction and lubrication*. Methuen, London, United Kingdom.

Bransby, M.F., Ireland, J. 2009. Rate effects during pipeline upheaval buckling in sand. *Proceedings of the Instituion of Civil Engineers: Geotechnical Engineering*, 162 (5), pp.247-256.

Brennodden, H. Lieng, J.T., Sotberg, T., Verley, R.L.P. 1989. An energy-based pipe-soil interaction model. In: *Proceedings of the Offshore Technology Conference*, Houston, Texas, USA.

Brennodden, H. Sveggen, D.A., Murff, J.D. 1986. Full-scale pipe-soil interaction tests. In: *Proceedings of the Offshore Technology Conference*, Houston, Texas, USA

Briscoe, B.J. 1992. Friction of organic polymers. *Fundamentals of friction: Macroscopic and microscopic processes*. I.L. Springs & H.M. Pollock (eds), Kluwer, Dordrecht, The Netherlands, pp.209-225.

Bromhead, E.N. 1979. A simple ring shear apparatus. *Ground Engineering*, 12 (5), pp.40-44.

Bruton, D.A.S., Carr, M. 2011. Overview of the SAFEBUCK JIP. In: *Offshore Technology Conference*, Houston, Texas, USA.

Bruton, D.A.S., Carr, M., Crawford, M., Poiate, E. 2005. The safe design of hot on-bottom pipelines with lateral buckling using the design guidance developed by the SAFEBUCK joint industry project. In: *Deep Offshore Technology Conference*, Vitoria, Brazil, pp.1-26.

Bruton, D.A.S., Carr, M., Sinclair, F. 2011. Geotechnical challenges for deepwater pipeline design – SAFEBUCK JIP. *Frontiers in Offshore Geotechnics*. Gourvenec & White (eds), London

Bruton, D.A.S., Carr, M., White, D.J. 2007. The influence of pipe-soil interaction on lateral buckling and walking of pipelines – the SAFEBUCK JIP. In: *Proceedings of the 6th International Offshore Site Investigation and Geotechnics Conference: Confronting New Challenges and Sharing Knowledge*, London, United Kingdom.

Bruton, D.A.S., White, D.J., Cheuk, J.C.Y. 2008. Pipe-soil interaction during lateral buckling and pipeline walking – the SAFEBUCK JIP. In: *Proceedings of the Offshore Technology Conference,* Houston, Texas, USA.

Bruton, D., White, D., Cheuk, C., Bolton, M., Carr, M., 2006. Pipe-soil interaction behavior during lateral buckling, including large-amplitude cyclic displacement tests by the SAFEBUCK JIP. *Offshore Technology Conference*. Houston, Texas, USA.

Bruton D., White D. J., Langford T. L., Hill A. 2009. Techniques for the assessment of pipe–soil interaction forces for future deepwater developments. In: *Proceedings of the Offshore Technology Conference*, Houston, Texas, USA.

BSI, 1990a. BS1377-2:1990 Methods of test for soils for civil engineering purposes - part 2: classification tests. *British Standards Institute*, London, United Kingdom.

BSI, 1990b. BS1377-4:1990 Methods of test for soils for civil engineering purposes - part 4: compaction related tests. *British Standards Institute*, London, United Kingdom.

BSI, 2016. PD8010-2:2015+A1:2016. Pipeline systems – part 2: Subsea pipelines - code of practice. *British Standards Institute*, London, United Kingdom.

Butterfield, R., Andrawes, K.Z. 1972. On the angles of friction between sand and plane surfaces. *Journal of Terramechanics*, 8(4), pp.15-23.

Carr, M., Bruton, D., Leslie, D. 2003. Lateral buckling and pipeline walking, a challenge for hot pipelines. In: *Proceedings of the Offshore Pipeline Technology Conference*, Amsterdam, The Netherlands, pp.1-36.

Cathie, D.N., Jaeck, C., Ballard, J.C., Wintgens, J.F. 2005. Pipeline geotechnics – state-of-the-art. In: *Proceedings of the International Symposium on the Frontiers in Offshore Geotechnics,* Perth, Australia, pp.95-114.

Chakraborty, T., Salgado, R., 2010. Dilatancy and shear strength of sand at low confining pressures. *Journal of Geotechnical and Geoenvironmental Engineering*, 136 (3), pp.527-532.

Chee, J., Walker, A., White, D. 2018. Controlling lateral buckling of subsea pipeline with sinusoidal shape pre-deformation. *Ocean Engineering*, 151, pp.170-190.

Cheuk, C.Y., Take, W.A., Bolton, M.D., Oliveira, J.R.M.S. 2006. Soil restraint on buckling oil and gas pipelines buried in lumpy clay fill. *Engineering Structures*, 29, pp.973-982.

Cheuk, C.Y., White, D.J., Dingle, H.R.C. 2008. Upper bound plasticity analysis of a partially-embedded pipe under combined vertical and horizontal loading. *Soils and Foundations*, 48 (1), pp.133-140.

Choi, H-S.,Do, C-H.,Young-Jang, N. 2010. Expansion spool design of an offshore pipeline by the slope deflection method. *Journal of Ocean Engineering and Technology*, 24 (5), pp.1-7.

Cole, E.R. 1967. *The behaviour of soil in the simple shear apparatus*. PhD thesis, University of Cambridge, United Kingdom.

Connolly, G., Gaiilard, G., Provou, Y. 1989. Three-layer epoxy-polypropylene pipe coatings for use at elevated surface temperatures. In: *Internal and External Protection of Pipes – Proceedings of the 8th International Conference*, pp.179-188.

Conroy, M., Armstrong, J. 2005. A comparison of surface metrology techniques. In: *Journal of Physics: Conference Series*, 13 (1), p.458. IOP Publishing.

Cosham, A., Carr, M., Bruton, D.A.S., Leslie, D. The reliable initiation of lateral buckles – SAFEBUCK JIP. *SUT Annual Conference*, Perth, Australia.

Cumming, G., Druzynski, A., Rathbone, A. 2009. Lateral walking and feed-in of buckled pipelines due to interaction of seabed features. In: *Proceedings of the ASME 28th International Conference on Ocean, Offshore, and Arctic Engineering*, Honolulu, Hawaii, USA.

Cumming, G., Rathbone, A. 2010. Euler buckling of idealized horizontal pipeline imperfections. In: *Proceedings of the ASME 29th International Conference on Ocean, Offshore, and Arctic Engineering*, Shanghai, China.

Daiyan, N., Kenny, S., Phillips, R., Popescu, R. 2011. Investigating pipeline-soil interaction under axial-lateral relative movements in sand. *Canadian Geotechnical Journal*, 48, pp.1683-1695.

Davis, E.R. 1967. Theories of plasticity and the failure of soil mases. In: *Soil Mechanics: Selected topics*, Ed I.K. Lee, Butterworth, London, pp.341-380.

De Brier, C., Ballard, J-C., Coliard, D. 2016. On the added value of advanced interface shear testing for pipeline walking mitigation. In: *Proceedings of the Offshore Technology Conference*, Amsterdam, The Netherlands.

DeJong, J.T., Frost, J.D. 2002. A multi-function sleeve attachment for the cone penetrometer. *Geotechnical Testing Journal*, 25 (2), pp.111-127.

DeJong, J.T., Frost, J.D., Saussus, D.R. 2002. Measurement of relative surface roughness at particulate-continuum interfaces. *Journal of Testing and Evaluation*, 30 (1), pp.8-19.

DeJong, J.T., Randolph, M.F., White, D.J. 2003. Interface load transfer degradation during cyclic loading: a microscale investigation. *Soils and Foundations,* 43 (4), pp.81-93.

DNV, 2013. Offshore Standard DNV-OS-F101 Submarine Pipeline Systems. Det Norske Veritas, Oslo, Norway.

DNVGL, 2017a. Recommended Practice DNV-RP-F109 On-bottom stability design of submarine pipelines. DNVGL AS, Oslo, Norway.

DNVGL, 2017b. Recommended Practice DNV-RP-F114 Pipe-soil interaction for submarine pipelines. DNVGL AS, Oslo, Norway.

Dhondt, G, 2014. *Calculix CrunchiX USER'S MANUAL version 2.7*. Available online: http://web.mit.edu/calculix_v2.7/CalculiX/ccx_2.7/doc/ccx/ccx.html [Accessed 25th July 2020].

Dietz, M.S. 2000. *Developing an holistic understanding of interface friction using sand within the direct shear apparatus*. PhD thesis, University of Bristol, United Kingdom.

Dietz, M.S., Lings, M.L. 2006. Postpeak strength of interfaces in a stress-dilatancy framework. *Journal of Geotechnical and Geoenvironmental Engineering*, 132, pp.1474-84.

Dingle, H.R.C., White, D.J., Gaudin, C. 2008. Mechanisms of pipe embedment and lateral breakout on soft clay. *Canadian Geotechnical Journal*, 45 (5), pp.636-652.

Dove, J.E., Frost, J.D. 1999. Peak friction behavior of smooth geomembrane-particle interfaces. *Journal of Geotechnical and Geoenvironmental Engineering*, 125 (7), pp.544-555.

Dove, J.E., Frost, J.D., Han, J., Bachus, R.C. 1997. The influence of geomembrane surface roughness on interface strength. In: *Proceedings of the Geosynthetic Institute*, 97 (1), pp.863-876.

Dove, J.E., Jarrett, J.B. 2002. Behaviour of dilative sand interfaces in a geotribology framework. *Journal of Geotechnical and Geoenvironmental Engineering*, 128 (1), pp.25-37.

Dove, J.E., Bents, D.D., Wang, J., Gao, B. 2006. Particle-scale surface interactions of non-dilative interface systems. *Geotextiles and Geomembranes*, 24 (3), pp.156-168.

Draper, S., Griffiths, T., Cheng, L., White, D., An, H. 2018. Modelling changes to submarine pipeline embedment and stability due to pipeline scour. In: *Proceedings of the ASME 2018 37th International Conference on Ocean, Offshore and Arctic Engineering*, Madrid, Spain.

Dyer, M.R. 1986. *Observation of the stress distribution in crushed glass with applications to soil reinforcement*. DPhil thesis, University of Oxford, United Kingdom

Fakharian, K., Evgin, E. 1997. Cyclic simple-shear behaviour of sand-steel interfaces under constant normal stiffness condition. *Journal of Geotechnical and Geoenvironmental Engineering*, 123 (12), pp.1096-1105.

Fannin, R.J., Eliadorani, A., Wilkinson, J.M.T. 2005. Shear strength of cohesionless soils at low stress. *Géotechnique*, 55 (6), pp.467-478.

Finch, M., Fisher, R., Palmer, A., Baumgard, A. 2000. An integrated approach to pipeline burial in the 21st century. *Deep Offshore Technology*.

Foray, P.Y., Colliat, J.Y., Nauroy, J.F. 1993. Bearing capacity of driven model piles in dense sands from calibration chamber tests. In: *Offshore Technology Conference*, Houston, Texas, USA.

Frost, J.D., DeJong, J.T. 2001. A new multi-friction sleeve attachment. In: *Proceedings of the 15th International Conference on Soil Mechanics and Geotechnical Engineering*, Vol. 1, Istanbul, Turkey.

Frost, J.D., DeJong, J.T., Recalde, M. 2002. Shear failure behavior of granular-continuum interfaces. *Engineering Fracture Mechanics*, 69, pp.2029-2048.

Frost, J.D., DeJong, J.T. 2005. In situ assessment of the role of surface roughness on interface response. *Journal of Geotechnical and Geoenvironmental Engineering*, 131 (4), pp.498-511.

Frost, J.D., Karademir, T. 2016. Shear-induced changes in smooth geomembrane surface topography at different ambient temperatures. *Geosynthetics International*, 23 (2), pp.113-128.

Fyrileiv, O., Collberg, L. 2005. Influence of pressure in pipeline design: effective axial force. In: *Proceedings of the ASME 2005 24th International Conference on Offshore Mechanics and Arctic Engineering*, Halkidiki, Greece, pp.629-636.

Ganesan, S., Kuo, M., Bolton, M.D. 2013. Influences on pipelines interface friction measured in direct shear tests. *Geotechnical Testing Journal*, 37 (1), pp.14.

Gilboy, G. 1936. Improved soil testing methods. *Engineering News Record*, 21.

Golder, H. Q. 1942. An apparatus for measuring the shear strength of soils. *Engineering*, 153, pp.501-503.

Griffiths, T., Draper, S., White, D., Cheng, L., An, H., Fogliana, A. 2018. Improved stability design of subsea pipelines on mobile seabeds: Learnings from the STABLEpipe JIP. In: *Proceedings of the ASME 2018 37th International Conference on Ocean, Offshore and Arctic Engineering*. Madrid, Spain.

Griffiths, T.J., White, D.J., Cheng, L. 2010. Progress in investigating pipe-soil-fluid interaction: The STABLEPIPE JIP. In: *Proceedings of the Twentieth (2010) International Offshore and Polar Engineering Conference*. International Society of Offshore and Polar Engineers.

Gudehus, G., Tejchman, J. 1988. Discussion. *Soils and Foundations*, 28 (3), pp.178-182.

Guidetti, G.P., Rigosi, G.L., Marzola, R. 1996. The use of polypropylene in pipeline coatings. *Progress in Organic Coatings*, 27, pp.79-85.

Hansen, J.B. 1970. A revised and extended formula for bearing capacity. Danish Geotechnical Institute, Lynby, Denmark.

Head, K. H. 1982. Manual of soil laboratory testing - Volume 2: Permeability, shear strength and compressibility tests. Pentech Press, London

Hebeler, G.L., Martinez, A., Frost, J.D. 2015. Shear zone evolution of granular soils in contact with conventional and textured CPT friction sleeves. *KSCE Journal of Civil Engineering*, 20 (4), pp.1267-1282.

Hill, A.J., White, D.J., Bruton, D.A.S., Langford, R., Meyer, V., Jewell, R., Ballard, J-C. 2012. A new framework for axial pipe-soil resistance, illustrated by a range of marine clay datasets. In: *Offshore Site Investigation and Geotechnics: Integrated Technologies – Present and Future*, London, United Kingdom

Hirsch, J.R., Wang, P.T. 1991. Texture and strength evolution in deformed polypropylene. *Texture Stress and Microstructure*, 13 (2), pp.101-122.

Hobbs, R.E. 1981. Pipeline buckling caused by axial loads. *Journal of Constructional Steel Research*. 1 (2), pp.2-10.

Hobbs, R.E. 1984. In-service buckling of heated pipelines. *Journal of Transport Engineering*, 110 (2), pp.175-189.

Hobbs, R.E., Liang, F. 1989. Thermal buckling of pipelines close to restraints. In: *Proceedings of the 8th International Conference on Offshore Mechanics and Arctic Engineering*, The Hague, The Netherlands.

Hodder, M.S., Cassidy, M.J. 2010. A plasticity model for predicting the vertical and lateral behaviour of pipelines in clay soils. *Géotechnique*, 60 (4), pp.247-263.

Houhou, R., Mjahed, R.B., Sadek, S., Najjar, S.S. 2020. Drained interface strength between pipelines and clays using tilt table and direct shear tests. In: *GeoCongress 2020: Geo-Systems, Sustainability, Geoenvironmental Engineering, and Unsaturated Soil Mechanics*, Reston, Virginia, USA.

Hryciw, R.D., Irsyam, M. 1993. Behaviour of sand particles around rigid ribbed inclusions during shear. *Soils and Foundations*, 33 (3), pp.1-13.

Hungr, O., Morgenstern, N.R. 1984. High velocity ring shear tests on sand. *Géotechnique*, 34 (3), pp.415-421.

Hvorslev, M.J., 1939. Torsion shear tests and their place in the determination of the shearing resistance of soils. In *Proceedings of the American Society of Testing Materials*, 39, pp.999.

Ibraim, E., Fourmont, S. 2007. Behaviour of sand reinforced with fibres. In: *Soil stress-strain behaviour: Measurement, modeling and analysis*. Springer, Dordrecht.

Ingold, T.S. 1982. Some observations on the laboratory measurement of soil-geotexile bond. *Geotechnical Testing Journal,* 5 (3/4), pp.51-67.

Irsyam, M., Hryciw, R.D. 1991. Friction and passive resistance in soil reinforced by plane ribbed inclusions. *Géotechnique,* 41 (4), pp.485-498.

Işık, A., Gürbüz, A. 2018. Assessment of behaviour of soil-geocell pullout capacity. In: *11th International Conference on Geosynthetics*, Seoul, Korea.

ISO, EN. 1998. 4288 – Geometrical Product Specifications (GPS) – Surface texture: profile methods – rules and procedures for the assessment of surface texture. *International Organisation for Standardisation: Geneva, Switzerland*.

Jardine, R.J., Lehane, B.M., Everton, S.J. 1993. Friction coefficients for piles in sands and silts. In: *Offshore Site Investigation and Foundation Behaviour* (pp. 661-677). Springer, Dordrecht.

Jewell, R.A. 1989. Direct shear tests on sand. *Géotechnique*, 39 (2), pp.25-37.

Jewell, R.A., Wroth, C.P. 1987. Direct shear tests on reinforced sand. *Géotechnique*, 37 (1), pp.53-68.

Jin, J., Audibert, J.M., Kan, W.C. 2010. Practical design process for flowlines with lateral buckling. In: *Proceedings of the ASME 29th International Conference on Ocean, Offshore and Arctic Engineering*, Shanghai, China.

Jukes, P. Eltaher, A., Sun, J. 2009. The latest developments in the design and simulation of deepwater subsea oil and gas pipelines using FEA. In: *Proceedings of the ISOPE 3rd International Deep-Ocean Technology Symposium: Deepwater Challenge*, pp. 70-82.

Jukes, P. Wang, S., Wang, J. 2008. The sequential reeling and lateral buckling simulation of pipe-in-pipe flowlines using finite element analysis for deep-water applications. In: *Proceedings of the 18th International Offshore (Ocean) and Polar Engineering Conference*.

Kelly, R.B., Byrne, B.W., Houlsby, G.T. 2004. Tensile loading of model caisson foundations for structures on sand. In: *The Fourteenth International Offshore and Polar Engineering Conference*, Toulon, France.

Kishida, H., Uesgui, M. 1987. Tests of the interface between sand and steel in the simple shear apparatus. *Géotechnique*, 37 (1), pp.45-52.

Klever, F.J., van Helvoirt, L.C., Sluyterman, A.C. 1990. A dedicated finite-element model for analysing upheaval buckling response of submarine pipelines. In: *Proceedings of the 22nd Annual Offshore Technology Conference*, Houston, Texas, USA, pp.529-538.

Kobayashi, M., Ando, H., Oguchi, N. 1995. Dependence of longitudinal subgrade reaction to buried pipe on displacement velocities and cycles of the ground. In: *Proceedings of the 6th US-Japan Workshop on Earthquake Disaster Prevention for Lifeline Systems*, pp.91-106.

Kuo, M. Y-H., Vincent, C.M., Bolton, M.D., Hill, A., Rattley, M. 2015. A new torsional shear device for pipeline interface shear testing. In: *Proceedings of the 3rd International Symposium on Frontiers in Offshore Geotechnics*, Oslo, Norway.

Kuwano, R. 1999. *The stiffness and yielding anisotropy of sand*. PhD thesis, Imperial College, London, United Kingdom.

Langford, T., Dyvik, R., Cleave, R. Offshore pipeline and riser geotechnical model testing: practice and interpretation. In: *ASME 2007 26th International Conference on Offshore Mechanics and Arctic Engineering,* San Diego, California, USA.

Lapidus, L., Pinder, G.F. *Numerical solution of partial differential equations in science and engineering*. John Wiley & Sons, New York, USA.

Leckie, S.H.F., Draper, S., White, D.J., Cheng, L., Fogliani, A. 2015. Lifelong embedment and spanning of a pipeline on a mobile seabed. *Coastal Engineering*, 95, pp.130-146.

Lee, D.H. 2013. 3-Dimensional profile distortion measured by stylus type surface profilometer. *Measurement*, 46 (1), pp.803-814.

Lehane, B.M., Jardine, R.J., Bond, A.J., Frank, R. 1993. Mechanisms of shaft friction in sand from instrumented pile tests. *Journal of Geotechnical Engineering*, 119 (1), pp.19-35.

Lemos, L.J.L. 1986. *The effect of rate of shear on residual strength of soil*. PhD Thesis, University of London, United Kingdom.

Lings, M.L., Dietz, M.S. 2004. An improved direct shear apparatus for sand. *Géotechnique*, 54, pp.467-478.

Lings, M.L., Dietz, M.S. 2005. The peak strength of sand-steel interfaces and the role of dilation. *Soils and Foundations*, 45, pp.1-14.

Liu, R., Xiong, H., Wu, X., Yan, S. 2014. Numerical studies on global buckling of subsea pipelines. *Ocean Engineering*, 78, pp.62-72.

Lopes, P.C., Lopes, M.L., Lopes, M.P. 2001. Shear behaviour of geosynthetics in the inclined plane test -influence of soil particle size and geosynthetic structure. *Geosynthetics International*, 8 (4), pp.327-342.

Lund, K.M. 2000. Effect of increase in pipe penetration from installation. In: *Proceedings of the 19th International Conference on Offshore Mechanics and Arctic Engineering*, New Orleans.

Lupini, J.F., Skinner, A.E., Vaughan, P.R. 1981.The drained residual strength of cohesive soils. *Géotechnique*, 31 (2), pp.181-213.

Martinez, A. 2015. *Multi-scale studies of particulate-continuum interface systems under axial and torsional loading conditions*. PhD Thesis, Georgia Institute of Technology, Georgia, USA.

Martinez, A. Frost, J.D., 2017. The influence of surface roughness form on the strength of sand–structure interfaces. *Géotechnique Letters*, *7* (1), pp.104-111.

Martinez, A., O'Hara, K.B., Sinha, S.K., Wilson, D., Ziotopoulou, K. 2019. Monotonic and cyclic centrifugre testing of snake skin-inspired piles. In: *Proceedings of the Biomediated and Bioinspired Geotechnics (B2G) Conference*, Atlanta, Georgia, USA.

Maugeri, L. 2006. *The Age of Oil: The Mythology, History, and Future of the World's Most Controversial Resource.* Greenwood Publishing Group.

McIntosh, J. 2008. The ancient Indus Valley: new perspectives. ABC-CLIO.

Merifield, R., White, D.J., Randolph, M.F. 2008. The ultimate undrained resistance of partially embedded pipelines. *Géotechnique*, 58 (6), pp.461-470.

Meyer, V.M., Dyvik, R., White, D.J. 2015. Direct shear interface tests for pipe-soil interaction assessment. In: *Frontiers in Offshore Geotechnics III*. Meyer (ed), London, United Kingdom, pp. 423-428.

Milewski, H., Dietz, M., Diambra, A., de Leeuw, L.W. 2019. Axial resistance of smooth polymer pipelines on sand. In: *Proceedings of the ASME 2019 38th International Conference on Ocean, Offshore and Arctic Engineering*, Glasgow, United Kingdom

Mirzaalimohammadi, A., Ghazavi, M., Roustaei, M., Lajevardi, S.H. 2019. Pullout response of strengthened geosynthetic interacting with fine sand. *Geotextiles and Geomembranes*, 47, pp.530-541.

Miura, S., Toki, S. 1982. A sample preparation method and its effect on static and deformation strength properties of sand. *Soils and Foundations*, 22, pp.61-77.

Miura, K., Maeda, K., Toki, S. 1997. Method of measurement for the angle of repose of sands. *Soils and Foundations*, 37, pp.89-96.

Mix, A.W., Giacomin, A.J. 2011. Standardized polymer durometry. *Journal of Testing and Evaluation*, 39 (4), pp.696-705

Mullilis, J.P., Chan, C.K., Seed, H.B. 1975. The effects of method of sample preparation on the cyclic stress-strain behaviour sands. *Report No. EERC 75-18*, Earthquake Engineering Research Centre, University of California, USA.

Murff, J.D., Wagner, D.A., Randolph, M.F., 1989. Pipe penetration in cohesive soil. *Géotechnique*, 39 (2), pp.213-229.

Najjar, S.S., Gilbert, R.B., Liedtke, E., McCarron, B., Young, A.G. 2007. Residual shear strength for interfaces between pipelines and clays at low effective normal stress. *Journal of Geotechnical and Geoenvironmental Engineering*, 133 (6), pp.695-706.

Nakamaru, S. Pradham, T.B.S., Fujitani, M. 1995. Strength and deformation properties of various sands in direct shear test. In: *Proceedings of the Symposium on Direct Shear Box Testing of Soils*, pp.111-118 (in Japanese).

Narejo, D.B. 2003. A simple tilt table device to measure index friction angle of geosynthetics. *Geotextiles and Geomembranes*, 21 (1), pp.49-57.

Nedderman, R.M., Laohakul, C. 1980. The thickness of the shear zone of flowing granular materials. *Powder Technology*, 25 (1), pp.91-100.

Negussey, D., Wijewickreme, W.K.D., Vaid, Y.P. 1989. Geomembrane interface friction. *Canadian Geotechnical Journal*, 26 (2), pp.165-169.

Nixon, J.F. 1994. PIPSOL, Stress analysis program for pipes subjected to ground displacements. Nixon Geotech Limited, Calgary, Canada.

Noorany, I. 1985. Side friction of piles in calcareous sands. In: *Proceedings of the 11th International Conference on Soil Mechanics and Foundation Engineering*, San Francisco, USA, pp.1611-1614.

Norbury, D. 2010. *Soil and Rock Description in Engineering Practice*. Whittles Publishing, Dunbeath, United Kingdom.

Nyman, K.J. 1984. Soil resistance against oblique motions of pipes. *ASCE Journal of Transportation Engineering*, 110 (2), pp.190-202.

Ooi, L.H., Carter, J.P. 1987. A constant normal stiffness direct shear device for static and cyclic loading. *Geotechnical Testing Journal*, 1 (10), pp.3-12.

O'Rourke, T.D., Druschel, S.J., Netravali, A.N. 1990. Shear strength characteristics of sand-polymer interfaces. *Journal of Geotechnical Engineering*, 116 (3), pp.451-469.

OSPAR, 2010. *Quality Status Report 2010*. Available online: http://qsr2010.ospar.org/en/index.html [Accessed 22nd October 2019].

Paikowsky, S.G., Player, C.M., Connors, P.J. 1995. A dual interface apparatus for testing unrestricted friction of a soil along solid surfaces. *Geotechnical Testing Journal*, 18 (2), pp.168-193.

Palmer, A.C., Steenfelt, J.S., Steensen-Bach, J.O., Jacobsen, V. 1988. Lateral resistance of marine pipelines on sand. In: *Proceedings of the Offshore Technology Conference*, Houston, Texas, USA.

Paramor, O.A.L., Allen, K.A., Aanesen, M., Armstrong, C., Hegland, T., Le Quesne, W., Piet, G.J., Raakær, J., Rogers, S., van Hal, R., van Hoof, L.J.W., van Overzee, H.M.J., Frid, C.L.J. 2009. MEFEPO North Sea Atlas. University of Liverpool, United Kingdom. ISBN 0906370604.

Pedersen, R.C.,Olsen, R.E., Rausch, A.F. 2003. Shear and interface strength of clay at very low effective stresses. *Geotechnical Testing Journal*, 26 (1), pp.71-78.

Perinet, D. Simon, J. 2011. Lateral buckling and pipeline walking mitigation in deep water. In: *Proceedings of the Offshore Technology Conference,* Houston, Texas, USA.

Porcino, D., Fioravante, V., Ghionna, V. N., Pedroni, S. 2003. Interface behaviour of sands from constant normal stiffness direct shear tests. *Geotechnical Testing Journal*, 26 (3), pp.289-301.

Potyondy, J.G. 1961. Skin friction between various soils and construction materials. *Géotechnique*, 11 (4), pp.339-353.

Psyrras, N., Kwon, O., Gerasimidis, S., Sextos, A. 2019. Can a buried gas pipelines experience local buckling during earthquake ground shaking? *Soil Dynamics and Earthquake Engineering*, 116, pp.511-529.

Psyrras, N., Sextos, A., Dietz, M., Mylonakis, G. 2020. Physical modelling of the seismic response of gas pipelines in laterally inhomogeneous soil. *Journal of Geotechnical and Geoenvironmental Engineering*, 146 (5).

Quinteros, S., Dyvik, R., Mortensen, N. 2017. Interface friction angle son-on-steel from ring shear tests on offshore North Sea sands. In: *Geotechnical Frontiers*, pp.258-367.

Ramsey, N., Jardine, R.J., Lehane, B., Ridley, A. 1998. A review of soil-steel interface testing with the ring shear apparatus. In: *Offshore Site Investigation and Foundation Behaviour*, Society of Underwater Technology, London, United Kingdom.

Randolph, M., Gourvenec, S. 2011. Pipeline and riser geotechnics. In: *Offshore Geotechnical Engineering*, Spon Press, Abingdon, Oxford, United Kingdom.

Randolph, M.F., White, D.J., Yan, Y. 2012. Modelling the axial soil resistance on deep-water pipelines. *Géotechnique*, 62 (9), pp.837-846.

Riks, E. 1979. An incremental approach to the solution of snapping and buckling problems. *International Journal of Solids and Structures*, 15 (7), pp.529-551.

Rowe, P.W. 1962. The stress dilatancy relation for static equilibrium of an assembly of particles in contact. *Proceedings of the Royal Society of London Series A*, 269, pp.500-527.

Rowe, P.W. 1969. The relation between the shear strength of sands in triaxial compression, plane strain and direct shear. *Géotechnique*, 19 (1), pp.75-86.

Saada, A. S., Townsend, F. C. 1981. State of the art: Laboratory strength testing of soils. *Laboratory shear strength of soil*, ASTM STP 740. R.N. Yong & F.C. Townsend (eds), pp.7-77.

Sagitaningrum, F.H.,Kamaruddin, S.A.,Nazir, R.,Soepandij, B.S.,Alatas, I.M. 2020. Soil-solid interface shear strength review and its possibility on interlayer slope stability analysis. In: *IOP Conference Series: Earth and Environmental Science*, 426 (1).

Sassa, K. 1985. The mechanism of debris flow. In: *Proceedings of the 11th International Conference on Soil Mechanics and Foundation Engineering*, San Francisco, California, USA.

Saxena, S.K., Wong, Y.T. 1984. Friction characteristics of a geomembrane. In: *Proceedings of the International Conference on Geomembranes*, Industrial Fabrics Association International, pp.187-190.

Schaminee, P.E.L., Zorn, N.F., Schotman, G.J.M. 1990. Soil response for pipeline upheaval buckling analyses: full-scale laboratory tests and modelling. *Offshore Technology Conference*, Houston, Texas, USA.

Schupp, J., Byrne, B.W., Eacott, N., Martin, C.M., Oliphant, J., Maconochie, A., Cathie, D. 2006. Pipeline unburial behaviour in loose sand. In: *Proceedings of the 25th International Conference on Offshore Mechanics and Arctic Engineering*, Hamburg, Germany

Seatools, 2020. *Subsea rock installation*. [Image] Available online: https://www.seatools.com/subsea-solutions/subsea-rock-installation/ [Accessed 12 June 2020].

Shadravan, A., Amani, M. 2012. HPHT 101 – What petroleum engineers and geoscientists should know about high pressure high temperature wells environment. *Energy Science and Technology*, 4 (2), pp.36-60.

Shibuya, S., Mitachi, T., Tamate, S. 1997. Interpretation of direct shear box testing of sands as quasi-simple shear. *Géotechnique,* 47 (4), pp.769–790.

Shooter, K.V., Tabor, D. 1952. The frictional properties of plastics. *Proceedings of the Physical Society – Section B*, 65, pp.661-671.

Simoni, A., Houlsby, G.T. 2006. The direct shear strength and dilatancy of sand-gravel mixtures. *Geotechnical & Geological Engineering*, 24 (3), pp.523.

Slade, A.L, Yip, C.M. 2005. Scanning probe microscopy – applications for the study of soft materials. In: *Molecular Interfacial Phenomena of Polymers and Biopolymers*, pp.161-213. Woodhead Publishing.

SPS, 2020. *Concrete Mattress Fleximats*. [Image] Available online: https://www.subseaprotectionsystems.co.uk/concrete-mattresses [Accessed 12 June 2020].

Stroud, M.A. 1971. *The behaviour of sand at low stress levels in the simple shear apparatus*. PhD thesis, University of Cambridge, United Kingom.

Structural Software Development Inc., 1981. PIPLIN-III Computer program for stress and deformation analysis of pipelines. Structural Software Developments Inc., Berkeley, California, USA.

Sture, S., Costes, N.C., Batiste, S.N., Lankton, M.R., AlShibli, K.A., Jeremic, B., Swanson, R.A., Frank, M. 1998. Mechanics of granular materials at low effective stresses. *Journal of Aerospace Engineering*, 11 (3), pp.67-72.

Stutz, H.H., Martinez, A., Heepe, L., Tramsen, H.T., Gorb, S.N. Strength anisotropy a soil-structure interfaces with snake skin inspired structural surfaces. In: *E3S Web of Conference*, Vol. 92, pp.13008. EDP Sciences.

Subba Rao, K.S., Allam, M.M., Robinson, R.G. 1998. Interfacial friction between sands and solid surfaces. *Proceedings of the Institution of Civil Engineers: Geotechnical Engineering*, 131 (2), pp.75-82.

Sun, J. Jukes, P., Kenny, W.G. 2011. The advancements of FEA in confronting the deepwater pipelines under high pressure and high temperature. In: *Proceedings of the Offshore Technology Conference*, Brazil.

Taylor, D.W. 1948. *Fundamentals of soil mechanics*. Wiley, New York.

Tika-Vassilikos, T. 1991. Clay-on-steel ring shear tests and their implications for displacement piles. *Geotechnical Testing Journal*, 14 (4), pp.457-463.

Tornes, K., Jury, J., Ose, B.A., Thompson, P. 2000. Axial creeping of high temperature flowlines caused by soil ratcheting. In: *Proceedings of the 19th International Conference on Offshore Mechanics and Arctic Engineering*, New Orleans, Louisiana, USA.

Uesugi, M., Kishida, H. 1986a. Influential factors of friction between steel and dry sands. *Soils and Foundations*, 26 (2), pp.33-46.

Uesugi, M., Kishida, H. 1986b. Frictional resistance at yield between dry sand and mild steel. *Soils and Foundations*, 26 (4), pp.139-149.

Vanden Berghe, J.F., Cathie, D., Ballard, J.C. 2005. Pipeling uplift mechanism using finite element analysis, *International Conference on Soil Mechanics and Foundation Engineering*, Osaka, Japan.

Verley, R., Lund, K.M., 1995. A soil resistance model for pipelines placed on clay soils. In: *Proceedings of the OMAE 1995 International Conference on Offshore Mechanics and Arctic Engineering*, Copenhagen, Denmark.

Verley, R.L.P., Sotberg, T., 1994. A soil resistance model for pipelines placed on sandy soils. *Journal of Offshore Mechanics and Arctic Engineering*, 116 (3), pp.145-153.

Wagner, D.A., Murff, J.D., Brennodden, H. 1987. Pipe-soil interaction model. In: *Proceedings of the Offshore Technology Conference*, Houston, Texas, USA, pp.181-190.

Wang, D., White, D.J., Randolph, M.F. 2010. Large deformation finite element analysis of pipe penetration and large-amplitude lateral displacement. *Canadian Geotechnical Journal*, 47, pp.842-856.

Wernick, E. 1979. A true direct shear apparatus to measure soil parameters of shear bands. In: *Proceedings of the 7th European Conference on Soil Mechanics and Foundation Engineering*, (2) Brighton, United Kingdom, pp.175-182

Westgate, Z.J., White, D.J., Savazzi, M. 2018. Experience with interface shear box testing for axial pipe-soil interaction assessment on soft clay. In: *Offshore Technology Conference*. Houston, Texas, USA.

White, D., Bruton, D.A., Bolton, M., Hill, A.J., Ballard, J.C., Langford, T. 2011. SAFEBUCK JIP – Observations of axial pipe-soil interaction from testing on soft natural clays. In: *Offshore Technology Conference*

White, D.J., Campbell, M., Boylan, N., Bransby, M.F. 2012. A new framework for axial pipe-soil resistance: illustrated by shearbox tests on carbonate soils. In: *Proceedings of the 8th International Conference on Offshore Site Investigation and Geotechnics*, London: Society for Underwater Technology.

White, D.J., Cathie, D.N. 2011. Geotechnics for subsea pipelines. In: *Frontiers in Offshore Geotechnics II*. Gourvenec & White (eds), Taylor & Francis Group, London, United Kingdom.

White, D.J., Cheuk, C.Y., Bolton, M.D. 2008. The uplift resistance of pipes and plate anchors buried in sand. *Géotechnique*, 58 (10), pp.771-779.

White, D.J., Dingle, H. 2011. The mechanism of steady friction between seabed pipelines and clay soils. *Géotechnique*, 61 (12), pp.1035-1041.

White, D.J., Gaudin, C. 2008. Simulation of seabed pipe-soil interaction using geotechnical centrifuge modelling. In: *Proceedings of the 1st Asia-Pacific Deep Offshore Technology Conference*, Perth, Australia.

White, D.J., Randolph, M.F. 2007. Seabed characterisation and models for pipeline-soil interaction. *International Journal of Offshore and Polar Engineering*, 17 (3), pp.193-204.

White, D.J., Take, W.A., Bolton, M.D., Munachen, S.E. 2001. A deformation measurement system for geotechnical testing based on digital imaging, close-range photogrammetry, and PIV image analysis. In: *Proceedings of the 15th International Conference on Soil Mechanics and Geotechnical Engineering*, Istanbul, Turkey.

Whitehouse, D.J. 2000. Stylus damage prevention index. *Proceedings of the Institution of Mechanical Engineers, Part C : Journal of Mechanical Engineering Science*, 214 (7), pp.975-980.

Williams, N.D., Houlihan, M.F. 1987. Evaluation of interface friction properties between geosynthetic and soils. In: *Proceedings of the 1987 Geosynthetic Conference*, Industrial Fabrics Association International, pp.616-627.

Wood, D.M. 1990. *Soil behaviour and critical state soil mechanics*. Cambridge University Press, United Kingdom.

Yogarajah, I., Yeo, K.C. 1994. Finite element modelling of pull-out tests with load and strain measurements. *Geotextiles and Geomembranes*, 13 (1), pp.43-54.

Yoshimi, Y., Kishida, T. 1981a. A ring torsion apparatus for evaluating friction between soil and metal surfaces. *Geotechnical Testing Journal*, 4 (4), pp.145-152.

Yoshimi, Y., Kishida, T. 1981b. Friction between sand and a metal surface. In: *Proceedings of the 10th International Conference on Soil Mechanics and Foundation Engineering*, 1, pp.831-834.

Youssef, B.S., Cassidy, M.J. 2014. Calibration of Verley and Sotberg soil resistance model for pipelines placed on calcareous soils. In: *Proceedings of the 24th International Ocean and Polar Engineering Conference*, Busan, Korea.

Zhang, J., Randolph, M.F., Stewart, D.P. 1999. An elasto-plastic model for pipe-soil interaction of unburied pipelines. In: *Proceedings of the International Offshore and Polar Engineering Conference*, Brest, France, pp.185-192.

Zhang, J., Stewart, D.P., Randolph, M.F. 2002. Modelling of shallowly embedded offshore pipelines in calcareous sand. *Journal of Geotechnical and Geoenvironmental Engineering*, 128 (5), pp.363-371.

Zhang, W. Tuohy, J. 2002. A three-dimensional finite element analysis of unburied flexible flow line: A case study. In: *Proceedings of the ASME 21st International Conference on Offshore Mechanics and Arctic Engineering*, Newcastle-Upon-Tyne, United Kingdom, pp.435-442.

Zhou, H., White, D.J., Randolph, M.F. 2008. Physical and numerical simulation of shallow penetration of a cylindrical object into soft clay. In: *Proceedings of the ASCE GeoCongress 2008 – Characterisation, Monitoring, and Modelling of GeoSystems*, New Orleans, Louisiana, USA, pp.108-177.

Appendix A – Profilometry Results

The individual texture measurements for each surface are recorded in this Appendix. First shows the variability across each individual specimen. Second is the variability across a typical example of each surface type. These are both measured by the Talysurf contact profilometer. The last table shows the Alicona measurements across a range of typical examples from each surface set which was used to determine the characteristic texture for that surface type. One specimen from "V" and "P" surfaces was tested due to the homogeneity of pristine polypropylene and that for "P" tests only one specimen was used for each test.

Talysurf measurements of each specimen from T, E, and S surfaces using L_c=8 mm.

T surfaces			E surfaces			S surfaces		
Surface	**T_a (µm)**	**T_{max} (µm)**	**Surface**	**T_a (µm)**	**T_{max} (µm)**	**Surface**	**T_a (µm)**	**T_{max} (µm)**
TCP01	0.31	4.0218	PP-002	12.0672	68.6629	PP-001	48.5609	197.9923
TCP02	0.41	5.4168	PP-007	12.2768	74.3800	PP-003	34.7826	153.1983
TCP03	0.30	5.0921	PP-008	14.6593	75.1639	PP-005	44.7179	194.2790
TCP04	0.36	6.6158	PP-009	15.1808	86.4037	PP-006	40.8557	202.0787
TCP05	0.38	7.5876	PP-011	16.0315	86.2344	PP-010	35.5905	184.0073
TCP06	0.36	7.738	PP-012	11.8444	61.9945	PP-015	25.5077	141.6482
TCP07	0.29	8.3656	PP-013	11.2375	67.6679	PP-019	43.1985	217.5165
TCP08	0.28	4.9599	PP-014	18.4464	81.4083	PP-022	44.2677	406.5259
TCP09	0.38	5.8787	PP-016	15.4201	83.5361	PP-023	29.8866	171.2870
TCP10	0.32	8.6648	PP-017	14.5298	74.9729	PP-024	30.5165	194.0046
TCP11	0.46	7.4198	PP-018	12.1372	71.8116	PP-026	34.7005	207.5245
TCP12	0.44	7.1991	PP-020	14.3098	84.3011	PP-029	19.8647	141.6388
TCP13	0.33	7.1084	PP-021	8.7993	48.6945	PP-031	40.5713	199.6802
TCP14	0.54	7.1613	PP-025	13.4074	65.1553	PP-033	32.2490	178.1771
TCP15	0.34	8.5297	PP-028	8.6518	61.8648	PP-035	52.3710	238.2191
TCP16	0.34	4.1958	PP-030	15.6623	71.9979	PP-040	40.3669	221.6822
TCP17	0.30	4.5259	PP-032	12.2085	73.3534	PP-041	42.4498	283.1610
TCP18	0.30	4.7843	PP-034	10.6727	53.0994	PP-043	33.4024	165.2045
TCP19	0.30	3.8646	PP-036	13.5124	75.5068	PP-045	15.2430	125.2375
TCP21	0.30	5.2575	PP-037	14.1417	72.6045	PP-046	16.9274	168.5819
TCP22	0.29	3.7828	PP-038	6.9791	49.9696	PP-052	12.1043	130.2969
TCP23	0.32	4.6266	PP-042	11.4994	61.9654	PP-054	43.2605	216.5821
TCP24	0.31	5.7413	PP-044	11.9199	63.7186	PP-056	21.6080	158.6427
TCP25	0.25	3.9548	PP-047	10.9811	66.9777	PP-058	42.1518	218.6358
TCP26	0.41	5.2959	PP-048	7.5227	65.0028	PP-059	17.0558	168.5401

TCP27	0.31	5.1407	PP-049	15.6543	68.6629	PP-062	40.7387	212.7944
			PP-051	11.3237	72.1244	PP-063	43.9141	226.6240
			PP-055	11.7081	52.4123	PP-064	56.3654	245.1185
			PP-057	19.0366	89.1128	PP-065	41.1861	219.1412
			PP-060	13.7328	60.6265	PP-066	46.5044	203.1400
			PP-070	10.8850	70.9325	PP-067	32.5044	203.1400
			PP-071	12.0030	69.8398	PP-068	38.0648	216.3891
			PP-073	11.1283	55.6683	PP-069	41.2129	239.3946
						PP-072	15.3758	115.4709

Talysurf measurements of a typical example from T, E, and S surfaces using L_c=8 mm.

T surfaces			E surfaces			S surfaces		
Traverse	**T_a (µm)**	**T_{max} (µm)**	**Traverse**	**T_a (µm)**	**T_{max} (µm)**	**Traverse**	**T_a (µm)**	**T_{max} (µm)**
X1	0.31	-	X1	10.6491	55.6095	X1	28.2536	167.3857
X2	0.30	-	X2	9.9373	65.0621	X2	43.8875	244.3024
X3	0.31	-	X3	10.9300	55.5395	X3	46.0803	199.9508
X4	0.30	-	X4	10.3338	61.5692	X4	23.5929	154.5591
X5	0.30	-	X5	10.0132	62.1322	X5	38.4234	202.9978
Average	0.30	-	*Average*	10.373	59.983	*Average*	36.048	193.839
St. Dev.	*	-	*St. Dev.*	0.376	3.790	*St. Dev.*	8.759	31.338

*standard deviation is within a rounding error so not reported

Alicona measurement of T_a with varying L_c.

	L_c filter length				
	8.00	**2.50**	**0.80**	**0.25**	**0.08**
V					
X1	0.0694	0.0587	0.0526	0.0416	0.0255
X2	0.0560	0.0458	0.0376	0.0278	0.0151
X3	0.0576	0.0454	0.0397	0.0302	0.0169
Average	0.061	0.049	0.043	0.033	0.019
T					
PP22	2.8176	1.0133	0.7649	0.6831	0.5381
PP21	4.913	1.2409	0.8269	0.7433	0.5709
PP23	3.2166	1.3846	0.9131	0.7854	0.5543
PP18	2.444	1.5126	1.1441	1.0052	0.6577
Average	3.348	1.288	0.912	0.804	0.580
E					
PP-048					
X1	9.8272	7.2971	3.6764	1.9056	1.3786
X2	9.6421	9.3092	2.1645	1.6997	1.2293
X3	12.7368	8.8813	3.4161	2.0949	1.5188
PP-055					

X1	15.6747	10.9874	3.4817	1.8185	1.2801
X2	15.1674	10.6515	3.2354	1.7654	1.2507
X3	13.1661	8.9411	2.8457	1.8167	1.2725
PP-060					
X1	12.6142	8.7185	2.4549	1.6821	1.1833
X2	8.4846	6.5485	2.7787	1.6581	1.1479
X3	11.6583	7.742	2.2376	1.5495	1.1283
PP-071					
X1	7.493	5.8231	2.6856	1.6484	1.2028
X2	12.2395	7.8833	2.4909	0.7963	1.2678
X3	14.1395	9.4424	3.3247	1.9482	1.2935
Average	11.922	8.268	2.799	1.645	1.215
S					
PP-062					
X1	26.0855	20.1827	9.2303	4.0288	1.6695
X2	42.717	32.2401	12.094	4.5926	1.8495
X3	38.269	29.5872	11.3113	4.2778	1.8309
PP-064					
X1	51.0478	39.8419	15.1245	4.9774	1.8644
X2	44.1451	32.9345	11.9102	4.3022	1.5787
X3	36.2627	27.2147	11.1223	4.4654	1.7308
PP-066					
X1	48.7622	36.9038	13.4601	4.6127	1.7775
X2	38.1247	28.4255	10.5402	4.1312	1.5933
X3	42.8238	38.0983	16.003	5.0351	1.9015
PP-068					
X1	35.6917	34.0787	14.9199	5.1203	2.0437
X2	21.8724	17.2113	8.6074	3.793	1.5788
X3	43.653	34.871	14.3648	4.9554	1.9031
Average	39.121	30.966	12.391	4.524	1.777
P					
PP-074					
X1	341.633	80.1979	18.255	6.548	2.733
X2	488.091	73.509	10.589	3.944	1.865
X3	402.865	79.843	16.434	6.161	2.257
PP-075					
X1	307.846	42.683	12.266	5.037	2.005
X2	316.851	50.351	13.755	5.585	2.197
X3	326.759	55.944	17.563	6.75	2.513
Average	364.01	63.75	14.81	5.67	2.26

Alicona measurement of T_{max} with varying L_c.

	L_c filter length				
	8.00	***2.50***	***0.80***	***0.25***	***0.08***
V					
X1	3.9362	3.8470	3.7161	3.0648	1.6434
X2	0.8929	0.8559	0.8091	0.7372	0.5617
X3	4.8379	4.8348	4.8184	4.6957	4.3843
Average	3.222	3.179	3.115	2.833	2.197
T					
PP22	27.7469	22.6761	15.2919	8.3057	4.2200
PP21	-	-	-	-	-
PP23	44.6621	23.6708	16.4538	12.2291	7.0715
PP18	41.9835	23.4187	19.7820	11.3241	5.2563
Average	38.131	23.255	17.176	10.620	5.516
E					
X1	57.3948	38.9683	20.2976	15.5137	10.7776
X2	72.4176	58.4797	29.0827	14.3725	9.4648
X3	85.9653	67.1683	52.0460	26.3378	14.7177
Average	71.926	54.872	33.809	18.741	11.653
S					
X1	159.9624	149.5636	95.5929	44.5593	20.7233
X2	164.3654	166.1054	134.1654	68.6193	26.4064
X3	208.7660	181.7097	139.7172	51.9973	16.2663
Average	177.698	165.793	123.159	55.059	21.132

Appendix B – Soil-only direct shear tests

Soil tests result tables include some cardinal test parameters and results. The $D_{r\ fab}$ and $D_{r\ con}$ are the soil sample relative densities as fabricated and post consolidation after the application of the pertinent normal load and represents the relative density as at the start of shearing. The same applies for e_{fab} and e_{con} with regard to the sample void ratio. The peak shear stress, τ_{peak}, is the maximum shear stress recorded during the test and the ultimate shear stress, τ_{ult}, is the average shear stress between 10 mm and 12 mm of horizontal displacement. For each soil, two nominal relative density were tested (D_r approximately 15% and 70%) at five levels of vertical confining stress(σ_n approximately 2, 5, 10, 20, 35 kPa). For soil tests a three part naming convention has been adopted to uniquely identify each test consisting of a soil type reference [S0, S15, S35, LG, LB, HS, RH], a density reference [L (for loose), D (for dense)], and a nominal stress level reference [2, 5, 10, 20, 35 (kPa)]. The horizontal displacement rate was 0.8 mm/minute.

S0, S15, and S35 soil direct shear tests

Test reference	σ_n (kPa)	$D_{r\ fab}$ (%)	$D_{r\ con}$ (%)	e_{fab}	e_{con}	τ_{peak} (kPa)	τ_{ult} (kPa)	τ_{peak}/σ_n	τ_{ult}/σ_n
S0_L02	2.87	15.6	21.0	0.870	0.859	1.84	1.76	0.64	0.61
S0_L05	5.94	8.4	14.9	0.884	0.871	3.92	3.82	0.66	0.64
S0_L10	11.91	6.1	30.2	0.889	0.841	8.04	7.11	0.68	0.60
S0_L20	22.13	-0.2	14.6	0.901	0.872	14.48	13.30	0.65	0.60
S0_L35	37.45	0.5	28.5	0.900	0.844	24.99	23.43	0.67	0.63
S0_D02	2.89	67.1	69.1	0.767	0.763	3.62	2.06	1.25	0.71
S0_D05	5.26	64.0	74.0	0.773	0.753	5.51	3.74	1.05	0.71
S0_D10	11.49	62.3	73.3	0.776	0.754	9.70	7.51	0.84	0.65
S0_D20	22.14	55.5	73.1	0.790	0.755	17.28	13.44	0.78	0.61
S0_D35	37.46	62.3	84.1	0.776	0.733	29.26	23.27	0.78	0.62
S15_L02	2.90	16.8	21.2	0.729	0.721	2.32	2.02	0.80	0.70
S15_L05	5.28	11.0	27.2	0.740	0.710	3.60	3.54	0.68	0.67
S15_L10	11.19	15.3	18.6	0.732	0.726	7.49	7.14	0.67	0.64
S15_L20	22.15	8.7	9.3	0.745	0.743	15.21	15.15	0.69	0.68
S15_L35	37.48	8.7	11.0	0.745	0.740	24.30	23.93	0.65	0.64
S15_D02	2.92	69.5	73.6	0.630	0.622	3.26	2.32	1.12	0.79
S15_D05	5.29	60.5	63.3	0.647	0.641	5.13	4.68	0.97	0.88
S15_D10	11.95	61.5	70.1	0.645	0.628	10.69	8.29	0.89	0.69
S15_D20	22.16	54.8	76.2	0.657	0.617	18.51	14.23	0.84	0.64

S0, S15, and S35 soil direct shear tests

Test reference	σ_n (kPa)	$D_{r\,fab}$ (%)	$D_{r\,con}$ (%)	e_{fab}	e_{con}	τ_{peak} (kPa)	τ_{ult} (kPa)	τ_{peak}/σ_n	τ_{ult}/σ_n
S15_D35	37.46	61.1	73.9	0.646	0.621	30.53	24.73	0.82	0.66
S35_L02	2.91	-7.2	3.2	0.652	0.634	2.45	2.03	0.84	0.70
S35_L05	5.29	1.4	0.2	0.637	0.639	3.69	3.42	0.70	0.65
S35_L10	11.95	-9.0	15.5	0.655	0.613	8.94	8.84	0.75	0.74
S35_L20	22.16	-15.8	3.0	0.667	0.635	14.77	14.37	0.67	0.65
S35_L35	37.49	-19.5	11.8	0.673	0.620	24.59	24.10	0.66	0.64
S35_D02	2.95	52.1	48.8	0.550	0.556	3.47	2.50	1.18	0.85
S35_D05	5.32	52.1	54.7	0.550	0.545	4.89	3.45	0.92	0.65
S35_D10	11.99	64.4	68.9	0.529	0.521	11.16	7.78	0.93	0.65
S35_D20	22.20	51.4	65.2	0.551	0.527	18.20	16.12	0.82	0.73
S35_D35	37.52	49.4	77.6	0.555	0.506	27.65	24.25	0.74	0.65

LG, LB, HS, and RH sand direct shear tests

Test reference	σ_n (kPa)	$D_{r\,fab}$ (%)	$D_{r\,con}$ (%)	e_{fab}	e_{con}	τ_{peak} (kPa)	τ_{ult} (kPa)	τ_{peak}/σ_n	τ_{ult}/σ_n
LG_L02	2.89	22.1	27.2	0.854	0.834	2.46	2.27	0.85	0.79
LG_L05	5.31	16.3	19.8	0.876	0.863	3.98	3.78	0.75	0.71
LG_L10	11.39	19.7	24.5	0.863	0.844	8.02	7.12	0.70	0.63
LG_L20	21.62	24.6	32.0	0.844	0.815	14.88	13.75	0.69	0.64
LG_L35	36.96	25.3	34.7	0.841	0.805	24.22	23.02	0.66	0.62
LG_D02	2.93	53.7	56.4	0.730	0.720	3.02	2.26	1.03	0.77
LG_D05	5.34	60.2	62.0	0.705	0.698	5.05	3.68	0.94	0.69
LG_D10	11.42	62.7	67.3	0.695	0.678	10.59	7.34	0.93	0.64
LG_D20	21.65	52.0	62.9	0.737	0.695	17.85	13.87	0.82	0.64
LG_D35	37.00	60.9	69.5	0.703	0.669	29.88	22.16	0.81	0.60
LB_L02	2.89	19.1	29.4	0.781	0.749	2.24	1.99	0.77	0.69
LB_L05	5.31	21.9	27.6	0.772	0.754	3.72	3.51	0.70	0.66
LB_L10	11.38	21.2	29.1	0.774	0.750	7.73	7.08	0.68	0.62
LB_L20	21.61	20.2	45.8	0.777	0.698	14.75	12.56	0.68	0.58
LB_L35	36.96	26.7	44.0	0.757	0.704	23.93	22.10	0.65	0.60
LB_D02	2.92	70.4	71.2	0.622	0.619	2.84	2.12	0.97	0.73
LB_D05	5.34	63.2	64.6	0.644	0.640	5.14	3.34	0.96	0.63
LB_D10	11.41	61.4	74.7	0.650	0.608	9.53	7.10	0.83	0.62
LB_D20	21.64	70.3	76.0	0.622	0.604	17.94	12.44	0.83	0.57
LB_D35	36.99	70.6	85.1	0.621	0.576	31.08	21.54	0.84	0.58
HS_L02	2.86	9.1	19.2	0.965	0.927	2.73	2.04	0.96	0.71
HS_L05	5.27	17.4	24.4	0.934	0.907	4.58	3.77	0.87	0.72

LG, LB, HS, and RH sand direct shear tests

Test reference	σ_n (kPa)	$D_{r\,fab}$ (%)	$D_{r\,con}$ (%)	e_{fab}	e_{con}	τ_{peak} (kPa)	τ_{ult} (kPa)	τ_{peak}/σ_n	τ_{ult}/σ_n
HS_L10	11.35	11.5	26.0	0.956	0.901	8.74	7.19	0.77	0.63
HS_L20	21.58	13.9	31.1	0.947	0.882	15.99	14.00	0.74	0.65
HS_L35	36.92	18.3	32.4	0.930	0.877	25.91	22.97	0.70	0.62
HS_D02	2.88	57.4	57.7	0.782	0.781	3.00	2.13	1.04	0.74
HS_D05	5.30	54.7	55.5	0.792	0.789	5.21	3.74	0.98	0.71
HS_D10	11.38	59.2	60.8	0.775	0.769	10.49	7.25	0.92	0.64
HS_D20	21.61	62.5	69.5	0.763	0.736	18.67	12.77	0.86	0.59
HS_D35	36.95	55.8	60.5	0.788	0.770	29.75	22.86	0.81	0.62
RH_L02	2.85	19.2	30.2	0.957	0.910	2.76	1.86	0.97	0.65
RH_L05	5.27	23.4	39.6	0.939	0.870	4.05	3.67	0.77	0.70
RH_L10	11.34	25.3	40.7	0.931	0.865	8.25	7.26	0.73	0.64
RH_L20	21.57	24.8	46.0	0.933	0.842	15.45	13.45	0.72	0.62
RH_L35	36.92	23.0	44.7	0.941	0.848	25.70	23.17	0.70	0.63
RH_D02	2.88	64.3	64.7	0.764	0.762	3.00	2.16	1.04	0.75
RH_D05	5.30	62.1	66.7	0.773	0.753	4.97	3.58	0.94	0.68
RH_D10	11.37	66.6	70.2	0.754	0.738	9.66	7.52	0.85	0.66
RH_D20	21.61	61.8	70.4	0.774	0.737	17.73	14.07	0.82	0.65
RH_D35	36.95	60.8	67.3	0.779	0.750	27.74	24.26	0.75	0.66

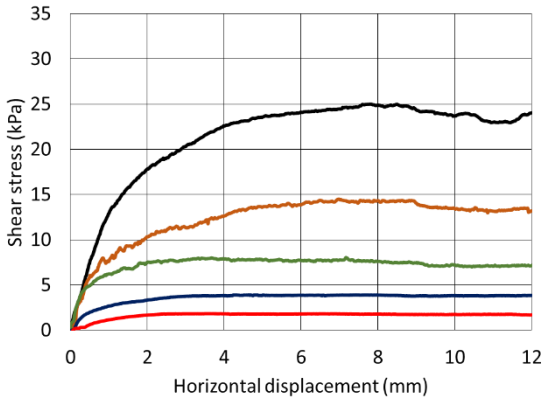

(a) loose shear stress-displacement

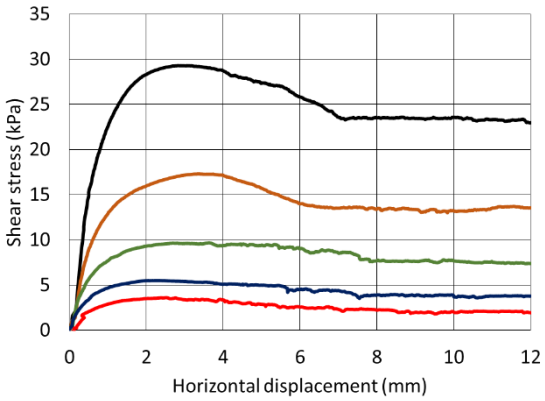

(b) dense shear stress-displacement

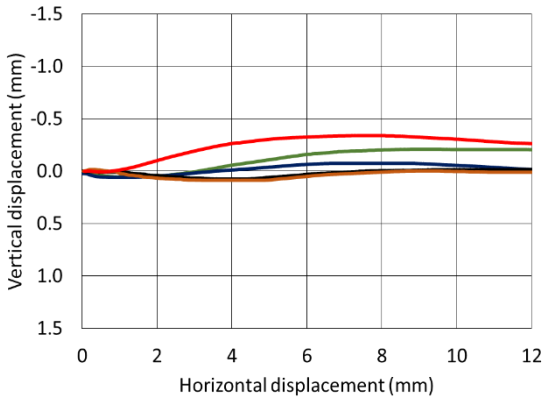

(c) loose vertical-horizontal displacement

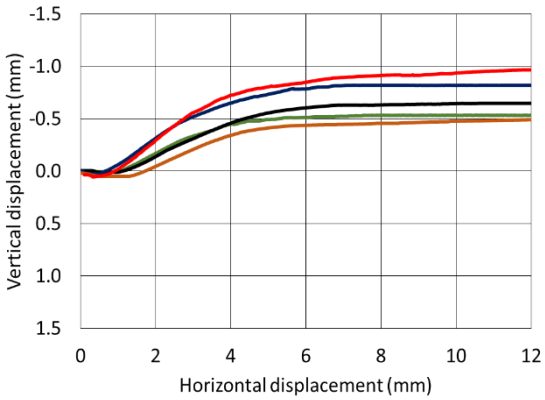

(d) dense vertical-horizontal displacement

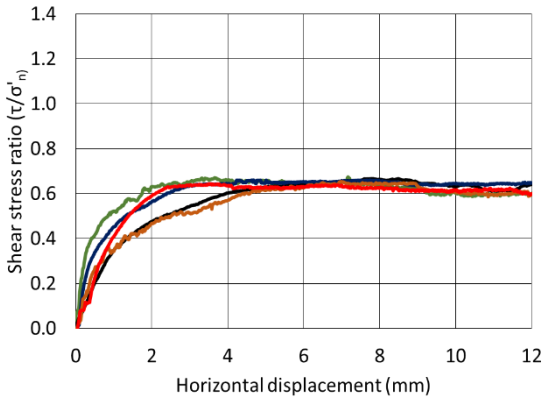

(e) loose stress ratio-displacement

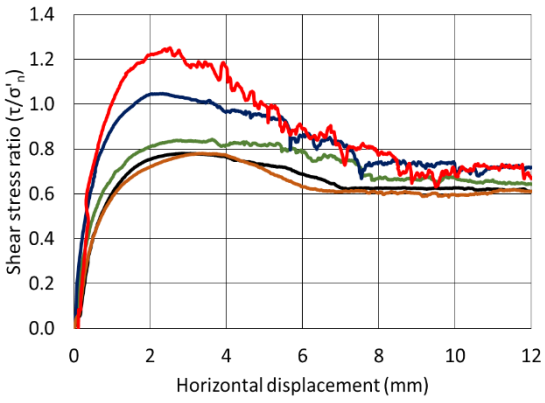

(f) dense stress ratio-displacement

S0 soil direct shear test results of loose and dense (a, b) shear stress displacement, (c, d) vertical-horizontal displacement, and (e, f) shear stress ratio, τ/σ_n.

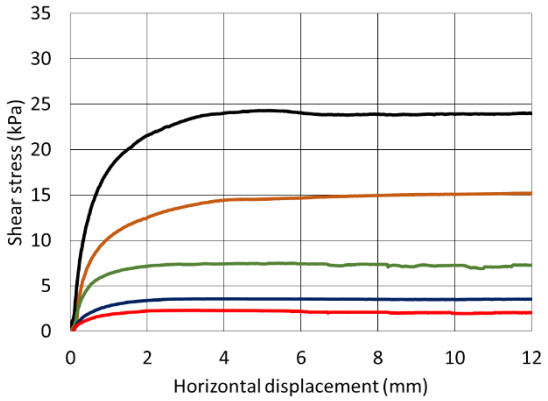

(a) loose shear stress-displacement

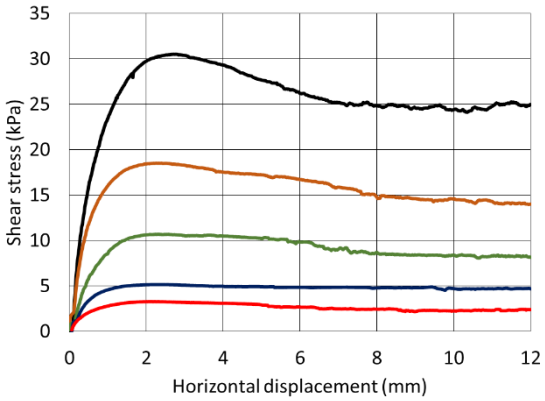

(b) dense shear stress-displacement

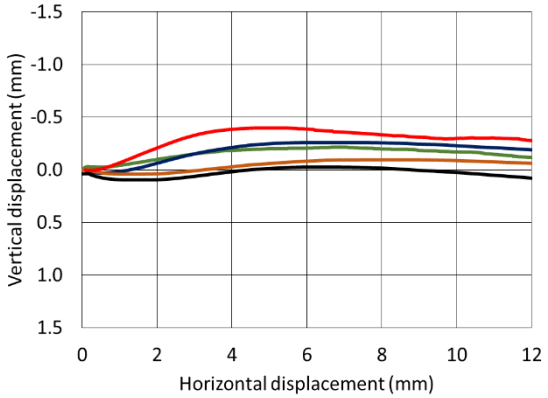

(c) loose vertical-horizontal displacement

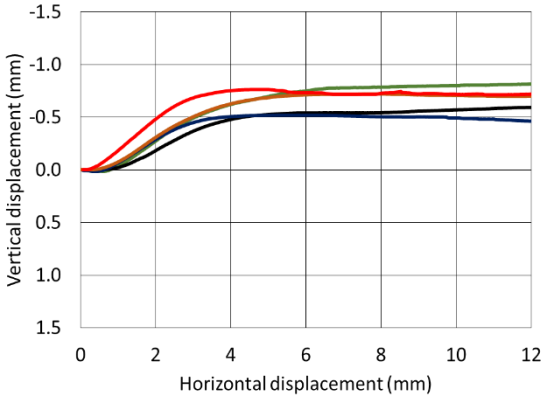

(d) dense vertical-horizontal displacement

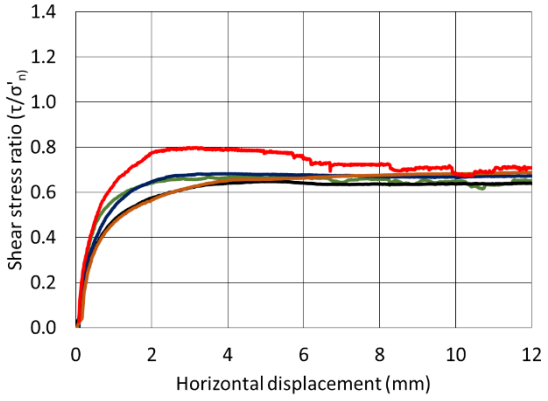

(e) loose stress ratio-displacement

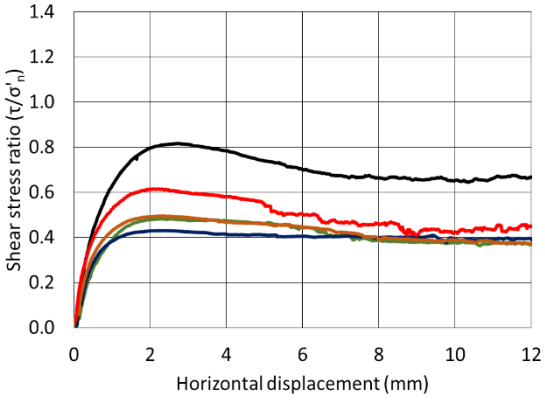

(f) dense stress ratio-displacement

S15 soil direct shear test results of loose and dense (a, b) shear stress displacement, (c, d) vertical-horizontal displacement, and (e, f) shear stress ratio, τ/σ_n.

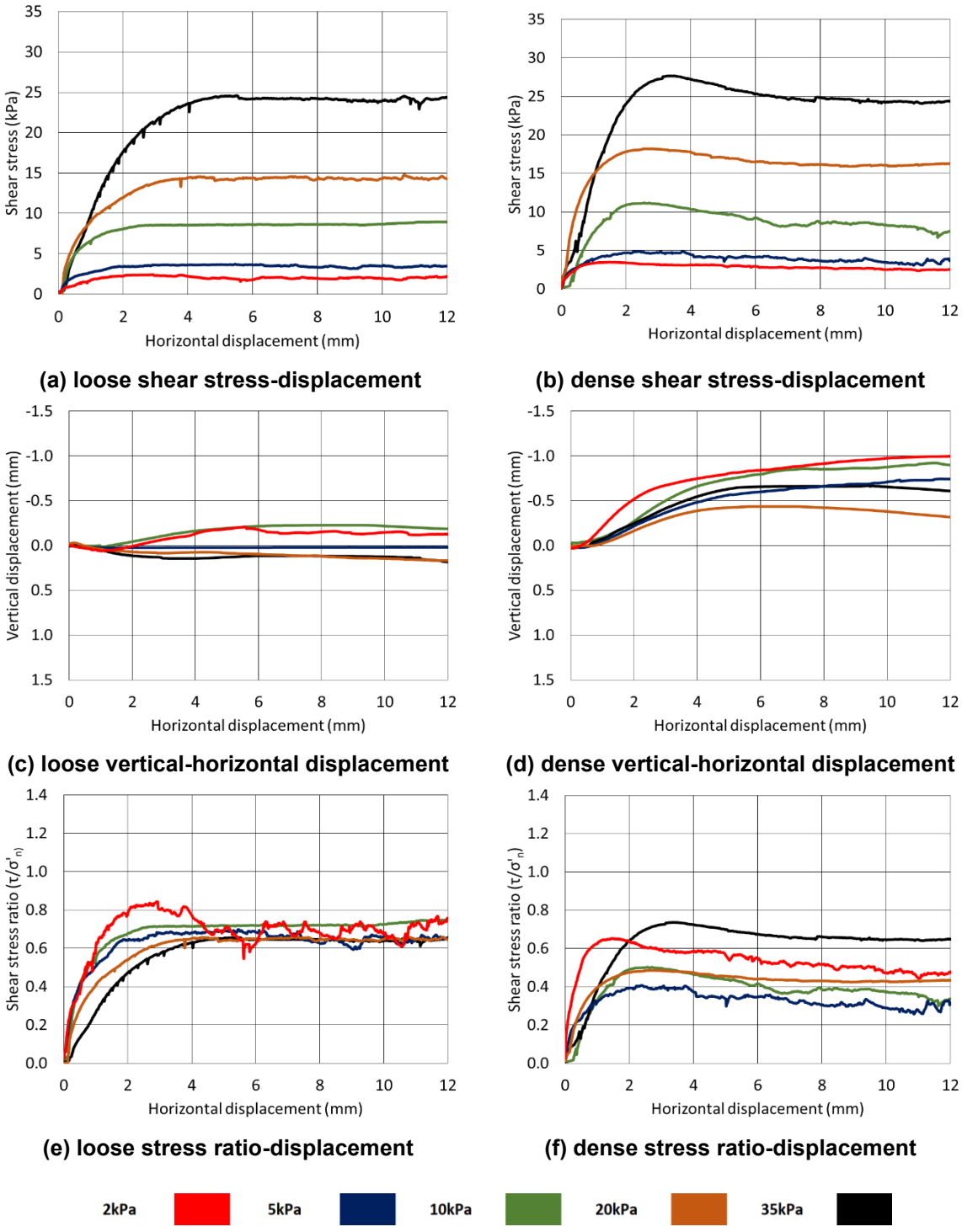

(a) loose shear stress-displacement

(b) dense shear stress-displacement

(c) loose vertical-horizontal displacement

(d) dense vertical-horizontal displacement

(e) loose stress ratio-displacement

(f) dense stress ratio-displacement

S35 soil direct shear test results of loose and dense (a, b) shear stress displacement, (c, d) vertical-horizontal displacement, and (e, f) shear stress ratio, τ/σ_n.

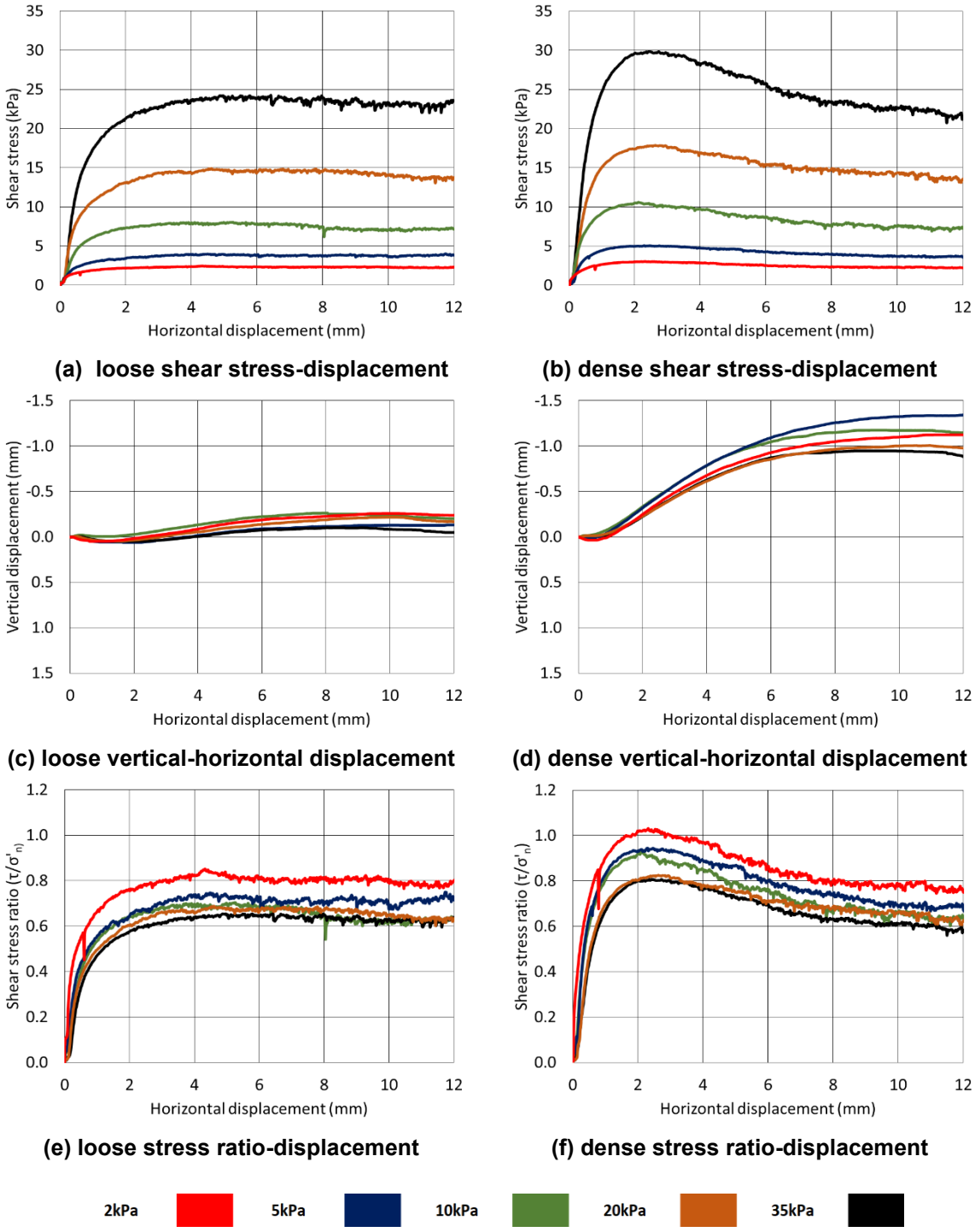

Lowestoft Gravel direct shear test results of loose and dense (a, b) shear stress displacement, (c, d) vertical-horizontal displacement, and (e, f) shear stress ratio, τ/σ_n.

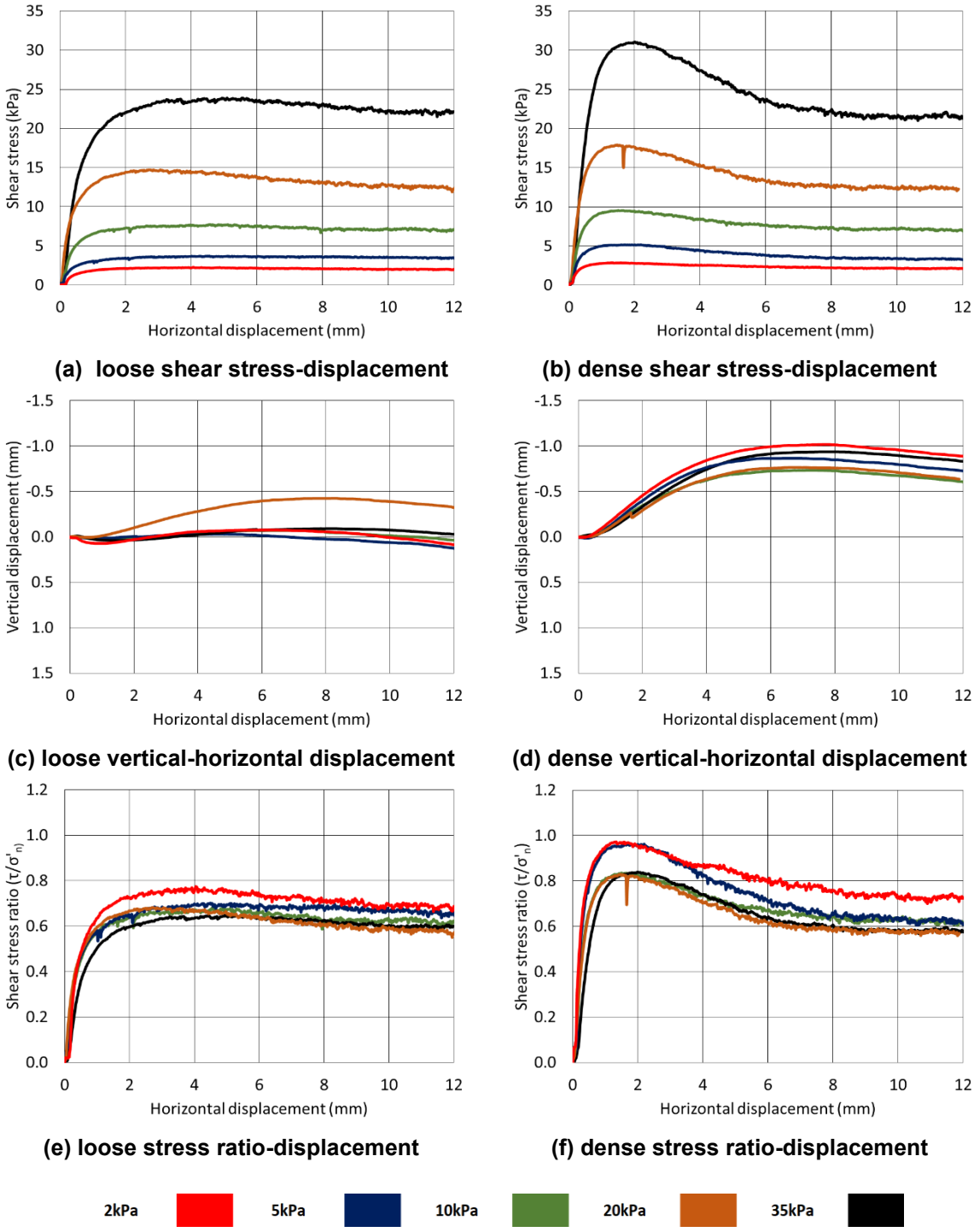

Leighton Buzzard direct shear test results of loose and dense (a, b) shear stress displacement, (c, d) vertical-horizontal displacement, and (e, f) shear stress ratio, τ/σ_n.

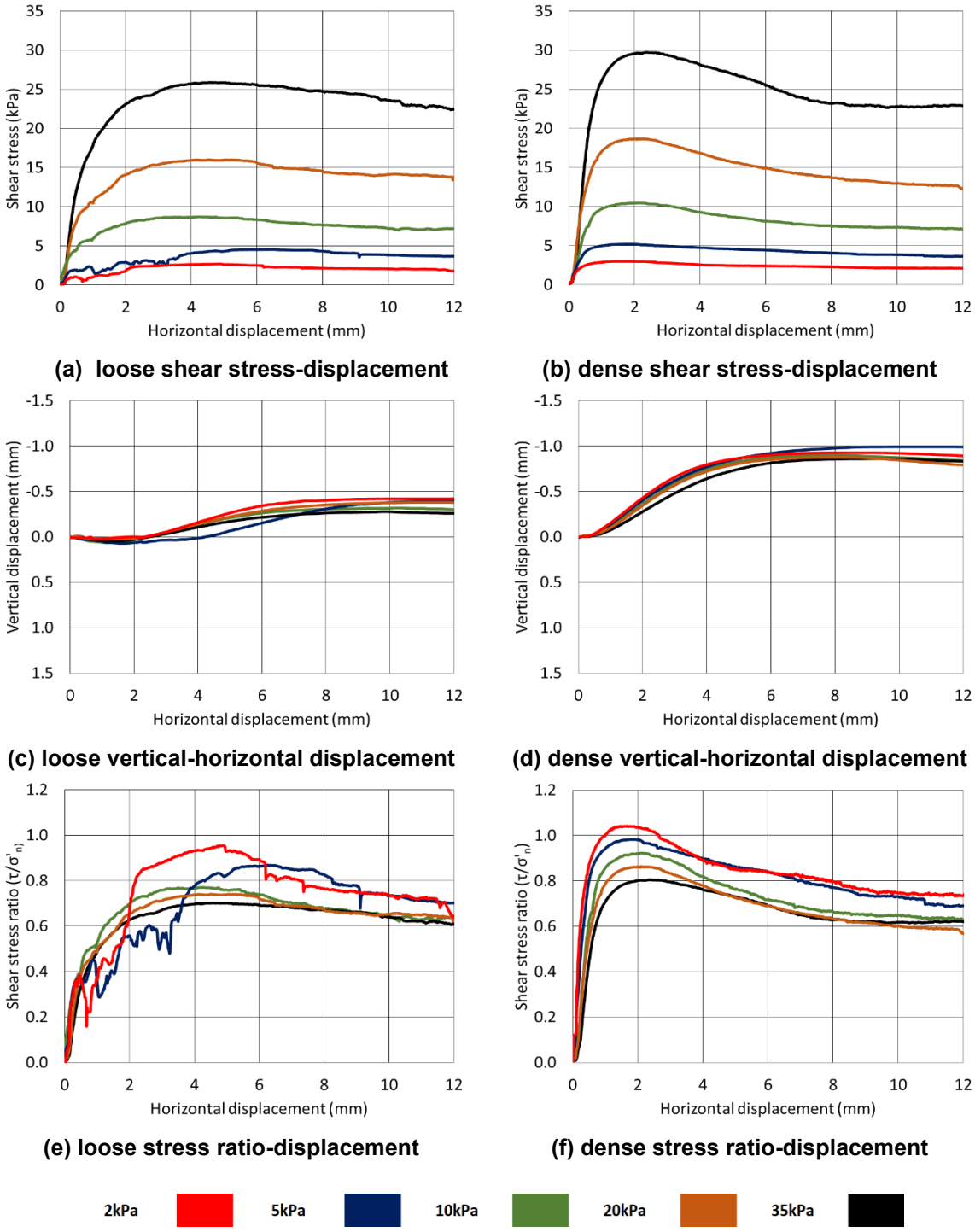

Hostun Sand direct shear test results of loose and dense (a, b) shear stress displacement, (c, d) vertical-horizontal displacement, and (e, f) shear stress ratio, τ/σ_n.

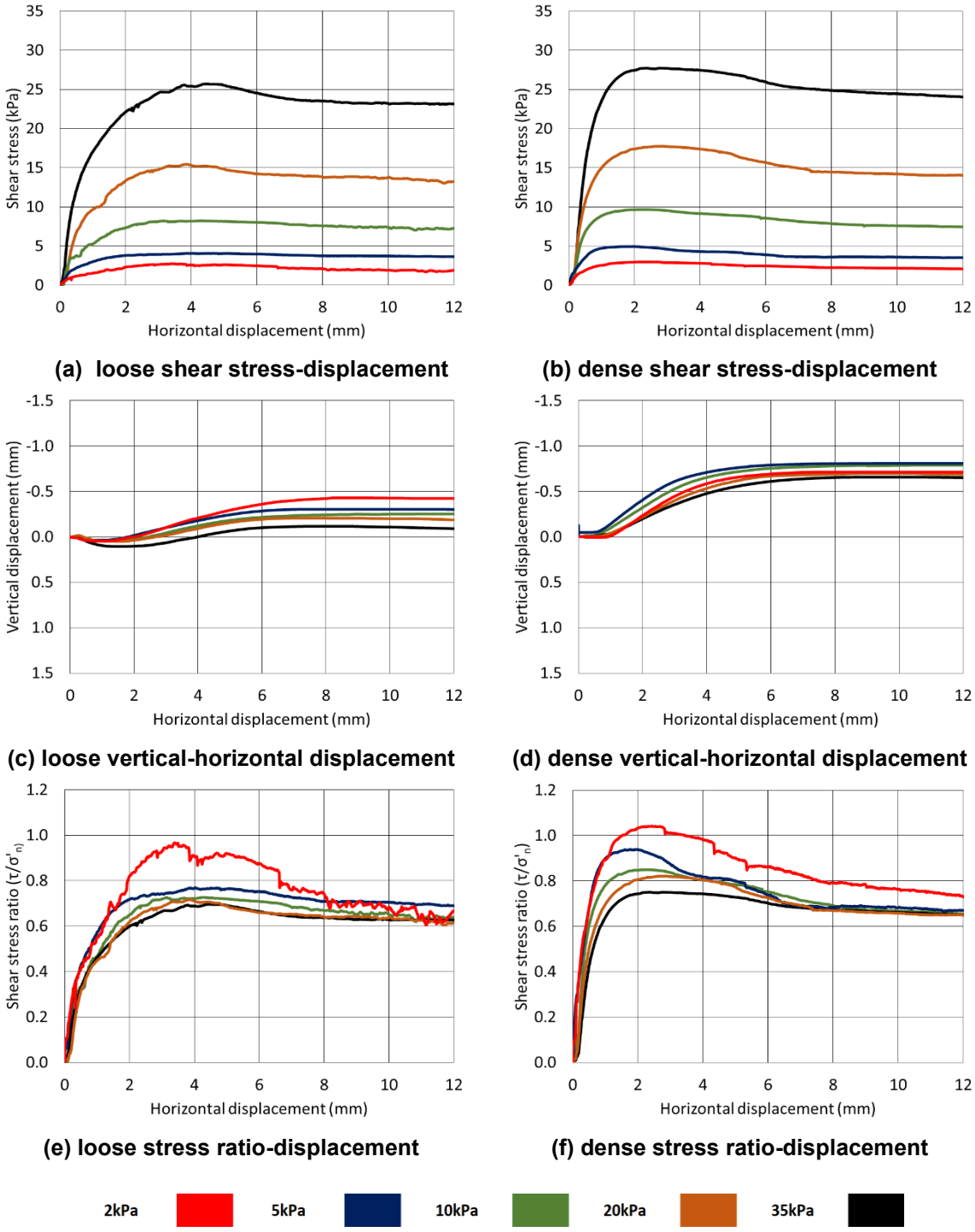

Redhill Sand direct shear test results of loose and dense (a, b) shear stress displacement, (c, d) vertical-horizontal displacement, and (e, f) shear stress ratio, τ/σ_n.

Appendix C1 – "T" interface test results

"T" interface tests result tables include some cardinal test parameters and results. The $D_{r\ fab}$ and $D_{r\ con}$ are the soil sample relative densities as fabricated and post consolidation after the application of the pertinent normal load and represents the relative density as at the start of shearing. The same applies for e_{fab} and e_{con} with regard to the sample void ratio. The peak shear stress, τ_{peak}, is the maximum shear stress recorded during the test and the ultimate shear stress, τ_{ult}, is the average shear stress between 10 mm and 12 mm of horizontal displacement. For each surface, two nominal relative density were tested (D_r approximately 15% and 70%) at five levels of vertical confining stress(σ_n approximately 2, 5, 10, 20, 35 kPa). For interface tests a four part naming convention has been adopted to uniquely identify each test consisting of a soil type reference [S0, S15, S35, LG, LB, HS, RH], a density reference [L (for loose), D (for dense)], and a nominal stress level reference [2, 5, 10, 20, 35 (kPa)]. Test references end with the surface type reference. A suite of tests using soil S0 was also conducted at a displacement rate of 0.2 mm/minute to investigate rate effects.

"T" interface tests with soils S0, S15, and S35

Test reference	σ_n (kPa)	$D_{r\ fab}$ (%)	$D_{r\ con}$ (%)	e_{fab}	e_{con}	τ_{peak} (kPa)	τ_{ult} (kPa)	τ_{peak}/σ_n	τ_{ult}/σ_n
S0_L02_T	2.26	-4.3	17.1	0.910	0.867	0.93	0.90	0.41	0.40
S0_L05_T	5.89	4.6	23.7	0.892	0.854	2.41	2.37	0.41	0.40
S0_L10_T	12.01	-14.8	19.8	0.931	0.861	4.14	0.00	0.35	0.33
S0_L20_T	22.22	-33.5	11.3	0.968	0.878	7.96	7.39	0.36	0.33
S0_L35_T	37.54	-29.1	10.5	0.959	0.880	14.30	13.39	0.38	0.36
S0_D02_T	2.27	70.3	77.6	0.760	0.746	1.08	1.04	0.47	0.46
S0_D05_T	5.9	68.7	80.3	0.764	0.740	3.00	2.93	0.51	0.50
S0_D10_T	12.03	60.1	74.7	0.781	0.752	5.19	4.80	0.43	0.40
S0_D20_T	22.24	47.8	73.7	0.805	0.754	8.85	8.60	0.40	0.39
S0_D35_T	37.56	41.0	69.4	0.819	0.762	14.45	12.68	0.38	0.34
S15_L02_T	2.28	5.9	14.1	0.750	0.734	0.87	0.86	0.38	0.38
S15_L05_T	5.9	5.9	32.7	0.750	0.699	2.41	2.30	0.41	0.39
S15_L10_T	12.03	12.4	28.0	0.738	0.708	4.75	4.57	0.39	0.38
S15_L20_T	22.24	-22.0	14.1	0.803	0.734	7.83	7.69	0.35	0.35
S15_L35_T	37.56	-11.4	15.1	0.783	0.732	12.80	12.39	0.34	0.33
S15_D02_T	2.29	71.5	74.5	0.626	0.620	1.28	1.24	0.56	0.54
S15_D05_T	5.92	74.9	82.1	0.620	0.606	3.37	3.29	0.57	0.56
S15_D10_T	12.04	68.2	74.6	0.626	0.620	4.99	4.93	0.41	0.41
S15_D20_T	22.26	56.5	75.4	0.654	0.619	11.69	11.50	0.53	0.52
S15_D35_T	37.58	57.0	69.4	0.653	0.608	16.00	14.67	0.43	0.39

"T" interface tests with soils S0, S15, and S35

Test reference	σ_n (kPa)	$D_{r\ fab}$ (%)	$D_{r\ con}$ (%)	e_{fab}	e_{con}	τ_{peak} (kPa)	τ_{ult} (kPa)	τ_{peak}/σ_n	τ_{ult}/σ_n
S35_L02_T	2.29	15.7	25.7	0.613	0.596	0.87	0.83	0.38	0.36
S35_L05_T	5.92	3.8	33.7	0.633	0.582	2.26	2.19	0.38	0.37
S35_L10_T	12.04	3.1	21.5	0.635	0.603	4.79	4.65	0.40	0.39
S35_L20_T	22.25	-11.3	23.1	0.660	0.600	8.56	7.91	0.38	0.36
S35_L35_T	37.58	-6.3	31.4	0.651	0.586	13.68	13.34	0.36	0.36
S35_D02_T	2.3	59.6	64.4	0.537	0.529	1.11	1.07	0.48	0.47
S35_D05_T	5.93	68.2	82.2	0.522	0.498	3.15	3.06	0.53	0.52
S35_D10_T	12.06	67.5	73.0	0.523	0.514	5.39	5.25	0.45	0.44
S35_D20_T	22.27	52.1	69.7	0.550	0.519	9.56	8.95	0.43	0.40
S35_D35_T	37.59	54.1	76.0	0.546	0.509	16.54	16.26	0.44	0.43
LG_L02_T	2.08	37.5	47.1	0.794	0.756	0.74	0.72	0.35	0.35
LG_L05_T	5.15	37.6	40.5	0.793	0.782	1.34	1.29	0.26	0.25
LG_L10_T	11.29	37.4	47.1	0.794	0.756	2.46	2.14	0.22	0.19
LG_L20_T	21.51	29.2	48.7	0.826	0.750	4.61	4.26	0.21	0.20
LG_L35_T	36.85	25.5	41.4	0.840	0.778	8.22	7.50	0.22	0.20
LG_D02_T	2.08	84.5	84.5	0.610	0.610	0.82	0.73	0.39	0.35
LG_D05_T	5.15	83.9	83.9	0.613	0.613	1.68	1.30	0.33	0.25
LG_D10_T	11.29	82.6	82.9	0.618	0.617	3.94	3.42	0.35	0.30
LG_D20_T	21.51	78.0	80.0	0.636	0.628	5.00	4.15	0.23	0.19
LG_D35_T	36.85	74.4	76.1	0.650	0.643	8.30	7.68	0.23	0.21
LB_L02_T	2.02	-1.8	22.2	0.845	0.771	0.63	0.61	0.31	0.30
LB_L05_T	5.09	-1.4	20.7	0.844	0.776	1.25	1.20	0.25	0.24
LB_L10_T	11.23	22.9	56.6	0.769	0.665	2.29	2.18	0.20	0.19
LB_L20_T	21.45	22.0	54.0	0.772	0.673	3.75	3.30	0.18	0.15
LB_L35_T	36.79	15.3	53.8	0.793	0.673	6.53	6.19	0.18	0.17
LB_D02_T	2.02	77.2	80.7	0.601	0.590	0.79	0.76	0.39	0.38
LB_D05_T	5.09	77.6	83.7	0.599	0.581	1.45	1.37	0.28	0.27
LB_D10_T	11.23	79.4	81.8	0.594	0.586	2.69	2.28	0.24	0.20
LB_D20_T	21.45	75.6	83.7	0.606	0.581	3.82	2.97	0.18	0.14
LB_D35_T	36.79	72.9	87.8	0.614	0.568	7.47	5.96	0.20	0.16
HS_L02_T	2.10	17.0	30.3	0.936	0.885	0.83	0.82	0.40	0.39
HS_L05_T	5.16	16.2	35.4	0.938	0.866	2.09	2.04	0.40	0.40
HS_L10_T	11.30	16.9	39.5	0.936	0.850	3.98	3.93	0.35	0.35
HS_L20_T	21.52	15.7	39.2	0.940	0.851	7.80	6.97	0.36	0.32
HS_L35_T	36.86	15.3	43.6	0.942	0.834	13.00	11.77	0.35	0.32
HS_D02_T	2.10	70.1	71.0	0.734	0.730	0.96	0.94	0.46	0.45

"T" interface tests with soils S0, S15, and S35

Test reference	σ_n (kPa)	$D_{r\ fab}$ (%)	$D_{r\ con}$ (%)	e_{fab}	e_{con}	τ_{peak} (kPa)	τ_{ult} (kPa)	τ_{peak}/σ_n	τ_{ult}/σ_n
HS_D05_T	5.16	70.3	70.7	0.733	0.731	2.09	2.02	0.40	0.39
HS_D10_T	11.30	70.2	75.4	0.733	0.714	4.49	4.27	0.40	0.38
HS_D20_T	21.52	69.8	75.5	0.735	0.713	8.47	7.68	0.39	0.36
HS_D35_T	36.86	70.5	83.6	0.732	0.682	15.25	13.25	0.41	0.36
RH_L02_T	2.05	18.1	41.0	0.962	0.864	0.89	0.78	0.43	0.38
RH_L05_T	5.11	15.5	38.2	0.973	0.876	2.21	1.54	0.43	0.30
RH_L10_T	11.25	18.9	46.4	0.959	0.841	4.19	3.87	0.37	0.34
RH_L20_T	21.47	17.3	45.9	0.965	0.843	6.73	6.48	0.31	0.30
RH_L35_T	36.81	18.2	56.7	0.962	0.796	12.43	11.98	0.34	0.33
RH_D02_T	2.05	70.1	70.2	0.739	0.738	1.18	1.04	0.58	0.51
RH_D05_T	5.11	70.0	72.9	0.739	0.726	2.10	2.07	0.41	0.41
RH_D10_T	11.25	70.4	78.1	0.737	0.704	3.89	3.51	0.35	0.31
RH_D20_T	21.47	69.4	77.3	0.742	0.708	7.36	7.12	0.34	0.33
RH_D35_T	36.81	70.6	77.1	0.736	0.708	11.44	11.33	0.31	0.31

S0 soil tests at 0.2 mm/min displacement rate

Test reference	σ_n (kPa)	$D_{r\ fab}$ (%)	$D_{r\ con}$ (%)	e_{fab}	e_{con}	τ_{peak} (kPa)	τ_{ult} (kPa)	τ_{peak}/σ_n	τ_{ult}/σ_n
S0_L02_T(0.2)	2.08	14.9	31.6	0.871	0.838	1.00	0.96	0.48	0.46
S0_L05_T(0.2)	5.15	16.7	31.4	0.869	0.838	2.04	1.93	0.40	0.37
S0_L10_T(0.2)	11.29	14.9	41.5	0.871	0.818	4.03	3.89	0.36	0.34
S0_L20_T(0.2)	21.51	14.2	44.3	0.871	0.812	8.09	7.87	0.38	0.37
S0_L35_T(0.2)	36.85	14.9	48.4	0.871	0.804	13.62	13.08	0.37	0.36
S0_D02_T(0.2)	2.08	70.1	77.3	0.761	0.746	1.00	0.95	0.48	0.46
S0_D05_T(0.2)	5.15	71.0	75.3	0.759	0.750	2.24	2.14	0.43	0.42
S0_D10_T(0.2)	11.29	70.5	78.3	0.760	0.744	4.67	4.41	0.41	0.39
S0_D20_T(0.2)	21.51	70.8	90.0	0.760	0.721	8.65	8.26	0.40	0.38
S0_D35_T(0.2)	36.85	70.1	87.7	0.761	0.726	14.45	13.94	0.39	0.38

S0 interface test on seamed and unseamed surfaces

Test reference	σ_n (kPa)	$D_{r\ fab}$ (%)	$D_{r\ con}$ (%)	e_{fab}	e_{con}	τ_{peak} (kPa)	τ_{ult} (kPa)	τ_{peak}/σ_n	τ_{ult}/σ_n
S0_D02_T(uS)	2.26	-4.3	17.1	0.910	0.867	0.93	0.90	0.41	0.40
S0_D05_T(uS)	5.89	4.6	23.7	0.892	0.854	2.41	2.37	0.41	0.40
S0_D10_T(uS)	12.01	-14.8	19.8	0.931	0.861	4.14	0.00	0.35	0.33
S0_D20_T(uS)	22.22	-33.5	11.3	0.968	0.878	7.96	7.39	0.36	0.33

S0 interface test on seamed and unseamed surfaces

Test reference	σ_n (kPa)	$D_{r\ fab}$ (%)	$D_{r\ con}$ (%)	e_{fab}	e_{con}	τ_{peak} (kPa)	τ_{ult} (kPa)	τ_{peak}/σ_n	τ_{ult}/σ_n
S0_D35_T(uS)	37.54	-29.1	10.5	0.959	0.880	14.30	13.39	0.38	0.36
S0_D02_T(S)	2.27	70.3	77.6	0.760	0.746	1.08	1.04	0.47	0.46
S0_D05_T(S)	5.9	68.7	80.3	0.764	0.740	3.00	2.93	0.51	0.50
S0_D10_T(S)	12.03	60.1	74.7	0.781	0.752	5.19	4.80	0.43	0.40
S0_D20_T(S)	22.24	47.8	73.7	0.805	0.754	8.85	8.60	0.40	0.39
S0_D35_T(S)	37.56	41.0	69.4	0.819	0.762	14.45	12.68	0.38	0.34

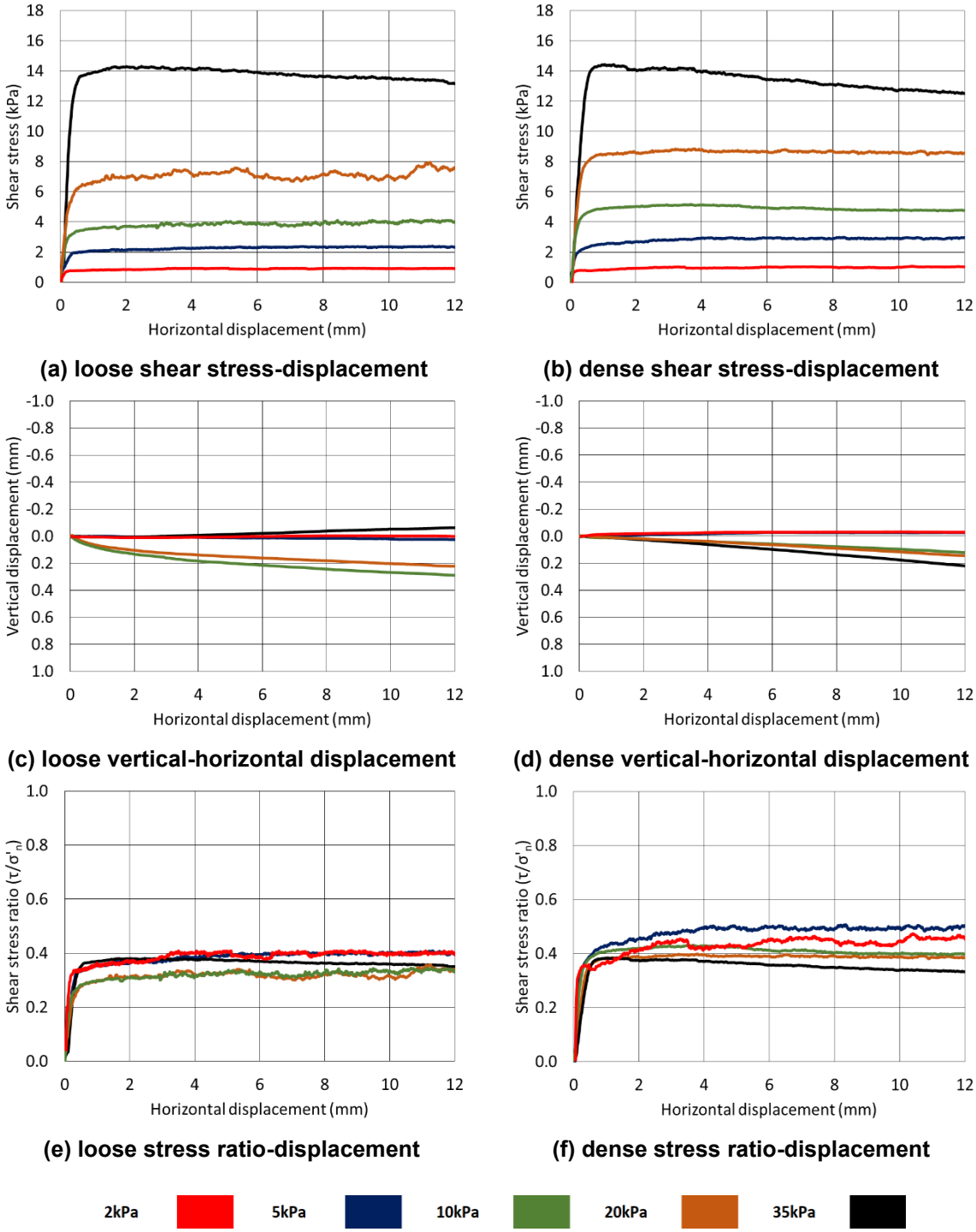

S0 soil interface test results of loose and dense (a, b) shear stress displacement, (c, d) vertical-horizontal displacement, and (e, f) shear stress ratio, τ/σ_n.

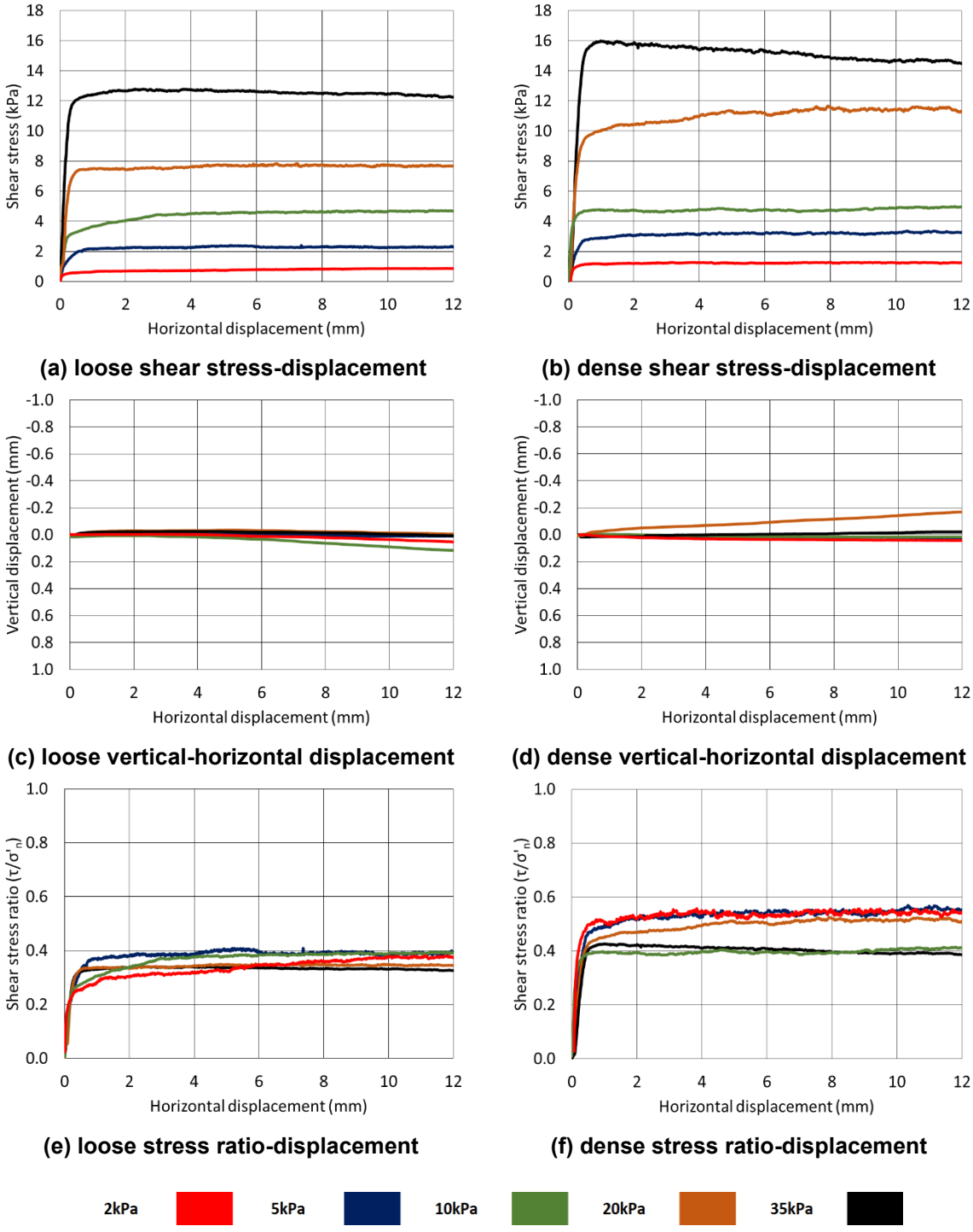

S15 soil interface test results of loose and dense (a, b) shear stress displacement, (c, d) vertical-horizontal displacement, and (e, f) shear stress ratio, τ/σ_n.

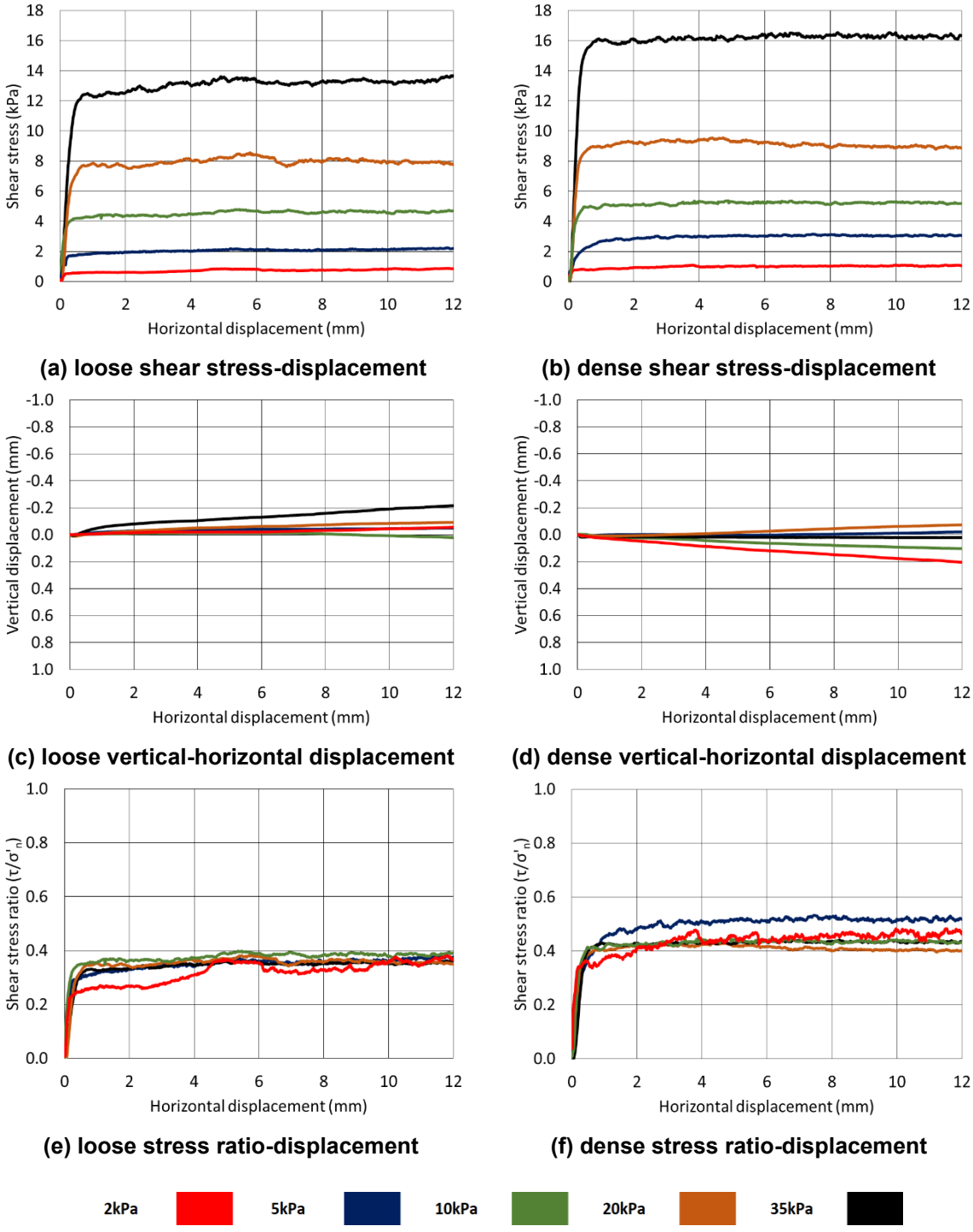

S35 soil interface test results of loose and dense (a, b) shear stress displacement, (c, d) vertical-horizontal displacement, and (e, f) shear stress ratio, τ/σ_n.

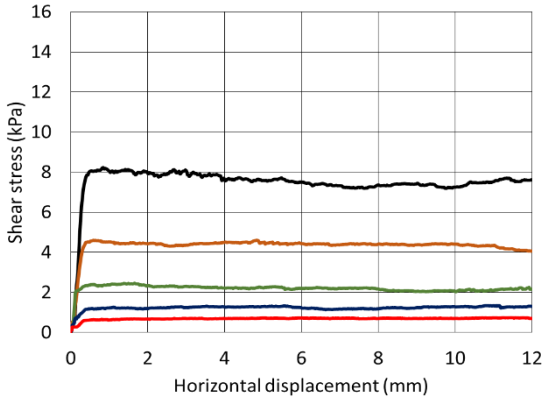

(b) loose shear stress-displacement

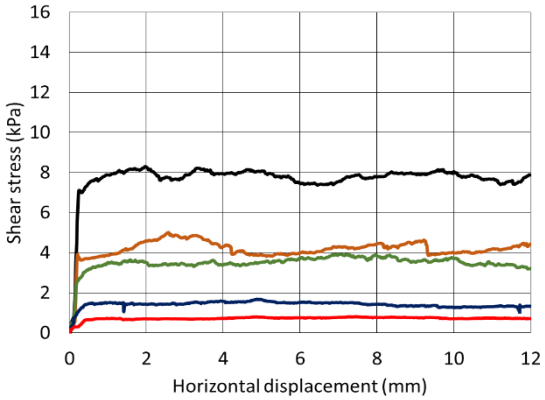

(b) dense shear stress-displacement

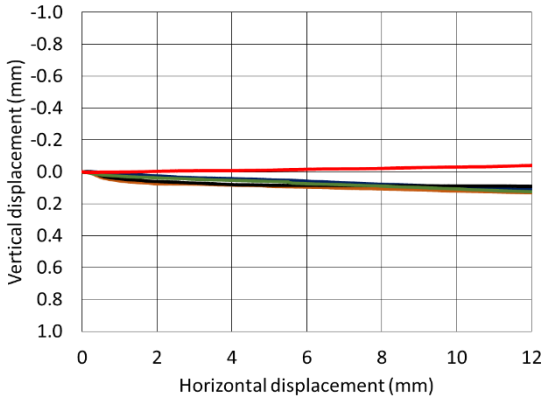

(c) loose vertical-horizontal displacement

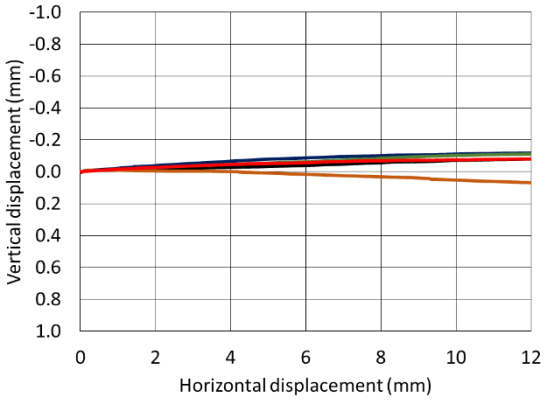

(d) dense vertical-horizontal displacement

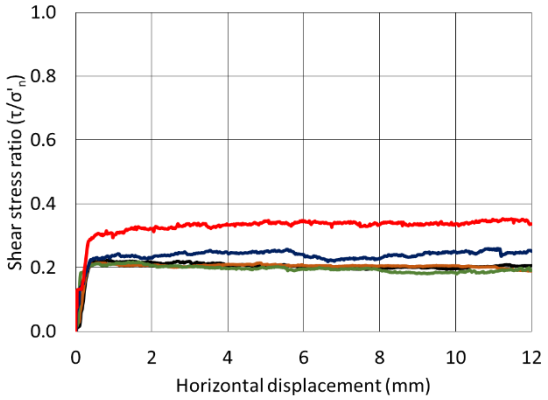

(e) loose stress ratio-displacement

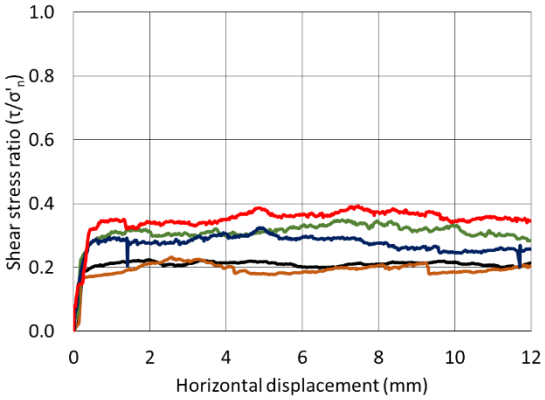

(f) dense stress ratio-displacement

Lowestoft Gravel "T" interface test results of loose and dense (a, b) shear stress displacement, (c, d) vertical-horizontal displacement, and (e, f) shear stress ratio, τ/σ_n.

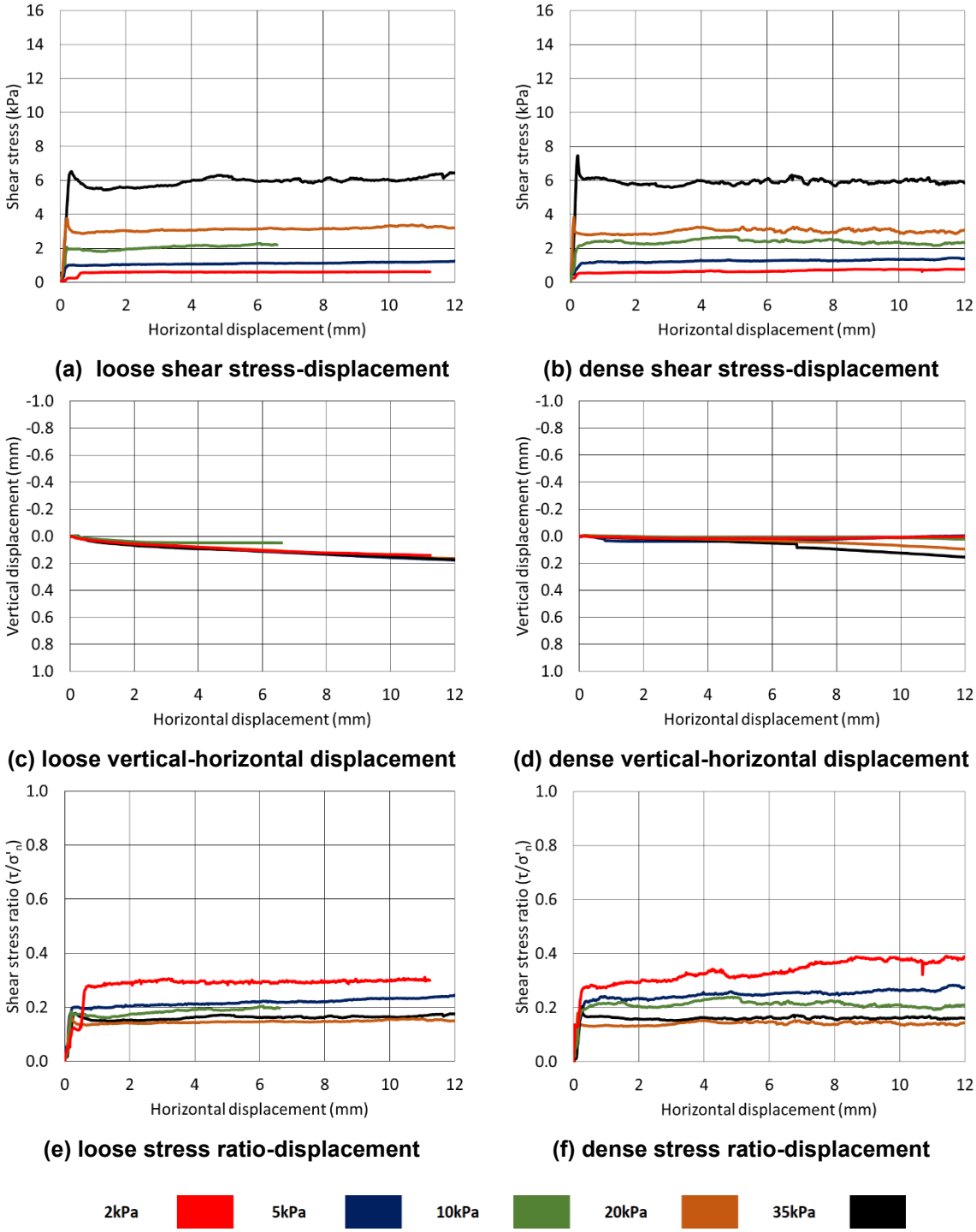

Leighton Buzzard "T" interface test results of loose and dense (a, b) shear stress displacement, (c, d) vertical-horizontal displacement, and (e, f) shear stress ratio, τ/σ_n.

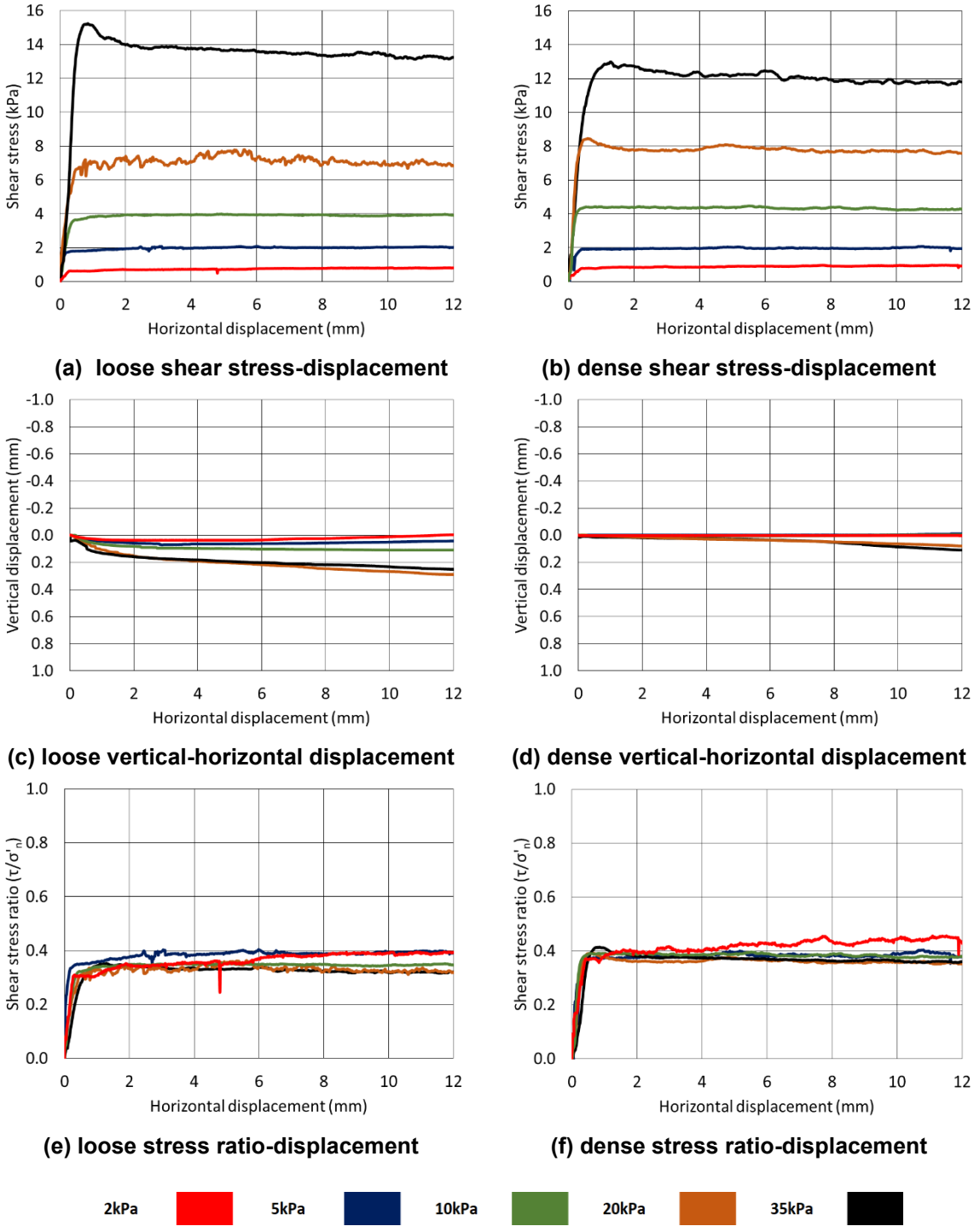

Hostun Sand "T" interface test results of loose and dense (a, b) shear stress displacement, (c, d) vertical-horizontal displacement, and (e, f) shear stress ratio, τ/σ_n.

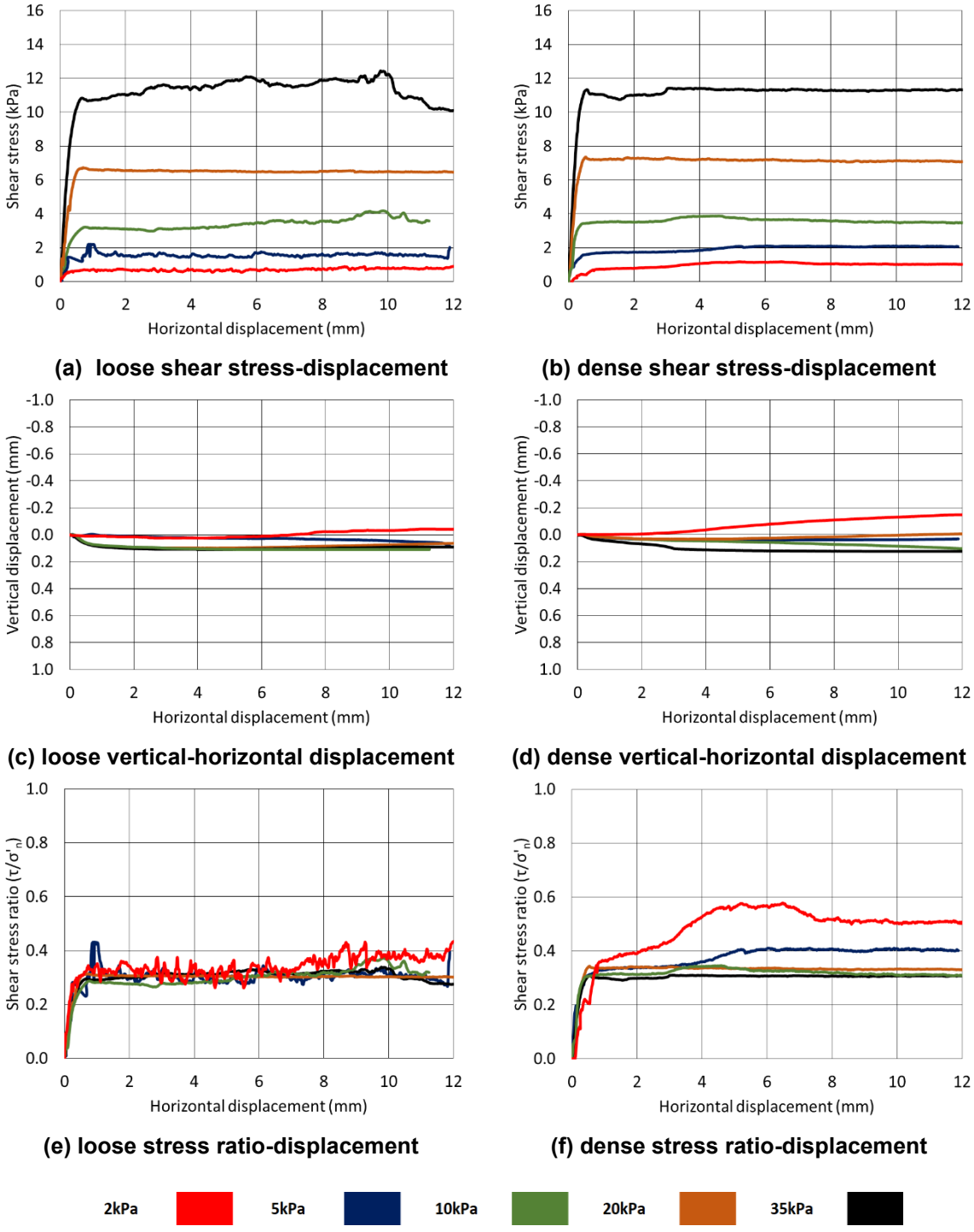

Redhill Sand "T" interface test results of loose and dense (a, b) shear stress displacement, (c, d) vertical-horizontal displacement, and (e, f) shear stress ratio, τ/σ_n

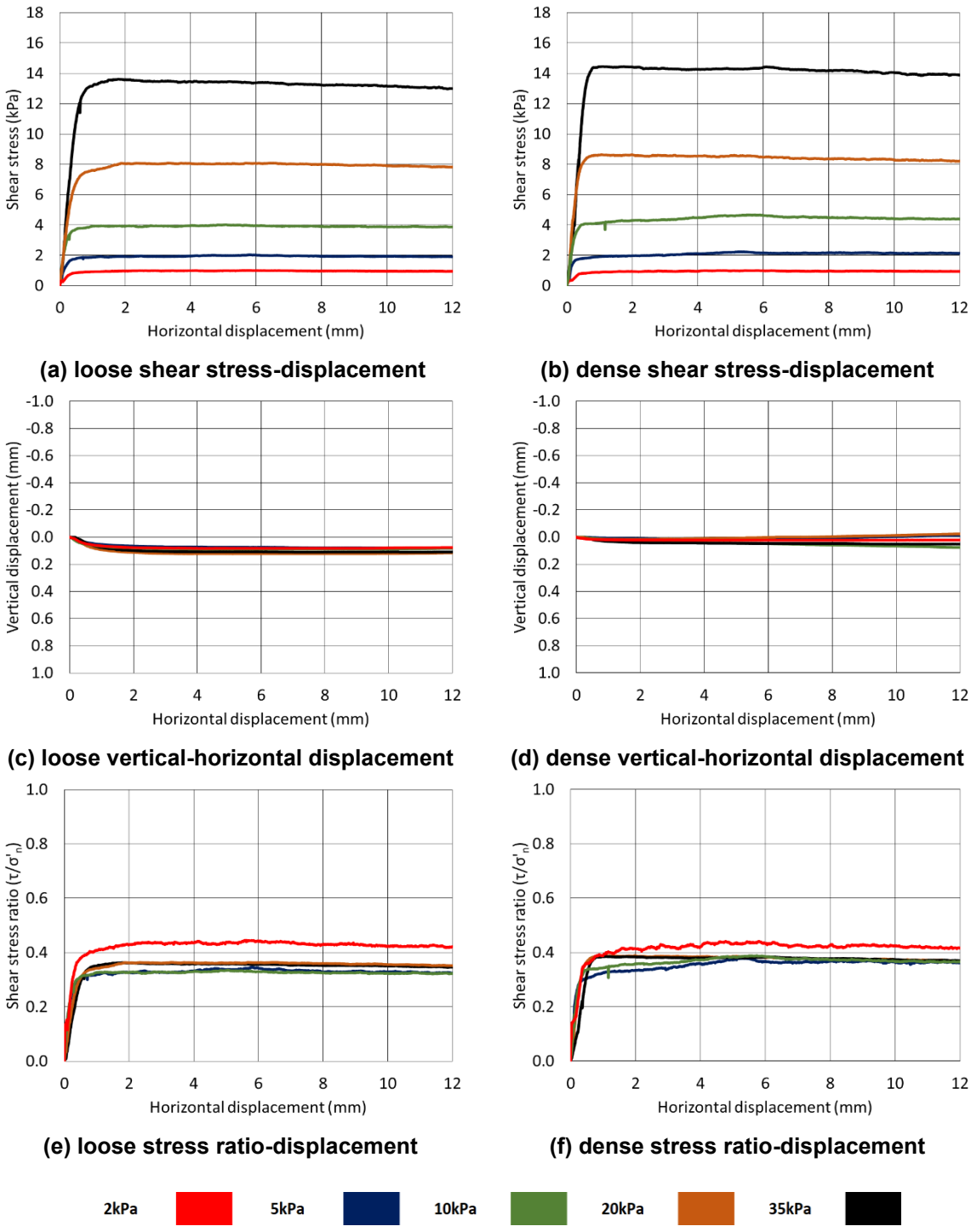

Soil S0 0.2 mm/minute horizontal displacement rate interface test results of loose and dense (a, b) shear stress displacement, (c, d) vertical-horizontal displacement, and (e, f) shear stress ratio, τ/σ_n.

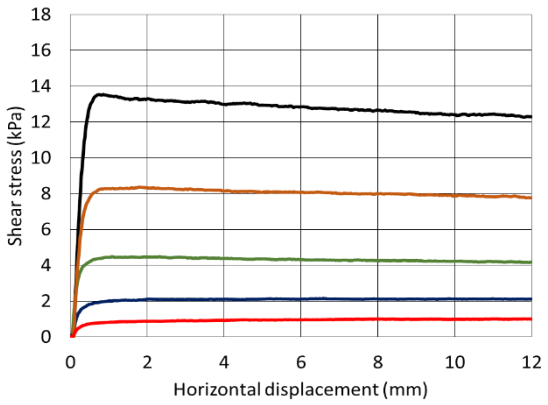

(a) loose shear stress-displacement

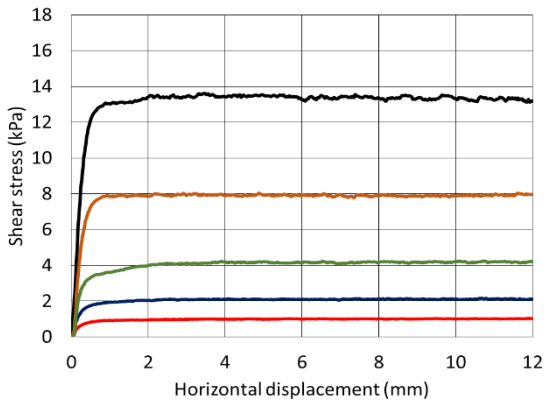

(b) dense shear stress-displacement

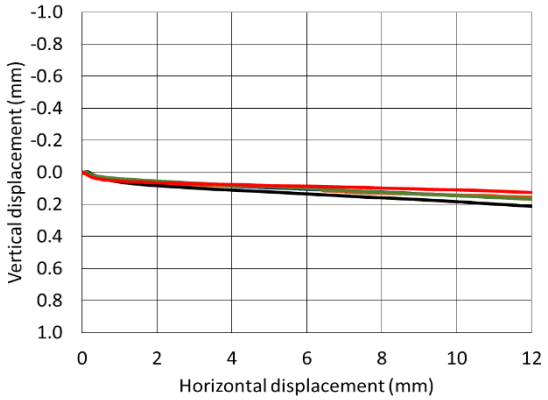

(c) loose vertical-horizontal displacement

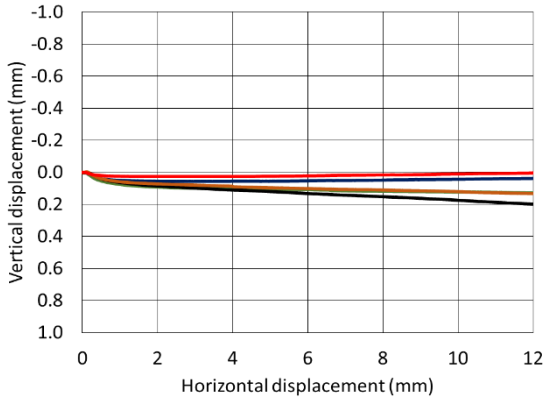

(d) dense vertical-horizontal displacement

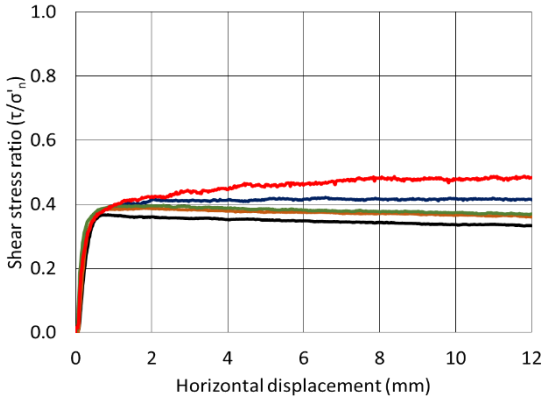

(e) loose stress ratio-displacement

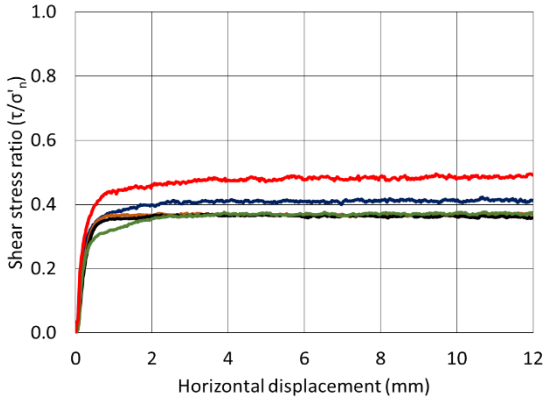

(f) dense stress ratio-displacement

Seamed-unseamed interface test results of loose and dense (a, b) shear stress displacement, (c, d) vertical-horizontal displacement, and (e, f) shear stress ratio, τ/σ_n.

Appendix C2 – "V" interface test results

"V" interface tests result tables include some cardinal test parameters and results. The $D_{r\ fab}$ and $D_{r\ con}$ are the soil sample relative densities as fabricated and post consolidation after the application of the pertinent normal load and represents the relative density as at the start of shearing. The same applies for e_{fab} and e_{con} with regard to the sample void ratio. The peak shear stress, τ_{peak}, is the maximum shear stress recorded during the test and the ultimate shear stress, τ_{ult}, is the average shear stress between 10 mm and 12 mm of horizontal displacement. For each surface, one nominal relative density was tested (D_r approximately 70%) at four levels of vertical confining stress(σ_n approximately 2, 5, 10, 20 kPa). For interface tests a four part naming convention has been adopted to uniquely identify each test consisting of a soil type reference [LG, LB, HS, RH], a density reference [L (for loose), D (for dense)], and a nominal stress level reference [2, 5, 10, 20 (kPa)]. Test references end with the surface type reference. Loose tests using Redhill Sand on this surface type were no possible due to excessive settlements causing unreliable results.

Summary of "V" virgin interface tests

Test reference	σ_n (kPa)	$D_{r\ fab}$ (%)	$D_{r\ con}$ (%)	e_{fab}	e_{con}	τ_{peak} (kPa)	τ_{ult} (kPa)	τ_{peak}/σ_n	τ_{ult}/σ_n
LG_L02_V	1.96	15.0	32.7	0.881	0.813	0.39	0.35	0.20	0.18
LG_L05_V	5.03	15.1	35.4	0.881	0.802	0.82	0.53	0.16	0.11
LG_L10_V	10.14	15.1	36.2	0.881	0.799	1.60	1.17	0.16	0.12
LG_L20_V	20.37	15.1	36.7	0.881	0.797	3.76	3.34	0.18	0.16
LG_D02_V	1.96	70.1	68.5	0.667	0.673	0.54	0.50	0.28	0.25
LG_D05_V	5.03	70.0	72.1	0.667	0.659	1.07	0.95	0.21	0.19
LG_D10_V	10.14	70.0	69.0	0.667	0.671	2.03	1.78	0.20	0.18
LG_D20_V	20.37	70.0	70.4	0.667	0.666	4.32	3.95	0.21	0.19
LB_L02_V	1.96	15.0	37.8	0.793	0.723	0.31	0.28	0.16	0.15
LB_L05_V	5.03	18.8	34.3	0.782	0.734	1.00	0.96	0.20	0.19
LB_L10_V	10.14	15.3	39.8	0.793	0.717	3.01	2.94	0.30	0.29
LB_L20_V	20.36	15.0	38.6	0.793	0.720	4.32	3.44	0.21	0.17
LB_D02_V	1.96	70.0	70.3	0.623	0.622	0.65	0.62	0.33	0.32
LB_D05_V	5.03	70.0	73.4	0.623	0.612	1.25	1.12	0.25	0.24
LB_D10_V	10.14	70.1	75.1	0.623	0.607	2.20	1.856	0.22	.018
LB_D20_V	20.36	70.0	73.3	0.623	0.613	4.19	3.14	0.21	0.15
HS_L02_V	1.96	15.0	33.1	0.943	0.874	0.51	0.49	0.26	0.25
HS_L05_V	5.02	15.1	35.8	0.943	0.864	1.53	1.49	0.31	0.30
HS_L10_V	10.14	15.1	35.2	0.943	0.866	3.52	3.43	0.35	0.34
HS_L20_V	20.36	15.0	38.1	0.943	0.855	6.99	6.41	0.34	0.31
HS_D02_V	1.96	70.0	69.6	0.734	0.736	0.80	0.79	0.41	0.40
HS_D05_V	5.02	70.1	72.3	0.734	0.725	1.74	1.71	0.35	0.34

Summary of "V" virgin interface tests

Test reference	σ_n (kPa)	$D_{r\ fab}$ (%)	$D_{r\ con}$ (%)	e_{fab}	e_{con}	τ_{peak} (kPa)	τ_{ult} (kPa)	τ_{peak}/σ_n	τ_{ult}/σ_n
HS_D10_V	10.14	70.1	72.1	0.734	0.726	3.70	3.63	0.36	0.36
HS_D20_V	20.36	70.1	73.6	0.734	0.720	8.24	7.40	0.40	0.36
RH_D02_V	1.95	70.1	71.4	0.739	0.733	0.68	0.67	0.35	0.34
RH_D05_V	5.02	70.0	71.9	0.739	0.731	1.49	1.47	0.30	0.29
RH_D10_V	10.13	70.1	72.8	0.739	0.727	2.82	2.79	0.28	0.28
RH_D20_V	20.36	70.0	77.9	0.739	0.705	4.96	4.93	0.24	0.24

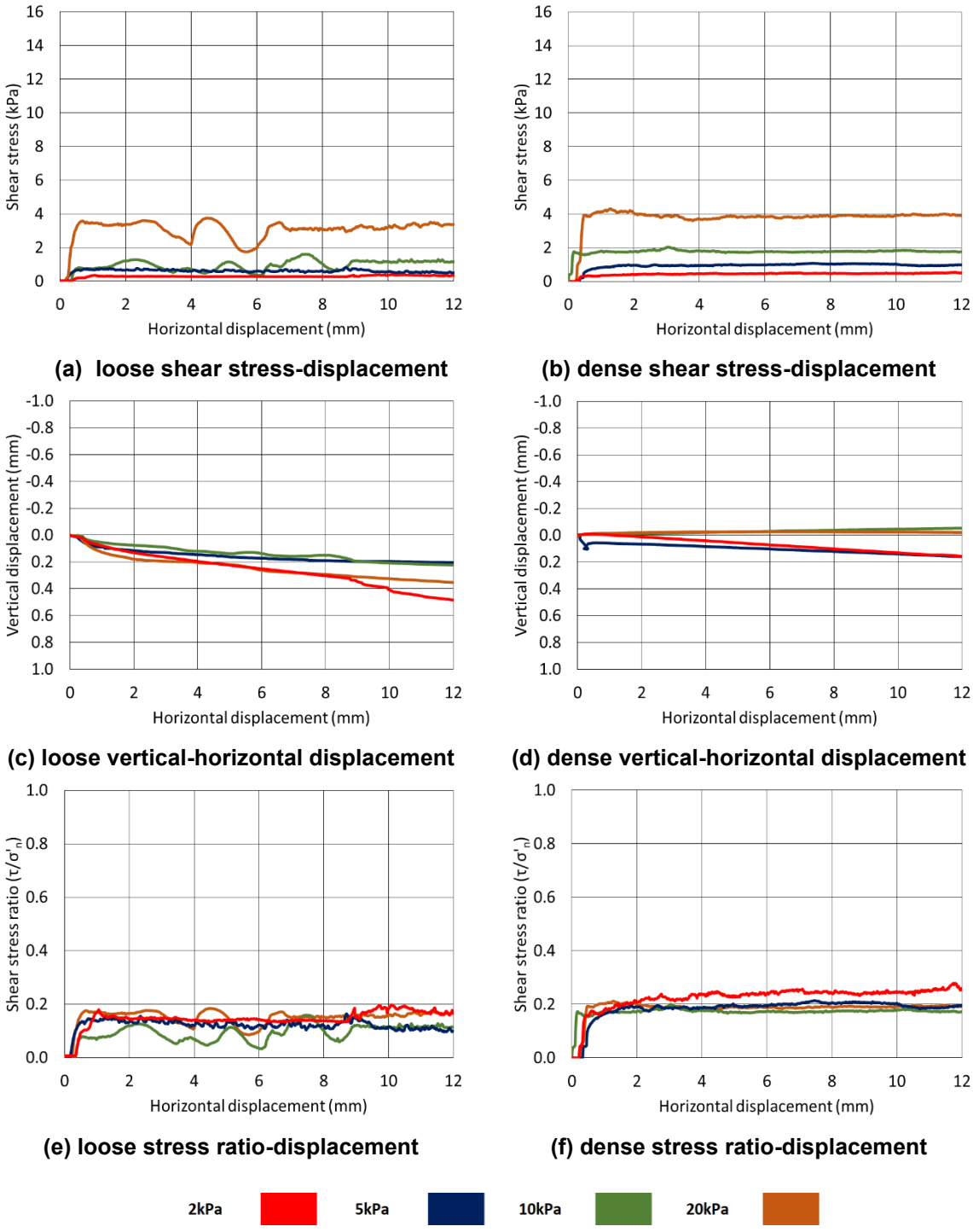

Lowestoft Gravel "V" interface test results of loose and dense (a, b) shear stress displacement, (c, d) vertical-horizontal displacement, and (e, f) shear stress ratio, τ/σ'_n.

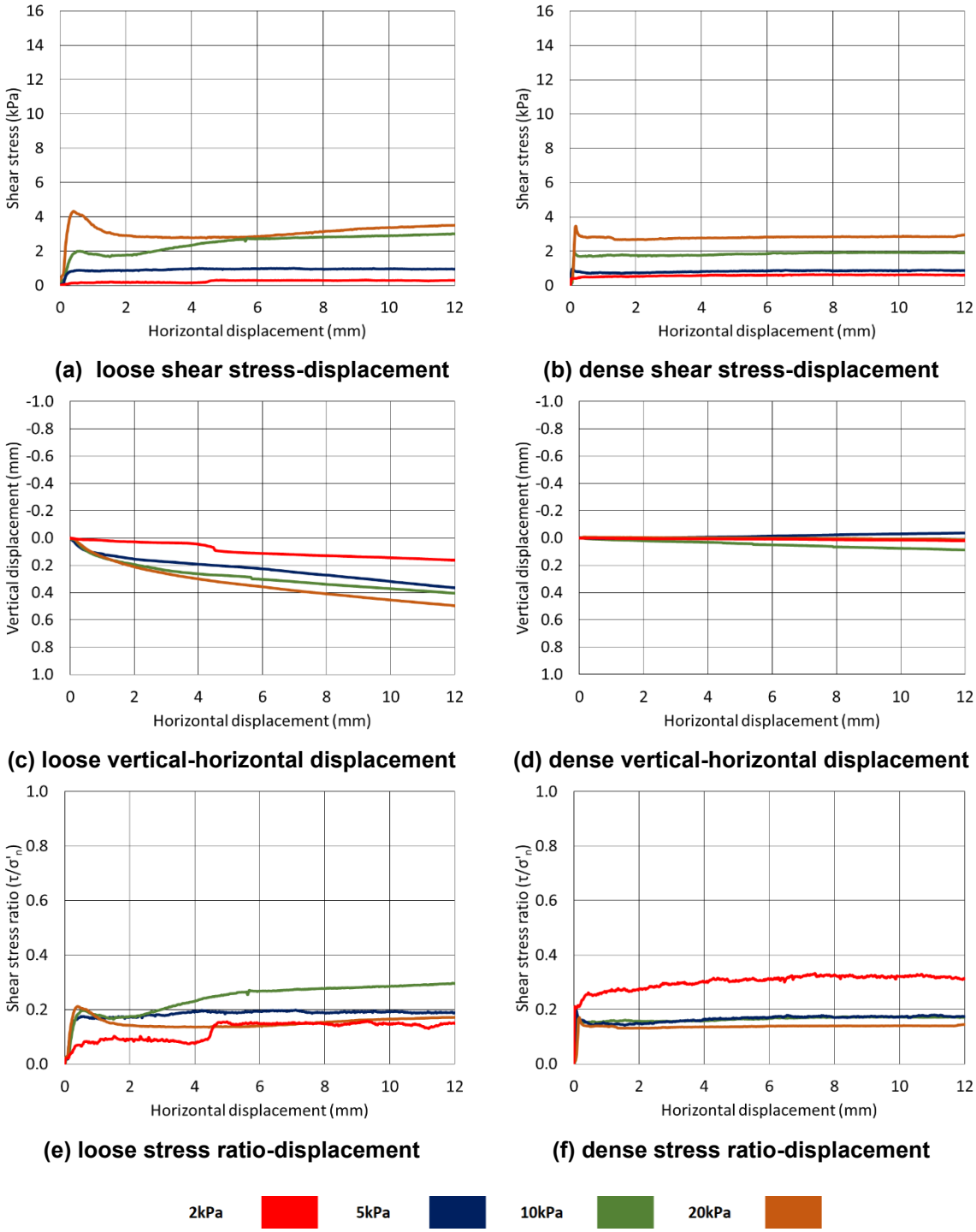

Leighton Buzzard "V" interface test results of loose and dense (a, b) shear stress displacement, (c, d) vertical-horizontal displacement, and (e, f) shear stress ratio, τ/σ_n.

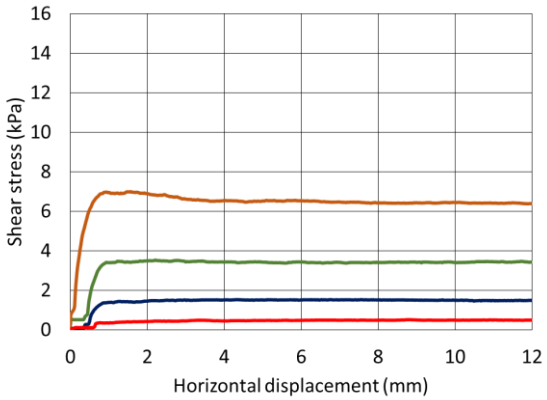

(a) loose shear stress-displacement

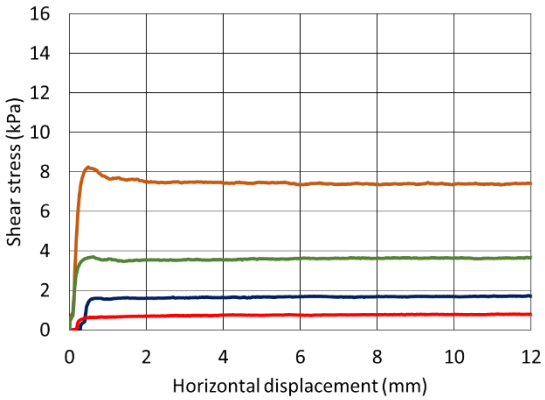

(b) dense shear stress-displacement

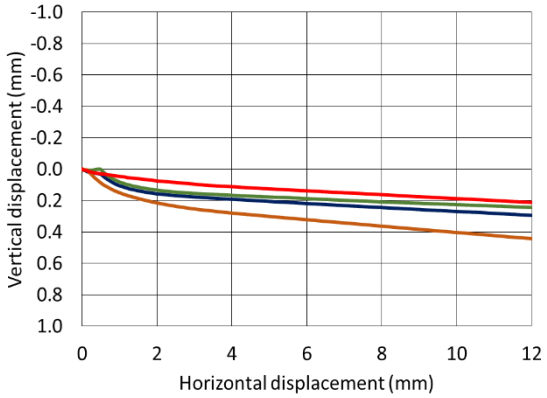

(c) loose vertical-horizontal displacement

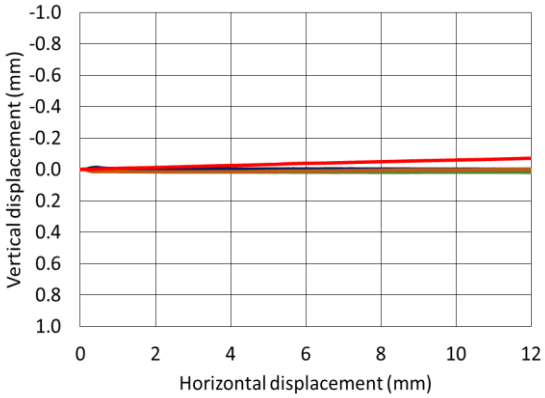

(d) dense vertical-horizontal displacement

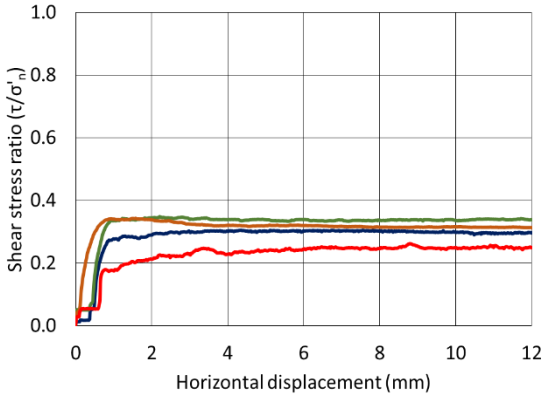

(e) loose stress ratio-displacement

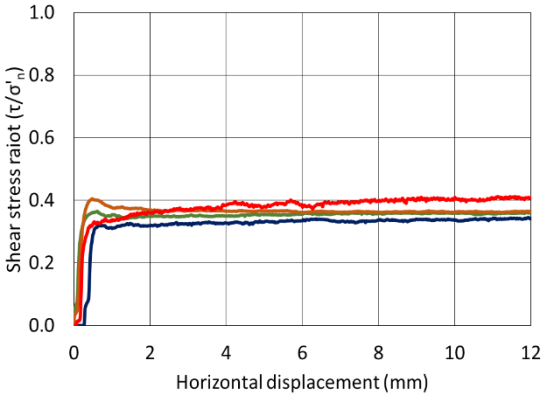

(f) dense stress ratio-displacement

Hostun Sand "V" interface test results of loose and dense (a, b) shear stress displacement, (c, d) vertical-horizontal displacement, and (e, f) shear stress ratio, τ/σ_n.

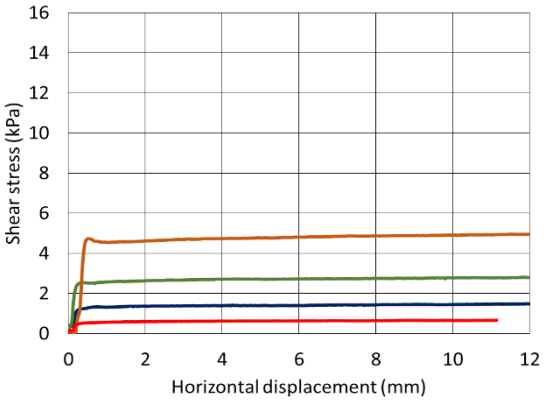

(a) dense shear stress-displacement

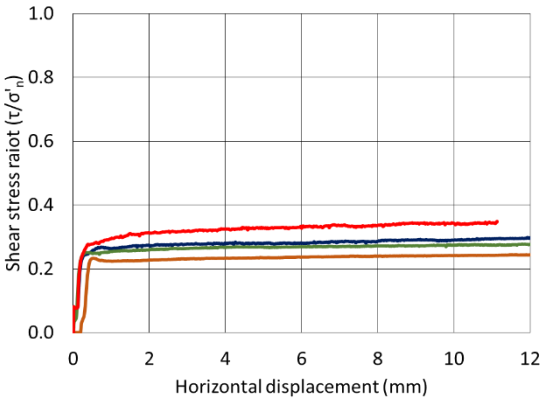

(b) dense vertical-horizontal displacement

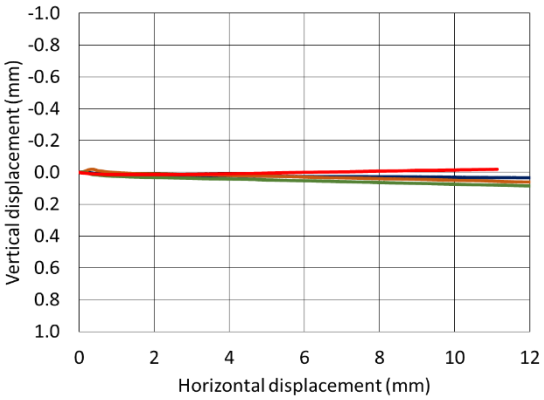

(c) dense stress ratio-displacement

Redhill Sand "V" interface test results of dense (a) shear stress displacement, (b) vertical-horizontal displacement, and (c) shear stress ratio, τ/σ_n.

Appendix C3 – "E" interface test results

"E" interface tests result tables include some cardinal test parameters and results. The $D_{r\ fab}$ and $D_{r\ con}$ are the soil sample relative densities as fabricated and post consolidation after the application of the pertinent normal load and represents the relative density as at the start of shearing. The same applies for e_{fab} and e_{con} with regard to the sample void ratio. The peak shear stress, τ_{peak}, is the maximum shear stress recorded during the test and the ultimate shear stress, τ_{ult}, is the average shear stress between 10 mm and 12 mm of horizontal displacement. For each surface, two nominal relative density were tested (D_r approximately 15% and 70%) at four levels of vertical confining stress(σ_n approximately 2, 5, 15, 20 kPa). For interface tests a four part naming convention has been adopted to uniquely identify each test consisting of a soil type reference [LG, LB, HS, RH], a density reference [L (for loose), D (for dense)], and a nominal stress level reference [2, 5, 15, 20 (kPa)]. Test references end with the surface type reference.

Summary of "E" engraved interface tests

Test reference	σ_n (kPa)	$D_{r\ fab}$ (%)	$D_{r\ con}$ (%)	e_{fab}	e_{con}	τ_{peak} (kPa)	τ_{ult} (kPa)	τ_{peak}/σ_n	τ_{ult}/σ_n
LG_L02_E	1.95	15.1	28.3	0.881	0.830	0.89	0.86	0.45	0.44
LG_L05_E	5.02	15.1	27.3	0.881	0.833	1.89	1.80	0.38	0.36
LG_L15_E	15.25	15.0	33.0	0.881	0.811	5.61	5.31	0.37	0.35
LG_L20_E	20.36	15.1	37.4	0.881	0.794	6.86	6.51	0.34	0.32
LG_D02_E	1.95	70.1	70.1	0.667	0.667	0.97	0.90	0.50	0.46
LG_D05_E	5.02	70.0	70.3	0.667	0.666	2.00	1.94	0.40	0.39
LG_D15_E	15.25	70.0	70.2	0.667	0.666	5.77	5.45	0.38	0.36
LG_D20_E	20.36	70.1	71.7	0.667	0.660	7.87	7.36	0.39	0.36
LB_L02_E	1.95	15.0	34.2	0.793	0.734	0.82	0.75	0.42	0.38
LB_L05_E	5.02	15.1	34.7	0.793	0.732	1.69	1.58	0.34	0.31
LB_L15_E	15.25	15.0	42.7	0.793	0.708	4.92	4.53	0.32	0.30
LB_L20_E	20.36	15.0	39.6	0.793	0.717	6.09	5.92	0.30	0.29
LB_D02_E	1.95	70.1	71.9	0.623	0.617	0.99	0.96	0.51	0.49
LB_D05_E	5.02	70.0	74.5	0.623	0.609	2.08	2.01	0.41	0.40
LB_D15_E	15.25	70.1	76.4	0.623	0.603	5.68	5.34	0.37	0.35
LB_D20_E	20.36	70.1	76.6	0.623	0.602	7.45	7.07	0.37	0.35
HS_L02_E	1.95	15.1	32.0	0.943	0.878	0.95	0.92	0.49	0.47
HS_L05_E	5.02	15.1	34.2	0.943	0.870	2.29	2.24	0.46	0.45
HS_L15_E	15.25	15.1	49.1	0.943	0.814	6.20	6.12	0.41	0.40
HS_L20_E	20.36	15.1	38.8	0.943	0.853	8.50	8.25	0.42	0.41
HS_D02_E	1.95	70.0	72.1	0.734	0.726	1.14	1.11	0.58	0.57
HS_D05_E	5.02	70.1	74.2	0.734	0.718	2.61	2.53	0.52	0.50

Summary of "E" engraved interface tests

Test reference	σ_n (kPa)	$D_{r\ fab}$ (%)	$D_{r\ con}$ (%)	e_{fab}	e_{con}	τ_{peak} (kPa)	τ_{ult} (kPa)	τ_{peak}/σ_n	τ_{ult}/σ_n
HS_D15_E	15.25	70.1	77.3	0.734	0.706	7.83	7.45	0.51	0.49
HS_D20_E	20.36	70.0	73.7	0.734	0.720	10.32	9.85	0.51	0.48
RH_L02_E	1.95	15.7	42.6	0.973	0.857	0.92	0.90	0.47	0.46
RH_L05_E	5.02	15.7	41.9	0.972	0.860	1.97	1.92	0.39	0.38
RH_L15_E	15.25	15.0	44.3	0.975	0.850	5.99	5.91	0.39	0.39
RH_L20_E	20.36	15.1	46.7	0.975	0.839	7.53	6.46	0.37	0.32
RH_D02_E	1.95	70.0	71.4	0.739	0.733	1.02	1.01	0.52	0.52
RH_D05_E	5.02	70.1	73.2	0.739	0.725	2.25	2.19	0.45	0.44
RH_D15_E	15.25	70.1	75.0	0.739	0.717	6.48	6.32	0.42	0.41
RH_D20_E	20.36	70.1	72.2	0.739	0.730	8.99	8.95	0.44	0.44

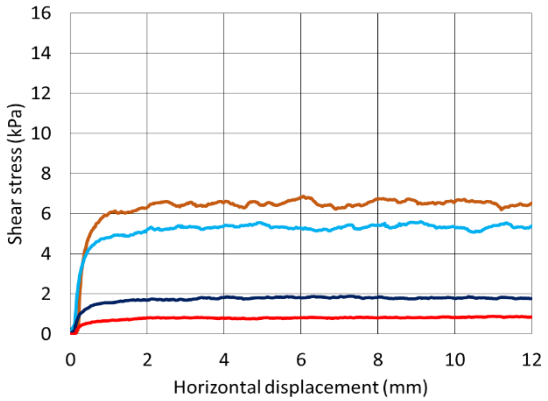

(c) loose shear stress-displacement

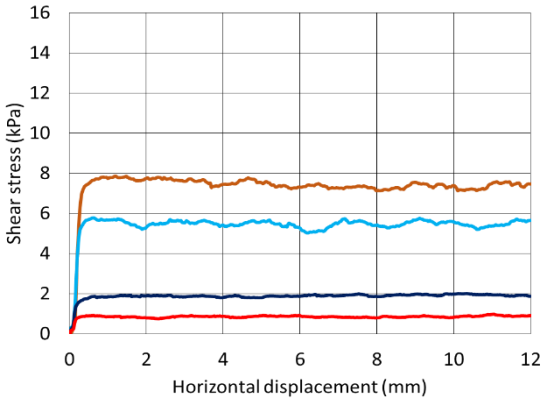

(b) dense shear stress-displacement

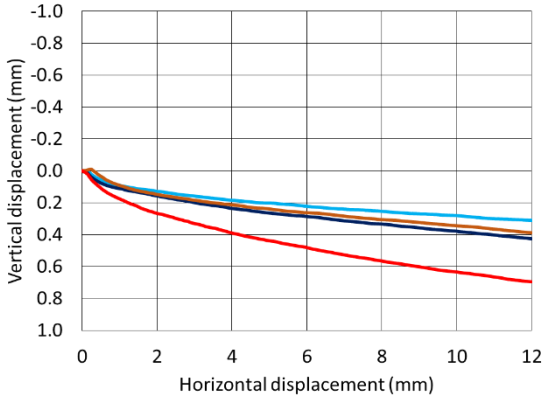

(c) loose vertical-horizontal displacement

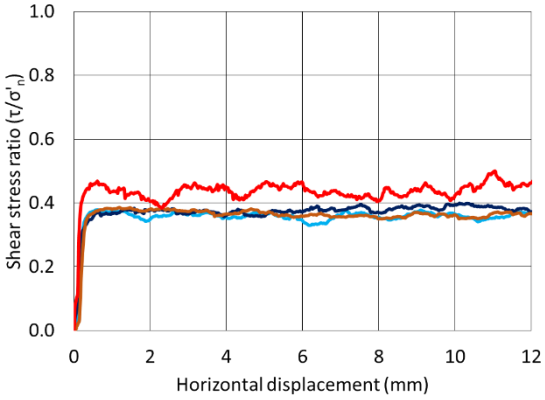

(d) dense vertical-horizontal displacement

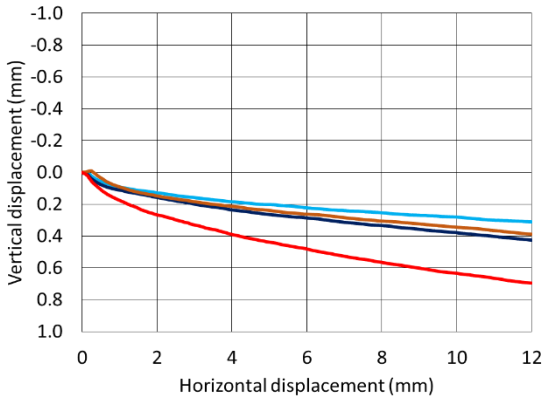

(e) loose stress ratio-displacement

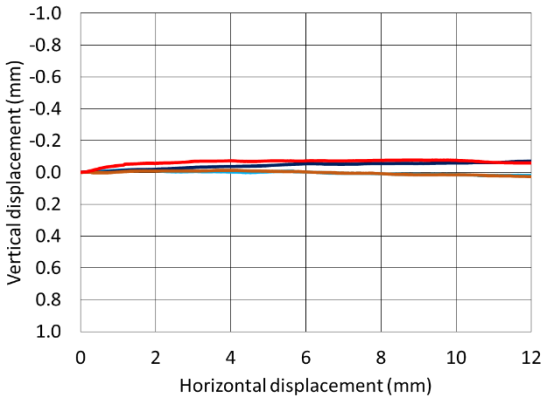

(f) dense stress ratio-displacement

Lowestoft Gravel "E" interface test results of loose and dense (a, b) shear stress displacement, (c, d) vertical-horizontal displacement, and (e, f) shear stress ratio, τ/σ_n.

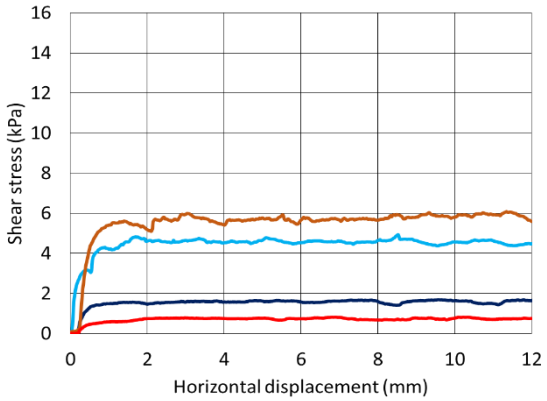

(b) loose shear stress-displacement

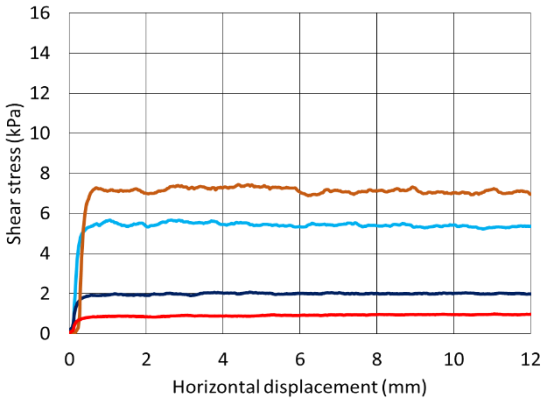

(b) dense shear stress-displacement

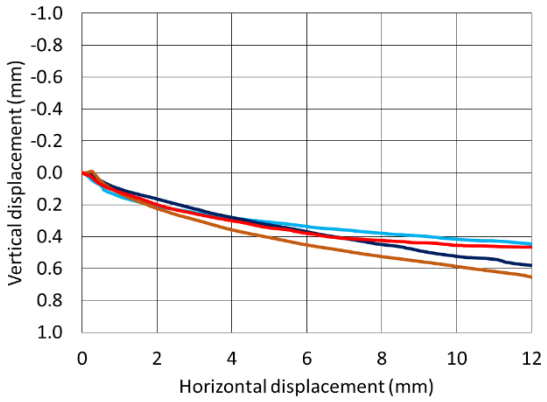

(c) loose vertical-horizontal displacement

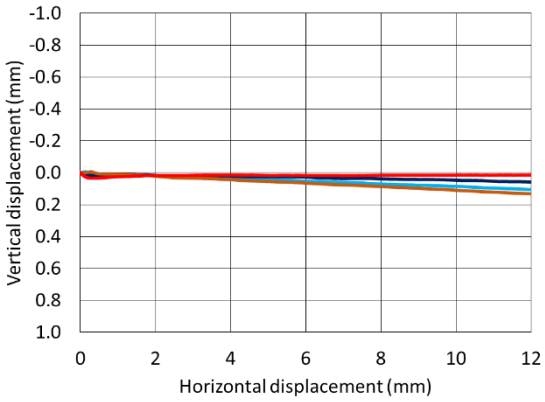

(d) dense vertical-horizontal displacement

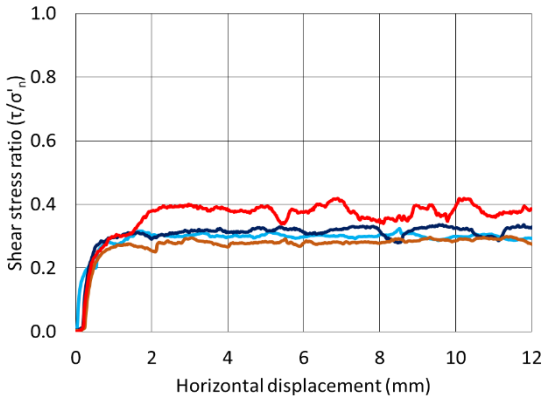

(e) loose stress ratio-displacement

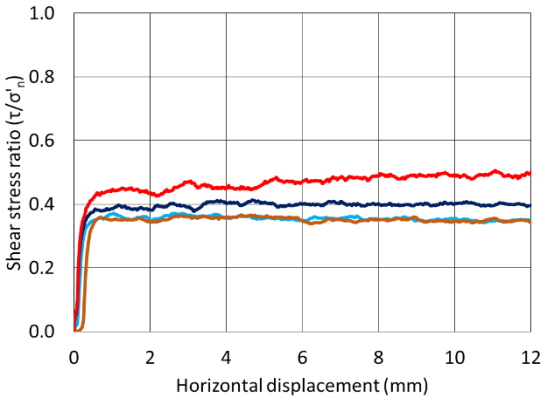

(f) dense stress ratio-displacement

Leighton Buzzard "E" interface test results of loose and dense (a, b) shear stress displacement, (c, d) vertical-horizontal displacement, and (e, f) shear stress ratio, τ/σ_n.

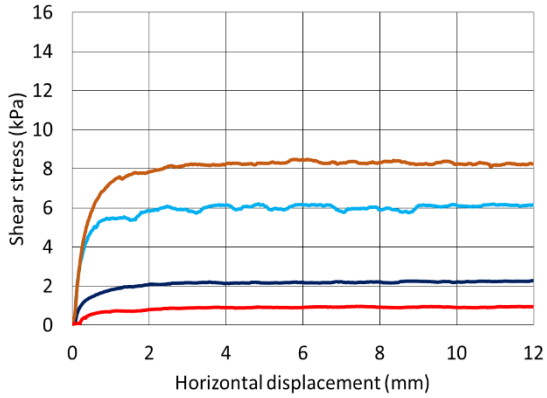

(b) loose shear stress-displacement

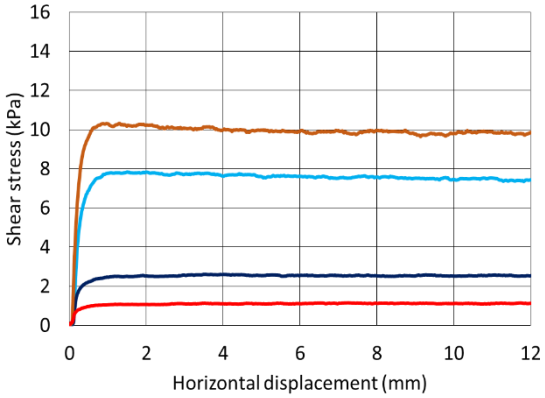

(b) dense shear stress-displacement

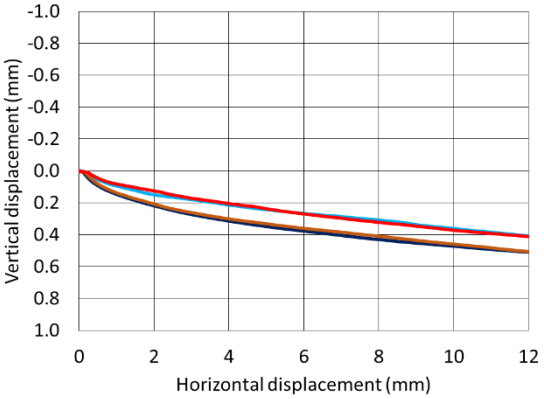

(c) loose vertical-horizontal displacement

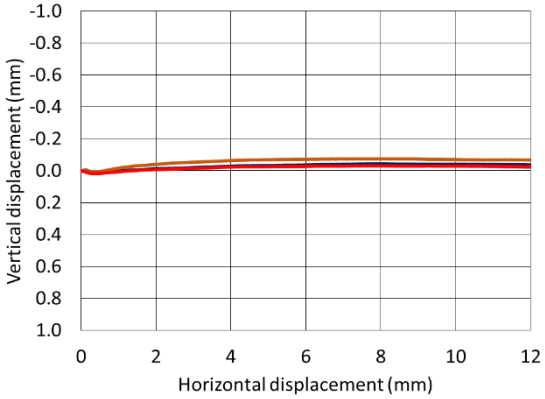

(d) dense vertical-horizontal displacement

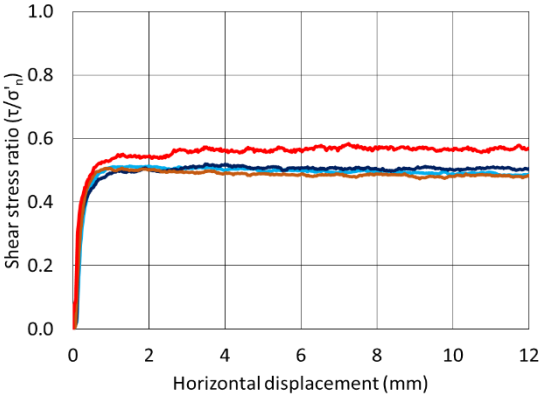

(e) loose stress ratio-displacement

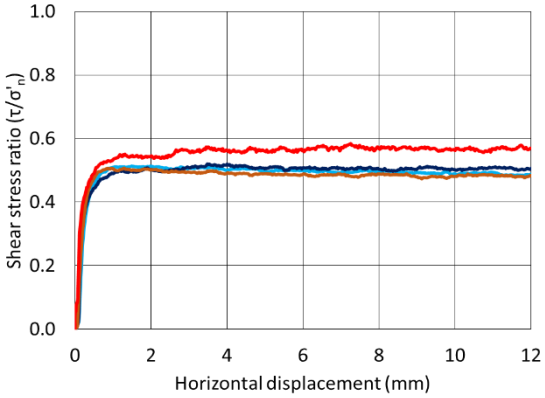

(f) dense stress ratio-displacement

Hostun Sand "E" interface test results of loose and dense (a, b) shear stress displacement, (c, d) vertical-horizontal displacement, and (e, f) shear stress ratio, τ/σ_n.

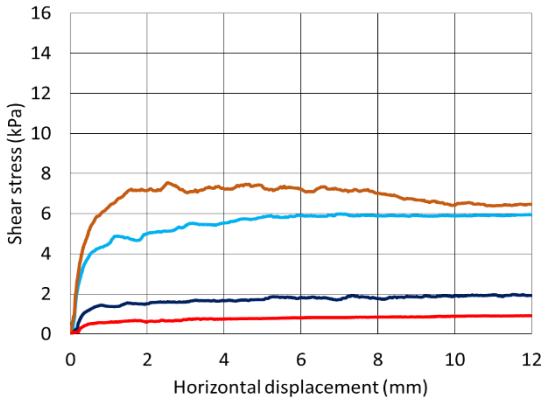

(b) loose shear stress-displacement

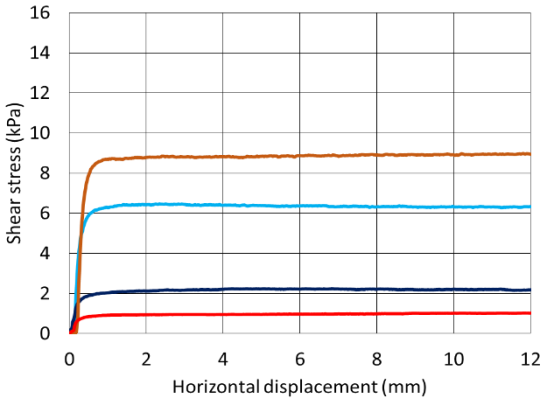

(b) dense shear stress-displacement

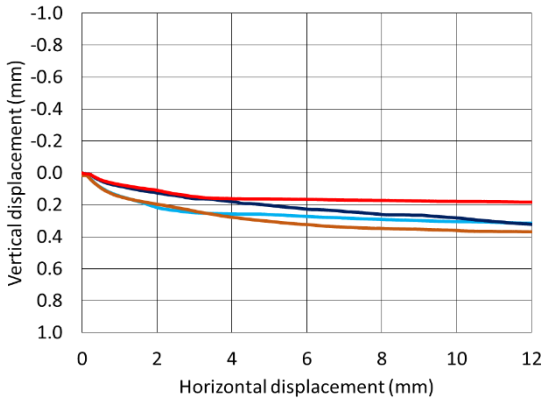

(c) loose vertical-horizontal displacement

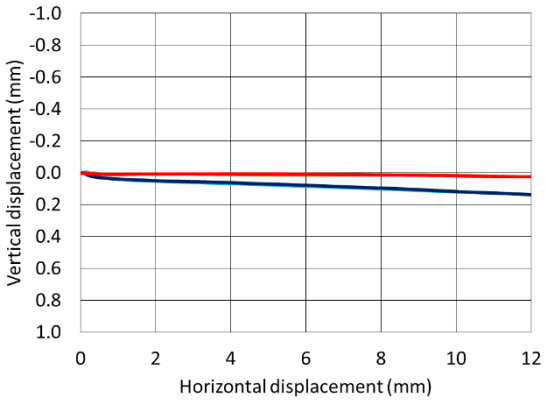

(d) dense vertical-horizontal displacement

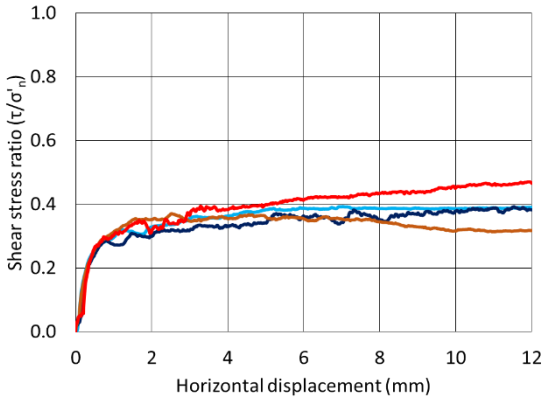

(e) loose stress ratio-displacement

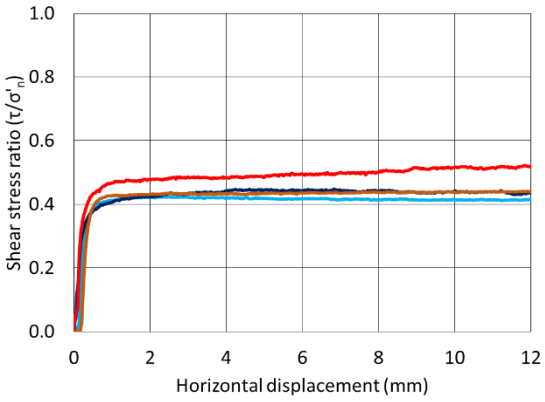

(f) dense stress ratio-displacement

Redhill Sand "E" interface test results of loose and dense (a, b) shear stress displacement, (c, d) vertical-horizontal displacement, and (e, f) shear stress ratio, τ/σ_n.

Appendix C4 – "S" interface test results

"S" interface tests result tables include some cardinal test parameters and results. The $D_{r\ fab}$ and $D_{r\ con}$ are the soil sample relative densities as fabricated and post consolidation after the application of the pertinent normal load and represents the relative density as at the start of shearing. The same applies for e_{fab} and e_{con} with regard to the sample void ratio. The peak shear stress, τ_{peak}, is the maximum shear stress recorded during the test and the ultimate shear stress, τ_{ult}, is the average shear stress between 10 mm and 12 mm of horizontal displacement. For each surface, two nominal relative density were tested (D_r approximately 15% and 70%) at four levels of vertical confining stress(σ_n approximately 2, 5, 15, 20 kPa). For interface tests a four part naming convention has been adopted to uniquely identify each test consisting of a soil type reference [LG, LB, HS, RH], a density reference [L (for loose), D (for dense)], and a nominal stress level reference [2, 5, 15, 20 (kPa)]. Test references end with the surface type reference.

Summary of "S" sandblasted interface tests

Test reference	σ_n (kPa)	$D_{r\ fab}$ (%)	$D_{r\ con}$ (%)	e_{fab}	e_{con}	τ_{peak} (kPa)	τ_{ult} (kPa)	τ_{peak}/σ_n	τ_{ult}/σ_n
LG_L02_S	1.95	15.0	25.9	0.881	0.839	1.27	1.15	0.65	0.59
LG_L05_S	5.02	15.1	26.6	0.881	0.836	3.34	3.10	0.66	0.62
LG_L15_S	15.25	15.1	31.8	0.881	0.816	9.25	8.93	0.61	0.59
LG_L20_S	20.36	15.0	37.8	0.881	0.793	10.89	10.57	0.53	0.52
LG_D02_S	1.95	70.0	68.8	0.667	0.672	1.43	1.16	0.73	0.60
LG_D05_S	5.02	70.0	68.5	0.667	0.673	3.44	2.89	0.69	0.58
LG_D15_S	15.25	70.0	70.5	0.667	0.665	10.86	9.18	0.71	0.60
LG_D20_S	20.36	70.0	79.1	0.667	0.632	12.98	10.55	0.64	0.52
LB_L02_S	1.95	15.1	34.2	0.793	0.734	1.26	1.20	0.64	0.62
LB_L05_S	5.02	15.1	34.3	0.793	0.734	2.81	2.75	0.56	0.55
LB_L15_S	15.25	15.1	39.0	0.793	0.719	8.49	8.20	0.56	0.54
LB_L20_S	20.36	15.1	39.8	0.793	0.717	11.39	11.04	0.56	0.54
LB_D02_S	1.95	70.0	72.5	0.623	0.615	1.46	1.20	0.75	0.62
LB_D05_S	5.02	70.0	72.9	0.623	0.614	3.73	2.91	0.74	0.58
LB_D15_S	15.25	70.1	76.0	0.623	0.604	11.33	8.42	0.74	0.55
LB_D20_S	20.36	70.1	73.8	0.623	0.611	15.36	11.40	0.75	0.56
HS_L02_S	1.95	15.1	30.3	0.942	0.885	1.14	1.12	0.58	0.57
HS_L05_S	5.02	15.0	37.8	0.943	0.856	3.00	2.90	0.60	0.58
HS_L15_S	15.25	15.0	37.0	0.943	0.859	8.41	8.28	0.55	0.54
HS_L20_S	20.36	15.5	46.7	0.941	0.823	11.93	11.82	0.59	0.58
HS_D02_S	1.95	70.0	71.5	0.734	0.728	1.90	1.40	0.97	0.72
HS_D05_S	5.02	70.0	70.4	0.734	0.733	4.30	3.45	0.86	0.69

Summary of "S" sandblasted interface tests

Test reference	σ_n (kPa)	$D_{r\ fab}$ (%)	$D_{r\ con}$ (%)	e_{fab}	e_{con}	τ_{peak} (kPa)	τ_{ult} (kPa)	τ_{peak}/σ_n	τ_{ult}/σ_n
HS_D15_S	15.25	70.0	74.2	0.734	0.718	11.43	9.17	0.75	0.60
HS_D20_S	20.36	70.0	75.3	0.734	0.714	14.63	12.60	0.72	0.62
RH_L02_S	1.95	15.8	39.6	0.972	0.870	1.04	1.00	0.53	0.51
RH_L05_S	5.02	16.4	46.2	0.969	0.841	2.76	2.66	0.55	0.53
RH_L15_S	15.25	15.8	45.6	0.972	0.844	7.78	7.59	0.51	0.50
RH_L20_S	20.36	17.2	48.4	0.966	0.832	9.80	9.15	0.48	0.45
RH_D02_S	1.95	70.0	71.4	0.739	0.733	1.43	1.28	0.73	0.65
RH_D05_S	5.02	70.1	73.6	0.739	0.724	3.25	2.84	0.65	0.57
RH_D15_S	15.25	70.0	74.1	0.739	0.721	9.93	8.84	0.65	0.58
RH_D20_S	20.36	70.0	74.2	0.739	0.721	13.78	12.10	0.68	0.59

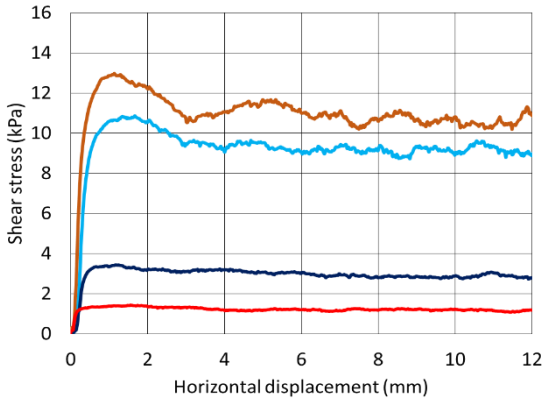

(d) loose shear stress-displacement

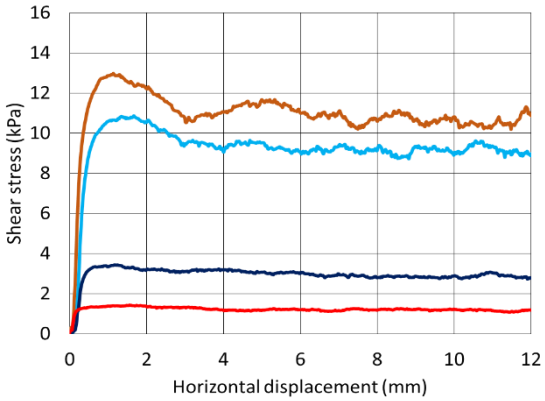

(b) dense shear stress-displacement

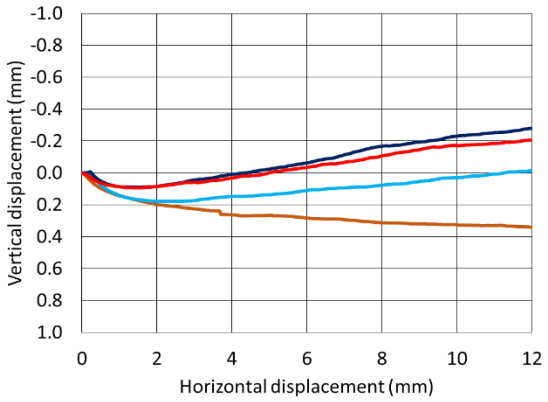

(c) loose vertical-horizontal displacement

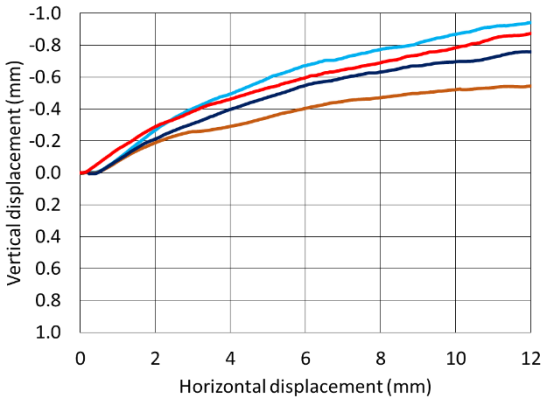

(d) dense vertical-horizontal displacement

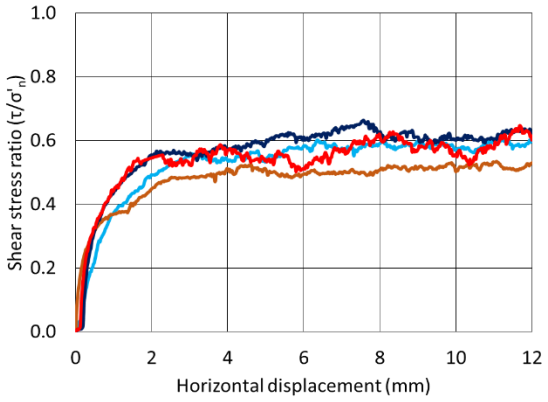

(e) loose stress ratio-displacement

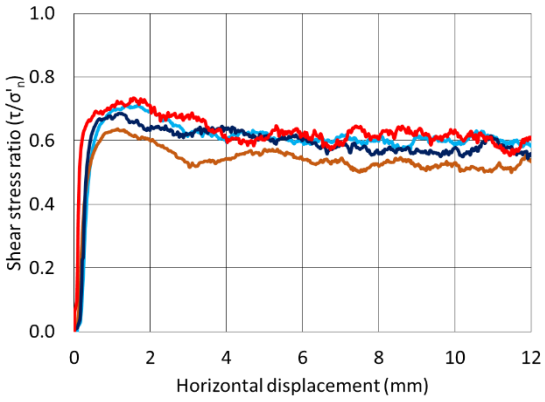

(f) dense stress ratio-displacement

Lowestoft Gravel "S" interface test results of loose and dense (a, b) shear stress displacement, (c, d) vertical-horizontal displacement, and (e, f) shear stress ratio, τ/σ_n.

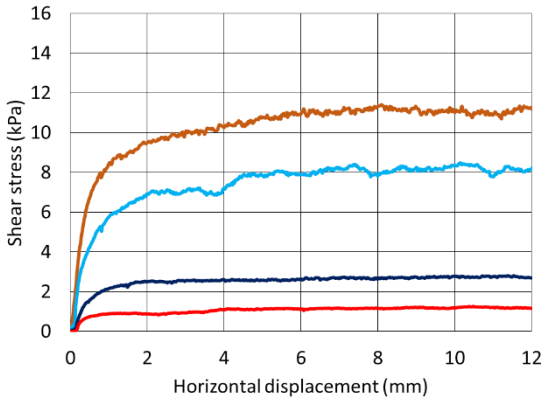

(c) loose shear stress-displacement

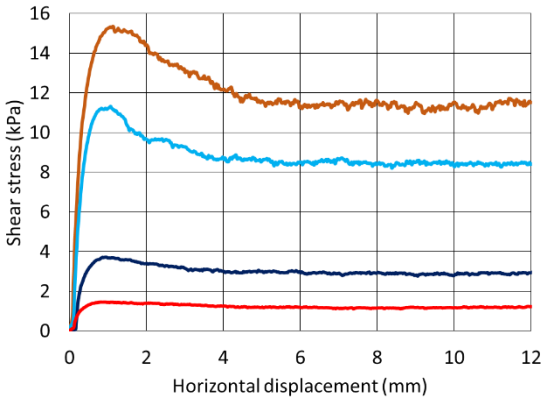

(b) dense shear stress-displacement

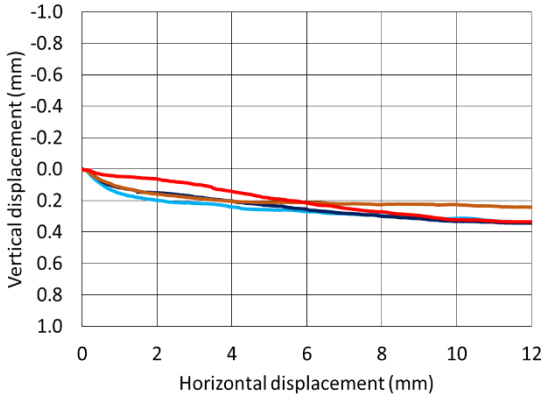

(c) loose vertical-horizontal displacement

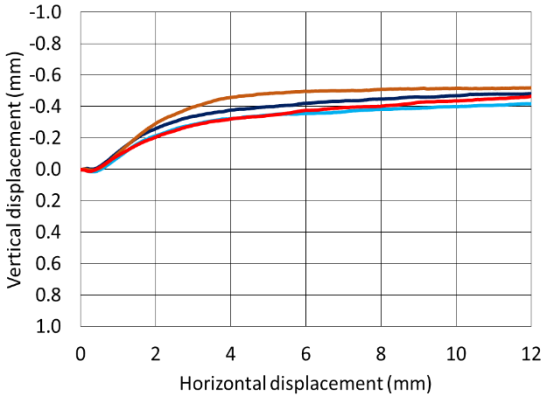

(d) dense vertical-horizontal displacement

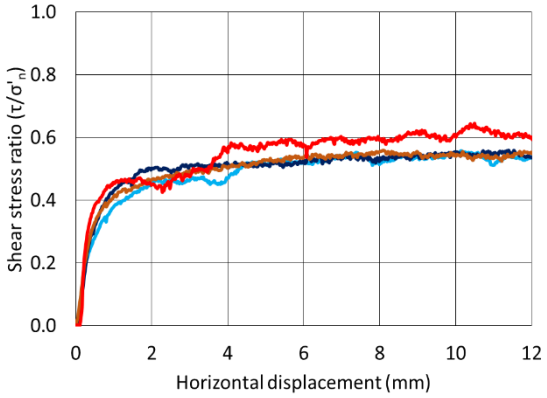

(e) loose stress ratio-displacement

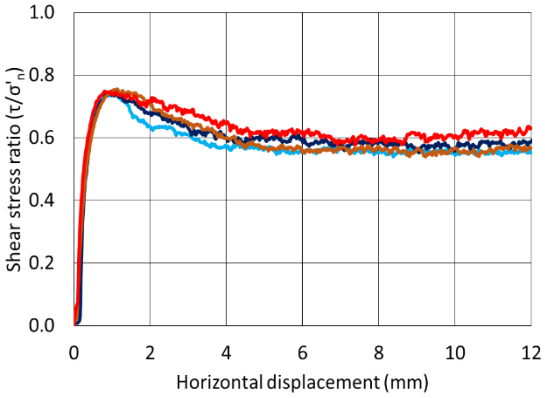

(f) dense stress ratio-displacement

Leighton Buzzard "S" interface test results of loose and dense (a, b) shear stress displacement, (c, d) vertical-horizontal displacement, and (e, f) shear stress ratio, τ/σ_n.

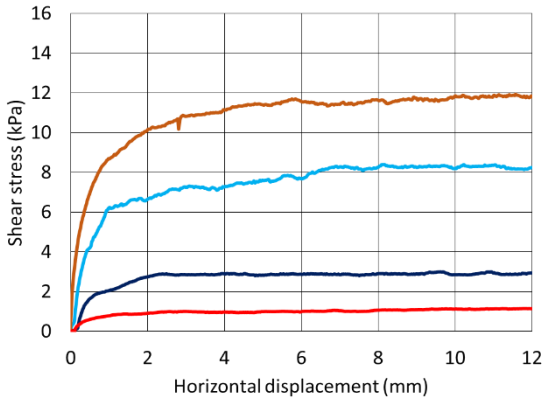

(c) loose shear stress-displacement

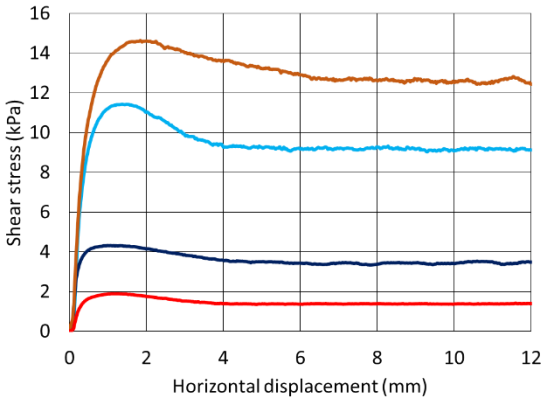

(b) dense shear stress-displacement

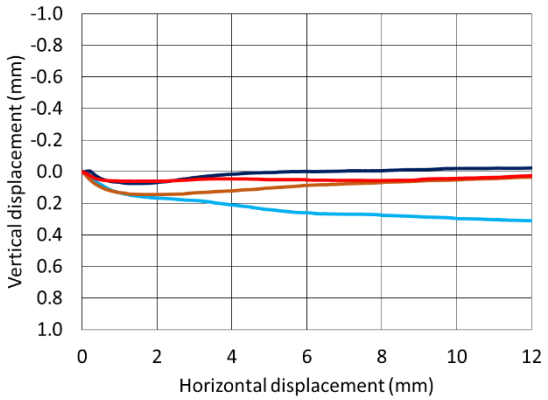

(c) loose vertical-horizontal displacement

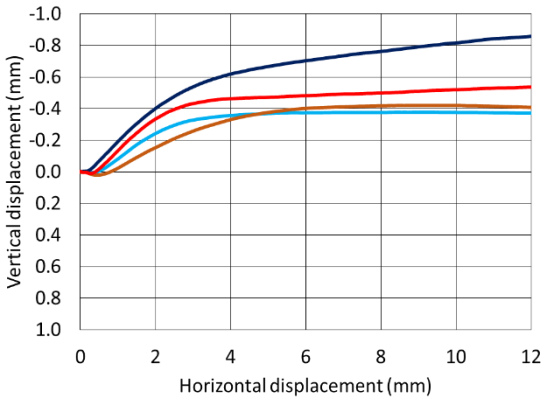

(d) dense vertical-horizontal displacement

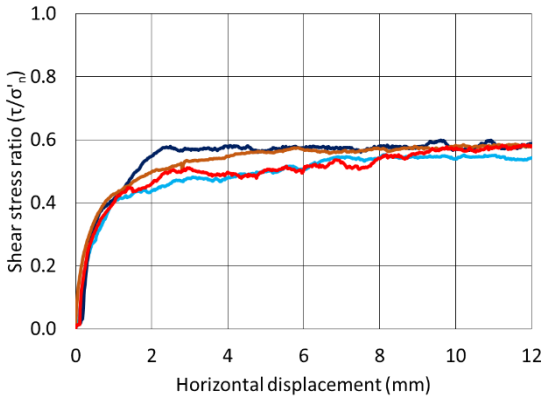

(e) loose stress ratio-displacement

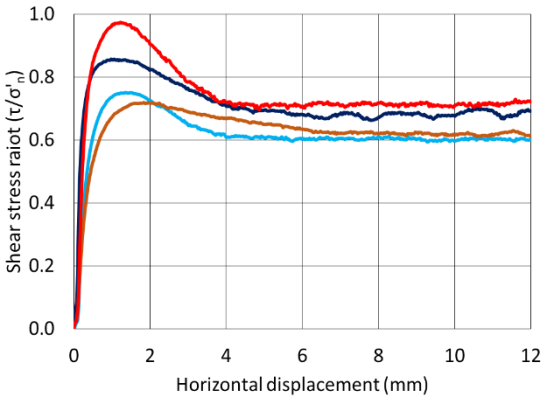

(f) dense stress ratio-displacement

Hostun Sand "S" interface test results of loose and dense (a, b) shear stress displacement, (c, d) vertical-horizontal displacement, and (e, f) shear stress ratio, τ/σ_n.

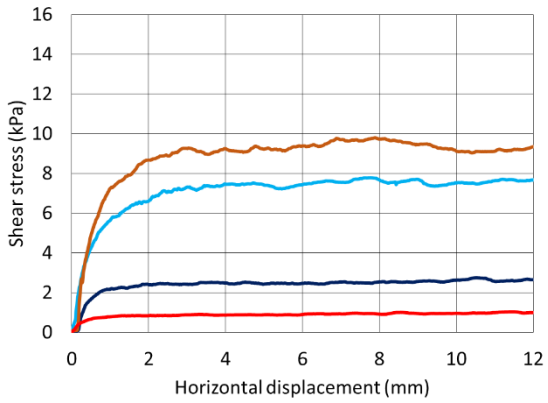

(c) loose shear stress-displacement

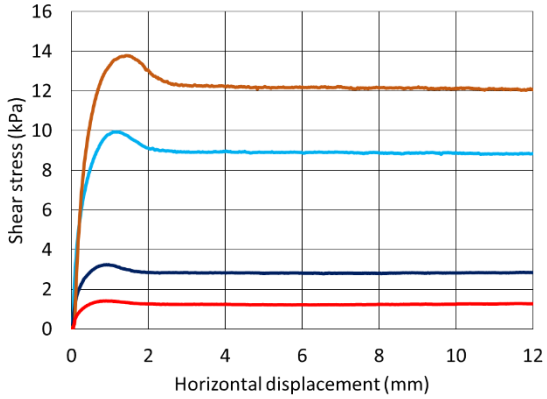

(b) dense shear stress-displacement

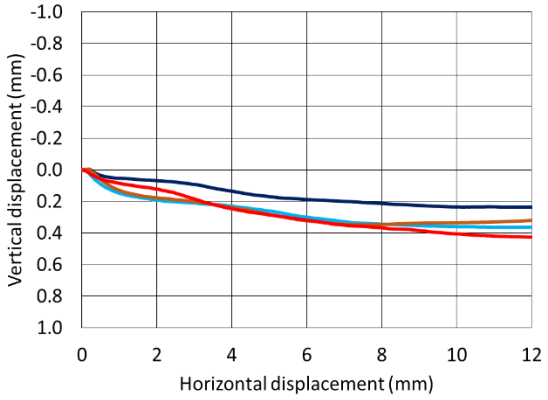

(c) loose vertical-horizontal displacement

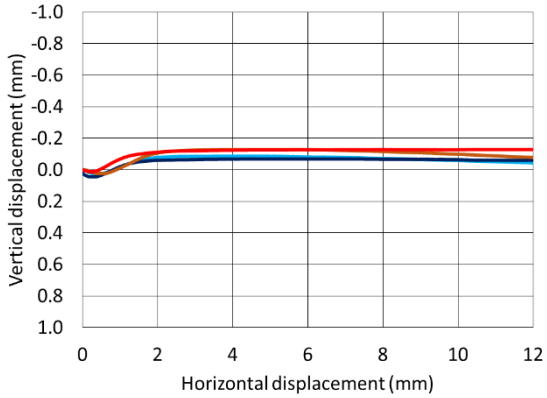

(d) dense vertical-horizontal displacement

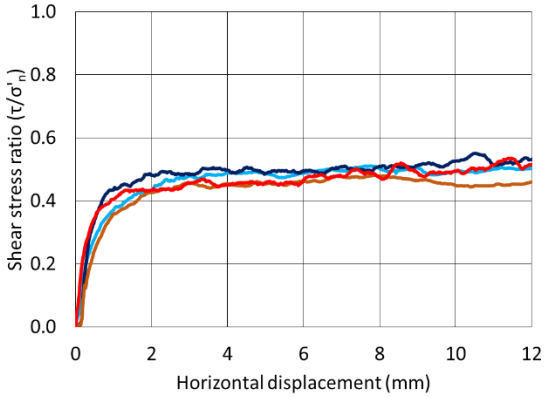

(e) loose stress ratio-displacement

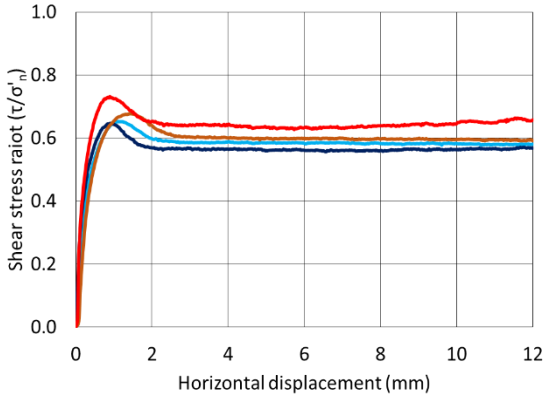

(f) dense stress ratio-displacement

Redhill Sand "S" interface test results of loose and dense (a, b) shear stress displacement, (c, d) vertical-horizontal displacement, and (e, f) shear stress ratio, τ/σ_n.

Appendix C5 – "P" interface test results

"P" interface tests result tables include some cardinal test parameters and results. The $D_{r\,fab}$ and $D_{r\,con}$ are the soil sample relative densities as fabricated and post consolidation after the application of the pertinent normal load and represents the relative density as at the start of shearing. The same applies for e_{fab} and e_{con} with regard to the sample void ratio. The peak shear stress, τ_{peak}, is the maximum shear stress recorded during the test and the ultimate shear stress, τ_{ult}, is the average shear stress between 10 mm and 12 mm of horizontal displacement. For each surface, one nominal relative density was tested (D_r approximately 70%) at four levels of vertical confining stress(σ_n approximately 2, 5, 15, 20 kPa). For interface tests a four part naming convention has been adopted to uniquely identify each test consisting of a soil type reference [LG, LB, HS, RH], a density reference [L (for loose), D (for dense)], and a nominal stress level reference [2, 5, 15, 20 (kPa)]. Test references end with the surface type.

Summary of "P" pressed interface tests

Test reference	σ_n (kPa)	$D_{r\,fab}$ (%)	$D_{r\,con}$ (%)	e_{fab}	e_{con}	τ_{peak} (kPa)	τ_{ult} (kPa)	τ_{peak}/σ_n	τ_{ult}/σ_n
LG_D02_P	1.95	70.0	70.0	0.667	0.667	1.87	1.45	0.96	0.74
LG_D05_P	5.02	70.0	70.5	0.667	0.665	4.16	3.46	0.83	0.69
LG_D15_P	15.25	70.1	71.3	0.667	0.662	11.76	9.83	0.77	0.65
LG_D20_P	20.36	70.0	71.5	0.667	0.661	16.26	12.73	0.80	0.63
LB_L02_P	1.95	15.1	30.6	0.793	0.745	1.18	1.14	0.60	0.59
LB_L05_P	5.02	15.0	34.5	0.793	0.733	2.79	2.66	0.56	0.53
LB_L15_P	15.25	15.1	36.9	0.793	0.726	9.33	9.16	0.61	0.60
LB_L20_P	20.36	15.9	37.8	0.791	0.723	12.83	12.38	0.63	0.61
LB_D02_P	1.95	70.1	70.2	0.623	0.623	1.88	1.38	0.96	0.71
LB_D05_P	5.02	70.1	72.0	0.623	0.617	3.97	3.28	0.79	0.65
LB_D15_P	15.25	70.0	72.3	0.623	0.616	12.04	9.47	0.79	0.62
LB_D20_P	20.36	70.1	72.0	0.623	0.617	15.76	12.43	0.77	0.61
HS_L02_P	1.95	15.1	36.4	0.943	0.862	1.18	1.14	0.60	0.59
HS_L05_P	5.02	15.1	33.6	0.943	0.872	2.87	2.74	0.57	0.55
HS_L15_P	15.25	15.1	37.5	0.943	0.858	9.13	8.87	0.60	0.58
HS_L20_P	20.36	15.0	39.7	0.943	0.849	11.87	11.67	0.58	0.57
HS_D02_P	1.95	70.1	70.2	0.734	0.733	1.86	1.46	0.96	0.75
HS_D05_P	5.02	70.0	71.4	0.734	0.729	3.91	3.11	0.78	0.62
HS_D15_P	15.25	70.1	74.2	0.734	0.718	11.48	9.48	0.75	0.62
HS_D20_P	20.36	70.0	73.2	0.734	0.722	15.46	12.78	0.76	0.63
RH_D02_P	1.95	70.0	71.9	0.739	0.731	1.55	1.36	0.79	0.69
RH_D05_P	5.02	70.0	72.9	0.739	0.727	3.45	3.07	0.69	0.61
RH_D15_P	15.25	70.1	73.2	0.739	0.725	10.60	9.23	0.70	0.61
RH_D20_P	20.36	70.0	76.8	0.739	0.710	13.99	12.06	0.69	0.59

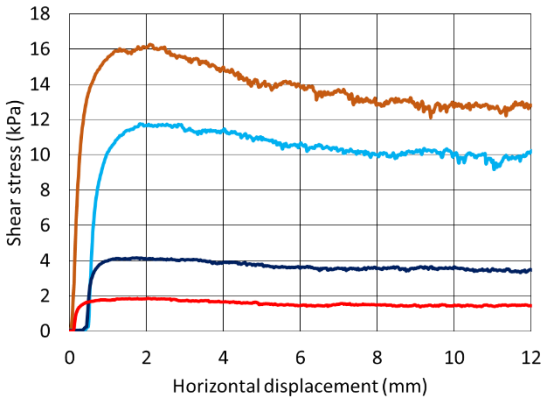

(a) dense shear stress-displacement

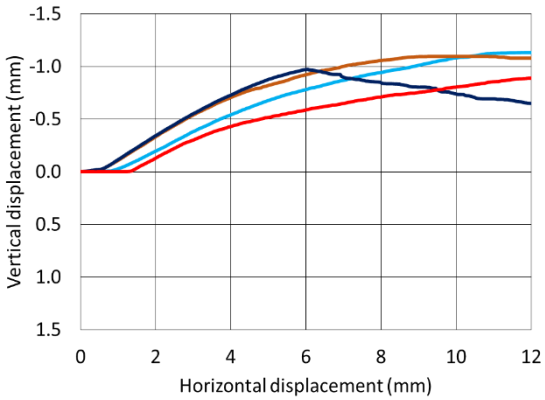

(b) dense vertical-horizontal displacement

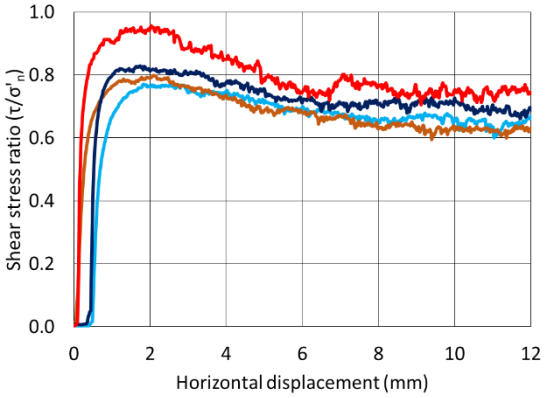

(c) dense stress ratio-displacement

Lowestoft Gravel "P" interface test results of dense (a) shear stress displacement, (b) vertical-horizontal displacement, and (c) shear stress ratio, τ/σ_n.

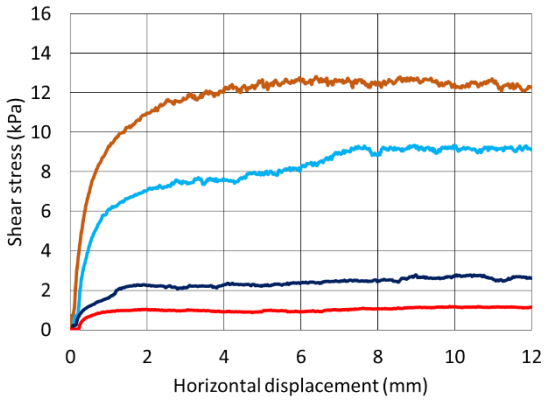

(d) loose shear stress-displacement

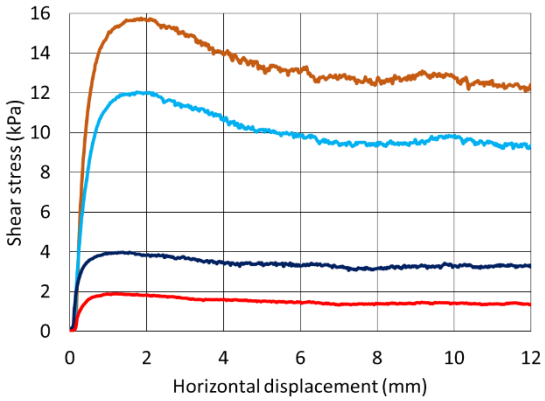

(b) dense shear stress-displacement

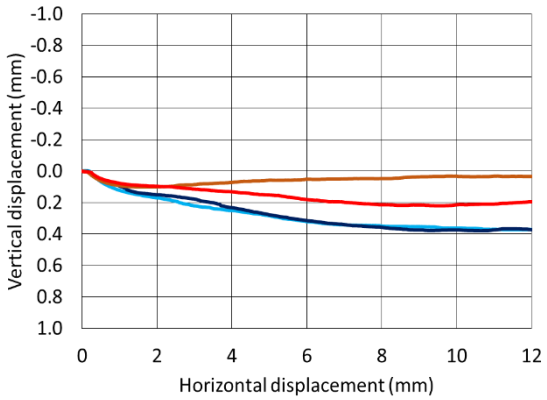

(c) loose vertical-horizontal displacement

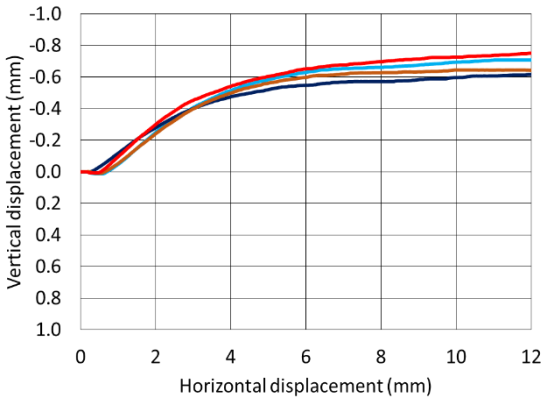

(d) dense vertical-horizontal displacement

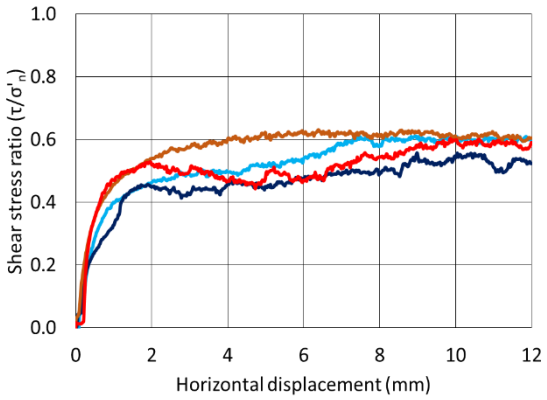

(e) loose stress ratio-displacement

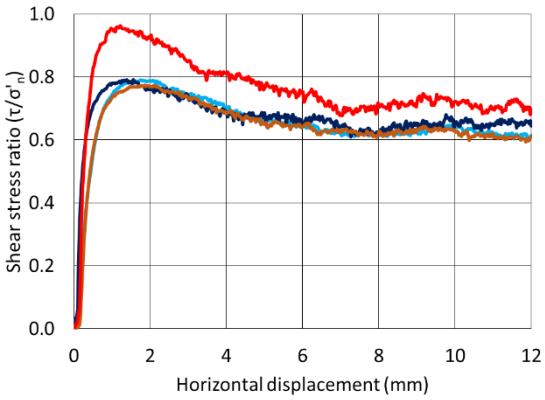

(f) dense stress ratio-displacement

Leighton Buzzard "P" interface test results of loose and dense (a, b) shear stress displacement, (c, d) vertical-horizontal displacement, and (e, f) shear stress ratio, τ/σ_n.

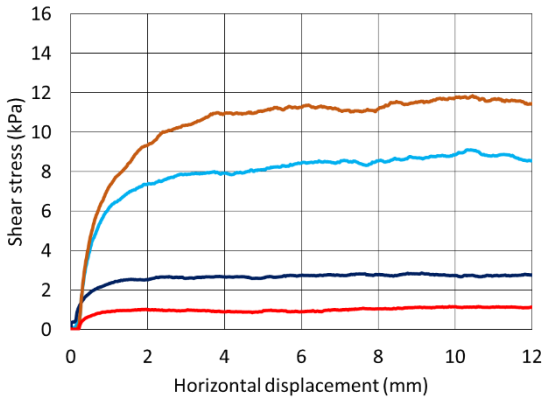

(d) loose shear stress-displacement

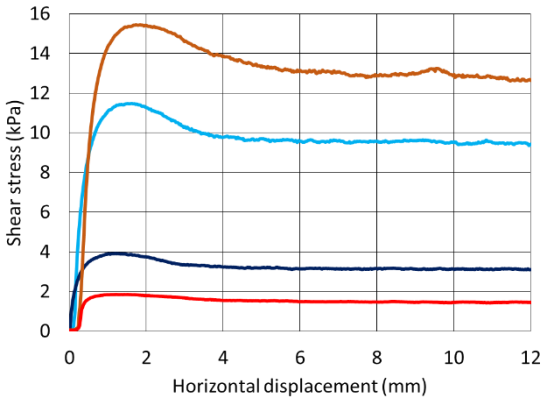

(b) dense shear stress-displacement

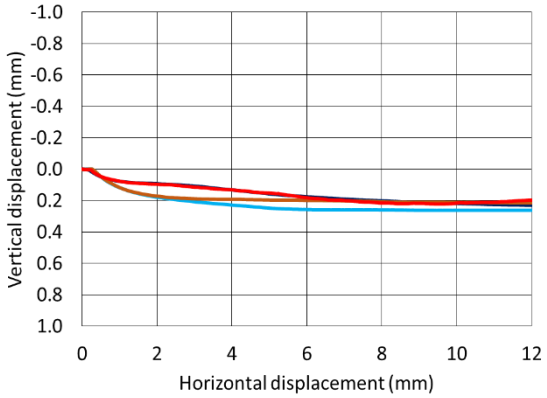

(c) loose vertical-horizontal displacement

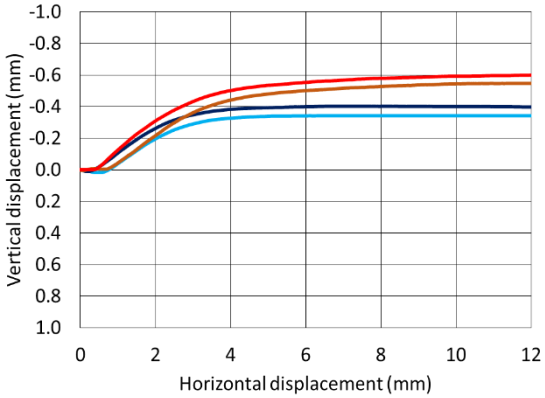

(d) dense vertical-horizontal displacement

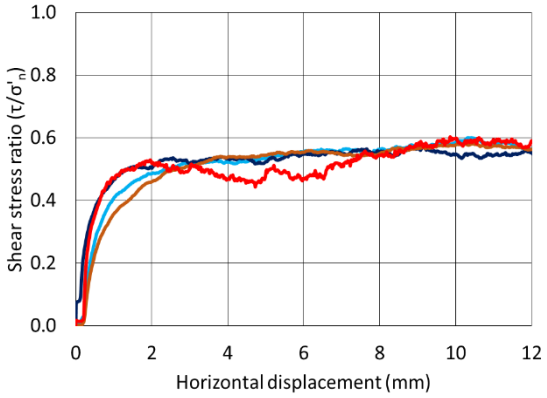

(e) loose stress ratio-displacement

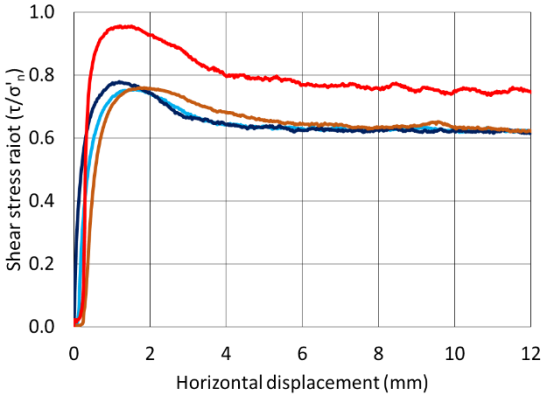

(f) dense stress ratio-displacement

Hostun Sand "P" interface test results of loose and dense (a, b) shear stress displacement, (c, d) vertical-horizontal displacement, and (e, f) shear stress ratio, τ/σ_n.

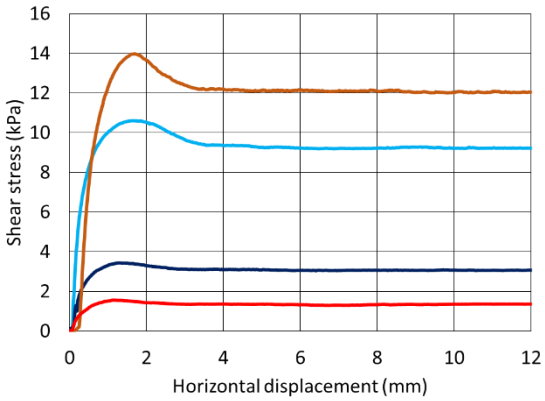

(a) dense shear stress-displacement

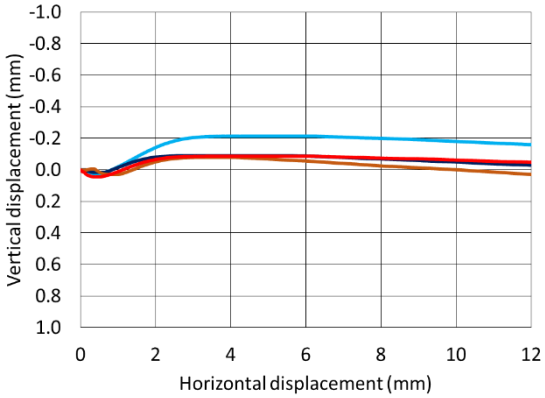

(b) dense vertical-horizontal displacement

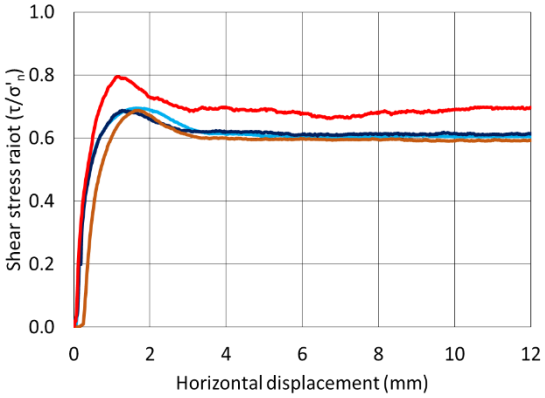

(c) dense stress ratio-displacement

Redhill Sand "P" interface test results of dense (a) shear stress displacement, (b) vertical-horizontal displacement, and (c) shear stress ratio, τ/σ_n.

Appendix D – Interface cyclic and reloaded results

Cyclic interface tests result tables include some cardinal test parameters and results. The $D_{r\,fab}$ and $D_{r\,con}$ are the soil sample relative densities as fabricated and post consolidation after the application of the pertinent normal load and represents the relative density as at the start of shearing. The same applies for e_{fab} and e_{con} with regard to the sample void ratio. The peak shear stress, τ_{peak}, is the maximum shear stress recorded during the test and the ultimate shear stress, τ_{ult}, is the average shear stress of the last two mm of horizontal displacement for each cycle. For each surface, one nominal relative density was tested (D_r approximately 70%) at three levels of vertical confining stress(σ_n approximately 2, 10, 35 kPa). For interface tests a four part naming convention has been adopted to uniquely identify each test consisting of a soil type reference [S0, LB, HS], a density reference [D (for dense)], and a nominal stress level reference [2, 10, 35 (kPa)].

Summary of pipe coating interface cyclic tests

Test reference	σ_n (kPa)	$D_{r\,fab}$ (%)	$D_{r\,con}$ (%)	e_{fab}	e_{con}	τ_{peak} (kPa)	τ_{ult} (kPa)	τ_{peak}/σ_n	τ_{ult}/σ_n
S0_D35_T-MR									
First cycle	37.56	53.4	73.1	0.794	0.754	15.59	13.89	0.42	0.37
Last cycle	37.56					13.46	12.39	0.36	0.33
LB_D02_ T-MR									
First cycle	2.04	70.0	71.5	0.623	0.618	0.52	0.43	0.25	0.21
Last cycle	2.04					0.37	0.35	0.18	0.17
LB_D10_ T-MR									
First cycle	11.24	70.0	75.8	0.623	0.605	2.32	2.02	0.21	0.18
Last cycle	11.24					2.02	2.01	0.18	0.18
LB_D35_ T-MR									
First cycle	36.80	70.0	78.3	0.623	0.597	8.79	6.62	0.24	0.18
Last cycle	36.80					5.30	5.15	0.14	0.14
HS_D02_ T-MR									
First cycle	2.09	70.1	71.8	0.734	0.727	1.01	0.92	0.48	0.44
Last cycle	2.09					0.88	0.86	0.42	0.41
HS_D10_ T-MR									
First cycle	11.30	70.1	75.7	0.734	0.712	4.43	4.18	0.39	0.37
Last cycle	11.30					4.09	3.96	0.36	0.35
HS_D35_ T-MR									
First cycle	36.86	70.0	75.3	0.734	0.714	16.54	14.74	0.45	0.40
Last cycle	36.86					15.45	13.64	0.42	0.37

Summary of enhanced textures cyclic interface tests

Test reference	σ_n (kPa)	$D_{r\ fab}$ (%)	$D_{r\ con}$ (%)	e_{fab}	e_{con}	τ_{peak} (kPa)	τ_{ult} (kPa)	τ_{peak}/σ_n	τ_{ult}/σ_n
LB_D35_E-MR									
First traverse	34.96	70.2	80.2	0.622	0.591	11.71	10.80	0.33	0.31
Last traverse		-	-	-	-	14.96	14.61	0.43	0.41
LB_D02_S-MR									
First traverse	1.96	70.0	72.6	0.623	0.615	1.36	1.18	0.70	0.61
Last traverse		-	-	-	-	1.16	0.97	0.60	0.50
LB_D35_S-MR									
First traverse	35.70	70.5	77.8	0.622	0.599	21.38	18.13	0.60	0.51
Last traverse		-	-	-	-	17.46	17.07	0.49	0.48
LB_D35_P-MR									
First traverse	35.70	69.5	72.4	0.624	0.615	30.26	21.65	0.85	0.61
Last traverse		-	-	-	-	15.71	14.33	0.44	0.40

Cyclic "T" interface strength for soil S0 at 35 kPa.

Forward shearing		Reverse shearing		Forward shearing		Reverse shearing	
Cycle #	τ_{ult}/σ_n	Cycle #	τ_{ult}/σ_n	Cycle #	τ_{ult}/σ_n	Cycle #	τ_{ult}/σ_n
1	0.373	2	0.400	45	0.321	46	0.343
3	0.357	4	0.390	47	0.323	48	0.343
5	0.347	6	0.380	49	0.323	50	0.341
7	0.342	8	0.373	51	0.322	52	0.342
9	0.338	10	0.368	53	0.323	54	0.341
11	0.334	12	0.365	55	0.322	56	0.339
13	0.332	14	0.363	57	0.322	58	0.340
15	0.332	16	0.359	59	0.336	60	0.350
17	0.329	18	0.356	61	0.334	62	0.349
19	0.327	20	0.354	63	0.334	64	0.349
21	0.325	22	0.353	65	0.333	66	0.350
23	0.324	24	0.350	67	0.329	68	0.347
25	0.336	26	0.357	69	0.33	70	0.345
27	0.332	28	0.355	71	0.326	72	0.343
29	0.329	30	0.353	73	0.327	74	0.342
31	0.328	32	0.351	75	0.327	76	0.341
33	0.327	34	0.351	77	0.324	78	0.339
35	0.326	36	0.349	79	0.322	80	0.339
37	0.324	38	0.348	81	0.322	82	0.337
39	0.323	40	0.346	83	0.324	84	0.338
41	0.324	42	0.345	85	0.321	86	0.334
43	0.325	44	0.343	87	0.321	88	0.334

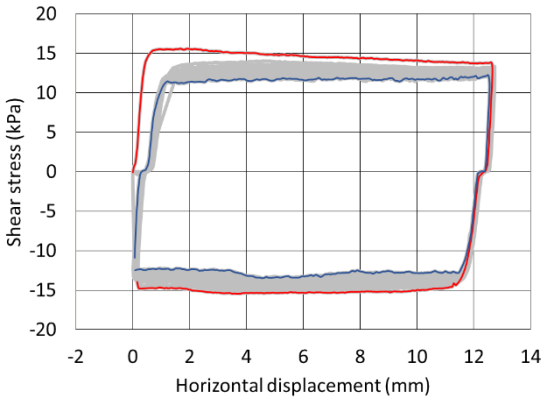

(a) shear stress-displacement

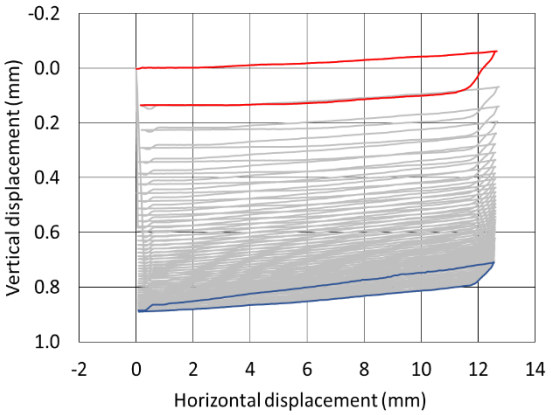

(b) vertical-horizontal displacement

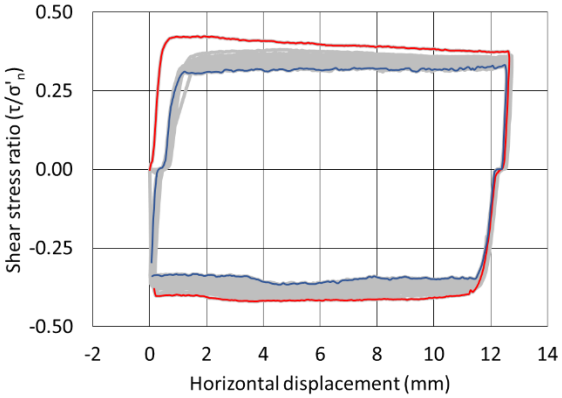

(c) stress ratio-displacement

First cycle **Last cycle**

Soil S0 ~35 kPa "T" surface cyclic interface test results dense (a) shear stress displacement, (b) vertical-horizontal displacement, and (c) shear stress ratio, τ/σ_n.

Cyclic "T" interface strength for Leighton Buzzard at 2 kPa

Forward shearing		Reverse shearing		Forward shearing		Reverse shearing	
Cycle #	τ_{ult}/σ_n	Cycle #	τ_{ult}/σ_n	Cycle #	τ_{ult}/σ_n	Cycle #	τ_{ult}/σ_n
1	0.214	2	0.198	51	0.162	52	0.157
3	0.184	4	0.171	53	0.162	54	0.147
5	0.191	6	0.160	55	0.162	56	0.159
7	0.188	8	0.153	57	0.168	58	0.147
9	0.180	10	0.158	59	0.165	60	0.144
11	0.174	12	0.144	61	0.166	62	0.154
13	0.174	14	0.138	63	0.169	64	0.161
15	0.173	16	0.138	65	0.164	66	0.147
17	0.177	18	0.145	67	0.173	68	0.149
19	0.168	20	0.152	69	0.166	70	0.150
21	0.169	22	0.147	71	0.167	72	0.148
23	0.175	24	0.144	73	0.167	74	0.148
25	0.179	26	0.136	75	0.169	76	0.149
27	0.177	28	0.138	77	0.163	78	0.146
29	0.170	30	0.134	79	0.169	80	0.144
31	0.169	32	0.141	81	0.167	82	0.151
33	0.162	34	0.142	83	0.167	84	0.147
35	0.164	36	0.150	85	0.167	86	0.150
37	0.165	38	0.143	87	0.172	88	0.147
39	0.167	40	0.144	89	0.168	90	0.146
41	0.170	42	0.166	91	0.169	92	0.144
43	0.164	44	0.154	93	0.169	94	0.142
45	0.163	46	0.157	95	0.178	96	0.138
47	0.167	48	0.166	97	0.172	98	0.143
49	0.164	50	0.155	99	0.167	100	0.138

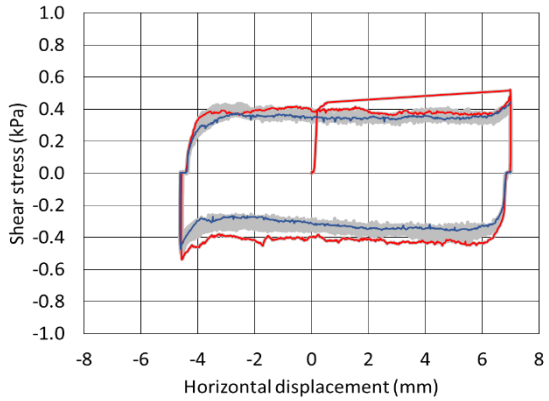

(a) shear stress-displacement

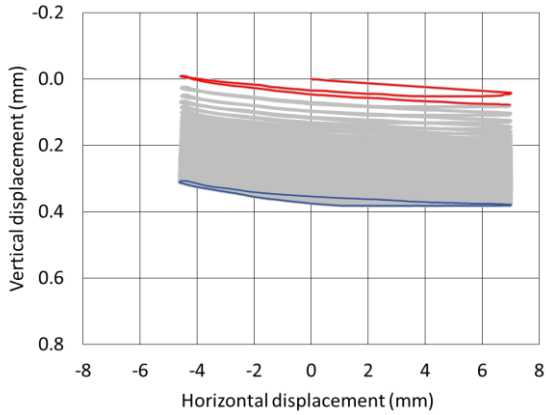

(b) vertical-horizontal displacement

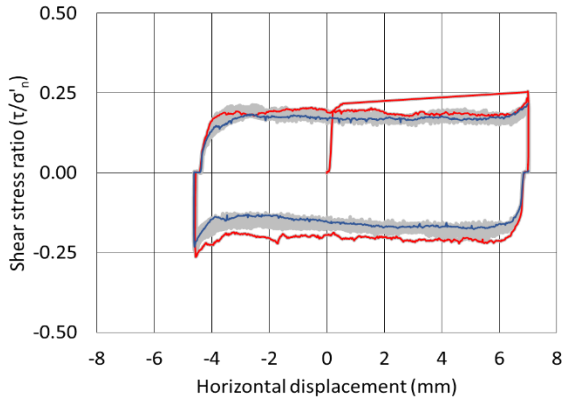

(c) stress ratio-displacement

Leighton Buzzard ~2 kPa "T" surface cyclic interface test results dense (a) shear stress displacement, (b) vertical-horizontal displacement, and (c) shear stress ratio, τ/σ_n.

Cyclic "T" interface strength for Leighton Buzzard at 10 kPa

Forward shearing		Reverse shearing		Forward shearing		Reverse shearing	
Cycle #	τ_{ult}/σ_n	Cycle #	τ_{ult}/σ_n	Cycle #	τ_{ult}/σ_n	Cycle #	τ_{ult}/σ_n
1	0.189	2	0.200	51	0.162	52	0.180
3	0.180	4	0.199	53	0.165	54	0.179
5	0.175	6	0.188	55	0.159	56	0.178
7	0.174	8	0.190	57	0.162	58	0.179
9	0.174	10	0.189	59	0.162	60	0.178
11	0.171	12	0.190	61	0.168	62	0.181
13	0.170	14	0.189	63	0.163	64	0.177
15	0.169	16	0.184	65	0.160	66	0.180
17	0.168	18	0.187	67	0.163	68	0.180
19	0.166	20	0.183	69	0.167	70	0.177
21	0.163	22	0.183	71	0.159	72	0.177
23	0.168	24	0.181	73	0.158	74	0.186
25	0.164	26	0.180	75	0.161	76	0.179
27	0.166	28	0.179	77	0.161	78	0.179
29	0.167	30	0.181	79	0.161	80	0.180
31	0.164	32	0.183	81	0.159	82	0.181
33	0.166	34	0.182	83	0.163	84	0.179
35	0.161	36	0.182	85	0.160	86	0.176
37	0.160	38	0.189	87	0.161	88	0.178
39	0.160	40	0.178	89	0.162	90	0.177
41	0.159	42	0.179	91	0.161	92	0.178
43	0.160	44	0.178	93	0.160	94	0.175
45	0.164	46	0.177	95	0.159	96	0.177
47	0.158	48	0.177	97	0.159	98	0.177
49	0.159	50	0.178	99	0.160	100	0.178

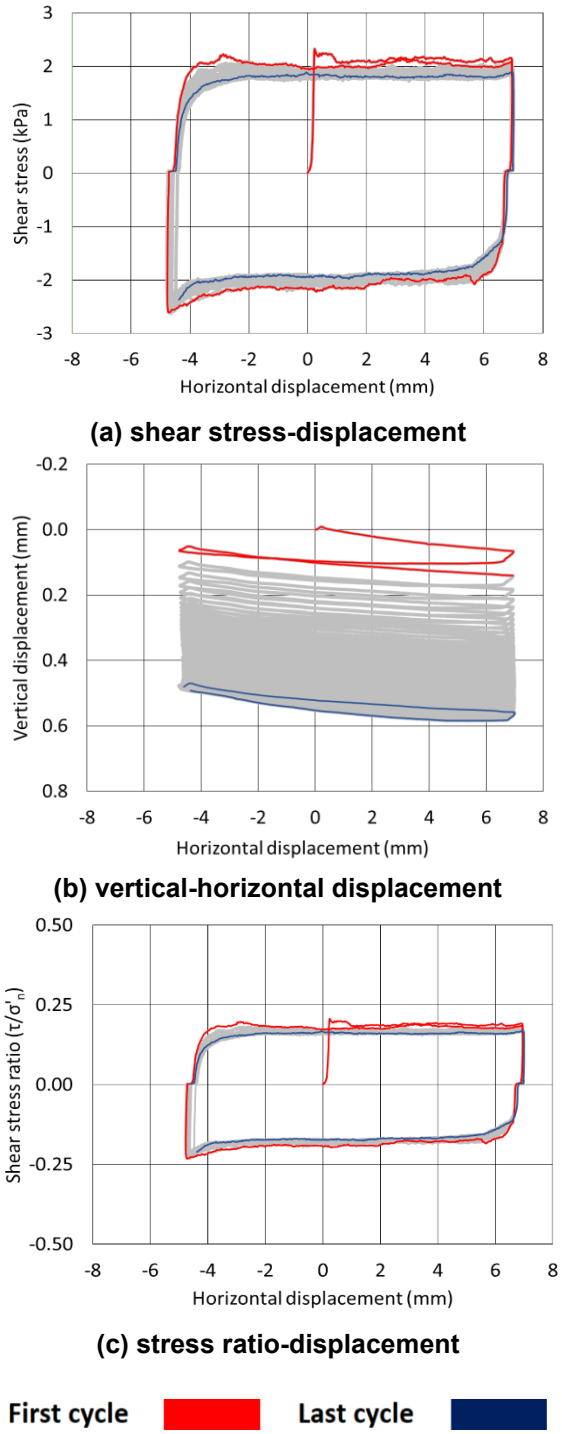

Leighton Buzzard ~10 kPa "T" surface cyclic interface test results dense (a) shear stress displacement, (b) vertical-horizontal displacement, and (c) shear stress ratio, τ/σ_n.

Cyclic "T" interface strength for Leighton Buzzard at 35 kPa

Forward shearing		Reverse shearing		Forward shearing		Reverse shearing	
Cycle #	τ_{ult}/σ_n	Cycle #	τ_{ult}/σ_n	Cycle #	τ_{ult}/σ_n	Cycle #	τ_{ult}/σ_n
1	0.182	2	0.167	51	0.143	52	0.132
3	0.168	4	0.161	53	0.142	54	0.134
5	0.160	6	0.153	55	0.142	56	0.133
7	0.155	8	0.150	57	0.142	58	0.133
9	0.154	10	0.146	59	0.144	60	0.134
11	0.153	12	0.144	61	0.146	62	0.135
13	0.149	14	0.142	63	0.148	64	0.131
15	0.147	16	0.140	65	0.144	66	0.132
17	0.142	18	0.143	67	0.143	68	0.134
19	0.143	20	0.139	69	0.145	70	0.134
21	0.149	22	0.136	71	0.146	72	0.135
23	0.140	24	0.136	73	0.143	74	0.134
25	0.145	26	0.134	75	0.144	76	0.136
27	0.145	28	0.134	77	0.148	78	0.134
29	0.150	30	0.134	79	0.142	80	0.133
31	0.146	32	0.136	81	0.143	82	0.132
33	0.142	34	0.135	83	0.143	84	0.133
35	0.144	36	0.136	85	0.141	86	0.137
37	0.143	38	0.134	87	0.141	88	0.131
39	0.141	40	0.135	89	0.142	90	0.134
41	0.142	42	0.135	91	0.142	92	0.134
43	0.141	44	0.136	93	0.145	94	0.136
45	0.142	46	0.135	95	0.143	96	0.132
47	0.143	48	0.134	97	0.141	98	0.133
49	0.142	50	0.133	99	0.140	100	0.132

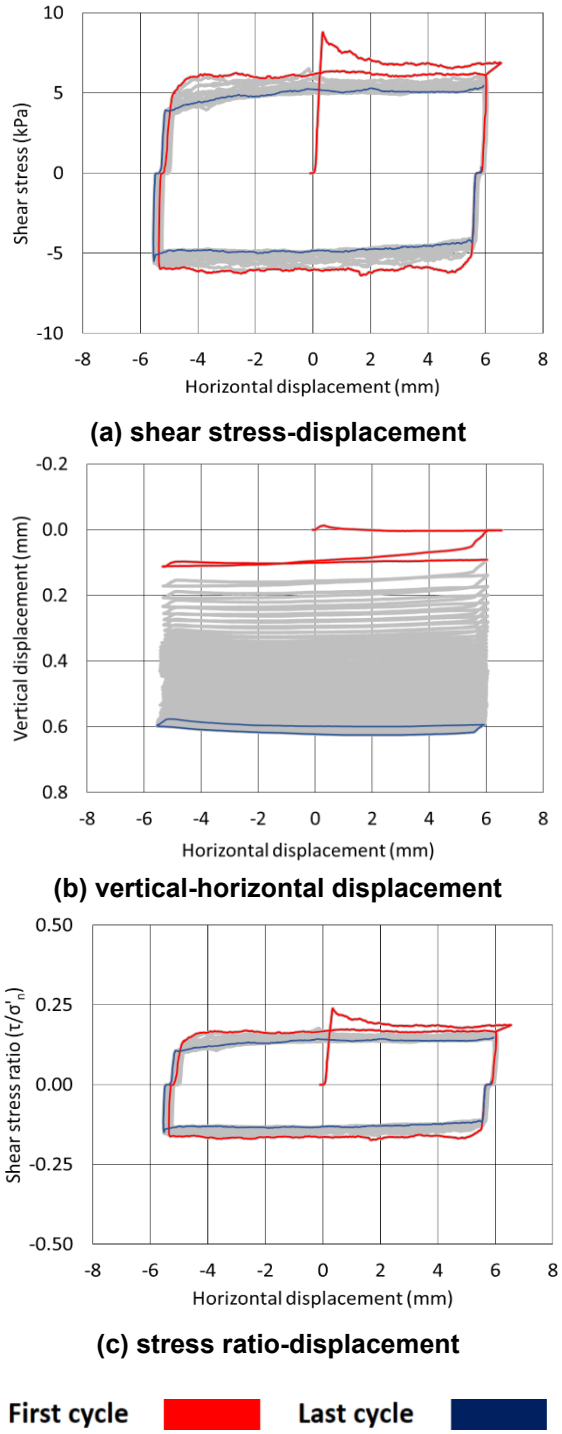

Leighton Buzzard ~35 kPa "T" surface cyclic interface test results dense (a) shear stress displacement, (b) vertical-horizontal displacement, and (c) shear stress ratio, τ/σ_n.

Cyclic "T" interface strength for Hostun Sand at 2 kPa

Forward shearing		Reverse shearing		Forward shearing		Reverse shearing	
Cycle #	τ_{ult}/σ_n	Cycle #	τ_{ult}/σ_n	Cycle #	τ_{ult}/σ_n	Cycle #	τ_{ult}/σ_n
1	0.436	2	0.470	51	0.408	52	0.425
3	0.431	4	0.457	53	0.402	54	0.424
5	0.428	6	0.446	55	0.397	56	0.426
7	0.426	8	0.452	57	0.402	58	0.420
9	0.419	10	0.447	59	0.401	60	0.426
11	0.423	12	0.444	61	0.404	62	0.426
13	0.421	14	0.452	63	0.406	64	0.434
15	0.417	16	0.447	65	0.410	66	0.429
17	0.411	18	0.435	67	0.409	68	0.431
19	0.412	20	0.433	69	0.411	70	0.432
21	0.417	22	0.430	71	0.409	72	0.434
23	0.410	24	0.432	73	0.411	74	0.437
25	0.408	26	0.428	75	0.409	76	0.434
27	0.407	28	0.430	77	0.412	78	0.432
29	0.406	30	0.427	79	0.415	80	0.446
31	0.406	32	0.429	81	0.412	82	0.441
33	0.402	34	0.428	83	0.412	84	0.434
35	0.405	36	0.425	85	0.414	86	0.421
37	0.404	38	0.423	87	0.401	88	0.427
39	0.397	40	0.425	89	0.401	90	0.424
41	0.398	42	0.429	91	0.401	92	0.422
43	0.406	44	0.426	93	0.397	94	0.429
45	0.404	46	0.415	95	0.396	96	0.424
47	0.397	48	0.426	97	0.402	98	0.424
49	0.402	50	0.428	99	0.401	-	-

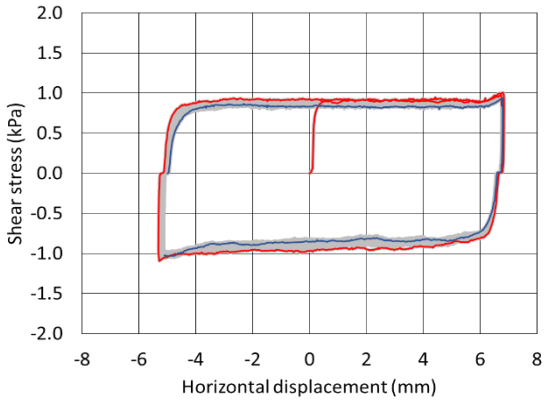

(a) shear stress-displacement

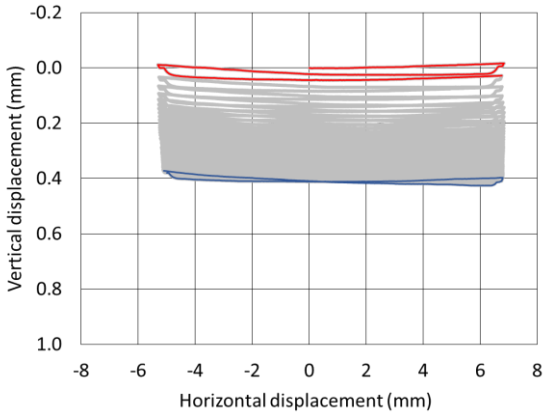

(b) vertical-horizontal displacement

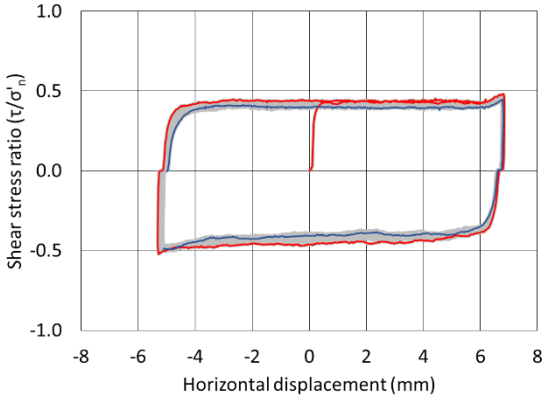

(c) stress ratio-displacement

First cycle **Last cycle**

Hostun Sand ~2 kPa "T" surface cyclic interface test results dense (a) shear stress displacement, (b) vertical-horizontal displacement, and (c) shear stress ratio, τ/σ_n.

Cyclic "T" interface strength for Hostun Sand at 10 kPa

Forward shearing		Reverse shearing		Forward shearing		Reverse shearing	
Cycle #	τ_{ult}/σ_n	Cycle #	τ_{ult}/σ_n	Cycle #	τ_{ult}/σ_n	Cycle #	τ_{ult}/σ_n
1	0.371	2	0.360	51	0.346	52	0.347
3	0.363	4	0.357	53	0.344	54	0.348
5	0.363	6	0.360	55	0.342	56	0.350
7	0.362	8	0.358	57	0.346	58	0.351
9	0.363	10	0.360	59	0.346	60	0.350
11	0.366	12	0.358	61	0.344	62	0.352
13	0.361	14	0.356	63	0.349	64	0.352
15	0.365	16	0.356	65	0.348	66	0.354
17	0.361	18	0.353	67	0.347	68	0.350
19	0.358	20	0.354	69	0.348	70	0.354
21	0.360	22	0.352	71	0.347	72	0.353
23	0.355	24	0.353	73	0.346	74	0.354
25	0.357	26	0.352	75	0.342	76	0.351
27	0.353	28	0.352	77	0.346	78	0.357
29	0.352	30	0.354	79	0.346	80	0.352
31	0.354	32	0.350	81	0.347	82	0.355
33	0.349	34	0.352	83	0.346	84	0.356
35	0.348	36	0.351	85	0.344	86	0.353
37	0.352	38	0.348	87	0.347	88	0.352
39	0.351	40	0.349	89	0.344	90	0.351
41	0.348	42	0.351	91	0.343	92	0.353
43	0.344	44	0.350	93	0.344	94	0.357
45	0.345	46	0.349	95	0.342	96	0.353
47	0.345	48	0.351	97	0.345	98	0.350
49	0.342	50	0.349	99	0.345	-	-

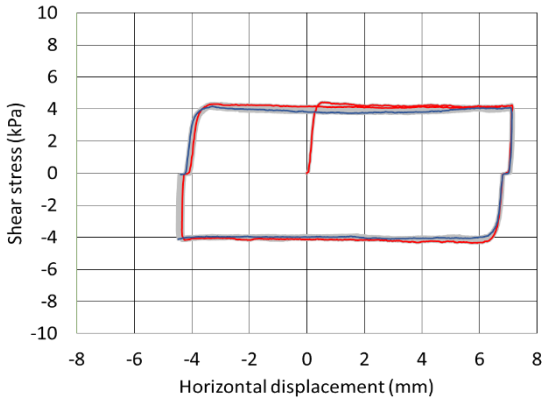

(a) shear stress-displacement

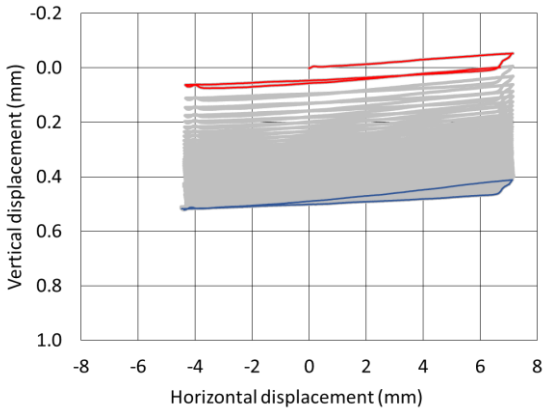

(b) vertical-horizontal displacement

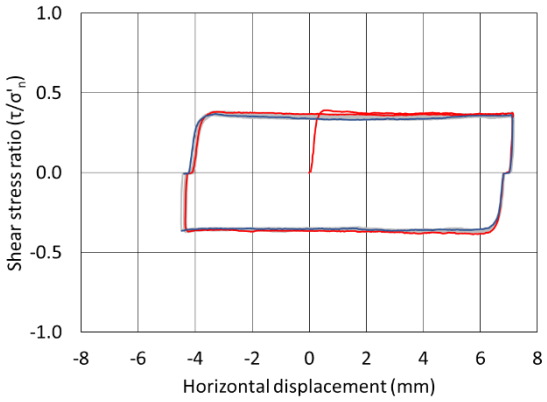

(c) stress ratio-displacement

Hostun Sand ~10 kPa "T" surface cyclic interface test results dense (a) shear stress displacement, (b) vertical-horizontal displacement, and (c) shear stress ratio, τ/σ_n.

Cyclic "T" interface strength for Hostun Sand at 35 kPa

Forward shearing		Reverse shearing		Forward shearing		Reverse shearing	
Cycle #	τ_{ult}/σ_n	Cycle #	τ_{ult}/σ_n	Cycle #	τ_{ult}/σ_n	Cycle #	τ_{ult}/σ_n
2	0.383	1	0.406	52	0.367	51	0.365
4	0.383	3	0.381	54	0.370	53	0.367
6	0.381	5	0.382	56	0.367	55	0.366
8	0.380	7	0.377	58	0.366	57	0.364
10	0.374	9	0.373	60	0.367	59	0.368
12	0.375	11	0.371	62	0.368	61	0.365
14	0.374	13	0.371	64	0.369	63	0.367
16	0.373	15	0.369	66	0.369	65	0.364
18	0.370	17	0.369	68	0.369	67	0.366
20	0.369	19	0.367	70	0.369	69	0.366
22	0.369	21	0.369	72	0.367	71	0.364
24	0.368	23	0.371	74	0.369	73	0.367
26	0.366	25	0.366	76	0.367	75	0.371
28	0.368	27	0.366	78	0.369	77	0.366
30	0.366	29	0.366	80	0.368	79	0.367
32	0.366	31	0.362	82	0.365	81	0.369
34	0.371	33	0.364	84	0.368	83	0.371
36	0.366	35	0.363	86	0.367	85	0.368
38	0.368	37	0.361	88	0.366	87	0.369
40	0.366	39	0.364	90	0.366	89	0.368
42	0.365	41	0.363	92	0.367	91	0.368
44	0.365	43	0.364	94	0.364	93	0.366
46	0.369	45	0.364	96	0.365	95	0.369
48	0.367	47	0.365	98	0.367	97	0.368
50	0.368	49	0.364	-	-	99	0.365

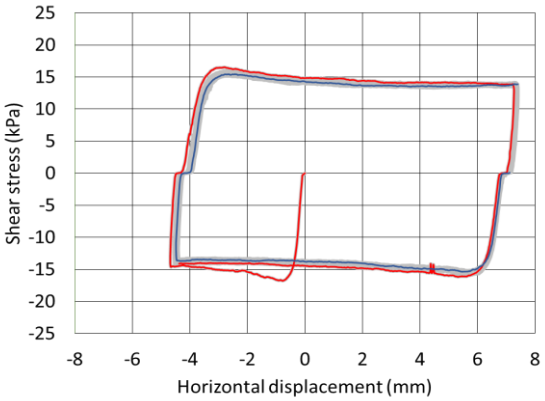

(a) shear stress-displacement

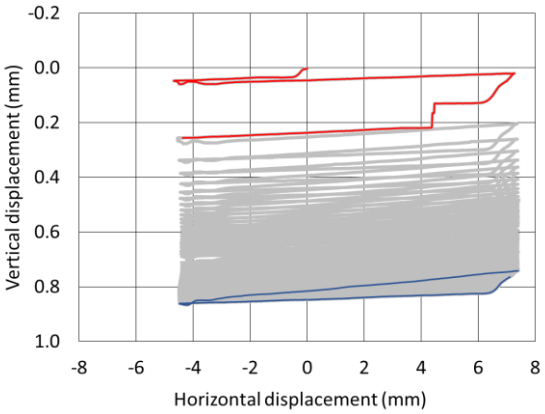

(b) vertical-horizontal displacement

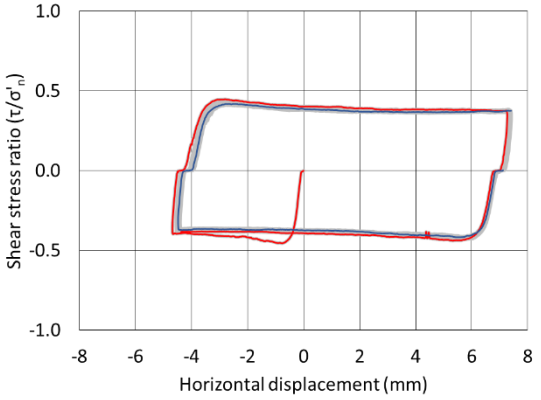

(c) stress ratio-displacement

Hostun Sand ~35 kPa "T" surface cyclic interface test results dense (a) shear stress displacement, (b) vertical-horizontal displacement, and (c) shear stress ratio, τ/σ_n.

Cyclic "E" interface strength for Leighton Buzzard at 35 kPa

Forward shearing		Reverse shearing		Forward shearing		Reverse shearing	
Cycle #	τ_{ult}/σ_n	Cycle #	τ_{ult}/σ_n	Cycle #	τ_{ult}/σ_n	Cycle #	τ_{ult}/σ_n
1	0.304	2	0.354	43	0.368	44	0.406
3	0.320	4	0.359	45	0.370	46	0.406
5	0.328	6	0.367	47	0.390	48	0.414
7	0.337	8	0.370	49	0.381	50	0.412
9	0.339	10	0.374	51	0.387	52	0.414
11	0.344	12	0.374	53	0.395	54	0.416
13	0.344	14	0.378	55	0.392	56	0.416
15	0.350	16	0.381	57	0.398	58	0.420
17	0.353	18	0.385	59	0.384	60	0.421
19	0.351	20	0.387	61	0.391	62	0.418
21	0.351	22	0.390	63	0.401	64	0.423
23	0.362	24	0.396	65	0.403	66	0.421
25	0.358	26	0.393	67	0.390	68	0.433
27	0.360	28	0.398	69	0.401	70	0.431
29	0.365	30	0.396	71	0.406	72	0.429
31	0.363	32	0.400	73	0.406	74	0.431
33	0.364	34	0.403	75	0.408	76	0.431
35	0.368	36	0.401	77	0.407	78	0.430
37	0.371	38	0.405	79	0.409	80	0.432
39	0.374	40	0.403	81	0.409	82	0.438
41	0.368	42	0.400	-	-	92	0.434

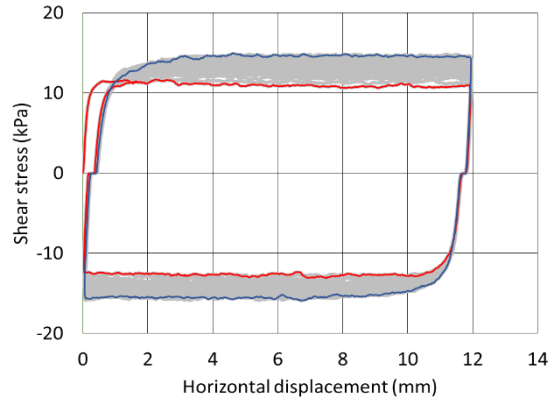

(a) shear stress-displacement

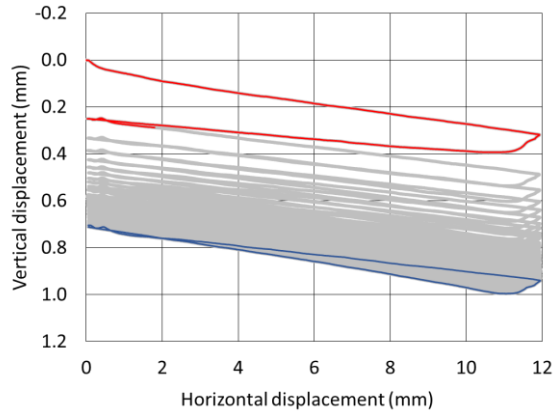

(b) vertical-horizontal displacement

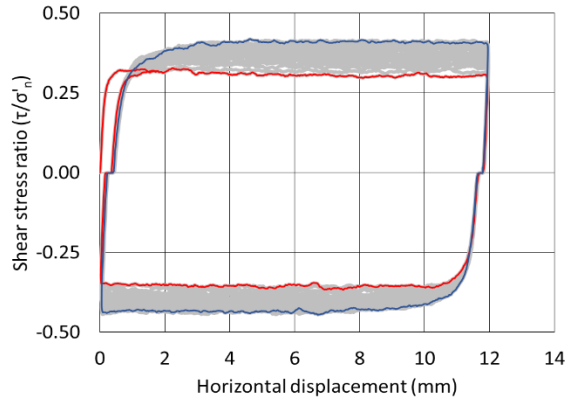

(c) stress ratio-displacement

First cycle **Last cycle**

Leighton Buzzard ~35 kPa "E" surface cyclic interface test results dense (a) shear stress displacement, (b) vertical-horizontal displacement, and (c) shear stress ratio, τ/σ_n.

Cyclic "S" interface strength for Leighton Buzzard at 2 kPa

Forward shearing		Reverse shearing		Forward shearing		Reverse shearing	
Cycle #	τ_{ult}/σ_n	Cycle #	τ_{ult}/σ_n	Cycle #	τ_{ult}/σ_n	Cycle #	τ_{ult}/σ_n
1	0.605	2	0.573	51	0.580	52	0.591
3	0.593	4	0.578	53	0.562	54	0.603
5	0.603	6	0.571	55	0.569	56	0.593
7	0.584	8	0.573	57	0.560	58	0.585
9	0.583	10	0.576	59	0.561	60	0.604
11	0.593	12	0.575	61	0.577	62	0.580
13	0.597	14	0.564	63	0.572	64	0.571
15	0.586	16	0.607	65	0.551	66	0.597
17	0.594	18	0.598	67	0.517	68	0.588
19	0.587	20	0.590	69	0.555	70	0.564
21	0.602	22	0.590	71	0.540	72	0.575
23	0.576	24	0.585	73	0.549	74	0.574
25	0.583	26	0.576	75	0.528	76	0.562
27	0.602	28	0.583	77	0.523	78	0.551
29	0.583	30	0.600	79	0.535	80	0.548
31	0.574	32	0.594	81	0.538	82	0.523
33	0.589	34	0.584	83	0.531	84	0.525
35	0.582	36	0.602	85	0.534	86	0.508
37	0.586	38	0.613	87	0.543	88	0.485
39	0.591	40	0.601	89	0.504	90	0.512
41	0.590	42	0.607	91	0.506	92	0.505
43	0.578	44	0.610	93	0.514	94	0.509
45	0.580	46	0.604	95	0.520	96	0.488
47	0.570	48	0.599	97	0.523	98	0.503
49	0.574	50	0.594	99	0.542	100	0.507

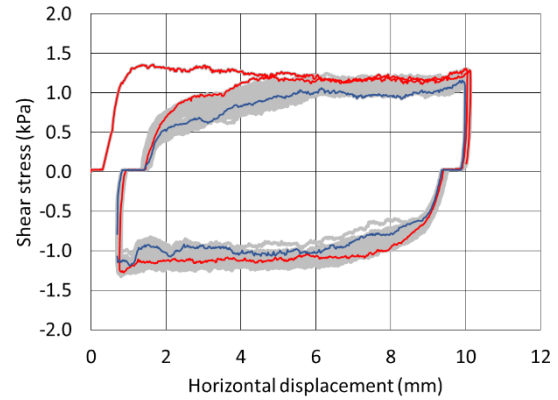

(a) shear stress-displacement

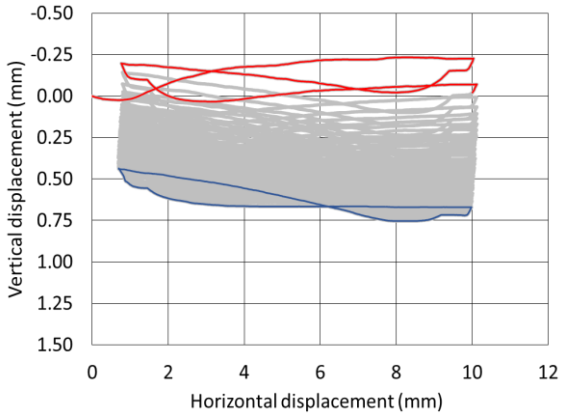

(b) vertical-horizontal displacement

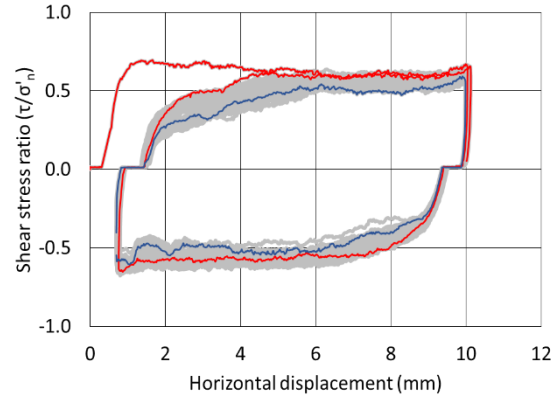

(c) stress ratio-displacement

Leighton Buzzard ~2 kPa "S" surface cyclic interface test results dense (a) shear stress displacement, (b) vertical-horizontal displacement, and (c) shear stress ratio, τ/σ_n.

Cyclic "S" interface strength for Leighton Buzzard at 35 kPa

Forward shearing		Reverse shearing		Forward shearing		Reverse shearing	
Cycle #	τ_{ult}/σ_n	Cycle #	τ_{ult}/σ_n	Cycle #	τ_{ult}/σ_n	Cycle #	τ_{ult}/σ_n
1	0.508	2	0.551	51	0.484	52	0.519
3	0.508	4	0.558	53	0.474	54	0.500
5	0.512	6	0.558	55	0.482	56	0.517
7	0.506	8	0.560	57	0.487	58	0.518
9	0.504	10	0.563	59	0.484	60	0.507
11	0.506	12	0.567	61	0.479	62	0.502
13	0.507	14	0.563	63	0.479	64	0.500
15	0.509	16	0.557	65	0.478	66	0.497
17	0.508	18	0.565	67	0.475	68	0.496
19	0.504	20	0.572	69	0.479	70	0.501
21	0.501	22	0.562	71	0.476	72	0.509
23	0.495	24	0.552	73	0.482	74	0.497
25	0.500	26	0.553	75	0.476	76	0.487
27	0.499	28	0.549	77	0.467	78	0.486
29	0.501	30	0.544	79	0.481	80	0.507
31	0.497	32	0.538	81	0.472	82	0.491
33	0.490	34	0.544	83	0.469	84	0.494
35	0.499	36	0.516	85	0.475	86	0.490
37	0.483	38	0.531	87	0.468	88	0.490
39	0.488	40	0.524	89	0.468	90	0.490
41	0.486	42	0.521	91	0.473	92	0.495
43	0.492	44	0.512	93	0.472	94	0.476
45	0.477	46	0.519	95	0.471	96	0.475
47	0.481	48	0.511	97	0.472	98	0.486
49	0.480	50	0.508	99	0.478	100	0.485

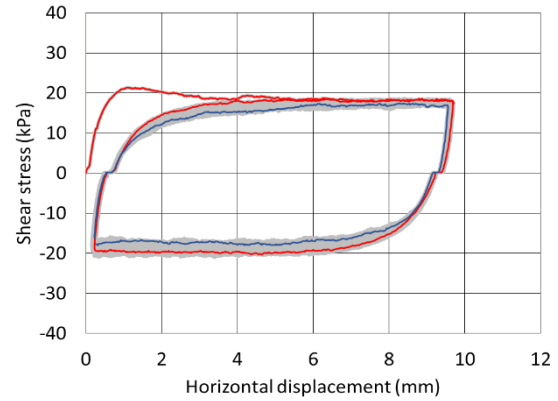

(a) shear stress-displacement

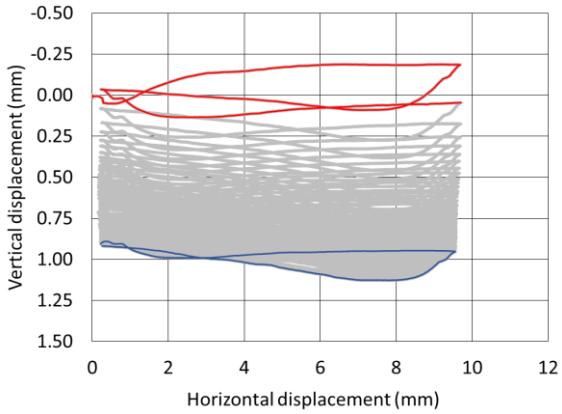

(b) vertical-horizontal displacement

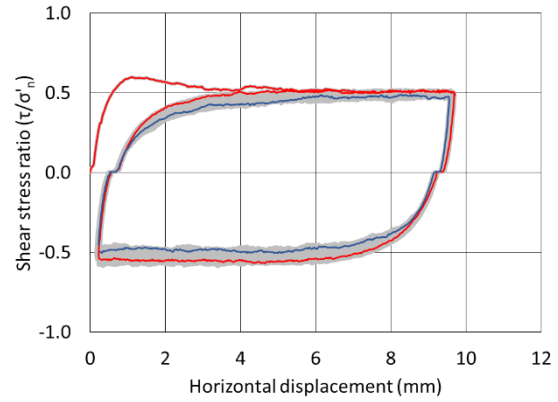

(c) stress ratio-displacement

First cycle **Last cycle**

Leighton Buzzard ~35 kPa "S" surface cyclic interface test results dense (a) shear stress displacement, (b) vertical-horizontal displacement, and (c) shear stress ratio, τ/σ_n.

Cyclic "P" interface strength for Leighton Buzzard at 35 kPa

Forward shearing		Reverse shearing		Forward shearing		Reverse shearing	
Cycle #	τ_{ult}/σ_n	Cycle #	τ_{ult}/σ_n	Cycle #	τ_{ult}/σ_n	Cycle #	τ_{ult}/σ_n
1	0.606	2	0.610	39	0.057	40	0.472
3	0.609	4	0.611	41	0.452	42	0.435
5	0.599	6	0.601	43	0.453	44	0.437
7	0.574	8	0.585	45	0.449	46	0.350
9	0.564	10	0.583	47	0.454	48	0.379
11	0.557	12	0.571	49	0.441	50	0.329
13	0.546	14	0.574	51	0.439	52	0.345
15	0.540	16	0.565	53	0.430	54	0.006
17	0.529	18	0.546	55	0.406	56	0.432
19	0.524	20	0.544	57	0.418	58	0.430
21	0.520	22	0.532	59	0.430	60	0.423
23	0.508	24	0.530	61	0.422	62	0.431
25	0.512	26	0.525	63	0.423	64	0.430
27	0.497	28	0.495	65	0.425	66	0.440
29	0.489	30	0.351	67	0.430	68	0.379
31	0.477	32	0.424	69	0.428	70	0.414
33	0.458	34	0.481	71	0.425	72	0.414
35	0.433	36	0.479	73	0.420	74	0.407
37	0.322	38	0.470	-	-	-	-

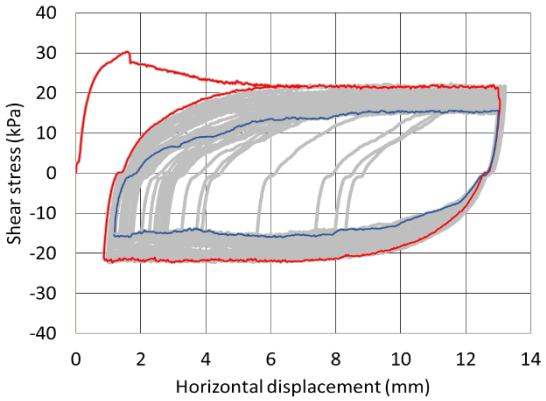

(a) shear stress-displacement

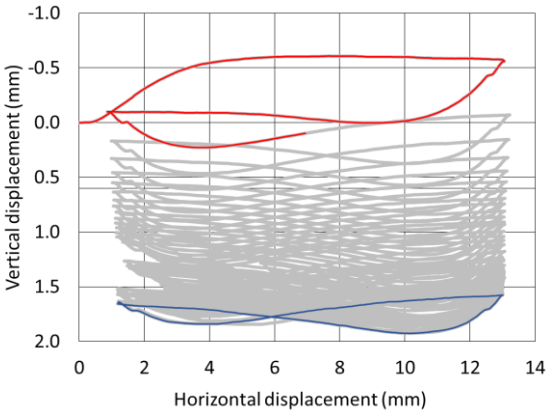

(b) vertical-horizontal displacement

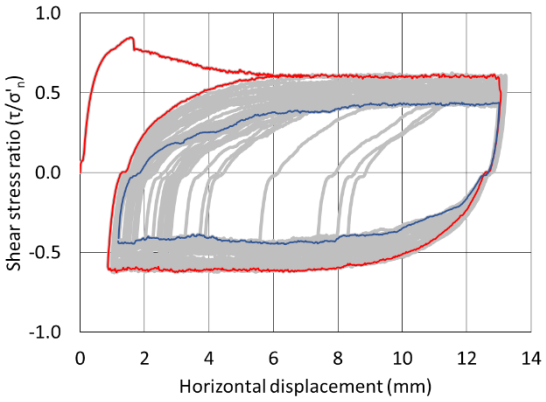

(c) stress ratio-displacement

Leighton Buzzard ~35 kPa "P" surface cyclic interface test results dense (a) shear stress displacement, (b) vertical-horizontal displacement, and (c) shear stress ratio, τ/σ_n.

Summary of post cyclic reloading tests

Test reference	σ_n (kPa)	$D_{r\ fab}$ (%)	$D_{r\ con}$ (%)	e_{fab}	e_{con}	τ_{peak} (kPa)	τ_{ult} (kPa)	τ_{peak}/σ_n	τ_{ult}/σ_n
LB_D02_T-pMR	2.10	70.1	70.4	0.623	0.622	0.72	0.59	0.34	0.28
LB_D10_T-pMR	11.30	70.0	72.2	0.623	0.616	2.88	2.40	0.26	0.21
LB_D35_T-pMR	36.87	70.1	78.4	0.623	0.597	7.50	6.28	0.20	0.17
HS_D02_T-pMR	2.09	70.1	70.2	0.734	0.733	1.04	1.00	0.50	0.48
HS_D10_T-pMR	11.29	70.1	74.8	0.734	0.716	5.04	4.37	0.45	0.39
HS_D35_T-pMR	36.85	70.0	79.0	0.734	0.700	16.35	13.83	0.44	0.38
LB_D35_E-pMR	35.70	70.0	77.8	0.623	0.599	15.93	15.21	0.45	0.43
LB_D35_S-pMR	35.70	70.0	76.2	0.623	0.604	20.68	17.84	0.58	0.50

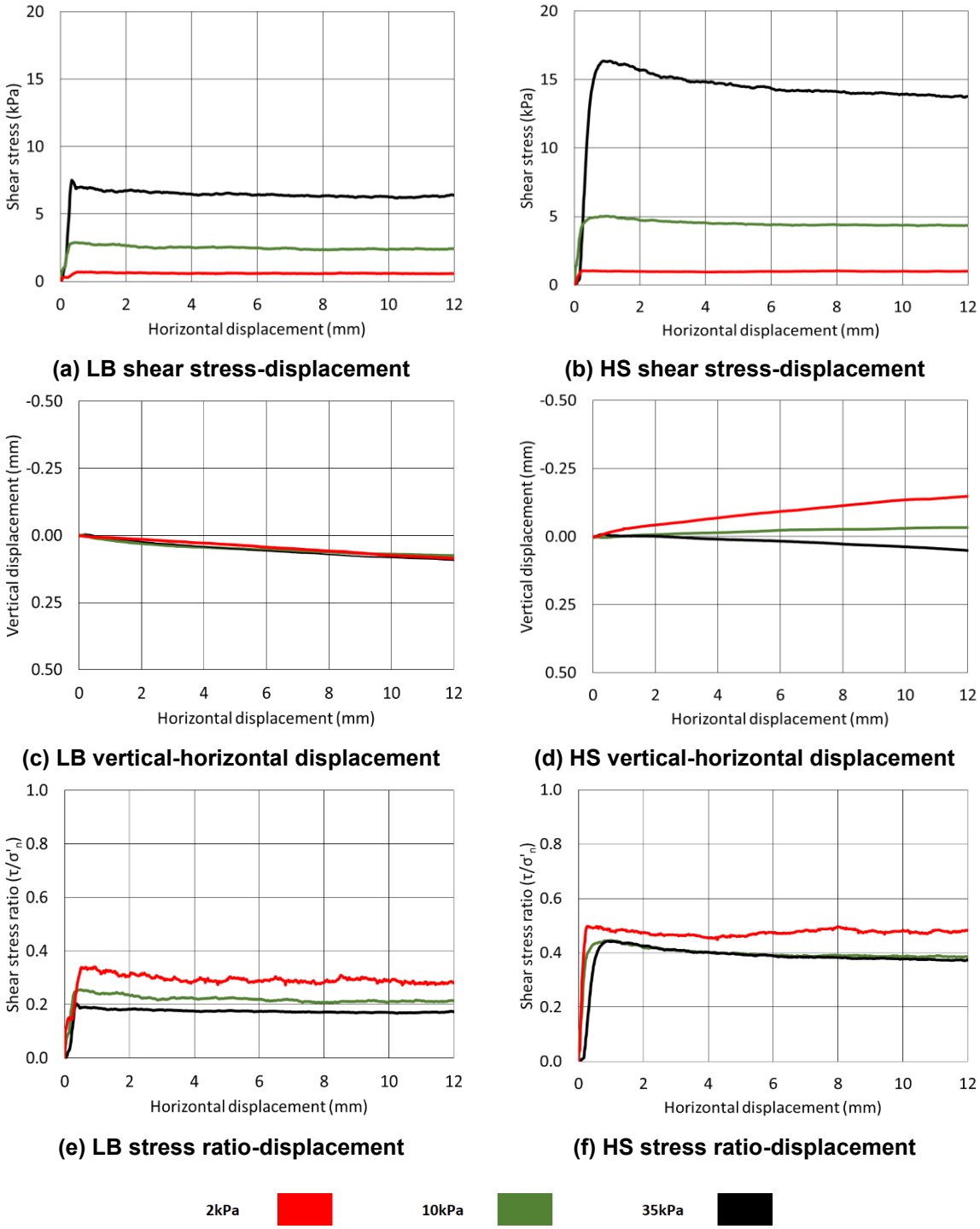

Post-cyclic reloaded "T" surface interface test results dense LB and HS (a, b) shear stress displacement, (c, d) vertical-horizontal displacement, and (e, f) shear stress ratio, τ/σ_n.

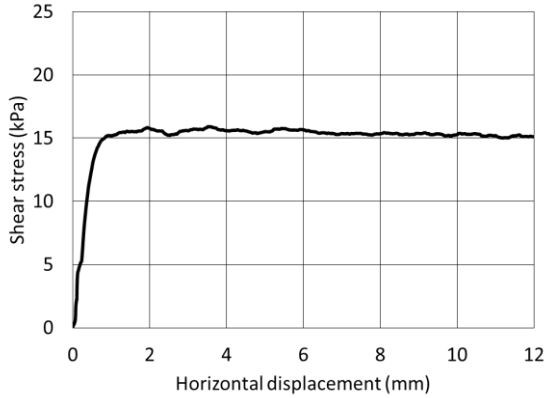

(a) "E" shear stress-displacement

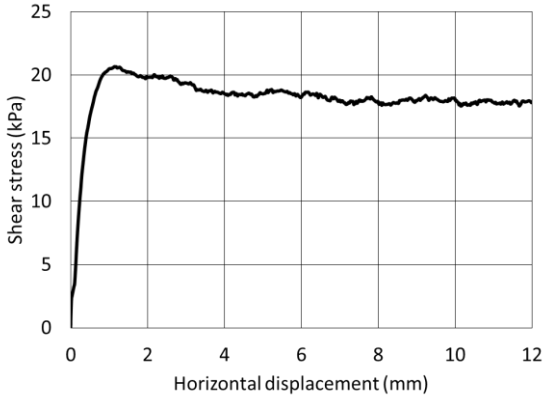

(b) "S" shear stress-displacement

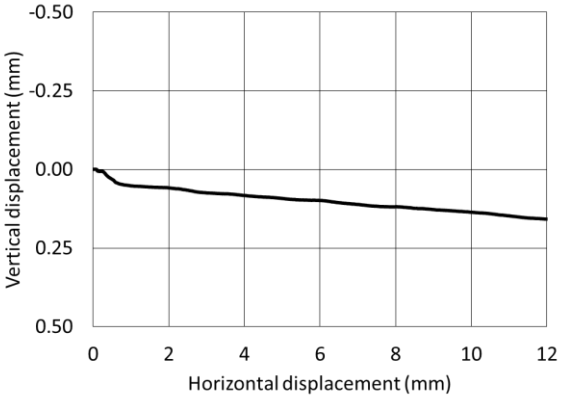

(c) "E" vertical-horizontal displacement

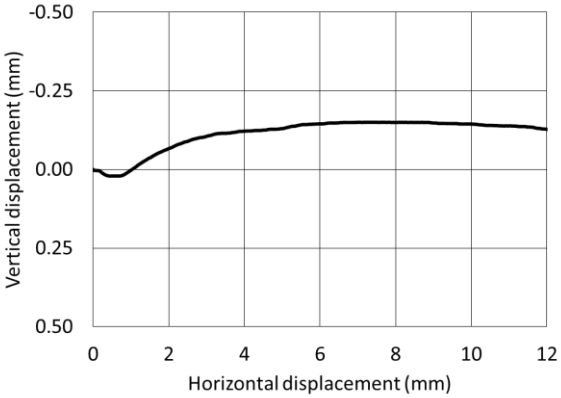

(d) "S" vertical-horizontal displacement

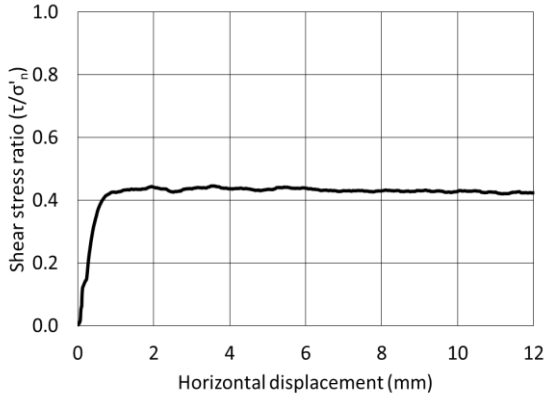

(e) "E" stress ratio-displacement

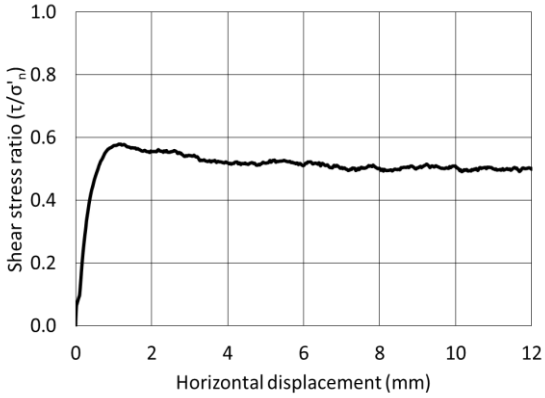

(f) "S" stress ratio-displacement

Post-cyclic reloaded Leighton Buzzard interface test ~35 kPa results dense "E" and "S" surface (a, b) shear stress displacement, (c, d) vertical-horizontal displacement, and (e, f) shear stress ratio, τ/σ_n.